Transactions of the ASME®

Journal of Engineering for Gas Turbines and Power

Published Quarterly by The American Society of Mechanical Engineers

VOLUME 111 • NUMBER 4 • OCTOBER 1989

Transactions of the ASME, Journal of Engineering for Gas Turbines and Power (ISSN 0022-0825) is published quarterly (Jan., Apr., July, Oct.) for $120 per year by The American Society of Mechanical Engineers, 345 East 47th Street, New York, NY 10017. Second class postage paid at New York, NY and additional mailing offices. POSTMASTER: Send address change to Transactions of the ASME, Journal of Engineering for Gas Turbines and Power, c/o The AMERICAN SOCIETY OF MECHANICAL ENGINEERS, 22 Law Drive, Box 2300, Fairfield, NJ 07007-2300.
CHANGES OF ADDRESS must be received at Society headquarters seven weeks before they are to be effective. Please send old label and new address.
PRICES: To members, $29.00, annually; to nonmembers, $120.00.
Add $12.00 for postage to countries outside the United States and Canada.

INDEXED by Applied Mechanics Reviews and Engineering Information, Inc.

TECHNICAL PAPERS

(Contents Continued on p. 594)

ANNOUNCEMENTS

A Parametric Analysis Microcomputer Model for Evaluating the Thermodynamic Performance of a Reciprocating Brayton Cycle Engine

G. A. Tsongas
Mechanical Engineering Department,
Portland State University,
Portland, OR 97207

T. J. White
Bonneville Power Administration,
Portland, OR 97006
Mem. ASME

A novel Brayton open-cycle engine is under development. It operates similarly to a gas turbine engine, but uses reciprocating piston compressor and expander components. The design appears to have a number of advantages, including multifuel capability, the potential for lower cost, and the ability to be scaled to small sizes without significant loss in efficiency. An interactive microcomputer model has been developed that analyzes the thermodynamic performance of the engine. The model incorporates all the important irreversibilities found in piston devices, including heat transfer, mechanical friction, pressure losses, and mass loss and recirculation. There are 38 input parameters to the model. Key independent operating parameters are maximum temperature, compressor rpm, and pressure ratio. While the development of the model and its assumptions are outlined in this paper, the emphasis is on model applications. The model has demonstrated itself to be a powerful tool for evaluating engine thermal efficiency, net specific work, and power. It can be used to analyze the performance of individual engine designs, to generate performance "maps" that graphically represent engine operating characteristics, and to perform sensitivity analysis to compare the relative effects of various input parameters. Examples of each of these model applications are discussed. Recommendations for model improvements and for further engine development work are made. The need for better experimental data to verify some critical model assumptions is stressed.

Background

In recent years a novel engine, called the PACE, has been under development. PACE (originally called the Britalus) is an acronym for Piston All-Fuels Ceramic Engine. This engine is based on an open Brayton cycle but uses reciprocating piston components for compression and expansion (work output) rather than axial compressors and turbines as in the gas turbine engine. Unlike conventional spark-ignition and Diesel engines, the PACE separates compression, expansion, and combustion into three different components and does not have the temperature and pressure profiles seen within the cylinders of IC engines.

Private funding has been used to construct and test a working prototype PACE I compressor. The compressor has run for over 500 hours without significant problems. Preliminary analysis indicates operational adiabatic efficiencies up to 80 percent should be possible. Meanwhile, a modified design PACE II compressor prototype has just recently been built and is being tested.

Contributed by the Advanced Energy Systems Division and presented at the ASME COGEN-TURBO II International Symposium, Montreux, Switzerland, August 30–September, 1988. Manuscript received by the Advanced Energy Systems Division December 19, 1988.

A series of technical papers on a number of distinct performance aspects of the PACE engine design and operation have been completed by Decher [1–5]. These analytic studies, as well as the prototype testing of the PACE I compressor, suggest that the PACE concept has considerable merit and warrants further development.

Compared to the gas turbine design, the PACE has several potential advantages. Piston components can be scaled over a wide range, making the PACE more versatile for small-scale power applications, compared to turbomachinery, which is limited to higher scale power (upward of 500 kW and beyond). PACE has a broader acceptance of different combustion fuels because the combustor can be isolated from the working fluid process stream to avoid contamination problems. Combustion can also be carefully controlled, getting better burn efficiency while eliminating most pollutants. As for cost, less design complexity could make the PACE lower in cost than its gas turbine cousins. Increased durability and, therefore, reliability and maintainability may be a benefit of reduced temperature and pressure stresses compared to IC engines.

With the prospect of incorporating ceramic liners into PACE cylinders, it may be possible for higher temperatures to

be tolerated, and thermal efficiency might be improved. The PACE does not have the same metallurgical temperature limits of conventional gas turbine systems because it does not use turbine blades. Higher pressure ratios than those possible with axial or centrifugal compressors will also improve efficiency. Part-load characteristics are favorable because power is tied to mass flow rate, which can be adjusted over a wide range of rpm without severe performance penalty.

There are certain disadvantages that a piston-style Brayton cycle engine suffers over its aerodynamic gas turbine analog. Friction losses associated with piston movement and flow losses at the entry and exit ports of the cylinders are two potentially significant penalties. However, the use of specially designed sleeve valves for both the expander and compressor should largely eliminate the loss of work availability from pressure drops typically experienced by IC engines with cam-operated valves. Operating at relatively low engine rpm can reduce both pressure losses and friction irreversibilities, which are primarily speed dependent.

Description of the PACE Engine. The compressor and expander of the PACE engine have a common design, but the expander operates in reverse fashion from the compressor. There are three key parts of the original PACE I design: a three-lobed cam, a rotor with six pistons encased within the cam, and a central manifold. As the rotor turns around the manifold, each piston moves up and down within its respective cylinder in simple harmonic motion as it contacts the inside surface of the cam.

The central manifold channels allow for both induction and expulsion of the working fluid. The amount of mass flow entering the cylinder is controlled by the duration and timing of exposure the cylinder port sees at the manifold–piston interface. Intake or exhaust manifold openings can be advanced or retarded, inducting or expelling more air. More air in the cylinder at a given compression ratio means higher pressure ratios. By adjusting the intake and exhaust period in this way, the pressure ratio in the expander or the compressor can be easily modified, and a great deal of control can be exerted over engine operation.

A second-generation PACE II compressor and expander design is now being emphasized; it differs somewhat from the first design in that it has a planetary gearing system rather than a cam casing. Instead of having the pistons turn with the rotor, the pistons remain stationary and the manifold, connected to the gears, rotates instead. This design eliminates the piston forces due to angular and Coriolis accelerations but requires a more complex gearing arrangement to transmit the torque from the pistons.

PACE Performance Modeling. Analytic work completed to date by Decher [1–5] on the PACE engine design concept has emphasized individual compressor and expander characteristics. Decher modeled nonideal, irreversible processes to determine certain performance capabilities such as specific work versus efficiency. As part of the ongoing development of the PACE, White [6] refined the equations describing pressure losses, heat transfer, and mechanical friction irreversibilities for an operating PACE engine. The algorithms are based on thermodynamic principles and empirical data derived from experiments with IC engines. White has integrated Decher's previous work into a comprehensive system model for an operating PACE engine. By combining the influences of all principal operating parameters into this model, a user can evaluate the effects of a set of operating conditions on certain performance indices such as efficiency, specific work, or power.

An IBM PC-compatible microcomputer version of the model has been developed and tested by Martin [7], which is capable of performing parametric analyses of the influences of design and operating parameters on the PACE thermodynamic performance. Martin built upon White's work [6], and the result is a software package with graphics, which simulates the performance of the PACE engine under a wide variety of possible operating conditions. It also allows for easy interactive input and rerunning of varying sets of engine design and operating parameters. Once a preferred PACE design configuration is determined, the software model can be used to work toward an optimum design by looking at tradeoffs and interactive effects among various design and operating parameters.

Thermodynamic Foundations and PACE Model Methodology

As noted earlier, most of the previous analytic work on the PACE engine has been conducted by Decher [1–5]. As for similar engines, the literature reports on at least two designs [8–10] that use reciprocating pistons for both compressor and

Nomenclature

A_i = piston/valve area ratio, inlet
A_e = piston/valve area ratio, exit
B = number of cycles per revolution, rev^{-1}
b = bore, in.
C_i = mean inlet flow coefficient
C_e = mean exit flow coefficient
c.v. = clearance volume (percent of stroke volume), percent
c_p = constant pressure specific heat, Btu/lb_m-°F
c_v = constant volume specific heat, Btu/lb_m-°F
e_H = combustion efficiency (heat input efficiency)
e_t = engine thermal efficiency
f = friction coefficient, fmep/(ft/s)
K = overall heat transfer coefficient
k = gas conductivity (standard air values), Btu/sec-ft-°F
N = number of cylinders
n = modified polytropic exponent (for mass loss)
P = power density (based on expander displacement), HP/in^3
p = pressure, psia
R = gas constant, $ft\text{-}lb_f/lb_m$-°F
R_C = pressure ratio, compressor operating parameter
rpm = revolutions per minute, min^{-1}
s = stroke, in.
T = temperature, °F
T_{max} = maximum cycle temperature at combustor, °F
u = mean piston speed, ft/sec
V = volume, ft^3
VSD = variable speed drive coupling
VVE = variable volume expander
w = net specific work, $ft\text{-}lb_f/lb_m$

Subscripts, Superscripts, and Greek Symbols

C, E, H = refers to the compressor, expander, and combustor (heater)
1, 2 = refers to compressor and expander
i, e = inlet and exit
′ = denotes postcombustion gas properties
γ = ratio of specific heats
δP_1 = pressure drop at compressor inlet, psia
δP_2 = pressure drop across the combustor, percent
μ = dynamic viscosity, $lb_m/ft\text{-}sec$
ρ = gas density, lb_m/ft^3

expander components of a Brayton cycle engine. A study by Rosa [11] has tied these designs together into a framework for analyzing a piston-component Brayton cycle engine.

The literature also abounds with detailed information on heat transfer, valve losses, friction, and volumetric efficiency in IC engines. Out of necessity, some of this information was adapted to model the PACE engine's unique design and operating characteristics because good empirical data are not yet available for an operating PACE engine.

The analysis of the PACE engine performance was divided into three basic processes: compression, heat addition, and expansion. Compression is divided into admission, compression, discharge, and re-expansion of residual gases. Similarly, the expander processes are intake, expansion, exhaust, and recompression of residual gases. In principle, the expander's operation is just the reverse of the compressor, except it sees much higher temperatures at lower gas densities.

Figure 1 is a schematic diagram of the engine design modeled in [6], comprising the three basic components: the compressor (C), the combustor or heater (H), and the expander (E). Each irreversibility, and where it occurs, is designated by a two-letter code. The equations and thermodynamic relationships derived by White [6] establish the engine model, and account for the four sources of irreversibility in the compression, expansion, discharge, admission, and heat addition process of the PACE engine:

1. *Pressure Losses* (PR):
   - entry and exit losses at the cylinder port/manifold interface of both the compressor and expander
   - duct losses into and out of combustor burner (or heater)
   - includes flow work necessary to induct or expel working fluid through valve openings
2. *Heat Losses* (*Nonadiabatic Processes*) (HT):
   - heat transfer from the gas to the cylinder walls, both compressor and expander (high-pressure gas temperature loss in the expander being the most important)
   - heat losses from the combustor, or combustor inefficiency
3. *Friction Work Losses* (FR):
   - work necessary to overcome mechanical friction in the compressor and in the expander (piston rings and valve/gear systems)
4. *Mass Leakages and Mass Recirculation* (MA):
   - compressor and expander – recirculation of gases trapped in the clearance volume after discharge
   - compressor and expander – effectiveness of piston and valve seals separating cylinder from manifold.

Note that the important working fluid properties are segregated into two sets of average values: those for the working fluid prior to heat addition, and those afterward (designated by the prime notation). These properties are average values of specific heats c_v and c_p (both constant volume and constant pressure), dynamic viscosity (μ), gas conductivity (k), modified polytropic expansion and compression exponents (n), and gas constants (R).

All of the irreversibilities are functions of two key parameters, speed and pressure ratio. The irreversibilities account for all the excess work or loss of work availability as the working fluid progresses through the compressor, combustor, and expander. It is the interrelationships among these nonideal processes, under varying operating conditions, that give the PACE its particular performance characteristics.

Modeling Approach and Assumptions. Although the compressor and expander components were treated separately, both have a similar analytic foundation. Both were modeled as two-part components, with an adiabatic part and a heat transfer part. The approach taken was to analyze the adiabatic part first, including the pressure loss irreversibilities during induction and discharge of the compressor, and during intake and exhaust of the expander. The actual expansion and compression strokes, which are only a small part of the overall compressor and expander cycles, are modeled as adiabatic and reversible. Then, the heat loss irreversibility was included and friction losses were added. Mass loss was calculated using a modified polytropic exponent to determine a reduced working fluid volume due to a reduction in mass. Then, an average total mass was used to determine mass flow rate through the compressor and expander to calculate power.

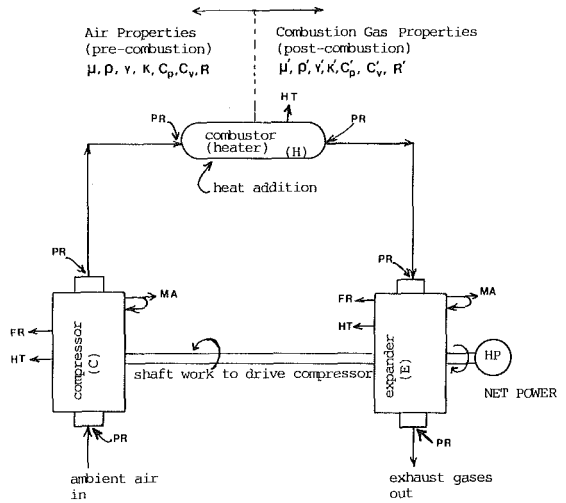

Fig. 1 PACE engine diagram with irreversibilities; HT = heat transfer; FR = friction; PR = pressure losses; MA = mass loss and recirculation

While the details of the model development are omitted here, the key model assumptions are important to mention:

1. Constant (average) specific heats are used for all processes. Constant values of specific heats and other gas properties are used up to the point of combustion, then new values are substituted that correspond to a higher gas combustion temperature.
2. All results are based on air standard analysis.
3. Heat transfer accounts for energy lost from the working fluid in the cylinders during the compression and expansion cycles. Heat loss is treated as a total quantity for an entire cycle for both compressor and expander and is calculated after the adiabatic work of compression or expansion has been calculated.
4. The heat generated by friction work is presumed lost without being reabsorbed into the working fluid, transferred directly to the cooling system. Friction is calculated as a mean effective pressure in compression or expansion and treated as a net work loss per cycle, or load, for both the compressor and the expander.
5. All valves open and close instantaneously. The model assumes an average port area exposed for the inlet and exit of gases.
6. All port expansion processes (pressure losses) are treated as isothermal, isenthalpic expansions – essentially throttling processes.
7. Mean inlet and exit flow coefficients are treated as constants for a particular design configuration.
8. Empirical data, derived from studies of IC engines, are used where appropriate information is lacking for corresponding aspects of the proposed PACE engine. In particular, data on friction, heat transfer, and pressure losses in IC engines are assumed applicable to the PACE.

Table 1 Pace model input parameters

Symbol	Notes	Parameter Name	Units	Range (Notes)
b	(1)	bore	inches	no restrictions, but 0.8 < b/s < 1.25
s	(1)	stroke	inches	no restrictions, but 0.8 < b/s < 1.25
A_i	(1)	piston/valve area ratio (inlet)	dimensionless	1 < A_i < 20; 5 to 10 common
A_e	(1)	piston/valve area ratio (exit)	dimensionless	1 < A_e < 20; 5 to 10 common
C_i	(1)	mean inlet flow coefficient	dimensionless	0.3 < C_i < 0.8; 1.0 theoretical maximum
C_e	(1)	*mean exit flow coefficient*	dimensionless	0.3 < C_e < 0.8; 1.0 theoretical maximum
c.v.	(1)	clearance volume (% of swept volume)	%	.001 < c.v. < .25
B	(1)	number of cycles per revolution	--	depends on design gearing or cams; PACE I has 3
N	(1)	number of cylinders	--	design dependent
f	(2)	friction coefficient	lbf-sec/ft^2	0 < f < 10; must be determined empirically
K	(2)	overall heat transfer coefficient	BTU/sec-ft^2-^{o}F	.05 < K < 3; 10.4 for IC engines; regime-specific
À	(2)	mass loss factor	dimensionless	if .95 < À < 1.0, then mass loss is < 5%
e_H	--	combustor (heater) efficiency	dimensionless	typical .75 < e_H <.95
δP_1	--	pressure drop at compressor inlet	psia	< 5 psia is reasonable
δP_2	--	pressure drop across combustor	%	<10% is reasonable
c_p	(3)	average constant pressure specific heat	BTU/lbm-^{o}F	for air, see Obert [12], Fig.11, p.732
$c_{p'}$	(4)	average constant pressure specific heat	BTU/lbm-^{o}F	for air, see Obert [12], Fig.11, p.732
c_v	(3)	average constant volume specific heat	BTU/lbm-^{o}F	for air, see Obert [12], Fig.11, p.732
$c_{v'}$	(4)	average constant volume specific heat	BTU/lbm-^{o}F	for air, see Obert [12], Fig.11, p.732
T_0	--	ambient temperature	^{o}F	T_0 > 32^{o}F
p_0	--	ambient pressure	psia	approximately atmospheric
RPM_C	(5)	compressor speed	rev/min	no restrictions except u < 3000 ft/min
T_{max}	(5)	maximum temperature (at expander inlet)	^{o}R	limited by material tolerance
R_C	(5)	pressure ratio (compressor)	dimensionless	maximum R_C dictated by clearance volume
X_E	--	variable volume expander (VVE) multiplier	--	depends on expander design configuration
MODE	--	VSD or VVE (one or the other)	--	software switch for two different expanders

NOTES:
(1) This parameter applies to both expander and compressor (design characteristics).
(2) This parameter applies to both expander and compressor (operation characteristics).
(3) This parameter applies to compressor processes.
(4) This parameter applies to processes after the compressor (combustor and expander).
(5) This is one of three independent operating parameters.

9. Working fluid flow velocities greater than sonic are not allowed. The engine is constrained to operate at average piston speeds below 3000 ft/min (15.2 m/s), which is the maximum found in the literature.

10. All analysis is for steady-state conditions; the model does not incorporate transient analysis.

11. The PACE expander accommodates all the mass flow from the compressor (thus reaching full expansion volume), by using either a variable speed drive (VSD) with fixed expander volume, or a variable volume expander (VVE) with fixed expander rpm.

Analysis and Results of Modeling the PACE Engine

Model parameters were organized into four groups, as listed in Table 1. The PACE engine model has a total of 38 inputs, which the user can specify. Table 1 specifies the nomenclature and symbols used for these variables and defines reasonable ranges for each variable, or a suitable reference where an appropriate value can be found.

In using the software model one can take several approaches in analyzing a particular PACE engine design:

1. Development of an engine design configuration;
2. Performance analysis and the creation of an engine "map";
3. Sensitivity analysis of input parameters;
4. Comparative analysis of parametric performance curves; and
5. Evaluation of interactive and separate effects of parameter groups.

Each of these approaches is described briefly here.

Development of an Engine Design Configuration. Although this model has tremendous analysis capability, it cannot design an engine. It will not optimize combinations of parameters nor will it match PACE compressor and expander components for best performance.

What the model can do is analyze a given engine's performance at specified operating conditions. For example, after specifying an engine design configuration, the user will input the three independent operating parameters: pressure ratio (R_C), compressor rpm (rpm_C), and maximum temperature (T_{max}). Then, after choosing operation characteristics and working fluid properties (see Table 1), the user can "run" the engine. The output – efficiency (e_t), net specific work (w), and power density (P) – will tell the user right away whether the engine performs to meet expectations. The user can vary the three operating parameters over a reasonable range and see whether the engine operates satisfactorily over the range given, and how well it does perform. Based on this interactive feedback information, the user can then adjust engine design or input specifications in order to increase expander volume, change compressor stroke, try a larger piston/valve area ratio, or vary some other parameter.

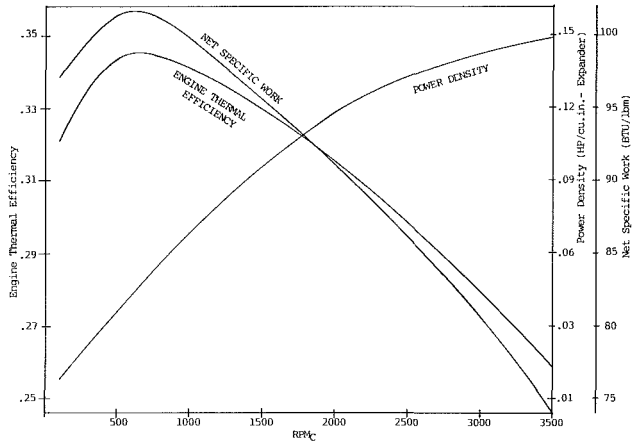

Fig. 2 PACE engine performance curves

A particular engine design configuration was chosen as the base case for analysis. The parameters selected are listed in the second column of Table 2, the base case values. In all cases, a variable speed drive engine configuration was used. This means the compressor and expander can operate at different rpm's, the expander reaches full expansion, and the compressor rpm is the independent variable. All base case parameter values were selected as midvalues over the range representing average values one might expect to use in modeling a PACE engine.

Performance curves for the base case engine design configuration are presented in Fig. 2. In this graph, the power density and efficiency curves show typical performance profiles similar to IC engines. The power density curve increases less than linearly with rpm, and, starts to taper off as the parasitic losses become more pronounced at higher rpms. But the efficiency curve reaches a maximum at about 600 rpm,

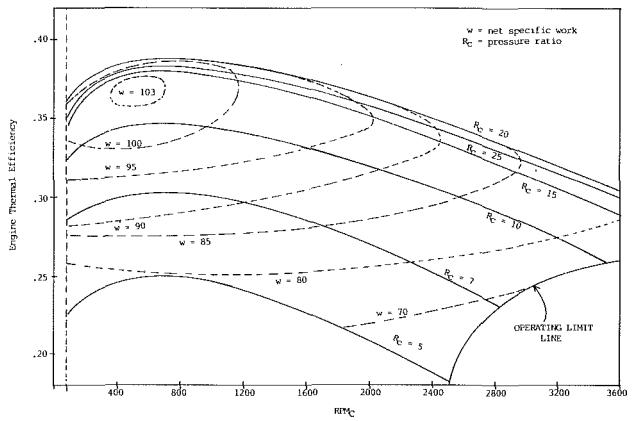

Fig. 3 PACE engine performance map

then drops dramatically as the irreversibilities due to speed begin to take over. Heat transfer, in particular, increases more than linearly at higher speeds, as do pressure losses, which increase with the square of engine speed.

The approach to engine design described here is clearly interactive and makes use of the model's parametric analysis capability. It is also very helpful to run the model first to determine whether a particular engine design configuration can actually operate at the extreme ends of the desired ranges of pressure ratio, compressor rpm, and maximum temperature.

Performance Analysis and Creation of an Engine "Map." By specifying both compressor and expander design characteristics, as well as the values for the engine operation characteristics and working fluid properties, an analyst can vary pressure ratio as a parameter with rpm as the independent variable. Then, the analyst can plot efficiency, net specific work, or power density as functions of compressor (or expander) rpm. Once the performance curves for each pressure ratio parameter are plotted, curves connecting constant values of net specific work or efficiency can be overlaid to complete the map, as shown in Fig. 3, for example. Note that this engine map represents performance for a single maximum temperature (1500°F or 816°C) and for a particular engine design configuration.

There are several features of the engine map that merit discussion. First, in the lower right corner of the map, there is a "performance limit line." This line identifies the operating limits for the engine that are due, primarily, to insufficient expander capacity to accommodate the mass flow from the compressor. Generally, this means the expander is undersized for operating points to the right of this demarcation.

The combination of optimum efficiency and net specific work lies around $R_C = 12$ and $\text{rpm}_C = 600$. Note also the crowding of the pressure ratio curves at the top of the map. The gains in efficiency as pressure ratio gets higher and higher become less and less.

For this particular PACE engine configuration, it appears there may be a maximum operating pressure ratio. Note how the efficiency curve for $R_C = 25$ is lower than the curve for $R_C = 20$. The effects of diminishing returns aside, this anomaly could be attributed to the effects of heat transfer and pressure losses as they begin to dominate at higher pressure ratios. In particular, the relative proportion of heat lost at higher pressure ratios may exact a higher efficiency penalty than is worth paying for.

Sensitivity Analysis of Input Parameters. One of the most valuable applications of this model is its ability to run sensitivity analyses on the several input parameters that drive it. In doing the sensitivity analysis, the objective is to determine

Table 2 Base case and sensitivity analysis

PARAMETERS		PARAMETER RANGE LOW VALUE	BASE CASE	HIGH VALUE	THERMAL EFFICIENCY BASE CASE=.314		NET SPECIFIC WORK BTU/lbm BASE = 90.75		POWER DENSITY HP/cu.in. BASE = .140	
Compressor Design Characteristics	b	2.0	2.5	3.125	.326	.287	94.7	82.6	.094	.200
	s	2.0	2.5	3.125	.326	.297	94.5	85.5	.119	.160
	A_i	1	5	9	.312	.317	90.2	91.8	.149	.119
	A_e	1	5	9	.322	.295	93.1	85.1	.143	.134
	C_i	.3	.6	.9	.319	.313	92.1	90.4	.111	.145
	C_e	.3	.6	.9	.287	.319	82.9	92.2	.132	.142
	c.v.	.001	.05	.10	.303	.318	86.1	94.0	.174	.100
Expander Design Characteristics	b	2.4	3.0	3.75	.285	.329	82.1	95.3	.199	.094
	s	2.4	3.0	3.75	.314	.314	90.7	90.7	.175	.112
	A_i	1	5	9	.319	.300	92.3	86.6	.143	.134
	A_e	1	5	9	.322	.298	93.0	86.1	.144	.133
	C_i	.3	.6	.9	.295	.317	85.2	91.6	.132	.142
	C_e	.3	.6	.9	.293	.318	84.6	91.9	.131	.142
	c.v.	.001	.05	.10	.331	.283	95.8	81.6	.148	.126
Operation Characteristics	r	0	5	10	.326	.301	94.3	87.0	.146	.135
	f_1	0	5	10	.340	.287	98.3	83.0	.152	.128
	K_1	0	1	2	.315	.312	88.8	92.5	.137	.143
	K_2	0	.25	.50	.355	.272	102.6	78.7	.159	.122
	A_1	.98	.99	1.00	.312	.316	90.2	91.4	.137	.144
	A_2	.98	.99	1.00	.308	.319	90.1	91.2	.138	.143
	e_H	.85	.90	.95	.296	.331	90.6	90.6	.140	.140
	δp_1	0	1	2	.311	.316	89.9	91.6	.152	.128
	δp_2	0	2	4	.319	.308	92.3	89.0	.143	.138
Working Fluid Properties	c_p	.250	.255	.260	.344	.282	99.8	81.3	.163	.119
	$c_{p'}$	.265	.270	.275	.270	.357	78.1	103.2	.121	.160
	c_v	.180	.185	.190	.289	.336	80.8	100.2	.119	.163
	$c_{v'}$	.195	.200	.205	.353	.273	102.1	79.0	.158	.122
	T_0	460	519	578	.324	.300	98.8	82.7	.171	.115
	P_0	13.7	14.7	15.7	.311	.317	89.8	91.6	.129	.152

which parameters have the most significant effect on engine performance. The incremental change in a parameter is the change from the midrange value to the high or low range values for each parameter. This approach allows one to see the relative effects of each parameter change at the high and low range, or best and worst case, of one parameter compared to another. Table 2 presents the results of a comprehensive sensitivity analysis of all the input parameters used in analyzing performance for this particular engine design. Table 2 lists the base case values used in the analysis (the same as the engine design), the extreme values of the parameters (both high and low), as well as the output parameter results.

As for the operation characteristics, the most profound changes are indicated by the friction and heat transfer factors (f and K) of the expander. Engine efficiency appears to be most sensitive to heat transfer and friction factors, so this only underscores the need to have good empirical input data for the model.

Small changes in specific heats, both for constant pressure and constant volume, also appear to be significant. One way to reduce the margin for error in c_v and c_p inputs is to include algorithms within the model to calculate these parameters as a function of temperature rather than have them user-specified.

Results also highlight the importance of valve design and operation, as represented by the mean flow coefficients (C_i and C_e) and piston/valve area ratio parameters (A_i and A_e). One would expect that maximum valve area and maximum flow coefficient values would result in the best performance because pressure losses and flow resistance would be minimized. However, the results show this is not so in all cases.

Neither mass loss effects nor pressure drop through the combustor are very significant. Parameters that affect pressure losses have less influence on overall performance than friction and heat transfer losses. However, pressure drop (δp_1) at the compressor inlet can be significant. This means that engine derating would have to be considered at nonstandard applications, such as at higher altitudes. Supercharging will also have a profound effect on thermodynamic performance.

What really matters is how the pressure drops are calculated at compressor admission and at the expander intake. The pressure drop during compressor admission influences volumetric efficiency probably more than clearance volume.

Both the compressor and the expander bores appear to influence efficiency strongly, but the effects are opposite for the compressor and expander. Overall, the relative effects of the

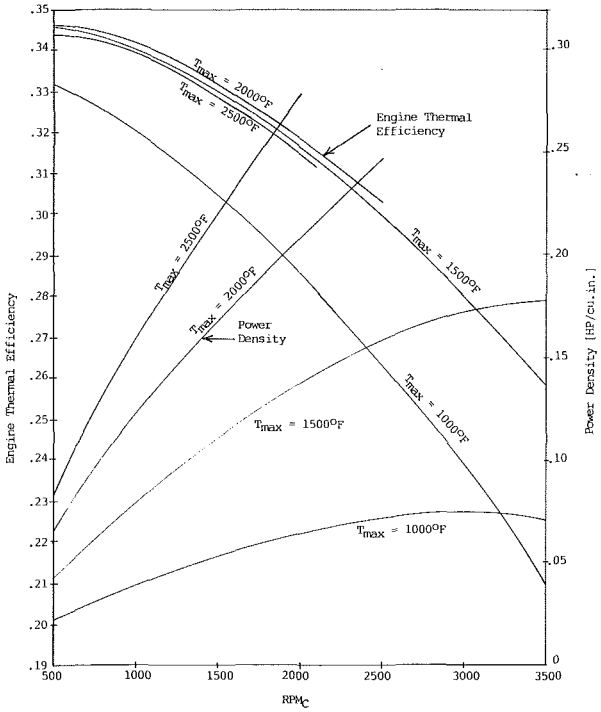

Fig. 4 Influence of temperature on power density and engine thermal efficiency (note: truncated curves indicate performance limit of this particular PACE engine design with this parameter)

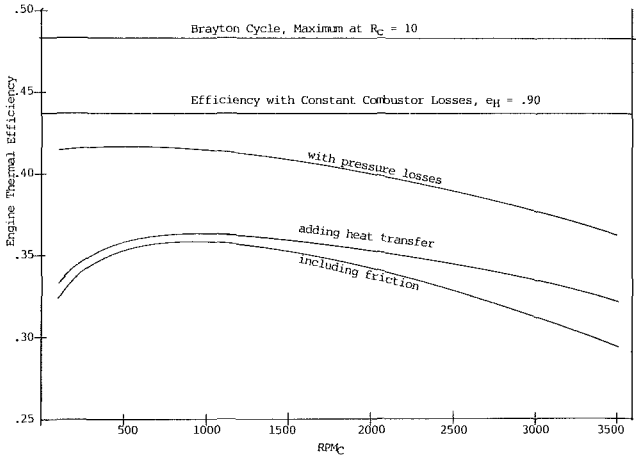

Fig. 5 Interactive effects of various parametric groups on engine thermal efficiency

compressor design and operation characteristics have less effect on engine performance than comparable changes in expander parameters. Since the compressor work rate is about equal to 40–60 percent of the expander power output, it stands to reason that the irreversibility losses associated with the compressor would be proportionately less.

Investigating performance sensitivity to small changes in parametric values is a very straightforward and simple, but powerful, analysis procedure. The one serious limitation to this approach is that the results are only valid for the operating point defined (in this case rpm_C = 2000, R_C = 10, and $T_{\max}$ = 1500°F or 816°C). Interactive effects among parameters may cause differing results at different ranges of the operating parameters.

Comparative Analysis of Parametric Performance Curves. Another approach one can use to assess the relative effects of various parameters is to actually vary a specific parameter over the operating range (rpm_C and R_C) of the engine and compare performance curves. Figure 4 is one example of how parametric curves may be plotted; it shows efficiency and power density versus rpm_C with $T_{\max}$ as the parameter. The truncated lines for $T_{\max}$ of 2000°F (1094°C) and 2500°F (1371°C) are due to insufficient expander capacity to operate beyond the points indicated. What is most interesting is the lack of thermal efficiency advantage at the higher temperatures. This may well be due to heat transfer effects.

Figure 4 is one small example of the kind of parametric analysis one could perform to investigate the relative effects of varying parameters. Other important parameters one might want to analyze in evaluating a particular engine configuration's performance are piston/valve area ratios, mean inlet and outlet flow coefficients, and inlet pressure and temperature. In cases where parameteric curves tend to indicate constant proportional differences (a linear relation), the results will not be very interesting. It is where parametric curves manifest different peaks, crossovers, or unusual shapes that the analysis can reveal important insights.

Interactive and Separate Parametric Effects. Another analysis approach is to take groups of parameters and test them, one group at a time, to investigate their relative effects. Then, once the largest parametric effects have been determined, the parametric groups can be run in seqeuence to see their interactive effects as shown in Fig. 5. This curve was developed using the base case parameter values in Table 2. Here, the maximum Brayton cycle efficiency is 0.482. A constant drop in efficiency, down to 0.435, is represented by adding a combustor efficiency e_H of 0.90. Next, all the parameters that affect pressure losses are incorporated: the mean flow coefficients, the piston/valve area ratios, and the combustor and compressor pressure drops. Then the heat transfer coefficients are added. Lastly, the friction coefficients are included.

What is clear from this interactive composite profile is that the proportion of pressure losses increases dramatically, and friction less so, as speed increases, and heat transfer losses are somewhat greater at low speed.

Scale Effects. In scaling the PACE engine up from its nominal 15 hp (11.2 kW) size represented here in the base case engine, there are three ways to change the power output: increase piston displacement, increase rpm, or increase the number of cylinders.

One might argue that the analysis described here for one engine configuration cannot possibly cover the gamut of engine performance capabilities from a small 1 hp (0.7 kW) engine all the way up to, say, 500 hp (373 kW), which is the operating range for other IC engines. However, there are several key points to keep in mind about the relative effects of the model parameters that are likely to be significant as engine scale varies.

As far as increasing displacement, the critical parameters are the bore and stroke of both the compressor and the expander. The effects of these parameters can be compared by examining the influence of the piston aspect ratio *b/s*. This ratio ranges from about 0.8 to 1.25. If the aspect ratio remains about constant as the piston is scaled up, the changes in bore and stroke will not significantly alter performance results (efficiency, net specific work, and power density). Power will, of course, scale up nearly proportional to displacement because the mass flow rate increases in almost direct proportion to displacement. The main factor that changes when the *b/s* ratio changes is heat transfer, which is affected primarily by bore. Because volume displacement increases with the square of the bore, the heat loss increase is almost compensated for by the net increase in power. If the stroke change is large relative to the bore, then all speed effects will be more pronounced.

As for number of cylinders (N) and cycles per revolution (B), these parameters are linearly related to power and rpm, respectively. In this model, multiplying the number of cylinders will multiply the power proportionately and not affect efficiency or net specific work. Changing the value of B for a component will only affect the rpm (of compressor or expander) in direct inverse proportion. In other words, the performance indicated at, say, 2000 rpm with $B=2$, is the same as that at 4000 rpm, $B=1$, or 1000 rpm with $B=4$. Both rpm and cycles per revolution are directly related to average piston speed u. B is determined by the gearing arrangement in the PACE design.

On the other hand, the relative number of cylinders and cycles per revolution (B and N) for the compressor compared to the expander may make a significant difference. Since the relative work of the compressor is only a portion of the work output of the expander, all irreversibilities due to B and N differences between the compressor and expander should be less important when associated with the compressor rather than with the expander.

By modeling a representative engine of four cylinders and two cycles per revolution, as done here, the resulting analysis should apply just as well to larger power output engines of more cylinders, which have values of N and B that are multiples of the base engine configuration. As far as this model works, scale effects will not be significant unless piston aspect ratio changes. However, the effect on efficiency over the range of $0.8 < b/s < 1.25$ is not very significant, as shown by White [6], when the aspect ratio change applies to both compressor and expander. However, it appears efficiency and net specific work can be enhanced by minimizing the compressor piston aspect ratio while maximizing this ratio for the expander.

One should also bear in mind that the PACE engine is not limited to low-horsepower size as described in this analysis. Piston displacement (bore and stroke) and number of cylinders are entirely open-ended design parameters, and power can be scaled upward accordingly. In the case of the PACE engine, though, power density should be carefully considered in proposing engine applications. The critical differences between a PACE and a comparable-displacement IC engine are, first, air density and mass flow rate, then pressure–temperature profile. The PACE may not reach comparable power densities of common IC engines, but this might be compensated for by better thermal efficiency at higher average operating temperatures. Moreover, common IC engines do not have the same potential multifuel capability, which may be particularly important in cogeneration applications.

The one irreversibility that probably is not constant, even if the piston aspect ratio remains constant, is friction. The empirical values for hte friction factor are probably strongly correlated to total cylinder surface area (circumference of the cylinder) and charge density. Although friction mean effective pressure (mep) is linear with piston speed for a particular engine configuration, the friction coefficient is bound to vary with different engine designs.

While friction effects due to scale are not accounted for in the model, the piston aspect ratio should still affect the friction coefficient. But empirical values related to scale effects are not available for making these comparisons without further experimental data.

Summary and Conclusions

A microcomputer model has been developed that predicts the thermodynamic performance of a Brayton cycle engine with reciprocating piston compressor and expander components. The model is based on an air-standard open Brayton cycle without regeneration.

The model incorporates all important irreversibilities, including: heat transfer, pressure losses, mass loss and recirculation, and mechanical friction. Each irreversibility is modeled as a function of pressure ratio or average piston speed, which in turn is a linear function of rpm. Key independent operating parameters are maximum temperature, compressor rpm, and pressure ratio. Other input parameters are divided into four groups, which include design characteristics of both the compressor and expander, parameters that characterize the irreversibilities, and properties of the working fluid. There is a total of 38 input parameters. Output parameters include: engine thermal efficiency, net specific work, and power (or power density).

Applicable data from research on IC engines have been adapted to model PACE engine performance. Data from studies on heat transfer, friction, and pressure losses, in particular, have been used. Certain empirical parameters appear to influence PACE engine performance very strongly, yet IC data based on these values may not be applicable to the PACE engine. The most critical parameters, notably friction and heat transfer coefficients, must be determined experimentally if accurate model results are to be expected. This underscores the need to obtain good empirical data to validate the PACE model.

The PACE model is a powerful tool for comparative analysis and develolping insight into the interactive effects of key operating and design parameters. It can be used as a tool to do preliminary engine design and to compare different engine designs using the performance maps. It can be used for sensitivity and parametric analyses to evaluate the relative influence of different parameters on engine performance. Comparative analyses can be run interactively, and the user gets immediate feedback.

Once the key parameters that influence engine performance are tested, improved engine designs can be developed, at least in principle. Good empirical data for parameters that may have a dramatic effect in swaying engine performance are critical to the development of optimum engine designs.

As presented here, the PACE engine microcomputer model has demonstrated itself to be very useful for evaluating the effects of different input parameters on engine performance.

Recommendations for Follow-on Work

There is the opportunity to analyze many more design configurations of the PACE engine than presented here, and this should be undertaken. Recommendations offered here as a result of completing this work include: additional analysis or further research to narrow uncertainty in values for model parameters; improvements in model methodology and algorithms, including specific heats that vary with temperature and real gas chemistry; and enhancement of model software and hardware. In particular, testing is also needed to determine appropriate model input values for the heat transfer and friction coefficients.

The PACE compressor and expander need to be matched to satisfy certain design or performance criteria, especially mass continuity. The expander must accept all the mass the compressor delivers, while still getting full expansion out of the pistons. If compressor and expander maps were available for a range of component sizes and designs, a user could decide which two components to put together to satisfy the mass continuity criterion while meeting other design criteria. These criteria might include meeting overall power density requirements while still achieving a certain efficiency level over a given rpm range.

Efficiencies of any Brayton cycle engine can be enhanced using supercharging, intercooling in multistage compressors, a recuperator to recover the heat in the exhaust, and closed-

cycle operation. These also could be added to the model. Of course, there are always software and hardware enhancements that could be incorporated into the model to make it more flexible, faster, and more accurate.

The next steps in the PACE development are to design and build an expander and test it. A well-designed series of tests is planned, starting with cold air testing, continuing with heated air tests, and, finally, concluding with tests using hot combustion product gases as the working fluid for the expander. Following these tests, a compressor will be added, then a combustor to complete a prototype engine design. Full-scale engine testing will follow. Ultimately, a prototype PACE engine design should be available and lead to a marketable product.

Acknowledgments

The authors wish to thank Al Albert of Combustion Research Technology, Inc. for his financial support, and Reiner Decher of the University of Washington for his advice in developing the analytical foundations for this work.

References

1 Decher, R., "The Britalus Brayton Cycle Engine," ASME Paper No. 84-GT-258, 1984.

2 Decher, R., "Optimization of the Britalus Brayton Cycle Engine for Part Load Performance," presented at the 16th International Congress on Combustion Engines (CIMAC), Oslo, Norway, 1985.

3 Decher, R., "Part Load Operation of a Displacement Brayton Cycle Engine With Variable Volume Ratio Expander," unpublished paper, Department of Aeronautics and Astronautics, University of Washington, Seattle, WA, 1985.

4 Decher, R., "Power Scaling Characteristics of a Displacement Brayton Cycle," presented at the 19th Intersociety Energy Conversion Engineering Conference, San Francisco, CA, 1984.

5 Decher, R., "Port Passage Losses in Britalus Compressors and Expanders," *Proceedings of the International Gas Research Conference*, Washington, DC, 1984.

6 White, T. J., "Development of a Parametric Analysis Microcomputer Model for Evaluating the Thermodynamic Performance of a Reciprocating Brayton Cycle Engine," M.S. Thesis, Portland State University, Portland, OR, 1987.

7 Martin, L., "PACE Performance Optimization," M.S. Project Report, Portland State University, Portland, OR, 1987.

8 Fryer, B. C., and Smith, J. L., "Design, Construction and Testing of a New Valved, Hot-Gas Engine," *Proceedings of the 8th Intersociety Energy Conversion Engineering Conference*, 1973, pp. 174–181.

9 Lee, K. R., and Smith, J. L., "Influence of Cyclic Wall-to-Gas Heat Transfer in the Cylinder of the Valved, Hot-Gas, Engine," *Proceedings of the 13th Intersociety Energy Conversion Engineering Conference*, 1978, pp. 1798–1804.

10 Warren, G. B., and Bjerklie, J. W., "Proposed Reciprocating Internal Combustion Engine With Constant Pressure Combustion," SAE Paper No. 690045, 1969.

11 Rosa, R. J., "Characteristics of a Closed Brayton Cycle Piston Engine," *Journal of Energy*, Vol. 7, Mar.–Apr., 1983, pp. 147–151.

12 Obert, E. F., *Internal Combustion Engines*, Harper & Row, New York, 1973, p. 732, Fig. 11.

Inhomogeneity of Fluid Flow in Stirling Engine Regenerators

J. D. Jones[1]
University of Reading,
Whiteknights, Reading,
United Kingdom

The literature relating to inhomogeneity of flow in regenerators is briefly reviewed. It is noted that, in contrast to other applications of regenerators, relatively little attention has been paid to the consequences of flow inhomogeneity for thermal regeneration in Stirling cycle machines. The construction of regenerator capsules for a large stationary Stirling engine is described. A test rig is developed to measure the gas velocity profile across the face of the packed regenerator capsules under steady flow conditions. Measured flow profiles for a number of different matrix materials and construction techniques are presented, and it is noted that stacked-mesh regenerator matrices tend to display marked inhomogeneities of flow. The consequences of flow inhomogeneity for flow friction and regenerator effectiveness are analyzed theoretically, and approximate formulae deduced. One method for reducing flow inhomogeneity in stacked-screen matrices is described.

Introduction

A considerable literature exists on the occurrence of flow maldistribution in heat exchangers. Mueller and Chiou (1987) provide an excellent review of the field. In the subset of this literature dealing with regenerative heat exchangers, one of the primary issues addressed is the nonuniform distribution of voids within beds of spheres or irregular particles. The details of voidage distribution depend strongly on the small-scale geometry of the regenerator filling, and are hence of limited relevance to Stirling-cycle regenerators, in which stacked screens of wire mesh are more commonly used than packed particle beds. Nevertheless, the existence of this work does serve to draw attention to the possibility of nonuniform voidage and its importance for regenerator performance.

Several of the papers in the literature deal with questions less closely linked to a particular geometry, and hence of potentially greater interest to Stirling-machine designers. Mickley et al. (1965) use hot-wire anemometry to investigate velocity and turbulence profiles within a packed bed of spheres and show that a velocity maximum exists close to the wall, even when the voidage fraction is uniform over any cross section of the bed. Schertz and Bischoff (1969) use a hot-wire anemometer to show that the radial temperature profile over a cross section of the bed can have a significant effect on the velocity profile. Stanek and Szekely (1973) present theoretical arguments to show that this effect can produce inhomogeneous flow even in a uniformly packed bed. These issues merit experimental and theoretical investigation for the conditions typical of Stirling-cycle machine operation.

Stirling-cycle machine design has drawn on numerous analyses of the thermal performance of regenerators and their associated flow losses. The great majority of these analyses have treated flow through the regenerator as one-dimensional, on the assumption that flow velocities are uniform over any cross section through the regenerator. Two recent studies examine the consequences of dropping that assumption.

Wolfs et al. (1986) evaluate the effect of the "residence time distribution" (RTD) on regenerator performance. This effect may be attributed to a fine-scale inhomogeneity of flow. As the working fluid passes over the extended surfaces making up the regenerator matrix, boundary layers and wakes are formed, and the fluid in these volumes passes through a different thermodynamic cycle than does the mainstream fluid. The effect of RTD is to increase the enthalpy flow through the regenerator, the magnitude of this effect depending on the phase angle between piston and displacer movement.

Gedeon (1985) examines the consequences of flow inhomogeneity resulting from the pressure distribution in the manifolds connecting the regenerator to the adjacent heat exchangers, and derives mathematical methods for calculating its effects.

The present paper examines flow inhomogeneity at a scale intermediate between these two extremes, arising from large-scale nonuniformities in the structure of the regenerator matrix. The effects discussed in this paper may thus be expected to occur *in addition to* those documented by Wolfs and Gedeon.

Experimental Investigation

We prepared twelve regenerator capsules for use in the U.K. Consortium Stirling engine (Dunn et al., 1982; Rice et al., 1983; Jones, 1982) and in the permeability test rig (Fig. 1). These capsules were of type 316 stainless steel, 50 mm high and 90 mm in external diameter, having a wall thickness of 0.5 mm. A retaining flange was machined at one end of the capsule, with a layer of stainless steel mesh with 15 strands to the inch spot-welded to it. A tightly fitting lid, also flanged and

[1]Present address: School of Engineering Science, Simon Fraser University, Burnaby, British Columbia, Canada.

Contributed by the Advanced Energy Systems Division for publication in the JOURNAL OF ENGINEERING FOR GAS TURBINES AND POWER. Manuscript received by the Advanced Energy Systems Division June 16, 1987.

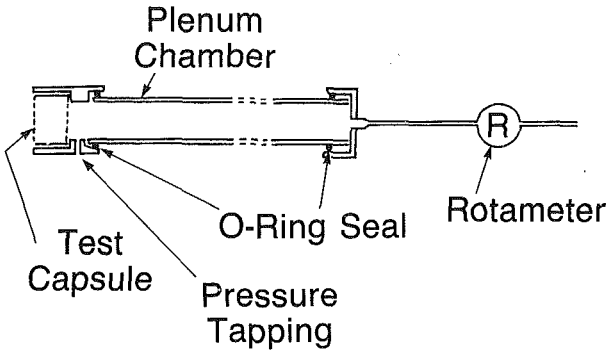

Fig. 1 Permeability test rig

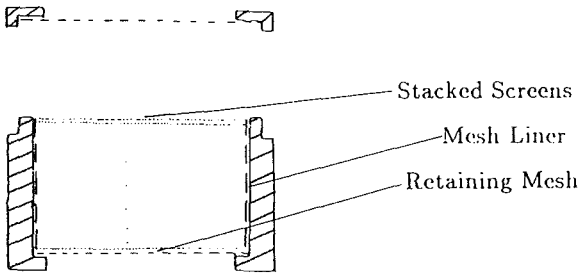

Fig. 2 Regenerator capsule

fitted with a retaining screen, was prepared to seal the other end (Fig. 2).

Matrix Assembly

The first series of tests was conducted using stainless steel wire screens, 100 meshes to the inch, with a wire diameter of 110 μm. The screens were prepared using a punch as described by Steiner (1978) to cut disks from strips of mesh. The disks were punched 0.5 mm oversize, in the hope that any leakage paths around the edge of the capsule would be closed off. We stacked the disks in the capsules, making no attempt to line up the wires in successive screens. Using the same method, we filled other capsules with screens of a finer mesh having 200 meshes to the inch and a wire diameter of 68 μm.

The same punch was used to cut disks of carbon-fiber felt, having a fiber diameter of 20 μm, and of nickel felt, with a fiber diameter of 10 μm. Several other capsules were manufactured from slabs of foamed metal, a porous material formed by electroplating nylon foam and subsequent baking. The metal foam had an irregular tetrahedral structure, with a mean fiber diameter of 70 μm. Approximate disks were cut from a slab of the foam $\approx$ 10 mm thick, turned to size on a lathe and stacked within the prepared capsules. Lastly, we packed several capsules with fine steel wool, made up of ribbonlike fibers approximately 100 μm wide by 20 μm thick, and with knitted mesh 100 μm in diameter. In the case of the wool and knitted mesh matrices, packing was evidently inhomogeneous despite all precautions taken to pack the capsules evenly.

Flow Measurements

We used the rig shown in Fig. 1 to investigate flow through the prepared capsules. Air from a compressed-air supply flowed through the plenum chamber and a hot-wire anemometer was moved across the outer face of the regenerator capsule at a distance of about 2 mm from the outermost screen. We measured flow velocity at a range of radii and along several different diameters to check for radial and circumferential inhomogeneity. The capsule was then removed from the apparatus and the flow profile emerging from the plenum chamber measured. Finally, we reversed the axial orientation of the capsule and repeated the measurements. Measurements were made at a range of flow velocities, corresponding to Reynolds numbers of 10–20 in the 100-mesh matrices, and of 4000–8000 in the plenum chamber leading up to the matrix.

Results

We found flow through the foamed metal, carbon, and nickel felt matrices to be homogeneous, within the accuracy of experimental measurement, under all conditions investigated. Flow through the wire wool and knitted-mesh matrices was

Nomenclature

A = frontal area of regenerator matrix, m^2
A_f = mean flow area of regenerator matrix $= \epsilon A$, m^2
A_H = heat transfer area of regenerator matrix, m^2
A_m = minimum flow area of regenerator matrix $= \frac{(s-d)^2}{s^2} A$, m^2
C = coefficient in empirical correlation for friction factor
c_p = specific heat of working fluid, J/kg•K
d = wire diameter, m
D = hydraulic diameter of regenerator matrix, m
E = regenerator effectiveness
f = Fanning friction factor
F = dimensionless correction factor
G = mean mass flow rate through matrix, based on A_f, kg/m^2•s
G_m = maximum mass flow rate through matrix, based on A_m, kg/m^2•s
h = film heat transfer coefficient, W/m^2•K
H = enthalpy flow, W
k = conductivity of working fluid, W/m•K
L = length of the regenerator, m
Δp = pressure drop across regenerator, Pa
n = exponent in empirical correlation for friction factor
$\dot{m}$ = mass flow rate, kg/s
u = flow velocity based on frontal area A, m/s
U_m = maximum flow velocity based on cross-sectional area of minimum screen opening A_m, m/s
α = specific area of regenerator matrix, m^2/m^3
ϵ = matrix porosity
μ = viscosity of working fluid, Pa•s
ρ = density of working fluid, kg/m^3
ϕ = ratio of flow velocities through annular and central regions of composite matrix
ψ = ratio of frontal area of annular region of matrix to total frontal area
Pr = Prandtl number $= \mu c_p/k$
Re = Reynolds number based on hydraulic diameter $= GD/\mu$
Re$_l$ = Reynolds number based on screen opening $= G_m(s-d)/\mu$
St = Stanton number $= h/Gc_p$
Λ = reduced length of matrix, as defined by Nusselt (1928)

Subscripts

a = denotes the annular region of the inhomogeneous matrix
b = denotes the central region of the inhomogeneous matrix
c = denotes the inhomogeneous matrix as a whole
d = denotes an equivalent homogeneous matrix

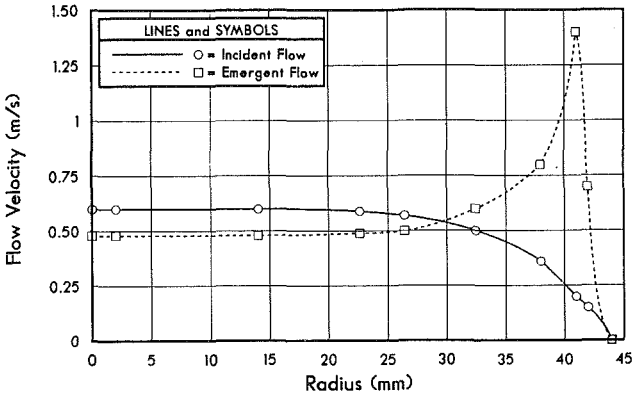

Fig. 3 Flow through a 100-mesh matrix

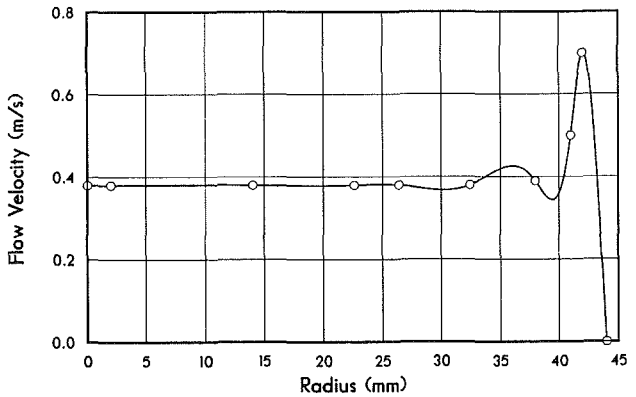

Fig. 4 Flow through a lined matrix

markedly inhomogeneous, both radially and circumferentially. The pattern of inhomogeneity varied from one capsule to another, but the highest flow rates tended to be at the periphery of the capsule. Both the 100-mesh and the 200-mesh stacked-screen matrices displayed consistent inhomogeneity; a representative flow distribution is shown in Fig. 3. This pattern of flow is similar to the flow profiles measured in packed sphere beds reported by Schertz and Bischoff (1969). Inhomogeneity was typically more serious in the case of the finer mesh. There was no measurable circumferential inhomogeneity for either of the stacked-screen matrices. Reversing the axial orientation of the capsule produced no measurable change in any of the cases investigated.

Remedial Measures

Because of the calculated consequences of inhomogeneity on performance, we investigated ways of ensuring a more homogeneous flow through the mesh matrices. After investigating various options, we found that the expedient of spot-welding a single layer of coarser mesh (30 meshes to the inch) to the inner circumference of the regenerator capsule produced satisfactory results (Fig. 4). No method of assembly we investigated would ensure homogeneous flow through knitted mesh or steel wool matrices.

Assessing Effects of Inhomogeneity

Given a method for manufacturing regenerator capsules, and given data similar to Figs. 3 and 4 on the inhomogeneity of flow through the finished capsule, we require some quantitative method of estimating its impact on performance. Such a method has been provided for gas turbine regenerators by London (1970). We seek to develop a similar method for stacked-screen matrices. We shall compare the net enthalpy flow from the hot to the cold end of the regenerator and the power lost in overcoming flow friction within it to the corresponding values for a perfectly homogeneous matrix installed in an otherwise identical engine operating at the same speed. This is approximately equivalent to comparing the two matrices when subject to the same volumetric flow.

Work by Tong and London (1957) and the re-interpretation of their data by Chen and Griffin (1983) indicate that the Colburn analogy does not hold for stacked-screen matrices: Heat transfer and flow friction behavior depend on matrix geometry in different ways. In order to deduce the effect of inhomogeneity on heat transfer from its measured effects on flow friction, we must therefore make certain assumptions about the physical structure of the inhomogeneous region.

Assumptions

(*i*) The inhomogeneous matrix can be represented as two homogeneous submatrices arranged in parallel, corresponding to the annular region, through which leak paths exist, and a central region, assumed to be well-packed. These notional submatrices are considered to have the same wire diameter d, but different spacing between the centerlines of adjacent wires s. Definitions for other matrix properties in terms of s and d are worked out in the Appendix.

(*ii*) The flow friction and heat transfer coefficients for each submatrix can be calculated from the formulae derived by Chen and Griffin (1983) and Tong and London (1957), respectively.

(*iii*) The friction factors and heat transfer coefficients for each submatrix are constant over its length and cross section.

(*iv*) Entrance and exit losses are negligible.

(*v*) Fluid properties μ, ρ, and Pr are the same throughout each submatrix.

Assumption (*ii*) may be challenged. It implies a geometric similarity between the central and annular regions that the demonstrated presence of leak paths renders doubtful. However, Tong and London (1957) observe that the heat transfer correlation they deduce for stacked screens is relatively insensitive to details of geometry and applies reasonably well even to packed spheres and granular beds, particularly at low Reynolds number.

We denote the submatrices corresponding to the annular and central regions of the inhomogeneous matrix by the subscripts a and b, respectively. By hypothesis, the measured flow velocity over each submatrix is uniform. We denote these velocities by u_a and u_b and their ratio by

$$\phi = u_a/u_b \tag{1}$$

Suppose the annular region to represent a fraction ψ of the total frontal area of the matrix. These two numbers, ϕ and ψ, characterize the measured pattern of inhomogeneity through the matrix. The annular and central regions taken together form a single composite matrix, whose properties will be denoted by the subscript c. Flow through this composite matrix is shown in Fig. 5. The performance of the composite, inhomogeneous matrix is to be compared with that of a uniformly well-packed matrix exposed to the same incident flow. The uniformly well-packed matrix will be denoted by the subscript d.

Frictional Losses

Chen and Griffin (1983) show that the friction factor measurements of Tong and London (1957) can be plotted with very little scatter on the basis of a Reynolds number defined by

$$\mathrm{Re}_l = \frac{\rho U_m (s-d)}{\mu} \tag{2}$$

where $(s-d)$ is the minimum screen opening and U_m is the flow velocity based on the cross-sectional area of that opening. It will be found mathematically convenient to fit an empirical equation of the form

$$f = C\mathrm{Re}_l^n \tag{3}$$

to the replotted data, choosing C and n to give the best fit in the region of interest.

The pressure drop across the two submatrices is the same and is given by

$$\Delta p = \frac{f_a L u_a^2 \rho}{D_a} = \frac{f_b L u_b^2 \rho}{D_b} \tag{4}$$

where D denotes hydraulic diameter and L regenerator length.

Comparing this pressure drop with that across a perfectly homogeneous matrix exposed to the same volumetric flow, we may write

$$Au_d = A\psi u_a + A(1-\psi)u_b$$

$$\Rightarrow u_d = \psi u_a + (1-\psi)u_b \tag{5}$$

where A is the frontal area of the matrix. The ratio of the actual pressure drop to that over the homogeneous matrix is therefore

$$\frac{\Delta p_b}{\Delta p_d} = \frac{f_b u_b^2}{f_d u_d^2} = \left(\frac{1}{\psi(\phi-1)+1}\right)^{2+n} \tag{6}$$

Frictional work in the regenerator will be reduced by the same ratio.

Enthalpy Losses

Inhomogeneity must be expected to lead to an increase in the net flow of heat from the heater to cooler, and a corresponding degradation of thermal efficiency. To estimate this we first calculate s_a, the effective spacing between centerlines of adjacent wires in the annular region of the matrix. Combining equations (1)-(4) and equations (A1)-(A4) from the Appendix yields

$$\left(\frac{s_b}{s_a}\right)^{2n}\left(\frac{s_a-d}{s_b-d}\right)^{n}\left(\frac{4s_a-\pi d}{4s_b-\pi d}\right) = \phi^{2+n} \tag{7}$$

s_a is the only unknown quantity in equation (7) and may readily be calculated.

We next calculate the ratio of the mass flows, $\dot{m}$, through the annular and central regions of the inhomogeneous matrix to the mass flow through the equivalent homogeneous matrix

$$\frac{\dot{m}_a}{\dot{m}_d} = \frac{u_a A\psi\rho}{u_d A\rho} = \frac{\phi\psi}{(\phi-1)\psi+1}$$

$$\frac{\dot{m}_b}{\dot{m}_d} = \frac{1-\psi}{(\phi-1)\psi+1} \tag{8}$$

The corresponding ratios for the average mass velocities are then

$$\frac{G_a}{G_d} = \left(\frac{\dot{m}_a}{\epsilon_a A\psi}\right)\left(\frac{\epsilon_d A}{\dot{m}_d}\right) = \frac{\epsilon_d}{\epsilon_a}\,\frac{\phi}{(\phi-1)\psi+1}$$

$$\frac{G_b}{G_d} = \frac{1}{(\phi-1)\psi+1} \tag{9}$$

where ϵ denotes matrix porosity.

We now make use of the heat transfer correlation derived by Tong and London (1957):

$$\mathrm{StPr}^{2/3} = 0.375\left(\frac{1-F\epsilon}{F\epsilon}\mathrm{Re}\right)^{-0.375} \tag{10}$$

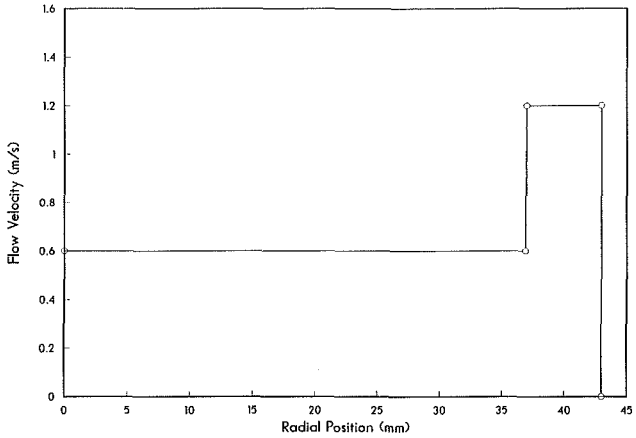

Fig. 5 Idealized flow profile for the matrix of Fig. 3

where

$$\mathrm{Re} = \frac{DG}{\mu} \tag{11}$$

and F is a correlation factor, which for the level of accuracy required in the present analysis may be set to unity. From equations (9)-(11) we obtain the following expressions for the heat transfer coefficients in the submatrices compared with that in the perfectly homogeneous matrix:

$$\frac{h_a}{h_d} = \left(\frac{\epsilon_d}{\epsilon_a}\,\frac{\phi}{(\phi-1)\psi+1}\right)^{0.625}$$

$$\frac{h_b}{h_d} = \left(\frac{1}{(\phi-1)\psi+1}\right)^{0.625} \tag{12}$$

Using the method dervived by Nusselt (1928) for calculating enthalpy flow through a matrix, we define the matrix *effectiveness* E by

$$1-E = \frac{\text{Net enthalpy flow through matrix}}{\text{Total energy deposited in matrix by gas}}$$

For the present level of accuracy, it is sufficient to use Nusselt's expression for regenerator ineffectiveness (Nusselt, 1928) $1-E = 2/(\Lambda+2)$, neglecting the effect of finite matrix mass, pressure fluctuations, and so on. Λ, the *reduced length* of the matrix, is defined by

$$\Lambda = \frac{hA_H}{\dot{m}c_p} \tag{13}$$

where A_H is the total area of the matrix available for heat transfer.

For Stirling engine regenerators this is typically large, so Nusselt's expression may be further approximated to $1-E = 2/\Lambda$.

The ratio of reduced lengths between the submatrices and the perfectly homogeneous matrix is therefore, using equation (A4)

$$\frac{\Lambda_a}{\Lambda_d} = \left(\frac{s_d}{s_a}\right)^{0.375}\left(\frac{4s_d-\pi d}{4s_a-\pi d}\right)^{0.625}\left(\frac{(\phi-1)\psi+1}{\phi}\right)^{0.375}$$

$$\frac{\Lambda_b}{\Lambda_d} = ((\phi-1)\psi+1)^{0.375} \tag{14}$$

Thus the net enthalpy H flowing through the two regions of the composite matrix can be expressed as a fraction of that flowing through the homogeneous matrix by

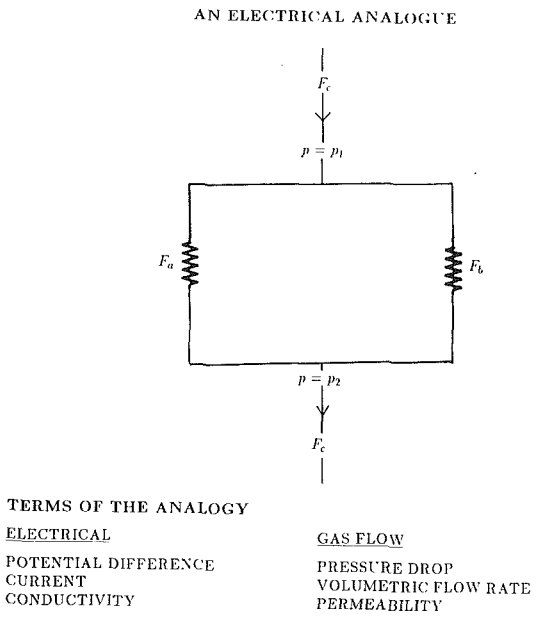

Fig. 6 Electrical analog

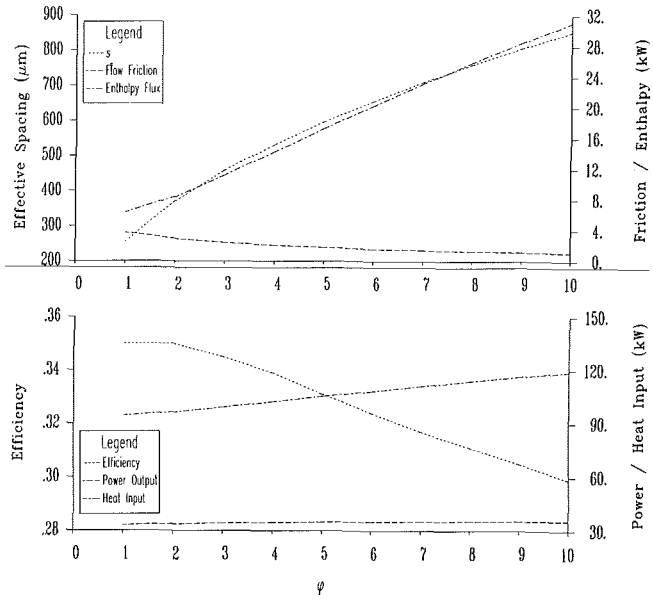

Fig. 7 Effects of inhomogeneity

$$\frac{H_a}{H_d}=\frac{\Lambda_d \dot{m}_a}{\Lambda_a \dot{m}_d}=\psi\left(\frac{4s_d-\pi d}{4s_a-\pi d}\right)^{-0.625}\left(\frac{s_a}{s_d}\right)^{0.375}\left(\frac{\phi}{(\phi-1)\psi+1}\right)^{1.375}$$

$$\frac{H_b}{H_d}=(1-\psi)\left(\frac{1}{(\phi-1)\psi+1}\right)^{1.375} \tag{15}$$

Summing the two parts of equation (15) yields an expression for the total enthalpy loss through the composite, inhomogeneous matrix compared with that lost through a perfect, homogeneous matrix

$$\frac{H_c}{H_d}=\left(\frac{1}{(\phi-1)\psi+1}\right)^{1.375}\left(1+\psi\left(\phi^{1.375}\left(\frac{4s_d-\pi \mathrm{d}}{4s_a-\pi d}\right)^{-0.625}\left(\frac{s_a}{s_d}\right)^{0.375}-1\right)\right) \tag{16}$$

Example

To illustrate the use of the above formulae, we calculate the performance of wire mesh matrices having various degrees of inhomogeneity. These calculations are based on the U.K. Consortium engine (Jones, 1982) operating at its design point, at which the indicated power output is 33 kW and the efficiency is 0.35. We will consider matrices having the same wire diameter as the experimental matrix, 110 μm, and flow distributions similar to that shown in Fig. 6, for which

$$\psi=\frac{(43^2-37^2)}{43^2}=0.26$$

The value of ϕ actually measured was 2; we will consider a range of values from 2 to 10. We take $f=60\mathrm{Re}_l^{-1}$.

Figure 7 shows the results of this calculation for ten values of ϕ. In the upper part of the figure the right-hand axis shows the effective wire spacing in the annular region of the matrix, which increases with increased inhomogeneity. The fluid frictional losses in the matrix decrease rapidly at first, then more slowly, while there is a steady increase in the net enthalpy flow through the regenerator. The consequences for the engine as a whole are shown in the lower part of the figure. The efficiency is insensitive to moderate degrees of inhomogeneity, but falls off markedly as leakage increases. For the measured value of inhomogeneity, $\phi=2$, the reduction in efficiency is slight.

The insensitivity of engine efficiency to a moderate degree of matrix inhomogeneity should not be surprising. In designing the regenerator to obtain maximum engine efficiency, we vary the wire spacing until the reduction in flow friction obtained by a slight increase in spacing is just balanced by the concomitant increase in net enthalpy loss. So to first order, a small change in effective wire spacing will not affect efficiency.

Implications for Design

In determining how much effort is justified to reduce inhomogeneity, the designer must consider the cost of reduced engine efficiency. Equations (6) and (16) should be evaluated and their net effect on power and efficiency assessed. If the slope around the optimum design is fairly flat, a moderate degree of inhomogeneity may be acceptable. If maximization of efficiency is critical, then special procedures must be devised to ensure near-perfect packing of the regenerator. In the case of severe inhomogeneity, the increased enthalpy loss through the regenerator may increase the thermal load on heater and cooler beyond their capacity to maintain design temperature. This will lead to a loss in power and a further decline in efficiency.

Conclusions

Measurements of flow inhomogeneity on a range of regenerator matrices have been described. Inhomogeneity has been shown to be a problem with stacked-screen, knitted mesh, and wire-wool matrices. In the case of stacked-screen matrices, remedial action has been suggested.

Approximate formulae have been deduced for assessing the effects of measured inhomogeneity.

Acknowledgments

I would like to acknowledge the contribution of my colleagues at the University of Reading. Thanks in particular to Dr. Graham Rice for several helpful discussions and to Alan Priest for help with construction of the test rigs. I would also

like to thank David Gedeon, who reviewed this paper in draft and made a number of useful suggestions.

References

Chen, N. C., and Griffin, N. P., 1983, "Effects of Pressure Drop Correlations on Stirling Engine Predicted Performance," *Proceedings of the 18th IECEC*, Orlando, FL, pp. 708–713.

Dunn, P. D., et al., 1982, "20 kW U.K. Consortium Stirling Engine—Specifications and Manufacture," *I Mech E Conference Publications*, 1982-2, pp. 65–76.

Gedeon, D., 1985, "Computational Techniques for the Two-Dimensional Gas Dynamic Equations in Stirling Engine Regenerators and Associated Manifolds," *Proceedings of the 20th IECEC*, Miami Beach, FL, Paper No. 859434, pp. 3.354–3.359.

Jones, J. D., 1982, "Thermodynamic Design of the Stirling Engine," PhD Thesis, University of Reading, United Kingdom.

London, A. L., 1970, "Laminar Flow Gas Turbine Heat Exchangers—The Influence of Manufacturing Tolerances," ASME JOURNAL OF ENGINEERING FOR POWER, Vol. 92, pp. 46–56.

Mickley, H. S., Smith, K. A., and Korchak, E. I., 1965, "Fluid Flow in Packed Beds," *Chemical Engineering Science*, Vol. 20, pp. 237–246.

Mueller, A. C., and Chiou, J. P., 1987, "Review of Various Types of Flow Maldistribution in Heat Exchangers," in: *Maldistribution of Flow and Its Effect on Heat Exchanger Performance*, J. B. Kitto, ed., ASME HTD Vol. 75.

Nusselt, N., 1928, "Die Theorie des Winderhitzers," *Z. Ver. Dt. Ing.*, Vol. 71.

Rice, G., et al., 1983, "U.K. Consortium Stirling Engine: Regenerator Effectiveness and Engine Performance," *Proceedings of the 18th IECEC*, Los Angeles, CA, Paper No. 839115, pp. 714–719.

Schertz, W. W., and Bischoff, K. B., 1969, "Thermal and Material Transport in Nonisothermal Packed Beds," *AIChE Journal*, Vol. 15, No. 4, pp. 597–604.

Stanek, V., and Szekely, J., 1973, "Flow Maldistribution in Two-Dimensional Packed Beds Part II: The Behavior of Non-isothermal Systems," *The Canadian Journal of Chemical Engineering*, Vol. 51.

Steiner, J. C., 1978, "Stirling Thermal Engine Regenerator Cost Reduction Program Report 1—Wire Cloth Matrix Materials," GMR Research Publications GMR-2690, Section 6.002, published by NASA-Lewis as N78-26261, N78-26262, N78-26284, N78-26299, N78-26312, N78-26318.

Tong, A. S., and London, A. L., 1957, "Heat Transfer and Flow Friction Characteristics of Woven-Screen and Crossed-Rod Matrices," *Transactions of the ASME*, Vol. 79, No. 7, pp. 1558–1570.

Wolfs, M. J. M., Dijkstra, K., and de Jonge, H., 1986, "On the Determination of the Regenerator Losses in Stirling Cycles," *Proceedings of the Eighth International Heat Transfer Conference*, San Francisco, CA, pp. 3043–3047.

APPENDIX

In this Appendix, expressions are deduced for all geometric matrix properties of interest in terms of wire diameter d, and the space between centerlines of adjacent wires s.

Porosity ϵ is given by

$$\epsilon = \frac{4s - \pi d}{4s} \tag{A1}$$

α, the heat transfer area density, is given by

$$\alpha = \frac{\pi}{s} \tag{A2}$$

Hydraulic diameter D is defined as

$$\frac{4LA_f}{\text{Total heat transfer area}}$$

which becomes

$$D = \frac{4\epsilon}{\alpha} = \frac{4s - \pi d}{\pi} \tag{A3}$$

A_H, the total heat transfer area, is given by

$$A_H = \frac{AL\pi}{s} \tag{A4}$$

Reliability Evaluation of Shrouded Blading Using the SAFE Interference Diagram

M. P. Singh

J. J. Vargo

Dresser-Rand Company,
Wellsville, NY 14895

The SAFE Interference Diagram is shown to be useful in the design reliability evaluation of shrouded blading, including long-arc shrouding construction. This method provides an alternate method to the widely used Campbell diagram and also brings in more information for easier design evaluation. The SAFE diagram uses the natural frequencies of an entire bladed disk rather than individual blade or packet frequencies. In addition, it compares frequencies, mode shapes, and speed to evaluate whether a resonance occurs. Theoretical arguments are provided for the validity of the SAFE Diagram and its usefulness is shown by practical examples. This method provides an easier means to show why long-arc shrouding works and also when it might not.

Introduction

A rotating turbine blade (bucket) is the component that converts the energy of the flowing fluid into mechanical energy. Thus the reliability of these blades is very important for the successful operation of a turbine. Metallurgical examinations of failed blades show that almost all the failures can be attributed to metal fatigue. Fatigue failure is caused by fluctuating forces in combination with steady forces.

Turbine blades experience fluctuating forces when they pass through nonuniform fluid flow from the stationary vanes (nozzles). The basic design consideration is to avoid or to minimize the dynamic stresses produced by the fluctuating forces.

The dynamic response (e.g., stress, displacements, etc.) levels experienced by the blades depend on:

(a) the natural frequencies of the bladed disk and their associated mode shapes;

(b) the frequency, the shape, and the magnitude of the dynamic force, which are a function of the turbine speed, number of stationary vanes and their location around the annulus, and/or the number of interruptions in the flow passage, e.g., struts and their location around the annulus; and

(c) the energy-dissipating properties (damping) provided by blade material, frictional slip between joints, aerodynamic damping from steam, etc.

A turbine bladed disk may get into a state of vibration where the energy buildup is a maximum. This is exemplified by maxima in its response (stress, displacement, etc.) and minima in its resistance to the exciting force. This condition is called a state of "resonance." There are two simultaneous conditions for the energy buildup per cycle of vibration to be a maximum. These conditions are:

1 the frequency of the exciting force equals the natural frequency of vibration, and

2 the exciting force profile has the same shape as the associated mode shape of vibration.

These have been demonstrated by theoretical calculations and also by measured responses of turbine bladed disks.

Thus, for a resonance to occur, both of the above conditions must be met.

A large number of theoretical and experimental studies have been reported (Dye and Henry, 1968; El-Bayoumy and Srinivasan, 1975; Ewins, 1969, 1970, 1975), describing the behavior of a bladed disk. These studies also included the effect of manufacturing tolerances known as mistuning or detuning. These studies were mostly concerned with the axial modes of vibration where the flexibility of the disk becomes a factor in the determination of natural frequencies. Mode shapes were characterized as nodal diameters or nodal circles traditionally used for a circular disk. These studies demonstrated that the whole bladed disk should be considered as a system for the vibrational behavior determination in place of a single blade or a packet of blades on rigid foundation. These studies included the case of 360 deg arc shrouding of free standing blades.

Singh and Schiffer (1982) presented results of a finite element calculation of a packeted bladed disk. They showed the correlation of natural frequencies and mode shapes of a single packet to the whole bladed disk as one system. This was reported for tangential vibration. The disk is virtually, infinitely stiff in this direction, i.e., the stiffness of the disk does not influence the natural frequencies. But in the calculation for response of the system, the mode shapes of the whole system should be taken into account even though frequencies could be predicted by a single packet calculation. The nodal diameter descriptions for the mode shapes were found to be convenient even when the disk might not deflect in the tangential direction.

Contributed by the Power Division and presented at the Joint ASME/IEEE Power Generation Conference, Miami Beach, Florida, October 4–8, 1987. Manuscript received by the Power Division August 1987. Paper No. 87-JPGC-Pwr-48.

Natural frequencies of a packeted bladed disk assembly were found to be bracketed by 360 deg arc shrouding and free-standing blading cases. Calculations for a packeted bladed disk assembly are an order of magnitude more complex compared to 360 deg arc shrouding or free-standing blade designs depending on number of blades in a packet. Thus the behavior of a packeted bladed disk could be predicted by the knowledge of abovementioned cases and the calculations are less complex.

Ortolano and co-workers (1977, 1986a, 1986b) have shown improvement in the reliability of blading by utilizing long arc shrouding or, as it is also called, harmonic shrouding. Justification was based on field experience and a force balance type of calculation. The concept of the SAFE Diagram also helps in understanding the success of harmonic shrouding. The successes seem to depend on the fact that in most of the cases the forcing was low order harmonics of the running speed. However, if the forcing is nozzle passing excitation, this type of construction might not work. This kind of situation is also easily explained by the use of the SAFE Diagram. The design evaluation and/or reliability improvements for any type of construction, i.e., 360 deg arc or any other size, can be made on the basis of the SAFE Diagram.

Mode Shape

The deflected shape attained by a vibrating bladed disk at its natural frequency is called its mode shape. This is shown by plotting the relative displacements of different points of the structure.

For a circular symmetric system (e.g., Bladed Disk), there are points that remain stationary in the vibration cycle. These points fall on either a diametral line(s) or a circle(s). The characterization of mode shapes of a packeted bladed disk is done by specifying the number of the nodal diameter (D) and nodal circle (C), e.g., 0C1D, 0C2D, etc. (Fig. 1).

The maximum number of nodal diameters in the bladed disk assembly is half the number of blades (for an even number of blades). For a disk having an odd number of blades, the maximum nodal diameter is (number of blades—1)/2.

There are three variables describing a mode of a bladed disk assembly, namely the natural frequency of vibration, its shape (e.g. 0C1D, 0C3D, etc.), and the speed of the turbine. This information can be displayed as shown in Fig. 2.

The two vertical projections of this surface are shown in Figs. 3(*a*) and 3(*b*). The first plane is the Campbell plane and the other is the SAFE plane.

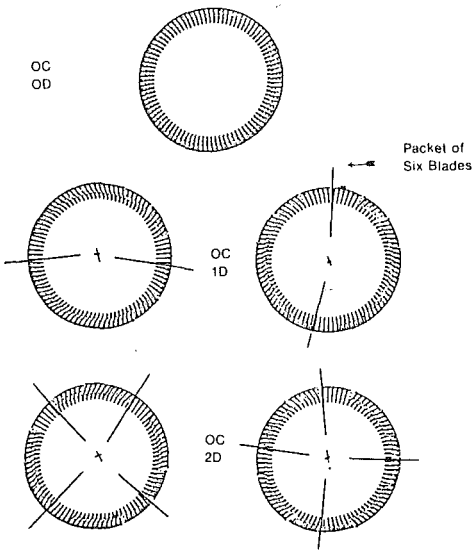

Fig. 1 Typical tangential vibration

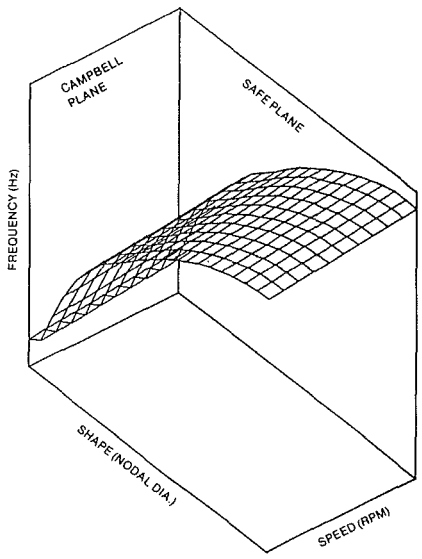

Fig. 2 Mode shape characterization as a surface

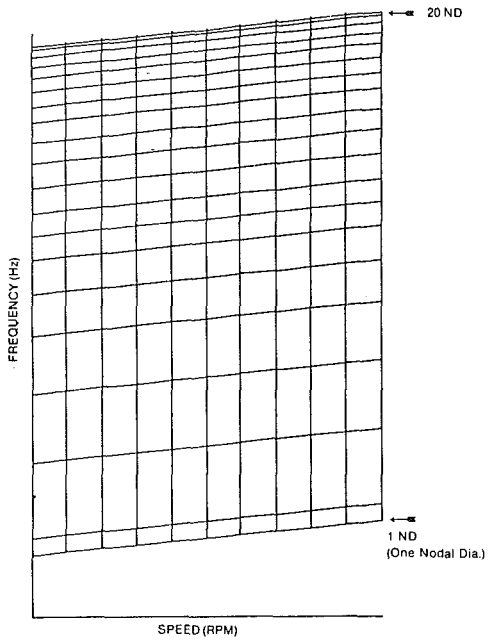

Fig. 3(*a*) Campbell plane

SPEED (RPM)

FIGURE 3a. Campbell Plane

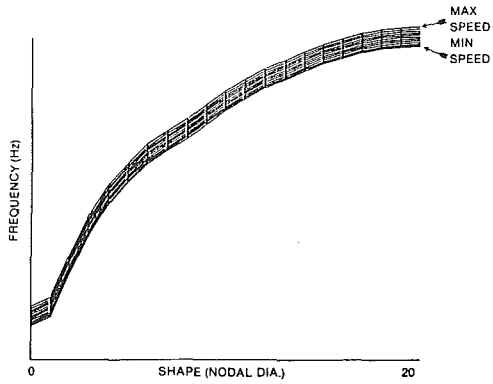

Fig. 3(*b*) SAFE plane

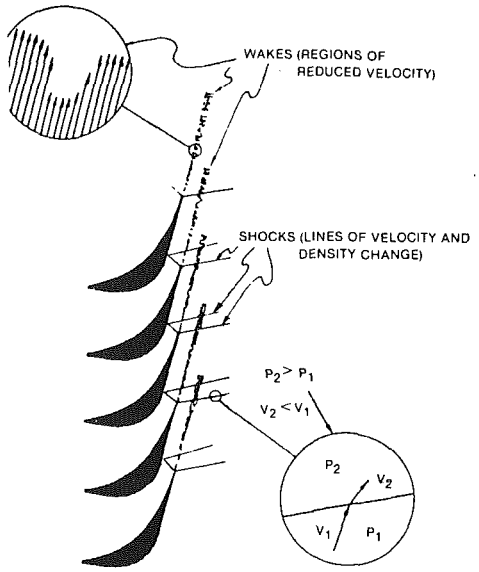

Fig. 4 Flow distortion due to stationary vanes

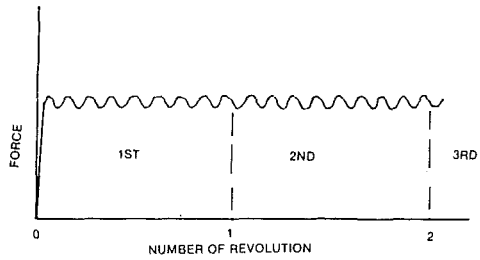

Fig. 5 Force pattern due to nozzles

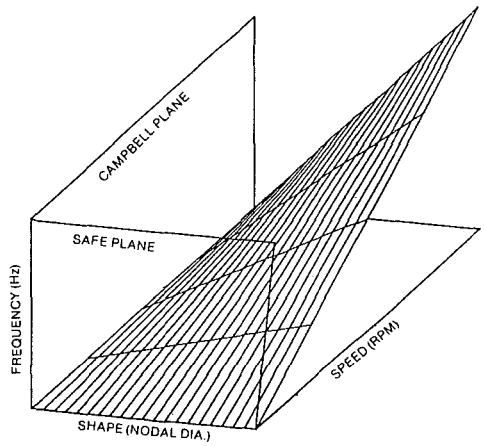

Fig. 6

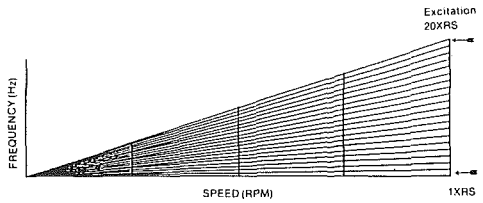

Fig. 7 Projection on Campbell plane

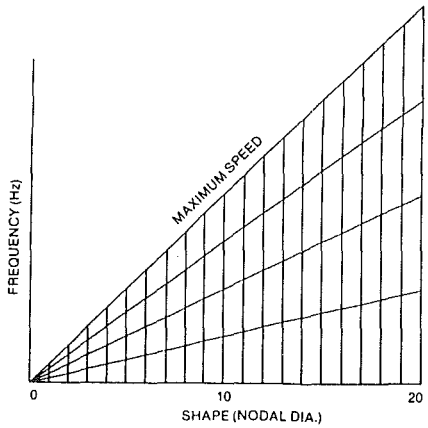

Fig. 8 Projection on SAFE plane

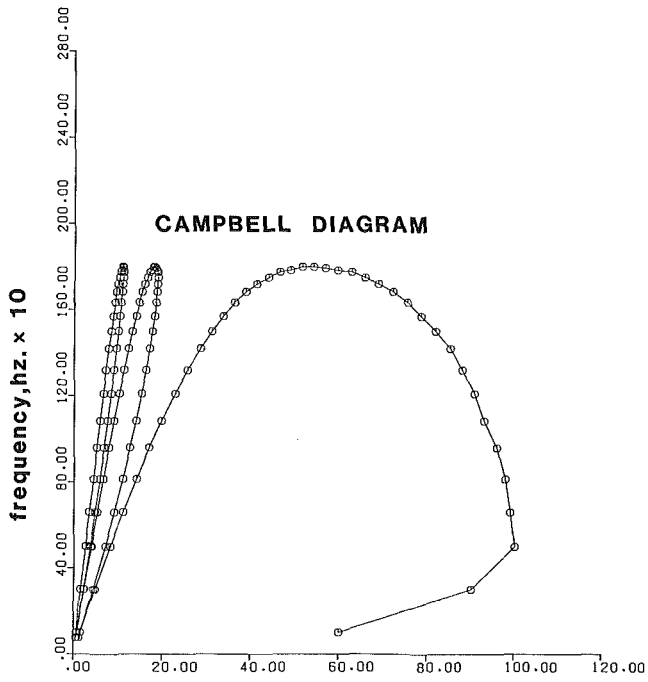

Fig. 9

Fluctuating Forces

Circumferentially oriented flow distortion due to stationary vanes (nozzles) is shown in Fig. 4.

The forces experienced by the blade depend on its relative position with respect to nozzles in one complete revolution. Under the steady-state condition, the same pattern of the force is repeated in successive revolutions making it a periodic force. Such a force is shown in Fig. 5.

These time-periodic forces may be composed of many harmonics. The frequencies of these harmonics are integer multiples of the angular speed of the turbine and also depend on the number of interruptions around the annulus

$$F = F_0 + F_1 \sin(\omega t + \phi_1) + F_2 \sin(2\omega t + \phi_2) + \ldots$$

The frequency (ω) of dynamic forces experienced by the blading is expressed mathematically as follows:

$$\omega = \frac{(M)\ (N)}{60} \text{ Hz}$$

where ω = frequency, Hz; M = number of nozzles, number of interruptions; N = turbine speed, rpm. A three-dimensional view and two vertical projections of the surface represented by the above equations are shown in Figs. 6–8.

One can find the points of resonance by superimposing the

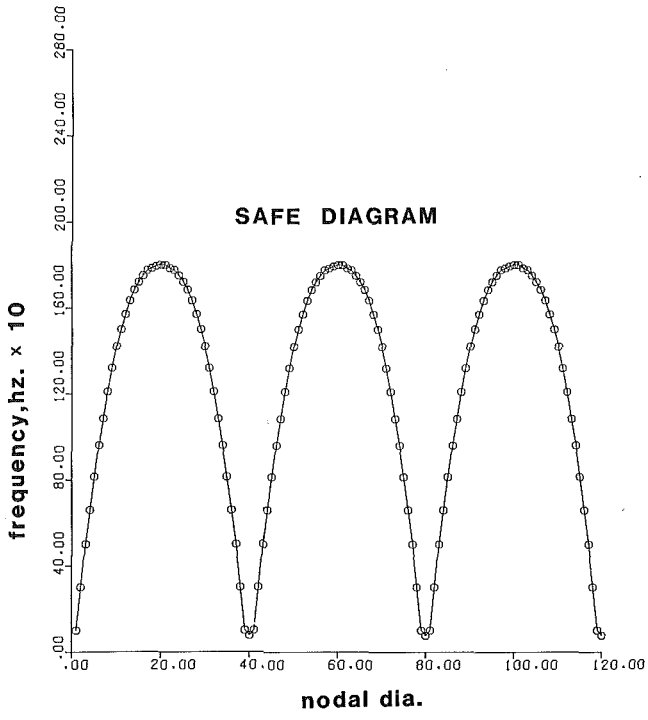

Fig. 10

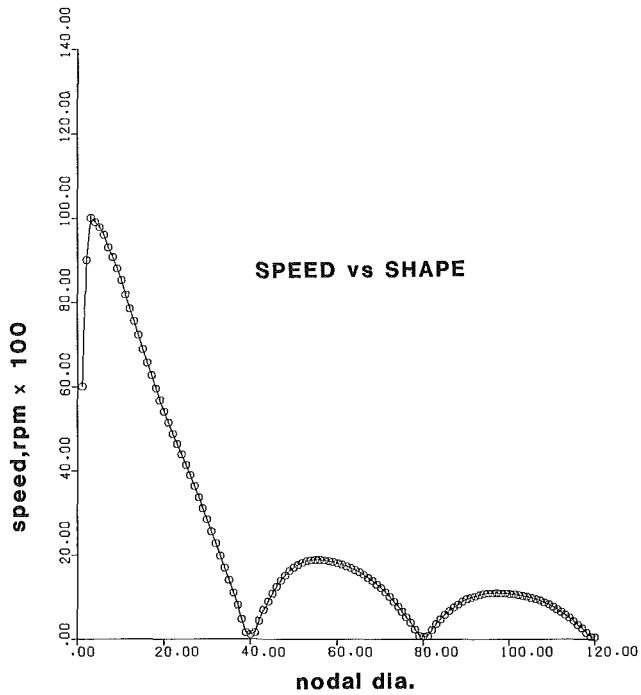

Fig. 11

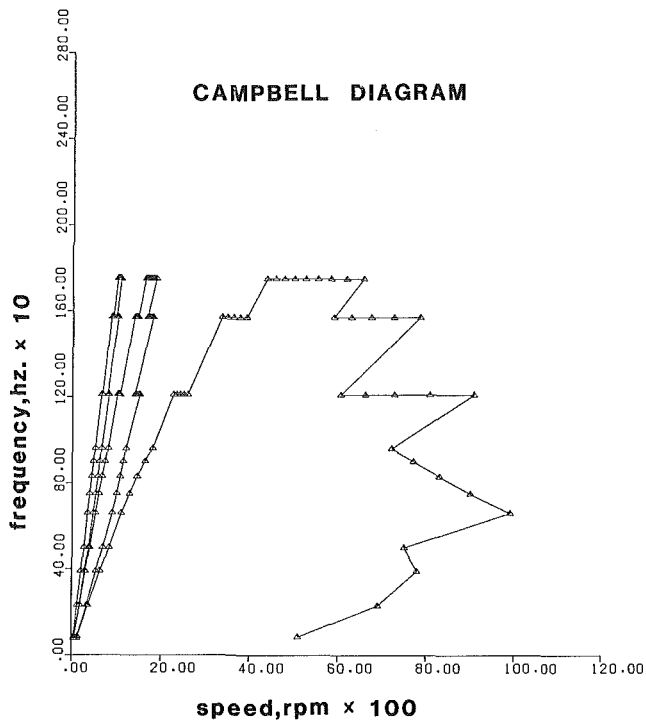

Fig. 12

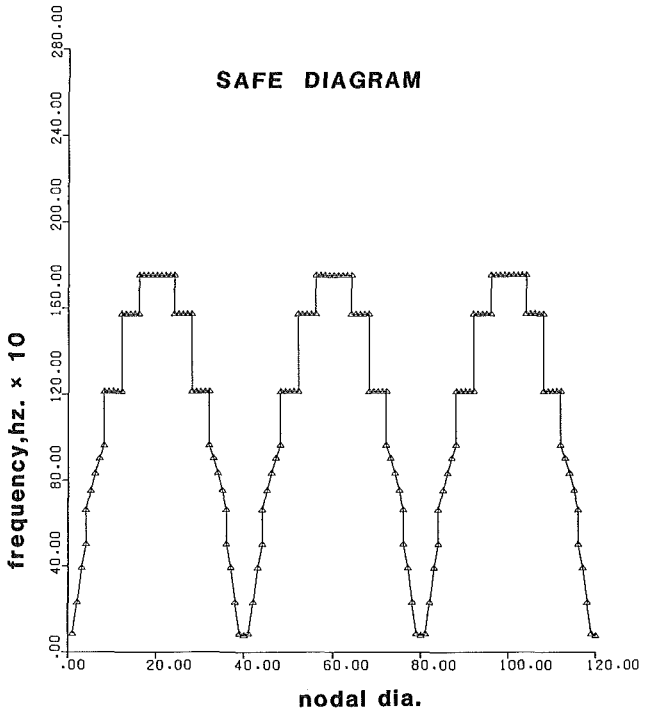

Fig. 13

three-dimensional surfaces of Fig. 2 and Fig. 6. The points of intersection define the resonance points. Planar projections (two vertical and one horizontal) of these points for a case of 360 deg arc shrouding (40 blades) are shown in Figs. 9, 10, and 11 with nodal diameters plotted up to 120. Higher harmonics of excitation (above 20 nodal diameters in this case) can be shown to excite lower orders of disk natural frequency. There is a relationship (Singh, 1984) between mode shapes, shapes of the exciting force, and total number of blades that can be described as follows: The M nodal diameter mode will be excited by a force having a shape of cos $M\theta$, cos $(N-M)\theta$, cos $(N+M)\theta$, cos $(2N-M)\theta$, cos $(2N+M)\theta$, etc. In this case if M is assumed to be 15 and N (the number of blades) is 40, a force of cos 15θ, cos 25θ, cos 55θ, cos 65θ, cos 95θ, etc., will excite the 15 nodal diameter modes but at different speeds. Hence, the M nodal diameter mode can be excited by a force having a cos $L\theta$ shape when $L = n \times N \pm M$, where $n = 0$, 1, 2, etc., and N is the number of blades.

Based on the correlation of frequencies between a blade packet and packeted bladed disk, Singh (1984) and Dello (1987) describe a method to draw the SAFE Diagram. Figures 12, 13,

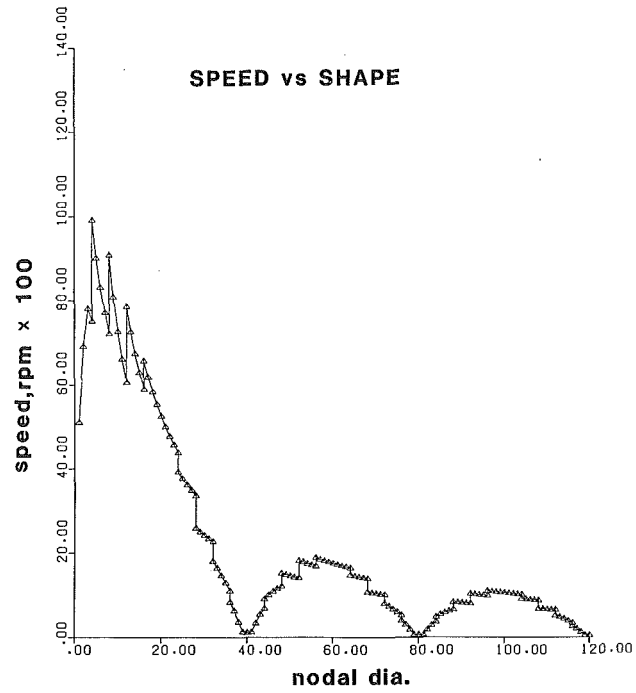

Fig. 14

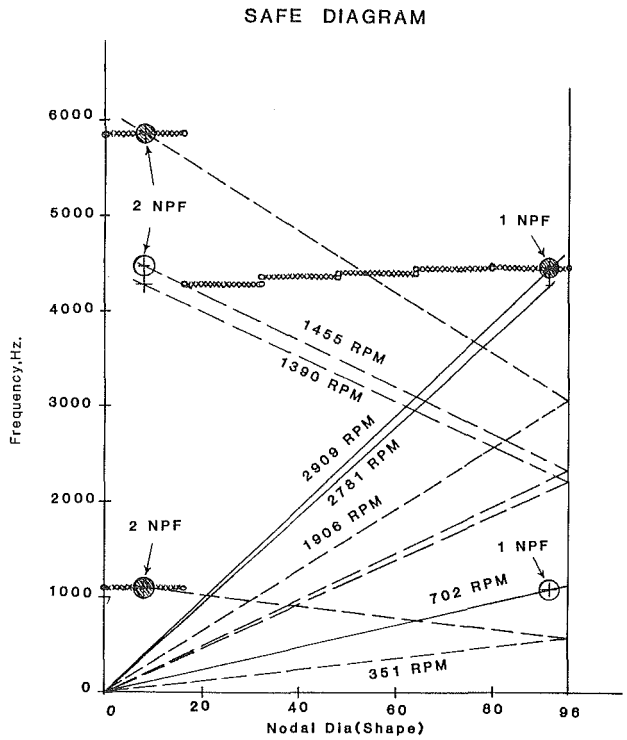

Fig. 16 Explanation of published data by the use of the SAFE diagram

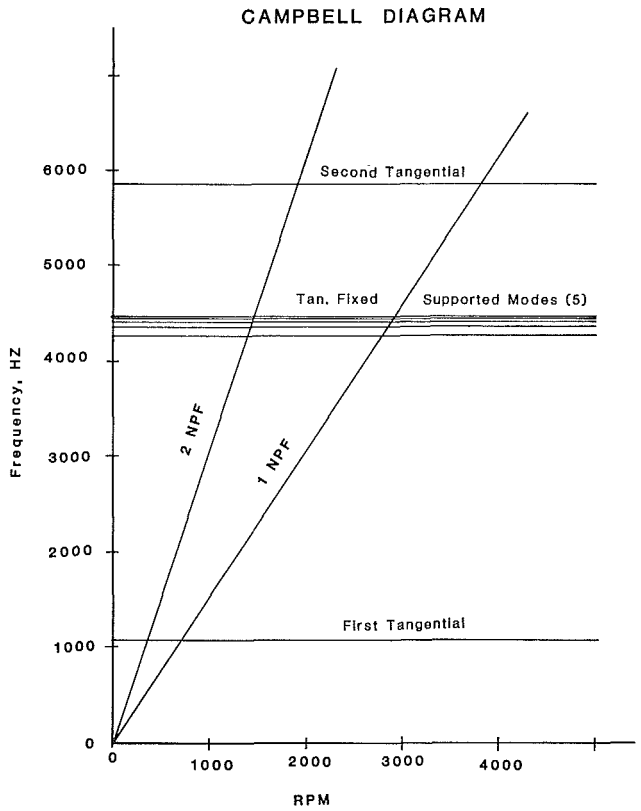

Fig. 15 Campbell diagram

and 14 are similar to Figs. 9, 10, and 11 except now the bladed disk has a packeted assembly of 45 deg arc shrouding. There are five blades in each packet with eight total packets.

Inspection of Figs. 9–14 reveals that the projection of interference points on the SAFE plane shows a remarkable symmetry and repeatability. Information from zero nodal diameter to 20 nodal diameters contains all the essential information.

The usefulness of the SAFE Diagram is demonstrated by published results of other researchers. Data from three ASME publications (Weaver and Prohl, 1956; Provenzale and Skok, 1973; Ortolano and co-workers, 1977, 1986a, 1986b) have been used.

Weaver and Prohl (1956), using an energy method, calculated the response of a packet of blades due to nozzle passing excitation. The turbine disk in their paper contained 6 blades per packet with a total of 192 blades. The number of nozzles was 92. Their response calculations showed that the response of the blades was highest when the nozzle passing frequency coincided with the tangential fixed supported modes. The first tangential mode's response was very low compared to the tangential fixed supported mode's response. A Campbell Diagram is drawn using their data (Fig. 15). A SAFE Diagram using their frequency numbers (assuming that the disk is very stiff in tangential direction) has been constructed. Assuming that the excitation comes from flow distortion due to nozzles, the modes and frequency of concern have been marked by large shaded circles (Fig. 16).

Results from Weaver and Prohl's paper are reproduced alongside the SAFE Diagram (Fig. 17).

The shaded circles are the modes and frequencies where the SAFE Diagram predicts higher responses. Specifically, higher resonances are predicted at the locations listed in Table 1.

Comparing this with Weaver and Prohl's results, it is easily seen that predictions by the SAFE Diagram correlate very well with their results, which were arrived at after numerous calculations. Hence the SAFE Diagram quickly helps locate points of concern that might warrant a further look.

Provenzale and Skok (1973) provided data obtained by a response calculation of the blades under the action of aerodynamic forces. Forces were defined by a frequency and a shape defined by a parameter β. The relationship between β and nodal diameters is β = 360 deg = N nodal diameter (N is the number of blades).

The total number of blades based on the data provided in the paper is estimated to be 264. Based on the theory of bladed disk vibration, there should be 264 frequencies; each of these

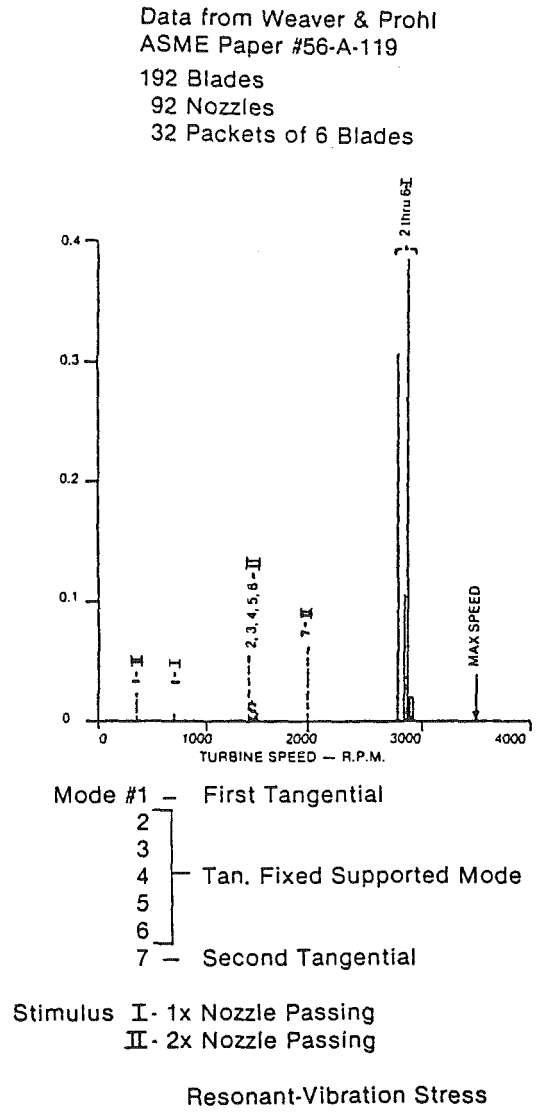

Fig. 17 Resonant-vibration stress

Table 1 Prediction of high resonance points by SAFE diagram

Mode	rpm/frequency	Excitation	Response
First tangential	351/1077	2 × NPF	High
	702/1077	1 × INPF	Low
Tangential fixed support	2909/4461	1 × NPF	High
	1455/4461	2 × NPF	Low
Second tangential	1906/5845	2 × NPF	High

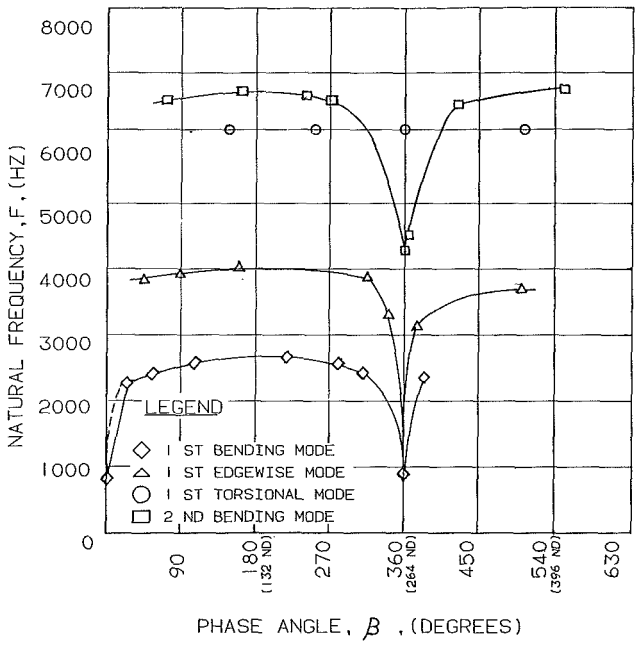

Fig. 18

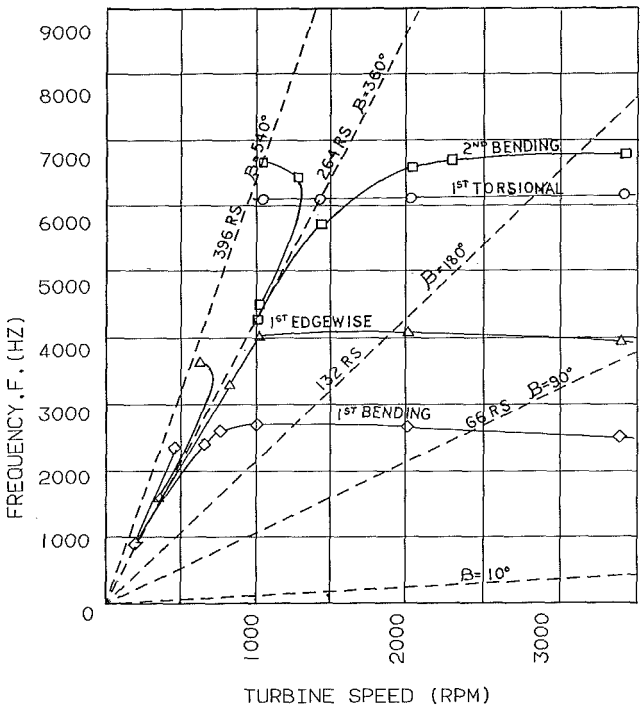

Fig. 19

will be excited by a force shape matching the mode shapes provided frequencies coincide. Figures 2 and 3 of the paper are reproduced here as Figs. 18 and 19 with the addition of definitions followed in this paper. Figure 19 is a Campbell diagram with resonance points (partial). Figure 18 is a SAFE Diagram (partial) showing the periodicity every 180 deg or *N*/2.

This confirms that the SAFE Diagram shows all the resonant points in a bladed disk structure. The final example is based on the work of Ortalano and co-workers (1977, 1986a, 1986b) using long arc shrouding to avoid first tangential mode blade failures caused by low harmonic of running speed excitation. The next to last stage (L-1) of Southern California Edison's Huntington Beach Station unit No. 2 experienced blade failures after many years of operation. The failure was attributed to an upward shift in the blade frequency due to changes in the root fixity. This was caused by a corrosion buildup in the root groove clearances. A design change was made to long arc shrouding of 42 and 43 blades (four groups) from the previous 5 and 6 blades per group. It is estimated that there are 170 blades per wheel. The SAFE Diagram can be used to explain why the six-blade packet is more susceptible to failure than the 42-blade packet. It also can be used to identify test frequency mode shapes and tell what frequencies may have been missed in the modal test.

The test and analytical data available from the Huntington Beach Station unit No. 2 (Ortolano and co-workers, 1986a, 1986b) are Table 2—Stationary Blade Frequency for a Six-Blade Group, Table 3—Rap Test of a 42-Blade Group, and Table 4—A Finite Element Blade Frequency Calculation of a

Table 2 SCE Huntington Beach model test results, Stage L-1, six-blade group

Mode	Frequency	Shape
1	98.4	Tangential
2	101.2	Tangential
3	103.5	Tangential
4	114.2	Axial
5	121.9	Axial
6	122.1	Axial
7	129.7	Axial
8	137.8	Axial
9	143.6	Axial
10	147.2	Axial
11	149.1	Axial
12	152.7	Axial
13	153.70	Axial
14	199	Axial X Mode
15	206.8	Axial
16	236.78	Axial
17	238.2	Axial
18	241.3	Axial
19	258.1	Axial
20	259.9	Axial
21	284.6	Axial
22	306.2	Axial
23	310.0	Axio-Torsional
24	324.5	Axio-Torsional
26	341.4	Axio-Torsional
27	344.5	Axio-Torsional
28	347.9	Axio-Torsional
29	351.3	U-Mode
30	353	Axio-Torsional

Table 3 SCE/Huntington Beach station, stage L-1, 42-blade group, rap test

Mode	Frequency (Hz)	Description
1	102–105	Predominantly tangential with axial *X*
2	119	Similar to axial *U* (closely coupled with a mode at 113 Hz)
3	126	Axial 4th or 5th nodal diameter
4	134.8	Axial 5th or 6th nodal diameter
5	149.5	Axial 8th nodal diameter
6	168.9	Axial 10th nodal diameter
7	197.1	Axio-torsional with large disk rim motion
8	225	Tangential fixed support
9	243	Tangential fixed support
10	246	Tangential fixed support
11	271.2	Tangential fixed support
12	281.0	Tangential fixed support
13	303.0	Axial and tangential fixed support
14	331	Axial and tangential fixed support
15	346.0	Tangential fixed support
16	371.2	Tangential fixed support with disk motion
17	393.0	Large disk motion with tangential fixed support
18	453.5	Tangential fixed support with disk motion
19	474	Unidentifiable due to nonlinearities in system

Table 4 Calculated frequency (Hz) from finite element analysis

0. rpm	Mode	1800. rpm	Difference	Percent
94	Tangential	110.	16	17.0
124	Axial	137.	13	10.5
191	Axial	108.	17	8.9
237	Axial	257.	20	8.4
357	Axial	375.	18	5.0
447	Axial	462.	15	3.4

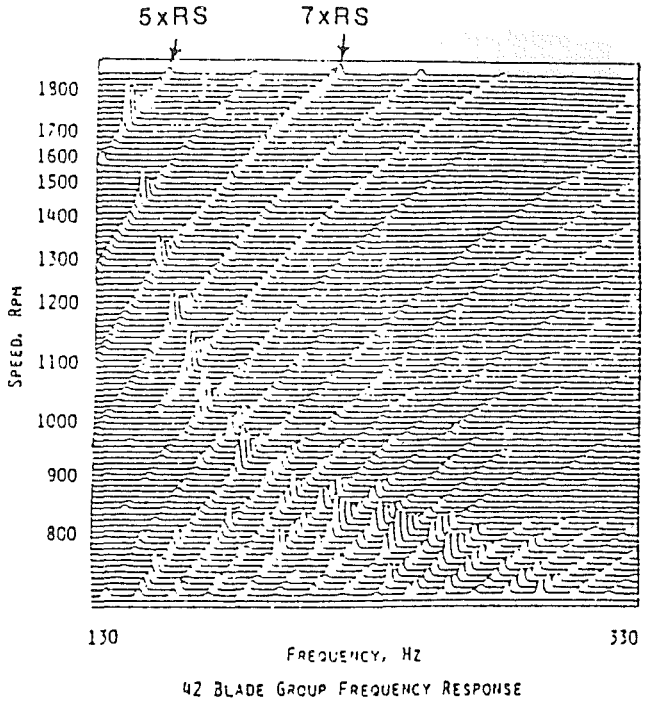

Fig. 20 Cascade plot

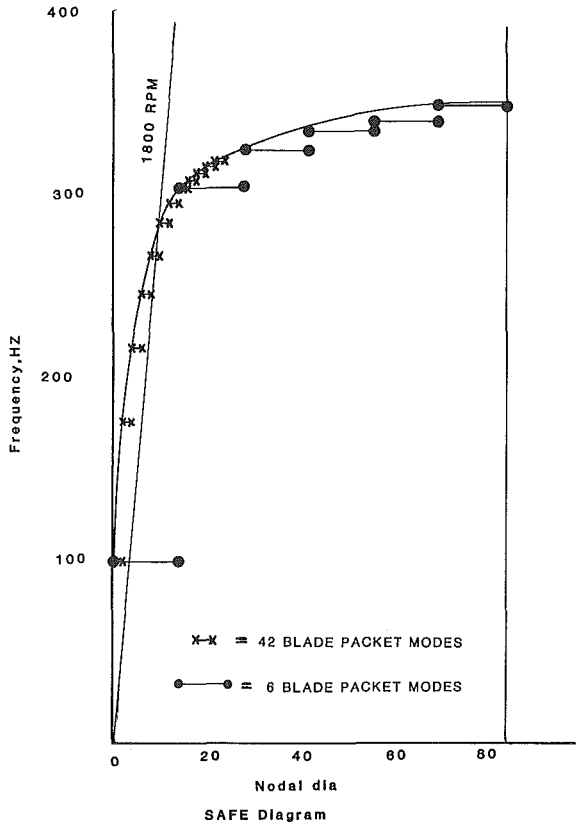

Fig. 21 SAFE diagram

Six-Blade Group at Zero and 1800 rpm. Using the modal test data of the six-blade group in Table 2, a SAFE Diagram can be drawn for tangential frequencies only using the rules of Singh and Schiffer (1982), Singh (1984), and Dello (1987). This is shown in Fig. 21. The behavior of a completely shrouded disk can be approximated by joining the extreme left points of Fig. 21. The behavior of a 42-blade group (four groups per wheel) can now be predicted. This is possible to do for tangential modes because the disk is very stiff and does not influence the tangential natural frequencies. There will be 42 first family basic modes, and at each of these basic modes (steps) there will be four additional modes because there are four blade groups in the wheel. The estimated frequencies with the associated mode shapes are shown in the SAFE Diagram of Fig. 21. By drawing in the operating speed line of 1800 rpm

in the SAFE Diagram it can be seen that it falls between the third and fourth nodal diameters (running speed harmonic) of the first tangential frequency of the six-blade group. Since the six-blade group has first tangential frequency mode shapes up to 14 nodal diameters (14 × RS) the blade frequency must remain tuned between 90 Hz and 120 Hz (3 × RS and 4 × RS) in order to remain resonance free. For the 42-blade group the first tangential frequency only has mode shapes up to two nodal diameters and therefore will never be resonant with 3 or 4 times running speed excitation. The 42-blade group disk will have higher modes with 8, 9, and 10 nodal diameter mode shapes that will be resonant at 1800 rpm as shown in Fig. 21. However, their resonant response will be lower than a first tangential mode resonance, thus making it a more reliable design.

The estimated frequencies and mode shapes of the 42-blade group disk from the SAFE Diagram of Fig. 21 will now be compared with the RAP test data of Table 3, which was also done on a 42-blade group disk. Notice how the tangential fixed supported modes of the six-blade group disk in Table 2 were in the 310 to 348 Hz range. For the 42-blade group disk the tangential fixed supported modes have dropped to the 225 to 281 Hz range as is shown in Table 3. This frequency change was predicted in the SAFE Diagram of Fig. 21. Table 5 gives a correlation between the predicted tangential fixed-supported frequencies of the SAFE Diagram and the rap test results of Table 3.

The cascade plot of Fig. 20 can be used to plot frequencies on the SAFE Diagram when it is realized that 4 × RS will excite a four-nodal diameter bladed disk frequency, 5 × RS

Table 5 Frequency and mode prediction by SAFE diagram

Frequency, Hz, 42-blade rap test	Estimated from SAFE diagram	Mode designation
102–105	Same data	0, 1, 2 ND
–	185.	2, 3, 4 NC
225	225.	4, 5, 6
243	–	
246	–	
	253	6, 7, 8
270	270	8, 9, 10
281	–	
	285	10, 11, 12
	295	12, 13, 14
303	303	14, 15, 16
	307.5	16, 17, 18
	313.	18, 19, 20
	315.	20, 21, 22

Table 6 Frequency and mode prediction from cascade plot

XRS	rpm	Frequency (Hz)	Mode shapes; nodal diameter
5	1686	141.	5
6	1470	147.	6
7	1307	152.5	7
8	1181	157.5	8
9	1093	164.	9
10	1020	170.	10
11	970	178.	11
12	920	184.	12
13	900	195.	13
14	869.,910	203.,212.	14
15	870.	217.5	15
16	830	221.	16
17	831	238.	17
18	810	243.	18
19	808.	255.	19
20	780.,790	260,263	20
21	770.	269.5	21
22	757	277.5	22
23	750.	287.5	23
24	750.	300.	24
25	738	307.5	25
26	733	318.	26

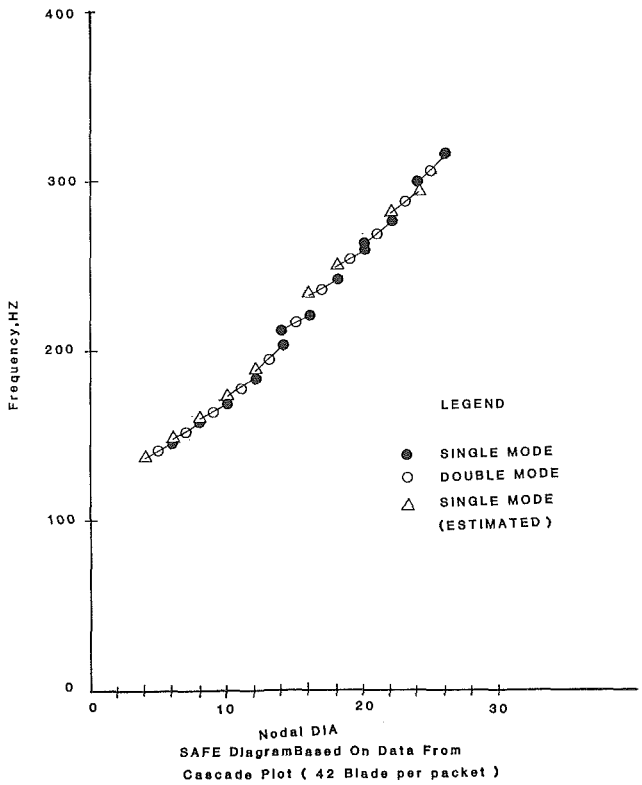

Fig. 22 SAFE diagram based on data from cascade plot (42 blades per packet)

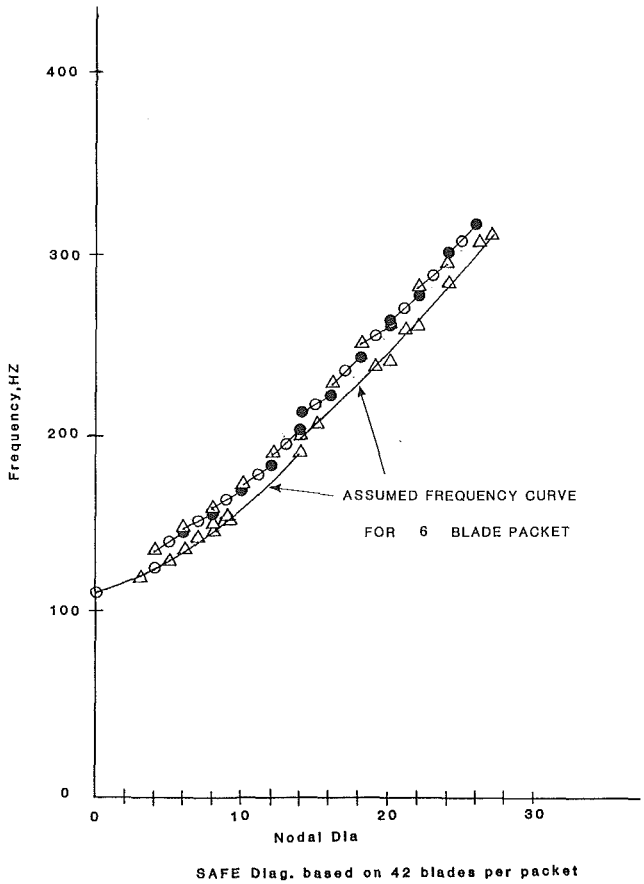

Fig. 23 SAFE diagram based on 42 blades per packet

Table 7 Inferred frequency from SAFE diagram based on Fig. 23

Frequency (Hz)		
Modal test	SAFE diagram (inferred)	Mode shape
114		0 ND
–	115	1 ND
–	118	2 ND
121.9	–	2 ND/3 ND
122.9	123.3 ND	2 ND/3 ND
–	127.	4 ND
129.7	132.	5 ND
137.8	137.5	6 ND
143.6	143.5	7 ND
147.2		8 ND
149.1	149.	8 ND
152.7	155.	9 ND
153.7		
–	162.	10
–	169.	11
–	176.	12
–	184.	13
199.	199.,190	14
206.8	205.	15
–	213.	16
–	221.	17

will excite a five-nodal diameter bladed disk frequency, etc. Identifying the frequency and running speed harmonic provides the necessary data points to plot the SAFE Diagram of Fig. 22. Table 6 has the same data reduced to tabular form of frequency, mode shape, and speed for the 42-blade group. The open circles of Fig. 22 represent two modes and the solid circles represent a single mode. The staircaselike feature is typical of packeted bladed disk. For a bladed disk with only four-blade groups, the even-numbered nodal diameters modes will split in two distinct frequencies while the odd-numbered nodal diameters will have two modes with equal frequencies (Singh and Schiffer, 1982; Singh, 1984; Dello, 1987). The SAFE Diagram of Fig. 22 can be compared to the rap test data of Table 3 since both are for a 42-blade group disk. The cascade plot shows axial modes and when these frequencies are compared to the rap test axial frequencies of the same nodal diameter (Table 3 versus Table 6), the results are very close, except for centrifugal stiffening effects, which are included in the cascade plot.

The SAFE Diagram can also be used to help identify mode shapes of blade frequency test data even with a minimum of information. The axial frequency data in Table 2 were plotted on the SAFE Diagram of Fig. 23 using only the assumption that the 114.2 Hz blade frequency is the zero nodal diameter axial mode and the 199 Hz blade frequency is the first axial x (or axial rocking) mode. This would make it the 14th nodal diameter or 29th mode assuming there are 28 packets of six-blade groups. Knowing the typical behavior of a packeted bladed disk, a curve can be drawn between these two points. The intermediate frequency data between these two points can be plotted to see how close it lines up with the estimated curve. Table 7 lists the inferred frequency for each nodal diameter (mode shape) from Fig. 23 and also shows how the test data of Table 2 line up very closely with the inferred frequencies. Also shown on Fig. 23 are the data from Fig. 22 for comparison. The difference is that Fig. 22 includes centrifugal stiffening and is for a 42-blade packet. In this manner the mode shapes of test frequencies can be identified very closely or exactly by using the SAFE Diagram concept.

References

Dello, J., 1987, "Frequency Evaluation of a Steam Turbine Bladed Disk," *Turbomachinery International*, Jan/Feb.

Dye, R. C. F., and Henry, T. A., 1968, "Vibration Amplitudes of Compressor Blades Resulting From Scatter in Blade Natural Frequencies," ASME Paper No. 68-WA/GT-3.

El-Bayoumy, and Srinivasan, A. V., 1975, "Influence of Mistuning on Rotor-Blade Vibrations," *AIAA Journal*, Vol. 13, No. 4, pp. 460–464.

Ewins, D. J., 1969, "The Effects of Detuning Upon the Forced Vibration of Bladed Discs," *Journal of Sound Vibration*, Vol. 9, pp. 65–79.

Ewins, D. J., 1970, "A Study of Resonance Coincidence in Bladed Discs," *Journal of Mechanical Engineering Science*, Vol. 12, No. 5.

Ewins, D. J., 1975, "Vibration Modes of Mistuned Bladed Discs," ASME Paper No. 75-GT-114.

Ortolano, R. J., LaRosa, J. A., and Welch, W. P., 1977, "Long Arc Shrouding—A Reliability Improvement for Untuned Steam Turbine Blading," ASME Paper No. 77-JPGC-Pwr-12.

Ortolano, R. J., and Burton, W. A., 1986a, "Field Testing of Long Arc Shrouding and Continuous Tied Blading in a L-1 Stage at SCE," Steam Turbine Blade Reliability Workshop, Electric Power Research Institute.

Ortolano, R. J., Burton, W. A., and McCloskey, T. H., 1986b, "Design and Field Evaluation of L-1 Blades Using Long Arc Shrouding," ASME Paper No. 86-JPGC-Pwr-39.

Provenzale, G. E., and Skok, M. W., 1973, "A Cure for Steam Turbine Blade Failures," ASME Paper No. 73-PET-71.

Singh, M., and Schiffer, D., 1982, "Vibrational Characteristics of Packeted Bladed Disc," ASME Paper No. 82-DET-137.

Singh, M., 1984, "Safe Diagram—A Turbodyne Evaluation Tool for Packeted Bladed Disc Assembly," Dresser-Rand, Steam Turbine Technology, Paper No. ST-16.

Weaver, F. L., and Prohl, M. A., 1956, "High Frequency Vibration of Steam Turbine Buckets," ASME Paper No. 56-A-119.

R. Bahree
Graduate Student.

A. M. Sharan
Associate Professor.

Faculty of Engineering
Memorial University of Newfoundland,
St. John's, Newfoundland, Canada A1B 3X5

J. S. Rao
Professor.
Dept. of Mechanical Engineering,
I.I.T., Hauz Khas,
New Delhi, India

The Design of Rotor Blades Taking Into Account the Combined Effects of Vibratory and Thermal Loads

The present work involves the design of rotor blades based on the thermal as well as centrifugal and nozzle excitation forces in the transient state. The finite element analysis has been used to calculate these stresses. The nozzle excitation forces have been modeled as a series of impulses occurring at instants of time known from the solution of kinematic equations.

1 Introduction

It is quite desirable to have increased gas pressures and temperatures for the efficient operation of turbomachinery. However, the higher temperatures are limited by a lack of suitable materials that can withstand higher temperatures. If a turbine blade is heated too rapidly it causes uneven temperature distribution, and as a result of this, severe thermal stresses are developed within the material. Since the three-dimensional geometry of the blade is quite complicated, the analysis of the thermal process also becomes very involved. In addition, the material properties vary with temperature and the radiative heat transfer process adds to the complexity of the problem.

Calculation of the vibratory stresses for a twisted, asymmetric, and tapered turbine blade, without even considering the thermal effects, would itself be a challenging work. This is because the stresses vary from point to point at any cross section and also along the height of the blade. In addition, the modeling of the transient forces requires solution of kinematic equations. Even the centrifugal forces in the transient region are time variant.

The heat transfer process in gas turbine blades has been studied by Mukherjee (1978) and Maya et al. (1978). In their work they considered the heat exchange process at the surface by convection only. They also calculated the transient thermal stresses; however, their analyses lack accuracy in predicting thermal stresses and temperature distributions because the radiative heat exchange mechanism is quite significant at the operating temperatures. In addition, they investigate the stresses at only a few points, such as the leading edge, and trailing edge, and at the core of the a cross section of the blade, and base their analyses on the assumption that the maximum stresses would take place at one of these points during the transient period. In their work they do not include the effect of forces due to nozzle excitation and centrifugal effects.

Contributed by the Power Division for publication in the JOURNAL OF ENGINEERING FOR GAS TURBINES AND POWER. Manuscript received at ASME Headquarters May 12, 1988.

To study the dynamics of the rotor blade, Subrahmanyam and Leissa (1985) and Hutchinson and Zillmer (1986) modeled the blade as having a rectangular cross section and carried out the free vibration analysis in terms of the bending modes. The influence of taper was studied by Banerji and Williams (1985). Sisto and Chang (1984) used a finite element method to calculate the natural frequencies; however, their modeling was only appropriate for thin, high-aspect-ratio blades. Among other works one should refer to the research carried out by Sato (1980) and Gupta (1985).

Considering the works of the researchers mentioned above, it would be an important contribution to calculate the stresses not only due to thermal effects but also due to other dynamic forces, and at every instant of time one should look for the locations where the blade is subjected to the maximum stresses in three-dimensional space. This is the objective of the present investigation.

2 Mathematical Formulation

2.1 Transient Thermal Analysis. The governing three-dimensional partial differential equation for heat conduction in any solid can be written as

$$\frac{\partial}{\partial x}\left(K_x\frac{\partial T}{\partial x}\right)+\frac{\partial}{\partial y}\left(K_y\frac{\partial T}{\partial y}\right)+\frac{\partial}{\partial z}\left(K_z\frac{\partial T}{\partial z}\right)+Q=\rho c\frac{\partial T}{\partial t} \quad (1)$$

with the boundary condition

$$K_x\frac{\partial T}{\partial x}l_x+K_y\frac{\partial T}{\partial y}l_y+K_z\frac{\partial T}{\partial z}l_z$$

$$+q+h(T-T_\infty)+\sigma_s\epsilon(T^4-T_\infty^4)=0 \quad (2)$$

on the pressure and suction surfaces of the turbine blade.

The equivalent functional formulation of equation (1) and its boundary condition can be written in the form shown by Reddy and Sharan (1985) as

$$X=\int_V \frac{1}{2}\left[K_x\left(\frac{\partial T}{\partial x}\right)^2+K_y\left(\frac{\partial T}{\partial y}\right)^2+k_z\left(\frac{\partial T}{\partial z}\right)^2+\rho cT\frac{\partial T}{\partial t}\right]dV$$

$$+\int_S\left[qT+\frac{h}{2}(T-T_\infty)^2+\sigma_s\epsilon\left(\frac{T^5}{5}-T_\infty^4T\right)\right]dS \tag{3}$$

Here V is the volume of the rotor blade and S is its surface area.

The functional X can be minimized by equating its first derivative with respect to vector $\{T^G\}$ to zero and can be rewritten in terms of the global matrices using finite element analysis as

$$[CP^G]\frac{\partial\{T^G\}}{\partial t}+[A^G]\{T^G\}=\{F_C^G\}-\{F_R^G\} \tag{4}$$

Here $\{F_R^G\}$ is the global force vector due to radiative heat transfer and contains terms of higher powers of the nodal temperatures. Equation (4) becomes nonlinear due to these higher powers of the nodal temperatures. The details of the global force vector due to radiative heat transfer can be found in Appendix A. These nonlinear systems of equations are solved in the time domain using the Crank-Nicolson finite difference scheme, which is unconditionally stable. Thus equation (4) can be rewritten as

$$\left[[A^G]+\frac{2}{\Delta t}[CP^G]\right]\{T^G\}_{t+\Delta t}=\left[\frac{2}{\Delta t}[CP^G]-[A^G]\right]\{T^G\}_t+\{F_C^G\}_{t+\Delta t}+\{F_R^G\}_{t+\Delta t}+\{F_R^G\}_t \tag{5}$$

Equation (5) can be solved for the unknown nodal temperature vector at time $t+\Delta t$ since the nodal temperatures at time t are known. Initially the vector $\{T^G\}_{t+\Delta t}$ is assumed and substituted on the right-hand side of equation (5). This makes the right-hand side of equation (5) a constant and thus the resulting system of equations can now be solved for the unknown temperatures $\{T^G\}_{t+\Delta t}$. If the calculated and the assumed nodal temperatures at $t+\Delta t$ do not meet the convergence criteria then the calculated nodal temperatures become the assumed nodal temperatures for the next iteration.

In the present problem, there is no heat generation and also there are no specified heat fluxes; hence the terms containing Q in equation (1) and q in equations (2) and (3) are respectively equal to zero. The heat transfer problem here has been modeled as a two-dimensional heat flow problem. This is because it has been shown by Maya et al. (1978) that in the transient analysis of turbine blades, the heat flow in the z direction is negligible in comparison to other directions. Hence, the $\partial T/\partial z$ terms in equations (1), (2), and (3) would respectively be equal to zero.

The thermal stresses in the blade are caused by the uneven temperature distribution in any cross section. It has been established by Maya et al. (1978) that the most important stress component is σ_z and all other normal and shear stresses are negligible in comparison to this stress. If the temperature distribution across any cross section is known, then σ_z can be calculated according to Littler (1969) and Mukherjee (1978) as

$$\sigma_z=E(T)\left[\frac{\sum_{e=1}^{n}A^eE(T)\alpha_t(T)\Delta T_{av}}{\sum_{e=1}^{n}A^eE(T)}+x_c\frac{\sum_{e=1}^{n}A^eE(T)\alpha_t(T)\Delta T_{av}x_c^e}{\sum_{e=1}^{n}A^eE(T)(x_c^e)^2}+y_c\frac{\sum_{e=1}^{n}A^eE(T)\alpha_t(T)\Delta T_{av}y_c^e}{\sum_{e=1}^{n}E(T)(y_c^e)^2}-\alpha_t(T)\Delta T_{av}\right] \tag{6}$$

In this equation, T_{av} is the average temperature of the three nodes of a triangular element shown in Fig. 2 and ΔT_{av} is the difference of T_{av} at any instant of time and T_{av} at the initial temperature when there was no stress. In the present analysis, the modulus of elasticity $E(T)$ and the coefficient of thermal expansion $\alpha_t(T)$ are evaluated at every time instant at the average temperature of the element. The variation of the material properties of the blade with its temperature is shown in Table 1 (Cubberly, 1980).

2.2 Finite Element Model for Vibratory Analysis. The

Nomenclature

$[D]$ = material property matrix
$[B]$ = strain-displacement matrix
$[N]$ = shape function matrix
$[CP]$ = capacitance matrix
$[A]$ = conduction matrix
$[C]$ = damping matrix
$[K]$ = stiffness matrix
$[M]$ = consistent mass matrix
$[J]$ = Jacobian matrix
$[\psi]$ = Transformation matrix
$[\bar{K}]$ = reduced stiffness matrix
$[\bar{M}]$ = reduced mass matrix
$[\bar{C}]$ = reduced damping matrix
$\{T\}$ = nodal temperature vector
$\{\gamma\}$ = strain vector
$\{F_R\}$ = force vector due to radiation
$\{F_C\}$ = force vector due to convection
$\{F\}$ = dynamic force vector
$\{\bar{F}\}$ = reduced dynamic force vector
$\{u\}$ = nodal displacement vector
T_∞ = gas temperature
S = surface subjected to convection, radiation, and specified heat flux
X = a functional
θ_p = angle of pretwist
θ = angle between two nozzles
θ_R = angle of pretwist at root
θ_T = angle of pretwist at tip
θ_N = angle subtended by a nozzle at the center of rotation
ω = angular speed of the rotor
ω_{nk} = natural frequency of k^{th} mode
ω_{dk} = damped natural frequency of k^{th} mode

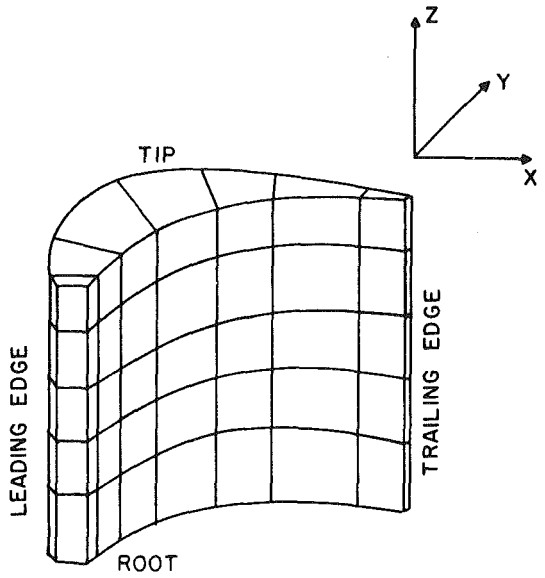

Fig. 1 Turbine blade finite element model

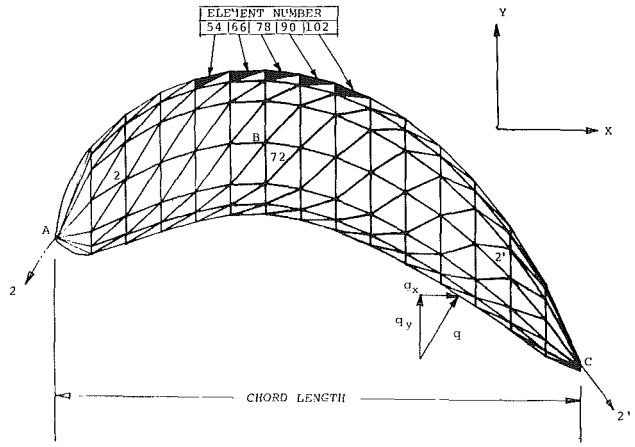

Fig. 2 Finite element discretization of the turbine blade cross section

Table 1 Variation of the material properties of the blade with temperature ($\rho = 8562$ kg/m^3)

Temperature (°C)	E (GPa)	σ yield (MPa)	α (μm/m°k)	c (J/Kg)	K (W/m°K)
21	220	840	11.9	400	12.7
93	215	842	12.07	400	13.0
205	215	844	12.29	395	13.5
315	195	846.3	12.4	420	13.8
425	190	848.4	12.8	440	15.1
540	185	850	13.1	420	15.2
650	175	855	13.5	460	17.3
760	170	840	14.0	480	14.0
870	160	760	14.8	500	21.6
980	145	470	15.8	525	24.9

mathematical modeling for the three-dimensional vibratory analysis of the turbine blade was accomplished through use of three-dimensional solid finite elements. In order to map the complex geometry of the turbine blade, accurately, the 20-noded, C° continuity, curved, "serendipity" isoparametric finite element can be chosen. This type of element is shown in Figs. 3(*a*) and 3(*b*), respectively. C° continuity implies that the field variables (displacements) here are continuous across the faces of the element. The advantage of this isoparametric element is that the same quadratic interpolation functions are used to describe the geometry of the element and its displacement field. The interpolation functions for this 20-noded element were obtained from Zienkiewicz (1977) and can be seen in Appendix B.

The element stiffness matrix $[K^e]$ for a 20-noded isoparametric element can be expressed as

$$[K^e] = \underset{60\times 60}{\int_{-1}^{+1}\int_{-1}^{+1}\int_{-1}^{+1}} [B(\xi,\eta,\zeta)]^T[D][B(\xi,\eta,\zeta)]\,|J(\xi,\eta,\zeta)|\,d\xi d\eta d\zeta \tag{7}$$

$60\times 6 \quad 6\times 6 \quad 6\times 60$

The $[B]$, matrix which relates the nodal displacements to the strains in the element, is given by

Nomenclature (cont.)

ξ_κ = damping ratio of k^{th} mode
n = number of elements
c = specific heat
h = convective heat transfer coefficient
K_x = thermal conductivity in the x direction
K_y = thermal conductivity in the y direction
K_z = thermal conductivity in the z direction
l_x, l_y, l_z = direction cosines normal to the surface
Q = heat generated within the body
q = specified heat flux
W_i, W_j, W_k = weights used in Gaussian quadrature
t = time
Δt = time increment
Δt_{imp} = duration of the impulse
Δt_0 = time gap between occurrence of two impulses
ρ = mass density of the material
σ_s = Stefan-Boltzmann constant
$\sigma_x, \sigma_y, \sigma_z$ = normal stresses
$\tau_{xy}, \tau_{yz}, \tau_{xz}$ = shear stresses
α_t = coefficient of thermal expansion
α = acceleration
ϵ = emissivity of the body
ξ, η, ζ = local coordinate directions
V = volume of the blade
NG = number of Gauss points
x_c, y_c = coordinates of the centroid of the triangular element
E = modulus of elasticity
A = area of cross section
R = radius of the rotor
σ_d = distortion energy stress
σ_d^* = normalized distortion energy stress
G = global
e = elemental

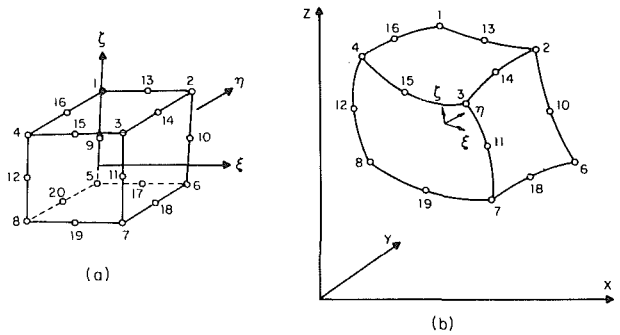

Fig. 3 Solid isoparametric "serendipity" 20-noded element: (*a*) local coordinate system; (*b*) global Cartesian coordinate system

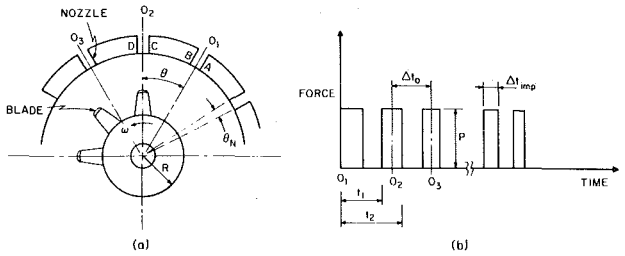

Fig. 4(*a*) Schematic of the blade, nozzle, and rotor configuration; (*b*) representation of the nozzle excitation forces as a series of impulses

The [*B*], matrix which relates the nodal displacements to the strains in the element, is given by

$$[B] = \underset{6\times 60}{[P]} \quad \underset{6\times 9}{[Q]} \quad \underset{9\times 9}{[R]} \quad \underset{9\times 60}{} \tag{8}$$

The details of matrices [*P*], [*Q*], and [*R*] can be seen in Appendix B.

Similarly, the elemental mass matrix $[M^e]$ for a 20-noded isoparametric element can be expressed as

$$\underset{60\times 60}{[M^e]} = \int_{-1}^{+1}\int_{-1}^{+1}\int_{-1}^{+1} \underset{60\times 3}{[N(\xi,\eta,\zeta)]^T} \underset{3\times 3}{\rho} \underset{3\times 60}{[N(\xi,\eta,\zeta)]} |J(\xi,\eta,\zeta)|\, d\xi d\eta d\zeta \tag{9}$$

The Jacobian matrix [*J*] is

$$[J] = \begin{bmatrix} \dfrac{\partial x}{\partial \xi} & \dfrac{\partial y}{\partial \xi} & \dfrac{\partial z}{\partial \xi} \\ \dfrac{\partial x}{\partial \eta} & \dfrac{\partial y}{\partial \eta} & \dfrac{\partial z}{\partial \eta} \\ \dfrac{\partial x}{\partial \eta} & \dfrac{\partial y}{\partial \eta} & \dfrac{\partial z}{\partial \eta} \\ \dfrac{\partial x}{\partial \zeta} & \dfrac{\partial y}{\partial \zeta} & \dfrac{\partial z}{\partial \zeta} \end{bmatrix} \tag{10}$$

The element J_{11} of [*J*] can be written as

$$J_{11} = \frac{\partial x}{\partial \xi} = \frac{\partial}{\partial \xi} \underset{1\times 20}{([N_i]^e)} \quad \underset{20\times 1}{\{x\}^e} \tag{11}$$

where $e = 1, 2, \ldots, 20$; and the vector $\{x\}^e$ contains Cartesian coordinates of the 20-noded element along the *x*-direction. Similarly, other elements of the [*J*] matrix can be evaluated.

Numerical integration for the elemental mass and stiffness matrices given in equations (7) and (9) can be carried out by using Gaussian quadrature (Huebner and Thorton, 1982). Thus the final expressions for the matrices $[K^e]$ and $[M^e]$ are

$$[K^e] = \sum_{i=1}^{NG}\sum_{j=1}^{NG}\sum_{k=1}^{NG} W_i W_j W_k [B(\xi,\eta,\zeta)]^T [D]\, [B(\xi,\eta,\zeta)]\, |J(\xi,\eta,\zeta)| \tag{12}$$

and

$$[M^e] = \sum_{i=1}^{NG}\sum_{j=1}^{NG}\sum_{k=1}^{NG} W_i W_j W_k \rho [N(\xi,\eta,\zeta)]^T [N(\xi,\eta,\zeta)]\, |J(\xi,\eta,\zeta)| \tag{13}$$

The details of the matrix $[N(\xi, \eta, \zeta)]$ are given in Appendix B.

2.3 Transient Vibrational Analysis. *2.3.1 Formulation of Transient Equations.* The elemental mass and stiffness matrices obtained are assembled to form the global matrices, and the dynamic equation of motion for the entire system is written as

$$[M^G]\{\ddot{u}\} + [C^G]\{\dot{u}\} + [K^G]\{u\} = \{F^G(t)\} \tag{14}$$

Since the system matrices $[K^G]$ and $[M^G]$ for this three-dimensional problem become very large, it is quite desirable that a coordinate reduction scheme be employed to reduce the size of these matrices without any significant loss of accuracy in terms of the lower modes.

A useful scheme to reduce these matrices is called the Guyan reduction scheme (Guyan, 1965). In this scheme the reduced system matrices are obtained by using the following equations:

$$[\bar{M}^G]_{m\times m} = [\psi]^T_{m\times n}[M^G]_{n\times n}[\psi]_{n\times m} \tag{15a}$$

$$[\bar{K}^G]_{m\times m} = [\psi]^T_{m\times n}[K^G]_{n\times m}[\psi]_{n\times m} \tag{15b}$$

$$[\bar{C}^G]_{m\times m} = [\psi]^T_{m\times n}[C^G]_{n\times n}[\psi]_{n\times m} \tag{15c}$$

$$\{\bar{F}^G\}_{m\times 1} = [\psi]^T_{m\times n}\{F^G\}_{n\times 1} \tag{15d}$$

In all the above equations, the matrix $[\psi]$ is obtained by partitioning the stiffness matrix after arranging this matrix in terms of master and slave degrees of freedom. Further details of this arrangement can be seen in Guyan (1965).

2.3.2 Modeling of Transient Excitation Forces. Figure 4 shows the position of a rotor blade at 0_2. The blade has started from rest at 0_1 with an angular acceleration α. The location of the position of the rotor at various instants of time can be found by solving kinematic equations. The time taken by the blade to move from 0_1 to C will be given by

$$t_1 = \left(\frac{2(\theta - \theta_{N/2})}{\alpha}\right)^{1/2} \tag{16}$$

Similarly, the blade will be at D at the instant

$$t_2 = \left(\frac{2(\theta + \theta_{N/2})}{\alpha}\right)^{1/2} \tag{17}$$

Therefore the duration of the impulse Δt_{imp} will be equal to $(t_2 - t_1)$. In this way the occurrence of the impulses can be calculated using equations (16) and (17). It should be borne in mind that θ is the total angle measured counter clockwise from 0_1 to the center line of the nozzle. The instantaneous speed of the rotor can also be calculated as

$$\omega_i = \omega_{i-1} + \alpha(t_i - t_{i-1}) \tag{18}$$

The ω_i is needed in the calculation of vibration response of the blade due to centrifugal forces in the next section.

The time gap between the occurrence of any two impulses will be

$$\Delta t_0 = t_{1_i} + \frac{(\Delta t_{\text{imp}})_i}{2} - \left(t_{1_{i-1}} + \frac{(\Delta t_{\text{imp}})_{i-1}}{2}\right) \tag{19}$$

where i in equations (18) and (19) represents the sequential order of the impulses.

The forces due to gas pressure are distributed along the entire length of the blade. The actual magnitude of the pressure distribution would depend upon the type and operating conditions of the turbine. To demonstrate the applicability of the present work, the values for the magnitude of the height of the impulse were taken from Rao (1985).

One of the convenient ways of calculating the response due to the series of impulses occurring at variable instants of time would be by using the following equation:

$$q_k(t) = \frac{P\Delta t_{\text{imp}}}{m_k \omega_{nk}(1-\xi_k^2)^{1/2}} e^{(-\xi_k \omega_{nk} t)} \sin[(1-\xi_k^2)^{1/2}\omega_{nk} t] \tag{20}$$

Equation (20) can be used for each mode by decoupling the equations of motion (14). In equation (20) the subscript k corresponds to the mode number. In Fig. 4(b) the displacement response at any instant of time between 0_1 and 0_2 can be calculated using equation (20) and the velocity response by differentiating this equation. The displacement and the velocity response values between 0_2 and 0_3 can be calculated due to the occurrence of the impulse at 0_2 and the velocity and the displacement values at 0_2 due to the previous impulse. In this way one can calculate the response at any instant of time.

2.3 Transient Response Due to Centrifugal Forces. The centrifugal forces in the rotor blade arise due to the radial location of the element with reference to the axis of rotation of the rotor shaft. If the mass of the element is m, then the centrifugal force acting on this mass will be

$$F_{\text{cen}} = m\omega_{\text{rotor}}^2 (R+z) \tag{21}$$

where R is the radius of the rotor disk and z is the distance from the root to the center of gravity of the element. This force, which acts at the center of gravity, can be replaced by eight equivalent forces, each of which act at the corner nodes.

To calculate the dynamic response due to the centrifugal forces, one has first to recognize that these are time variant, because ω_{rotor} in equation (21) is a variable and is calculated using equation (18). To calculate the response one has to decouple the equations of motion and the forcing function corresponding to equation (21) will be

$$F_{\text{cen}} = (R+z)(\alpha t)^2 m \tag{22}$$

To calculate the modal response one has to use the convolution integral, which is of the form

$$q_k(t) = \frac{1}{\omega_{dk}} \int_0^t (R+z)(\alpha\tau)^2 m e^{(-\xi_k \omega_{nk}(t-\tau))} \sin[\omega_{dk}(t-\tau)] d\tau \tag{23}$$

The solution for this equation can be written as

$$q_k(t) = \frac{(R+z)}{\omega_{dk}} \alpha^2 \sin(\omega_{dk} t) e^{(-\xi_k \omega_{nk} t)} \left[e^{(\xi_k \omega_{nk} \tau)} \right.$$

$$\sum_{r=0}^{2} \frac{(-1)^r 2! (\tau)^{2-r}}{(\xi_k^2 \omega_{nk}^2 + \omega_{dk}^2)^{\frac{r+1}{2}} (2-r)!} \cos\left[\omega_{dk}\tau \right.$$

$$\left. \left. - (r+1)\tan^{-1}\left(\frac{\omega_{dk}}{\xi_k \omega_{nk}}\right)\right]\right]_0^t$$

$$- \frac{(R+z)\alpha^2}{\omega_{dk}} \cos(\omega_{dk} t) e^{(-\xi_k \omega_{nk} t)} \left[e^{(\xi_k \omega_{nk} \tau)} \right.$$

$$\sum_{r=0}^{2} \frac{(-1)^r 2! (\tau)^{2-r}}{(\xi_k^2 \omega_{nk}^2 + \omega_{dk}^2)^{\frac{r+1}{2}} (2-r)!} \sin\left[\omega_{dk}\tau \right.$$

$$\left. \left. - (r+1)\tan^{-1}\left(\frac{\omega_{dk}}{\xi_k \omega_{nk}}\right)\right]\right]_0^t \tag{24}$$

2.3.4 Calculation of Dynamic Stresses. Once the total response of the turbine blade due to various excitation forces is known, the strains in each element can be obtained from the isoparametric finite element formulation as

$$\{\gamma\} = [B]\{u\} \tag{25}$$

$$6\times 1 \quad 6\times 60 \quad 60\times 1$$

and the vibratory stresses can then be evaluated as

$$\{\sigma\} = [D]\{\gamma\} \tag{26}$$

$$6\times 1 \quad 6\times 6 \quad 6\times 1$$

This stress vector can then be used to obtain the principal stresses in each element of the blade by solving the following cubic equation:

$$S^3 - (\sigma_x + \sigma_y + \sigma_z)S^2 + (\sigma_x\sigma_y + \sigma_y\sigma_z + \sigma_x\sigma_z - \tau_{yz}^2 - \tau_{xz}^2 - \tau_{xy}^2)S$$

$$- (\sigma_x\sigma_y\sigma_z + 2\tau_{yz}\tau_{xz}\tau_{xy} - \sigma_x\tau_{yz}^2 - \sigma_y\tau_{xz}^2 - \sigma_z\tau_{xy}^2) = 0 \tag{27}$$

The roots of the above equation yield the three principal stresses as σ_1, σ_2, and σ_3. In order to calculate the design stress for safe operation of the blade, various failure theories can be used. One commonly used theory is the distortion energy theory. This theory can be used to calculate the design stress from the principal stresses as

$$\sigma_d = \frac{1}{\sqrt{2}}[(\sigma_1 - \sigma_2)^2 + (\sigma_2 - \sigma_3)^2 + (\sigma_3 - \sigma_1)^2]^{1/2} \tag{28}$$

Thus σ_d would be a reliable indicator of the state of stress in each element.

3 Results and Discussion

3.1 Thermal Stress Analysis of Turbine Blade. The thermal stresses can be calculated once the temperature distribution at any cross section of the blade is known. For the cross section shown in Fig. 2, the temperature distribution was calculated using equation (5); once the temperature distribution at various elements was known, the thermal stresses were calculated using equation (6). The variations of temperatures and stresses with time are shown in Fig. 5 at some of the important points of this cross section. One can clearly see in this figure that the stresses build up to a maximum value and then decrease as the temperatures of various points on the blade approach the gas temperature. The maximum stresses occur at element number 78, the location of which is shown in Fig. 2. The stress values in this figure have been normalized with respect to the yield stress of the element, which itself varies as the element temperature changes. It should be added here that these stresses will become negligible when the blade temperature approaches the steady-state temperature. Figure 6 shows the temperature contours on this cross section of the blade at $t = 70$ s.

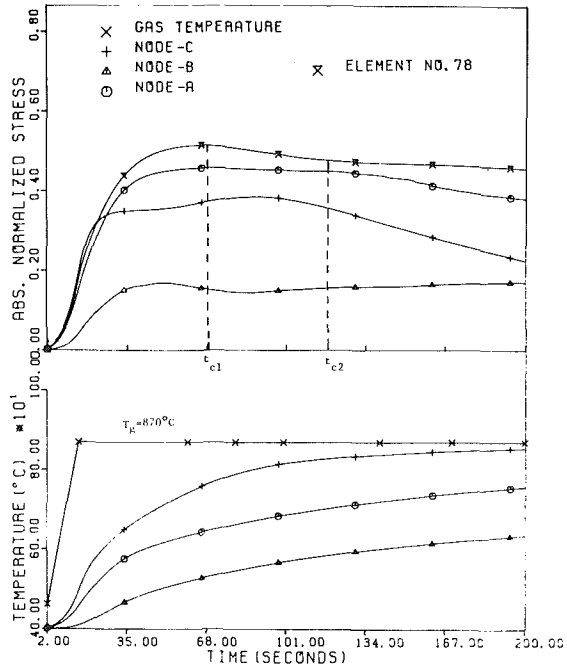

Fig. 5 Transient temperature and thermal stress distribution in the blade

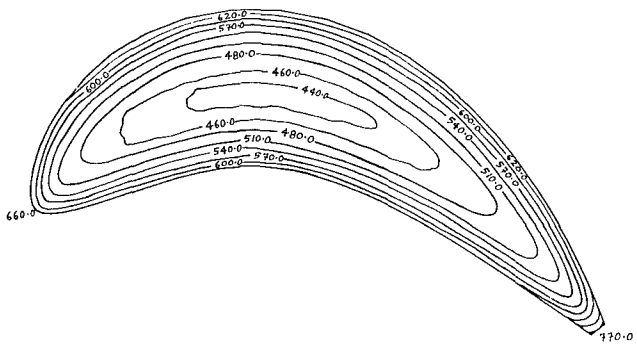

Fig. 6 Temperature contours across the airfoil section at $t = 70$ s

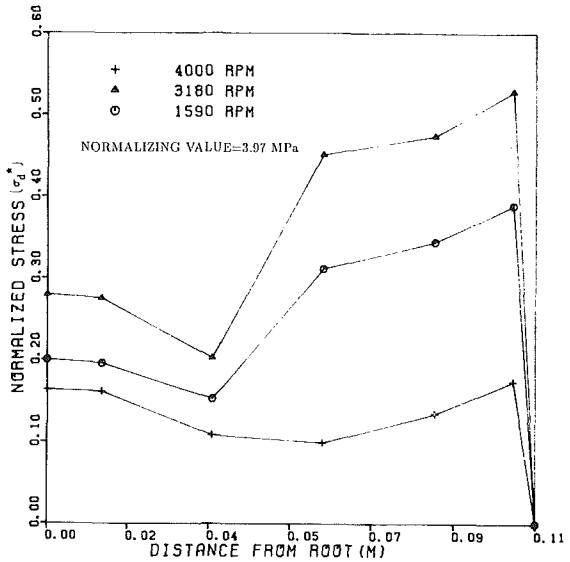

Fig. 7 Variation of dynamic stresses at the leading edge at various speeds

Table 2 Geometric properties of the blade; $\theta = 30$ deg, $\theta_N = 7.5$ deg, $R = 0.5$ m

Section	Distance From Root x 10^2, (m)	A x 10^4,(m^2)	I_{xx} x 10^8,(m^4)	I_{yy} x 10^8,(m^4)	θ_p (DEGREES)
1	0.0	2.127	0.3447	0.9489	0.0
2	2.5	1.738	0.3651	0.6717	10.2
3	5.0	1.647	0.4927	0.5174	21.6
4	7.5	1.263	0.5054	0.3097	33.8
5	10.0	1.008	0.4356	0.1543	38.2
6	11.0	0.736	0.3258	0.0858	42.0

Table 3 Variation of natural frequencies (Hz) with time

Mode Number	The Natural Frequencies After					
	1 (sec)	30 (sec)	50 (sec)	100 (sec)	120 (sec)	Steady State
I	661.08	651.74	648.48	613.65	603.35	564.58
II	2081.02	2047.43	2001.58	1929.53	1912.24	1784.95
III	3371.59	3310.57	3230.26	3116.24	3094.99	2888.35
IV	4230.02	4171.99	4077.06	3928.37	3900.07	3623.50
V	7159.01	7040.37	6865.78	6629.0	6588.2	6134.51
VI	8891.83	8762.97	8592.89	8261.54	8205.29	7618.53
VII	10956.95	10731.32	10486.71	10118.61	10054.18	9385.74
VIII	13301.75	13118.97	12829.29	12359.61	12280.01	11395.4
IX	15014.76	14777.74	14488.46	13942.27	13848.89	12861.76
X	14232.5	14011.57	13695.39	13198.16	13118.21	12192.42
XI	21803.25	21463.58	21048.37	20259.3	20122.5	18680.02

3.2 Dynamic Stress Analysis of Turbine Blade. To carry out the dynamic analysis, the rotor blade was divided into 35 20-noded elements, which were arranged in five layers as shown in Fig. 1. The various other details of the turbine blade, etc., are given in Table 2. Since the total number of degrees of freedom for this system was 924, the Guyan reduction technique was used to reduce the size of the system matrices. After reduction, the number of degrees of freedom was 200, and the criterion for this reduction was that the change in the first five natural frequencies was less than 1 percent.

To get some idea about the effect of the thermal process on the natural frequencies, the modulus of elasticity of various elements was varied at various instants of time due to the change in temperature and the corresponding undamped natural frequencies were calculated. These are shown in Table 3. One can clearly see in this table that the thermal environment has a pronounced effect on the natural frequencies.

The value of E used in this section only was 2.0×10^{11} Pa and the corresponding first natural frequency was 636.01 Hz (3180 rpm). The transient vibration response was calculated with this value in mind. Figures 7–9 show the variations of the stresses along the height of the blade at the leading edge, trailing edge, and at element number 78. In Fig. 7 the maximum stresses occur close to the tip of the blade, and among all the maxima, the global maximum takes place at 3180 rpm, which corresponds to the first natural frequency. At half-order excitation, i.e., at 1590 rpm, the stresses are again quite significant. This figure also shows reasonably low value of stresses of 4000 rpm, which is the maximum operating speed for the present analysis. Similar behavior as far as the speeds are concerned can be seen in Figs. 8 and 9. The maximum stresses in

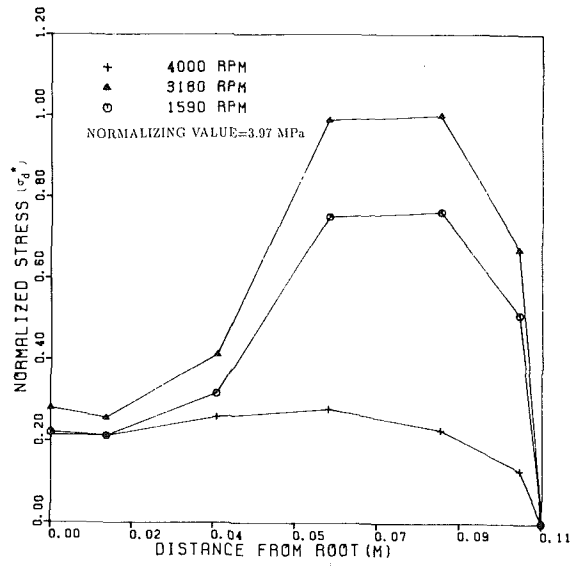

Fig. 8 Variation of dynamic stress at the trailing edge at various speeds

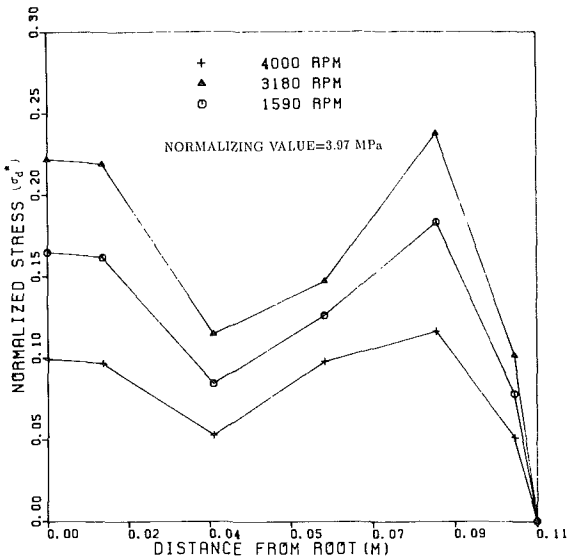

Fig. 9 Variation of dynamic stresses at element number 78 at various speeds

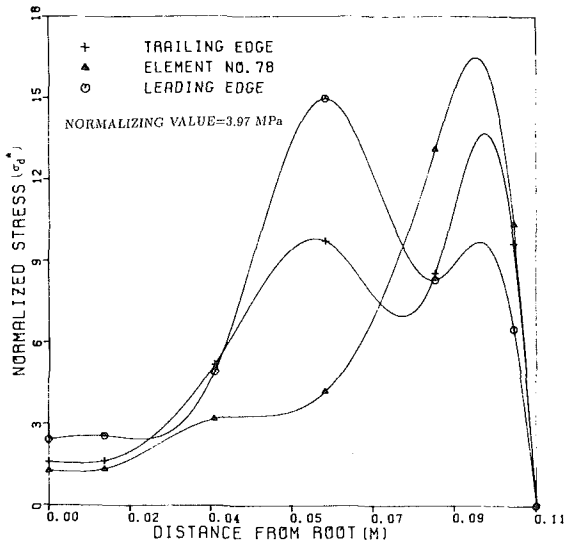

Fig. 10 Variation of centrifugal stresses at a rotor speed of 4000 rpm

these two figures are also nearer to the tip than the root. Among all the peaks in these three figures, the maximum peak values of the stress is in Fig. 8. The stress values in these three figures have been normalized with respect to the global maximum of Fig. 8.

In all three figures, the stress values have been connected by straight lines and each point corresponds to the element joint along the height of the blade. If one desires to know the value of stress at any other point, one can calculate this value using polynomial interpolation for this particular finite element. It should be noted in all these figures that the maximum stress does not occur at the root. This is because the cross-sectional area of the root is higher, which is generally the case, and the variation of the stress along the height is not very regular because of the complicated three-dimensional geometry of the blade.

Figure 10 shows the centrifugal stress distribution when the rotor speed reaches 4000 rpm. At this speed the peak value of the stress was more than the peak value at other speeds. Among the leading edge, trailing edge, and element number 78, the peak stress of each occurs at a different distance from the root. From the design point of view, even in this case the magnitudes of the stresses are greater near the tip than the root. This figure has also been normalized with the same value as that used in Figs. 7–9.

3.3 Stress Analysis of Turbine Blade Due to Combined Effects. In section 3.1, the stresses due to thermal effects were discussed and the maximum transient stresses were found to be quite significant. In the vibratory analysis, the value for the height of the impulse P was chosen to be a low value, and it was used just to illustrate the calculation of the transient stresses. In the design of an actual turbine blade, the transient forces have to be known exactly, and for this type of a linear system the vibratory stresses would be in the same proportion as the actual force is to P. Therefore, the actual design would involve the summation of all the stresses first of all at any instant of time, and then finding the global maxima of these types of combined stress as the time varies.

To understand the critical instants of time from the stress point of view, one should look at Figs. 5 and 7–10. The rotor accelerates from rest, and at $t = 70$ s that shaft speed is 933.33 rpm. At this instant the maximum thermal stress occurs at element number 78 (refer to t_{cl} in Fig. 5). These stresses decrease very slowly with time. The second critical event occurs due to the half-order excitation at 1590 rpm ($t = 119.25$ s). Here the critical point is the trailing edge. This is due to the vibratory stresses as shown in Fig. 8. The centrifugal stresses, not shown in any of the figures, are very low at this speed. The thermal stress at the trailing edge is also quite significant (refer to t_{c2} in Fig. 5). The most critical stresses take place at 3180 rpm ($t = 238.5$ s) as the rotor goes through the first natural frequency. The maximum vibratory stresses shown in Fig. 8 are again at the trailing edge. In addition the thermal stresses are also not very low. At 4000 rpm the vibratory stresses in Figs. 7–9 are much lower. The thermal stresses, however, are still quite high (not shown in the figures) but the peaks of the centrifugal stresses are significant. If we compare the magnitudes of the peaks of the centrifugal stresses shown in Fig. 10 and the thermal stresses, the centrifugal stresses are still much lower. Therefore, the blade is not under very high stress at 4000 rpm as compared to the first critical instant of time (t_{cl}). From all this discussion one can see that thermal stresses are quite important in the design of the turbine blades. As a point of clarification it should be restated that the dynamic stresses in Figs. 7–9 were low because the value of P in Fig. 4(b) was very small. In actual operation of the turbomachinery P would be very large, whereas the stresses in Figs. 5 and 10 are not affected by the value of P.

4 Conclusion

In the present work the transient temperature variations were obtained using a finite element analysis in two dimensions. The finite element equations also included the effect of nonlinear variation of properties as well as the nonlinear radiative boundary conditions. From the temperature distribution the normal thermal stresses in the z direction were calculated. To calculate the stresses due to the pressure and centrifugal forces the three-dimensional solid finite elements were used. The transient forces were modeled as a series of impulses occurring at instants of time that were found by solving kinematic equations. The response due to these forces was calculated using modal analysis. The response values were then used to calculate the dynamic stress vector. The principal stresses in three dimensions were obtained by solving the cubic equation. The design criterion for the blade was based on the distortion energy theory.

Based on the study carried out in this work the following conclusions can be drawn:

1 The maximum values of the thermal stresses occur at element number 78 during the transient period.

2 The peak values of the distortion energy stress σ_d occur at the trailing edge along the blade, and among these maximum, the global maximum takes place close to the tip.

3 The stresses σ_d due to centrifugal force increase with increase in speed.

4 The thermal stresses are quite significant during the acceleration period and must be included in the design of rotor blades.

Acknowledgments

The authors are thankful to the National Science and Engineering Council of Canada for their grant No. A5549, which was used as a financial support for this work.

References

Banerji, J. R., Williams, F. W., 1985, "Exact Bernoulli-Euler Dynamic Stiffness Matrix for a Range of Tapered Beams," *Int. J. Numerical Methods in Engineering*, Vol. 21, p. 2289.

Cubberly, W. H., 1980, *ASM Metals Reference Book*, 9th ed., American Society for Metals, Metals Park, OH, Vol. 3, pp. 248-249.

Gupta, A. K., 1985, "Vibration of Tapered Beams," *ASCE J. Structural Engineering*, Vol. 11, p. 19.

Guyan, R. J., 1965, "Reduction of Stiffness and Mass Matrices," *AIAA Journal*, Vol. 3, No. 2, p. 380.

Huebner, K. H., and Thorton, E. A., 1982, *The Finite Element Method for Engineers*, Wiley, p. 187.

Hutchinson, J. R., and Zillmer, S. D., 1986, "On the Transverse Vibration of Beams of Rectanglar Cross Section," ASME *Journal of Applied Mechanics*, Vol. 53, p. 278.

Littler, D. J., 1969, "Thermal Stresses and Thermal Fatigue," *Proceedings of the Intl. Conference*, Gloucestershire, United Kingdom, Sept. 22-26, pp. 374-386.

Maya, T., Katsumata, I., and Itoh, M., 1978, "A Study of Thermal Fatigue Life Prediction of Air-Cooled Turbine Blades," ASME Paper No. 78-GT-63.

Mukherjee, D. K., 1978, "Stresses in Turbine Blades Due to Temperature and Load Variation," ASME Paper No. 78-GT-158.

Rao, J. S., and Vyas, N. S., 1985, "Response of Steam Turbine Blades Subjected to Distributed Harmonic Nozzle Excitation," 3rd Intl. Modal Analysis Conference, Orlando, FL, pp. 618-626.

Reddy, B. S., and Sharan, A. M., 1985, "The Transient Heat Transfer Analysis of Solids With Radiative Boundary Conditions Using Finite Element Analysis," *Int. Comm. Heat Mass Transfer*, Vol. 12, pp. 169-178.

Sato, K., 1980, "Transverse Vibrations of Linearly Tapered Beam With Ends Restrained Elastically Against Rotation and Subjected to Axial Force," *Int. J. Mech. Sci.*, Vol. 22, p. 109.

Sisto, F., and Chang, A. T., 1984, "A Finite Element for Vibration Analysis of Twisted Blades Based on Beam Theory," *AIAA Journal*, Vol. 22, pp. 1646-1651.

Subrahmanyam, K. B., and Leissa, A. W., 1985, "An Improved Finite Difference Analysis of Uncoupled Vibrations of Cantilever Beams," *J. Sound and Vibration*, Vol. 98, p. 1.

Zienkiewicz, O. C., 1977, *The Finite Element Method*, McGraw-Hill, United Kingdom, pp. 167-171.

APPENDIX A

The force vector due to radiative heat transfer $\{F_R\}$ can be expressed as

$$\{F_R\} = \int_{S_2} \sigma\epsilon T_\infty^4 [N]^T ds - \int_{S_2} \sigma\epsilon [N]^T ([N]\{T\})^4 dS$$

For side i-j of the triangular element shown in Fig. A1, the force vector due to radiation can be written as

$$\{F_R^e\} = \frac{\sigma\epsilon L_{ij}}{2} T_\infty^4 \begin{bmatrix} 1 \\ 1 \\ 0 \end{bmatrix} - \frac{\sigma\epsilon L_{ij}}{30} \begin{bmatrix} 5T_i^4 + 4T_i^3 T_j + 3T_i^2 T_j^2 + 2T_i T_j^3 + T_j^4 \\ 5T_j^4 + 4T_j^3 T_i + 3T_j^2 T_i^2 + 2T_i T_j^3 + T_i^4 \\ 0 \end{bmatrix}$$

where L_{ij} is the length of side i-j of the triangle subjected to radiation.

APPENDIX B

The interpolation functions for the 20-noded isoparametric element can be expressed as

Corner Nodes:

$$N_i = \frac{1}{8}(1+\xi\xi_i)(1+\eta\eta_i)(1+\zeta\zeta_i)(\xi\xi_i+\eta\eta_i+\zeta\zeta_i-2)$$

Typical Mid-side Node:

$$N_i = \frac{1}{4}(1-\xi^2)(1+\eta\eta_i)(1+\zeta\zeta_i)$$

for the case when $\zeta_i = 0$, $\eta_i = \pm 1$, and $\zeta_i = \pm 1$. Here the subscript i represents the ith node of the 20-noded element.

As stated earlier, the $[B]$ matrix is a product of three matrices $[P]$, $[Q]$, and $[R]$. The expressions for these matrices are

$$[P]_{6\times 9} = \begin{bmatrix} 1 & 0 & 0 & 0 & 0 & 0 & 0 & 0 & 0 \\ 0 & 0 & 0 & 0 & 1 & 0 & 0 & 0 & 0 \\ 0 & 0 & 0 & 0 & 0 & 0 & 0 & 0 & 1 \\ 0 & 1 & 0 & 1 & 0 & 0 & 0 & 0 & 0 \\ 0 & 0 & 1 & 0 & 0 & 0 & 1 & 0 & 0 \\ 0 & 0 & 0 & 0 & 0 & 1 & 0 & 1 & 0 \end{bmatrix}$$

$$[Q]_{9\times 9} = \begin{bmatrix} J_{11}^{-1} & J_{12}^{-1} & J_{13}^{-1} & 0 & 0 & 0 & 0 & 0 & 0 \\ J_{21}^{-1} & J_{22}^{-1} & J_{23}^{-1} & 0 & 0 & 0 & 0 & 0 & 0 \\ J_{31}^{-1} & J_{32}^{-1} & J_{33}^{-1} & 0 & 0 & 0 & 0 & 0 & 0 \\ 0 & 0 & 0 & J_{11}^{-1} & J_{12}^{-1} & J_{13}^{-1} & 0 & 0 & 0 \\ 0 & 0 & 0 & J_{21}^{-1} & J_{22}^{-1} & J_{23}^{-1} & 0 & 0 & 0 \\ 0 & 0 & 0 & J_{21}^{-1} & J_{22}^{-1} & J_{23}^{-1} & 0 & 0 & 0 \\ 0 & 0 & 0 & 0 & 0 & 0 & J_{11}^{-1} & J_{12}^{-1} & J_{13}^{-1} \\ 0 & 0 & 0 & 0 & 0 & 0 & J_{21}^{-1} & J_{22}^{-1} & J_{23}^{-1} \\ 0 & 0 & 0 & 0 & 0 & 0 & J_{31}^{-1} & J_{32}^{-1} & J_{33}^{-1} \end{bmatrix}$$

$$[R]_{9\times 60} = \begin{bmatrix} \frac{\partial N_1}{\partial \xi} & 0 & 0 & \frac{\partial N_2}{\partial \xi} & 0 & 0 & \frac{\partial N_3}{\partial \xi} & - & - & - & - \\ \frac{\partial N_1}{\partial \eta} & 0 & 0 & \frac{\partial N_2}{\partial \eta} & 0 & 0 & \frac{\partial N_3}{\partial \eta} & - & - & - & - \\ \frac{\partial N_1}{\partial \zeta} & 0 & 0 & \frac{\partial N_2}{\partial \zeta} & 0 & 0 & \frac{\partial N_3}{\partial \zeta} & - & - & - & - \\ 0 & \frac{\partial N_1}{\partial \xi} & 0 & 0 & \frac{\partial N_2}{\partial \xi} & 0 & 0 & - & - & - & - \\ 0 & \frac{\partial N_1}{\partial \eta} & 0 & 0 & \frac{\partial N_2}{\partial \eta} & 0 & 0 & - & - & - & - \\ 0 & \frac{\partial N_1}{\partial \zeta} & 0 & 0 & \frac{\partial N_2}{\partial \zeta} & 0 & 0 & - & - & - & - \\ 0 & 0 & \frac{\partial N_1}{\partial \xi} & 0 & 0 & \frac{\partial N_2}{\partial \xi} & 0 & - & - & - & - \\ 0 & 0 & \frac{\partial N_1}{\partial \eta} & 0 & 0 & \frac{\partial N_2}{\partial \xi} & 0 & - & - & - & - \\ 0 & 0 & \frac{\partial N_1}{\partial \zeta} & 0 & 0 & \frac{\partial N_2}{\partial \zeta} & 0 & - & - & - & - \end{bmatrix}$$

The shape function matrix used in the evaluation of the elemental consistent mass matrix $[M^e]$ can be expressed as

$$[N]_{3\times 60} = \begin{bmatrix} N_1 & 0 & 0 & N_2 & 0 & 0 & N_3 & 0 & 0 & - & - & - \\ 0 & N_1 & 0 & 0 & N_2 & 0 & 0 & N_3 & 0 & - & - & - \\ 0 & 0 & N_1 & 0 & 0 & N_2 & 0 & 0 & N_3 & - & - & - \end{bmatrix}$$

A Ruggedized Design Approach to Reduce Maintenance and Enhance the Efficiency of High and Intermediate Pressure Steam Turbines

L. Conway

H. F. Martin

A. L. Stock

F. R. Vaccaro

Westinghouse Electric Corp.,
Generation Technology Systems Division,
Orlando, FL 32817

The industry issues of minimizing maintenance and maintaining turbine performance with operating time have been systematically addressed using creative approaches to control wear, erosion, vibration, and distortion of critical High-Pressure (HP) and Intermediate-Pressure (IP) Steam Turbine components. The important components were identified utilizing a new technique to analyze turbine high maintenance areas. New technology advances were utilized to understand the causes of the maintenance, and to reduce or eliminate it. The technology advances discussed in the paper are in the area of three-dimensional computer programs, materials, coatings, modern computer-aided drafting, and verification testing. These, in conjunction with new creative design approaches for the critical components, have resulted in a ruggedized HP and HP/IP turbine design, which is retrofittable in today's operating units. Of special interest are the steps taken to give rapid and individually customized attention from design through manufacturing to each unique situation and utility. Among the benefits achieved are up to a 50 percent overall reduction in maintenance, up to 120 Btu/kWh (30 kcal/kWh) reduction in heat rate, and an increased cyclic duty capability for the ruggedized turbines.

Introduction

The reliability and availability of turbine-generator units gained increasing importance in the early 1970s when the entire electric utility industry was rapidly forced to adapt to dramatically different economic conditions. To respond to the changing priority of needs of utilities, Westinghouse instituted systematic programs that took full advantage of the tremendous advances in testing, analyses, and materials technologies that had become available for turbine development. Some of the resultant development programs that were introduced were for the Ruggedized HP and combined HP/IP Rotors, the Ruggedized HP Inlet Features, including the Control Stage, and new more efficient HP and IP blading. New technology was successfully developed and applied for a cost-effective, retrofittable package, with the goals of improving the performance and availability, as well as extending the life of existing base loaded and cyclic duty units.

The design package resulting from the Ruggedized HP and HP/IP Turbine Programs have been developed with the objectives of improving reliability and availability, and greatly reducing the performance degradation that results from exfoliation, thermally induced differential expansion, and flow induced vibration. The programs focused on the components of the turbine that had the greatest potential for reducing unavailability and improving performance. These main components were the inlet features, the blading, and the rotor. Advances in key areas resulted in new HP and IP turbine features, such as:

- 180 deg ring-type nozzle chambers
- Improved inlet seals
- Pinned control stage blades
- Erosion resistant coatings
- More effective aerofoil shapes for blading
- Integral shrouded blades
- No-bore rotors

The introduction of these new features is intended to produce the most effective attack on unavailability, maintenance, and performance aging according to studies of industry needs and turbine unavailability issues.

Westinghouse "STARS" System

Some of the most important questions that must be answered in the consideration of improving the reliability of a

Contributed by the Power Division and presented at the Joint ASME/IEEE Power Generation Conference, Portland, Oregon, October 19–23, 1986. Manuscript received by the Power Division January 29, 1988. Paper No. 86-JPGC-Pwr-31.

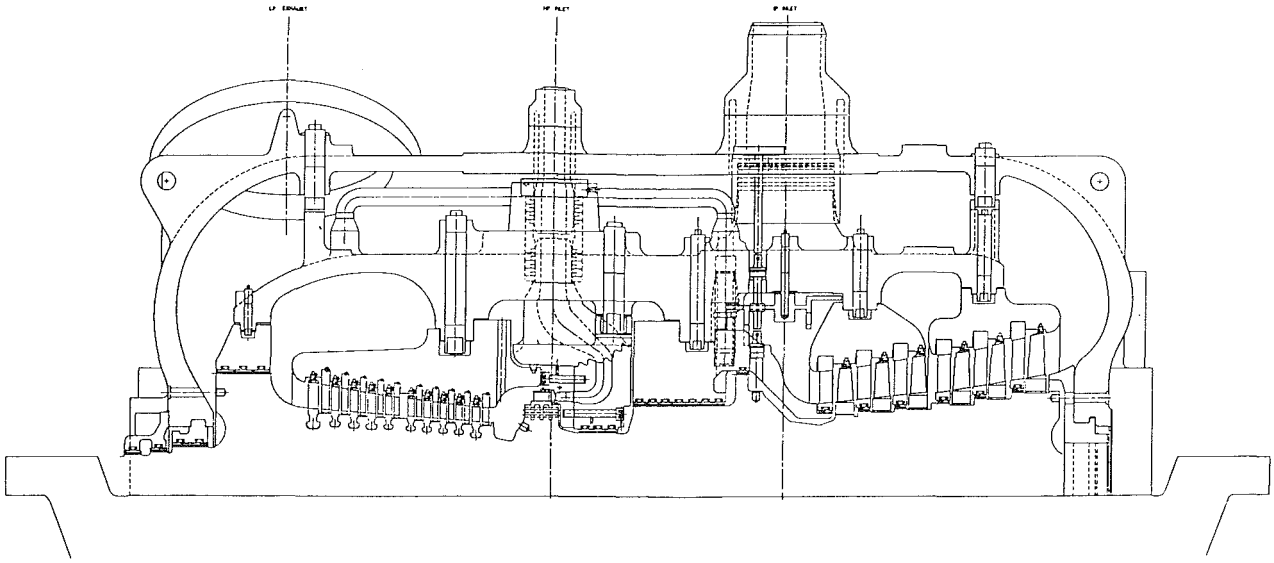

Fig. 1 Longitudinal ruggedized HP/IP turbine

turbine element, whether it be a retrofit design, or a new ruggedized element, are the questions of:

- Are the correct issues being addressed?
- What features or components in the design are the important contributors affecting the issues?
- What are the effective solutions that eliminate the issues?

In other words the designers must determine issues and causes of turbine generator unreliability or unavailability. Once these questions have been answered properly, the areas with the greatest potential return on invested effort can be determined.

A turbine generator designer and manufacturer such as the authors' company, with over a thousand operating units of many and varied designs, has a great resource in its operating experience and service records. Years of service and operating experience have been analyzed into meaningful data on reliability of features and components. This vital pool of data is one important resource used in considering solutions and new features or components to address the issues determined.

Another vital source of data begins with the NERC Unavailability and Forced Outage data compiled and available on turbines and generators. These data, while useful, are not detailed enough for effective analysis of the causes of unavailability issues, maintenance issues, or contributing components.

The authors' company has expanded the NERC reporting system, using it as a base. This expanded system for Westinghouse turbines is known as "STARS": Steam Turbine Availability and Reliability System. STARS expands the NERC data eightfold by making contacts with over 100 utilities every 2 weeks for specifics. The personnel making the contacts are trained and experienced in determining the correct causes and components involved in any outage or maintenance.

STARS therefore can draw on this extensive service and maintenance experience, as well as over five years of the expanded NERC unavailability and forced outage data, to identify unavailability issues and associated maintenance hours. Analysis of this data identifies the components that contribute to the significant outages or maintenance in a systematic process. After these components have been determined, the advanced technology and experience, not available at the time of the original design, can now be utilized to provide solutions and address the issues properly.

At this point new technology and creative conceptual design focus on the issues, the components, and their functions, to eliminate, or significantly reduce, the maintenance required. Components are redesigned with new features added or combined to address the issues and causes determined by the analysis. These new low-maintenance component features are now built into a new turbine element in what has been termed a "Ruggedized System." In like manner similar components and features can be adapted or retrofitted to older operating machines in the form of retrofittable "Ruggedized" products. These new products are offered to utilities to improve their efficiency and reliability, as well as significantly reduce maintenance and forced outage hours, and thus modernize and extend the life of their older machines.

Performance Improvements

In addition to improved reliability and maintainability, thermodynamic performance can also be improved. This is possible due to the technological improvements in recent years, and the concept of optimizing the blade path for a specific customer application. Units that were designed twenty or more years ago applied nearly standardized blade paths to control manufacturing processes. The benefit of this new unit by unit optimization and new technology is an improvement in unit heat rate up to 120 Btu/kWh. The revised longitudinal section and blade path for a ruggedized HP/IP unit is shown in Fig. 1.

The efficiency improvements of the reaction blade path are made up of five basic ingredients: overall blade path thermodynamic optimization, improved aerofoil design, improved aerodynamic analysis, improved sealing, and reduced windage losses. The new technology is being applied to both high-pressure and intermediate-pressure steam turbines.

The blade path optimization procedure is computerized. The procedure produces a blade path, which determines the most advantageous thermodynamic configuration that will satisfy mechanical constraints. Blading performance data in terms of flow incidence angle, aspect ratio (blade height/blade width), and surface velocity are used in this analysis. This type of data is obtained by cascade performance tests and is verified from turbine tests. Many high-pressure turbine modernizations include retrofitted blade paths that have an additional stage and taller blade heights as a result of the optimization study findings.

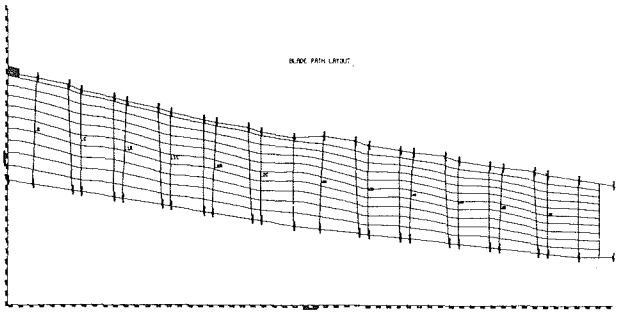

Fig. 2 IP turbine blade path flow field

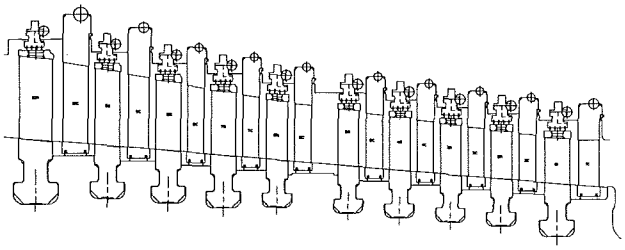

Fig. 3 BB44R HP blade path

Another important aspect of the optimization of HP performance is selecting the proper work split between the control stage and reaction blade path. Since this selection affects rotor and blade path temperatures, the first-stage exit temperature is optimized for both mechanical and thermodynamic variables.

Improved aerofoil design and aerodynamic analysis combine the best blade section with proper incidence angles, and flow area distribution. An analytical tool developed for this purpose is a three-dimensional flow field analysis (Steltz et al., 1974). This approach has been used extensively in low-pressure turbines with great success (Steltz et al., 1979). Figure 2 shows the streamline distribution for an IP turbine blade path. This figure illustrates the effect of twisted stationary blades on suppressing radially outward flow and thus controlling the radial distribution of reaction. This analysis tool provides the turbine designer with the radial area variation and incidence angle information to use a twisted stationary blade foil properly in the HP or IP turbine to replace the previous parallel-sided stationary blades.

The rotating blades of the HP turbine are parallel-sided reaction blades. The newest design information and computerized techniques are used to produce blade sections. Cascade tests have shown that the new design has a better efficiency and is less sensitive to inlet angle variations. New blade sections have also been developed for application in intermediate turbine blade paths. These designs use integral shrouded blades and tapered twisted rotating blades for improved performances. The new technology applied to these blade designs is discussed in Thomas and Pigott (1984).

In HP turbines the mechanical reliability of the tee root riveted blade has been excellent. Therefore, new designs build on this proven success. However efficiency improvements are possible with improved sealing. This is accomplished through the use of countersunk rivets, which produces a flat sealing surface along the outside diameter of the blade path; this permits the use of multistrip springback seals.

A typical HP reaction bladepath is shown in Fig. 3. Leakage flow is reduced through the reduced flow coefficient of the multistrip seal and the fact that smaller radial clearances are possible with the use of springback seals. Turbine test data have shown that springback seal designs maintain high efficiency longer than staked-in seals and are easier to replace.

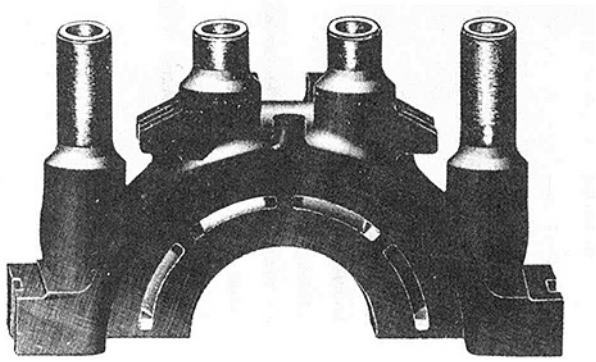

Fig. 4 180 deg nozzle chamber ring structure

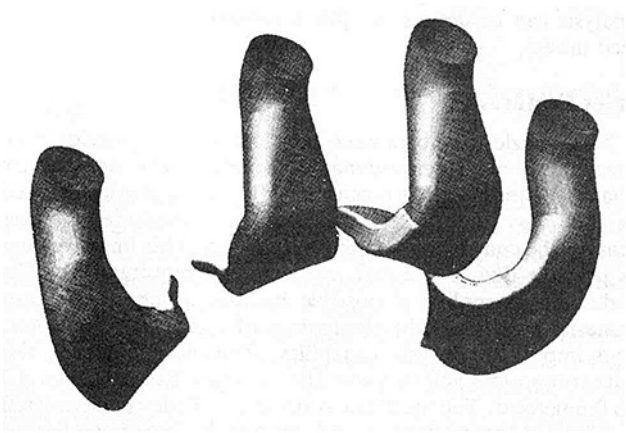

Fig. 5 Nozzle chamber flow passages

Springback seal designs are also used throughout the IP turbine section.

The tee root design also minimizes leakage paths, which is particularly important with the shorter blade height HP turbines.

Mechanical Drawings

Extending the life and modernizing HP turbines of up to 35 years of age requires interfacing with the technology of the 1950s. Significant changes have occurred since then. One of the most dramatic changes is in the method of producing modern mechanical drawings. Computer-aided drawing (CAD) has changed the scope, speed, and quality of part descriptions. The most apparent success of the process in this particular upgrade has been the ability to customize parts rapidly and accurately for different customers. For example the blade path shown in Fig. 3 is the result of a CAD plot for specific customized requirements.

Some of the more complicated steam passages that conduct the steam historically have had a great deal of pattern maker input in determining their profiles, and this frequently restricted the number of iterations possible to optimize the profiles from a pressure drop perspective. The nozzle chamber shown in Fig. 4 was actually designed inside out. The passages were first constructed with a uniformly increasing area (Fig. 5), despite the widely changing sections, to optimize performance, and then the shell was constructed around it. The entire assemblage, together with blade rings and other parts, was then installed by the computer into the layout in Fig. 1, which then self-corrected the parts and layout. It is of interest to note that the isometric views shown in Figs. 4 and 5, and several other uncommon views, helped describe the part to

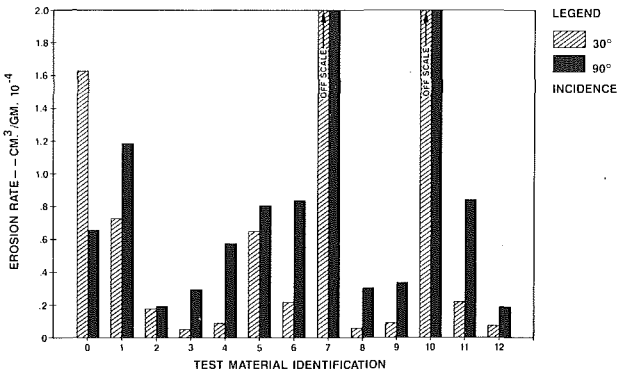

Fig. 6 Elevated temperature erosion rates of various coatings

casting vendors much more completely than conventional two-dimensional drawings. In addition, more accurate stress analysis can be done from this three-dimensional computerized model.

Inlet Features

New nozzle chambers have been designed to provide both mechanical and thermodynamic benefits. The new nozzle chamber eliminates the turnaround flow path previously used in this class of turbines. The straight-through design after leaving the control stage is shown in Fig. 1. This improvement is possible due to reduced rotor cooling requirements. The reduction in cooling is possible because of improved rotor material properties, the elimination of the bore in the rotor, and improved analysis capability. The elimination of this turnaround loss will improve HP turbine efficiency from 0.3 to 0.6 percent. The mechanical structure of the chamber itself has been substantially changed. Originally, in anticipation of thermal expansion constraints, the nozzle chamber assembly was split into six individual chambers welded into the inner cylinder in a flexible manner to reduce thermal stresses. Modern analysis and design techniques have shown a better approach to this problem. A much more robust and rugged design has evolved that reduces the six segments to two 180 deg ring structures, symmetric about the horizontal joint. A three-dimensional picture of the nozzle chamber ring is shown in Fig. 4. It is supported and aligned within the inner cylinder in a manner similar to a blade ring. The nozzle chamber ring structures are now physically separate and demountable from the inner cylinder for access and inspection. The support features, which provide high damping, and the ring structure, which is separate from the inner cylinder, significantly reduce any potential for flow-induced vibration of the chambers, and therefore should significantly reduce their required maintenance.

The thermodynamic benefit of the chamber design is an improved flow area control in the transition between the round inlets to the annular passage at the nozzle inlets. The better control of diffusion provides for reduced pressure loss and improved efficiency. Another benefit is the improved sealing potential of this design. The manner in which the ring structure is supported allows control stage sealing arrangements that much more nearly match thermal expansions. The effective service life of these seals should be significantly extended.

The steam inlet features that direct steam flow into the nozzle chambers have been redesigned. The inlet sleeves are now short and rugged with a diffused exit to enhance stability. New high damping inlet seal rings based on past proven designs replace the "Bell Seal" feature formerly utilized. Improved resistance to vibration is further achieved by sealing both the nozzle chamber inlet and the inlet sleeve in a common bore located in the stationary inner cylinder. The sealing surfaces are hard surfaced to reduce wear and galling.

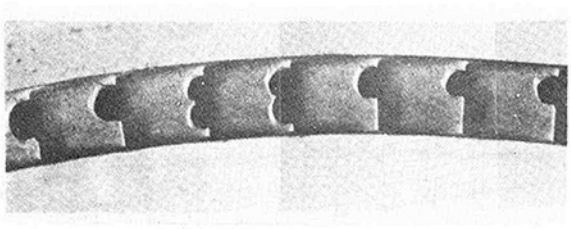

Fig. 7 Chipping of trailing edge of nozzle vanes

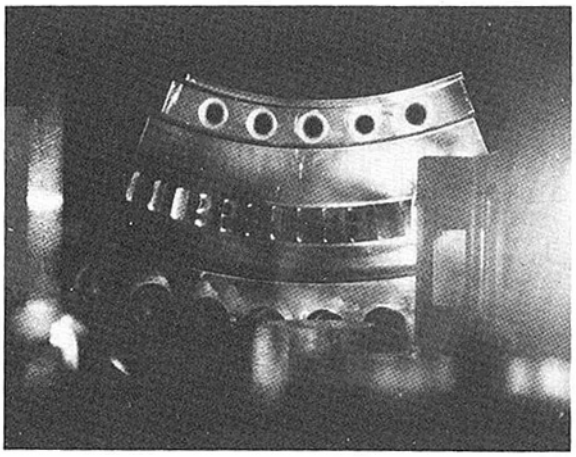

Fig. 8 Holographic image of vane panel mode vibration

Control Stage

The purpose of operating the control stage of a turbine is to have it act like an isentropic valve and thus avoid throttling losses at part-load operation. This is normally accomplished by controlling the arc of steam admission to the first stage. Impulse stages are most suitable for this service because the blades have a low pressure drop and therefore peripheral leakage out of the arc of admission is low. The inherent problem with any impulse stage is the high steam velocities across both nozzle and rotating blade, which lead to lower efficiencies and susceptibility to hard particle erosion and mechanical damage. Three approaches have been used to alleviate these problems and increase reliability, which are:

- Coating of inlet nozzles and blades
- Ruggedizing the nozzle vane profile
- Confining the use of impulse blades to the control stage region

Coating materials and process applications have been exhaustively investigated for consistency, application ease, erosion resistance, creep, and fatigue resistance (Quershi et al., 1986; Kramer et al., 1983). An example of erosion testing results is shown in Fig. 6.

The coatings investigation program evaluated twelve different coatings, and six different processes. The most attractive coating is now in the final verification phase.

The nozzle vane has an extremely harsh duty cycle. It needs to be thin and aerodynamically shaped for efficiency reasons, but robust to resist thermal shock and vibration. A common consequence of service is erosion and chipping of the trailing edge of the vanes shown in Fig. 7. This results in declining efficiency with time. Both holographic testing shown in Fig. 8 and finite element analysis have demonstrated that the chipping is due to a second panel mode vibration of the vane trailing edge, with a frequency of about 25 kHz. A new design of the vane section will reduce this as a concern.

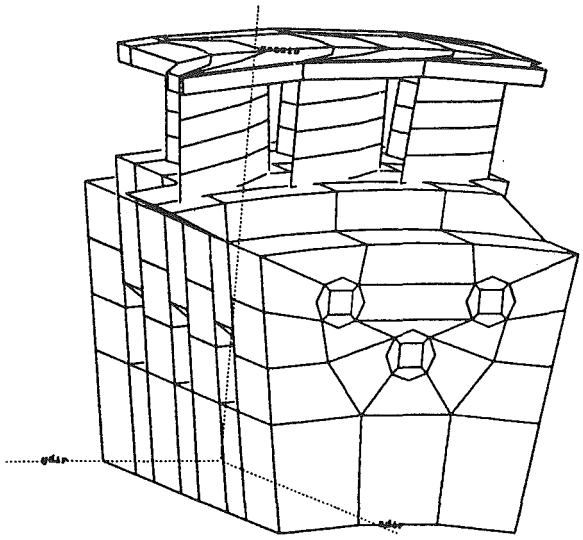

Fig. 9 Finite element model of triple pin, four-prong, control stage blade group

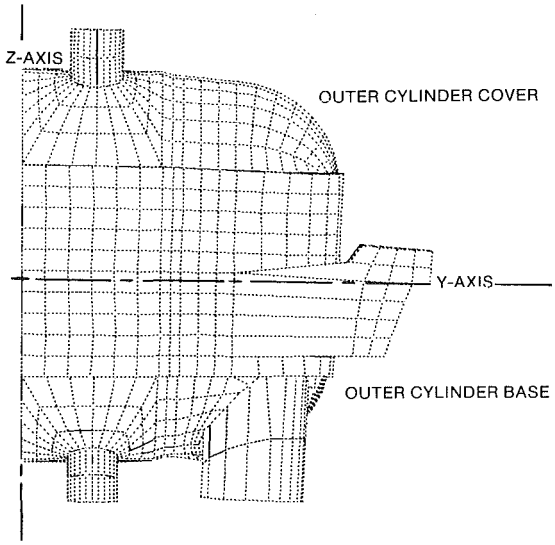

Fig. 10 Deformation pattern of outer cylinder showing cylinder humping

The new inlet nozzles also have a contoured end wall. This design reduces the secondary flow and improves aerodynamic efficiency. A new nozzle and rotating blade section have been developed. The new designs employ a passage velocity control philosophy outlined in Tran (1986), which significantly improves efficiency.

The feature of containing the control stage inlet nozzle vane in a mechanically demountable nozzle block for access and complete inspection has been maintained.

The new rotor is equipped with a rugged monoblock, pinned root, control stage rotating blade assembly. The blades, in clusters of three, have three large prongs, which engage in four rotor prongs machined in the control stage rotor region. The assembly and design technique is well proven in service and provides a fivefold improvement in mechanical strength over other control stage configurations (Partington, 1982). Control stage conditions are one of the most strongly varied elements as a machine is adjusted to individual utility requirements. The design process is now automated to the extent that an engineer need only input a handful of parameters and the entire finite element mesh required for optimization is produced automatically. A typical mesh of rotor and control stage blade is shown in Fig. 9. This has been proven invaluable in customizing to individual utility requirements.

As a result of these more rugged designs and more accurate analysis techniques, an eight-valve machine may now operate at 38 percent admission instead of the more common 50 percent. This produces an improvement in part-load efficiency, which is especially important for cycling units. The erosive environment for control stage rotating blades is somewhat less aggressive than for inlet nozzle vanes because of the lower relative velocities. However, for extended service life, the rotating blades are to be diffusion coated as part of the coating program discussed earlier.

Performance Aging

Unit efficiency will always change with age due to the effect of deposits on blade surfaces. However, some units have experienced significantly more aging than the industry average. This has been brought about by the following factors:

- Hard particle erosion
- Seal rubs and seal damage
- Nozzle vane trailing edge chipping

As previously discussed, the control stage nozzle and rotating blades have been the most susceptible to hard particle erosion. The new ruggedized designs use coated nozzles and rotating blades. The direct result is a reduction of performance aging in the control stage.

The use of reaction versus impulse blades in the remainder of the HP and IP blade paths is much less susceptible to hard particle erosion because of much lower turning angles for the hard particles.

A common problem with all turbine cylinders, but especially HP cylinders with their wide temperature extremes, is to control the location of the cylinder relative to the rotor and thus protect the blade path seals. Excessive displacements between rotor and cylinder parts can cause seal rubs that get progressively worse with time. The result is a significant decline in blade path efficiency with service due to leakage past the seals. Analytic investigations and field testing have shown a potential for generating cylinder displacements during shut-down unless care is taken with the isolation of the turbine. A typical deformation pattern is shown in Fig. 10, where the most common displacement is to curve the cylinder upward, relative to the rotor. This condition is called "cylinder humping," and can be corrected by applying heat at proper times and locations to the cylinder base. Several forms of heat input and protective measures were considered to accommodate the contributing factors to cylinder humping. The measures were required to be broad in application and also compensate for unusual operation. The final selection was a temperature feedback system based on cylinder temperature differentials. Electric resistance heating blankets attached to the cylinder base are activated by temperature difference and controlled with a microprocessor control system integrated with the start-up system. This process then permits control of cylinder position within wide latitude of shut-down system operation.

Seal damage due to rubs is also significantly reduced through the use of springback seals. The new designs use heavier seal strip sections to resist debris damage. The springback feature allows the seals to move with rub conditions at turning gear speeds, reducing wear on the strips.

Rotor

New advances in rotor forging steel making have brought about a significant reduction in flaws and discontinuities in the basic forging. The forging is also chemically and physically

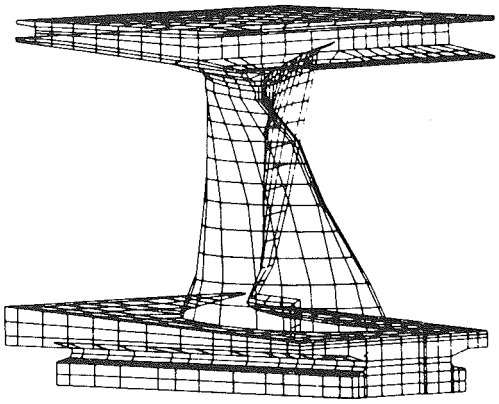

Fig. 11 Mesh for finite element stress calculations of integral shrouded blade

more homogeneous, with improved creep, fatigue, and fracture toughness properties (Swaminathan and Landos, 1984). These improvements combine to eliminate the main reason for a bore in the rotor. The rotor bore was utilized to improve the rotor forging by machining out the impurities and flaws that concentrated at the center of the forging. The immediate benefit of the no-bore rotors is the elimination of the stress concentration of the bore that is inherent in the geometry. This benefit and the improved properties may be utilized to enhance any or all of several features. Specifically:

- Improved rotor life due to higher fatigue properties and larger acceptable critical flaw sizes.
- Elimination of time-consuming boresonic examinations.
- Faster start-up times (in particular for cold starts) due to lower peak stresses.
- More tolerance for cyclic duty due to lower stress concentration and improved properties.
- Higher allowable temperature operation eliminates need for rotor cooling features and the turned around flow of the control stage.

In practice, a design compromise was evolved that balanced the gains of all of the desirable features without focusing exclusively on one element.

The restrictions that come with these benefits are:

- No test material from the interior.
- Sonic inspection from the exterior.
- More elaborate metallurgical preparation of the basic material.

The in-service inspection referred to is a requirement for satisfactory service. To accomplish this, the rotor geometry was carefully designed for acoustic patterns so that all critical regions are accessible for ultrasonic inspection from the rotor surface. For an example, an extra blade width was placed in midblade path in the HP turbine as a consequence of this consideration.

Consideration was given to the use of a 12 percent Cr rotor material, with the intention of reducing creep rate and potential in-service deformation. Both the open literature and the author's company testing gave no indication of improvement and as a consequence, it was not used. The creep-rupture strength of 12 percent Cr material may be higher, but this is more easily addressed by other mechanical design alternatives. In addition, producing an acceptable CrMoV no-bore rotor is a more predictable and cost effective process.

Integral Shroud IP Blades

Recently there has been a move toward blading with a minimum of mechanical attachments to remove as much craft content as possible in blade assembly. A blade row then becomes more predictable and analyzable. As blades get longer in the blade path there is a choice between free-standing blades and integral shrouded blades. Intermediate pressure turbines may use free standing blades but the width becomes excessive, and there is a heat rate penalty associated with this choice. A much more satisfactory selection is to use the integral shroud style and gain the strength and damping characteristics of a shroud while retaining the benefits of a single piece structure. A typical blade is shown in Fig. 11.

An extensive test program was undertaken to verify a design base that incorporated service and analytic experience. The products of this research are integral shroud blades, running successfully in numerous units. The design is now reduced to a well-defined process, automated from drafting through analysis and fabrication of the blades.

Conclusion

Major improvements in HP and HP/IP turbine reliability, availability, and efficiency have been made possible by a decade of intensive technology development in analysis and manufacturing.

The result is a ruggedized high-pressure turbine design for application to new units and retrofittable to operating units. Important benefits of the new design are significantly reduced maintenance, enhanced availability, and increased inspection intervals. In addition, heat rate reductions of 80–120 Btu/kWh (approximate 20–30 kcal/kWh) are possible when the technology is retrofittably applied to present operating older machines.

Acknowledgments

Special thanks are due to J. I. Quershi and V. P. Swaminathan for metallurgical advice, and A. J. Partington and J. P. Thomas for blading advice.

References

Kramer, L. D., Quershi, J., Rousseau, R. A., and Ortolano, R. J., 1983, "Improvements of Steam Turbine Hard Particle Eroded Nozzles Using Metallurgical Coating," ASME Paper 83-JPG-PWR-29.

Quershi, J., Levy, A., and Wang, B., 1986, "Characterization of Coating Processes and Coatings for Steam Turbine Blades," presented at the International Conference on Metallurgical Coatings, San Diego, CA, Apr.

Partington, A. J., 1982, "Vibration Analysis of Steam Turbine Pinned Root Control Stage Blades," International Federation for the Theory of Machines and Mechanisms Proceedings of the Meeting on Dynamics of Rotating Machines, Rome, Italy, Sept.

Steltz, W. G., Evans, D. H., and Desai, K. J., 1979, "Low Pressure Steam Turbine Efficiency Improvements as Verified by Field and Full Scale Laboratory Test Results," presented at the Institution of Mechanical Eng. 1979 Design Conference of Steam Turbines for the 1980s.

Steltz, W. G., Evans, D. H., and Stahl, W. F., 1974, "The Aerodynamic Design of High Performance Low Pressure Steam Turbine," Third Scientific Conference on Steam Turbine of Great Output, Gdansk, Poland, Sept.

Swaminathan, V. P., and Landos, J. D., 1989, "Temperature Dependence of Fracture Toughness on Large Steam Turbine Forgings by Advanced Steel Melting Processes," *Fracture Mechanics Fifteen Symposium,* ASTM STP833, R. J. Sanford, ed., American Society for Testing and Materials, Philadelphia, pp. 315–332.

Thomas, J. P., and Pigott, R., 1984, "Turbine Blade Design and Analysis for Reliability," presented at the First Parsons International Turbine Conference, Dublin, Ireland, June.

Tran, M. H., 1986, "Recent Development in Blading to Improve Turbine Efficiency," ASME Paper No. 86-JPGC-Pwr-35.

DISCUSSION

R. J. Ortolano[1]

The authors are complimented on their paper, which depicts a number of significant design improvements that are expected to produce both efficiency and reliability benefits. It is noted that the use of countersunk riveted blading to accommodate multiple radial seals on the spring-backed rings also avoids rivet erosion from abrasion.

The reversal of the nozzle chamber is intended to improve the HP turbine efficiency. Hopefully, this is achieved without creating an excessively high partial arc stimulus on the downstream reaction blading due to the shorter steam path.

The 180 deg ring-type nozzle chambers with removable nozzle blocks should be a distinct structural advantage while retaining access and ease of repair for the blocks.

Monoblock constructed blading is another significant feature, which should reduce assembly distortion and associated stress. Care should be given to stresses at the axial pin holes in the blades and disk, particularly at the corners and with respect to an interference fit pin. Of course, since the blading is manufactured as a set, it requires diffusion alloying rather than plasma spray for abrasion protection.

Spring-back seals, particularly of the repairable type, should be an attractive feature, along with the other improvements mentioned. Spring-backed seals for use in the IP turbine also appear to be quite compatible with the integral covered blading, due to the absence of tenon rivets.

The authors have clearly shown that the current lull in power plant construction can be effectively used to develop needed improvements, which can be applied to both existing and future units.

T. H. McCloskey[2]

The authors are complimented for their very interesting and useful paper, which promises substantial steam turbine reliability and performance improvements utilizing modern state-of-the-art design techniques.

The following comments and questions relate to several design modifications presented in the paper and are intended to clarify certain features of the ruggedized HP/IP turbine.

We concur with the authors' use of the triple-pin, control stage blade root attachment in lieu of the more conventional axial "Fir Tree" root construction. Independent finite element analyses have shown that high cycle fatigue stresses caused by partial arc admission and coupled with high temperature creep are much less likely to occur with the triple pin design as compared to the axial fir tree design (Reiger et al., 1986).

The elimination of the rotor bore represents a significant step advance in conventional large turbine rotor technology resulting in extended operating life, increased cyclic duty operation, and reduced maintenance inspection. This metallurgical advance was made possible in large part by a joint Westinghouse/EPRI research project, which developed and qualified the advanced low impurity rotor forging techniques employed in the ruggedized rotor (Swaminathan and Jaffee, 1986).

Many utilities have retrofitted provisions for fiberscopic examination of internal turbine components without the added need and expense of cylinder cover removal (Ortolano, 1986). Have the authors considered making any provisions in the ruggedized design to include fiberscope provisions to minimize downtime during periodic maintenance inspection?

The projected 120 Btu/kWh heat rate improvement is based solely on aero and thermodynamic design optimization studies. What is the original cycle heat rate from which this gain is projected, and do the authors have any plans to conduct an ASME PTC-6 field performance test to verify this efficiency improvement?

[1]Consulting Engineer, Southern California Edison Company, Rosemead, CA, 91770.

[2]Manager, Steam Turbines and Related Auxiliaries, Coal Combustion System Division, EPRI, Palo Alto, CA 94303.

References

Ortolano, R., 1986, "Inspection, Modification, and Repair of Steam Turbine Blading," EPRI Workshop on Steam Turbine Blade Reliability, Mar.

Reiger, N. F., Steel, J. M., and Lam, T. C., 1986, "Development and Testing of a General Purpose Finite Element Code for Stress and Vibration Analysis of Steam Turbine Blade Groups," ASME Paper No. 86-JPGC-Pwr-34.

Swaminathan, V. P., and Jaffee, R. I., 1986, "Significant Improvements in the Properties of CrMoV HP Rotors by Advanced Steel Making," EPRI Workshop on Life Assessment and Improvement of Turbo-Generator Rotors for Fossil Plants, Paper No. CS-4169.

Authors' Closure

The writers wish to thank Mr. Ortolano and Mr. McCloskey for their discussions. Their comments are generated from an extensive industry information base.

Prior to adopting the straight-through control stage design, considerable attention was given to the shock potential on the reaction blades. Flow distribution test and mechanical analyses were performed to ensure blading reliability. In addition, the stress of all areas of the triple pin control stage design were investigated. The authors' company has never experienced a control stage problem with a triple pin design of this type.

While no-bore rotors will require less inspection, provisions have been provided for ultrasonic inspection of the rotor body from the surface. These no-bore rotors provide cyclic duty benefits, as well as permitting performance improvements.

The possibility of fiberscopic inspection has not been specifically provided for in the cylinder design of the first application of this technology. This capability, however, is available for the inlet nozzles and control stage blades with modifications to the turbine inlet piping.

The 120 Btu/kWh heat rate improvement is developed when modifications are made with a basic turbine heat rate of approximately 7800 Btu/kWh. This heat rate improvement is developed from all of the features discussed in the paper for a combined HP-IP element and the reduction in the existing levels of performance aging for this type of equipment. The efficiency improvements will be verified with enthalpy drop test before and after the installation of the ruggedized design.

A New Concept for Operation of a Pulverized Coal Fired Boiler Using Circulating Fluidized Bed Firing

P. Basu
Centre for Energy Studies.

P. K. Halder
Department of Mechanical Engineering.

Technical University of Nova Scotia,
Halifax, Nova Scotia,
Canada B3J 2X4

The feasibility of adapting existing pulverized coal fired boilers slated for life extension to circulating fluidized bed firing is examined by considering the case of a 150 MWe tangentially fired pulverized coal boiler. The proposed modifications call for a minimum of change in existing units. Thermal calculations are presented to show how heat absorption in different sections of the converted boiler can be matched to that in the pre-existing pulverized coal fired boiler. Data for two load conditions are presented to identify problems associated with low loads. Fuel flexibility in the converted circulating fluidized bed unit is shown by repeating the thermal calculations for coal washery rejects. It is concluded that the adoption of circulating fluidized bed firing is thermodynamically feasible.

Introduction

Zylkowski et al. (1985) reported that about 200 pulverized coal fired (PC) utility units in the USA with a total capacity of 20,000 MWe are due for life extension. At a time when foreseeable future stringent environmental regulations may require a large capital investment in the utility sector for setting up new boilers that are environmentally acceptable, there are two choices. Utility boilers, due for life extension, could either be converted to bubbling fluidized bed firing, or new items like flue gas desulfurization equipment, low NO_x burners, etc., could be added to the existing plants. The first choice involves time and money but the second requires costlier equipment and forces the user to compromise on fuel flexibility. The present work is a search for a third alternative for adoption of a more advanced coal burning system into existing PC boilers. The examination of the feasibility of a new concept has two steps. The first step is an examination of the scientific and technical feasibility. If feasible, one goes to the second step of examining whether it is economical. The present paper concerns the first step.

When in search of an advanced coal burning system, one looks for both bubbling and circulating fluidized bed systems that are known for fuel flexibility and their compliance with environmental constraints. The circulating fluidized bed process is favored by industries because of its several additional advantages, for example: simpler fuel feed system, better sorbent utilization, better load following, and higher combustion efficiency. Attempts would be made to explore whether an existing PC boiler can be adapted to CFB firing.

Here, the combustion and heat transfer features of a pulverized boiler are compared with those of a circulating fluidized bed combustor. Also the paper examines, through a thermodynamic study, whether a 150 MWe PC boiler could be modified for CFB firing.

The paper also discusses some engineering aspects of the modifications of the PC boiler that would be necessary to adapt it to CFB firing.

Compatibility

Basu (1987) noted similarities between some key design features of pulverized coal (PC) and circulating fluidized bed (CFB) boilers. For any new firing process to be compatible with existing PC units the following important design criteria must be similar:

1 Furnace heat absorption rate (on the basis of both effective projected surface area and furnace volume).

2 Furnace heat release rate based on the grate (furnace cross section) area.

3 Table 1 shows the degree of similarity when the above

Table 1 Similarity between PC and CFB firing

	PC furnace[1]	CFB firing[2]
Grate heat release rate, MW/m^2	4.4–6.3	2–6.0
Volumetric heat release, MW/m^3	0.15–0.23	0.1–0.25
Average height of the furnace, m	27–45	15–45
Average heat absorption rate based on effective projected radiant surface of wall, MW/m^2	0.05–0.25	0.05–0.17

[1]Data taken from Singer (1981).
[2]Data taken from Basu (1986).
[3]Based on actual area of fin and tube = 1.475 × projected area.

Contributed by the Power Division for publication in the JOURNAL OF ENGINEERING FOR GAS TURBINES AND POWER. Manuscript received by the Power Division May 28, 1987.

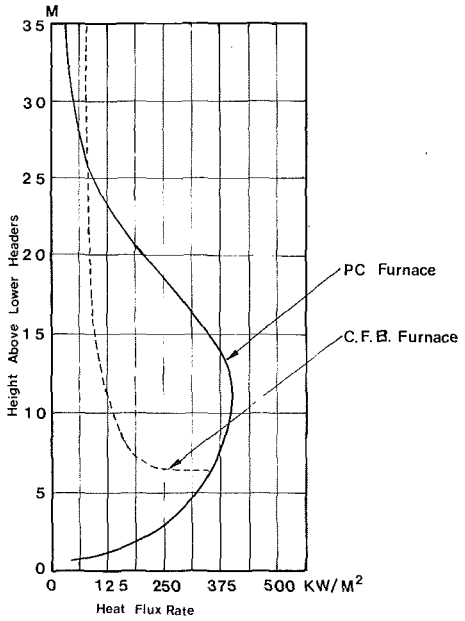

Fig. 1 Heat flux rates at different elevations in a typical PC furnace at maximum output, and that in a CFB furnace of similar height

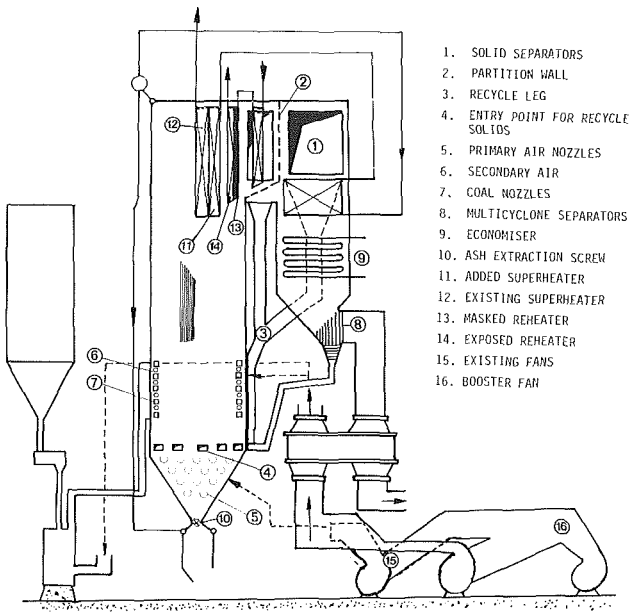

Fig. 3 A 150 MWe PC boiler when fired as a CFB boiler

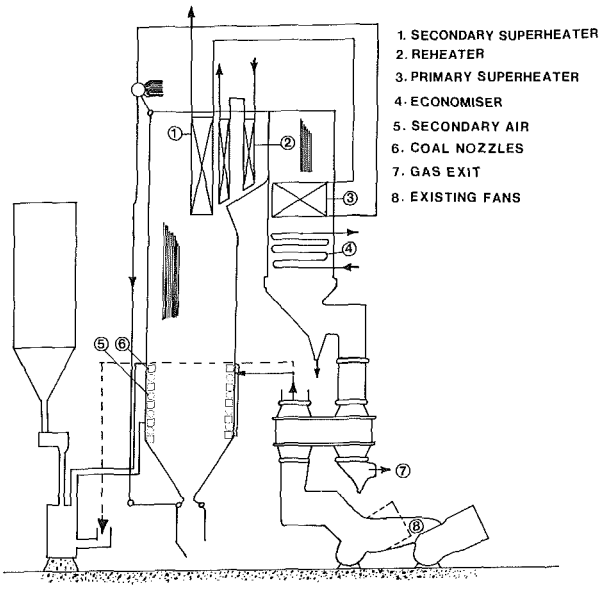

Fig. 2 A 150 MWe PC boiler when fired as a PC boiler

three criteria for PC firing are compared with those for CFB firing. Other areas where compatibility is required are discussed below.

The residence time of a 0.1 mm particle in a 45-m-tall PC boiler is about 2-3 s. Since it takes about 0.5 s for a carbon particle of this size to burn completely (Field et al., 1967), virtually no unburned carbon leaves a PC furnace. Assuming kinetic control, the burnout time in a CFB for a 0.1 mm carbon particle is about 8 s (Basu, 1986). Since the particles are backmixed, the mean residence time could be as high as 26 s in a 45-m-tall unit. Thus the 0.1 mm particle could be expected to burn completely before it leaves the furnace. Large-size particles may leave the CFB furnace before complete burnup, but these would be captured in the gas–solid separation section of the system and recycled to the furnace for further combustion. Thus large particles will follow a number of cycles before they are burned completely.

Flue gas enters the second pass of a PC boiler at about 800°C, which is about the same as for a CFB. Since the mass flow of gas is also the same in the two firing systems, it may be possible to extract the same quantity of heat in the second pass containing an air heater, economizer, primary reheater, or superheater tubes after adaptation to CFB firing. Thus systems become compatible if the first pass of CFB can absorb the same heat as the PC. However, differences may exist in the heat transfer rates in the combustion chamber.

In a PC boiler there is a wide variation of heat flux over the height of the furnace (Fig. 1). However, the average heat absorption is generally in the range of 0.05 to 0.22 MW/m^2 (Singer, 1981). The average absorption in CFB boiler furnace is in the range of 0.20–0.17 MW/m^2. Thus there is a considerable overlap in the furnace heat absorption rate between these two firing systems.

The heat transfer rate to the radiant superheater and reheater in a PC boiler is above the average absorption in the furnace. Also it is much higher than heat flux on the superheater and reheater surfaces beyond the furnaces. In a CFB the heat transfer in the furnace is uniform. Thus after adaptation to CFB firing there would be fewer secondary superheater and evaporator tubes and more reheater tubes than in the original PC boiler.

Scheme of Adapting to CFB Firing

The foregoing discussion will show that it is thermodynamically feasible to adapt CFB firing to some types of PC boilers. A specific case study based on a 150 MWe PC boiler will be made, but the method and rationale can be generalized to other PC boiler units. The following section shows what mechanical modifications are necessary.

Figure 2 is a sectional elevation of the 150 MWe PC boiler before conversion and Fig. 3 is a schematic diagram of the same boiler after adaptation to CFB firing. As discussed earlier, the secondary superheater and reheater heating surfaces had to be readjusted for the difference in the heat absorption rates in a CFB. About 20 percent of the reheater tubes had to be masked with refractory and the secondary superheater heating surface had to be increased by about 100

percent. Since the transverse tube pitching is 68 mm, there is enough room to add the additional heating surface in the secondary superheater.

The bottom tapered section of the furnace on conversion will be covered by refractory. This section acts as a thermal flywheel and provides additional heat for any sudden surge in the demand. The screen tubes after the reheater are masked with refractory to form a barrier, and the side panel walls of the space up to the masked reheater tubes are opened to allow flue gas to enter the solid separation system. Here the gas flows first through a series of impingement-cum-inertial separators. An array of multicyclone-type dust collectors is placed below the economizer.

Figure 4 is a plane view of the separation system proposed for the conversion, which extends up to 4.3 m from the boiler surface and covers the entire 6 m back pass from the outlet of the reheater. Four rows of 50 mm o.d. impingement separators are proposed, which may give about 93 percent efficiency for 75 μm particles. To capture the fines, 1120 geometrically similar 150 mm multiclone collectors are placed at a pitch of 305 mm below the economizer. These will give about 99 percent efficiency for 10 μm particles (Perry and Chilton, 1973).

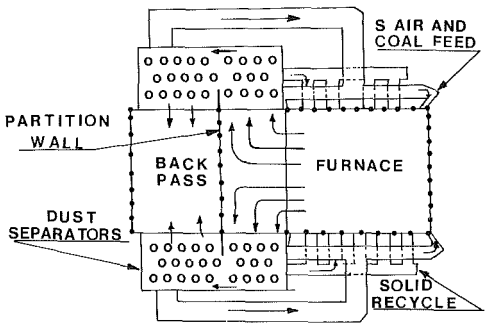

Fig. 4 Plan view of a 150 MWe PC boiler when fired as a CFB boiler

This adaptation does not affect the performance of the backpass elements such as primary superheater, economizer, and air heater. Enclosures covering the separators will be connected to a refractory-lined common hopper across the depth of the furnace. The total solid flow in this boiler will be about 1068 kg/s, assuming 10 kg/m^{2}s recycle rate (Kobro and Brereton, 1986). This will require about four L-valves of 1 m diameter each placed at two elevations at the rear side of the refractory-lined section of the furnace. These valves will require about 240 m^3/h air, which will be injected around this periphery of the L-valve. Fines collected below the economizer are pneumatically injected to the bed at the same level as that of the L-valves.

Table 2 Analyses of fuels used in the calculations

Proximate analysis, percent	Coal (Type A[1])	Washery rejects (Type B[2])
Moisture	8.9	---
Ash	13.01	---
Volatile matter	29.79	---
Fixed carbon	45.0	---
Sulfur	3.3	---
Gross calorific value, kcal/kg	6158	4280
Ultimate analysis, percent	(dry basis)	
C	68.05	36.9
H	4.19	2.4
N	1.22	0.06
A	14.3	52.2
S	3.63	5.4
O	8.61	3

[1]Type A: Blend of 60 percent Raw Prince and 40 percent Lingan washed middlings.
[2]Type B: Coal washery rejects.

Table 3 Projected performance of 150 MWe PC boiler when fired as a CFB with Type A coal

Firing system	PC		CFB	
Boiler load	100 percent	60 percent	100 percent	60 percent
Main steam:				
Flow, kg/s	132.3	79.4	132.3	79.4
Pressure, MPa	13.2	13.2	13.2	13.2
Temperature, C	540	540	540	535
Reheat steam:				
Flow, kg/s	120	73	120	73
Pressure, MPa	3.3	2.0	3.3	2
Temperature, C	540	540	540	540
Coal feed, kg/s	16.6	10.8	17.2	11.0
Excess air, percent	18	25	15	15
Combustible loss, percent	0.4	0.4	2	2
Boiler efficiency, percent	86.7	85.9	83.8	82.7
Superficial velocity, m/s	---	---	5.6	3.6
Number of burner or feeder	12	8	12	8
Temperature °C				
Air leaving preheater	292	272	292	272
Flue leaving furnace	1165	1079	871	843
Flue leaving secondary S.H.	1011	917	871	843
Flue leaving high-temperature R.H.	---	---	871	843
Flue leaving low-temperature R.H.	812	726	809	787
Flue entering primary S.H.	774	690	773	751
Flue leaving primary S.H.	525	478	507	501
Flue leaving economizer	357	313	365	334
Flue leaving air preheater	171	171	171	182
Steam leaving primary S.H.	421	414	421	410
Water entering economizer	237	212	237	212
Water leaving economizer	290	272	290	276

Table 4 Projected performance of 150 MWe PC boiler when fired as a CFB with Type B fuel

Firing system	CFB	
Boiler load	100 percent	60 percent
Main steam:		
Flow, kg/s	132.3	79.4
Pressure, MPa	13.2	13.2
Temperature, °C	540.0	535.0
Reheat steam:		
Flow, kg/s	120.9	73.1
Coal feed, kg/s	25.14	16.05
Excess air, percent	30.0	30.0
Combustible loss, percent	3.5	3.5
Boiler efficiency, percent	82.5	81.5
Superficial velocity, m/s	5.43	3.44
Number of burner or feeder	12	8
Temperature, °C		
Air leaving preheater	292	272
Flue leaving furnace	871	843
Flue leaving secondary superheater	871	843
Flue leaving high-temperature reheater	871	843
Flue leaving low-temperature reheater	809	787
Flue entering primary superheater	773	746
Flue leaving primary superheater	507	498
Flue leaving economizer	357	331
Flue leaving air preheater	171	179
Steam leaving primary superheater	421	407
Water entering economizer	237	212
Water leaving economizer	290	274

The primary air will be supplied by ducts placed at the bottom of the furnace. The secondary air will be supplied through the existing coal nozzles along with the pulverized coal. The air pressure may be raised by using a separate booster fan to about 3.5 m H_2O as required for any CFB system. The air for the nonmechanical L-valve and fine injection will be supplied by a separate fan.

Performance After Conversion

The analyses of two types of coal used in the performance calculations are shown in Table 2. Using these two types of coal, heat and mass balance calculations were carried out for 100 and 60 percent of maximum continuous rating of the boiler. Projected efficiencies, steam and local gas temperatures, and other parameters before and after the conversion are reported in Tables 3 and 4. Thermal calculations show no difference in steam and exit gas temperatures. A drop in the boiler efficiency after conversion to CFB firing is noticed here. This is attributed to the conservative estimate of 98 percent combustion efficiency for CFB firing. The gas side heat transfer coefficients were taken from Ganapathy (1982).

In a PC furnace, the mode of heat transfer is radiative and its peak value is much higher than the average value in a CFB, where the heat transfer is primarily through particle convection. Unlike a PC furnace, the solids in a CFB are backmixed. These solids are the major heat carrier, and transfer heat to the entire height of the furnace, maintaining a uniform temperature throughout the furnace. The heat transfer in CFB depends primarily on the bulk density of gas–solid suspension in the furnace. Since the density of this suspension is relatively high, even immediately after leaving the furnace, the heat transfer coefficient in the reheater and secondary superheater region of CFB furnace is much higher than that in PC systems. The steam generation in a CFB may be increased by operating the CFB boiler at a higher bed density, which gives a higher heat transfer coefficient. Additional steam generation may

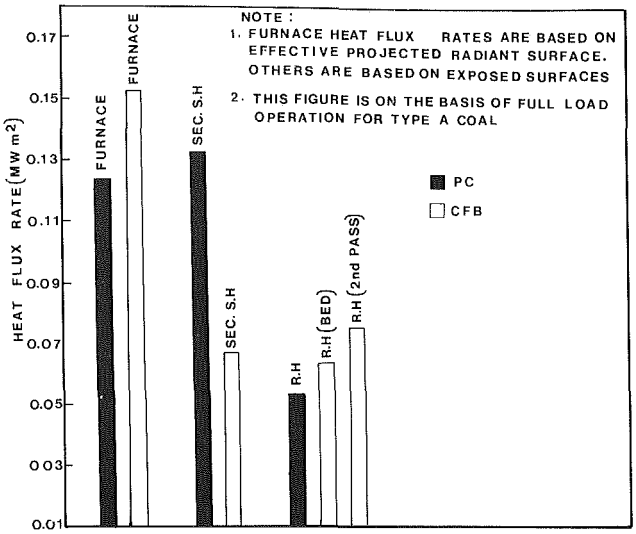

Fig. 5 Heat flux rates at different sections of the boiler before and after adaptation: calculations based on bituminous coal

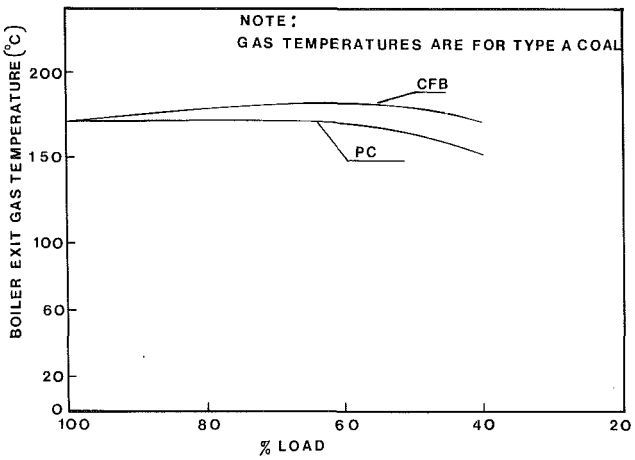

Fig. 6 Variation of boiler exit gas temperature with load before and after adaptation

take place in the cyclone enclosure where the gas temperature drops by about 90°C.

It is impossible to run a PC boiler with coal washery rejects alone. Therefore, performance calculations for this fuel were not made for PC boilers. Conversion to CFB firing makes the performance of an existing PC boiler less sensitive to the quality of coal. Thus the performance calculation for the CFB fired PC boiler was also extended to washery rejects. However, the boiler efficiency will be a little lower for firing washery rejects due to the high excess air required for this low-quality fuel. Figure 5 shows the rate of heat transfer at different sections of the PC boiler before and after adaptation.

Part-Load Operation

The heat transfer in a CFB is greatly influenced by the bed density. At full load the average value of the heat transfer coefficient could be as high as 0.176 kW/m^2 K when the bed density is 52 kg/m^3. On the other hand it could be as low as 0.096 kW/m^2 K when the bed operates in the transition to dilute phase transport with a bed density of 5 kg/m^3. The correlation of Basu (1986) has been used for these calculations. For full load the higher value of heat transfer coefficient is chosen. For 60 percent load, the bed density is reduced to 25

kg/m^3 to reduce the heat transfer coefficient to 0.13 kW/m^3 K. Thus the boiler load is controlled by adjusting the solid recycling rate, which in turn changes the bed density.

The thermodynamic calculation with coal washery rejects suggests that it is technically feasible to operate the boiler down to 60 percent load without any auxiliary fuel support. However, it was observed that for both fuels, operations below 40 percent load may create problems with fast fluidization in the furnace, as the velocity drops below the minimum velocity for fast fluidization. The bed may have to be operated under entrained bed conditions.

From Tables 3 and 4 it is apparent that steam and exhaust gas temperatures do not change appreciably with load. Figure 6 is a plot of boiler exit gas temperature with load, and a slight increase in the exit gas temperature for less than 100 percent load is observed. Primary air at the bottom of the CFB furnace should not exceed the stoichiometric air requirement. For full load and 60 percent load, the velocities at the bottom of the bed are 4.7 m/s and 3.0 m/s, while the corresponding superficial velocities are 5.6 m/s and 3.6 m/s, respectively. In view of this low fluidization velocity the size of coal and sorbents must be chosen to yield fast fluidization at the operating velocities.

Conclusions

A thermodynamic study has shown that it is conceptually feasible to adapt a tangentially fired 150 MWe PC fired boiler to CFB firing and that from the heat transfer and combustion standpoint, the performance of the converted unit is comparable with the original PC fired boiler. This conclusion is valid for the two loading conditions calculated. Boiler efficiencies are lower with CFB firing but this is associated with assuming a value of 98 percent for combustion efficiency. An examination of the boiler hardware reveals that most of the existing equipment can be used. The only additional space required would be to install two dust collectors at two locations.

It is emphasized that the study was primarily a thermodynamic one and that detailed engineering aspects of conversion, such as structural rigidity, etc., and techno-economic studies, have not been addressed here. For a full feasibility study of the adaptation of CFB firing in PC boilers slated for life extension further studies are required.

References

Babcock & Wilcox, 1972, *Steam—Its Generation & Use*, 38th ed., B&W, USA.

Basu, P., 1986, "Design Consideration of a Circulating Fluidized Bed Boiler," *Journal of Institute of Energy*, Dec., pp. 179–183.

Basu, P., 1987, "Operation of an Existing Pulverized Coal Fired Boiler as a Circulating Fluidized Bed Boiler," *Journal of Institute of Energy*, pp. 77–87.

Field, M. A., Morgan, D. W., and Hawksley, B. B., 1967, *Combustion of Pulverized Coal*, Institute of Energy, pp. 350–369.

Ganapathy, V., 1982, *Applied Heat Transfer*, Pennwell Publishing Company, OK, pp. 426–474,

Kobro, H., and Brereton, C., 1986, *Control and Fuel Flexibility of Circulating Fluidized Bed Technology*, Pergamon Press, P. Basu, ed., p. 266.

Perry, R. H., and Chilton, C. H., 1973, *Chemical Engineering Handbook*, 5th ed., McGraw-Hill, pp. 18–85.

Singer, J. G., 1981, *Combustion—Fossil Power System*, 3rd ed., Combustion Engineering Ins., Windsor.

Zylkowski, R. J., Krippene, B. C., and Gramble, R. L., 1985, "Black Dog AF BC Retrofit for Emission Reduction, Capacity Increase, and Life Extension," *Proceedings of the Eighth International Conference on Fluidized Bed Combustion*, Vol. 1, DOE/METC-85/6021, pp. 350–369.

C. M. Grondahl
Senior Engineer,
General Electric Co.,
Turbine Technology Department,
Schenectady, NY 12345

R. D. Linnell
Service Supervisor,
General Electric Co.,
Industrial Sales & Service Division,
Harahan, LA 70123

T. J. Martin
Chief Power Engineer,
Louisiana Plant,
Texaco, USA,
Convent, LA 70723

The Modernization of a 1965 MS5001 Gas Turbine: New Life for an Old Unit

Application of the GE MS5001 gas turbine performance improvement uprate package has been extended to an early model "K" unit at Texaco's Convent, LA, refinery. This extensive modification required replacement of the turbine shell in addition to the installation of new technology components developed for more recent MS5001 models. This paper presents the customer's motivation to refurbish a 22-year-old gas turbine. Gas turbine component design improvements and interfaces are discussed with performance and reliability gains. Field service engineering experience installing the uprate is also related.

Introduction

Significant advances in gas turbine technology have been applied to new unit production in the past 15 years. Application of these improvements to field units can increase ouput with better heat rate and fewer inspections per year. A gas turbine performance improvement package for the MS5001 machine series was introduced in 1984 [1]. It specifically addressed the model "L" and newer units, shipped since 1966, that have many similar features. While some 30 of these units have now been uprated and operate with enhanced performance and reliability [2], there are earlier MS5001 models that continue in profitable service that are prime candidates for uprate and modernization (see Table 1). However, the assembly of new or advanced design gas path components in an early design turbine shell was considered a barrier to the new technology performance uprate package until 1986 when Texaco sought to modernize one of these older units, an MS5001 model "K," at the Convent, LA, refinery.

Operator Needs and Objectives

The Texaco facility at Convent, LA, is designed to process 240,000 barrels per day of crude oil into fuel products. There are two gas turbines in the plant, which operate as process compressor drivers. Both are General Electric Machines, one a MS3002 and the other a MS5001. The MS3002 was upgraded from a model "G" to an "F" in 1984 after 142,800 operating hours to meet a higher horsepower requirement. The MS5001 model "K" unit had 168,000 operating hours at this upgrade in 1987.

The MS5001 train consists of the following equipment (see Fig. 1): a 934 hp GE starter turbine; the MS5001 gas turbine; a Cooper Bessemer RFS process compressor rated 8419 hp; a Lufkin 2.024 ratio gear box rated 10,000 hp; a Cooper Bessemer RCS process compressor rated 6,032 hp; and two fired process heaters.

The upgrade project was aimed at improving unit availability and increasing the process compressor throughput. The project included complete new aerodynamic assemblies for both process compressors, a new speed increaser gear box, an upgrade of the gas turbine and process compressor controls, and the gas turbine uprate to the MS5001 model R, new technology turbine, i.e., the "R/NT" performance uprate package.

Prior to the upgrade, Texaco experienced significant process curtailments caused by the deteriorated condition of the gas turbine after 160,000 operating hours and the resulting unscheduled shutdowns. There also has been an increase in process compressor horsepower requirement during summer

Table 1 MS5001 fleet operation, Jan. 1988

Units Shipped & Commercial			Units Operated More Than			
Models	Units	Avg. FH	50,000 Hrs.	100,000 Hrs.	150,000 Hrs.	200,000 Hrs.
A-K	130	69,000	67	40	17	3
L-M	575	48,000	190	116	13	—
N-R	1080	33,000	235	18	1	—

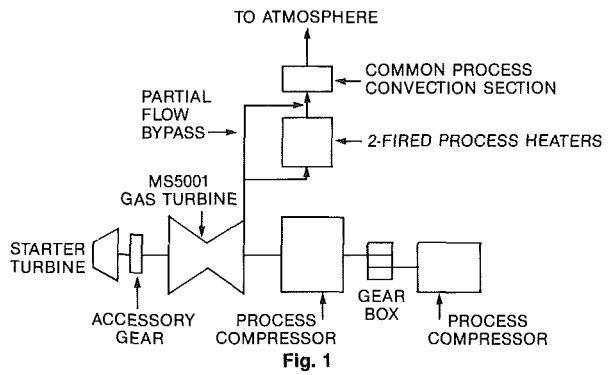

Fig. 1

Contributed by the International Gas Turbine Institute and presented at the 33rd International Gas Turbine and Aeroengine Congress and Exhibition, Amsterdam, The Netherlands, June 5-9, 1988. Manuscript received by the International Gas Turbine Institute October 8, 1987. Paper No. 88-GT-143.

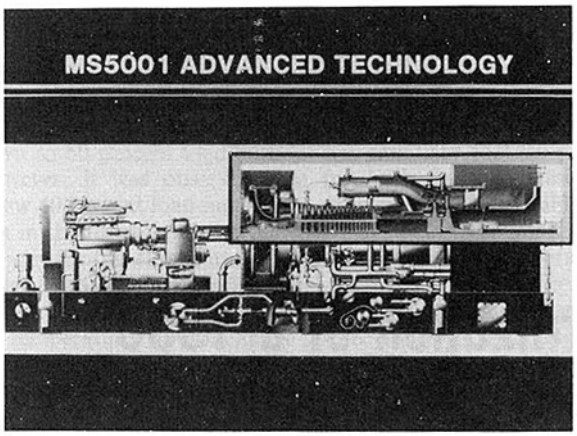

Fig. 2

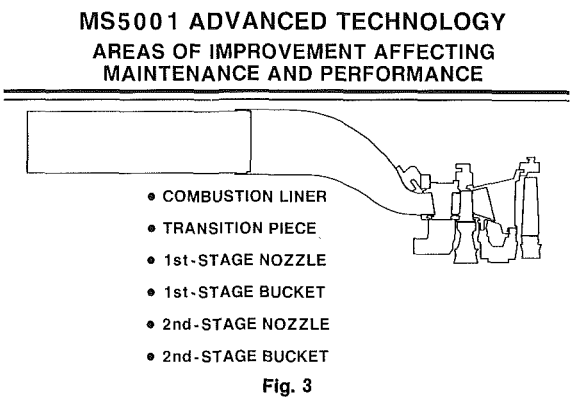

Fig. 3

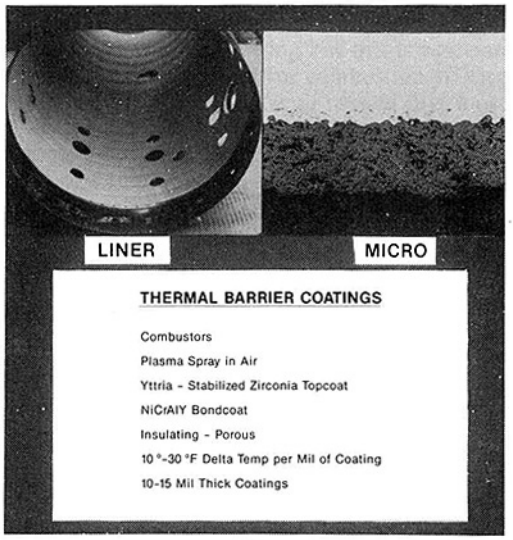

Fig. 4

Table 2 MS5001 performance history

MODEL	SHIP DATES	KW (NEMA)[1]	FIRING TEMP (F)	AIR FLOW (LBS/S)
A	1957–1961	10,000	1500	184
C	1961–1964	10,250	1500	184
D	1961–1963	10,750	1500	184
E	1963	10,750	1500	193
G	1963–1964	12,000	1500	193
H,J	1964	12,500	1500	193
K	1965	12,500	1500	195
L	1966–1967	14,000	1600	195
LA	1968–1970	15,250	1650	197
M	1969–1970	16,100	1700	199
		KW (ISO)[1]		
R	1970–1987	19,400	1720	201
R-N/T	1987–	20,500	1755	201
N	1970–1972	24,700	1730	263
P	1972–1978	25,280	1730	263
P	1978–1986	25,890	1730	269
P-N/T	1987–	26,930	1755	273

(1) In the early 1970's, Rating Standards were changed from NEMA (1000 ft. altitude and 80 F) to ISO (Sea level and 59 F) conditions. To convert from NEMA to ISO ratings for approximate comparison, multiply NEMA rating by 1.12.

months when gas turbine horsepower output is minimum and the refinery wants to produce maximum gasoline. Such an operating restriction is extremely costly.

After the last major turbine overhaul in 1982, Texaco planned to replace the stationary inlet guide vanes and the first and second-stage nozzles at the next overhaul, as well as nondestructive testing or replacement of first and second-stage buckets. Testing, however, does not predict remaining component life and Texaco decided to replace these buckets due to the critical nature of this machine and the desire to operate for a minimum of four years between overhauls.

During June 1986 a major process unit upgrade was defined and funded. This project called for a 24 percent increase in compressor flow and a 10 percent increase in compressor head. With a desire to cover this increased horsepower requirement at summertime operating conditions and to improve the availability of spare parts, GE was contracted to upgrade the gas turbine to "R/NT."

During Oct. 1986, a secondary project was approved to upgrade the gas turbine and compressor controls. This part of the project was justified by a sudden increase in train tripouts caused by control problems. Sixteen tripouts were experienced in the first nine months of 1986. An average of 3.3 tripouts per year had been experienced the previous three years. Texaco wanted to upgrade to the Mark IV SPEEDTRONIC™ control system, but delivery could not be made by the March 1987 outage.

MS5001 "New Technology" Performance Uprate Components

The MS5001 gas turbine, shown in Fig. 2, was first produced in 1957. Performance improvements associated with design enhancement of the MS5001 turbine over the years are shown in Table 2. (Changes of GE gas turbine designs have traditionally been designated alphabetically as a suffix to the basic model series; hence the MS5001 Model A, B, etc.). Until the introduction of a 17-stage compressor with the model N in 1969, which is now used in model P, there had been essentially no change in the aerodynamic design of the turbine section of MS5001 models. This stable aerodynamic design was the basis for the development of a package of uprate components incorporating recent developments, i.e., "new technology," in terms of material advancements and design improvements that have been introduced on the latest GE gas turbine products. Areas of improvement affecting maintenance and performance are illustrated in Fig. 3 and discussed below.

Combustion Liner. Two major advances to the louvered liner concept are a thermal barrier coating and a splash plate crossfire tube collar.

The thermal barrier coating on the internal surfaces of the liner reduces liner operating temperatures and peak thermal strains (Fig. 4). The coating's insulating quality averages out peak thermal strains and increases liner life. This yttria-stabilized zirconia coating is porous and has a low thermal conductivity.

The splash plate concept replaces the small louvers surrounding the crossfire tube collar with cooling holes. This configuration reduces stress concentrations and adds to liner life.

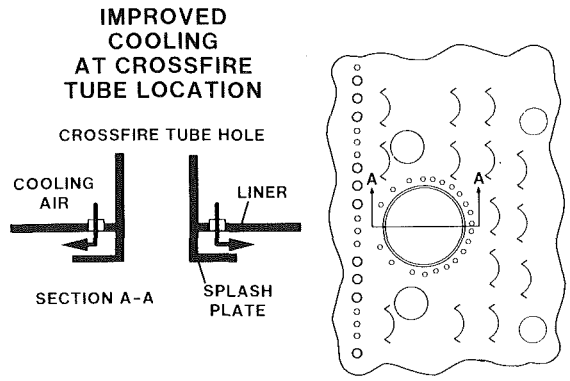

Fig. 5

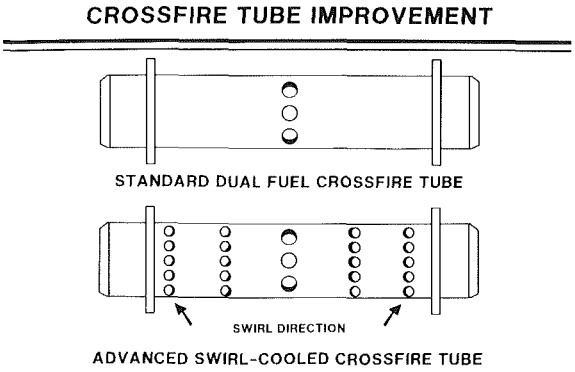

Fig. 6

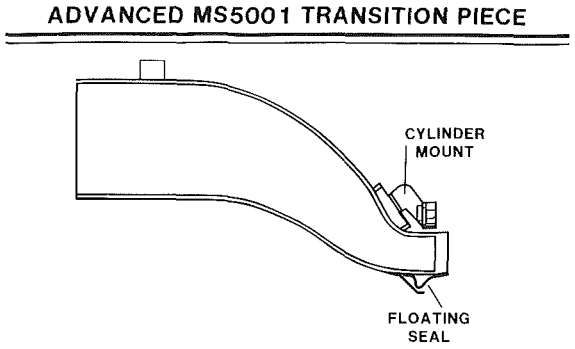

Fig. 7

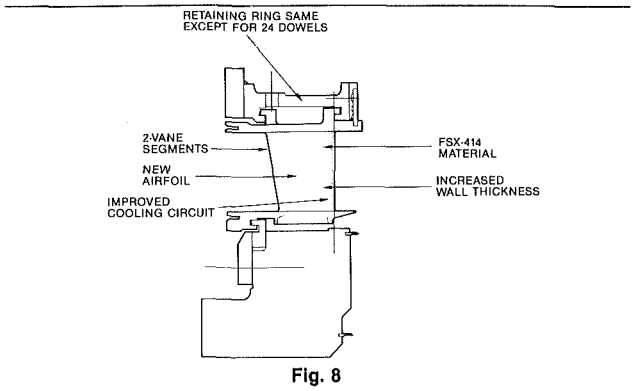

Fig. 8

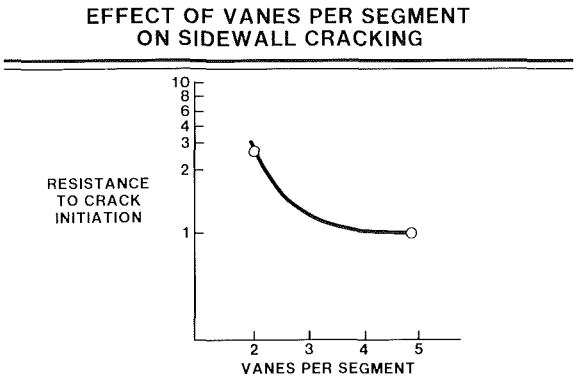

Fig. 9

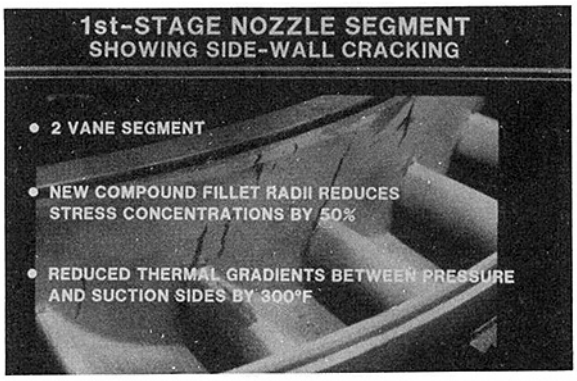

Fig. 10

The cooling air impinges on the splash plate and increases the effectiveness of the cooling air at the collar location (Fig. 5).

Crossfire Tubes. Air introduced into the tubes via swirl-cooling holes improves cooling effectiveness. More uniform cooling air flow and lower metal temperatures increase crossfire tube life by reducing burning and end nibbling. Crossfire tube improvements are illustrated in Fig. 6.

Transition Piece. A cylinder mount has been added to the transition piece as shown in Fig. 7. This mounting eliminates stress concentrations where the transition piece body joins the mounting arrangement. The attachment weld is now at the top of the cylinder mount – an area of reduced temperature. This extends the life between repairs for the transition piece, particularly during cyclic operation. The transition piece to nozzle seal is the "floating" seal design.

First-Stage Nozzle. The first-stage nozzle is a key element of the MS5001 New Technology package. Since it is stationary during operation, the first-stage nozzle contacts the highest gas temperature downstream from the combustion system. By comparison, a rotating turbine bucket is exposed to a lower relative gas temperature, and an average temperature profile.

Major improvements to the first-stage nozzle include a new aerodynamic airfoil design, a new cooling hole grouping arrangement, and improved component mechanical design (Fig. 8).

Figure 9 shows the relative effect on starts to crack initiation as a function of the number of airfoil vanes per segment. The new design two-vane segment, reduced from five vanes per segment, has a significant impact on cycles to crack initiation with acceptable seal leakage. Experience with two vane segments indicates that improvements in cycle to crack initiation by a factor of almost 3 to 1 can be realized. This type of cracking is shown in Fig. 10.

Wall thickness material has been added to the areas where "ballooning" type cracking can occur. This type of cracking is shown in Fig. 11. The new design increases wall thicknesses up to 50 percent to reduce this mode of cracking.

The overall cooling circuit to the nozzle was redesigned and the cooling holes have been moved closer to the side walls to reduce cracking in the trailing edges shown in Fig. 12. This

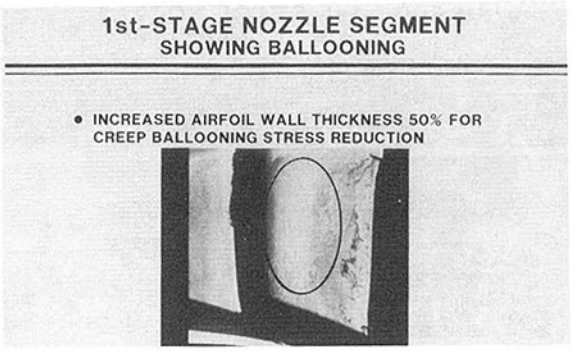

Fig. 11

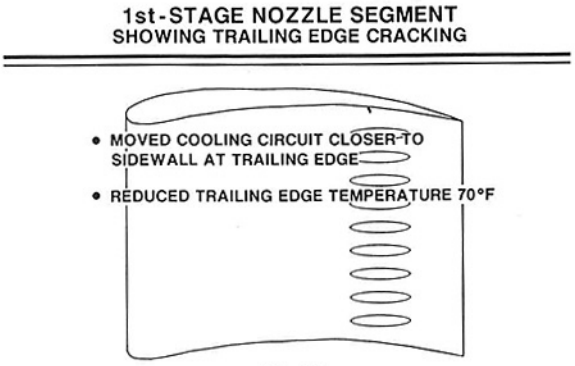

Fig. 12

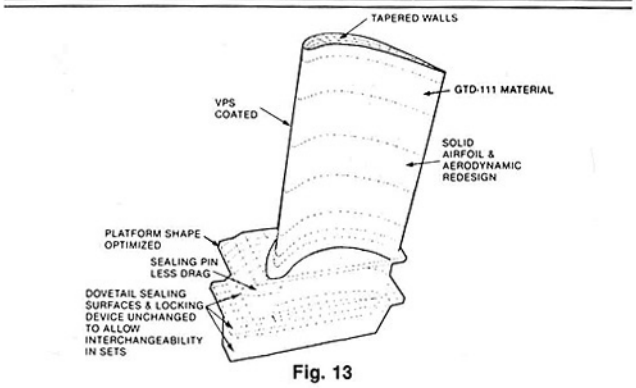

Fig. 13

change significantly improves the recommended intervals for hot-gas-path inspections.

First-Stage Bucket. The redesigned and more aerodynamically efficient first-stage bucket is shown in Fig. 13. The solid bucket design made possible by stronger GTD-111 bucket material dramatically improves resistance to foreign object and corrosion damage that can occur in operation. The bucket is coated with PLASMAGUARD™ coating – a vacuum plasma spray coating that doubles its bucket life in corrosive environments compared to uncoated buckets.

Second-Stage Nozzle. The fabricated second-stage nozzle with 28 vanes per segment has been redesigned to four vanes per segment casting. The nozzle material is FSX414. The present two-segment design tends out of roundness during startup, eventually resulting in bucket seal rubs. The design shown in Fig. 14 is supported by new first and second-stage bucket shrouds to ensure the design remains concentric throughout operation. The new design eliminates leak paths that have resulted in high first-stage aft wheelspace temperatures.

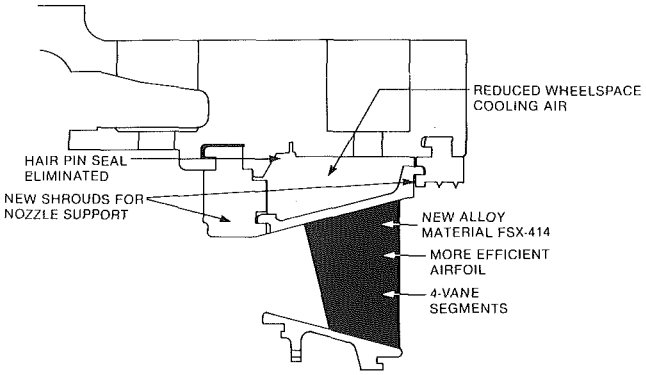

Fig. 14

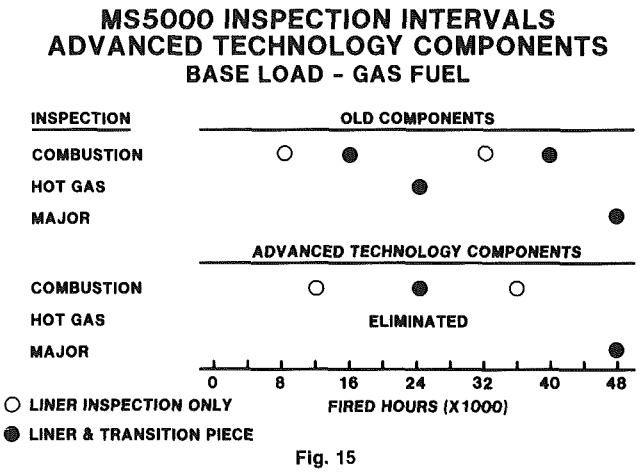

Fig. 15

Inspection Intervals. The MS5001 New Technology Package extends the combustion and hot-gas-path recommended inspection intervals. Figure 15 shows the combustion and hot-gas-path intervals made possible by applying today's technology to machines shipped years ago.

Uprate Application on MS5001 Models "A-K"

A number of uprate options are available for model "A-K" units depending on service requirements, output and efficiency improvement objectives, and extent of refurbishment desired by a customer. Table 3 summarizes a range of options evaluated for this particular Texaco turbine. As previously stated, service objectives of extended maintenance intervals, spare part availability, operating reliability, and power reserve for process expansion were all contributing factors in selection of option 5C from Table 3 for the "R/NT" uprate.

Application of the "R/NT" uprate to the model "K" turbine is somewhat more involved than the changes on more recent models, as shown on Table 4. This is because mechanical design features changed substantially even though the aerodynamic design of the MS5001 turbine had remained essentially unchanged until the introduction of the 17-stage Model "N" compressor. Turbine rotor and stator component materials and design evolved with increasing firing temperature. For example, compressor high-pressure packing shifted from the first-stage turbine wheel to a cooler location at the last stage of the compressor; the power output flange shifted from the compressor end of the machine to the turbine as torque increased with the same basic compressor design; clamped combustion casings, prone to leakage, became bolted flanges; transition piece tie bars gave way to the floating seal design; and the turbine shell became a heavy wall casting instead of a thinner fabrication that tended to be distorted in service. Most of these significant mechanical design changes

Table 3 Estimated uprate performance summary

Original NEMA	Option 1	Option 2 (1+2)	Option 3 (1+2+3)	Option 4 A at 4860 RPM	Option 4 B at 5100 RPM	Option 5 A at 1720°F at 4860 RPM	Option 5 B at 1720°F at 5100 RPM	Option 5 C at 1755°F at 4860 RPM
Output of 14,800 H.P.	+14.9%	+17.5%	+23.5%	+43.8%	+49.6%	+48.6%	+54.6%	+57.0%
Heat Rate of 10,830 BTU/HP-HR	-4.9%	-7.5%	-8.5%	-7.4%	-8.4%	-8.9%	-9.9%	-11.4%
Design Changes								
High-Flow IGV	X	X	X	X	X	X	X	X
Shrouded Stg. 2 Bucket	-	X	X	X	X	X	X	X
Turbine Speed, RPM	4860	4860	5100	4860	5100	4860	5100	4860
Model Uprate	5001K	5001K	5001K	5001M	5001M	5001R-N/T	5001R-N/T	5001R-N/T
Firing Temp. (F)	1500	1500	1500	1700	1700	1720	1720	1755

Table 4 MS5001 models A through P: advanced-technology hardware changes

	MODELS		
	A/K	L/LA/M	N/P/R
Combustion Liners (TBC & Splash Plate)	X	X	X
Cylinder-mount Transition Pieces	X	X	X
Swirl-cooled Cross-Fire Tubes	X	X	X
2-Vane Stage 1 Nozzle	X	X	X
GTD111 Stage 1 Buckets	X	X	X
Stage 2 Nozzle	X	X	X
Shrouded-Tip Stage 2 Buckets	X	X	-
Stage 2 Turbine Wheel	X	X(1)	-
Distance Piece	X	-	-
Turbine Shell	X	-	-
Stage 1 Turbine Wheel	X	-	-
Outer Combustion Casing	X	-	-
Exhaust Frame	X	-	-

(1) Stage 2 turbine wheel replacement is only required for models L, LA & M units if uprating to a full "R" advanced technology rating. An intermediate uprating to an "M" advanced technology-configuration is also available which does not require Stage 2 wheel replacement.

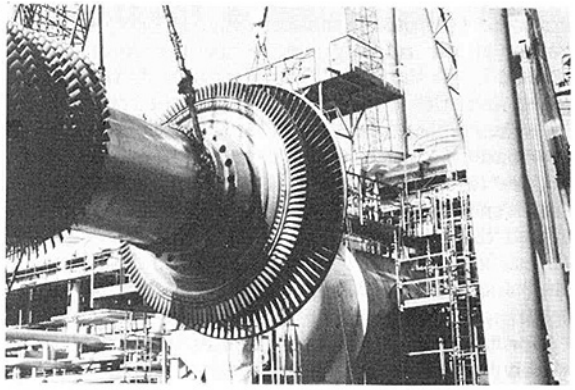

Fig. 16

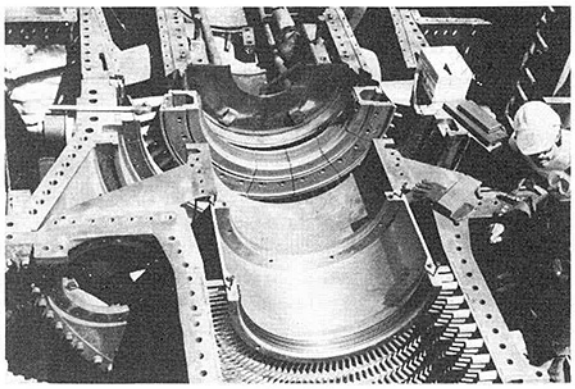

Fig. 17

were in place with the Model "L," thereby facilitating the application of uprate components to many more recent turbines. However, as application barriers are overcome, the uprate potential for earlier model "A-K" units is substantial. The "R-N/T" rating, Table 2, represents a 46 percent to over 80 percent output increase possibility. These model "A" through "K" machines require replacement of more major components as listed in Table 4 to apply the new technology uprate package. Of major impact is the turbine shell replacement that is required to mount the uprate second-stage nozzle that is supported concentrically from the first and second-stage shroud blocks as shown in Fig. 14. The current production cast turbine shell is compatible with these early machines as far as overall length, bolt circle diameter, and axial location of stages is concerned. Modification is required at the horizontal flange to provide a flexplate trunnion attachment, the gib key interface with the base and vertical flange bolt spacing pattern. Alignment and doweling of the turbine shell is done as part of field assembly. This major barrier to application of the "new technology" uprate package has been overcome. However, all interfaces need to be carefully evaluated – especially if there has been significant modification over the years that may not be in the manufacturers' record of changes. These interfaces include the compressor discharge casing attachment to both turbine shell and combustion casings, exhaust frame to turbine shell flanges, turbine shell gib to base configuration, and output flange.

Site Installation Experience

Job management, craft labor, and technical direction for the field modification of this gas turbine were provided by GE Utility and Industrial Sales and Service in New Orleans. The modification of the gas turbine rotor to incorporate replacement axial flow compressor blades and a new turbine section was accomplished in GE's Houston Service Shop. Extensive field modifications were also performed on the Cooper Bessemer process compressors including the installation of a new rotor in the low-pressure compressor and the replacement of the speed increaser gear. The high-pressure compressor was removed and sent to Cooper Bessemer's shop in New Orleans for modification.

Technical direction was provided by Cooper Bessemer for compressor work. Texaco, with assistance from GE controls specialists, completely revamped the gas turbine control system with the installation of Option I control upgrade compounds TEMCON I, II, III, TEMPRO, and GASCON I and II. See [1] for a brief description of these modifications and [6] for more complete discussion of these improvements. A new control building had been built prior to the outage in which GE's TEMCON, TEMPRO, and GASCON electronic control modules were installed, replacing the original pneumatic control components. The existing inlet silencer and filtration system were replaced with a new silencer having stainless steel

internals and a filter house with replaceable high-efficiency filter cartridges.

The planning effort for the gas turbine modernization began several months prior to the scheduled outage. Work planned for the gas turbine was only a part of a large upgrade project undertaken by Texaco. After several planning sessions a schedule was established that was compatible with Texaco's overall project needs. It called for one ten-hour shift per day, six days per week for a duration of 45 working days. This schedule allowed for escalation to two shifts per day and/or Sunday work should work scope increase or problems be encountered. In order to save time, the upgrade rotor was assembled in the Houston Service Shop using axial flow compressor wheels stocked by the shop and compressor blades, turbine rotor, and hardware supplied by GE Turbine Business Operations. The rotor is shown in Fig. 16 being lifted for installation at the refinery site. While the rotor was being assembled in the shop, major field activity on the gas turbine included axial flow compressor stator blade replacement and turbine shell replacement. Modifications were made to the gas turbine base to accommodate relocation of the centerline gib of the new turbine shell and to the aft support legs because of the difference in turbine shell support trunion height. Figure 17 shows the turbine half shell with the new turbine shell, lower half in place. The complete new turbine shell was bolted in place and the unit assembled without the rotor. GE Service Shop personnel, using optical alignment equipment, provided the information required for alignment and doweling of the new turbine shell.

The turbine rotor was shipped to the site on the 23rd day of the outage and reassembly of the unit, including all new combustion system components, began. The gas turbine assembly was completed on the 58th day of the outage. Some problems were encountered with other components that necessitated extension of the work schedule, and the gas turbine compressor train was turned over to operations five days late.

Summary

Texaco realized their goal of removing a major process restriction by uprating this gas turbine compressor train. It has been in operation since June 1987, meeting peak power requirements with improved reliability. Relative to the original unit rating, expected turbine output capability has increased 57 percent with a heat rate improvement of 11.4 percent. Customer satisfaction is high on this successful project that has demonstrated major turbine component replacement required to uprate early MS5001 units with the new technology performance improvement package. Reliable operation can be restored to these units with improved performance and extended maintenance intervals.

Acknowledgments

The authors are indebted to the assistance provided by Sarah Bures, the project coordinator for Texaco at Convent.

References

1 Johnston, J. R., "Performance and Reliability Improvements for Heavy Duty Gas Turbines," ASME Paper No. 87-GT-24, 1987.

2 Allen, R. P., and Smit, H. C. M., "New Techology Uprating of Process Compressor and Generator Drive Gas Turbine," ASME Paper No. 86-GT-40, 1986.

3 Johnston, J. R., and Freeman, M. A., "MS5000 Gas Turbine Modernization With Advanced Technology Parts," GER-3528, 1987.

4 "Gas Turbine Parts and Performance Technology," GER-3414, 1984.

5 Whittaker, R. A., "Application of Advanced Technology to In-Service Gas Turbines," ASME Paper No. 85-GT-148, 1985.

6 Jurczynski, G. E., "Controls Upgrade for GE Gas Turbine," GER 3514, 1988.

A Method of Evaluating Life Cycle Costs of Industrial Gas Turbines

R. B. Spector
Marine & Industrial Engine
Projects Dept.,
General Electric Co.,
Evendale, OH 45215

When aeroderivative gas turbines were first introduced into industrial service, the prime criterion for assessing the "relative value" of equipment was derived by dividing the initial (or capital) cost of the equipment by the number of kilowatts produced. The use of "dollars per kilowatt" as an assessment parameter emanated from the utility sector and is still valid providing that the turbomachinery units under consideration possess similar performance features with regard to thermal efficiency. Second-generation gas turbines being produced today possess thermal efficiencies approximately 45 percent greater than those previously available. Thus, a new criterion is required to provide the purchaser with a better "value" perspective to differentiate the various types of turbomachinery under consideration. This paper presents a technique for combining the initial cost of equipment with the costs of fuel consumed, applied labor, and parts to arrive at an assessment parameter capable of comparing the relative merits of varying types of turbomachinery. For simplicity, this paper limits the life cycle cost derivation and discussion to turbogenerator units; however, the principles of this type of life cycle analysis can also be applied to gas turbines in mechanical drive applications and/or combined cycles.

Introduction

The first gas turbines introduced into industrial service in the early 1950s represented a blend of steam turbine design coupled with the aerothermodynamic technology evolved from the embryonic military aircraft gas turbine industry that began in the latter stages of World War II. In the late 1950/early 1960 time period, lightweight industrial gas turbines derived directly from aircraft engines were introduced into electrical power generation, marine propulsion, and pipeline compression applications. These units possessed performance characteristics similar to their steam turbine based counterparts: pressure ratios on the order of 12 to 1, firing temperatures of approximately 1200–1500°F, and thermal efficiencies in the range of 23 to 27 percent. In the 1970 time period, a new breed or "second generation" of aeroderivative gas turbines entered industrial service. These units with simple cycle thermal efficiencies in the 32–37 percent bracket represented a new technological approach to aero-thermo design. Today, these second-generation units are joined by hybrid designs that utilize some of the aeroderivative design advancements but still maintain the basic structural concepts of the heavy frame of Type H units. These hybrid units are now approaching the simple cycle thermal efficiency levels reached by some of the early second-generation aeroderivative units when first introduced into industrial service.

Traditionally, the major cost focus was on the acquisition phase of gas turbines with little emphasis placed on the operational cost factors. Experience with higher technology equipment indicates that a low initial capital investment cost does not mean a lower total cost during the life expectancy of the purchased equipment (Baughn and Kerwin, 1986). The degree of quality, achieved reliability, and demonstrated availability of the equipment will be remembered long after the emotional distress associated with high initial cost is long forgotten. The utility sector is credited with the establishment of a measure of relative value received. This measure, "'dollars per kilowatt," was adopted in the late 1940s and is still in use. Today, there is need for a new assessment parameter that recognizes and credits the advancements that have taken place since the post-World War II time period. This assessment parameter must also consider all of the cost elements in the operating life of the equipment.

Life Cycle Cost Criteria

The life cycle cost model must consider the following elements:

- initial investment cost
- cost of financing
- variations in equipment availability
- cost of fuel
- cost of fuel treatment and/or preparation
- direct operating labor costs
- spare parts for preventive and corrective actions.

The economic factors governing life cycle costs tend to vary from one period to another. Foreign exchange rates, inflationary factors, interest, fuel costs, etc., are some of the factors that can be of importance in influencing the life cycle cost analysis of the equipment (Televen et al., 1983). Equipment availability is included in the analysis in order to assure that overall system economy is obtained. In addition, a life cycle cost model must be able to differentiate between the value received for varying levels of technological innovations em-

Contributed by the International Gas Turbine Institute and presented at the 33rd International Gas Turbine and Aeroengine Congress and Exhibition, Amsterdam, The Netherlands, June 5-9, 1988. Manuscript received by the International Gas Turbine Institute October 1987. Paper No. 88-GT-324.

bodied into the equipment and yet be simple enough to be clearly understood.

A life cycle cost model, meeting the above criteria, can be established for a turbogenerator unit as follows:

$$\text{Production Cost} = \text{Annual Investment Cost} + \text{Annual Fuel Cost} + \text{Annual Maintenance Cost} \quad (1)$$

Anual Investment Cost Term

There are several approaches to evaluating the comparative capital cost of an electrical generating package. One of the more popular approaches (used both domestically and internationally) is the capital recovery factor technique. This technique spreads the initial investment and interest costs for the repayment period into an equal annual expense using the time value of money. This approach allows for the comparison of other periodic expenses (i.e., fuel costs and maintenance costs) on a comparable basis. The equation for determining the annual annuity equivalent to the initial investment is

$$T = I\left[\frac{i}{1-(1-i)^{-n}}\right]\frac{1}{G} \quad (2)$$

where

T = total cost of the equipment including financing
i = interest rate
n = number of payment periods
I = initial capital cost of the equipment
G = efficiency of the associated electrical alternator

There are several methodologies that can be used to compare the availability of competing equipment. One very conservative approach is to define the equivalent capital cost, and thus equate a unit that generates more kilowatt-hours of electricity over the life cycle of the unit to an equivalent lower initial (or capital) cost (Jackson, 1985). This can be accomplished by dividing the annual investment cost (T) from equation (2) by the stated availability

$$T_{\text{adj}} = \frac{T}{A} \quad (3)$$

where

A = availability (expressed as decimal)

From equation (3), the production cost per kilowatt-hour of electricity produced resulting from the total equipment purchase debit is

$$C_p = \frac{T_{\text{adj}}}{(\text{kW})\ (8760)} \quad (4)$$

where

kW = number of kilowatts of electricity produced

Combining equations (2) through (4) results in establishing the annual investment cost term of equation (1)

$$C_p = \frac{I\left[\frac{i}{1-(1-i)^{-n}}\right]}{(A)\ (\text{kW})\ (8760)\ (G)} \quad (5)$$

Annual Fuel Cost Term

Inspection of the life cycle cost formula of equation (1) reveals that fuel cost is a predominant factor. The fuel cost term of the life cycle cost model is expressed as

$$C_f = \frac{F}{E}\ (\text{mils/Btu}) \text{ or}$$

$$= \frac{F}{(293)(E)}\ (\text{mils/kWh}) \quad (6)$$

where

F = fuel cost expressed in dollars per million Btu (higher heating value basis)
E = thermal efficiency of the unit

Of importance is the fact that the fuel price used in this expression must include any associated costs for fuel treatment and/or fuel preparation or neutralization required to condition the fuel such that it may be utilized by the gas turbine (Kovacik, 1984).

Annual Maintenance Cost

Gas turbine maintenance cost includes such items as material and labor for both preventive and corrective maintenance through the life span of the equipment and is generally expressed in terms of dollars per operating hour. Maintenance cost in terms of dollars per kilowatt hour is

$$C_m = \frac{M}{\text{kW}} \quad (7)$$

where

M = maintenance cost expressed in dollars per operating (fired) hour

Life Cycle Cost Model

Combining equations (5), (6), and (7) results in the overall life cycle model as defined in equation (1)

$$C_T = C_p + C_f + C_m \quad (8)$$

$$C_T = \frac{I\left[\frac{i}{1-(1-i)^{-n}}\right]}{(A)\ (\text{kW})\ (8760)\ (G)} + \frac{F}{(293)(E)} + \frac{M}{\text{kW}} \quad (9)$$

From equation (9), it can be noted that there are ten independent variables to be considered, and although a single-point solution can be easily attained, multiple solutions require repeated calculations. Curves depicting simultaneous variations in all variables would be difficult to interpret. Simplified diagrams can, however, be constructed to illustrate the relative importance of these different variables. The simplified diagrams included in this paper are based on a case of continuous operation (8760 hours per year) at 21,000 kilowatts with an equipment life expectancy of twenty years.

Analysis of Simplified Diagrams

• **Thermal Efficiency.** Figure 1 depicts the cost per kilowatt-hour of electricity produced as a function of initial investment (or capital) cost for varying levels of gas turbine thermal efficiency. It is evident from Fig. 1 that the initial investment cost is somewhat limited in its effect at a given thermal efficiency. For a given gas turbine thermal efficiency, a doubling of the initial investment cost results in approximately a 2.1 mil (or 4.5 percent) increase in the cost per kilowatt-hour produced. The effects of increases or decreases in gas turbine efficiency are staggering. As shown in Fig. 1, an increase in gas turbine fuel efficiency of 2 percent is equivalent to a decrease of $200.00/kW in initial investment cost for a constant cost/kWh produced. Figure 1 also shows that a 36 percent (thermal efficiency) unit costing $500/kW will produce a kilowatt-hour of electricity for the same cost as a 32 percent (thermal efficiency) unit costing $100/kW. The overall effect of fuel efficiency on the life cycle cost equation can also be noted. The incremental difference between any two curves shown in Fig. 1 increases as an inverse function of thermal efficiency.

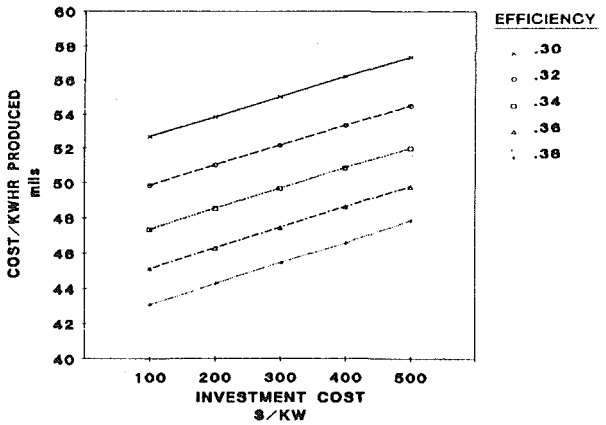

Fig. 1 Production costs versus initial investment for varying thermal efficiencies

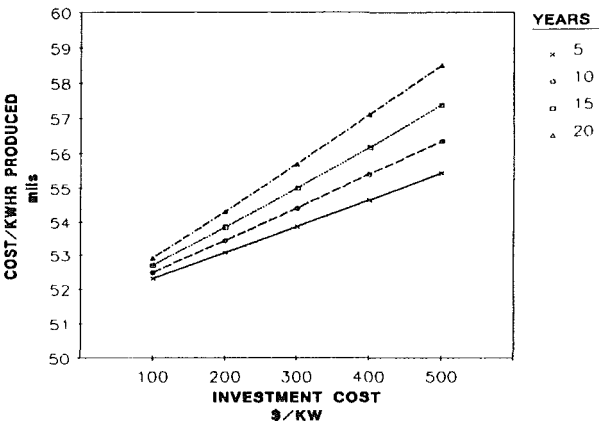

Fig. 2 Production costs versus initial investment for varying payment periods (30 percent thermal efficiency)

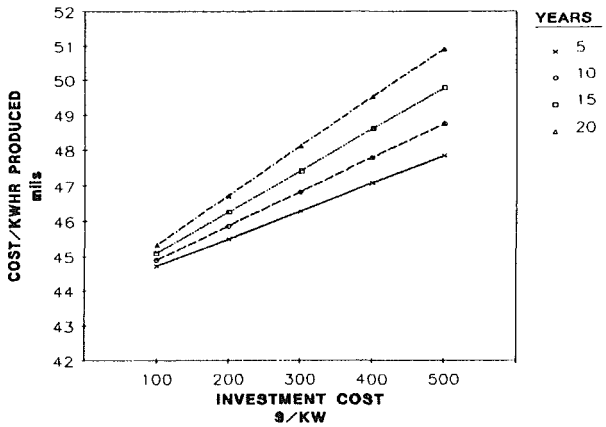

Fig. 3 Production costs versus initial investment for varying payment periods (36 thermal efficiency)

• **Loan Repayment Period.** Figures 2 and 3 show the nonlinear relationship between a reduction in loan repayment period at varying initial investment costs. The total variation (expressed in mils per kilowatt-hour produced) between a five and twenty-five year repayment period varies from 0.6 mils at an initial investment cost of \$100/kW to 3.0 mils at an initial investment cost of \$500/kW for thermal efficiencies varying between 30 and 38 percent. In the range from \$200 to \$300/kW initial investment cost, a decrease of five years in loan repayment period is equivalent to a \$50/kW incremental decrease in initial investment cost.

• **Availability.** The effects of variations in availability are

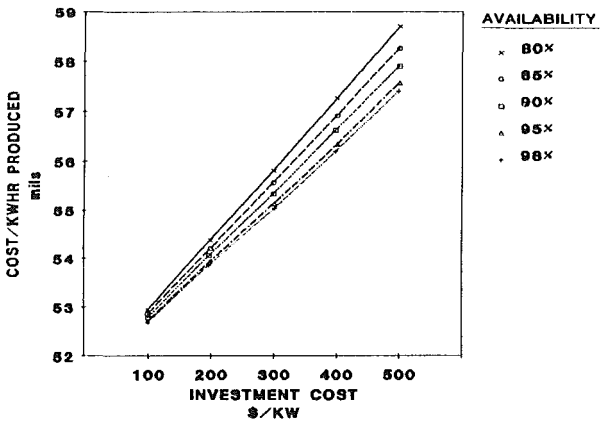

Fig. 4 Production costs versus initial investment for varying availability (30 percent thermal efficiency)

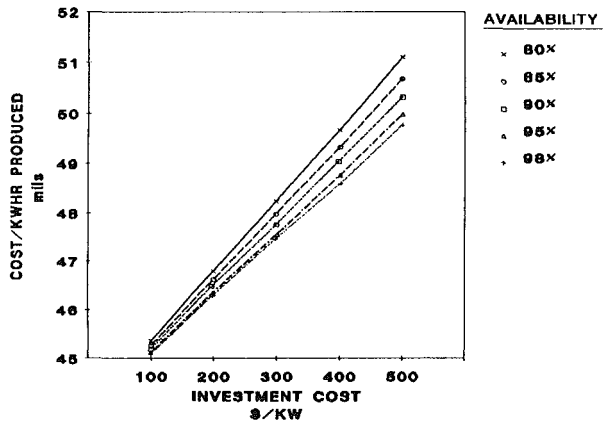

Fig. 5 Production costs versus initial investment for varying availability (36 percent thermal efficiency)

illustrated in Figs. 4 and 5. A nonlinear relationship can be noted between an increase in availability at varying initial investment costs. The total variation (expressed in mils per kilowatt-hour) between $A = 0.90$ to $A = 0.98$ varies from 0.35 mils at an initial investment cost of \$100/kW to 1.4 mils at an initial cost of \$500/kW. In the \$200 to \$300/kW initial investment cost range an increase in availability of 0.05 is equivalent to a \$20/kW incremental decrease in initial investment cost.

• **Fuel Costs.** The effect of fuel cost is depicted in Figs. 6 and 7. Each of the figures indicates that at a constant initial investment cost, a \$0.50 increase/decrease in the price of fuel will have an approximate 4.5 mils (or 9.0 percent) increase/decrease in the cost per kWh produced. It should also be noted that at a constant investment cost, a unit with a 0.36 thermal efficiency using fuel costing \$4.00 per million Btu is equivalent, at a constant cost per kilowatt-hour produced basis, to another unit with a thermal efficiency of 0.30 using fuel costing \$3.40 per million Btus. These figures once again show the large effect of thermal efficiency upon the life cycle cost model.

• **Interest Rate.** As shown in Fig. 8, the effect of interest rate on the life cycle cost model is nonlinear and minimal, ranging from less than 0.025 mils per percent increase in interest rate at the lower initial investment costs to a value of approximately 0.20 mils per percent interest increase of the higher initial investment costs. In the \$200 to \$300/kW (Fig. 8*A*) initial investment cost range a decrease of 0.5 percent in interest is equivalent to a \$5/kW incremental decrease in initial investment cost.

• **Generator Efficiency.** Within the bounds of electric

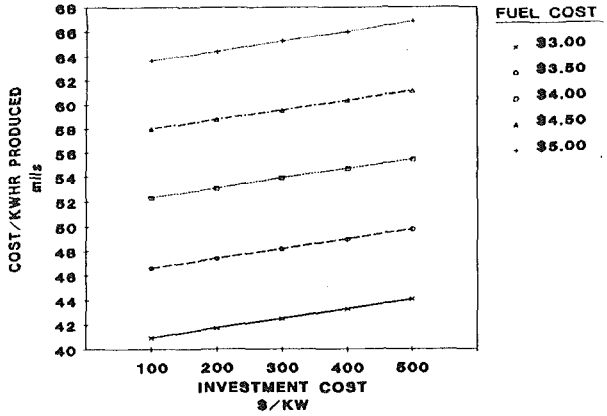

Fig. 6 Production costs versus initial investment for varying fuel costs (30 percent thermal efficiency)

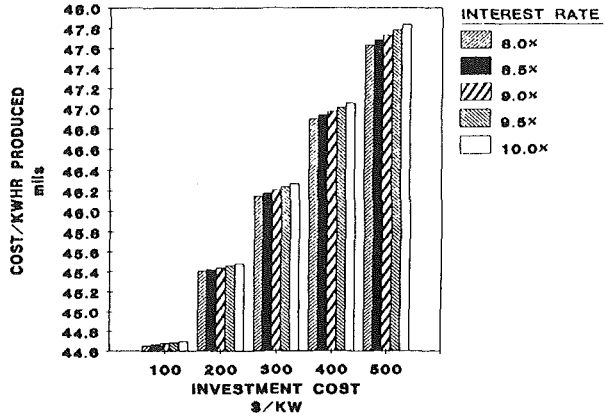

Fig. 8 Production costs versus initial investment for varying interest rates (36 percent thermal efficiency)

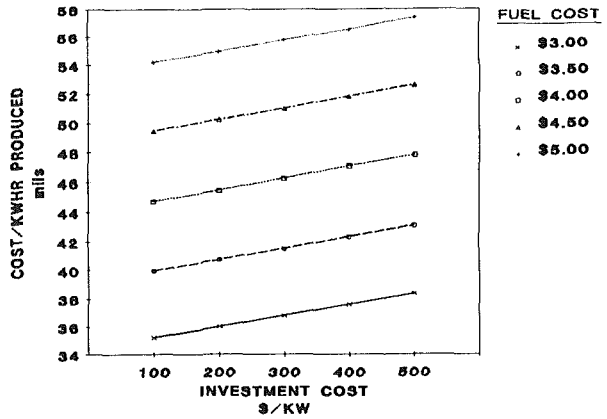

Fig. 7 Production costs versus initial investment for varying fuel costs (36 percent thermal efficiency)

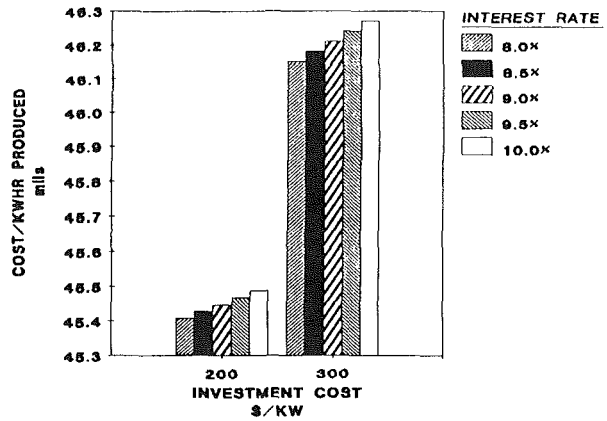

Fig. 8(*A*) Production costs versus initial investment for varying interest rates (36 percent thermal efficiency)

generator efficiencies ranging from 0.95 to 0.99, generator efficiency has a relatively small effect on the life cycle model of all the input parameters. As depicted in Fig. 9, the effect of generator efficiency on the cost per kilowatt-hour produced varies from less than 0.1 mils at the lower initial investment costs to 0.2 mils at the higher initial investment costs. In the range of $200–300/kW (Fig. 9*A*) initial investment cost, an increase in generator efficiency of 0.01 (one percent) is equivalent to a decrease in the cost per kilowatt-hour produced of approximately 0.025 mils. For a constant cost per kilowatt-hour, in the same initial investment range, a 0.01 increase in generator efficiency is equivalent to an initial investment cost decrease of $3/kW.

• **Maintenance Cost.** From equation (9), it can be noted that the maintenance cost (in terms of dollars/kilowatt-hour produced) is a direct additive term. Therefore, any increase or decrease in maintenance cost directly raises or lowers the level of the cost per kilowatt-hour produced. A decrease of 1 mil in maintenance cost per kWh is equivalent to a $90/kW incremental reduction in initial investment cost. One must take care, however, to insure that the maintenance cost input to the life cycle cost model is a true representation of the average cost of maintenance within the twenty-year lifespan of the equipment (Donovan, 1984). For a typical unit, the maintenance cost term must include the associated costs for:

—preventive on-site maintenance
—hot section refurbishment
—corrective on-site maintenance
—overhaul.

Table 1 is included to illustrate the interactive parametric effects in the initial investment cost range of $200 to $300/kW and summarizes the data previously presented in the section of this paper entitled "Analysis of Simplified Diagrams." Although this table can be used as a "rough-cut" estimate when comparing equipments, it is recommended that the mathematical model of equation (9) be used.

Example

An example using the life cycle cost model for a typical procurement of a turbogenerator illustrates the utility of the model in determining "best relative value."

In Table 2 data are listed for five typical candidate units with initial investment costs ranging from $200 to $320 per kilowatt. From a dollar per kilowatt basis only unit E would be instantly selected; however, the life cycle cost model indicates the following:

Unit	Cost per kWh produced
A	48.3 mils
B	47.5
C	48.3
D	46.6
E	51.9

From a life cycle standpoint, the choice of unit E would result in the additional expenditure of approximately $975,000 per year during the lifespan of the equipment (i.e., $0.0053 \times 8760 \times 21{,}000$). Since the difference in initial cost between units E and D is $2,520,000, this cost differential will be equalized in approximately one eighth of the twenty-year lifespan assumed for the equipment. Additionally, it must be noted that the twenty-year differential in cost per kilowatt

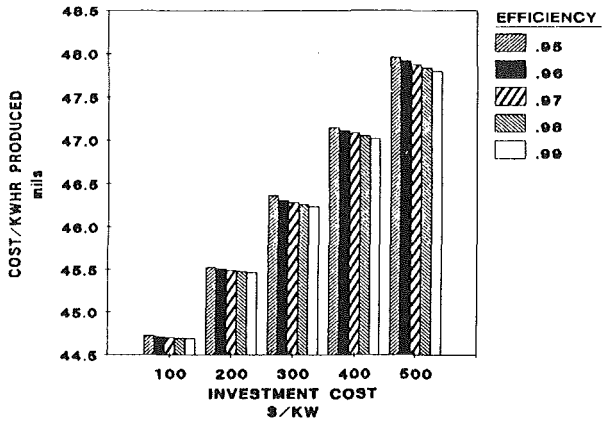

Fig. 9 Production costs versus initial investment for varying generator efficiency (36 percent thermal efficiency)

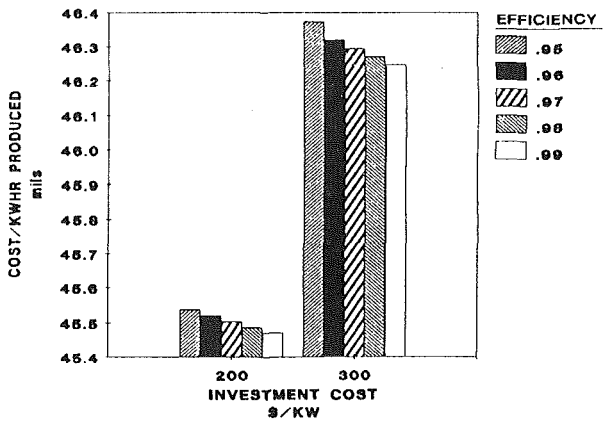

Fig. 9(A) Production costs versus initial investment for varying generator efficiency (36 percent thermal efficiency)

Table 1 Interactive parametric effects; initial investment cost $200 to $300/kW

Parameter	Net change	Effect on production cost (mils per kWh)	Equivalent effect on investment cost (dollars/kilowatt)
Thermal efficiency	+0.01	−1.3	−100
Loan repayment period	±1.0 year	±0.1	±10
Availability	+0.01	−0.05	−4
Interest	±0.05	±0.02	±5
Fuel cost	±0.10	±0.06	±125
Generator efficiency	+0.01	−0.025	−3
Maintenance cost	±1mil/kWh	±1	±90

Table 2 Various equipment attributes for typical candidates

	A	B	C	D	E
Initial cost/kW ($/kW)	205	320	275	320	200
Thermal efficiency	0.325	0.355	0.34	0.365	0.30
Loan periods (years)	20.0	20.0	20.0	20.0	20.0
Availability	0.96	0.94	0.95	0.94	0.96
Fuel cost ($/$10^6$ Btu)	4.00	4.00	4.00	4.00	4.00
Interest	0.065	0.080	0.070	0.085	0.075
Generator efficiency	0.980	0.985	0.985	0.980	0.985
Maintenance cost ($/kWh)	0.004	0.005	0.005	0.005	0.004

Equipment life: 20 years
Output: 21,000 kW

produced between units E and D is equivalent to over 4.6 times the initial equipment cost of Unit E. As a note of caution, it must also be realized that the values outputted by the life cycle model are only as valid as the data inputted and one must take care to input both reasonable and accurate data. Also one should take care in attempting to distinguish model outputs that vary less than 0.5 mils from each other.

Conclusions

This paper has presented the steps taken to establish the methodology for a mathematical model that is indicative of end-user costs during the lifespan of turbogenerator equipment. The purpose of the model is to provide a single assessment parameter that is capable of comparing and highlighting the relative merits of competitive turbogenerator units. The discussion of the mathematical derivation of the model, the effects of the parametric inputs when treated individually, and the included example clearly shows that the comparison of different turbogenerator units using the life cycle model results in a more thorough analysis and presents a more complete perspective than that obtained by merely comparing initial investment cost alone. Comparisons based solely on an initial investment cost basis can result in a scenario where the ultimate user of the equipment is presented with an equipment selection that does not address itself to the long-range operational and cost aspects associated with the equipment.

Since the predictions of this life cycle cost mathematical model cannot be compared to actual ultimate measurements at this time, a potential shortcoming of the model lies with the validity of the data and assumptions used for input. One cannot overemphasize the need for both reasonable and accurate input data. For this reason, the use of the life cycle model as an evaluational tool for the procurement of a single piece of equipment is not considered as valid as the use of the model to establish the "relative value perspective" to differentiate between several pieces of competing equipment.

References

Baughn, J. W., and Kerwin, R. A., 1987, "A Comparison of the Predicted and Measured Thermodynamic Performance of a Gas Turbine Cogeneration System," ASME JOURNAL OF ENGINEERING FOR GAS TURBINES AND POWER, Vol. 109, pp. 32-38.

Donovan, S. J., 1984, "Aircraft Derivative Maintenance Practices," GER3424, Gas Turbine Reference Library, General Electric Company, Schenectady, NY.

Jackson, J. A., 1985, "Reliability, Availability and Maintainability of the General Electric LM2500 System," ASME Paper No. 85-GT-140.

Kovacik, J. M., 1984, "Industrial Gas Turbine Cogeneration Application Considerations," GER3430, Gas Turbine Reference Library, General Electric Company, Schenectady, NY.

Televen, K., Baughn, J. W., and McKillop, A. A., 1983, "A Model for the Economic Analysis of Cogeneration Plants With Fixed and Variable Output," *Energy, The International Journal*, Vol. 8, No. 7, pp. 547-552.

M. Pluviose
Docteur d'Etat es Sciences,
Ingénieur-Conseil,
Centre Technique des Industries
Mécaniques,
Senlis, France

Stabilization of Flow Through Steam-Turbine Control Valves

After observing the abrupt variations in flow on an aerodynamic model having the form of a conventional valve, modifications in the basic geometry of the valve are proposed in order to stabilize the flow. The instabilities are almost completely eliminated by introducing an exergy-destructive element into the design of the valve head and seat.

Introduction

The control valves for steam turbines are located in the steam load between the steam generator and the turbine. They are intended to regulate the flow of steam to the turbine in accordance with the electrical load that is required of the turbogenerator. At maximum valve lift, which corresponds to the nominal operating regime of the steam turbine, the pressure drop caused by the control valve should be small so that the conversion of thermal energy into mechanical energy will be achieved with satisfactory efficiency.

In the case of small lifts, however, pressure drop is inherent to the system, since here the steam is throttled by the valve. This intentional decrease in the generating pressure is produced by viscous friction and by an increase in entropy through shock waves that are often unstable. The increase in the power of generators combined with the limitation on the inlet steam pressure have led to control devices of such dimensions that the problems of flow instability have become critical. They are responsible for:

- vibrations, in particular in the moving parts, which can lead to stem ruptures;
- additional stresses on the nozzles and the blades of the control stage;
- excessive noise that can reach or even exceed acceptable levels.

By way of example, it can be pointed out that the power lost through throttling in the six valves of a 1000 MW steam turbine can attain 130 MW at medium lift. Fortunately, only a part of this lost energy is transformed into vibration and noise. To analyze the mechanisms of these flows with the aim of stabilizing them, it is essential first to study them experimentally, since their complexity makes it impossible to set up a theoretical mathematical model. The mechanical problem of absorbing the shock to which structures are submitted under aerodynamic excitation is not dealt with in this study, which limits itself solely to the causes of and remedies for aerodynamic instability.

Contributed by the Power Division and presented at the Joint ASME/IEEE Power Generation Conference, Portland, Oregon, October 19-23, 1986. Manuscript received at ASME Headquarters May 12, 1988.

Steam is somewhat complicated to use in such tests. The difficulty is due to the formation of condensation waves after the steam crosses the saturation line, when, of course, conditions for expansion in the valve permit it. These conditions, which sometimes exist, would introduce an additional parameter that it was not judged essential to reproduce in order to understand the phenomena and find ways to counteract their effects. Therefore, the experiments were carried out using air. Finally, the supply elbow of the valve, which certainly has an influence on the phenomena being studied, without, however, altering them radically, was simplified. The wide variety of internal shapes used in industry would have increased the quantity of the experimental research considerably. An axisymmetric aerodynamic model is particularly useful in measuring the forces that act on the valve head. A two-dimensional model provides a means of visualizing the different internal flow patterns that are encountered and of observing the abrupt transitions from one flow to another. The compilation and synthesis of the experimental results are used to provide an initial interpretation of the observed phenomena.

The complete elimination of the divergent part of the nozzle, which is formed by the valve head and its seat, will improve the control valve's performance noticeably with regard to flow instability. The effectiveness of this modification has been proven in actual operating conditions. Nevertheless, instabilities are still present. Therefore, the effort to understand the complex and violently changing phenomena that occur in control valves has been pursued. By first making it impossible for the sheet of supersonic jets coming from the valve head to flow together, and by then eliminating the new instabilities created by the abrupt enlargement that has been introduced, it will be possible to propose a new geometry for control valves that will improve their performance decisively. The proposed design will produce significant energy losses in the fluid for small lifts without causing instability, and it will not create any problem at lifts where the valve must be very permeable.

Finally, it should be noted that in the customary classification of a single-phase fluid, the flow being studied is unsteady, three-dimensional, viscous, turbulent, and compressible.

The problem at the industrial level is therefore extremely complex and no claim is made to having solved it analytically. The only goal has been to make a contribution to the search

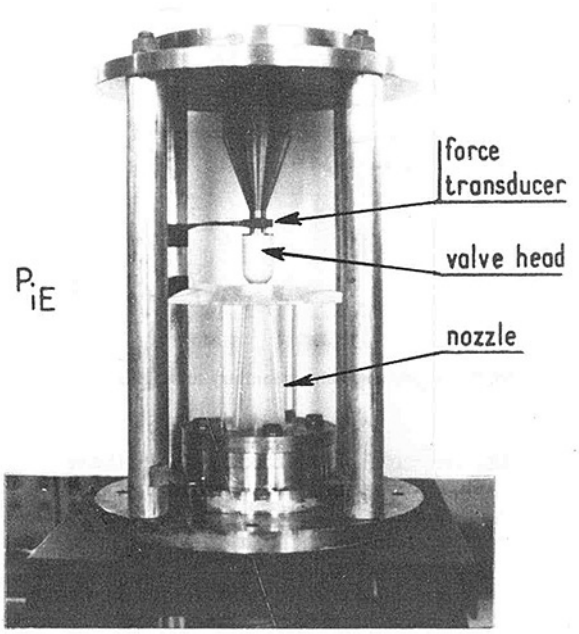

Fig. 1 Axisymmetric model

for a satisfactory technical solution for the short and middle term.

Problem Definition

Experimental Observations. These observations were made on either an axisymmetric model or a two-dimensional model that permitted visual observation of the flow. The axisymmetric reference model consists of a transparent valve body and a hemispherical valve head that is rigidly attached to the valve body (Fig. 1).

Both manufacturers and users have noted that this design produces serious flow instability and is prone to operational malfunctions. A force transducer is placed between the valve head and the nozzle support. This detector measures unsteady forces along the axis of the valve head and perpendicular to this axis. This model functions with a wind tunnel including an air tank downstream. Before the test, a vacuum is created in this tank. The experiment runs long enough so that the flow instabilities studied here occur under steady-state conditions. As the atmosphere is the upstream reference, the inlet conditions are excellent. Although the unsteady force acting along the axis of the valve are also very significant, only the forces perpendicular to the axis are chosen as an illustration of the problems.

In the lift-pressure ratio performance data, two humps of unsteady forces are observed. These two humps have also been observed by Khanin (1975). The axisymmetric model can also be equipped with a piezoelectric meter installed in a Wheatstone bridge, which can monitor the average force along the axis of the valve. This measurement is extremely instructive, as it shows that the hump appearing at the highest expansion ratios corresponds to a jump in this average force. At this stage of the research, it becomes necessary to observe the flows visually in order to describe them as accurately as possible. This can be accomplished by using hydraulic analogies or by viewing them on a two-dimensional model with a schlieren system (Pluviose, 1975).

It is incorrect to replace a three-dimensional flow with a two-dimensional flow by assuming the real valve to be a slice passing through the axis of symmetry. This arrangement no longer shows the flow in a valve: It shows a different flow, with different geometric limits, which has no apparent industrial application. The knowledge that can be gained from such schematizations must be used with caution. Once this warning has been made, however, the advantage of such a configuration for the researcher should be noted. The model, whose shape is derived from the preceding hemispheric valve, is connected to the atmosphere upstream and downstream to a vacuum vessel powerful enough to produce supersonic flows. A quick-closing valve located in the lower part of the circuit is opened at the beginning of the experiment, and the tank fills in a few minutes with air drawn through the model from the atmosphere.

The lift is maintained constant during the trial, and the expansion ratio across the model thus varies continuously. In the lift-pressure ratio field, it is then possible to photograph and film the different flow pattern images. Three distinctly different patterns are observed in the performance field. They are shown in photographs 2(*a–c*).

In photo 2(*a*), taken at high expansion ratio ($P_{iE}/P_{iS} = 5$; $L/R = 0.4$) supersonic flow can be observed in the second nozzle with nearly straight recompression shock wave. The passage from the pattern seen in Fig. 2(*a*) to the one in Fig. 2(*b*) is violent and corresponds to the second nozzle's cutting out when the expansion ratio decreases. Supersonic jets and their wave trains coming from the first nozzle, which is formed between the valve head and valve seat, are visible in Fig. 2(*b*). These two wave trains become particularly unstable between photos 2(*b*) and 2(*c*), and disappear when the expansion ratio continues to drop, but the jets remain dissymmetric (Fig. 2*c*: $P_{iE}/P_{iS} = 2$ and $L/R = 0.1$).

These two sudden changes in flow revealed in the flow pattern photographs seem to show that the same thing is occurring here as in the three-dimensional trials, where two humps of stress were recorded.

Possible Causes of Instability. Several causes of instability have been recorded by Pluviose (1984); the list is not exhaustive and certain of these causes are still unconfirmed. Nevertheless, it is known that:

- under certain conditions, and for different expansion ratios, oscillations in the flow through a convergent-divergent nozzle are observed;
- two convergent-divergent nozzles operating in series can, in certain cases, create a type of instability classic in double-throated nozzles. A pumping action accompanied by strong pulsations of pressure occurs during the filling and emptying of the space between the two throats. In a supersonic wind tunnel there is no question of reducing the volume between the two throats, as this is, in fact, the test chamber. In this case, care is taken never to close the second throat after decompression without leaving an adequate margin in relation to recompression. Therefore, no attempt is made to utilize the maximum energy available to avoid the risk of the chamber's returning violently to a subsonic level, which often results in damage. The principle on which a valve operates makes

Nomenclature

Fx, Fy = unsteady force perpendicular to the axis of the valve head (rms value)
L = valve lift
P_{IE} = valve inlet stagnation pressure
P_{IS} = valve outlet stagnation pressure
R = nozzle radius

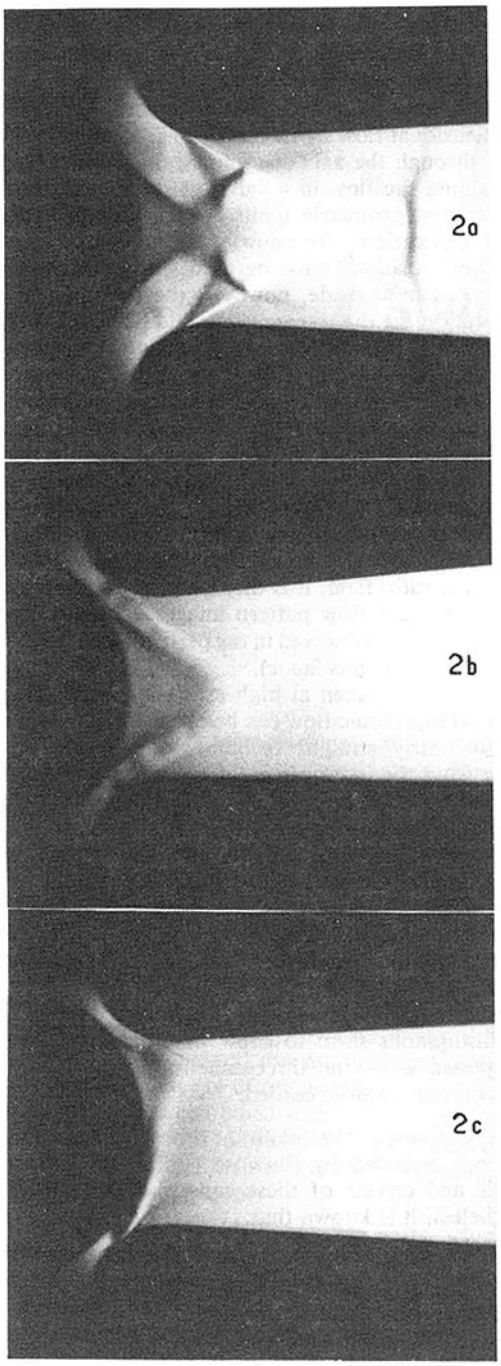

Fig. 2 Flow pattern photographs

recompression inevitable, and thus the diffuser, whose air supply is intermittent and irregular, functions unpredictably.

• two nozzles operating in parallel may also produce very serious instability at times.

As can be seen, the two-dimensional valve is composed of two convergent-divergent nozzles in parallel, followed by a convergent-divergent recovery nozzle. Thus, all the types of instability that have been recorded in the three situations described above may occur simultaneously and render it particularly difficult to make certain observations and interpretations.

A Preliminary Attempt to Stabilize Flow in Control Valves. While all types of instability are not identical in character, they do have the same cause: the divergence of the air stream downstream from the throat between the valve head and its seat. Therefore, in order to eliminate any possibility of recompression (whether subsonic or due to shock waves), a hollow-form valve head in conjunction with a nozzle that is also hollow is adopted (Fig. 3).

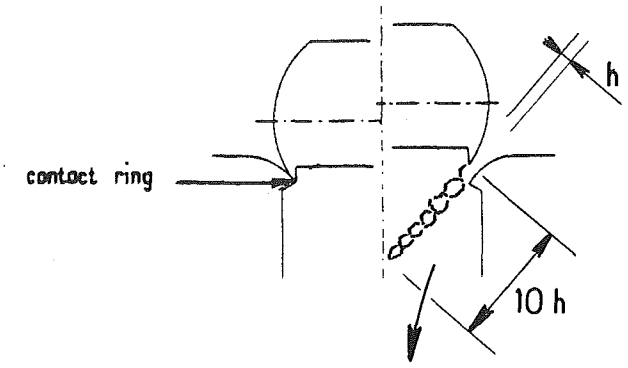

Fig. 3 Preliminary valve geometry to stabilize flow

It would be possible to cut the valve so that the first nozzle would always be appropriate to the expansion ratio. However, it seems preferable to make an even more radical change by hollowing out the valve head from the level of the contact ring or in the area immediately downstream.[1]

Notable improvement in performance was immediately observed as a result of this modification and its effectiveness has been verified in actual operation. Nevertheless, this solution is not totally successful, as instability continues to occur. There is: a possible pumping action on the cavity formed at the base of the valve head; and instability due to the abrupt enlargement that has been created.

An effort must now be made to deal with these two new types of instability in order to be able to stabilize the flow further, once the second throat is eliminated.

Influence of Jet Angle. The lifespan of a supersonic jet is equal to approximately 10 to 20 times the diameter of the exhaust. By applying this fact directly to the problem of valves, it can be seen schematically in Fig. 3 that above a certain lift the jets may meet along the axis.

When these confluent jets meet at the center, they form a sheet (three-dimensional in a real valve) that isolates the cavity created at the base of the valve head from the downstream flow. This sheet creates a depression by viscous entrainment in the cavity formed, and this, in turn, deforms the sheet. When the deformed sheet has created a vacuum that is incompatible with its capacity to resist the infiltrations of the higher-pressure fluid downstream, the sheet ruptures, and there is a return to the initial conditions. The cavity is then emptied once again and a new phase of instability begins.

A systematic study of the conditions surrounding the appearance of the pumping action was not undertaken. It was thought preferable to vary the angle of the flow by changing the valve radius.

The experiments show that indeed, the jets created by hemispherical valve heads with small radii have much less of a tendency to flow together, thus limiting the possibility of a pumping action on the cavity at the base of the valve head. In order to limit the instability due to the confluence of the streams, the hollow valve head must be abandoned in favor of an inward-sloping valve head, which may or may not be hollow depending on the design of the control device.

This solution reduces to a minimum the possibility of the valve's base being isolated from the downstream flow and thus

[1] Patent CETIM—Electricité de France.

improves performance by eliminating the interference of the jets. It should also be noted that the flow does not have the possibility of separating from the valve head before reaching its base. Keller (1980) has observed that this solution gives satisfactory results.

Instability Due to Abrupt Enlargement. Observations made both in actual operating conditions and in the laboratory show that hollowing the valve and the nozzle can result in notable improvement in performance as long as the cavities are not excessively large. Experiment shows that the stability of the valve is jeopardized when the cavity is too large.

In order to stabilize flow as fully as possible, more detailed studies had to be carried out on abrupt enlargements, as there were new ideas to be explored in this area. Particular attention has been given to this and the essential results are summarized below. In the case of a compressible fluid, the basic problem is created by the underexpansion of the supersonic flow between the sonic section at the end of the orifice and the downstream section. The consequence is a flared airflow, generated by a system of infinitesimal expansion waves coming from the edges of the orifice, which creates, at the moment it intersects with the downstream cavity, an organized system of oblique shock waves that is destroyed farther downstream by more or less steady pseudoshocks. It can be shown experimentally on a two-dimensional model that the airflow is disymmetric for low expansion ratios, where it is flattened against one of the walls (Fabri and Siestrunck, 1955). When the expansion ratio rises, the supersonic stream flares, and eventually it flattens against the other wall as well. This is the sudden change in flow (or start in this text), which is preceded by more or less violent disturbances related to geometry of the abrupt enlargement.

In order to stablilize the fluid stream and significantly decrease the quantity of usable energy in the fluid, the device shown below was designed. It is seen here (Fig. 4) for two-dimensional enlargement (Pluviose, 1984).

Supersonic nozzles with limited or no expansion area are placed on each side of the central supersonic stream. They are fed in the same way as the central stream and designed in such a way that a recompression shock wave (shown in the diagram as a straight shock wave) is formed before the throat of the nozzle. As the flow is subsonic behind this shock wave, significant differences in velocity are created between the supersonic central flow and the peripheral subsonic flows. The possibility of diversifying the supersonic jets was used. Each of the flows is blocked by a sonic throat. The system that has been created is not an ejector because there is no entrainment of a secondary fluid by a primary fluid. The two flow rates are independent of each other and are determined solely by the dimensions of the sonic throats. The system does not function as well as mixed-flow ejector because one fluid cannot entrain another. There is forced mixing with intense transfers of momentum; such a device is extremely inefficient. By taking care not to allow the flow coming from the nozzles to return to supersonic velocities, the walls are thus isolated from shock waves. The chances of separation and return flow are reduced; that is, stable flow and intense dissipation of energy are achieved, thus meeting the two objectives.

Nozzles with limited expansion areas are chosen because:

- they are short, and thus of obvious interest to industry;
- they are most likely to generate straight shock waves because the development of boundary layers upstream for the shock is weaker;
- when operating at partial load, during recompression they produce clear separations, which reduces the chance of internal instabilities in these nozzles.

Stabilization of Flow in Control Valves

In a control valve, the area ratio is very high for small lifts, which corresponds, unfortunately, to high pressure ratios. This enlargement ratio varies continually according to the lift. Instability and sudden changes in flow (which are particularly noticeable at the base of the valve) must be expected because of the changes in enlargement. The encouraging results that were obtained with the supersonic pressure reducer during the study of abrupt enlargement led to the adoption of modifications of a similar nature for valves[2] (Fig. 5). Notches in the form of divergent limited-expansion-area nozzles are cut into the nozzle beginning at the contact ring. They are distributed in the nozzle and separated from each other by normal nozzles of the same size (on the diagram shown).

Therefore, downstream from the throat formed by the valve head and seat, the fluid's flow will vary depending on its azimuthal penetration into the valve. An intense mixing occurs at the interface between the two flows. It invades, one after another, each of the layers of this stratification. If shocks still occur, they are very localized in the intermediate levels and have little effect, since they are muffled by the predominant viscous effects they have themselves helped to create. This viscous mixing is intense, proceeds from level to level in a very complex manner, and is a priori inaccessible to calculation.

Breaking up the flow to such an extent assures:

- the stability of the flow, which is no longer treated in a

[2]Patent pending, France.

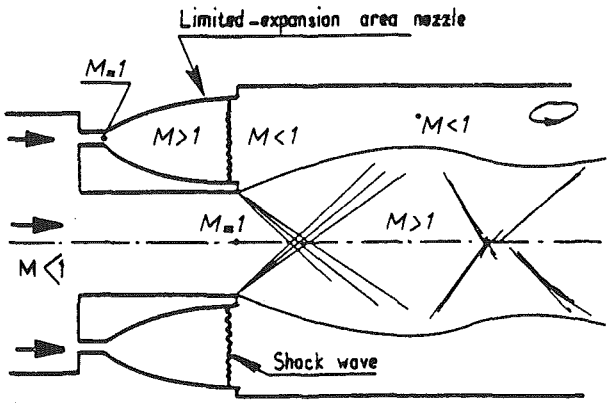

Fig. 4 Supersonic pressure reducer with mixing action

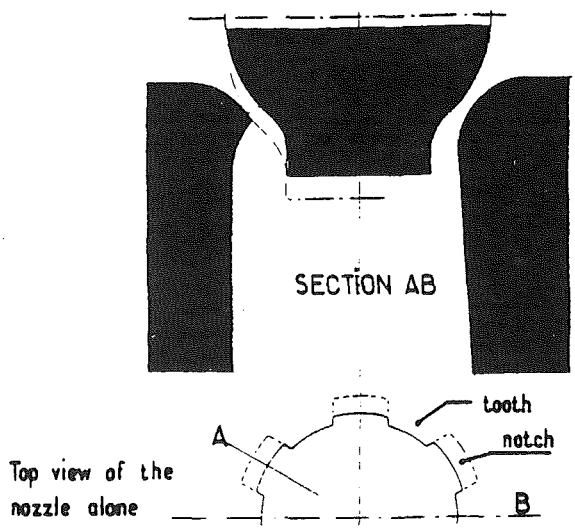

Fig. 5 Notched valve

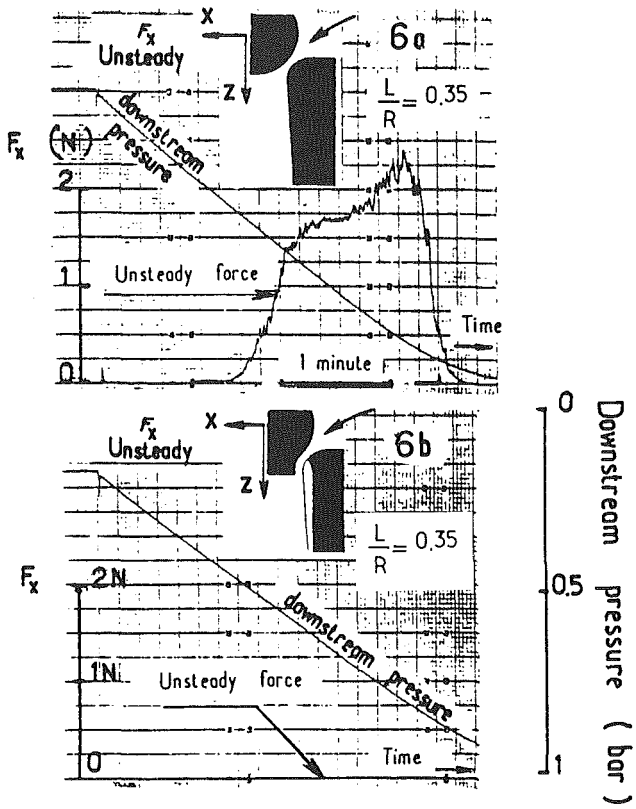

Fig. 6 Comparison of stress along the perpendicular to the valve head axis

single mass. Each micro-instability is destroyed the moment it appears by its immediate environment;

- an efficient mixing over a short distance;
- a flow devoid of any rotation of the fluid downstream.

During subsonic operation at nominal or nearly nominal levels, the notched nozzles will be definitely separated, which is an additional guarantee for the stability of the total flow. Finally, it should be noted that the valve head will not be notched so that any residual perturbance that might occur will be kept at a distance from this key part and dissipated near the fixed nozzle. A reduced lift of 0.35 was chosen to make a comparison between the reference design and the design proposed here.

Figure 6 gives the unanalyzed results obtained during an intermittent-burst test of stress perpendicular to the axis of the valve head. The results are spectacular: The signal transmitted by the detector is negligible in comparison with the signal for the initial design, and this regardless of the lift. The flow in the valves is stabilized. The result that seems the most significant is the following: The decisive improvement was achieved on the first attempt, which is undoubtedly the best justification of the solution chosen.

The utilization of a notched nozzle in conjunction with an inward-sloping valve produces higher pressure losses in the valve's control function, and no instabilities; and does not provoke any disturbance near the nominal operating point of the turbine. Thus, the notched nozzle in conjunction with an inward-sloping valve responds precisely to industrial requirements.

Conclusion

Enormous quantities of energy must be dissipated in control devices. If the walls are not designed to handle the fluid under all operating conditions, the fluid is free to vibrate the structures uncontrollably. Therefore, care must be taken to tame the fluid with simple forms that are adapted to all operating conditions so as to guarantee the reliability of the equipment.

Among the causes of structural vibration that are due to the shape of the fluid flow composed of two nozzles in series, of which one is annular, the following are of particular importance:

- the instabilities created by inappropriate nozzles;
- the violent movement of recompression shock waves from the nozzle onto the valve head;
- the start of nozzles;
- the potential instabilities of annular nozzles for certain expansion ratios;
- the unstable operation of open diffusers;
- the COANDA effects.

Instabilities at the level of the valve may occur simultaneously. They are not devoid of hysteresis and can interfere with the operation of the turbine. They must, therefore, be diminished or eliminated. An initial encouraging step involves removing any possibility of recompression, either subsonic or by shock wave, by eliminating the divergent formed by the valve and its seat. This solution is inadequate to the extent that it creates other instabilities due, in particular, to enlargements when they are too abrupt.

The more or less stable and violent starts in abrupt enlargements, which have been shown elsewhere, can be eliminated by using exergy destructors. An analogous device used in control valves nearly eliminates the unsteady forces on the valve head by organizing the flow in layers which expand at different rates, with intense mixing of these layers during expansion. This solution would seem to be decisive in solving in the short and middle term the problems of internal stability in control valves.

Acknowledgments

The author wishes to thank the French manufacturers of steam turbines and the Electricite of France for requesting him to carry out this study and for giving him their fullest support and cooperation.

References

Fabri, J., and Siestrunck, R., 1955, "Etude des divers régimes d'écoulement dans l'élargissement brusque d'une veine supersonique," *Revue générale des sciences appliquées*, Brussels, Vol. 2, No. 4.

Keller, H., 1980, "Design of Non-Rotating Parts," *Steam Turbines for Large Power Outputs*, Von Karman Institute for Fluid Dynamics, lecture series 1980/6, Brussels.

Khanin, G. A., 1975, "Simulation of Vibrations of Control Valves," *Thermal Engineering*, Vol. 22, pp. 60–63.

Pluviose, M., 1975, "Etude de l'écoulement dans une soupape fonctionnant en fluide compressible," Cetim-Information No. 42, pp. 33–41.

Pluviose, M., 1984, "Contribution á l'étude des instabilités d'écoulement dans les organes de réglage," Thèse de Doctorat d'Etat, Université Pierre et Marie Curie, Paris.

Development of a Thermal Analysis Model for a Nuclear Spent Fuel Storage Cask and Experimental Verification With Prototype Testing

J. Y. Hwang
Senior Engineer.
Mem. ASME

L. E. Efferding
Advisory Engineer.
Fellow ASME

Westinghouse Electric Corporation,
Nuclear Components Division,
Pensacola, FL 32596

A thermal analysis evaluation is presented of a nuclear spent fuel dry storage cask designed by the Westinghouse Nuclear Components Division. The cask is designed to provide passive cooling of 24 Pressurized Water Reactor (PWR) spent fuel assemblies for a storage period of at least 20 years at a nuclear utility site (Independent Spent Fuel Storage Installation). A comparison is presented between analytical predictions and experimental results for a demonstration cask built by Westinghouse and tested under a joint program with the Department of Energy and Virginia Power Company. Demonstration testing with nuclear spent fuel assemblies was performed on a cask configuration designed to store 24 intact spent fuel assemblies or canisters containing fuel consolidated from 48 assemblies.

Introduction

This paper describes a portion of the thermal analysis methodology employed in a Topical Safety Analysis Report for a dry storage cask (MC-10), which was reviewed and has recently been approved by the U.S. Nuclear Regulatory Commission. The Westinghouse MC-10 Cask was designed for dry storage of irradiated Pressurized Water Reactor fuel assemblies at a reactor site Independent Spent Fuel Storage Installation (ISFSI).

The analytical method was verified by comparison between analytical predictions and experimental results from a demonstration cask built by Westinghouse and tested under a joint program with the Department of Energy and Virginia Power Company. The demonstration cask (Figs. 1-4) is a self-contained storage system that provides necessary features of containment, shielding, criticality control, and passive heat removal for an ensemble of 24 intact spent fuel assemblies. A view of the cask loading operation in a hot cell with covers removed is shown in Fig. 5.

The cask is designed to provide a storage mode for containment of radioactive materials with use of a multiple, redundant closure barriers and a low alloy steel vessel. Shielding is provided by a thick wall of low alloy steel for gamma radiation absorption and by solid hydrogenous material and borated material for neutron absorption. Control of criticality in both spent pool-submerged and dry-storage modes is provided by neutron-absorbing material. Passive heat removal in the demonstration cask is provided by a heat-conducting matrix of aluminum grid plates in the cask interior and heat dissipation to the ambient environment at the cask exterior by convection and thermal radiation.

Thermal Analysis Basis

Passive heat rejection from the storage cask and internal structure (basket) was analyzed with the WECAN (Westinghouse Electric Computer ANalysis) finite element computer code. Cladding hot-spot temperature at the interior of the spent fuel assemblies was determined from experimental measurements on intact fuel and from assembly boundary temperature determined from WECAN conduction analysis.

Passive heat rejection mechanisms entail:

1 Convection/radiation from cask outer surface to ambient surroundings
2 Conduction via connecting ribs and fins (Fig. 2) from the cask body to the outer envelope and extended surface
3 Conduction radially through cask wall and circumferentially in the case of insolation (cosine distribution applied for solar heating)
4 Conductance at the interface configuration between the basket perimeter and vessel cavity (Fig. 3)
5 Conduction within basket grid structure
6 Conduction gap between basket plates and laminated cell enclosure (Fig. 4), which contains neutron-absorbing borated aluminum
7 Axial conduction along basket grid structure (three-dimensional correction), which attenuates the grid temperature at the peak heating location exhibited by the fuel assembly axial decay heat distribution

Contributed by the Nuclear Engineering Division and presented at the Joint ASME/ANS Nuclear Power Conference, Myrtle Beach, South Carolina, April 17-20, 1988. Manuscript received at ASME Headquarters September 2, 1988.

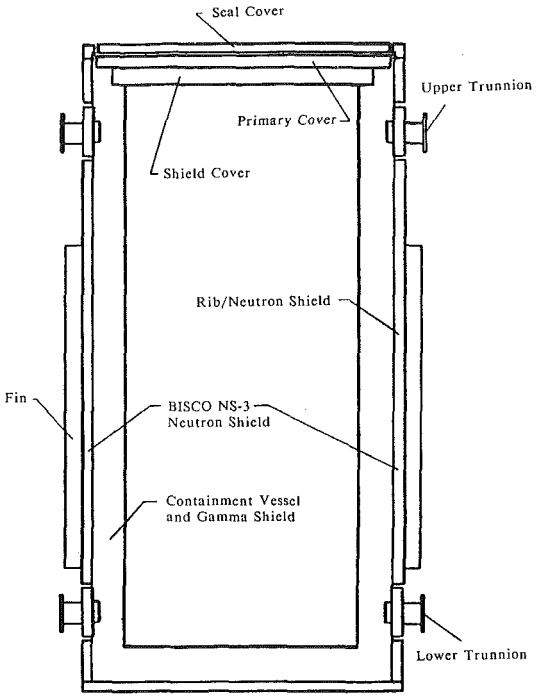

Fig. 1 Vertical cross section of cask

8 Fuel rod cladding temperature in the cell interior determined with the use of experimental data developed in tests

Items 4 through 8 above were based upon use of helium properties within the enumerated features in order to enhance heat conduction between adjacent surfaces and to minimize clad temperature at the fuel rod bundle centerline.

Heat rejection from the cask outer surface is based upon natural convection to the ambient air combined with thermal radiation to the environment. Heat transfer correlations are described for convection in air [1, 2, 3] and radiation to the atmosphere and ambient surroundings [5]. The correlations in reduced form are for convection and radiation, respectively

$$h_c = 1.451\ (T_S - T_A)^{1/3} \tag{1}$$

$$h_r = \frac{5.68\epsilon}{(T_S - T_A)}\left[(\bar{T}_S/100)^4 - (\bar{T}_A/100)^4\right] \tag{2}$$

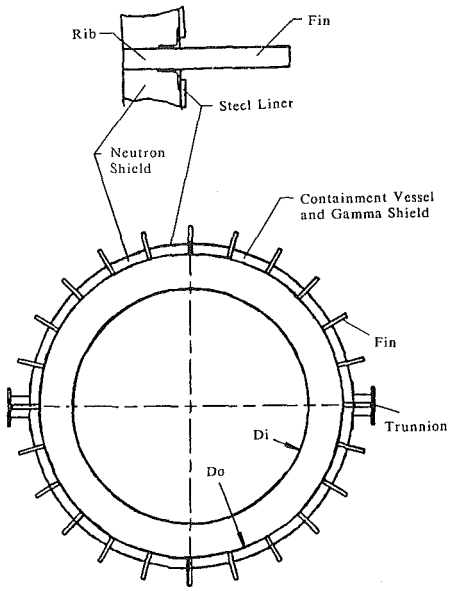

Fig. 2 Cross section of exterior geometry

$\bar{T}_S$ and $\bar{T}_A$ are cask surface and ambient absolute temperatures, respectively.

The resulting effective film coefficient at the cask outer surface is

$$h_{\text{eff}} = h_c + h_r \tag{3}$$

Conduction Via Ribs, Neutron Shielding, and Cask Wall

Carbon steel ribs serve to conduct heat radially from the cask vessel wall to the extended fin shown in Fig. 2. In addition, conduction through the neutron shield material, also shown in Fig. 2, forms a parallel heat transport path. The equivalent thermal conductivity for this combined parallel path is

$$K_g = \frac{K_B A_B + K_f A_f \lambda_w\ (C_{2D})}{A_B + A_f} \tag{4}$$

where $C_{2D} = 0.59$ is a two-dimensional conduction geometric factor determined by WECAN analysis.

Nomenclature

A_B = heat transfer area of neutron shielding, m^2
A_f = heat transfer area of ribs, m^2
b = thickness of the grid plate, cm
C_{2D} = two-dimensional conduction geometry factor
C_S = heat transfer correlation constant
D_i = inside diameter of vessel wall, m
D_o = outside diameter of vessel wall, m
h_c = heat transfer coefficient of convection, W/m^2-°C
h_r = equivalent heat transfer coefficient of radiation, W/m^2-°C
h_{eff} = $h_c + h_r$
K_B = neutron absorber thermal conductivity W/m-°C
K_f = thermal conductivity of rib, W/m-°C
K_{cell} = thermal conductivity of the cell, W/m-°C
K_{grid} = thermal conductivity of the grid plate, W/m-°C
K_g = equivalent thermal conductivity of ribs and neutron shield, W/m-°C
K_G = equivalent thermal conductivity of the grid plate (equation (7)) W/m-°C
K_V = thermal conductivity of the vessel wall, W/m-°C
L = length of the fuel assembly, m
Q = decay heat rate, KW
q'' = decay heat flux, W/m^2
q''' = volumetric decay heat rate, W/m^3
$\bar{T}$ = absolute temperature, K
T_A = ambient temperature °C
T_{can} = temperature of canister, °C
T_{fuel} = maximum temperature of each fuel assembly, °C
T_{grid} = temperature of the grid plate, °C
T_S = external surface temperature of the cask, °C
ΔT_V = temperature difference across the vessel wall, °C
X_{gap} = helium gap between the cell and grid plate, cm
Y = distance between two grid plates or finite element length, cm
y = variable distance along grid, cm
ϵ = thermal radiation emissivity
λ_w = rib/weld effectiveness = 0.94

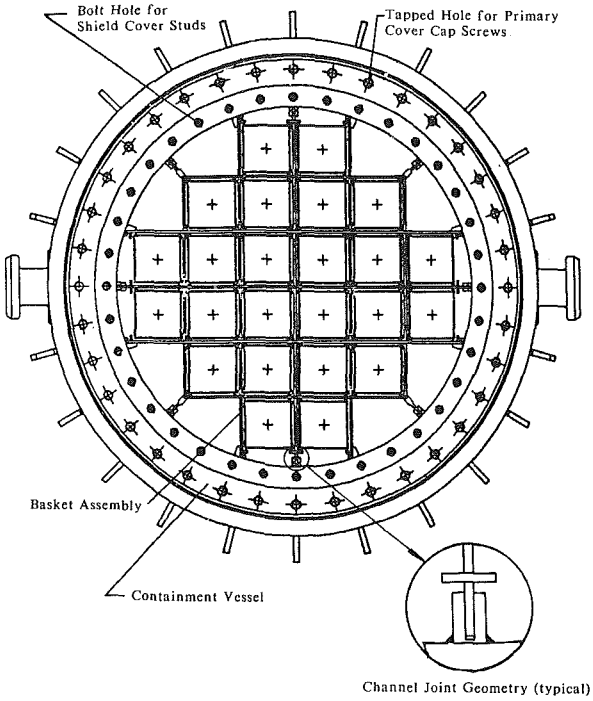

Fig. 3 Cross section of vessel and basket assembly

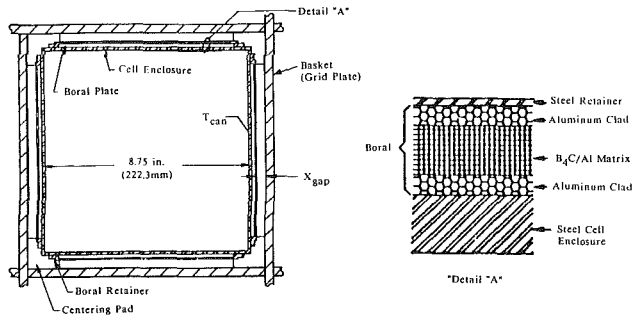

Fig. 4 Basket storage location

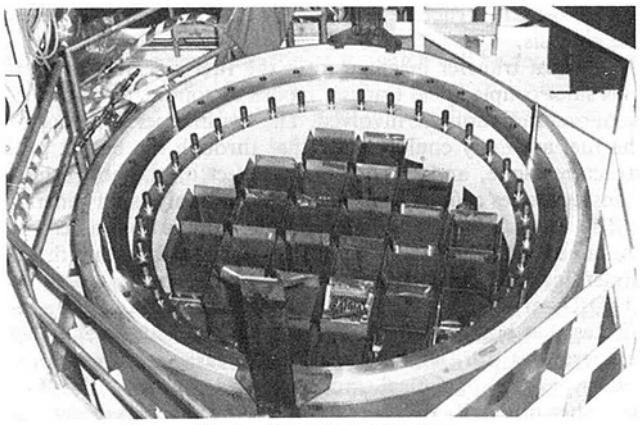

Fig. 5 View of cask loading

Basket/Vessel Contact Conductance and Vessel Wall Conduction

Vessel wall temperature difference is found from the expression [2]

$$q'' = \frac{2K_v \Delta T_v}{D_o \ln(D_o/D_i)} \tag{5}$$

The basket structure fitup relative to the cask vessel interior is a "captured" geometry whereby a channel welded to the vessel envelopes the periphery of the grid plates (Fig. 3) at 16

POWER UNIT: NORMALIZED

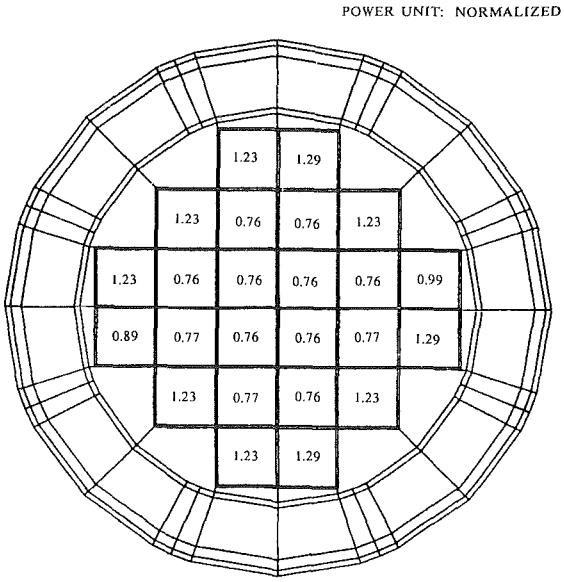

Fig. 6 WECAN code geometry and power distribution (total power = 13.5 kW)

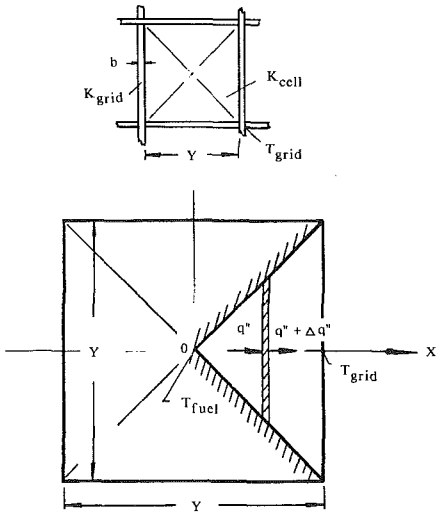

Fig. 7 Unit cell heat transfer model

peripheral locations. This design achieves maximum conductance for heat rejection to the vessel wall from the grid within the basket structure. Thermal expansion of the cask vessel relative to the basket grid structure during initial heatup is accommodated by the clearance provided between the channel opening and the grid plate thickness. The as-fabricated diametral gap and manufacturing tolerance with upper and lower bounds and relative axial motion between vessel and basket at hot ambient and cold ambient conditions was also accommodated. Contact conductance between aluminum and stainless steel surfaces within the "captured" joint has been analyzed assuming that the most conservative maximum gas gap appears between the mating surfaces.

Radial Conduction – Grid Structure

Radial transport of heat from interior cells to the vessel wall is modeled exclusively by conduction through grid plates during normal operation. The conduction model for radial

temperature difference considering uniform heat absorption over the length of each finite element (Fig. 7) is [2]:

$$K_G \frac{d^2T}{dy^2} + Q = 0 \tag{6}$$

where Q is heat absorption at the grid/cell interface, and K_G is the grid equivalent thermal conductivity

$$K_G = \frac{K_{\text{cell}} \text{Y} + \text{K}_{\text{grid}}\ b}{b} \tag{7}$$

Conductance at Grid/Storage Cell Interface Surface

The effective thermal conductance between basket plates and the cell envelope (Fig. 4) that encloses a spent fuel assembly is a combination of the helium gas conductance and the thermal radiation between parallel surfaces. The resulting temperature difference can be evaluated by the following equation:

$$q'' = \frac{5.68 \times 10^{-8}}{(1/\epsilon_1 + 1/\epsilon_2 - 1)} (\bar{T}^4_{\text{can}} - \bar{T}^4_{\text{grid}}) + \frac{K_{he}}{X_{\text{gap}}} (T_{\text{can}} - T_{\text{grid}}) \tag{8}$$

where ϵ_1 and ϵ_2 are the emissivities of the grid and cell wall, respectively [4]; $\bar{T}_{\text{grid}}$ and $\bar{T}_{\text{can}}$ are absolute temperatures of the grid and cell wall, respectively.

Fuel Rod Cladding Maximum Temperature

The relationship of peak fuel clad temperature for intact fuel assembly (as determined from center thermowell measured temperature) to cell temperature and assembly decay heat level is as follows [6]:

For helium:

$$T_{\text{fuel}} = T_{\text{can}} + Q(123.52 - 0.6325T_{\text{can}} + 0.001202T^2_{\text{can}}) \tag{9}$$

and for vacuum or air:

$$T_{\text{fuel}} = T_{\text{can}} + Q(172.6 \times 10^{-0.0000179T_{\text{can}}}) \tag{10}$$

This relationship is considered to be valid for a cell temperature range of 38°C to 316°C and fuel assembly decay heat level range of 0.1 to 2.0 kW for fuel stored and enveloped by a stainless steel cell (canister).

Computer Code Analysis and Results

The WECAN finite element analysis model of a cross section of the cask and basket grid structure is shown in Fig. 6. The code is used to predict the temperature distribution of the cross section with maximum heat generation in the cask.

The WECAN steady-state heat transfer analysis option for determining the steady-state temperature distribution in a heat conducting body was employed. In this analysis option, the boundary conditions may be specified temperatures or specified heat flow rates. Convection and radiation boundary conditions can be handled by convection and radiation elements or convection surfaces for certain elements. The material properties may be temperature dependent, which, along with the radiation element, causes a nonlinear problem and requires an iterative solution.

The basic equation for the steady-state heat transfer analysis is

$$[K_T]\{T\} = \{Q_{\text{app}}\} + \{Q_{\text{gen}}\} + [H]\{T_o\} \tag{11}$$

where $[K_T]$ is the structure thermal conductivity matrix, which includes the contribution due to convection (between T and T_o); $\{T\}$ is the nodal temperature vector, which is the solution of the set of simultaneous equations. Most heat transfer elements have one temperature per node; $\{Q_{\text{app}}\}$ is the applied heat flow rate at the node (if any); $\{Q_{\text{gen}}\}$ is the heat flow at the node due to internal heat generation in the element; $[H]$ is the structure thermal conductivity matrix due to the forced convection that is handled by convection surfaces; $\{T_o\}$ is the equivalent medium (bulk) nodal temperature vector.

For this analysis, internal heat generation (decay heat) within each cell of the cask is treated in the computer model as radiant deposition in a uniform heat flux applied to the cell envelope. The distribution is based on test data measured from an experimental geometry similar to that shown in Fig. 7. According to the heat generation distribution and the recorded ambient temperature, the basket temperature distribution in the cask is predicted by the computer code WECAN. The fuel temperature (clad temperature) is determined from equations (9), enclosure/canister temperature from equation (8), and grid temperature is based on these WECAN predictions.

Two cases for intact spent fuel storage in helium are analyzed. The first case assumes $K_{\text{cell}} = 0$ in equation (7) and $K_{\text{cell}} > 0$ for the second case, respectively. They are described as follows:

Case 1. $K_{\text{cell}} = 0$. This case considers a basket grid structure constructed of thick plates having high thermal conductivity, such as copper or aluminum material; thus heat transfer through the grid is much greater than that through the fuel assembly. Based on the use of a conservative thermal engineering model, the assumption of heat conduction through the basket grid alone is a practical approach as long as the degree of "conservatism" can be determined. This approach avoids a complex analysis of heat transfer modes within the fuel assembly.

Referring to the heating distribution in Fig. 6 and the ambient temperature of 28.2°C, the predicted temperatures of the basket and fuel locations are shown with test data in Fig. 8. The results indicate that the predicted fuel temperature can be as much as 19.5°C greater than the corresponding test data. The conservatism predicting the maximum fuel temperature in this case is calculated to be 18 percent.

Case 2. $K_{\text{cell}} > 0$. This case considers a cask basket grid structure constructed of thin plates with low thermal conductivity, such as stainless steel material. Heat transfer through the fuel assembly could be more effective than that through the basket grid structure and its effect cannot be neglected in the analysis.

The heat transfer mechanism in the fuel assembly is complex since coupled heat transfer modes of conduction, convection, and radiation are involved. The thermal performance of the fuel assembly could exceed that through the basket grid structure alone, and the combined effect of the above heat transfer modes cannot be neglected in the analysis, in general.

The thermal/hydraulic performance of the fuel assembly contained with the cask is generally predicted by using three-dimensional thermal/hydraulic computer codes such as HYDRA or COBRA-SFS [7]. Comparison with test data indicates that both codes perform well in predicting peak clad temperatures for a wide variety of cask configurations. However, the analytical model should simulate the fuel assembly in detail, which requires more than two nodes per rod. A change in rod emissivity from 0.8 to 0.6 can result in a 15°C temperature change in the prediction.

In this paper, a simplified method is introduced. Heat transfer through the entire internal structure of the basket and the fuel assembly continues to be simulated by heat conduction through the basket grid, but with use of an equivalent thermal conductivity. The grid equivalent thermal conductivity K_G is determined by combining heat transfer effects of the fuel assembly and the basket grid.

Considering the geometry of the cell shown in Fig. 4, the grid equivalent thermal conductivity K_G employed in the WECAN code can be written as a function of grid and cell

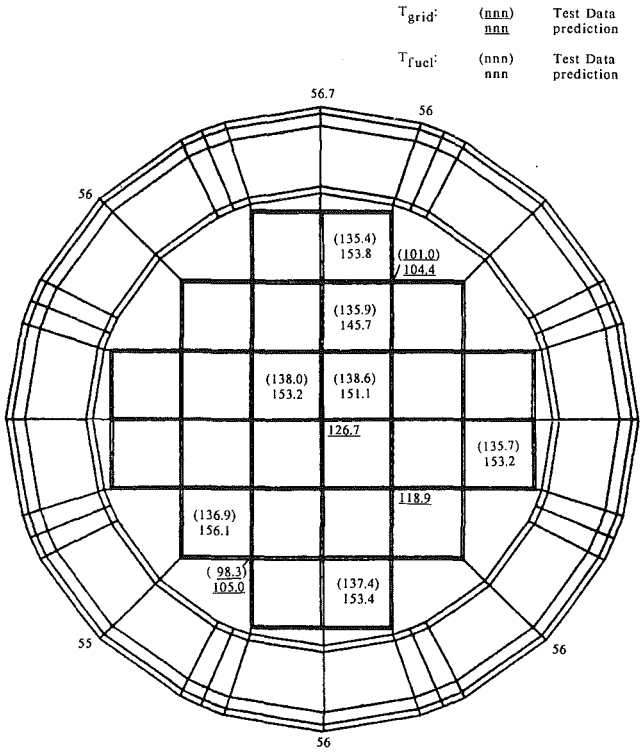

Fig. 8 Thermal analytical results ($K_{cell} = 0.0$)

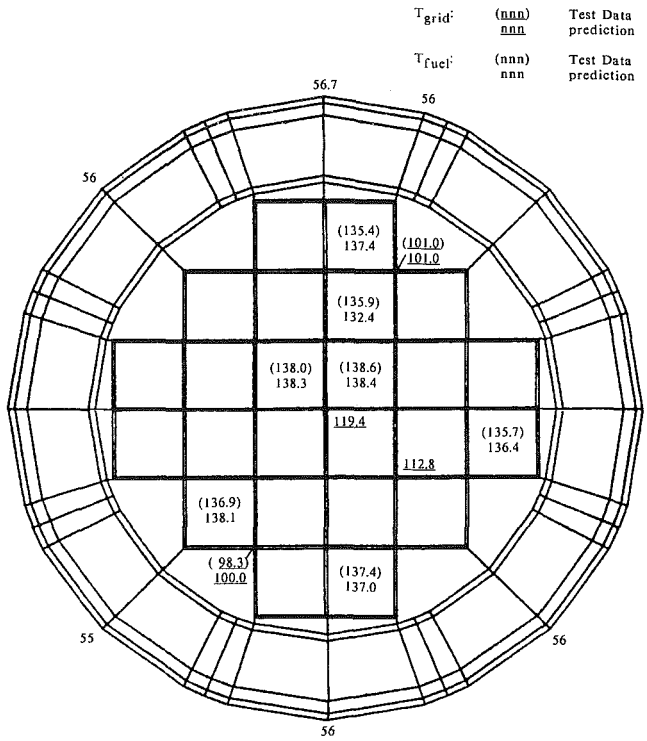

Fig. 9 Thermal analytical results ($K_{cell} = 1.2$ W/m·°C)

thermal conductivities and the corresponding dimensions of the cell and the grid as shown by equation (7).

The cell equivalent thermal conductivity is determined from a one-dimensional heat transfer solution of the cell. The solution is derived based on the heat transfer configuration as shown in Fig. 7 with the analyzed cell defined by the fuel assembly heat source. The heat transfer solution is

$$T_{fuel} - T_{grid} = \frac{q''' Y^2}{4 K_{cell}} \tag{12}$$

Equation (9) can be modified to the form

$$T_{fuel} - T_{grid} = C_S\, Q(123.52 - 0.6325\, T_{grid} + 0.001202\, T_{grid}^2) \tag{13}$$

where C_S is the correlation constant, which will be determined by comparison of the test data and the prediction. By combining equations (12) and (13), the final relation between K_{cell} and T_{grid} is

$$C_S\,(123.52 - 0.6325\, T_{grid} + 0.001202\, T_{grid}^2) = \frac{1000}{4L\, K_{cell}} \tag{14}$$

For a given value of C_S and using the estimated average grid temperature, K_{cell} and K_G can be calculated from equation (14) and (7) in sequence. According to the calculated value of K_G, the basket (grid) temperature distribution is predicted by WECAN. The fuel temperatures are calculated by using equation (13) based on the predicted grid temperatures.

The final analytical results $C_S = 0.83$ are shown with a comparison of the test data in Fig. 9. The results indicate that this prediction yields excellent agreement with the test data. The maximum grid temperature is 119°C, which is 7.2°C less than that of Case 1. The cell equivalent thermal conductivity is calculated from equation (14) to be 1.2 W/m-°C. The heat transfer partition conducted by the fuel assembly and by the aluminum plate is 15 and 85 percent, respectively. With the grid plate constructed of stainless steel material, heat transfer partition conducted by the fuel assembly changes to 65 percent with 35 percent through the plate material. This example demonstrates the fuel assembly heat conduction is significant when the grid structure is constructed of low thermal conductivity materials.

Conclusions

The following conclusions result from this analysis and experimental comparison:

1 The WECAN 2-D thermal model is able to predict fuel temperature accurately in a spent fuel storage cask.

2 In the case of a cask basket grid structure of aluminum or copper material, the heat transfer conducted by the fuel assembly is about 15 percent or less of the total heat transport through the structure.

3 The proposed method of calculating the cell equivalent thermal conductivity greatly simplifies the analysis and provides sufficient accuracy for predicting fuel temperature in a storage cask.

Acknowledgments

The authors appreciate the support of personnel at the Idaho National Engineering Laboratory in making information available to allow the evaluation of a simplified heat generation model.

References

1 Holman, J. P., *Heat Transfer*, 2nd ed., McGraw-Hill, New York, 1968.

2 Geidt, W. H., *Principles of Engineering Heat Transfer*, D. Van Nostrand Company, New York, 1957.

3 Eckert, E. R. G., and Drake, R. M., *Heat and Mass Transfer*, McGraw-Hill, New York, 1959.

4 "Tables of Emissivity of Surfaces," *International Journal of Heat and Mass Transfer*, Vol. 5, 1962, pp. 67–76.

5 Wiebelt, J. A., *Engineering Radiation Heat Transfer*, Holt, Rinehart and Winston, New York, 1980.

6 Driesen, G. E., Unterzuber, R., and Milnes, R. D., "Heat Transfer Associated With Dry Storage of Spent LWR Fuel," *Heat Transfer in Nuclear Waste Disposal*, ASME HTD-Vol. 11, 1980.

7 Wheeler, C. L., McCann, R. A., Lombardo, N. J., Rector, D. R., and Michener, T. E., "HYDRA and COBRA-SFS Temperature Calculations for CASTOR-1C, REA-2023, CASTOR-V121, and TN-24P Casks," 3rd International Spent Fuel Storage Technology Symposium/Workshop CONF-860417, UC-85, Apr. 8–10, 1986.

Rub Interactions of Flexible Casing Rotor Systems

F. K. Choy

J. Padovan

C. Batur

Department of Mechanical Engineering,
The University of Akron,
Akron, OH 44325

Rub interactions between a rotor assembly and its corresponding casing structure has long been one of the major causes for machine failure. Fracture/fatigue failures of turbine impeller blade components may even lead to catastrophic consequences. This paper presents a comprehensive analysis of a complex rotor-bearing-blade-casing system during component rub interactions. The modal method is used in this study. Orthonormal coupled rotor-casing modes are used to obtain accurate relative motion between rotor and casing. External base vibration input and the sudden increase of imbalance are used to simulate suddenly imposed adversed operating condition. Nonlinear turbine/impeller blade effects are included with the various stages of single/multiple blade participation. A variable integration time step procedure is introduced to insure both accuracy and efficiency in numerical solutions. The dynamic characteristics of the system are examined in both the time domain and the frequency domain using a numerical FFT procedure. Nonlinear bearing and seal forces are also included to enhance a better simulation of the operating system. Frequency components of the system spectral characteristics will be correlated with the localized rub excitations to enable rub signature analysis. A multibearing flexible casing rotor system will be used as an example. Conclusions will be drawn from the results of an extensive parametric study.

Introduction

Failure in high-performance turbomachinery involves a wide variety of mechanisms, namely erosion, corrosion, thermomechanically induced elastic/plastic creep/rupture, etc. Perhaps the least understood mode of failure and performance degradation evolves out of rub interactions between seal surfaces, compressor and turbine blades, and their associated casing seals, and in general between the rotor and casing. In general, rubs lead to excessive seal/blade wear and fatigue as well as to severe vibration environments and lost performance. Overall the occurrence of the rubs and their resulting degrading effects cause highly nonlinear rotor-blade-casing dynamics.

This paper presents a comprehensive analysis of rotor/bearing/blade/seal system response under extreme operating conditions, e.g., seismic events, blade losses, etc. This is facilitated through the use of the modal method in combination with numerical integration. The rub-induced nonlinear transient dynamics of a rotor-blade-seal-casing system is evaluated using a variable time-stepping numerical integration scheme. The overall features in modeling and analysis methodology consist of incorporating the bearing coupled rotor/casing vibration modes in the modal analysis. The basic forcing functions of the system are rotor imbalance eccentricities and external base motion through the flexible casing support systems. Rotor blade flexibilities and effects of various stages of single blade participations in rub interaction are also considered.

Based on such a methodology, the paper overviews an overall signature analysis methodology to enable pattern recognition for rub interaction problems in rotating equipment. A numerical FFT procedure is used to examine rub forces, system vibrations, bearing forces, and modal amplitudes. Response characteristics are developed to identify various stages of rub interactions. Correlation of such response/force spectral characteristics with localized rub excitations provides for system rub interaction signature analysis.

2 Equations of Motion

For the rotor-bearing-casing system shown in Fig. 1, the generalized equations of motion for the system can be written as

$$[M_o]\{\ddot{W}\} + [C_o]\{\dot{W}\} + [K_o]\{W\} = \{F_o(t)\} \tag{1}$$

where $[M_o]$, $[C_o]$, and $[K_o]$ are, respectively, the generalized mass-inertia, damping-gyroscopic, and stiffness matrices of the rotor, the casing, and its corresponding support system. $\{W\}$ is the generalized displacement vector of the rotor and casing components in the X and Y directions, and $\{F_o(t)\}$ is the forcing function vector, which includes the imbalance forces, nonlinear bearing forces, and external excitation, as well as the rub interaction forces. Note that the X and Y components account for circumferential and radial effects. Due to the generality of the methodology developed herein, axial effects (Li, 1978) can easily be introduced into the analysis. Using the normal mode expansion (Child, 1976; Choy, 1978) the displacement function can be approximated by

Contributed by the Power Division for publication in the JOURNAL OF ENGINEERING FOR GAS TURBINES AND POWER. Manuscript received by the Power Division September 15, 1987.

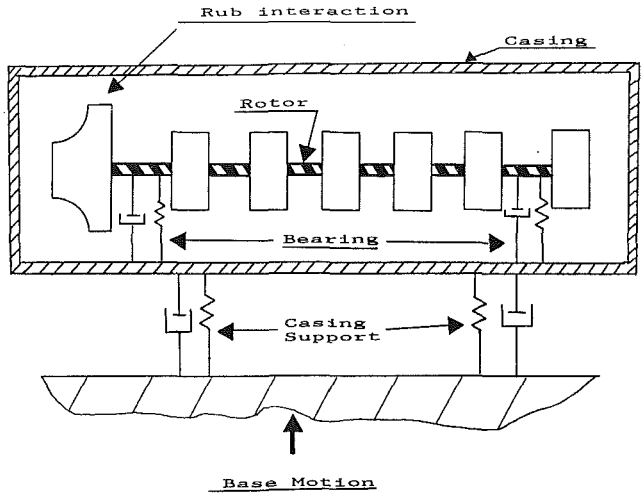

Fig. 1 Rotor-bearing-casing system

$$\{W\} = \begin{bmatrix} (X) \\ (Y) \end{bmatrix} = \sum_{I=1}^{N} \begin{pmatrix} A_I(t)\{\phi_I\} \\ B_I(t)\{\phi_I\} \end{pmatrix} \tag{2}$$

where $\{\phi\}$ are the orthonormal planar modes of the coupled rotor/casing system and A_I and B_I are, respectively, modal time functions for the X and Y coordinates. Employing the orthogonal conditions of the planar modes, namely

$$[\phi]^T[M][\phi] = [I] \tag{3}$$

$$[\phi]^T\{[K_s] + [K_b]\}[\phi] = [\lambda^2] \tag{4}$$

The equations of motion can be written in both the X-Z plane and the Y-Z plane, as X-Z plane equation

$$\{\dot{A}\} + [\phi]^T[C_x][\phi]\{\dot{A}\} + [\phi]^T[C_{xy}][\phi]\{\dot{B}\} + [\lambda^2]\{A\} + [\phi]^T\{[K_s] - [K_b]\}[\phi]\{A\} + [\phi]^T[K_{xy}][\phi]\{B\} = [\phi]^T\{F_x(t)\} + [\phi]^T\{F_{rx}(t)\} + [\phi]^T\{F_{Bx}(t)\} \tag{5}$$

and a Y-Z plane equation

$$\{\ddot{B}\} + [\phi]^T[C_y][\phi]\{\dot{B}\} + [\phi]^T[C_{yx}][\phi]\{\dot{A}\} + [\lambda^2]\{B\} + [\phi]^T\{[K_s] - [K_b]\}[\phi]\{B\} + [\phi]^T[K_{yx}][\phi]\{A\} = [\phi]^T\{F_y(t)\} + [\phi]^T\{F_{ry}(t)\} + [\phi]^T\{F_{By}(t)\} \tag{6}$$

where $[K_s]$ is the shaft and casing stiffness and $[K_b]$ is the average bearing stiffness such that

$$[K_b] = 1/2\{[K_x]_b + [K_y]_b\} \tag{7}$$

$\{F_x\}$, $\{F_{rx}\}$, and $\{F_{Bx}\}$ are, respectively, forcing functions due to imbalance and bearing/seal forces, rub interaction, and base motion (Choy et al., 1986; Choy and Padovan, 1987). Rearranging the above equations, the modal acceleration can be expressed as:

X-Z plane equation

$$\{\ddot{A}\} = [\phi]^T\{F_x(t)\} + [\phi]^T\{F_{rx}(t)\} + [\phi]^T\{F_{Bx}(t)\} - [\phi]^T[C_x][\phi]\{\dot{A}\} - [\phi]^T[C_{xy}][\phi]\{\dot{B}\} - [\lambda^2]\{A\} - [\phi]^T\{[K_s] - [K_b]\}[\phi]\{A\} - [\phi]^T[K_{xy}][\phi]\{B\} \tag{8}$$

Y-Z plane equation

$$\{\ddot{B}\} = [\phi]^T\{F_y(t)\} + [\phi]^T\{F_{ry}(t)\} + [\phi]^T\{F_{By}(t)\} - [\phi]^T[C_y][\phi]\{\dot{B}\} - [\phi]^T[C_{xy}][\phi]\{\dot{A}\} - [\lambda^2]\{B\} - [\phi]^T\{[K_s] - [K_b]\}[\phi]\{B\} - [\phi]^T[K_{yx}][\phi]\{A\} \tag{9}$$

Given the appropriate initial conditions, a Newmark Beta integration scheme is used to obtain the transient motion of equations (8) and (9). A variable time-stepping approach has been employed for numerical integration. In order to maintain solution accuracy and numerical stability, the step size will be reduced when the rotor is approaching the onset of rub interaction, and further reduced during the rub process.

3 Rotor-Casing Interaction

For the rotor/casing system shown in Fig. 2, the rub force vectors in the X and Y directions can be expressed as

$$F_{rx}(t) = f_n \cos\phi - f_t \sin\phi \tag{10}$$

and

$$F_{ry}(t) = f_n \sin\phi + f_t \cos\phi \tag{11}$$

where f_n and f_t are the rub force components in the normal and tangential directions of the rub area. For the case of a rigid casing with radial foundation stiffness K_g, the rub force can be calculated by employing the radial clearance c and the relative displacement δ of the rotor as given by

$$f_n = (\delta - c)K_g \tag{12}$$

and assuming Coulomb-type behavior (Bently, 1974; Choy et al., 1986; Childs, 1979; Muszynska, 1984)

$$f_t = \mu f_n \tag{13}$$

where μ is the coefficient of friction. Note that due to the generality of the analysis methodology, essentially any form of constitutive expansion (Bill and Ludwig, 1980; Marsches, 1982) defining friction and machining can be handled.

Nomenclature

A_I, B_I = modal parameters in x and y directions
$[C_x]$, $[C_y]$ = overall damping matrix in x and y directions
$[C_{xy}]$, $[C_{yx}]$ = overall cross-coupling damping matrix
$[C_o]$ = generalized damping matrix
$\{F_{rx}\}$, $\{F_{ry}\}$ = component rub force in x and y directions
$\{F_{Bx}\}$, $\{F_{By}\}$ = casing support force due to base motion
$\{F_N\}$, $\{F_t\}$ = normal and tangential rub force due to friction
$\{F_x\}$, $\{F_y\}$ = force vectors in x and y directions due to imbalance
$\{F_o(t)\}$ = generalized force vector
$[I]$ = identity matrix
$[K_b]$ = average bearing stiffness
$[K_s]$ = shaft stiffness matrix in x and y directions
$[K_{xy}]$, $[K_{yx}]$ = overall cross-coupling stiffness matrix
$[K_o]$ = generalized stiffness matrix
$[K_x]_b$, $[K_y]_b$ = bearing stiffness matrix in x and y directions
$[M]$ = mass matrix
$[M_o]$ = generalized mass-inertia matrix
$\{S_x\}$, $\{S_y\}$ = base motion displacement vectors in x and y directions
$[W]$ = generalized displacement and rotational vector
$[\lambda^2]$ = eigenvalue matrix
$[\phi]$ = orthonormal mode shape matrix
$\{\phi_I\}$ = Ith orthonormal mode

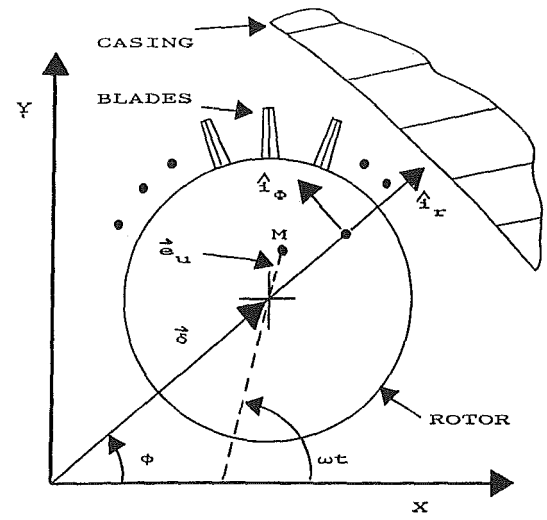

Fig. 2 Rotor-blade-casing coordinates

For the case of a rotor-blade-casing interaction event, the normal rub force (Choy and Padovan, 1986) can be calculated as

$$F_n = \frac{\pi^2 EI}{4l_b^2}\bar{F}_N \tag{14}$$

and

$$\bar{F}_N = \frac{\frac{\pi}{2}\sqrt{\frac{\delta_l}{l_b}}}{\mu + \frac{\pi}{2}\sqrt{\frac{\delta_l}{l_b}}} \tag{15}$$

where δ_l is the normal deflection and l_b, EI are the length and material/geometric properties of the blade. Note that the normal force F_N is in a nonlinear relationship with the normal blade deflection δ_l. A complete derivation of the blade rub force and deflection relationship, and criteria for various stages of single/multiple blade participation, are given by Padovan and Choy (1986).

4 Base Motion Excitation

The effects of base motion excitations can be simulated by an equivalent forcing function input at the support bearings. Hence, the equations of motion for base displacements $\{S_x\}$ and $\{S_y\}$ can be written as

X-Z plane

$$[M]\{\ddot{X}\} + [C_x]\{\dot{X}\} + [C_{xy}]\{\dot{Y}\} + [K_s]\{X\} + [K_x]_b\{X\} + [\bar{\bar{K}}_x](\{X\} - \{S_x\}) + [K_{xy}]\{Y\} = \{F_x(t)\} \tag{16}$$

Y-Z plane

$$[M]\{\ddot{Y}\} + [C_y]\{\dot{Y}\} + [C_{yx}]\{\dot{X}\} + [K_s]\{Y\} + [\bar{\bar{K}}_y]_b\{Y\} + [K_y](\{Y\} - \{S_y\}) + [K_{yx}]\{X\} = \{F_y(t)\} \tag{17}$$

where $[K_x]_b$, $[K_y]_b$, and $[\bar{\bar{K}}_x]$, $[\bar{\bar{K}}_y]$ are the coupling bearing and casing support stiffness in the X and Y directions, respectively.

Using the average bearing stiffness $[K_b]$ from (7), we see that

X-Z plane

$$[M]\{\ddot{X}\} + [C_x]\{\dot{X}\} + [C_{xy}]\{\dot{Y}\} + ([K_s] + [K_b])\{X\} + ([K_x]_b - [K_b])\{X\} + [K_{xy}]\{Y\} = \{F_x(t)\} + [\bar{\bar{K}}_x]\{S_x\} \tag{18}$$

Y-Z plane

$$[M]\{\ddot{Y}\} + [C_y]\{\dot{Y}\} + [C_{yx}]\{\dot{X}\} + ([K_s] + [K_b])\{Y\} + ([K_y]_b - [K_b])\{Y\} + [K_{yx}]\{X\} = \{F_y(t)\} + [\bar{\bar{K}}_y]\{S_y\} \tag{19}$$

Transient solutions can be obtained through a similar technique explained in Section 2.

5 Overall Signature Analysis Procedure

The overall requirements of signature analysis fall into several main categories. These include:

(*i*) proper definition of parameters defining system response/performance under both proper and anomalous conditions;

(*ii*) proper location and selection of transducers enabling ongoing description of response;

(*iii*) understanding of prototypical system response behavior for a wide variety of anticipated normal and anomalous operating environments;

(*iv*) complete evaluation/description of real time and frequency signatures of system response to both normal and anomalous operating environments; and,

(*v*) via spectrum analysis, define various types of generic response signatures so as to enable pattern recognition for normal and anomalous characteristics, thereby providing for improved system control.

In order to define a complex system response properly, the appropriate field parameters must be monitored. For high-performance rotating machinery, this includes such information as:

(*i*) bearing loads;
(*ii*) casing loads and motion;
(*iii*) rotor loads and motion;
(*iv*) rub site locations;
(*v*) rub forces;
(*vi*) ongoing assessment of all clearances;
(*vii*) monitoring single-multiple blade participation.

Generally, the response of real world system involves extremely rich spectral characteristics. In this context, it is typically difficult to extract out a given phenomenon from a general response. To improve such a process, it is necessary to evaluate the proper location of transducers. Additionally, to enable extraction of rub effects from the overall response, their own distinct signature must be identified. This can be achieved by employing the analytical modeling procedure described in the previous section to determine the response to prototypical operating environments. Such a procedure can also be used to locate zones of rubbing as well as define optimal sites for transducer location. Note that one of the benefits of the modal method follows from the fact that the nodes and peaks of the primary participating spectra are known. In this context, the response characteristics of a given mode can be extracted by placing the transducer at the zone of peak amplitude. Since typical rub bounce processes in rotating equipment involve strong time dependencies, a windowed FFT is necessary. Overall the FFT analysis consists of five main phases, namely:

(*i*) perform FFT for all pertinent signals;
(*ii*) define normal operating signatures;
(*iii*) establish windowing requirements to define various ranges of behavior;
(*iv*) establish unique features of various types of rub events; and
(*v*) distinguish between magnitude and components signatures.

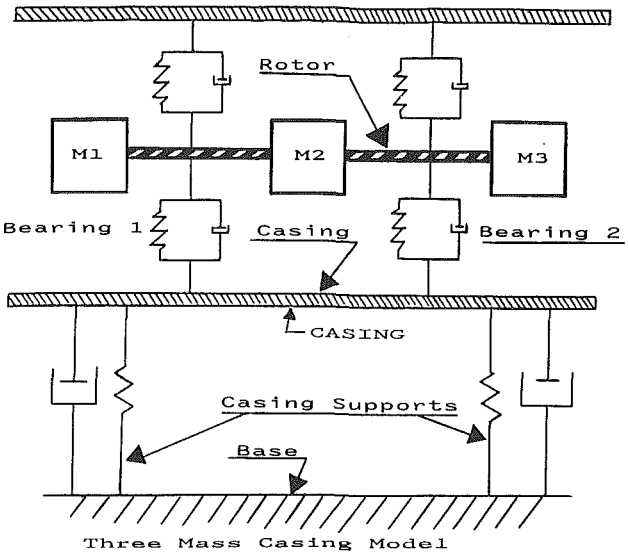

Fig. 3 Three-mass model rotor-bearing-casing system

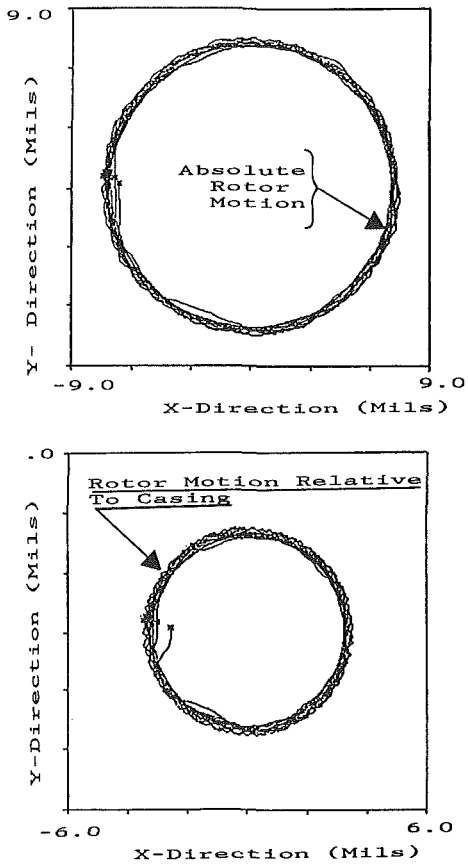

Fig. 4 Absolute and relative rotor transient trajectories

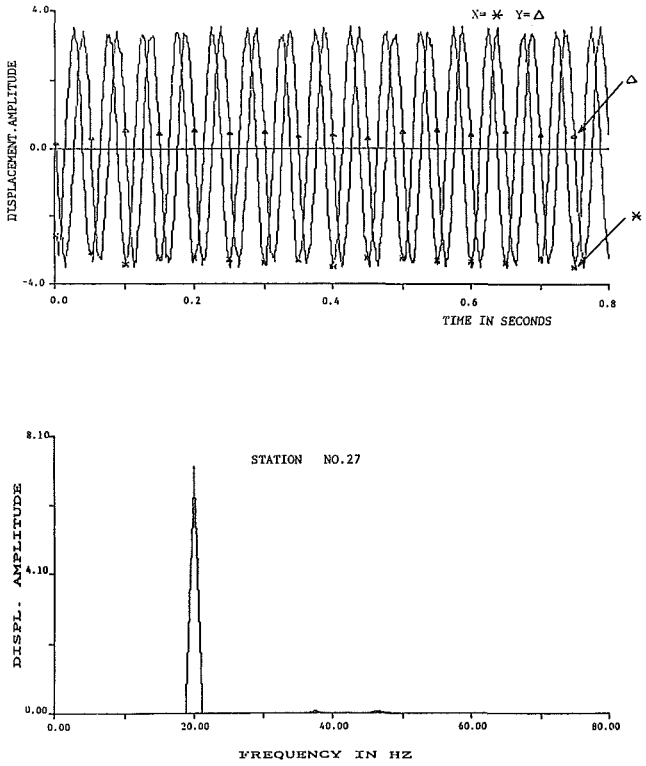

Fig. 5 Relative rotor motion in time and frequency domain

6 Discussion of Results

In the preceding sections, a modeling and signature analysis methodology was overviewed. To demonstrate the procedure, several sample problems will be considered. The basic emphasis of the case studies considered consists of:

(*i*) the system frequency shifts generated by the rubbing process;

(*ii*) the effects of directionally dependent (anisotropic) versus rotating (isotropic) exciting fields; and

(*iii*) the signature characteristics of such effects.

For current purposes, the directional dependence will be modeled by seismic events. The symmetric exciting field will be simulated by considering blade loss events.

Figure 3 illustrates the rotor-casing model used to perform the analysis. As a starting point, we shall consider the case of rub induced by rotatory (isotropic) exciting fields, i.e., blade loss events. Figures 4 to 7 illustrate various aspects of the rub bounce process. For instance, Fig. 4 shows the absolute and relative rotor motion. As can be seen, the trajectory depicted is very symmetric. This is further illustrated in Fig. 5, which depicts the X and Y component deflections.

To illustrate the frequency shifting induced by rubbing, we next consider the rub and bearing forces. This is achieved by evaluating the radial rub magnitude as well as both the bearing radial and component force responses. These are depicted in Figs. 6 and 7 along with their associated FFT signatures. Note that the original system frequencies are calculated as

$$N_1 = 46 \text{ Hz}$$

$$N_2 = 56 \text{ Hz}$$

$$N_3 = 240 \text{ Hz}$$

In order to provide a better understanding of the shifting of system frequencies during rub interactions, a set of modified system frequencies is also evaluated with an additional "fictitious" bearing support located at the rub site. The fictitious bearing support is created by introducing a set of linear springs at the rub location. The system frequencies for this modified model are calculated as

$$N_1 = 50 \text{ Hz}$$

$$N_2 = 160 \text{ Hz}$$

Figure 6 demonstrates that for the given case, the rub force induces significant interactions in a relatively narrow spectral range about the shifted second mode at about 160 Hz. The narrow band is an outgrowth of the intermittent nature of the rub process approaching the steady-state condition.

Considering the bearing force spectrum, similar spectral

shifting is noted. This is depicted in Fig. 7. Interestingly, the shifted second mode is present in the magnitude plots, while it appears to be missing in the X-component FFT spectrum. This is a direct outgrowth of the precessing of the rub site. In particular, employing the Dirac function $\delta(t)$, the steady-state magnitude and component rub forces can be cast in the form

$$F_{\text{rub}}(\text{mag}) \sim \sum_m F_m \, \delta(t-\tau_m) \tag{20}$$

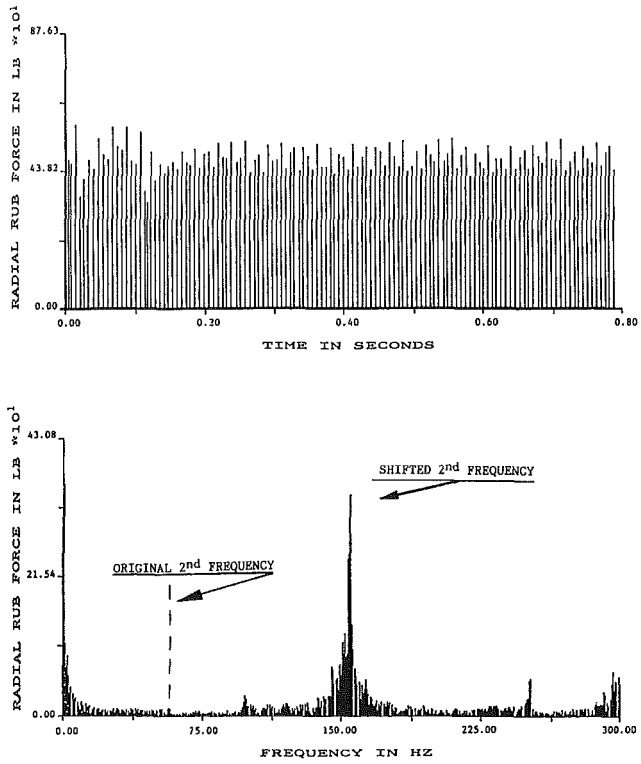

Fig. 6 Normal (magnitude) rub force in time and frequency domain

$$F_{\text{rub}}(\text{comp}) \sim \sum_m F_m \cos(\omega^* \tau_m)\delta(t-\tau_m) \tag{21}$$

where ω^* is related to the precessing rate. Taking the FFT of equations (20) and (21), we see that

$$F_{\text{rub}}(\text{mag}) \sim \sum_m F_m \, e^{j\omega\tau m} \tag{22}$$

$$F_{\text{rub}}(\text{comp}) \sim \sum_m F_m \cos(\omega^* \tau_m) e^{j\omega\tau m} \tag{23}$$

Recalling the various trigonometry identities, (23) can be recast in the form

$$F_{\text{rub}}(\text{comp}) \sim \sum_m F_m (e^{j(\omega-\omega^*)\tau m} - e^{j(\omega+\omega^*)\tau m}) \tag{24}$$

Comparing equations (22) and (24), we see that for the component version, various peaks may undergo ω^* shifts about the central magnitude FFT.

Next we shall consider the effects of directionally dependent (anisotropic) exciting fields, i.e., seismic events. Figure 8 illustrates the relative and absolute rotor motion. For the given problem, the overall motion appears to fit the attributes of a totally chaotic response. Viewed from a component basis (Fig. 9), the motion is seen to possess definite harmonic characteristics. This is seen from the FFT of the x component, also depicted in Fig. 9. As can be seen, the spectral outputs appear to be centered about the seismic, synchronous blade loss and first mode frequency effects. As noted earlier, despite the appearance of chaos in the rotor response trajectories, the rub forces depicted in Fig. 10 show very distinct order. Like an FM radio signal, the force magnitude varies about a given (carrier) frequency while the time period between successive rubs increases and decreases (frequency modulation). Noting the FFT depicted in Fig. 10, this leads to a spectrum that, while spread out in white noise sense, shows distinct concentrations about the seismic input and shifted second mode frequencies.

Furthermore, Fig. 11 also clearly illustrates the influence of the seismic, synchronous, and shifted first/second mode effects. As with the rub forces, the second mode effects in the

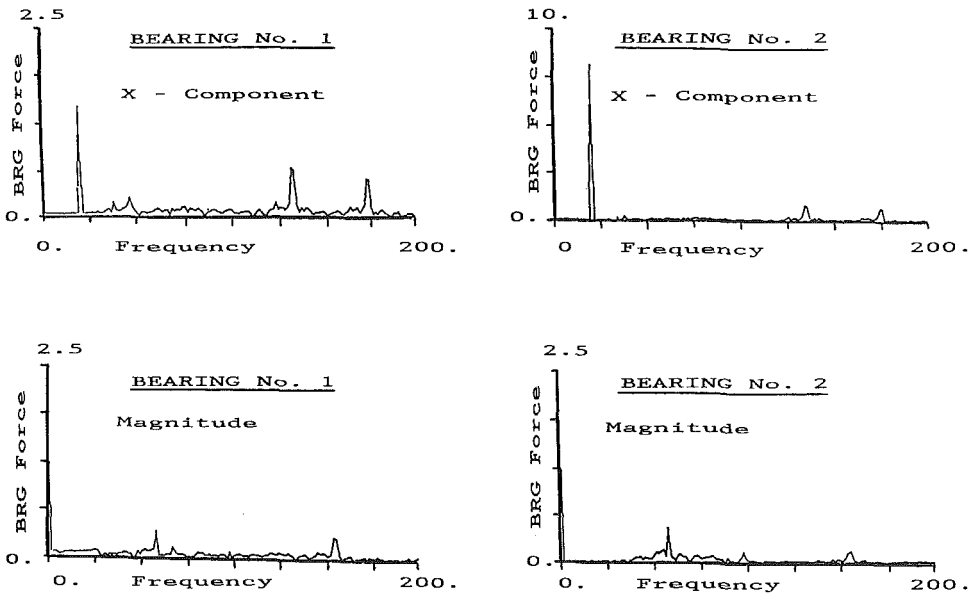

Fig. 7 X component (directional) and normal (magnitude) bearing force in frequency domain

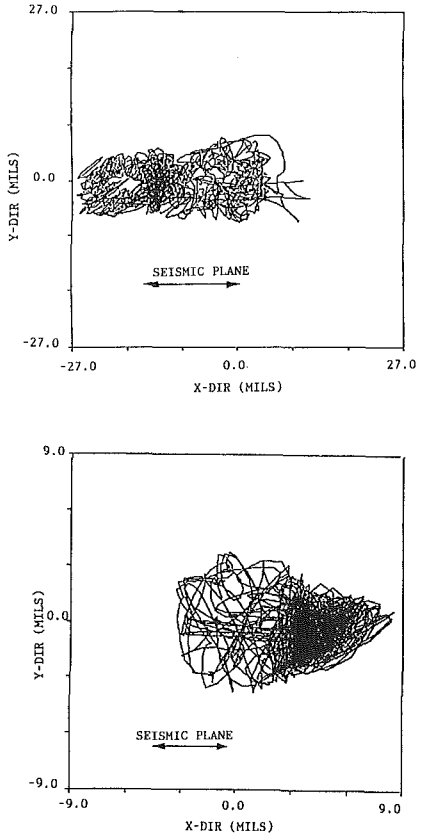

Fig. 8 Absolute and relative rotor transient trajectories under seismic effect

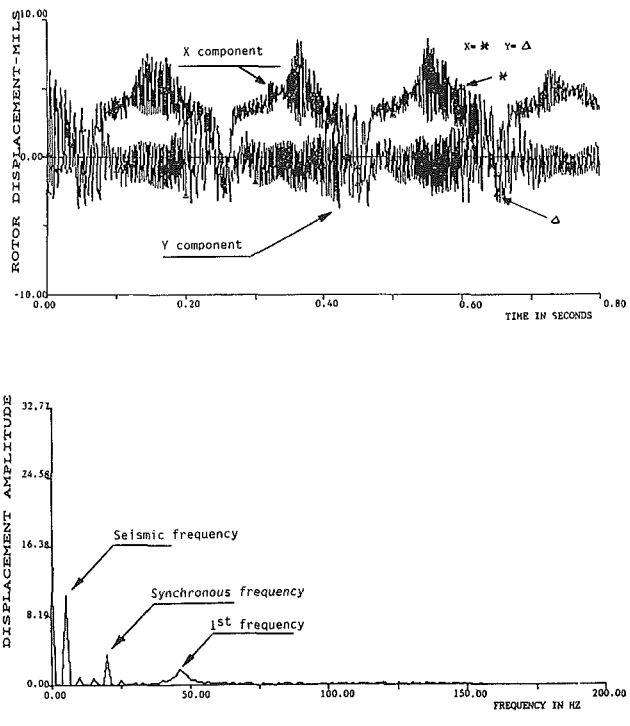

Fig. 9 Relative rotor motion in time and frequency domain under seismic effect

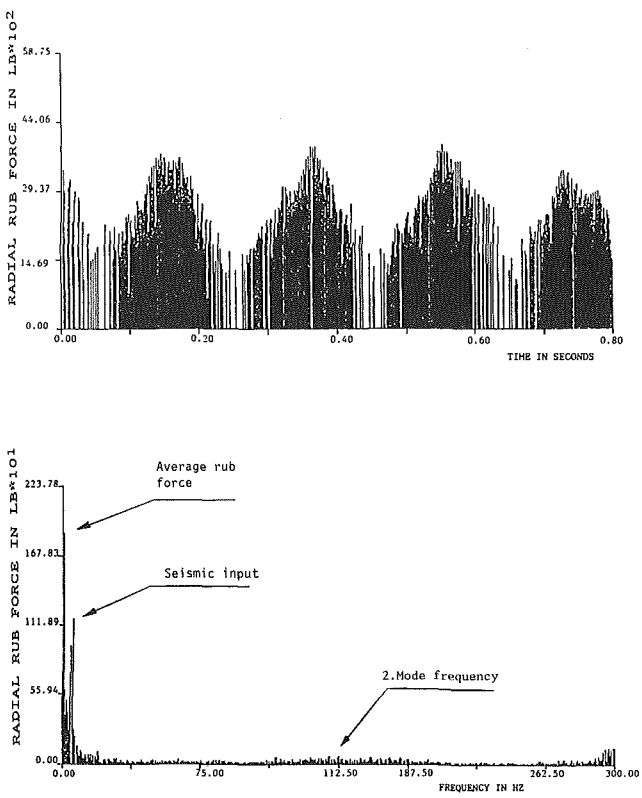

Fig. 10 Normal (magnitude) rub force in time and frequency domain under seismic effect

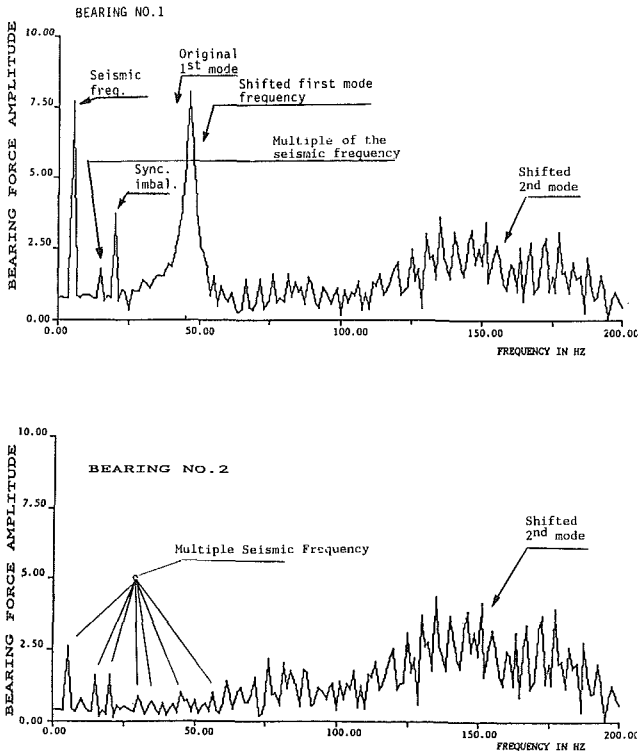

Fig. 11 X component bearing force in frequency domain under seismic effect

bearing forces are somewhat spread due to the strong response anisotropy induced by the seismic input. Upon closer investigation, we see that the FFT of the bearing forces depicted in Fig. 11 has close but evenly spread peaks whose periods are multiples of the seismic exciting field (5 Hz). This follows from the fact that the seismic field initiates a preferential rubbing process in the plane of loading. Hence the phase of the rubbing process tends to be strongly dependent on the seismic

input frequency and its various multiples. A further indication of this follows from the fact that the absolute, relative, and component rotor orbits are not symmetric (see Figs. 8 and 9). Rather they are aliased in the X direction, i.e., the direction of seismic loading.

In the context of the foregoing examples, we conclude that:

(*i*) Significant frequency shifting can be induced by rubbing; this is a direct outgrowth of the intermittent change in boundary conditions induced during the rub process;

(*ii*) Rotating exciting fields induce largely symmetric rub bounce trajectories; this is contingent on the symmetry of various support/casing stiffness; and

(*iii*) Seismic/directionally dependent exciting fields tend to cause asymmetric force and displacement fields; for such situations the directional fields tend to have a strong influence on the rub bounce frequency.

(*iv*) The component rub force recorded during rub events will be shifted from the actual rubbing frequency by both plus and minus rotor precession frequency.

References

Bently, D. E., 1974, "Forced Subrotative Speed Dynamic Action of Rotating Machinery," ASME Paper No. 74-DET-16.

Bill, R. C., and Ludwig, L. P., 1980, "Wear of Seal Materials Used Aircraft Propulsion System," *Wear*, Vol. 59, pp. 181–211.

Childs, D. W., 1976, "A Modal Transient Rotor Dynamic Model for Dual-Rotor Jet Engine Systems," ASME *Journal of Engineering for Industry*, Vol. 98, pp. 876–882.

Childs, D. W., 1979, "Rub Induced Parametric Excitation in Rotors," ASME *Journal of Mechanical Design*, Vol. 101, No. 4, pp. 640–644.

Choy, F. K., and Padovan, J., 1985, "Investigation of Rub Effects on Rotor-Bearing-Casing System Response," *Proceedings of the 40th Mechanical Failures Prevention Group Symposium*, National Bureau of Standards, Gaithersburg, MD, Apr.

Choy, F. K., Padovan, J., and Li, W., 1986, "Seismic Induced Nonlinear Rotor-Bearing-Casing Interaction of Rotating Nuclear Component," *Proceedings of the ASME 1986 PVP Conference*, Chicago, IL, July, PVP-Vol. 108, pp. 105–112.

Choy, F. K., and Padovan, J., 1987, "Nonlinear Transient Analysis of Rotor-Casing Rub Events," *Journal of Sound and Vibration*, Vol. 113, No. 2.

Choy, F. K., and Li, W., 1989, "Frequency Component and Modal Synthesis Analysis of Large Rotor/Bearing Systems With Base Motion Induced Excitations," *Journal of Franklin Institute*, in press.

Li, D. F., 1978, "Dynamic Analysis of Complex Multi-level Flexible Rotor Systems," Ph.D. Thesis, University of Virginia.

Marscher, W. D., 1982, "Test Simulation of Turbomachinery Rotor-Stator Interactions," presented at 1982 ASLE Annual Meeting.

Muszynska, A., 1984, "Partial Lateral Rotor to Stator Rubs," IMechE Conference Publication on Third Int. Conf. on Rotating Machinery, Sept.

Padovan, J., and Choy, F. K., "Nonlinear Dynamics of Rotor/Blade/Casing Rub Interactions," ASME Paper No. 86-DE-6.

Spray Automated Balancing of Rotors: Concept and Initial Feasibility Study

A. J. Smalley
Institute Engineer,
Applied Physics Division.

R. M. Baldwin
Senior Research Engineer,
Applied Physics Division.

W. R. Schick
Senior Research Engineer,
Engineering & Materials Sciences Division.

Southwest Research Institute,
San Antonio, TX 78284

This paper describes a new balancing concept: Spray Automated Balancing Of Rotors (SABOR). The Fuel Air Repetitive Explosion (FARE) process of metal film deposition is used to apply discrete amounts of metallic or ceramic particles to a spinning rotor at a controlled angular location on the rotor. In this way, without stopping the rotor, its mass eccentricity is changed in a manner designed to reduce the vibration sensed by a balancing machine. The system design and control for implementing SABOR are described. Preliminary results are presented from a demonstration rig that confirm the ability of the method to control both angle of application and rate of application to the extent necessary for effective automated balancing. The method is used to balance a spinning disk without stopping it. Results are presented which show that the bond strengths of materials deposited by the FARE process for use in small gas turbine engines are acceptable for the level of centrifugal stresses expected. Fatigue tests of sprayed samples show the data to be indistinguishable from those available for specimens hand-ground according to current balancing practice.

Introduction

Low-speed balancing methods are used to balance a very high majority of land-based and aircraft gas turbines. Low speed means well below operating speed of the engine and below any critical speeds of the rotor. As a result, the forces transmitted to the balancing machine's bearing supports are proportional to unbalance multiplied by the square of speed. The balance machine most commonly senses the transmitted force in terms of the vibration response of the support. Once calibrated to a known unbalance, the balancing machine provides a consistent readout of unbalance level. The phase difference between the vibration signal and a once per revolution phase reference signal indicates the angle of the unbalance.

To reduce unbalance, the balancing operator changes the mass eccentricity at one or two preselected planes in the rotor. On relatively large rotors, such as the high or low-speed turbine or the fan of a wide-body aircraft engine, the corrections are made by discrete weights, which are clipped or bolted in place. On smaller engines, such as are used in helicopters, the corrections are made by grinding on the turbine wheel, disk, blisk, or shaft.

In all these weight correction methods, the rotor must be brought to rest from its balancing speed, the balance machine must be opened, and the weight correction must be made. With add-on discrete weights, the correction is usually made while the rotor is on the balance machine. In the case of grinding, it is most common to remove the rotor to a separate grinding booth for weight change.

Contributed by the International Gas Turbine Institute and presented at the 33rd International Gas Turbine and Aeroengine Congress and Exhibition, Amsterdam, The Netherlands, June 5-9, 1988. Manuscript received by the International Gas Turbine Institute September 1987. Paper No. 88-GT-163.

The grinding process is almost always manual. In other words, the operator must apply the grinding wheel to the rotor or wheel for a period of time judged appropriate to make the necessary change in mass eccentricity. The angle for correction is usually marked with reasonable accuracy, but the amount of metal removed is strictly a matter of judgment. To bring the indicated level of unbalance on the balancing machine within tolerance frequently requires a number of iterations between balance machine and grinding booth. The number of iterations generally increases as the specified level of residual unbalance reduces. Some shops are balancing aircraft engine parts to within 0.0004 oz-in.

The use of computer-assisted balancing machines is increasing. The computer allows setup information, tolerances, etc., to be stored and provides a digital readout of residual unbalance weight and angle. It can subtract out tooling unbalance if required. It provides for record keeping and documentation, but with limited exceptions does not automate the weight change process. There are one or two examples in high-volume production where the computer is being used to provide grinding depth and angle information to a grinder for the balancing of specific parts. However, the part must still be transferred from balance machine to grinder, and a check balance must still be performed.

Schneider (1960) describes some approaches to semi-automated weight change; here the rotor is stopped and drilled or ground to a controlled depth at a controlled angle.

There is a distinct need to automate the weight correction process fully, such that mass eccentricity can be changed while the rotor is spinning. Such automatic weight change would include immediate feedback in terms of the change in recorded

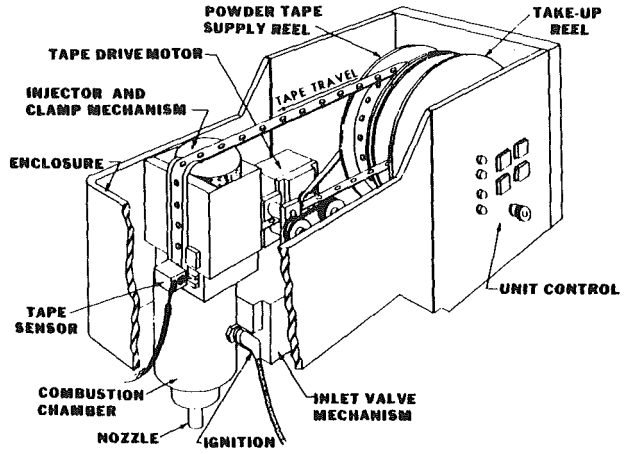

Fig. 1 Schematic of FARE gun

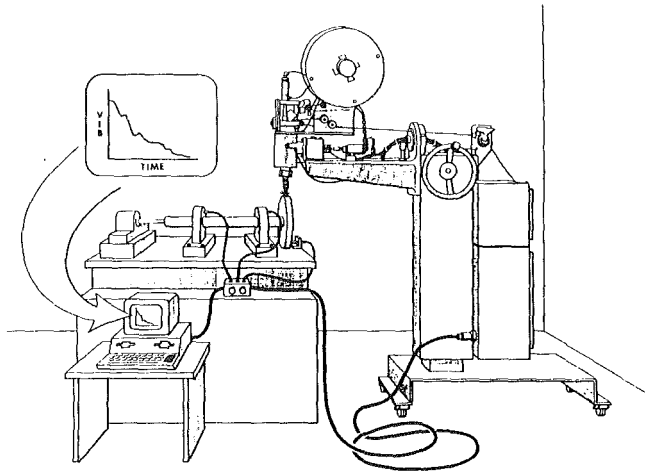

Fig. 2 FARE gun automated balancing concept

vibration. High-production-rate manufacturing processes would benefit greatly.

The concept of automatic weight change while the rotor is spinning has been addressed in the past. Gusarov and Shatalov (1980) have presented a number of conceptual approaches to this problem. The use of a laser for balance weight correction was proposed more than 10 years ago, and laser balancing has been demonstrated in the laboratory by DeMuth and Zorzi (1981). There has, apparently, been some successful application of laser balancing to small rotating components such as dental drills and gyroscopes.

For propulsion gas turbines, there is concern that the laser burns will lead to fatigue strength reduction. Test data presented by Martin (1986) show that the high cycle endurance limit can be reduced by a factor of two relative to hand-ground material as a result of laser burn marks.

This paper presents a promising alternative for automatic weight correction. Material is deposited on the spinning rotor with the amount and angle of weight addition under computer control. A high velocity thermal spray process named Fuel Air Repetitive Explosion (FARE) has been selected for the purpose. Figure 1 is a schematic that illustrates important elements of the FARE process. Discrete powder charges of the required spray material are encapsulated within a tape. A single capsule of powder is forced into the combustion chamber wherein a mixture of propane and air is ignited with a spark plug. The combustion melts the powder as it is expelled through a barrel at high velocity. As shown conceptually in Fig. 2, the barrel of the gun is located a short distance from the target area on the rotor, and the particles embed themselves in the rotor material. The rotor is spinning and, by appropriately accounting for all time delays, the control system causes the particles to be concentrated at a particular angular location on the rotor. Based on known sensitivity to mass eccentricity changes, the angle of weight addition is selected to reduce measured vibrations of the rotor. This paper describes the method in more detail; it presents results of some preliminary automated balancing experiments, and some preliminary results on bond strength and fatigue strength.

Requirements for Automated Balancing

This section of the paper addresses requirements for automated balancing. Some of these are general in nature, and some of them particular to the specific application. Following is a list of considerations that must be addressed:

- What is the maximum weight of material to be added?
- What is the minimum weight of material to be added?
- To what thickness must material be deposited to achieve the maximum possible required weight?
- At what speed should the rotor be balanced?
- What is the access to the area for weight addition?
- Will the process produce a concentration of weight at a selected angle?
- How repeatable is process timing?
- Will the deposited material stay in place under the operating environment of the rotor?
- Will the deposited material reduce the fatigue resistance of the part?
- What combinations of rotor and spray materials are appropriate for likely applications?

Maximum weight is dictated by the most extreme mass eccentricity that could occur as a result of machining and assembly tolerances. This can be estimated from specified tolerances or based on historical records. If a part is shown by the balancing machine to have the weight requirement outside the expected maximum, there is probably a basis for rejecting that part as out of tolerance, or making major corrections by other means.

The minimum weight to be added addresses the question of balance tolerance. It must be possible to make weight changes which are of the order of the balance tolerance. A reasonable value for the minimum weight to be added would be one-quarter to one-half of the balance tolerance expressed as a weight applied at the known radius.

Having established the maximum weight that might need to be added, this weight should be considered in terms of width, height, and extent of deposit. It should be possible to deposit the weight over a width and angular extent that is effective for balancing and with a depth to which the spray deposit maintains good integrity. For the FARE process, preliminary investigations indicate that satisfactory deposits of 20 or more mils (500 μm) can be made. It has been established that, for most small gas turbine parts, the required maximum correction weight can be accomplished within a 10 mil (250 μm) deposit.

The speed at which a component or assembly is typically balanced is normally a speed at which satisfactory sensitivity to unbalance is achieved in the readout of the balancing machine. Such a speed would be a suitable reference point for the speed at which automated balancing would be performed. It is expected, however, that automated balancing would achieve improved accuracy as a result of direct feedback between weight addition and vibration, and that it will sometimes enable effective balancing at a lower speed.

Access to the surface area where weight changes can be accomplished is an important issue in automated balancing. Clearly, the outside surface of a straight shaft is readily accessible. An axial facing surface on a disk is also likely to be readily accessible. In some cases, if balancing has previously

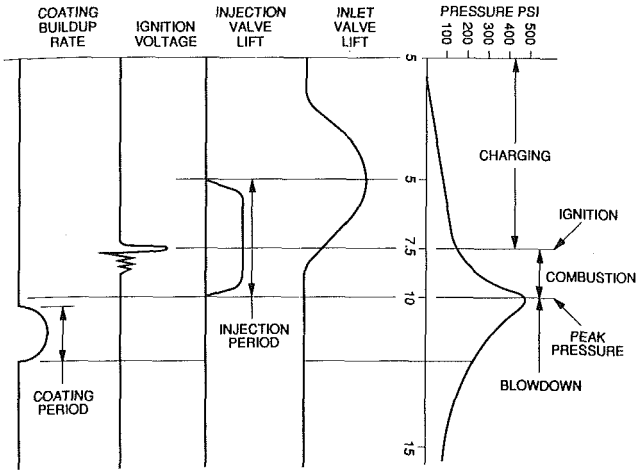

Fig. 3 Timing sequence

been accomplished by weight removal, there may be a ring of sacrificial material that is too narrow to act as a target area. In this case, automated balancing would probably require that this sacrificial ring be removed. This actually has benefits in terms of weight reduction; parts originally designed to be spray balanced could take advantage of avoiding sacrificial weight while accommodating spray access.

Large inside radii, such as on the disk of a turbine wheel, should also be manageable, but small inside radii present a challenging aspect of automated balancing. Specially designed spray nozzles may be needed for certain situations.

If we consider that the gun takes a finite length of time to deposit the sprayed material, then the deposit will spread over an angle proportional to the product of speed and pulse length, as follows:

$$\Delta\beta = 6N\Delta t$$

where $\Delta\beta$ is the angular extent of the deposit, deg; N is the speed in rpm; and Δt is the pulse width of the spray process.

In the case of continuous spray processes, the pulse width must be artificially created by some form of rotating window or shutter. The FARE process has the distinct advantage of being naturally discrete. Figure 3 shows the ideal sequence of events associated with the FARE process, and indicates that metal is deposited over a period of about 2 ms. For a rotor-balancing speed as high as 3000 rpm, according to the above equation, spray material will spread over 36 deg during a 2 ms pulse. A very high proportion of rotors are balanced at speeds below 3000 rpm, and the vector weight correction effectiveness of material spread over 36 deg is above 98 percent of that with all the material concentrated at a single location. Since normal low-speed balancing is performed in the range of 600 to 3000 rpm, the process should perform comfortably for low-speed balancing as far as pulse width discreteness and extent of deposit are concerned.

Repeatability and controllability of the process are also important considerations. If Δt is considered as the tolerance on when the midpoint of the deposit pulse occurs, then the above equation also provides an expression for the likely tolerance on the angle at which weight is deposited. Balancing test results presented later in the paper will quantitatively refine these expectations.

A significant concern for any new weight addition balancing process applied to high-speed aircraft propulsion systems is the effect of the process on the fatigue characteristic of the substrate and the metal film sprayed. A parallel concern is the ability of the material to bond to the substrate and stay in place under the mechanical stresses imposed during normal operation of a small gas turbine engine.

When considering balancing by spray addition, rather than

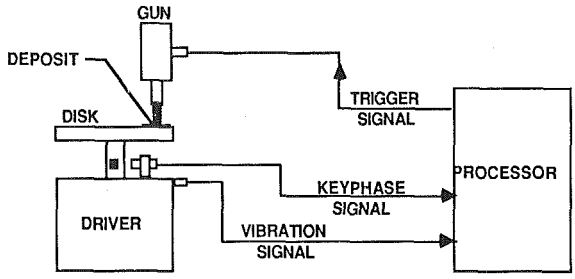

Fig. 4 Schematic of SABOR demonstration

by removal, a new consideration arises as to what materials to spray and on what base materials they will need to be sprayed. After a survey of current production helicopter gas turbine engines, we selected as representative substrate materials: (1) 17-4PH stainless steel for the compressor section, and (2) Inconel 718 for the turbine section.

When spraying metal powder for the purpose of balancing rather than the traditional spray objectives of hard-facing, the rules and options change somewhat. Weight density and spray efficiency become important to maximize the weight applied, and matching of thermal growth properties is important to prevent large relative growth and debonding forces. Hardness and erosion resistance are of reduced importance for balancing.

Based upon an analysis of these factors, we selected for initial evaluation one material combination for typical engine cold section application, tungsten carbide on 17-4PH, and one combination for hot section application, Inconel 718 powder on Inconel 718. The evaluation consisted of bond strength and fatigue life tests of sprayed test specimens.

Automated Balancing Concept

The SABOR automated balancing concept is presented in Fig. 2. The rotor itself is rotated in bearings and any vibrations of the bearing supports are sensed by a transducer on each bearing. A once per revolution phase reference signal is given by a sensor fixed to the balancing machine, which responds to an intentional discontinuity on the rotor at a particular angular location. Figure 4 illustrates, schematically, the main elements of the SABOR system interfaced to the test rotor for which results are presented in the paper. Both vibration signal and phase reference signal are transmitted to a processor, which performs several functions. The processor must detect the speed of the rotor, acquire the vibration wave form, and band pass filter this at the frequency of rotation to give synchronous amplitude and phase lag relative to the phase reference signal. When the processor determines that the speed is within the tolerance band at which balancing is to be performed, it must determine the angle relative to the phase marker at which weight should be deposited to correct the implied unbalance. It must, further, initiate a firing sequence at an appropriate instant to accomplish the deposition of metal at the appropriate angle.

The processor could, in fact, consist of discrete components, such as an analog filter, a tachometer, an A to D converter, a clock, a microprocessor to calculate the phase delay, and a triggering device. Alternatively, some of these functions, particularly the filtering and speed detection functions, can be incorporated in a digital processor. Such is the approach being developed for the present SABOR system.

The system and process described above imply knowledge of the total system response sensitivity, such that the appropriate angle and number of shots for weight addition can be precisely determined from the amplitude and phase signals. This knowledge would indeed exist to some tolerance for each component or assembly to be balanced. At the same time a

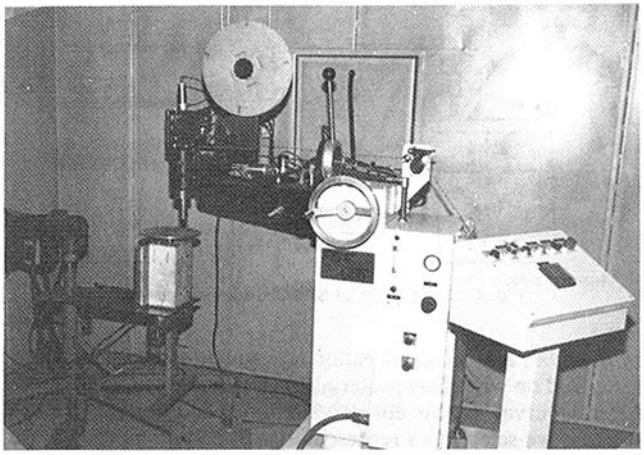

Fig. 5 Photo of FARE gun and test rotor disk

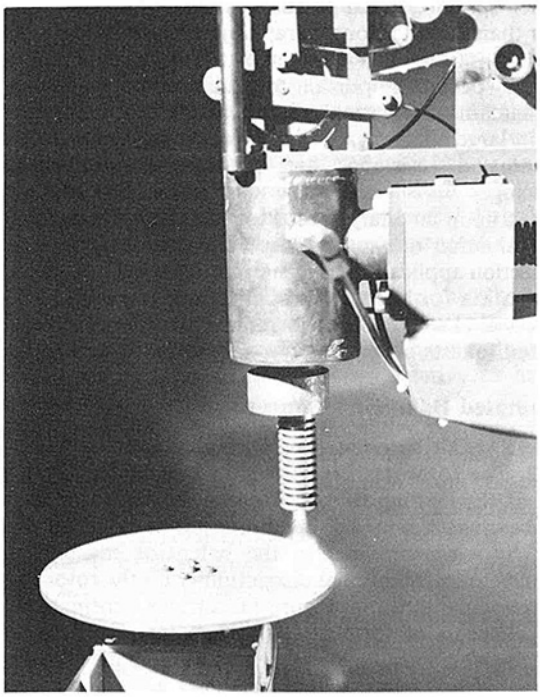

Fig. 6 Photo of FARE gun firing at disk

particularly attractive feature of the SABOR process is that it can provide a direct feedback on the total system sensitivity, such that after a few shots have been fired, their influence on vibration vector response can be determined and the initial factors used to drive the weight addition process can be adjusted on-line. This feedback feature is analogous to the trial weight and influence coefficient calculation process of influence coefficient balancing, but avoids the need to stop the rotor for each trial weight addition. Vibration measurement, influence coefficient calculation, and weight correction can all be made in sequence at a constant speed with fractional second time delays rather than the minutes or hours needed to achieve the same end manually. Various algorithms can be envisaged to control the feedback and adjustment process in both production or development balancing; optimum details will vary with balancing tolerances, typical initial unbalance, and production volume for the rotor in question.

Automated Balancing Test Rig

A test facility has been set up in which the FARE gun performance can be evaluated. A test rig has been assembled using a flat disk directly attached to a motor shaft and spun about a vertical axis. The gun fires downward onto the face of the disk. The disk is 10 in. (254 mm) in diameter. Material is deposited on the face of the disk at a radius of approximately 4.5 in. (115 mm). Firing of the gun is triggered by a once per revolution pulse off the spinning disk.

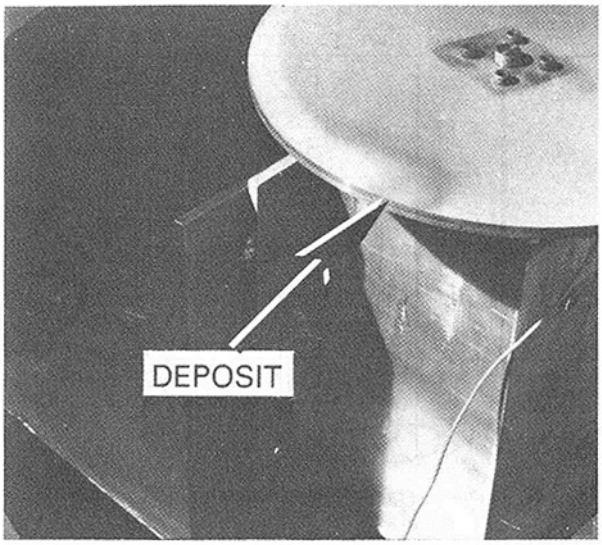

Fig. 7 Photo of sprayed disk

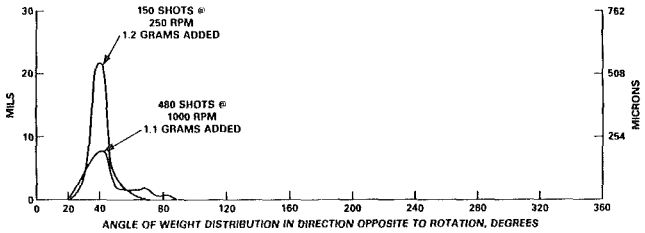

Fig. 8 Thickness of deposit as a function of angle at centerline of deposit

Figure 5 shows an overall photograph of the FARE gun and test rotor disk. The barrel of the gun may be seen in the left of the picture pointing down from the arm (the gun barrel can be rotated to a horizontal position as necessary). The spool above the arm of the gun carries the taped powder. Figure 6 shows a photograph of the gun firing at the disk on the test rotor, and Fig. 7 is a photograph of the deposit on the rotor. For these initial experiments, the disk material is carbon steel and the spray material is tungsten carbide.

Balancing Results

To evaluate repeatability and weight concentration, the thickness of the disk was measured, at a series of stations, before and after automated weight addition. The disk was also weighed before and after weight addition. The sprayed weight was added with the disk running at constant speed and the gun was set to fire repeatedly with constant phase delay. The test was performed at two speeds, 250 rpm and 1000 rpm, on separate disks.

Figure 8 presents the resultant deposit thickness, at the radius of maximum deposit thickness (4.5 in.; 11.43 cm), as a function of circumferential angle from a fixed point on the disk. Two lines are apparent, one for the 250 rpm test and one for the 1000 rpm test. For the 250 rpm test, 150 shots were deposited with a measured weight increase of 1.2 g. For the 1000 rpm test, 480 shots were added with a weight increase of 1.1 g. It is intuitively clear that, at both speeds tested, the thickness increase is concentrated over an angle that is sufficiently small to cause effective changes in mass eccentricity.

Table 1 Weight correction effectiveness at two speeds

SPEED	EFFECTIVENESS	ADDED WEIGHT PER SHOT, mg
250 rpm	99.3%	8.
1000 rpm	97.3%	2.3

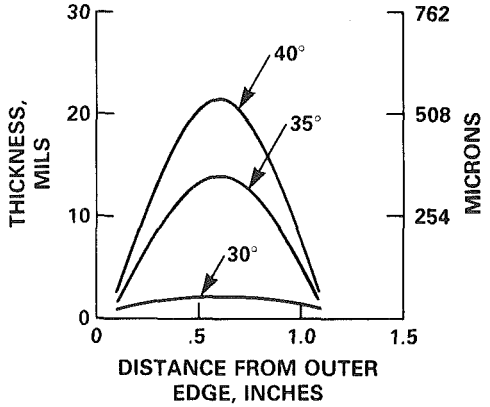

Fig. 9 Thickness of deposit versus distance from outer edge of disk for three angles, 250 rpm

To be more quantitative, a weight correction effectiveness η for a total deposit can be defined as the total vector magnitude of the added weight divided by the total weight added. If we assume that weight per unit angle is proportional to thickness at the radial center of deposit, then this effectiveness can be calculated as follows:

$$\eta \cong \left[\left(\Sigma(t \cos\theta)\right)^2 + \left(\Sigma(t \sin\theta)\right)^2 \right]^{1/2} / \Sigma t$$

where t is the measured thickness of deposit at angle θ.

Table 1 gives the weight correction efficiency for the two lines of Fig. 8, together with weight per shot information. This table shows that high effectiveness is achieved at speeds of 250 and 1000 rpm and suggests that significant increases in balancing speed could be undertaken before serious deterioration in effectiveness was encountered.

It is also clear that the rate of weight addition per shot decreases with speed. The full explanation for this has not yet been established, but it is likely due to centrifugal forces or the change in effective angle of attack of the particles on the surface. As will be discussed later, this rate reduction could be a beneficial feature of the process.

Figure 9 presents thickness as a function of distance from the outer edge of the disk at three angles around the location of maximum thickness. This shows that most of the measurable deposit falls well within a 1 in. radial band.

An experiment was conducted to verify that the automated weight addition concept could be used to change mass eccentricity and so to reduce the amplitude of synchronous response to unbalance on a spinning disk. Based on the previous investigations, it was known at what angular location the gun would deposit metal on the disk at a particular speed when directly triggered off the key phase pickup. An initially balanced disk was purposely unbalanced at a location opposite the known deposit location; the motor was run through a speed range of 600 to 1150 rpm and the resultant vibration amplitude and phase were recorded. Without subsequently stopping the motor, a series of shots was fired at 1000 rpm under control of the key phase trigger. After each 20 shots the synchronous vibration was recorded again. Vibration amplitude was steadily reduced as shown in Fig. 10. The experiment was terminated after vibration amplitude had been reduced from 1.7 mils to 0.6 mils (from 43 to 15 μm).

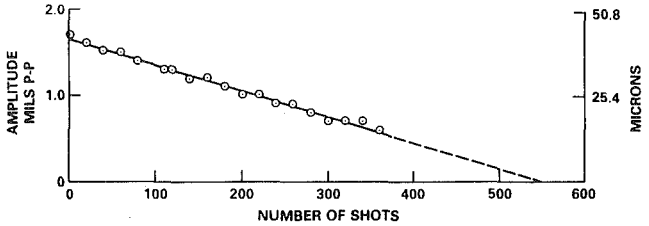

Fig. 10 Vibration amplitude as a function of number of shots deposited

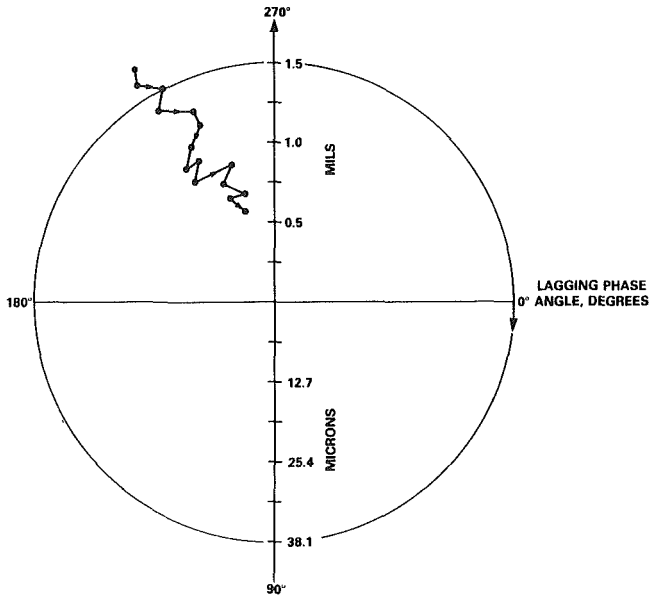

Fig. 11 Polar plot of vibration vector change during balancing experiment; data points every 20 shots; arrow indicates direction of increasing weight

The intent of this initial balancing experiment, rather than to demonstrate fully automated balancing, was to verify under controlled conditions that weight could be consistently added at a required angular location, thereby reducing vibration amplitude.

Figure 10 shows the results of this evaluation by presenting amplitude of vibration as a function of the number of shots deposited. It is clear that the vibration steadily and consistently reduces in a linear manner.

Figure 11 presents the changes in vibration vectorially in a polar plot. The data is plotted every 20 shots and shows typical phase angle scatter, but the overall trend is clearly to reduce the vibration vector consistently.

Figure 12 compares vibration as a function of speed for the rotor before and after balancing. It is clear that vibration has been reduced throughout the speed range.

Material Integrity

A series of bond and fatigue strength tests was conducted on the two spray-substrate material combinations selected as typical of applications in the hot and cold sections of small gas turbines. Bond strength tests were conducted according to ASTM C633 and four-point bending fatigue tests were performed on sprayed bars to develop fatigue life curves over the range of 10^4 to 10^7 cycles.

Table 2 gives the range of bond strengths for five samples of each of the two material combinations tested.

Preliminary analysis shows that the stress due to centrifugal loads imposed during normal operation of current inventory

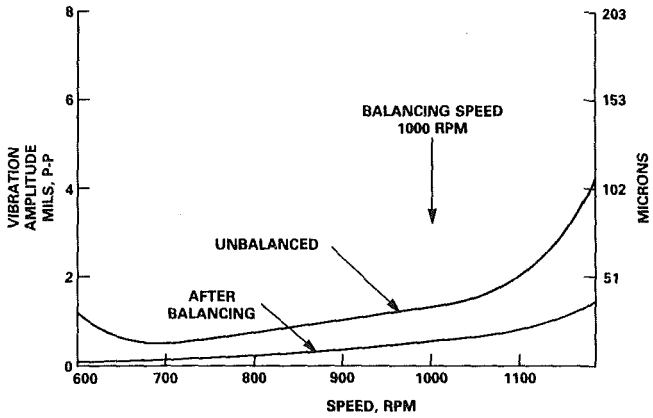

Fig. 12 Vibration amplitude as a function of speed comparing vibrations for imbalanced rotor with vibrations after balancing experiment

Table 2 Bond strength test data

MATERIAL COMBINATION	BOND STRENGTH, PSI (MPa) HIGHEST	LOWEST	AVERAGE
Tungsten Carbide on 17-4PH	10583 (73.0)	7410 (51.1)	8920 (61.6)
Inconel 718 on Inconel 718	6466 (44.6)	3312 (22.9)	5103 (35.2)

helicopter engines is unlikely to exceed 1000 psi (7 MPa), so the tensile bond strengths measured are expected to be adequate.

The fatigue strengths of these two material combinations have been evaluated in comparison with available data for the same substrate materials which have been hand-ground with a finish typical of the results of manual balance corrections, as presented by Martin (1986). Figure 13 presents the fatigue strength data for tungsten carbide on stainless, and Fig. 14 presents the fatigue strengths for Inconel 718 on Inconel 718. In each case, the data indicated as hand-ground represent the strength of the substrate with defects typical of hand-grinding, finished and radiused according to typical engine balancing procedures.

It is apparent that the strength data of the coated materials is coincident with that of the hand-ground material. It may be concluded that the fatigue strength of materials balanced by thermal spray will not be compromised.

Further evaluation is planned for other material combinations, including a high-cobalt alloy on Inconel 718.

Discussion

The first evaluations of the SABOR concept are most encouraging: It is possible to control firing of the FARE gun so that material is deposited at a consistent angular location on a spinning disk; weight correction effectiveness of over 97 percent has been achieved at 1000 rpm and satisfactory effectiveness is expected for speeds of at least 3000 rpm, fully fast enough for the great majority of balancing operations; a single disk has been balanced with very direct evidence of effectiveness.

Firing of the gun is presently triggered directly by a keyphase pulse. Computerized control, now under development, will provide flexibility to deposit the weight at any selected angle.

Bond strengths achieved with representative materials are much higher than required to withstand centrifugal stresses. Fatigue tests of the same material combinations indicate fatigue life margins can be maintained when balancing by grinding is replaced by balancing by thermal spraying.

The observed dependence on speed of weight deposited per shot requires further investigation. It appears that this feature can be exploited with benefit in effectiveness of balancing:

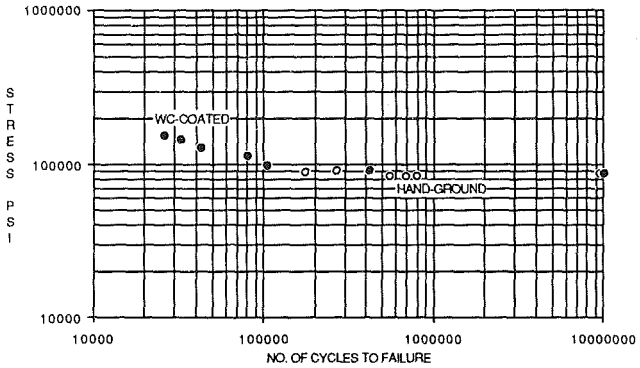

Fig. 13 17-4PH stainless fatigue data comparison: sprayed versus hand-ground

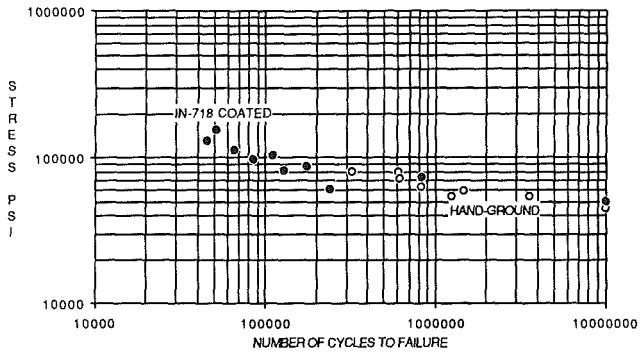

Fig. 14 Inconel 718 fatigue data comparison: sprayed versus hand-ground

Rapid weight correction is needed for parts with high unbalance while more gradual correction is needed to bring small unbalance within balancing tolerances.

If large unbalance is corrected at a lower speed than small unbalance, then this characteristic of the process will directly achieve the desired reduction in weight change rate. Automatic speed control on the basis of residual unbalance can be readily implemented. Increasing speed as unbalance is reduced will be of additional benefit, at least on hard bearing machines, by increasing the sensitivity of the machine for smaller unbalance levels.

A deposit rate as high as 8 mg/shot seems readily achievable from the lower-speed preliminary results. For most small gas turbine applications, the worst expected initial unbalances may require 500 shots at this rate to bring the unbalance close to tolerance. Although not yet tested in a balancing environment, past data on the FARE gun indicate 2 to 5 shots per second are achievable. Thus, the time to balance a seriously unbalanced part should be 2 to 5 min, which is five to ten times faster than typical manual time to balance such parts; less seriously unbalanced parts will be automatically balanced much faster.

The concept now needs to be applied, and appropriate early applications need to be identified. The developments necessary for production automated balancing need to be made. As discussed, initial feasibility evaluations for helicopter gas turbine engines are promising: Weight addition rates appear appropriate; weight distribution considerations (thickness, width, etc.) are satisfactory. A natural and planned next step is an application evaluation on some selected helicopter gas turbine hardware. Such an evaluation will include further investigation of long-term bond integrity under anticipated thermal and load cycles, and demonstration of the effectiveness of the process on real parts accounting for their geometry, assembly considerations, balance tolerances, need for two-plane balancing, etc. Some longer-term considerations

are the economics of an automated balancing facility for balancing of a variety of parts, the appropriate role for robotics, and needed developments in the process for small inside radii.

Looking more broadly at potential applications, we see turbochargers, automotive gas turbines, tank gas turbine engines, and cruise missile engines as appropriate candidates to benefit from this automated balancing process. For parts such as high-speed turbochargers, which may need very fine balance tolerances, the initial data suggest submilligram balance shots should be readily achievable.

It is our intention to pursue the technology vigorously in the future and to work at addressing the many practical considerations and problems involved in advancing from laboratory demonstration to a viable, economic, automated manufacturing process.

Conclusions

1 A new concept for automated balancing has received preliminary evaluation with encouraging results.

2 By triggering off a once per revolution pulse from a spinning disk, the FARE gun can be controlled to deposit metal at a consistent location on the disk.

3 The process has successfully been used to correct mass eccentricity of an unbalanced disk, while the disk was spinning at constant speed.

4 Weight deposit rates appear satisfactory for small gas turbine parts.

5 Weight deposit rate appears to decrease with speed, but this feature can be used to optimize the process for the state of balance of a part.

6 For tight balance tolerances 2.3 mg per balance shot has already been achieved, and submilligram shots should be readily achievable.

7 Bond strengths for tungsten carbide on 17-4PH stainless steel and for Inconel spray on Inconel 718 stainless are satisfactory for expected centrifugal loads in small gas turbines.

8 Fatigue strengths for both material combinations tested, tungsten carbide on 17-4PH and Inconel on Inconel, are equivalent to data from hand-ground specimens of the same materials.

9 Evaluation of the method in specific applications is needed.

10 Evaluation of bond integrity under thermal and load cycles is needed.

Acknowledgments

The authors wish to acknowledge the H. B. Zachry Company, San Antonio, TX (owner of the FARE gun) for loan of the gun used in the experiments, and for support in getting the process operational.

The authors wish to thank the U. S. Army Propulsion Directorate, AVSCOM, and NASA Lewis Research Center for permission to present bond strength and fatigue results, and for their support and encouragement; thanks particularly are due to David Fleming, John Yuhas, and Mark Raglin.

The authors wish to acknowledge Mr. Andrew Nagy of Southwest Research Institute for his significant technical contributions in the generation of material bond and fatigue strength characteristics.

The authors also wish to acknowledge the permission of Southwest Research Institute to publish results of the balancing experiments, which were supported by an internal research project.

References

DeMuth, R., and Zorzi, E., 1981, "Development of High-Speed Balancing Technology," NASA CR 165314.

Gusarov, A. A., and Shatalov, L. N., 1980, "Automatic Balancing of Rotors," in: *Vibrations of Rotating Machinery*, IMechE.

Martin, M. R., 1986, "Fatigue Life of Laser Cut Metals," USAAVSCOM Technical Report No. 86-C-34.

Schneider, H., 1960, *Balancing Technology*, translation of VDI-Taschenbücher T29 Auswuchttechnik, Carl Schenck AG, Darmstadt, Federal Republic of Germany.

Laboratory Study of a Steam Turbine Rotor Weld Repair

K. Fuentes
Staff Mechanical Engineer.

K. Oberle
Staff Metallurgical Engineer.

Radian Corporation,
Austin, TX 78720

In 1986, a large utility discovered a crack in its IP/LP steam turbine rotor and weld repair was chosen as the most cost-effective alternative. The repair consisted of severing the rotor between the 12th and 13th stages and welding a new forging, replacing the 9th and 12th stages, to the remaining original rotor. A test rotor was prepared from the scrapped rotor section using procedures similar to the actual rotor repair. The test rotor was subjected to a mechanical and metallurgical test program to determine the properties of the material in the weld-repaired area. Testing included: nondestructive examination of the rotor bore, chemical analysis of the rotor material, metallographic examination, hardness, tensile, rotating beam fatigue, fracture appearance transition temperature, J-integral fracture toughness, and stress rupture testing. In addition, boresonic inspection records were compared to the destructive examination of the scrapped section of the rotor and four disk sections from the original rotor were tested for evidence of a temper embrittlement gradient.

Introduction

Steam turbines are widely used throughout industry. Many of the steam turbine rotors used today were manufactured prior to 1960. These rotors were manufactured from steels that have different characteristics from those manufactured using modern steelmaking technology. By virtue of the number and increasing age of these older rotors, a study of their unique characteristics is warranted. The three major areas of interest are: correlation of boresonic inspection results with defects found during destructive examination, application of weld-repair techniques to old rotor materials, and temper embrittlement of old rotor steels.

Ultrasonic (UT) inspection of rotors has been a routine inspection technique for many years. UT inspection of material near the bore (boresonic inspection) has been of particular interest since the Gallatin rotor failure (Kramer, 1976). However, boresonic inspection techniques change from year to year and the interpretation of the results remains dependent upon the experience of the analyst. The significance of boresonic readings, therefore, remains controversial. The opportunity to examine a rotor section destructively and compare the actual defects present to the boresonic inspection would be of great value. The results could serve as a guide in the interpretation of boresonic data.

Weld repair of damaged rotors is increasingly used as an alternative to rotor replacement. Weld repair of rotors in the United States is a relatively new application of welding technology, although it has been used to manufacture rotors in Europe for many years. However, this welding technology is not readily transferable since European construction materials are different from the materials commonly used in this country. In addition, rotors that are being considered for repair in the United States differ in age, size, and material characteristics from those manufactured using welding techniques in Europe. While the technology transfer from Europe may not be complete, several successful repairs in the United States have shown that weld repair is a viable alternative to retirement. Many of these repairs have not included exhaustive testing of the welds by parties other than the repair firm. This lack of third-party test data has limited the application of rotor repair for many utilities and insurance companies.

The older rotors discussed above have been found to be temper embrittled after many years of service. Temper embrittlement results in a decrease in the fracture toughness and critical crack size, rendering the rotor more susceptible to catastrophic failure (Leslie, 1981; McMahan, 1980). Susceptibility to temper embrittlement is dependent upon the presence of tramp elements in the steel and results from exposure to certain temperature ranges during operation or manufacturing (Leslie, 1981). If it is service dependent, a temper embrittlement gradient should be evident and follow the temperature gradient along the length and radius of the rotor. Testing of sections along the length of the rotor should provide valuable information about the temper embrittlement phenomenon.

Project Background

The repaired rotor is the IP/LP (intermediate pressure/low pressure) rotor from the Valley Generating Station of Los Angeles Department of Water and Power, Unit No. 3. The rotor was manufactured by General Electric. Unit No. 3 is rated at 175 MW and was put into service in 1955. The unit ran

Contributed by the Power Division and presented at the Joint Power Generation Conference, Miami Beach, Florida, October 1987. Manuscript received at ASME Headquarters August 1, 1988. Paper No. 87-JPGC-Pwr-15.

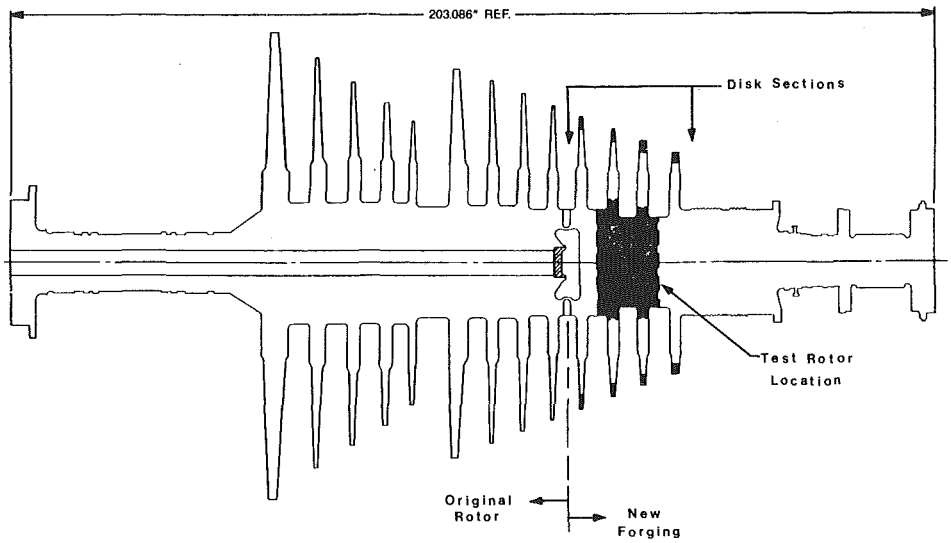

Fig. 1 Schematic of the repaired IP/LP rotor from L.A. Department of Water and Power, valley station, unit No. 3

for approximately 20 years base loaded (1955 to 1975), cycled for 5 years (80 percent on cold standby and 20 percent at minimum load), and has been on cold standby for the remaining years. During a routine outage in 1982–83, cracking was found in the balancing slot located on the ninth stage of the turbine, first stage of the IP/LP rotor. The cracks were originating from the corners of the slot. Samples of the cracks were not available for examination and a failure mode was, therefore, not determined.

On 4 Mar. 1986, Radian Corporation received a welded test rotor that duplicated the repair procedure performed on the IP/LP rotor. Additionally, Radian received four disk samples removed from the scrapped section of the rotor, 9th to 12th stages. The objective of this investigation was to evaluate the condition of the rotor material and the weld repair in the test rotor relative to the future usage of the actual repaired IP/LP rotor. The goals set forth to reach this objective were:

- compare boresonic records of the original rotor section with the destructive examination of that section;
- perform metallographic and extensive mechanical property testing of the welded test rotor; and
- perform metallographic and mechanical property testing of samples from the 9th to 12th stages to check for temper embrittlement.

Repair. The repair firm recommended that the rotor be sectioned between the 12th and 13th stages and a new forging containing the 9th to 12th stages be welded in place. This recommendation was based on the stress distribution and estimated operating temperature gradient of the rotor. The recommendation was followed and a new forging was welded onto the old rotor section. A schematic of the repaired rotor is shown in Fig. 1.

Test Rotor. The test rotor was made from the scrapped portion of the rotor at the 10th and 11th stage. The location of the test rotor is shown on the repaired rotor in Fig. 1. The locations of the disk sections received for temper-embrittlement examination are also shown in the figure.

The test rotor was prepared by the same firm that repaired the rotor. It was machined in preparation for welding, welded, and heat treated after welding using the same procedures used to repair the IP/LP rotor. The only difference between the test rotor and the actual IP/LP rotor was in the chemistry of the material that represented the new rotor forging. Instead of using a scrap end from the new forging, carbon steel was substituted. Even though the use of carbon steel in the test rotor did not duplicate the actual repair, the samples were located such that carbon steel did not significantly interfere with the testing program. A sketch of the test rotor is shown in Fig. 2, which includes the dimensions of the test weld and the relative location of subsequently removed test specimens.

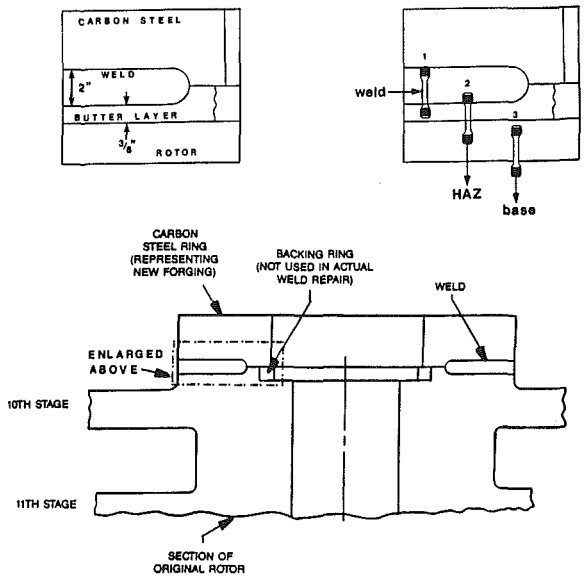

Fig. 2 Sketch of the test rotor weld repair and location of test specimens

The welding was completed in two steps. First, a layer of weld material, referred to as the butter layer, was placed on the prepared surface of the old rotor end. The butter layer serves as an intermediate layer between the old rotor material and the weld material used to join the new and old rotor sections. The HAZ (heat affected zone) specimens tested during this program refer to the HAZ between the butter layer and old rotor material. Second, the two sections, old rotor and carbon steel representing new forging, were welded together. The weld-repaired area was then post-weld heat treated.

Table 1 Chemical composition (in weight percent) of the IP/LP rotor from L.A. Department of Water and Power, valley station, unit 3

Element	Rotor	Chemical requirements per ASTM A293 Class 6	Chemical requirements per ASTM A470 Class 8
Carbon	0.37	0.37 max.	0.25 – 0.35
Phosphorus	0.044*	0.035 max.	0.012 max.
Sulfur	0.041*,**	0.035 max.	0.015 max.
Manganese	0.87	1.00 max.	1.00 max.
Silicon	0.30	0.15 to 0.35	0.15 – 0.35
Nickel	0.31	0.50 max.	0.75 max.
Chromium	0.92	0.85 to 1.25	1.05 – 1.50
Molybdenum	1.15	1.00 to 1.50	1.00 – 1.50
Copper	0.12	N.S.	N.S.
Aluminum	0.020	N.S.	N.S.
Tin	<0.01	N.S.	N.S.
Lead	<0.01	N.S.	N.S.
Vanadium	0.26	0.20 to 0.30	0.20 – 0.30
Arsenic	<0.01	N.S.	N.S.
Antimony	<0.01	N.S.	N.S.
Iron	Balance	Balance	Balance

N.S. = not specified.
*Does not exceed supplementary specification limit per ASTM A293.
**Exceeds both primary and supplementary specification limits for ASTM A470.

Test Program

The following tests were performed on the test rotor:

1 nondestructive examination of the test rotor bore;
2 chemical analysis of the original rotor (base metal);
3 metallographic examination and hardness testing of the weld-repair area;
4 tensile tests of the base metal, weld, and HAZ at ambient and 400°C (750°F) temperatures;
5 rotating beam fatigue testing of base metal, weld, and HAZ specimens in air at ambient temperature;
6 charpy V-notch impact testing of base metal, weld, and HAZ specimens at various temperatures to develop FATT (fracture appearance transition temperature) curves;
7 fracture mechanics J-integral testing on base metal, weld, and HAZ specimens in air at ambient temperature;
8 stress rupture testing of base metal and HAZ specimens at 552°C (1025°F) and 241.3 MPa (35 ksi); and
9 Charpy impact testing of specimens removed from the ring sections representing stages 9 to 12, before and after de-embrittling heat treatment to determine the embrittlement gradient.

The following sections will describe these tests and present the results.

Nondestructive Examination. The nondestructive examination of the test rotor bore consisted of ultrasonic scans taken at the bore surface of the original rotor material. The carbon steel section of the test rotor was not examined as no destructive testing of this section was planned. Ultrasonic attenuation measurements were made to establish the sound transmission characteristics of the rotor section relative to the sound transmission characteristics of the calibration standard. The ultrasonic scans consisted of the following sound beam orientations:

(*a*) A 0 deg longitudinal wave sound beam (straight beam) directed normal (90 deg) to the surface of the bore to detect reflectors (flaws) oriented parallel to the bore surface.

(*b*) Two 45 deg shear wave sound beams (angle beams) directed circumferentially around the bore, one in the clockwise direction and one in the counterclockwise direction, to detect reflectors (flaws) oriented axially.

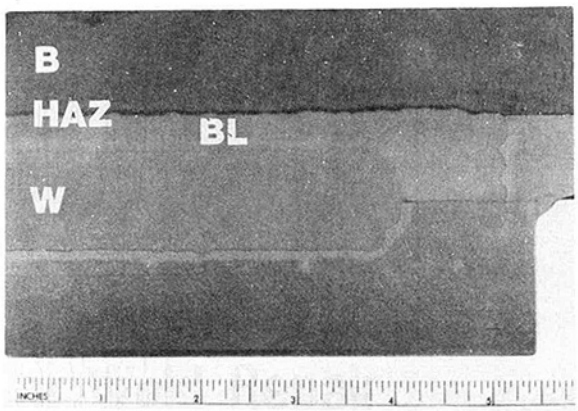

Fig. 3 Weld contour: magnification: 0.5 ×; etchant: Nital

The bore surface was prepared prior to ultrasonic examination by hand-honing using a portable honing machine. The honing process is used to remove surface deposits to provide effective surface coupling between the UT transducer and bore surface.

The ultrasonic attenuation measurements indicated that the rotor material was acoustically similar to the calibration standard and could be ultrasonically examined. The 0 deg longitudinal wave and two shear wave scans revealed no evidence of reflectors or material discontinuities within 10 in. of the bore surface. Since no flaws or other discontinuities were detected, the test rotor was sectioned to remove test specimens. Extensive subsequent sectioning of the test rotor revealed no flaws.

Chemical Analysis of the Rotor Material. The chemical composition of the rotor material is presented in Table 1 and is similar to ASTM A470 Class 8 or ASTM A293 Class 6. Although the rotor material has been compared to ASTM A470, a vacuum-melted steel, it is likely an air-melted steel such as ASTM A293 because of the high sulfur and phosphorus contents.

Although both the sulfur and phosphorus contents meet the supplementary requirements of A293 Class 6, they are exceptionally high by current steelmaking practices. High sulfur content can be detrimental both by promoting hot shortness and possibly reducing the impact toughness (Leslie, 1981; Rose, 1978). However, no metallurgical/mechanical test results or operational history indicate that the sulfur has adversely affected the rotor material. The high phosphorus content is also of concern since it indicates that the material may be susceptible to temper embrittlement mechanisms (Leslie, 1981; McMahan, 1980; Zhe, 1982).

The chemical composition of the weld and butter layer material is considered proprietary by the repair firm. However, it should be noted that the chemical compositions of the weld and butter layer were tested. There was concern that use of the carbon steel may have "contaminated" the weld other than the normal dilution at the fusion zone. The chemical composition of the weld or butter layer did not demonstrate any significant contamination by the carbon steel. The carbon, sulfur, and phosphorus contents of the weld were within the expected ranges, and in all cases, below the composition of the original rotor material.

Metallographic Examination and Hardness Tests. A profile of the weld contour is shown in Fig. 3. The different areas of the repair, including the base metal (B), weld (W), butter layer (BL), and HAZ, are labeled in Fig. 3.

The microstructures of the base metal, butter layer, weld, and HAZ consisted of tempered bainite. Both upper and lower bainitic structures were observed in the weld repair. Tempered bainite is the normal microstructure found in ASTM A293

Table 2 Tensile test results for L.A. Department of Water and Power test rotor

Test location	Temperature	Tensile* strength MPa (ksi)	Yield* strength MPa (ksi)	Elongation,* (percent)	Reduction in area, (percent)	Location of break
Base	Room	743.3 (107.8)	553.7 (80.3)	22.5	47.5	Base
Weld	Room	621.2 (90.1)	462.0 (67.0)	19.5	56.0	Butter layer
HAZ	Room	637.1 (92.4)	473.7 (68.7)	19.0	54.5	butter layer
Base	400°C (750°F)	606.1 (87.9)	433.7 (62.9)	21.8	47.7	Base
Weld	400°C (750°F)	517.1 (75.0)	397.1 (57.6)	14.3	45.0	Butter layer
HAZ	400°C (750°F)	532.3 (77.2)	413.0 (59.9)	12.5	48.3	Butter layer
ASTM A293 Class 6		758 (110)(min)	586 (85)(min)	16 (min)	40 (min)	

*Average of three tests.

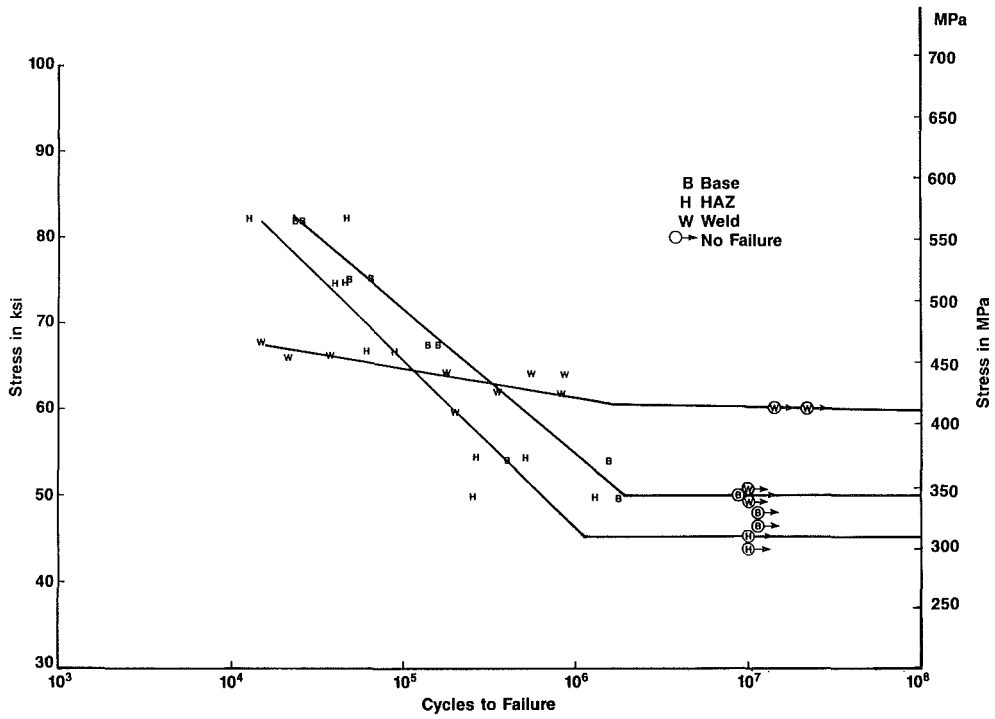

Fig. 4 Plot of all rotating beam fatigue test results

Class 6 material. It is also the expected microstructure for the butter layer and HAZ. The weld metal also contained dispersed spheroidal inclusions. The inclusions are normally observed in submerged arc weld filler metal and should not significantly detract from weld reliability.

Following microstructural documentation of the repair, the sample was measured for hardness using a diamond pyramid microhardness tester, and the results were converted to the Rockwell scale. The readings were consistent across the repair and ranged from an average of 97 Rockwell "B" in the base metal to 92 in the butter layer and 95 in the weld passes. There were no large deviations in the hardness across the repair, indicating a relatively uniform microstructure. All values measured are in the normal and expected range for the respective areas of the repair.

Tensile Tests. Tensile specimens were machined with a 0.6 cm (0.25 in.) gage diameter and tested according to ASTM A370 specifications. The smaller size was chosen so the specimens could be oriented such that the gage length contained primarily base or weld metal, depending on the test. Specimens were also machined with the HAZ in the center of the gage length. Three specimens from each group (base metal, weld, and HAZ) were tested at ambient and 400°C (750°F) temperatures. The results of the tensile tests are presented in Table 2. The base metal properties are similar to the tensile requirements for ASTM A293 Class 6 material, also shown in Table 2. The weld and HAZ samples all failed in the butter layer and within the gage length. Accordingly, both sets of samples exhibited similar tensile properties. The ultimate tensile strengths and yield strengths for all the elevated temperature tests were 11 to 18 percent lower than the room temperature values but exhibited good uniformity between the different areas of the weld repair.

Rotating Beam Fatigue Tests. Rotating beam fatigue tests were performed in air at ambient temperature on specimens composed of base and weld metal. Specimens were also tested with the HAZ positioned at the center of the test section. Rotating beam fatigue tests are used to determine the stress versus number of cycles to failure (S-N) curve for a particular material. This type of test also identifies the endurance limit of the test material. The endurance limit is the stress level below which the material will theoretically not fail by fatigue. Test results for the base metal, weld, and HAZ are shown in Fig. 4. The weld metal had the highest endurance limit, approximately 413.7 MPa (60 ksi). The base and HAZ samples had similar results with the endurance limit at approximately 358.5 MPa

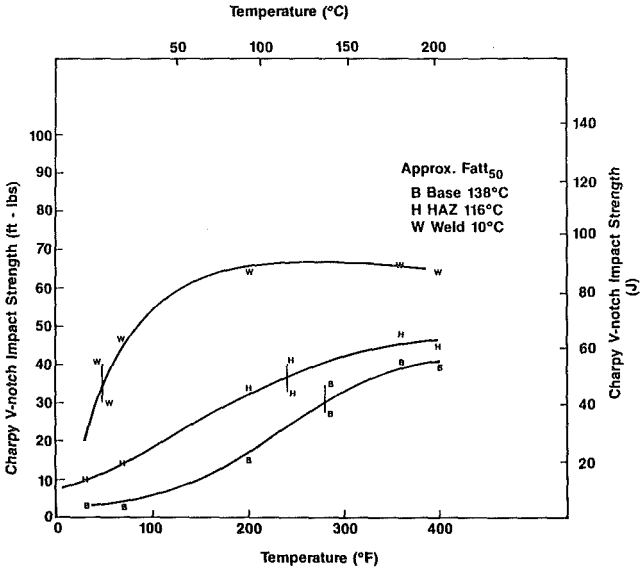

Fig. 5 Plot of charpy V-notch impact test results for the base metal, weld, and HAZ samples

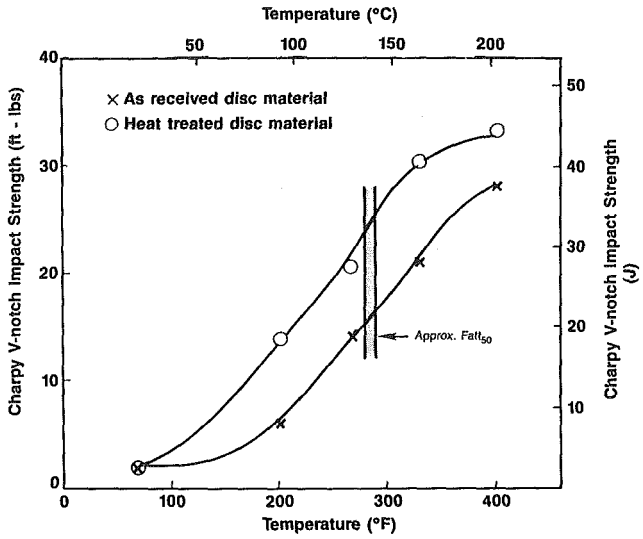

Fig. 6 Summary of the charpy V-notch impact test results for the 9th to 12th stage disk material in the as-received and heat-treated conditions

(52 ksi) and 331.0 MPa (48 ksi), respectively. The HAZ samples experienced failures both at the HAZ and in the butter layer.

Charpy V-Notch Impact Tests. Charpy V-notch impact tests were performed at various temperatures to determine the fracture appearance transition temperature, $FATT_{50}$, where the fracture is 50 percent ductile and 50 percent brittle. Figure 5 is a plot of the results. The $FATT_{50}$ for the weld is approximately 10°C (50°F) and the room temperature impact strength is 65 J (48 ft-lb). The HAZ and base metal tests were similar. The HAZ $FATT_{50}$ is approximately 115.6°C (240°F) and the $FATT_{50}$ for the base metal is approximately 137.8°C (280°F). The room temperature impact strength for the HAZ and base metal are 16 J (12 ft-lb) and 4 J (3 ft-lb), respectively. ASTM A293 Class 6 specifies a maximum $FATT_{50}$ of 121°C (250°F) and minimum room temperature impact strength of 8 J (6 ft-lbs).

J-Integral Fracture Mechanics Tests. J-integral fracture mechanics testing was performed to determine the fracture toughness, K_{IC}, of the base metal, weld, and HAZ. Fracture toughness is a material property that represents the material's resistance to crack propagation. The tests were performed at room temperature according to ASTM E813. The data were reduced in accordance with ASTM E813 except in instances where data reduction per ASTM E399 was valid. The tests show that the base metal had a fracture toughness of 39.6 MPa $\sqrt{m}$ (36.2 ksi $\sqrt{in.}$); the weld had a K_{Ic} of 140.7 MPa $\sqrt{m}$ (128.3 ksi $\sqrt{in.}$). The HAZ test was likely controlled by the butter layer material as a K_{Ic} of 120.9 MPa $\sqrt{m}$ (110 ksi $\sqrt{in}$), well above the base metal, was measured.

The fracture toughness values obtained for the weld were significantly higher than for the rotor base metal. The data imply that, compared to the weld, the critical crack size in the base metal may be relatively small. Typical room-temperature K_{Ic} values for Cr–Mo–V rotor steels range from 44 MPa $\sqrt{m}$ (40 ksi $\sqrt{in.}$) to 88 MPa $\sqrt{m}$ (80 ksi $\sqrt{in.}$) (Matthews, 1973), well above the value obtained for the rotor base metal. The quoted range provides a basis for comparison, but fracture toughness for a material can vary depending on grain size, impurities, anisotropy, and loading rate. In addition, K_{Ic} is influenced by temperature and behaves like Charpy impact energy, exhibiting a lower range value, an upper range value, and a transition region. Therefore, the K_{Ic} value at the operating temperature of the rotor will be slightly higher than those obtained at room temperature and reported in this paper.

Stress Rupture Tests. The time to rupture of the base metal, weld, and HAZ were determined at 241.3 MPa (35 ksi) and 552°C (1025°F). The parameters for testing were chosen for reasonable test periods, that is, less than 300 hours. The parameters, therefore, do not correspond to operating conditions of the rotor. They are merely to compare the stress rupture properties between the base metal, weld, and HAZ at an identical stress and temperature level.

Three specimens were tested from each repair loacation with samples similar to those used for the tensile tests. Each was machined such that the test area was located at the center of the 2.54 cm (1.0 in.), 0.6 cm (0.25 in.) diameter gage. However, in the weld samples, this size gage resulted in carbon steel (from the weld attached ring) in a threaded portion of the specimen. Since carbon steel has significantly lower stress rupture properties than the weld metal, the samples failed in the threads, not the gage. Therefore, stress rupture testing of the weld material was not possible.

The time to rupture for the base metal ranged from 156.2 to 224.9 hours, with an average of 188.0 hours. The HAZ samples failed in the butter layer at an average of 16.1 hours, approximately 10 times less than the base metal. The HAZ samples also exhibited less than half the elongation (16 percent) of the base metal (36 percent).

Charpy V-notch Tests—9th to 12th Stages. Two sets of Charpy V-notch impact specimens were tested from each disk, stages 9 to 12. The samples were machined from the disks such that the notch was oriented parallel to the axis of the rotor. The first set was tested at various temperatures using the disk material in the as-received condition. The second set was given a de-embrittling heat treatment and then tested at the same temperatures as the first set. The de-embrittling heat treatment consisted of heating the specimens to a temperature of 593°C (1100°F), holding at temperature for 2 hours, and water quenching (Kalderon, 1972). Any temper embrittlement in the as-received disk material should have been eliminated by the heating/quenching process. Figure 6 presents the impact results from all four stages. While there was a slight increase in the impact strength at any given temperature, likely due to increased tempering, there was no significant change in the $FATT_{50}$ and, therefore, no indication of temper embrittlement. Had the material been temper embrittled, the impact

curve and $FATT_{50}$ should have shifted to the left (Leslie, 1981). The relatively low impact values and transition temperature observed in the rotor steel are likely due to original manufacturing, i.e., a large prior austenite grain size resulting from a high normalizing temperature. There is no indication of temper embrittlement, i.e., in-service diffusion of tramp elements to the prior austenite grain boundaries.

Discussion

The goals of this investigation were to:

- compare boresonic records with the destructive examination of the test rotor;
- perform metallographic and mechanical property testing of the welded test rotor; and
- perform mechanical property testing of samples from the 9th to 12th stages of the scrapped portion of the rotor to determine the degree of temper embrittlement.

The first of these goals could not be achieved because ultrasonic inspection of the test rotor bore revealed no indications. Since no indications were detected by UT inspection techniques, no areas could be pinpointed for metallurgical investigation. However, during the remainder of the destructive examination and testing of the test rotor, no defects were identified that had been missed by the UT inspection.

The results of the testing performed to achieve the second goal indicate that weld-repaired areas possess some material properties that exceed the specified rotor values and some properties that are lower than the specified values. Generally, the weld metal exceeded the tensile strength, fatigue endurance limit, impact strength, and fracture toughness of the base metal. In addition, good uniformity between the weld, HAZ, and base metal elevated-temperature tensile properties was observed. The butter layer appeared to be the weak link in the repair, exhibiting lower room-temperature tensile strength and stress rupture properties than the base metal. Variability of properties in the weld-repaired area as compared to the base metal should be evaluated when considering future rotor weld repairs.

Two sets of test results are of particular interest. First, the fracture toughness of the base metal is lower than expected. This indicates that critical crack size for the actual rotor is relatively small. However, as previously discussed, the fracture toughness at operating temperature will be higher than the room-temperature test values. It is advisable to institute start-up procedures that allow for adequate heating of the actual weld-repaired rotor.

Second, the HAZ/butter layer exhibited relatively poor, accelerated stress rupture properties compared to the bulk base metal. Had these results been generated from an HP (high-pressure) turbine repair where operating temperatures are in the creep range, they would warrant concern and more detailed examination. However, it should not be a problem with this repair because of the relatively low operating temperatures in the IP/LP.

The third goal of this project was to determine whether the rotor material was temper-embrittled, and if it was, whether an embrittlement gradient existed in the 9th to 12th stages. Charpy impact testing performed on original and heat-treated disk material indicates the rotor was not temper embrittled and a temper-embrittlement gradient was not present. The low impact energy values observed in the material are likely a result of original manufacturing and not in-service degradation.

Acknowledgments

The authors wish to acknowledge the assistance of Mr. Mark Tanner in the performance of the J-integral fracture mechanics testing and data evaluation. We would like to acknowledge Mr. Tommy Scrimshire and Mr. Dave Tomlinson for their excellent laboratory work.

The authors also wish to acknowledge Mr. Walt Fishback of The Hartford Steam Boiler Inspection and Insurance Company and Mr. Don Treinen of Los Angeles Department of Water and Power for their support during this project.

References

Kalderon, D., 1972, "Steam Turbine Failure at Hinkley Point 'A'," Vol. 186(31), London, p. 352.

Kramer, L. D., et al., 1976, "Analysis of the Tennessee Valley Authority, Gallatin Unit No. 2 Turbine Rotor Burst," presented at the Winter Annual meeting of the American Society of Mechanical Engineers, New York, Dec. 5–10.

Leslie, W. C., 1981, *The Physical Metallurgy of Steels*, McGraw-Hill-Hemisphere Publishing, New York, 1981, pp. 236–240.

Matthews, W. T., 1973, *Plain Strain Fracture Toughness (K_{Ic}) Data Handbook for Metals*, Army Materials and Mechanical Research Center, Watertown, MA, Report No. AMMRC MS T3-6, p. 31.

McMahan, C. J., et al., 1980, "Elimination of Impurity-Induced Embrittlement in Steel, Part 1: Impurity Segregation and Temper Embrittlement," EPRI Interim Report, NP-1501, Part 1, Research Project 559, Palo Alto, CA, Sept. pp. 2–1.

Rose, G. J., et al., 1978, "Notch Toughness of Steels," *Metals Handbook Volume 1: Properties and Selections of Irons and Steels*, ASM, Metals Park, OH, p. 692.

Zhe, Q., et al., 1982, "Temper Embrittlement of CrMoV Turbine Rotor Steels," EPRI Interim Report CS-2242, Research Project 559, Palo Alto, CA, Feb.

R. K. Ahluwalia

K. H. Im

Argonne National Laboratory,
Argonne, IL 60439

R. A. Wenglarz

Allison Gas Turbine Division of
General Motors,
Indianapolis, IN 46206

Flyash Adhesion in Simulated Coal-Fired Gas Turbine Environment

A rich-quench-lean subscale turbine combustor has been used to expose specimens to the products of combustion from several beneficiated coal-water fuels. An analytical scheme is formulated to extract sticking coefficients from the measured weight gain data, particle size spectrum, and particle density and composition. The inferred sticking coefficients, appropriate for impaction on the pressure surface, range between 0.0003 and 0.11 and are strong functions of the gas and surface temperatures but rather insensitive to the impact angle. The implications of these results on coal-fired gas turbine operation are discussed.

Introduction

Deposition, erosion, and corrosion (DEC) due to inorganic contaminants pose major obstacles to the successful deployment of direct coal-fired gas turbines. There are two aspects to the deposition problem: particle delivery to the blade surface and particle adhesion. The second aspect is the principal focus of this investigation. Whereas the delivery mechanisms govern the arrival rate of particles, particle-blade surface interactions determine whether the incident particles build up a deposit. We define sticking coefficient as the mass fraction of incident particles to a surface that are retained on that surface.

Particle adherence under prototypical gas turbine environment has received limited attention in the literature. Anderson et al. (1984) employed a laminar entrained reactor to study adhesion characteristics of flyash on a target held perpendicular to the flow stream after acceleration through a nozzle. The experimental setup did not allow an independent control of the target temperature. For bituminous coals, they observed sticking coefficients varying between 0.04 and 0.10. These were sensitive to the coal type, reactor temperature (1370–1810 K), and gas velocity (50–225 m/s) but, surprisingly, rather insensitive to the gas temperature. The last observation is contrary to past experience with residual fuels and coal-derived liquids, which showed that deposition tendency often increases markedly with gas and surface temperatures (Rose, 1982; Whitlow, 1981; Spengler et al., 1983).

Particles are transported to blade surfaces by different mechanisms depending on their size. For a typical first-stage nozzle of a commercial gas turbine with 65 deg turning angle and surface maintained 300 K below the gas temperature, Fig. 1 shows the deposition mechanism and velocity for the throat pressure and suction surfaces (Ahluwalia et al., 1986). The diffusive mechanisms, thermophoresis and eddy impaction, are responsible for particle delivery to the suction surface and to the pressure surface if particle diameter is smaller than about 1 μm. The major fouling threat, however, is posed by inertial impaction because of the associated high depostion velocities and because flyash liberated from coal combustion is expected to have mass mean diameter larger than 1 μm (Wenglarz, 1985). Particles arriving at blade surface through diffusion processes are likely to adhere to the deposition surface but are subject to re-entrainment by the action of turbulent eddies. On the other hand, sticking coefficient for inertial impaction may be much less than unity since for capture to occur, a large amount of kinetic energy must either by dissipated through inelastic deformation or overcome by surface-particle interactions.

Figure 2 has been constructed with the help of the foregoing arrival rate data in order to quantify the significance of the sticking coefficient. It displays the variation of the throat area closure rate normalized by percent ash content of coal as a function of ash mass mean diameter and the pressure side sticking coefficient (η_p). It is assumed that the low-velocity contacts on the suction surface are completely sticky, throat height is 3.5 cm, and the deposit density is 2 g/cm^3. If one

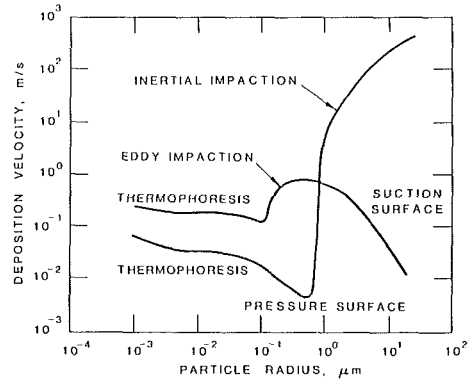

Fig. 1 Arrival velocities and mechanisms for first-stage stator throat

Contributed by the International Gas Turbine Institute and presented at the 33rd International Gas Turbine and Aeroengine Congress and Exhibition, Amsterdam, The Netherlands, June 5-9, 1988. Manuscript received by the International Gas Turbine Institute December 23, 1987. Paper No. 88-GT-135.

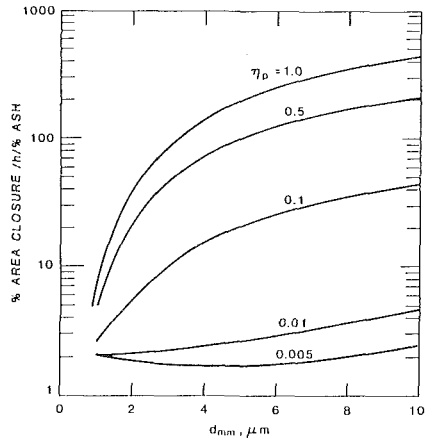

Fig. 2 Sensitivity of throat area closure to pressure side sticking coefficient for log-normal particle size distribution with geometric standard deviation of 1.5

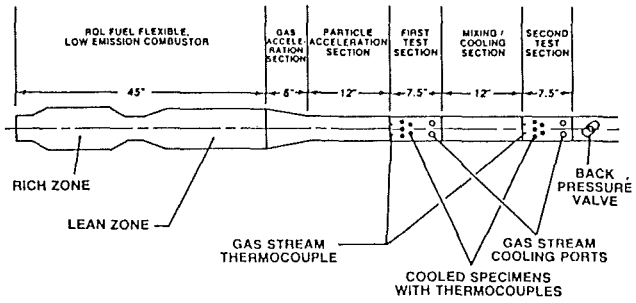

Fig. 3 DEC test facility

postulates a fouling criterion of 20 percent area closure in 200 h of operation, $\eta_p = 0.1$ and $d_{mm} = 4$ μm, the allowable equivalent ash content in beneficiated coal is a stringent 0.006 percent. The tolerance level relaxes to 0.04 percent if the sticking coefficient is reduced to 0.01. The equivalent content here refers to ash content expressed as percent of coal and may be lowered either by coal beneficiation (precombustion) or by hot gas cleanup processes (postcombustion). Quite clearly then, it is important to know the level of sticking coefficient to be expected from coal combustion in a gas turbine environment and the combinations of operating conditions that lead to η_p smaller than 0.01.

Experimental Facility

A rich-quench-lean (RQL) subscale turbine combustor was used to expose specimens to the products of combustion from several coal-water fuels (CWF). This combustor was developed to control NO emissions and provide fuel flexibility. The RQL combustor has operated with distillate, heavy petroleum residual, synthetic coal-derived liquid, and coal-water fuels. Reduced NO emissions have been achieved by staged combustion in fuel rich, rapid quench, and fuel lean zones of combustor (Wenglarz et al., 1987). Fuel flexibility has been facilitated by variable geometry control of air flows to the various combustion zones.

A schematic for the test facility is shown in Fig. 3. High-temperature combustion gases and entrained particles from the RQL combustor are accelerated to high velocities (155 m/s) by a reduction in flow area following the combustor outlet. Five specimens are exposed in the first test section to the high velocity products of combustion. Cooling air is injected at the exit of the first test section to reduce the gas temperature entering the second test section. The second test section is identical in construction to the first and exposes five additional specimens to lower-temperature gases. Coolant is injected at the exit of the second test section to protect the downstream back pressure valve, which controls the system pressure. Gas stream temperatures are measured with thermocouples located near the inlet of each test section. Specimen surface temperatures are individually controlled by internal cooling with air to maintain temperatures at prescribed values measured with thermocouples embedded in their surfaces. The RQL combustor was operated at the combustion residence times, inlet air temperature [vicinity of 753 K (900°F)] and exit gas temperature [excess of 1325 K (1925°F] of recuperated turbine powering a locomotive. The first test section gas temperature and most of the specimen surface temperatures represented the maximum gas and airfoil surface temperatures, respectively, of the first stator vanes of that turbine. The second test section gas temperature and most specimen surface temperatures represented the maximum gas and airfoil surface temperatures, respectively, of the first rotor blades.

One specimen in each test section was cooled from 83°C to 97°C lower temperature than the represented turbine vanes and blades. Data were thereby obtained to evaluate surface temperature effects (e.g., thermophoresis, boundary layer freezing of particles, etc.) on deposition and corrosion.

Most specimens were constructed of IN738 turbine alloy covered with a CoCrAlY coating, which has resisted erosion and corrosion during exposure to products of combustion from coal-fired PFBC pilot plants (Barkalow et al., 1980). One uncooled specimen in each test section was constructed of an SiC ceramic to evaluate the erosion/corrosion resistance to coal fuels of this potential future turbine blade material. Ceramics have experienced much lower erosion and corrosion rates than conventional turbine alloys and coatings in laboratory tests (Stringer et al., 1985).

All test specimens were constructed of hollow (to allow cooling air flows) cylindrical castings with machined flat surfaces exposed to the flow to control particle impact angles. The wedge-shaped upstream surfaces were oriented at a 30 deg angle (typical of maximum erosion angle for alloys) for most specimens. The angles for two specimens in each test section were machined at 10 and 45 deg to explore impact angle effects on particle "sticking fractions" and erosion, if experienced.

Nomenclature

d = diameter of the machined cylinder
d_p = particle diameter
d_{mm} = mass-mean diameter
n = size distribution function
Re_p = particle Reynolds number
s = stopping distance
Stk = Stokes number
u, v = gas velocities
u_∞ = free-stream velocity
w_p = particle relative velocity
W = theoretical weight gain
Y = mass fraction
x, y = coordinates from wedge nose
β = half wedge angle
δ = boundary layer thickness
ϵ = collection efficiency
η_p = pressure-side sticking coefficient
μ = dynamic viscosity
ν = kinematic viscosity
ρ_p = particle density
τ_p = particle relaxation time

Table 1 Fuel properties

	Fuel 1	Fuel 2	Fuel 3
Ultimate Analysis - wt % dry			
Carbon	82.76	82.79	82.89
Hydrogen	5.19	5.20	5.22
Nitrogen	2.11	2.08	2.15
Chlorine	0.19	0.15	0.17
Sulfur	0.91	0.96	0.71
Ash	1.25	0.97	0.69
Mineral Analysis of Ash - wt % of ash			
Phosphorus	0.88	0.57	0.23
Silicon	12.00	11.48	7.50
Iron	20.40	21.90	23.14
Aluminum	14.24	13.92	10.94
Titanium	0.83	0.83	1.00
Manganese	0.02	0.03	0.04
Calcium	3.82	3.37	4.73
Magnesium	0.82	0.98	1.40
Potassium	1.19	0.98	0.87
Sodium	0.58	0.73	0.98
Balance trace elements and oxygen			

Table 2 Deposit weight gains on specimens from fuel 1 (1.25 percent ash) test

Specimen Surface Temperature, K (°F)	Specimen Angle (degrees)	Specimen Weight Gains (mg/cm²h)
High Temperature Test Section [1325 K (1925°F) gas]		
1172 (1650)	30	202
1256 (1800)	30	256
1325 (1925)	30	507
1256 (1800)	10	306
1256 (1800)	45	257
Low Temperature Test Section [1256 K (1800°F) gas]		
1061 (1450)	45	2.25
1172 (1650)	30	2.52
1256 (1800)	30	SPALLED
1172 (1650)	10	1.72
1172 (1650)	30	1.40

Test Fuels

Table 1 gives characteristics of three coal-water fuels used in the deposition, erosion, and corrosion tests. All fuels were provided by the same supplier using the same cleaning process and additive type. The fuels were formulated from the same batch of coal to eliminate feedstock variation effects on deposition, erosion, and corrosion (DEC). The coal was cleaned to a range of levels from 1.25 percent ash to 0.69 percent ash in order to evaluate the effect of ash removal on DEC. This changed not only the ash levels but also the relative percentages of ash species as shown in Table 1. Fuel 1 was formulated with a larger coal particle size (top size of about 40 μm) than Fuels 2 and 3 (top size of about 15 μm) to determine possible effects on product of combustion particle sizes and DEC.

Test Results

Deposition Rates. Table 2 gives the specimen weight gains per unit area per unit time for the DEC test Fuel 1 containing 1.25 percent ash and coal particle sizes smaller than 40 μm. Since some deposits had spalled at test shutdown, the deposit weight gains included material remaining on the surfaces and large spalled pieces matched to specimen spall patterns that had collected at the bottom of the test sections. In some cases where spalled pieces were not found, specimen weight gains were adjusted to reflect full surface coverage of the thickness of deposits remaining on the specimens.

Table 2 shows the major effect of temperature on deposition rates. Deposition rates two orders of magnitude higher were observed in the first test section [average gas temperature of 1325 K (1925°F)] compared to the second test section [average gas temperature of 1256 K (1800°F)]. Deposition in the first test section reduced gas stream ash loading entering the second test section by only 5 to 10 percent. Consequently, upstream ash capture probably has a relatively minor effect on the greatly reduced deposition rates in the second test section.

A clear trend in increasing deposition with increasing surface temperature is seen for 1325 K (1925)°F) gas temperatures. The deposition at the surface temperature of 1325 K (1925°F) is about 2.5 times greater than at 1172 K (1650°F). No clear trend in deposition with surface temperature was seen at the lower gas temperature. The highest deposition rate on the uncooled SiC ceramic specimen at 1325 K (1925°F) gas temperature is probably due to its highest surface temperature and not its difference in material from the coated alloy specimens. Once an initial thin deposit is formed, additional deposition accumulates on underlying deposits and the original surface composition is probably of little consequence. The deposit density measured by water displacement was determined to be 1.9 ± 0.05 g/cm^3 for the 1325 K (1925°F) surface ceramic specimen and 1.85 ± 0.05 g/cm^3 for a 1256 K (1800°F) surface metallic specimen, both exposed at 1325 K (1925°F) gas temperature.

Table 2 shows that specimen surface orientation did not have a great effect on deposit weight gains/area. At an average gas temperature of 1325 K (1925°F) and surface temperature of 1256 K (1800°F), the maximum deviation was 12 percent from the average of deposition rates for the three orientation angles of the 10, 30, and 45 deg specimens. At an average gas temperature of 1256 K (1800°F) and surface temperature of 1172 K (1650°F), the maximum deviation was 34 percent from the average of deposition rates for the same three orientation angles.

As will be discussed later, the data from Table 2 for Fuel 1 and similar data for Fuels 2 and 3 were used to obtain combustion product particle sticking fractions.

Gas Stream Particulate Characteristics. Sticking fraction has been defined earlier as the mass fraction of particles delivered to a surface that are retained on that surface. Mass delivery rates depend on particle diameter and density. Consequently, it was necessary to determine the mass size distributions and densities of the combustion product particulate in order to estimate mass delivery rates to the specimens for sticking fraction computations.

Products of combustion volumetric size distributions were determined by using a particulate probe to capture gas stream particles in combustion experiments conducted with the fuels at the same conditions as the DEC tests. Even though carbon burnout efficiencies exceeded 90 percent, a major fraction of the particulate was char due to incomplete burnout and the low ash concentrations (order of 1 percent) in the test fuels. The approximate 3:1 ratio in densities of ash to porous combustion char and the concentration of char in larger unburned particles result in a significant difference between the desired mass size distributions and the measured volumetric size distributions. Furthermore, these factors cause a variation of combustion product particle density with diameter.

A procedure was developed to determine the mass size

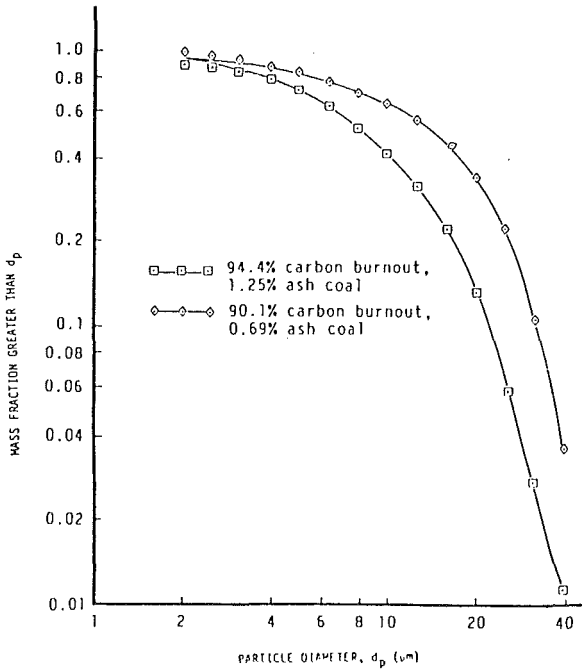

Fig. 4 Mass size distributions for combustion product particles for DEC test fuels

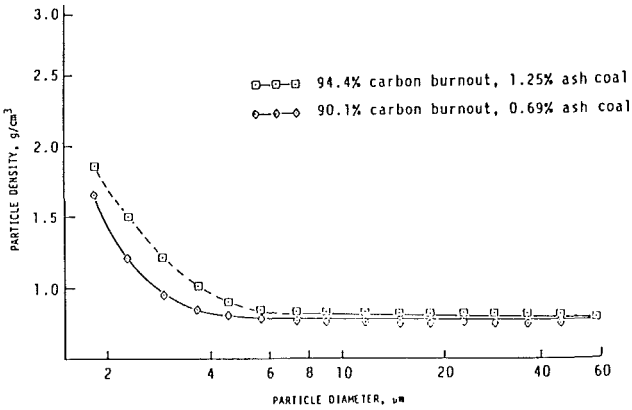

Fig. 5 Particle density versus diameter for combustion products of DEC tests

distributions and density variation with size from the captured particulate volumetric size distribution, the volumetric size distributions of the particulate after ashing, the char mass lost in ashing, and an estimated ash density of 2.91 g/cm^3. Figure 4 gives the mass size distributions determined in this manner for Fuels 1 and 3. Fuel 2 data are not shown because partial blockage of the fuel nozzle during the particulate probe combustion test resulted in poor combustion efficiency and a product of combustion size distribution that was not representative of that in the DEC test. Figure 4 shows that 72 and 83 percent of the combustion product particulate were larger than 5 μm for Fuels 1 and 3, respectively. Most of the particulate is in the inertial impaction range (larger than a few μm). Since inertial impaction delivery rates are much higher than for other mechanisms (e.g., eddy impaction, diffusion, etc.), these other transport mechanisms had a minor effect on total mass delivery to the specimens.

The size distribution for Fuel 1 was smaller than that for Fuel 3 even though larger coal particles were in Fuel 1. This suggests that combustion product particle sizes were primarily influenced by agglomeration of coal and ash in the atomized spray droplets and not coal particle sizes in the fuel. The smaller combustion particle size distribution for Fuel 1 reflects less unburned char due to higher burnout (94.4 percent) compared to Fuel 3 (90.1 percent).

Figure 5 gives the particle densities versus diameter that were determined in the manner indicated earlier from the particulate probe data for Fuels 1 and 3. The larger particles have low densities because they consist mostly of char remaining from incomplete combustion. The mass fraction of ash in the particulate increases with decreasing diameter. The ash begins to significantly influence particle density at diameters smaller than about 5 μm.

Sticking Fraction

In order to extract sticking fraction from deposition data, the arrival rate of particles needs to be determined. This involves mapping of the flow field around the wedge-shaped specimen, solution of particle trajectory equations, and a residual char burnout model. These aspects are discussed in the following sections.

Flow Field Description. Because of the large length-to-diameter ratio of the cylinder from which the wedges were cut, the flow field may be approximated as two-dimensional. A further simplification is effected by neglecting the boundary layer development along the wedge. This is justified for several reasons. The region of interest is confined to the upstream portion of wedge where inertial impaction of particulates is predominant. The boundary layer in this region is expected to be thin because of its vicinity to the front stagnation point. Furthermore, the pressure gradient in this region is favorable and large, resulting in thinning and laminarization of the boundary layer. The effect of neglecting viscous effects on particulate capture efficiency will be assessed later.

With the above simplifications, the problem of describing flow field reduces to two-dimensional inviscid flow about a bank of wedges with 3.05 cm spacing, half wedge angle β, length d, and height equal to $d \sin\beta \cos\beta$. This was accomplished by using a computer code TSONIC that solves the inviscid flow equations using a combination of finite difference solution of the stream function equation and velocity gradient solution (Katsanis, 1969).

Collection Efficiency. For prescribed flow field, particle trajectories are determined by solving the drag equations

$$\ddot{x} = (u - \dot{x})/\tau_p$$

$$\ddot{y} = (v - \dot{y})/\tau_p$$

where τ_p, the particle relaxation time, is a function of the local Reynolds number.

$$\mathrm{Re}_p = w_p d_p/\nu$$

$$w_p = [(\dot{x}-u)^2 + (\dot{y}-v)^2]^{1/2}$$

The particle trajectory equations are integrated numerically starting one specimen diameter upstream of the wedge nose. The integration is terminated if the particle contacts the wedge surface or if it travels beyond $d \cos^2\beta$ without contacting. In this manner, one can determine the location, velocity, and angle of impact as a function of particle size and initial location.

For sticking coefficient calculation, one needs to determine the critical trajectory for which the particle just touches the wedge at $x = d\cos^2\beta$. In other words, we seek the initial location, $y = y_c$ at $x = -d$, such that a particle originating from there reaches $y = d \sin\beta \cos\beta$ at $x = d\cos^2\beta$. Only particles between $y = 0$ and $y = \pm y_c$ reach the target. For unity sticking coefficient then, the collection efficiency is simply $y_c/d \sin\beta \cos\beta$. The computed theoretical collection efficiency has been

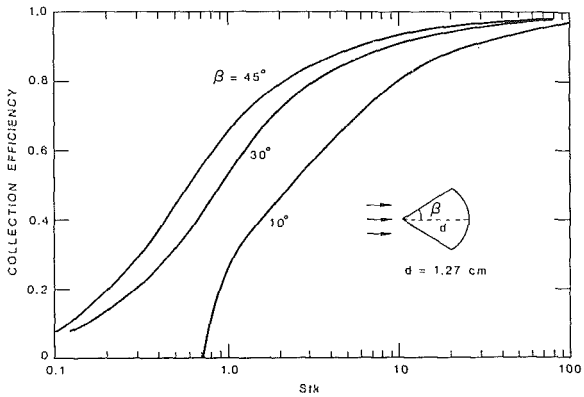

Fig. 6 Theoretical collection efficiency of wedge-shaped targets

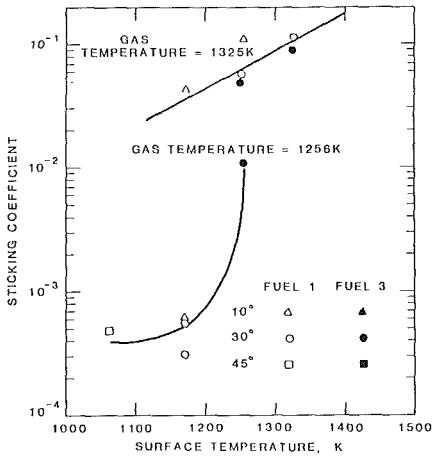

Fig. 7 Sticking coefficients extracted from weight gain data

generalized and plotted in Fig. 6 as a function of the wedge angle and particle Stokes number. The latter quantity is defined for convenience as

$$\mathrm{Stk} = \rho_p d_p^2 u_\infty / (36\,\mu d \sin\beta \cos\beta)$$

We are now in a position to assess the effect of neglecting the viscous effects. Quite obviously for viscous effects to be small, δ/y_c should be much smaller than unity. Alternatively, viscous effects are important whenever η approaches $\delta/d \sin\beta \cos\beta$. For laminar stagnation flow about a wedge, we calculated boundary layer thickness for accelerating (front) portion of the flow. Table 3 lists the calculated value near the turning point (edge) downstream of which the flow is expected to separate. When nondimensionalized by the wedge height, this represents the collection efficiency at which the boundary layer presence may be felt. As listed in Table 3, the critical collection efficiencies are 0.106 for $\beta = 10$ deg, 0.029 for $\beta = 30$ deg, and 0.018 for $\beta = 45$ deg. The corresponding Stokes numbers can be determined from Fig. 6 and are included in Table 3. For our experimental conditions, the total mass of particulates corresponding to sizes smaller than Stk_c is less than 5 percent.

A more quantitative estimate of error incurred due to neglect of boundary layer can be established by comparing the boundary layer thickness to the stopping distance (δ/s). This quantity approximates the reduction in deposition velocity by the viscous effects in boundary layer. It can be shown that

$$\frac{\delta}{s} = \frac{1}{\epsilon \mathrm{Stk}} \left(\frac{\delta}{\sin 2\beta}\right)$$

The calculated value of Stk number at which δ/s equals 0.05 (5 percent error in deposition velocity) is listed in Table 3. As

Table 3 Assessment of boundary layer effects

β	δ (mm)	$\epsilon_c = \frac{2\delta}{d \sin 2\beta}$	Stk_c	$\mathrm{Stk}_c\left(\frac{\delta}{s} = 0.1\right)$
10°	0.23	0.106	1.0	3.0
30°	0.16	0.029	<0.1	0.7
45°	0.11	0.018	<0.1	0.45

before, neglect of boundary layer is completely justified for 30 and 45 deg half-wedge angles but may be questionable for $\beta = 10$ deg.

Particle Size and Composition. As remarked earlier, a significant amount of residual char remained after combustion. On a mass basis, the char content of the entrained particles incident on the targets was larger than the ash content. Ashing tests were conducted on particulates sampled from gas stream. At the gas temperatures of interest, 1250–1350 K, the measured characteristic combustion time for residual char was of the order of minutes, which is two to three orders of magnitude larger than the gas transit time through the test section. Thus, a negligible amount of residual-char combustion occurred while the particles were flowing through the test section. On the other hand, very little carbon was detected in the deposits built up on the targets. This suggests that the residual char content of the particulates deposited on the target completes burnout on the target surface. The residence time available for char burnout on the target surface is essentially the same as test duration (i.e., hours) and is much larger than the measured combustion time (i.e., minutes). This is an important piece of information that has been utilized in inferring the sticking coefficient from the weight gain data.

Figure 5 can be utilized to determine the char and ash mass fractions of entrained particulates as a function of particle size. If ρ_{ash} and ρ_{char} designate reference ash and char densities, one can calculate the ash mass fraction spectrum from Fig. 5 data as

$$Y_{\mathrm{ash}}(d_p) = [1/\rho_{\mathrm{char}} - 1/\rho_p)]/[1/\rho_{\mathrm{char}} - 1/\rho_{\mathrm{ash}}]$$

For consistency, ρ_{ash} and ρ_{char} are referenced such that the particle size distribution and density data yield proper ash and char loadings in the gas entering the test section. It is satisfying to note that ρ_{ash} computed in this manner matches the asymptotic particle density at $d_p = 0$ and ρ_{char} matches the asymptotic ρ_p for large d_p adjusted for the initial ash content.

Sticking Coefficient. For unit sticking coefficient, the theoretical weight gain per unit time per unit target length can now be computed from the following equation:

$$W = u_\infty d \sin 2\beta \int_o^\infty \frac{\pi}{6} d_p^3 \rho_p(d_p) Y_{\mathrm{ash}}(d_p) \epsilon(\mathrm{Stk}) n(d_p) dd_p$$

where $d \sin 2\beta$ is the projected height of the target and n is the particle size distribution function defined as the number of particles per unit volume in the size range d_p to $d_p + dd_p$. The latter quantity is easily recovered from the measured cumulative size distribution and the residual char and ash burden in the gas.

The ratio of measured to theoretical weight gain yields the sticking coefficient. This quantity is plotted in Fig. 7 for Fuels 1 and 3. The gas and surface temperatures are seen to bear strong influence on the sticking coefficient. For example at 1256 K surface temperature, sticking coefficient increases by a factor of six when the gas temperature is raised to 1325 K from 1256 K. Similarly, at 1256 K gas temperature, it decreases by an order of magnitude when the surface temperature is lowered to 1172 K from 1256 K.

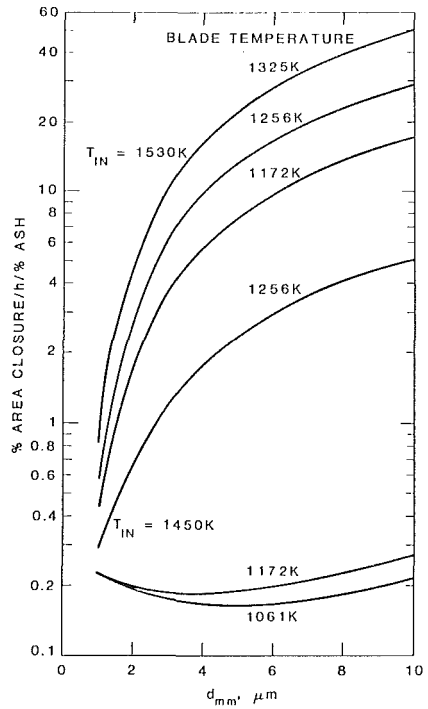

Fig. 8 Projection of data to coal-fired gas turbines

Sticking coefficients presented in Fig. 7 are based on overall weight gain even though they are meaningful only when inertial impaction is involved. At 1325 K gas temperature, and 1256 K gas and surface temperatures, deposit buildup was observed primarily on the frontal area. But at 1256 K gas temperature and surface temperature less than 1200 K, deposit buildup was quite uniform on the upstream and leeward surfaces. For these conditions, the inferred sticking coefficients for inertial impaction should be regarded as higher estimates.

According to the results presented in Fig. 7, wedge angle does not have a discernible influence on the sticking coefficient. To a first approximation then, only the approach velocity and not the angle of impact determines particulate deposition.

Application to a Gas Turbine

Pressure surface sticking coefficients presented in the previous section have been used to project the influence of operating temperatures on fouling potential of a utility-scale coal-fired gas turbine. The results are displayed in Fig. 8 in the form of percent throat area closure per hour per percent ash in coal as a function of flyash mass mean diameter. These are based on an assumed suction side sticking coefficient of 0.10 and a log-normal particle size distribution with a geometric standard deviation of 1.5. For a turbine operating with choked throat, the two gas temperatures used in deposition tests project to 1530 K and 1450 K turbine inlet temperatures. At the higher inlet temperature, fouling increases with d_{mm}, which is indicative of runaway fouling of the pressure surface. As indicated earlier, pressure surface deposition dominates (due to high delivery rates) for particle diameters larger than about 1 μm unless sticking fractions for the pressure surface are much smaller than for the suction surface. This is the case at 1450 K inlet temperature and blade temperature less than 1200 K for the assumed suction surface sticking fraction of 0.1. Area closure is almost independent of η_p and fouling is determined primarily by the suction surface deposits. In the suction fouling regime, the rate of deposit buildup decreases with d_{mm} provided that d_{mm} is larger than about 1 μm (see Fig. 4 for reference to the maxima in the eddy impaction regime). In this instance, fouling is also sensitive to the magnitude of the suction surface sticking coefficient appropriate for diffusive deposition.

From the standpoint of fouling, there is an uncertainty in projecting the gas temperatures (1256 K, 1325 K) to turbine inlet temperatures (1450 K, 1530 K). Particles conducive to inertial impaction have thermal response time much longer than the gas residence time in the first stage. At the throat location, these particles may not relax to the local gas temperature. They may exhibit fouling behavior more characteristic of gas temperature approaching the turbine inlet temperature. Thus, the inlet temperatures stated in Fig. 8 have an implicit uncertainty band of about −200 K.

In view of the foregoing reservations, proper projection of turbine fouling rate will require additional clarifications with respect to suction surface sticking coefficients for diffusive deposition and effect of incomplete particle temperature relaxation on the adhesion mechanism.

Discussion

Both particle delivery and adhesion influence the fouling behavior of coal-fired gas turbines. Flyash delivery rate to a blade surface is determined by airfoil aerodynamics and the particle size distribution. Our experimental data indicate that the size distribution of flyash liberated from micronized coal-water slurry combustion is related to atomization characteristics rather than the degree of coal grind. The insensitivity to coal grind derives from the apparent agglomeration of micronized coal particles contained within an atomized droplet. The agglomeration presumably occurs during the evaporation of the droplet water content. The subsequent combustion of coal is characteristic of the agglomerate rather than the individual parent coal particles. The slurry atomization characteristics are related to the nozzle design, coal grind, viscosity reduction additive used, and coal loading. The available experimental data point to the domineering effect of coal loading on slurry atomization. In general, the smaller the coal loading, the finer the spray. The intentional dilution of slurries, however, causes ignition difficulties, combustion instability, and loss of energy conversion efficiency.

Flyash adhesion is a function of many variables including the gas temperature, target temperature, particle contact velocity, contact angle, coal ash composition, and mode of coal combustion. For high-velocity impacts representative of inertial deposition on pressure surface, this work has established quantitatively the effect of gas and surface temperatures on the sticking coefficient whereas the impact angle has been relegated to secondary importance. The data of Anderson et al. (1984), although exhibiting a large uncertainty band, showed an interesting velocity dependence of the sticking coefficient. At low velocities, the sticking coefficient decreases with contact velocity, reaches a shallow minimum at about 50 m/s, and then rises again as the velocity is increased. They also observe a positive correlation between the sticking coefficient and the laboratory furnace/combustor temperature. Ash composition also plays an important role in determining the severity of fouling. It is generally agreed that for adhesion of energetic particles to occur, either they must be semimolten or a molten phase must be present on the blade surface to bind the impacting particles. Sodium sulfate has long been recognized for its glue action in conventional fossil fuel technology. The data of Anderson and Romanowski (1985) also suggests a correlation between the volatile sodium content of coal and flyash adhesion at velocities approaching particle impaction on pressure surface.

One paramount difficulty in interpreting gas/surface temperature effect on the sticking coefficient is caused by the limited turbine residence time (τ) in relation to particulate

thermal relaxation time (τ_t). From a simple heat transfer argument, one can derive the following equation for the variation of particle temperature (T_p) in transit through a turbine

$$T_p = \exp(-\tau/\tau_t)\left[T_{in} + \int_0^{\tau/\tau_t} T\exp(t)dt\right]$$

where

$$\tau_t = 1/12(k_p/k_g)(d_p^2/\alpha_p)$$

The above equation states that the relaxation of particle temperature from the inlet temperature T_{in} to the local gas temperature T is governed by the parameter τ/τ_t. For $\tau_t \ll \tau$, T_p approaches T, and for $\tau_t \gg \tau$, T_p retains the inlet value T_{in}. Thus, one can determine a critical particle size corresponding to $\tau_t = \tau$: Particles larger than the critical size have temperature intermediate between T_{in} and T, whereas the smaller particles have temperatures closer to the local gas temperature T. If one assumes that the particle thermal conductivity $k_p = 2$ W/mK, gas thermal conductivity $k_g = 0.07$ W/mK, particle thermal diffusivity $\alpha_p = 5 \times 10^{-7}$ m^2/s, and the gas residence time in the first-stage nozzle $\tau = 0.50$ ms, the critical particle diameter is calculated as 10 μm. We can then conclude that the fouling behavior of particles larger than 10 μm will be characteristic of gas temperature T_{in}, and of those smaller than 10μm will correspond to gas temperature T. This conclusion is tentative in that supporting experimental data are not available.

Unburnt char remaining after combustion of highly cleaned coals may constitute a significant fraction of the total particulate burden. As a reference, flyash liberated from 1 percent ash coal combusted at 99 percent efficiency will contain 50 percent char. The residual char modifies the combustion particulate size distribution. It shifts the distribution to the larger sizes, thereby enhancing the inertial delivery of ash to the pressure surface. Since the burnout time in the diffusion-controlled regime is directly proportional to the square of particle diameter, the larger particles are rich in unburnt char. Because of the density difference between char and ash, particles of different size and composition develop different densities and this too affects the delivery rate. The experimental evidence indicates that the residual char completes its combustion after depositing on the blade surface. Thus, it does not physically contribute to blockage of the blade passages but serves to enhance flyash delivery to the blade surface.

Summary and Conclusions

Adherence of flyash impacting on an inclined surface has been investigated under conditions prototypical of gas turbine operation. A rich-quench-lean subscale turbine combustor was used to expose targets to the products of combustion from several coal–water fuels. The slurry fuel was prepared from coals cleaned to 0.69–1.25 percent ash levels. Wedge-shaped targets were machined from hollow cylinders constructed of IN738 alloy covered with a CoCrAlY coating and of SiC ceramic. The alloy targets were cooled up to 200 K below the gas temperature. The gas velocity was in the vicinity of 150 m/s. The resulting impaction of entrained flyash on the flat surfaces of the targets simulated deposition on the pressure surface of a coal-fired gas turbine.

An analytical scheme was formulated to extract sticking coefficients from the measured weight gain, particle size distribution, and particle density. A burnout model accounted for residual char combustion on the target surface. The theoretical collection efficiency was computed by solving numerically the particle trajectory equations with gas flow field prescription obtained from the potential flow solution.

The inferred sticking coefficients were sensitive to gas temperature and surface temperature but not to the impact (wedge) angle. They ranged from 0.04 to 0.11 at 1325 K gas temperature and from 0.0003 to 0.01 at 1256 K gas temperature. The sticking coefficient also increases with surface temperature. At 1256 K gas temperature, it declines precipitously if the surface temperature is maintained below 1200 K.

The implications of the above results were assessed by projecting the data to the utility-scale coal-fired gas turbine. A particle delivery model appropriate for diffusive and inertial delivery to suction and pressure surfaces was used for this purpose. The projection was based on an assumed sticking coefficient of 0.1 for the diffusive deposition on the suction surface. At 1325 K gas temperature (1530–200 K turbine inlet temperature), throat area closure was primarily due to deposit buildup on the pressure surface. At 1256 K gas temperature (1450–200 K inlet temperature), surface temperature lower than 1200 K, and for the size distribution considered, fouling was ascribed to deposition on the suction side. In this instance, area closure rate is sensitive to the actual magnitude of the suction-side sticking coefficient. This points to the need of conducting experiments in the future, the data from which can be used to infer sticking coefficients for low-velocity particle–surface interactions characteristic of diffusive deposition on the suction side.

The above pressure surface sticking fraction data extrapolations to estimate throat rates are for a specific large turbine passage flowpath, particle size distribution spread, and suction surface sticking fraction. The same data could be applied to other turbine flowpaths operating with the same fuel at similar gas and surface temperatures but with different blade shapes, physical scales, and product of combustion size distributions. Such evaluations could demonstrate the sensitivity of throat closure rates to these variables.

Acknowledgments

This work was supported by the Morgantown Energy Technology Center of the U.S. Department of Energy. Fred Bauer was the contracting officer for the program at Argonne. Janna Thames, Nelson Nekos, and Larry Carpenter were the contracting officers for the work performed at Allison.

References

Ahluwalia, R. K., Im, K. H., Chuang, C. F., and Hajduk, J.-C., 1986, "Particle and Vapor Deposition in Coal-Fired Gas Turbines," ASME Paper No. 86-GT-239.

Anderson, R. J., Romanowski, C. J., and France, J. E., 1984, "The Adherence of Ash Particles From the Combustion of Micronized Coal," DOE/METC-85/2007.

Anderson, R. J., and Romanowski, C. J., 1985, "Deposition Tendencies for Selected Coals Combusted at Atmospheric Pressure," presented at the Second Annual Pittsburgh Coal Conference, Pittsburgh, PA.

Barkalow, R. H., Goebel, J. A., and Pettit, F. S., 1980, "Materials Problems in Fluidized-Bed Combustion Systems," EPRI CS-1448.

Katsanis, T., 1969, "Fortran Program for Calculating Transient Velocities on a Blade-to-Blade Stream Surface of a Turbomachine," NASA TN D-5427.

Rose, R. S., 1982, "Advanced Cooling Full-Scale Engine Demonstration Program," EPRI AP-2605.

Spengler, C. J., Whitlow, G. A., Lee, S. Y., Wenglarz, R. A., and Mulik, P. R., 1983, "Corrosion and Deposition Results From Pressurized Passage Tests With Heavy Ash Bearing Fuels From the SRC-II Process," ASME Paper 83-GT-185.

Stringer, J., McCarron, R., et al., 1985, "Results From the Turbine Materials Testing Program on the IEA Grimethorpe Experimental PFBC Facility," *Proceedings of 8th International Conference on Fluidized Bed Combustion*, Houston, TX.

Wenglarz, R. A., 1985, "Deposition, Erosion and Corrosion Protection for Direct Coal-Fuel Gas Turbines," ASME Paper 85-IGT-61.

Wenglarz, R. A., Ames, F. E., Williams, J. R., and Wilkes, C., 1987, "Combustion of Coal Water Fuels Under Gas Turbine Conditions," *Proceedings of 12th International Conference on Slurry Technology*, New Orleans, LA.

Whitlow, G. A., Lee, S. Y., Mulik, P. R., and Wenglarz, R. A., 1981, "The High-Temperature Combustion of Residual Fuel Oil—Some Deposition Product Considerations," *Proceedings of Second Conference on Advanced Materials for Alternate Fuel-Capable Heat Engines*, Monterey, CA.

Physical and Chemical Characteristics of Cenospheres From the Combustion of Heavy Fuel Oil

R. M. Clayton
Member of Technical Staff.

L. H. Back
Group Supervisor.

Jet Propulsion Laboratory,
California Institute of Technology,
Pasadena, CA 91109

Characterization of an existing sample of cenospheres produced during residual-oil-fired steam power plant combustion included: scanning electron microscopy of surface structure; photomicrography of particle cross sections; measurement of porosity, surface area, and density; and measurement of chemical composition. The studies showed that typical large (100–200 μm) and small (20–40 μm) cenospheres were spheroidal and hollow and had at least one blowhole. The sizes of the blowholes range from 10 to 50 percent of the diameters of the cenospheres. The ratio of outer to inner diameter of the shell was of the order of 1.3–1.4. The shells are porous, the larger ones appearing spongelike, the smaller ones appearing smoother but containing many pores a few micrometers in diameter. The solid portions of the shell appear flaky and layered. A typical cenosphere contained only about 18 percent solid material on a volumetric basis. A relatively concentrated percentage content of elements S, Fe, Na, and V was indicative of the potential contribution to high-temperature corrosion from cenosphere deposition on heat exchanger surfaces.

Introduction

Liquid-phase-cracking reactions, which occur in droplets of residual fuel oil during their combustion, produce particles called cenospheres, which burn much more slowly than the original liquid droplet. Cenospheres often contribute to operational problems in oil-fired furnaces and boilers, such as deposits, high-temperature corrosion, particulate emissions, and reduced combustion efficiency (e.g., Bellan and Elghobashi, 1985). Thus, it is desirable to eliminate these particulates. However, since it does not seem practical to prevent their formation due to the presence of heavy hydrocarbon ends in the fuel (Marrone et al., 1984), methods of enhancing the combustion of cenosphere particles are sought. Although no statistical data are known by the authors for droplet ensembles under power plant conditions, as much as 3 percent of the mass of the original fuel droplet has been reported to be left as a cenosphere in single droplet experiments (Marrone et al., 1984). Therefore, the task of consuming them may be significant.

Information on the formation of cenospheres has been reported in experimental studies of a single drop suspended from a filament and for monosize free-fall drops (Michael and El-Wakil, 1967; Jacques et al., 1976; Marrone et al., 1984). In most cases disruptive ejection of volatile fuel components from the droplet and thermal decomposition of heavy fuel components inside the droplet have been observed. Initially the volatile components at the surface and those that diffuse to the surface evaporate and form a diffusion-type flame. This diffusion and evaporation of the volatile components cause a viscous shell to form consisting of the remaining components of asphaltene and resin. The shell then slows further diffusion of volatile components from the interior, but as the interior temperature increases, additional volatile components vaporize, increasing the size of the drop with fuel eventually escaping through a weak portion of the shell. Surfce tension then causes contraction of the shell and eventually at the end of vaporization a hollow residue remains. Earlier work on cenospheres formed during coal devolatilization or combustion has been reported (e.g., Newall and Sinnatt, 1924; Lightman and Street, 1968).

The specific focus of this paper is on a description of the physical structure and chemical composition of cenospheres from the combustion of heavy fuel oil. There is little information in the existing literature in this regard. Such data are also important in analytical modeling of cenosphere combustion (Gavalas et al., 1985; Lowenberg et al., 1987). Accordingly, a mixed, bulk sample (~20 g) of cenospheres was located that had been obtained for other purposes from downstream of the boiler tubes of several residual-oil-fired steam power plants operating in the Southwestern area of the United States. The cenospheres were washed and cleaned, and the following characterization studies were performed:

1 Scanning electron microscopy of surface structure
2 Photomicrography of particle cross sections

Contributed by the Power Division for publication in the JOURNAL OF ENGINEERING FOR GAS TURBINES AND POWER. Manuscript received by the Power Division November 1987.

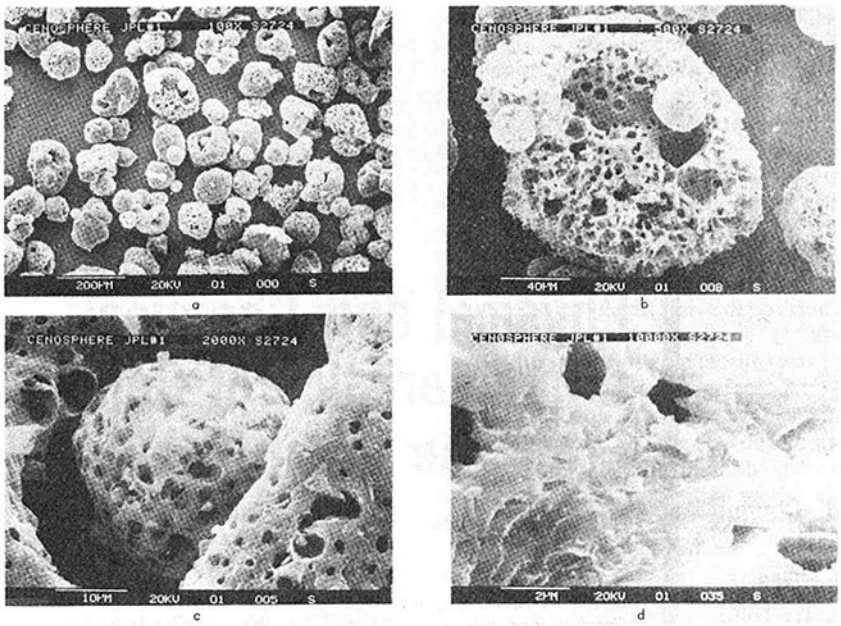

Fig. 1 SEM photographs of JPL group No. 1 cenospheres

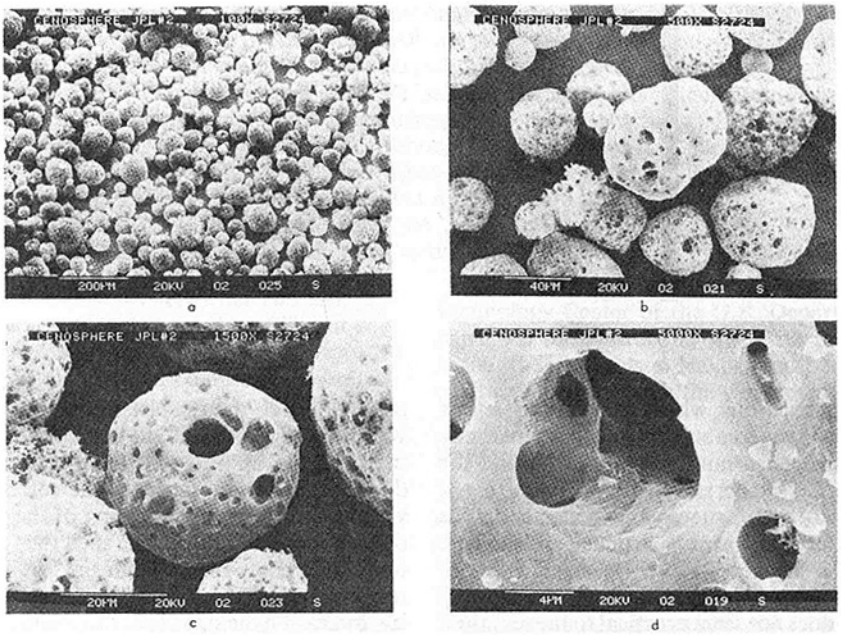

Fig. 2 SEM photographs of JPL group No. 2 cenospheres

3 Measurements of porosity, surface area, and density
4 Measurement of chemical composition

Although records of the composition of No. 6 fuel oil, detailed sampling locations and operating conditions of the plants were not available, the structural characteristics of the cenospheres are believed to be typical of heavy fuel oil-fired boilers and furnaces, but the detailed chemical composition would generally be variable.

Surface Structure Study

The surface structure of three groups of cenospheres from the bulk sample was studied using a Stereoscan 250, Mark 2[1] scanning electron microscope (SEM). Selected SEM photographs are shown in Figs. 1, 2, and 3 for the groups identified as JPL 1, 2, and 4, respectively. No distribution is implied by the group numbers other than identification. In each figure the magnification increases for the individual photographs from *a* through *d*; however, the photographs are not necessarily of the same scene. A length scale in micrometers and a magnification factor are shown in each photograph in the lower left-hand and upper right-hand regions, respectively.

The SEM photographs show that typical large (100–200 μm) and small (20–40 μm) cenospheres are spheroidal and hollow, and have at least one "blowhole" that extends from the hollow core through the shell of the cenosphere (Figs. 1*b*, 2*c*, and 3*b*). These blowholes have diameters in the range of 10–50 percent of the cenosphere diameter. The shells of large particles tend to be spongelike with an interconnected cellular structure (Figs. 1*b* and 3*b*), whereas the shell of the smaller particles is smoother but pitted by many small pores of the order of a few micrometers diameter (Figs. 1*c*, 1*d*, 2*c*, 2*d*, and 3*c*).

[1]Manufactured by Cambridge Instruments, Inc., Monsey, NY.

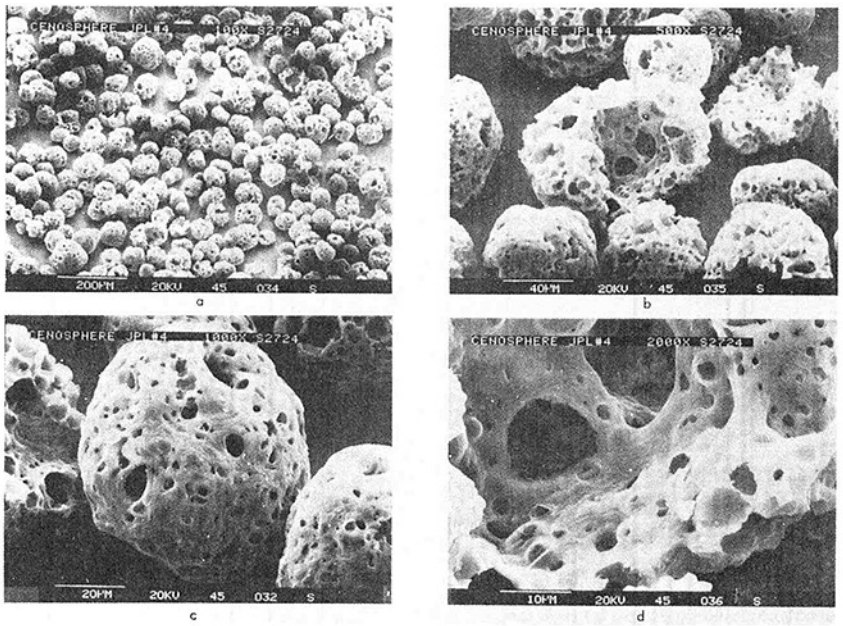

Fig. 3 SEM photographs of JPL group No. 4 cenospheres

Magnification up to $10^4\times$ revealed a somewhat flaky or layered appearance of the solid portions of the surface (Figs. 1*d*, 2*d*, and 3*d*). No microporosity appears in the latter photographs although interstitial spaces between flakes or layers might provide an effective microporosity.

Particle Cross Section Study

Cross sections of typical cenospheres were made by imbedding a few of the JPL Group #1 particles in a resin, under vacuum as the resin cured. After hardening, the surface of the resin was ground and polished, exposing various cross sections of the particles.

Photomicrographs ($500\times$) of a portion of the bulk sample and of typical cenosphere cross sections are shown in Fig. 4. A length scale is shown for each photograph. The light-colored, irregular shapes centrally located in the photographs in Fig. 4(*a*) are cross sections. These cross sections verify the hollow center of the cenosphere and the porosity of its shell that was observed by SEM (Figs. 1–3). Voids from 1 to 70 μm are clearly shown within the shell wall. The ratio of outer to inner diameter of the shell appears to be of the order of 1.3–1.4.

Surface Area, Porosity, and Density Analysis

Laboratory analyses of physical properties were made[2] using mercury intrusion porosimetry and nitrogen adsorption by static BET[3] apparatus to establish total pore volume, total surface area, and pore volume and area distribution as a function of pore opening size over the range of 0.0015 to 127 μm (15 to 1.27 $\times$ 10^6 Å). Density measurements were made in helium to obtain the true density of the carbonaceous shell material. The cenosphere samples were degassed at a temperature of 423–473 K prior to the analyses.

Mercury Intrusion Porosimetry Measurements. Mercury intrusion porosimetry provides standard porosity information for the larger void size range. An Autopore 9200 porosimeter

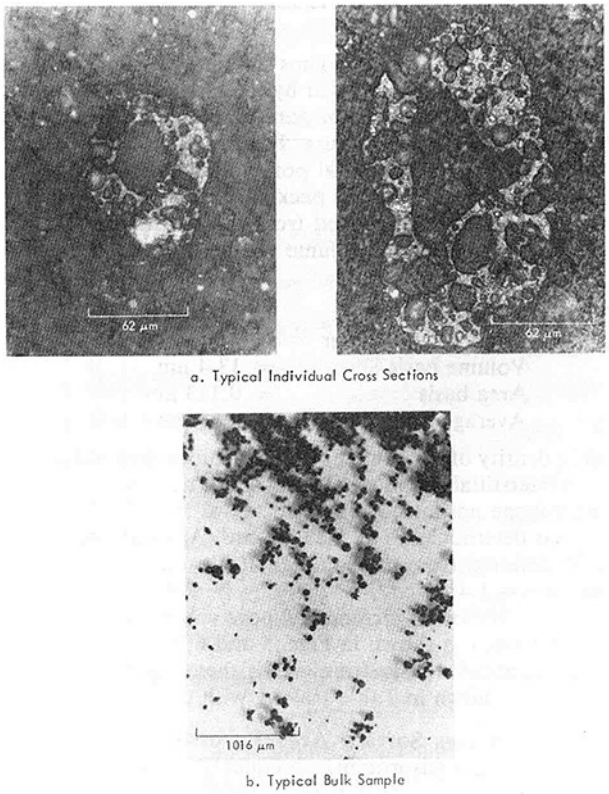

Fig. 4 Photomicrographs of JPL group No. 1 cenospheres; 500 × magnification

was used directly to measure the total pore volume of a 0.094-g sample of cenospheres over a mercury-pressure range of 9.7 kPa to 71.6 MPa (1.4 to 10,400 psia). The pressure was incrementally applied in sixteen steps in order to measure incremental intrusion volume changes. A total pore volume of 3.61 cm^3 per gram of sample was measured. The pressure range used corresponds to a pore-size range of 0.017 to 127-μm diameter on the basis of the standard assumption of a cylindrical pore shape. In reality, pore size refers to the diameter of the opening to a void and not to the size of the void behind

[2]Performed by the Materials Analysis Laboratory, Micromeritics, Norcross, GA. All analysis equipment identified in this Section is manufactured by Micromeritics. Details of equipment and laboratory procedures are available from the manufacturer.

[3]From the names of the originators of the technique, Brunauer, Emmett, and Teller (1938).

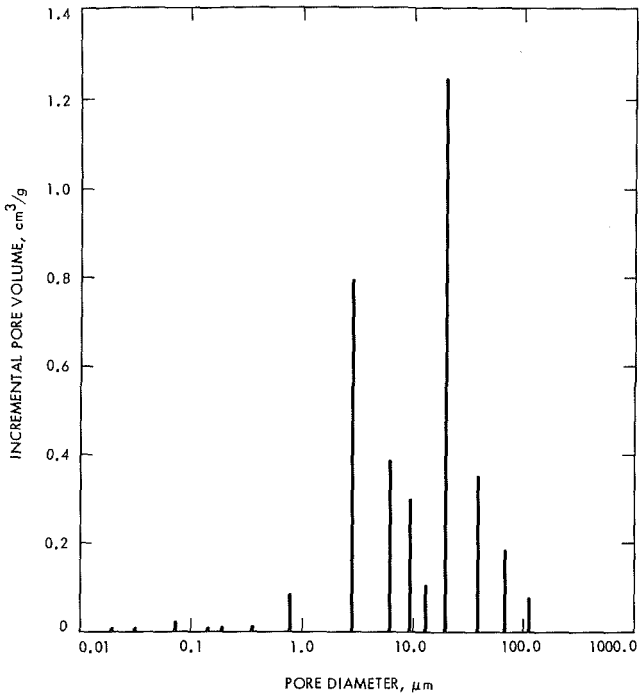

Fig. 5 Incremental pore volume versus pore diameter; mercury intrusion porosimetry

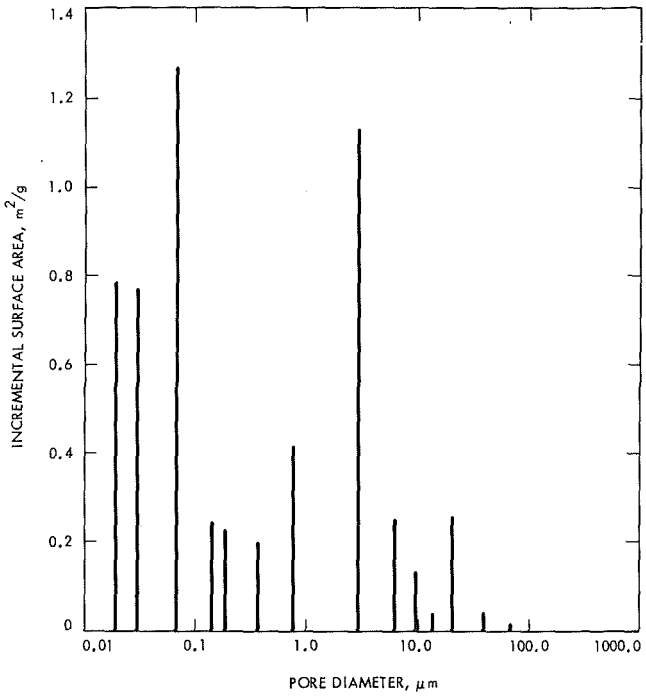

Fig. 6 Incremental surface area versus pore diameter; mercury intrusion porosimetry

it, which in general is larger. Thus total pore volume reported here includes all voids intruded by the mercury through pore openings above the 0.017-μm pore diameter associated with the maximum mercury pressure. For the packed bulk sample of cenospheres used, the total pore volume also includes the interstitial voids between the packed cenospheres.

Other parameters calculated from the measured total pore volume, the incremental volume changes, and the assumed cylindrical pore shape are:

Total pore area	=	5.71 m^2/g
Median pore diameter		
Volume basis	=	13.4 μm
Area basis	=	0.113 μm
Average pore diameter	=	2.53 μm

Bulk density of the sample, which includes the solid shell as well as interstitial and internal voids and is defined on the basis of all volume not intruded by mercury at the minimum pressure, was determined to be 0.232 g/cm^3. Apparent or skeletal density inferred from the volume not intruded at the highest pressure was 1.41 g/cm^3.

The distribution of incremental pore volume and pore area versus pore size is shown in Figs. 5 and 6, respectively. Tabulated distribution data from which these figures were constructed are shown in Table 1 along with cumulative values.

BET-Apparatus Surface Area/Porosity Measurements. Classical BET gas-adsorption techniques (Brunauer et al., 1938) yield a direct measurement of total surface area and also yield porosity distribution in the lower pore-size range based on the standard assumption of cylindrical voids. Briefly, this technique exposes the sample, which has been evacuated and cooled to near the boiling-point temperature of the adsorbate gas, to the gas in a series of controlled pressure increases (43 pressure steps were used for the present measurements). The equilibrium quantities of gas adsorbed are determined for each pressure, defining an isotherm. From the isotherm thus determined, the quantity of gas needed to cover the solid surfaces, both external and internal within voids accessible to the gas, with a monolayer of close-packed adsorbate molecules can be calculated. Finally, the total area of the solid is calculated using the summed projected area of all adsorbed gas molecules.

Table 1 Incremental data from mercury intrusion measurements

Average	Pore volume, cm^3/g		Pore area, m^2/g	
diameter, μm	Incremental	Cumulative	Incremental	Cumulative
126.6	0.0000	0.0000	0.0000	0.0000
104.6	0.0785	0.0785	0.0030	0.0030
65.9	0.182	0.261	0.0111	0.0141
38.2	0.350	0.611	0.0367	0.0508
19.9	1.25	1.86	0.252	0.302
12.0	0.115	1.98*	0.0383	0.341
9.62	0.297	2.28	0.124	0.464
6.25	0.385	2.66	0.246	0.710
2.84	0.797	3.46	1.12	1.83
0.794	0.0826	3.54	0.416	2.25
0.365	0.0171	3.56	0.188	2.44
0.179	0.0099	3.57	0.221	2.66
0.128	0.0077	3.58	0.242	2.90
0.0718	0.0228	3.60	1.27	4.17
0.0310	0.0059	3.60	0.764	4.93
0.0198	0.0039	3.61	0.781	5.71

*Interpreted as the interstitial space between cenospheres in the packed bulk sample.

The distributions of pore volume and pore surface area as a function of pore size are obtained by extending the process described above to cause gas condensation in the fine pores, cracks, and crevices of the samples. As pressure is increased beyond that for a monolayer of gas film molecules, a layer several molecules deep can be formed. If the sample contains fine pores and crevices, the gas condenses to fill these small voids from smaller to larger size as film thickness increases with pressure. This process can be continued until saturation conditions are reached. With the standard assumption of cylindrically shaped voids, the data obtained from the foregoing process can be converted to the distribution information desired. Note, however, that the conversion of the gas adsorption results to porosity statistics is dependent on the assumed pore geometry; therefore, the data on pore area distribution versus pore size are subject to some uncertainty.

A DigiSorb 2600 surface area analyzer was operated with

Table 2 Adsorption isotherm from BET-apparatus measurements using nitrogen

P/P_{sat}	N_2 volume adsorbed, cm^3/g @ STP
0.0311	3.54
0.0568	3.85
0.119	4.33
0.202	4.76
0.338	5.30
0.460	5.73
0.555	6.11
0.625	6.41
0.677	6.69
0.718	6.95
0.750	7.18
0.776	7.44
0.805	7.77
0.849	8.42
0.884	9.05
0.906	9.53
0.932	10.3
0.947	11.0
0.958	11.6
0.962	12.0
0.971	13.1
0.976	14.0
0.981	15.3
0.986	17.9
0.990	20.6

Table 3 Incremental data from BET-apparatus measurements using nitrogen

Average	Pore volume, cm^3/g		Pore area, m^2/g	
diameter, μm	Incremental	Cumulative	Incremental	Cumulative
0.160	0.00452	0.00452	0.113	0.113
0.117	0.00432	0.00884	0.148	0.261
0.0907	0.00220	0.0110	0.097	0.358
0.0752	0.00139	0.0124	0.074	0.432
0.0597	0.00186	0.0143	0.124	0.556
0.0502	0.000711	0.0150	0.057	0.613
0.0449	0.000535	0.0155	0.048	0.660
0.0404	0.000584	0.0161	0.058	0.718
0.0363	0.000581	0.0167	0.064	0.782
0.0320	0.000579	0.0173	0.073	0.855
0.0274	0.000670	0.0180	0.098	0.953
0.0236	0.000634	0.0186	0.108	1.060
0.0208	0.000440	0.0190	0.085	1.15
0.0189	0.000423	0.0194	0.090	1.24
0.0168	0.000567	0.0200	0.135	1.37
0.0148	0.000619	0.0206	0.167	1.54
0.0134	0.000452	0.0211	0.135	1.67
0.0118	0.000831	0.0219	0.283	1.96
0.0105	0.000458	0.0224	0.175	2.13
0.00981	0.000207	0.0226	0.084	2.21
0.00935	0.000246	0.0228	0.105	2.32
0.00886	0.000281	0.0231	0.127	2.45
0.00837	0.000234	0.0233	0.112	2.56
0.00790	0.000223	0.0236	0.113	2.67
0.00742	0.000236	0.0238	0.127	2.80
0.00694	0.000276	0.0241	0.159	2.96
0.00645	0.000308	0.0244	0.191	3.15
0.00598	0.000271	0.0246	0.181	3.33
0.00552	0.000291	0.0249	0.211	3.54
0.00505	0.000341	0.0253	0.270	3.81
0.00459	0.000403	0.0257	0.351	4.16
0.00414	0.000460	0.0261	0.444	4.61
0.00370	0.000490	0.0266	0.530	5.13
0.00328	0.000572	0.0272	0.697	5.83
0.00288	0.000844	0.0280	1.17	7.01
0.00253	0.000784	0.0288	1.24	8.25
0.00228	0.000666	0.0295	1.17	9.42
0.00209	0.000877	0.0304	1.68	11.1
0.00189	0.00117	0.0315	2.48	13.6
0.00172	0.000763	0.0323	1.77	15.4
0.00162	0.000596	0.0329	1.47	16.8
0.00154	0.000810	0.0337	2.10	18.9

nitrogen to measure the total BET surface area of a 3.23-g sample of cenospheres. An area of 16.8 m^2 per gram of sample was obtained. Part of the 43-point adsorption isotherm is tabulated in Table 2.

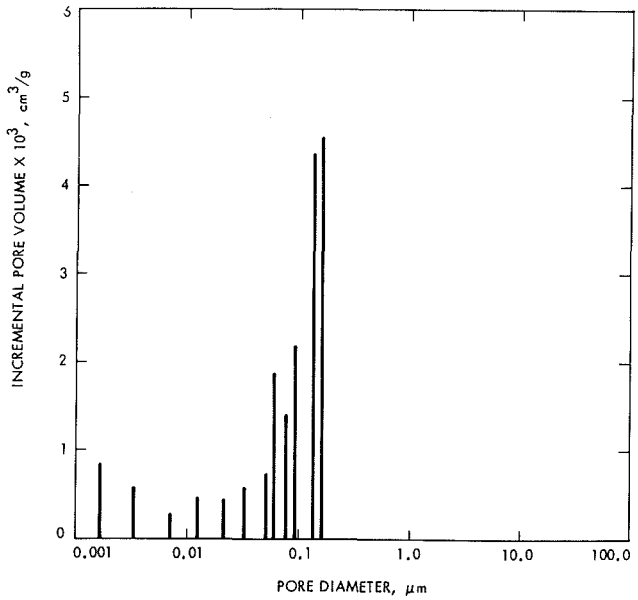

Fig. 7 Incremental pore volume versus pore diameter; BET apparatus

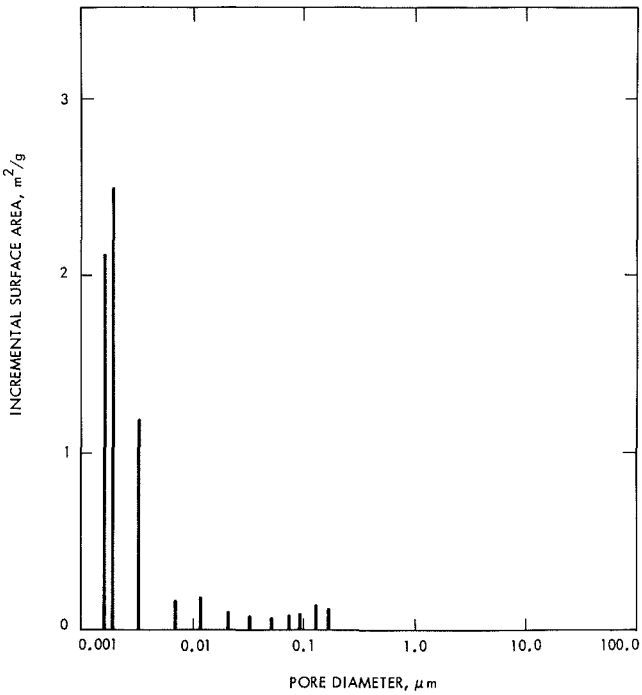

Fig. 8 Incremental surface area versus pore diameter; BET apparatus

The distribution of incremental pore volume and pore area over the pore-size range of 0.0015 to 0.23 μm (15 to 2300 Å) is shown in Figs. 7 and 8, respectively. Tabulated data are shown in Table 3 including cumulative values. Note that the cumulative value for pore area of 18.9 m^2/g differs from the more accurate total value of BET surface area of 16.8 m^2/g by virtue of the discussion above.

Pycnometer Density Measurement. The true density of the carbonaceous phase of the cenosphere material was determined by a helium gas displacement technique on the basis of the volume of the sample not penetrated by helium. An Auto-Pycnometer 1320 instrument was used to measure the density of a 4.02-g sample of cenospheres. A true density of 2.41 g/cm^3 was obtained.

From the measured values of true density (from He dis-

Table 4 Chemical analysis data

Elemental analysis*, percent						
C	H	N	P	S	0	Unidentified
59.1	0.76	0.62	0.025	3.81	7.14	28.6

Spectrographic analysis*, percent			
Fe	5.5	Ti	0.027
Mg	3.5	Ca	0.21
Si	0.28	Mo	0.0072
V	0.11	Sn	Trace < 0.001
B	0.0032	Cu	0.020
Al	0.34	Na	0.34
Mn	0.040	Zn	0.040
Pb	0.029	Ag	0.00068
Cr	0.12	Co	0.018
Ni	0.26	Sr	0.0044

Total identified	10.9
Loss on ignition	70.9
Unidentified	18.3

*The reported compositions do not include oxygen in any oxides.

placement) and bulk density (from Hg intrusion), and an interpreted value for interstitial space between cenospheres in the bulk samples (1.98 cm^3/g from Table 1 based on a theoretical packing factor of 0.74 and 100-μm diameter spheres) the following calculation provides an estimated volume fraction of the envelope of an individual cenosphere that is solid material. Note that volume is expressed as specific volume (i.e., cm^3/g) for the calculation.

$$\frac{\text{Solid volume}}{\text{Total envelope volume}} = \frac{1}{\text{True density}} \Big/ \left(\frac{1}{\text{Bulk density}} - \text{Interstitial space}\right)$$

$$= \frac{1}{2.41} \Big/ \left(\frac{1}{0.232} - 1.98\right)$$

$$= 0.18$$

Chemical Composition Measurements

Standard semiquantitative elemental[4] and spectrographic[5] chemical analyses of cenosphere samples yielded the compositions shown in Table 4. It is noted that the reported compositions do not include oxygen present in any oxides.

Summary and Concluding Remarks

Physical and chemical studies have been conducted to determine the structure and composition of cenospheres, the small, carbonaceous spheres produced by liquid-phase cracking of burning droplets of heavy fuel oil. The cenospheres, which burn more slowly than does the original fuel, contribute to deposits, high-temperature corrosion, emissions of particles, and reduced efficiency of combustion in oil-fired furnaces and boilers.

Examinations by optical and scanning electron microscopy showed that typical large (100–200 μm) and small (20–40 μm) cenospheres are spheroidal and hollow, and have at least one blowhole that extends from the hollow core through the shell of the cenosphere (Figs. 1–4). The sizes of the blowholes cover the range of 10–50 percent of the cenosphere diameter. The ratio of outer to inner diameter of the shell appears to be of the order of 1.3–1.4. The shells of large particles tend to be spongelike in appearance with an interconnected porous structure. The shells of the smaller particles are smoother but contain many pores of the order of a few micrometers in diameter. The solid portions of the shell in either case appear flaky or layered and the interstitial space between flakes or layers may contribute to microporosity.

Measurements of surface area and porosity distribution by mercury-intrusion porosimetry and adsorption of gases established, as expected, that the large pores contributed most to total pore volume, whereas the small pores contribute most to total surface area (Figs. 5–8). Density determinations based on mercury intrusion and helium displacement techniques indicate that a typical individual cenosphere contains only about 18 percent solid material on a volumetric basis. These observations are consistent with the hollow, porous structure established microscopically.

Chemical analyses yielded a relatively concentrated percentage content of the elements S (3.8), Fe (5.5), Na (0.3), and V (0.1) shown in Table 4 and is indicative of the potential contribution to high-temperature corrosion from cenosphere deposition on heat exchanger surfaces (Bellan and Elghobashi, 1985). The measured content of 3.5 percent Mg and 0.2 percent Ca might counteract the corrosive effects to some extent, however, as additives containing these elements are sometimes mixed with fuel oil to inhibit corrosion processes.

The results reported here are being used in developing an analytical model of cenosphere combustion that takes into account the geometric structure of the typical cenosphere (albeit in a simplified way) and the diffusion processes necessary to transport oxygen throughout the structure to the carbonaceous surfaces (Gavalas et al., 1985; Loewenberg et al., 1987). Insights gained from such a model hold promise of guiding future efforts to enhance the burnout of cenospheres within a furnace or boiler and thus reduce their deleterious effects on corrosion, emissions, and combustion efficiency.

Acknowledgments

The authors acknowledge the able contributions of Dr. George R. Gavalas of the California Institute of Technology in selecting the various characterization studies, in interpreting the results, and in carrying out modeling activities. The work described in this paper was carried out in the Applied Technologies Section of the Jet Propulsion Laboratory, California Institute of Technology, and was supported by the U. S. Department of Energy, Office of Energy Utilization Research, Energy Conversion and Utilization Technologies Program, Mr. Marvin Gunn, Jr., Program Manager, through an interagency agreement with the National Aeronautics and Space Administration.

References

Bellan, J., and Elghobashi, S., 1985, "Fuel Composition Effects on High Temperature Corrosion in Industrial/Commercial Boilers and Furnaces: A Review," ASME JOURNAL OF ENGINEEIRNG FOR GAS TURBINES AND POWER, Vol. 107, pp. 744–757.

Brunauer, S., Emmett, P. H., and Teller, E. J., 1938, "Adsorption of Gases in Multimolecular Layers," *J. Am. Chem. Soc.*, Vol. 60, pp. 309–319.

Gavalas, G. R., Loewenberg, M., Bellan, J., and Clayton, R. M., 1985, "Structure and Oxidation of Carbonaceous Cenospheres," AIChE Annual Meeting, Chicago, IL, Nov. 10–15, Paper No. 30d.

Jacques, M. T., Jordan, J. B., Williams, A., and Hadley-Coates, L., 1976, "The Combustion of Water-in-Oil Emulsions and the Influence of Asphaltene Content," *Sixteenth International Symposium on Combustion*, pp. 307–319.

Lightman, P., and Street, P. J., 1968, "Microscopical Examination of Heat Transfer Pulverized Coal Particles," *Fuel*, Vol. 47, pp. 7–28.

Loewenberg, M., Bellan, J., and Gavalas, G. R., 1987, "A Simplified Description of Char Combustion," *Chemical Engineering Communications*, Vol. 58, pp. 89–103.

Marrone, N. J., Kennedy, I. M., and Dryer, F. L., 1984, "Coke Formation in the Combustion of Isolated Heavy Oil Droplets," *Combustion Science and Technology*, Vol. 36, pp. 149–170.

Michael, M. I., and El-Wakil, M. M., 1967, "On the Self Ignition of Hydrocarbon Mixtures," *Eleventh International Symposium on Combustion*, pp. 1027–1035.

Newell, H. E., and Sinnatt, F. S., 1924, "The Carbonisation of Coal in the Form of Fine Particles—I. The Production of Cenospheres," *Fuel*, Vol. 3, pp. 424–434.

[4]Performed by Galbraith Laboratories, Inc., Knoxville, TN.

[5]Performed by Pacific Spectrochemical Laboratory, Inc., Los Angeles, CA.

On the Control Methods of Atmospheric Fluidized Bed Boilers for Power Generation

A. Kaya
Professor,
The University of Akron,
Akron, OH 44325

H. I. Sternberg
Senior Market Manager,
Bailey Controls Co.,
Wickliffe, OH 44092

This paper deals with the state of the art of controlling atmospheric fluidized bed steam generators. The emphasis has been placed on multivariable control to provide optimum performance within environmental constraints. A general multivariable model structure is used. The specific model parameters are determined from actual input-output relations (process reactions). Control and optimization methods for commercially implementable controls are presented. The usage of feedback, feedforward, cascade, and decoupling controls is discussed for the general model. A comparison is made between the proposed controls and those used for conventional boilers to identify areas where particular caution must be exercised in dealing with atmospheric fluidized bed boilers. The implementation and computational capabilities including the current challenges and the needs for further work are presented.

Introduction

Fluidized bed reactors are widely used in chemical and metallurgical industries, with applications such as material transportation, absorption, heating, and catalytic gas/solid reactions (Schlingman, 1979). Although the first commercial fluidized bed was introduced by Fritz Winkler in 1922 for powdered coal gasification, the state of knowledge relative to the modeling of fluidized beds is still modest.

Development of Fluidized Bed Boilers. All fossil fuel burners in energy converters face both cost and environmental problems. Relatively clean-burning fuels such as gas and oil are expensive and their supply is uncertain.

The current challenge is to be able to burn low quality coal, farm products, industrial and municipal waste, and other hydrocarbons with high efficiency and yet fully satisfy environmental constraints.

In addition to wet scrubber applications, fuel gas desulfurization processes have been considered (Ziegler and Meyers, 1979).

This frustration has supported the search for new processes to meet environmental challenges. One such new application has been to bring the scrubbing and combustion unit processes together into a single fluidized bed. Although the results of atmospheric fluidized bed boiler (AFBB) performance are promising, with regard to pollution performance, there are control problems under load and other disturbances. The most important control related issue has been to provide a relatively constant bed temperature to maximize the SO_x removal under wide load variations.

Current AFBB design challenges are; improved controllability, faster response, increased turn-down ratio, increased capacity, and higher unit availability. The variety of designs have been summarized by Makansi and Schwieger (1982). Figure 1 describes a typical AFBB. The boiler is equipped with FD and ID fans, air heaters, etc., which are not shown. For a fundamental development of the control system, Fig. 1 is sufficient.

Performance Requirements and Control Concepts. The main requirement is that the steam output must be modulated responsively while maintaining high efficiency and satisfying environmental limits. There are many variables that must be regulated and exogenous disturbances that must either be compensated for or rejected by advanced control methods. A major issue is the decoupling of combustion and heat transfer, Btu/h, since the temperature must be constant under varying heat transfer (load) conditions.

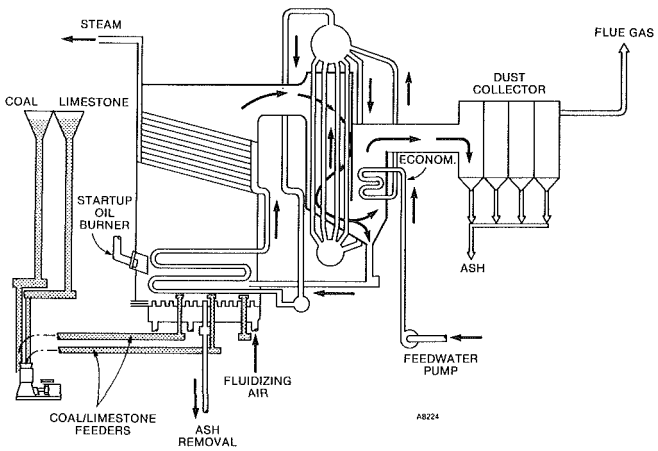

Fig. 1 Schematic of a typical AFBB

Contributed by the Power Division and presented at the Industrial Power Conference, Atlanta, Georgia, October 25–28, 1987. Manuscript received at ASME Headquarters July 8, 1988.

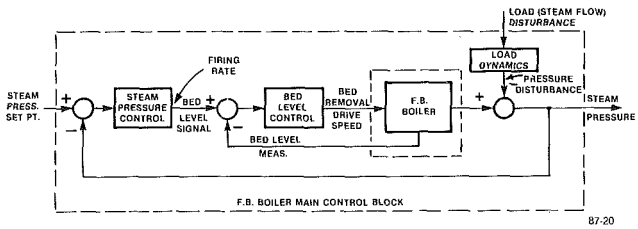

Fig. 2 Feedback control of primary process variable (steam pressure)

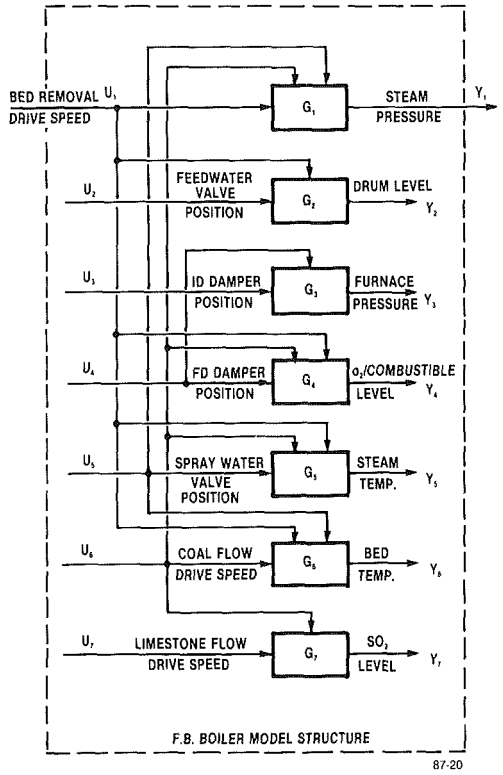

Fig. 3 Major process variables and their interaction in an AFB boiler

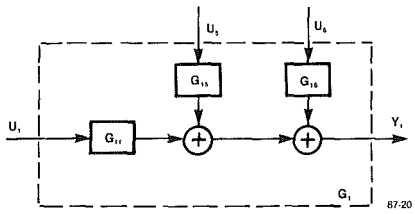

Fig. 4 Internal structure of blocks in Fig. 3 (shown for block G_1)

The specific task is to develop a model for AFBB process and the control functions for its most efficient (optimum) operation. Control diagrams will be generated that are implementable by distributed microprocessors. Furthermore, some selected control functions for solids circulating boilers will be presented.

Control Development for Load Control of AFBB

In conventional steam boilers the boiler load is varied by the fuel flow rate to maintain the header steam pressure. Figure 2 shows a conceptual and simplified block diagram for AFBB load control. This diagram is similar to that for conventional boilers except the boiler load is varied by changing the bed level. Now consider Fig. 2 and a load control concept based on the "boiler following" principle. As the steam valve for the cogeneration turbine or process conduit opens (load disturbance), the steam pressure drops. The pressure control reacts to restore the pressure. The signal from the pressure control block is named as the firing rate and is set point for bed level. This signal is compared with the actual bed level measurements and the error corrects the bed level to the set point through the bed level control (a cascade control loop). The output of bed level control is the bed removal speed signal. This signal is the set point for bed removal speed. It is a good practice to compare this set point signal with the actual bed removal speed and correct the speed to the set point (another cascade loop).

Decreasing the bed removal speed increases the bed level, which increases the heat transfer surface of tubes within the bed. The heat flux for in-bed tubes is four times that of tubes above the bed. The increased heat transfer causes increased steam generation. The preceding phenomena upset the values of other process variables such as drum level, O_2 level, steam temperature, and bed temperature. The variation from desired values causes poor boiler efficiency and safety problems. The main issue is to maintain the pressure and all other process variables at their desired values under varying loads. To develop a control system to meet such requirements, we start with a model structure of AFBB and demonstrate how this model can help the control engineer to design, improve, and evaluate the control system.

Structure of AFBB Dynamics. Figure 3 describes the structure of an AFBB model where major input and process variables are shown. Furthermore, the effects of input variables on process variables are indicated. There are seven major input variables and the same number of corresponding process variables they control. The blocks are the transfer functions in Laplace domain when the dynamics is described by a linearized system model.

Now, the AFBB dynamics can be represented by a transfer function matrix

$$GU = Y \tag{1}$$

where each element in equation (1) is described by equation (2). Note that the interactions between the input variables and the outputs variables rather than what they control are described by off-diagonal terms.

$$\begin{bmatrix} G_{11} & 0 & 0 & 0 & G_{15} & G_{16} & 0 \\ G_{21} & G_{22} & 0 & 0 & 0 & 0 & 0 \\ 0 & 0 & G_{33} & G_{34} & 0 & 0 & 0 \\ G_{41} & 0 & 0 & G_{44} & 0 & G_{46} & 0 \\ G_{51} & 0 & 0 & 0 & G_{55} & G_{56} & 0 \\ G_{61} & 0 & 0 & 0 & G_{65} & G_{66} & 0 \\ 0 & 0 & 0 & 0 & 0 & G_{76} & G_{77} \end{bmatrix} \begin{bmatrix} U_1 \\ U_2 \\ U_3 \\ U_4 \\ U_5 \\ U_6 \\ U_7 \end{bmatrix} = \begin{bmatrix} Y_1 \\ Y_2 \\ Y_3 \\ Y_4 \\ Y_5 \\ Y_6 \\ Y_7 \end{bmatrix} \tag{2}$$

(i.e., the interactions between U_5, U_6, and Y_1 by G_{15}, G_{16} respectively as shown in Fig. 4).

Referring to Fig. 2, the control signal to restore the steam pressure changes the value of the bed removal speed, which in turn disturbs the values of process variables Y_2, Y_4, Y_5, and Y_6. Then input signals U_2, U_4, U_5, and U_6 vary to restore those disturbed values. Furthermore, the variation in U_4 disturbs the process variable Y_3; the variable U_6 affects the value Y_7 and Y_1.

The model elements G_{ij} can be determined either by analytical derivations, which is an involved process or by experimental reaction curves. For the experimental approach, it is possible to give a step change to one of the input elements of u and find its effect on each element of output y. Then, specifically the effect on the output y_6 by the input u_5 determines the model element G_{65}. There are sufficient methods available in the literature to find the transfer function G. Some of them are: frequency response methods, reaction curve approximation methods, etc.

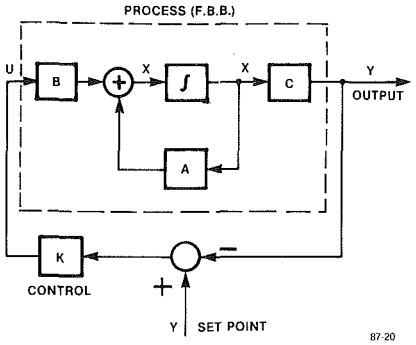

Fig. 5 Output feedback control design for multivariable system (note: variables and parameters are in vector and matrix form)

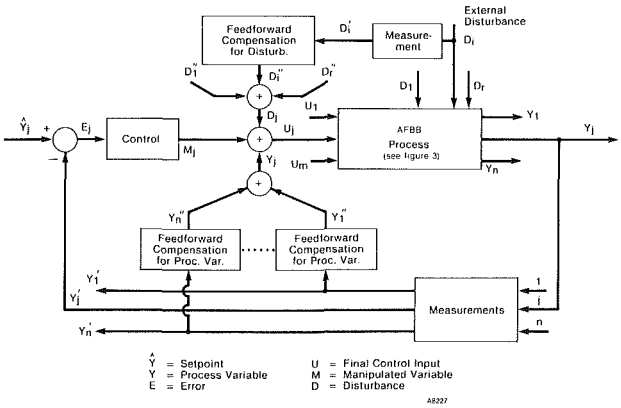

Fig. 6 Typical block diagram for AFBB control system

The combination of the model, the control techniques, and the performance requirements become the basis of control design for the control engineer. The interactions in model require that all major variables must be controlled at their desired values with a minimum deviation (error), and meet the load demand. The control techniques considered are described below.

Control Philosophy and Methods. There are two main approaches available:

1 State space control: a uniform method by which the boiler dynamics is described as a set of first-order differential equations with multiple variables in state space forms. The pole placement control design is pursued (Brogan, 1974) to deliver the expected performance.

2 Advanced process control: feedforward, decoupling, cascade control methods are utilized and a physical insight to the problem is maintained.

State Space Control Approach. This approach is uniform, and that is the only advantage. The number of variables may become very extensive as described in the Appendix. The method of derivation of the state space equations from the system matrix G (equations (1) and (2)) is described in the appendix for a simple case. That is, a state space form for matrix G is readily available similar to equation (A.6) except higher dimensions. The control problem is defined as follows: Given the state space equations similar to that in equation (A.6) in the appendix, design a feedback control K (an $r \times m$ matrix), as in Fig. 5, such that the system output Y changes as desired by the performance specifications of the AFBB. The design procedure of control matrix K is given by Brogan (1974). The pole placement method provides a specified closed-loop transient response (time constant) of each variable in the Y vector when it responds to a step change in setpoint input or disturbance.

The main problem with this approach is that no insight into the physical system is provided and number of variables may be very large. Furthermore, there is no applicable procedure when time delays are present in transfer function blocks. More work is needed to implement this technique in industry.

Advanced Process Control Approach. A typical control system is described in Fig. 6 in block form. Note that the AFBB already described in Fig. 3 is shown as a simple block where U is the input (controls), and Y is the output (process variables). The external disturbances are shown in D'. A process variable in Y is usually regulated by a feedback control loop and through a control variable in U. Variations to this convention are possible. That is, a process variable may be measured to regulate the other process variables as shown by the elements of Y''. External disturbances are those process inputs that may be measured, but may not be regulated by a feedback loop directly. These are compensated for by the elements of D''. The effects of external disturbances (the elements of D) on the process variables (the elements of Y) are found by the same method as G. There are variations to Fig. 6. It is possible that the output of compensations can be used to modify the set points instead of the manipulated variables, M. Also, the error E is frequently used as an input instead of the measurements, Y, into the control compensator. These variations are a matter of practical choice by the designer. In developing Y'' and D'' the feedforward compensation techniques are utilized. In developing the controller values M, the feedback control techniques are utilized.

Studies of modeling of AFBB for transient and steady state have been made by Schlingman et al. (1979), Bliss (1977), Datta and Rovnak (1978), and Ray et al. (1980). These studies are useful for design and development of AFBB. However, the control engineer is charged with designing and tuning a control system for an existing boiler. The modeling by the process reaction becomes more practical and is often exercised in industry. Referring to Fig. 6, the control inputs U drive the process variables. An input U will act as a control for a Y of the same control loop; but it will act as a disturbance for all other Y values either directly or through the process variable it controls. Such effects are described by the couplings in Figs. 3 and 4. Where the off-diagonal coefficients are significant (see equation (2)), the interaction must be accommodated with either feedforward compensation (Fig. 6) or by decoupling. External disturbances, such as variations in fuel, sorbent properties, and combustion air, can be compensated for as long as their effect on process variables are predicted. In this approach a good physical insight into the process structure exists. The control system can be designed at any degree of sophistication such as starting with feedback control and extending it into feedforward, cascade, decoupling, etc. Control loops can be individually tuned. Each control loop operates on its own and interacts with the other loops. Industry has been using this technique and will continue to do so. The action in the primary (pressure) control loop, as a result of load demand change, causes disturbances in other process variables. For a reliable performance, the other process variables are feedback controlled as well. Those other loops are called secondary loops. Within these secondary loops there are minor loops for "metering" the control values.

This approach of control philosophy has a good insight into the dynamic behavior of the process, and it is currently implemented in conventional boilers in industry. An experienced control designer saves on the control equipment by simplifying the compensations. This is accomplished by knowing the chain effects of the controls and the interactions between the process variables as described in Figs. 3 and 4. In the following section, the control of each process variable indicated in Fig. 3 will be described by the methods structured in Fig. 6. Attempts

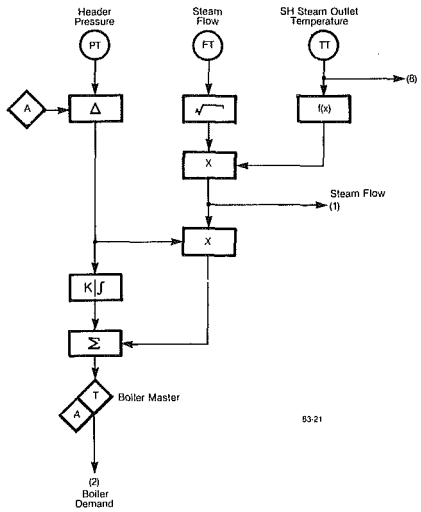

Fig. 7 Boiler master (steam pressure control loop)

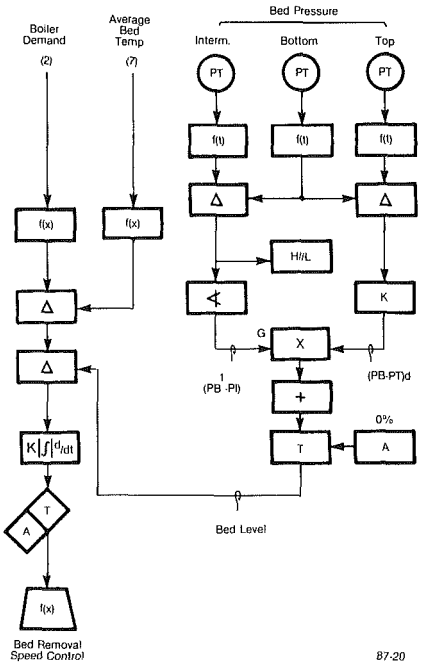

Fig. 8 Bed level control (steam pressure control loop)

will be made to tie the control logic to the model and the control structure.

Control Systems for AFBB

Based on the philosophy of advanced process control, the logic diagrams are developed in SAMA[1] symbols, which are widely used in the power industry and highly self explanatory.

Control Logics for a Typical AFBB. Referring to Fig. 3, there are seven feedback control loops, steam pressure control being the primary (outer) loop. The logic diagrams for those control loops, which are significantly different from conventional boilers, will be described here. The detailed explanations will be limited since the logic diagrams are self-explanatory.

Steam Pressure Control. Figures 7 and 8 describe the control logic. The boiler demand signal developed in Fig. 7 is used to control the bed removal speed (per Figs. 2 and 3) as described in Fig. 8. A signal is developed in Fig. 7 from steam pressure, and steam flow along with steam temperature for the account of Btu as a true demand signal. Here, the inclusion of steam temperature is also a compensatory (feedforward) signal to represent the interaction from the spray water valve position. The pressure error signal added to the compensated steam flow makes up the boiler demand signal. This signal becomes a set point for the bed level (Fig. 8). Due to interaction from the coal flow, the bed temperature is included to represent the coal flow as a compensation (feedforward) signal in developing the bed level setting. The bed level measurement is developed as shown in Fig. 8, and compared with the bed level setting to result in a signal for bed removal speed control mechanism.

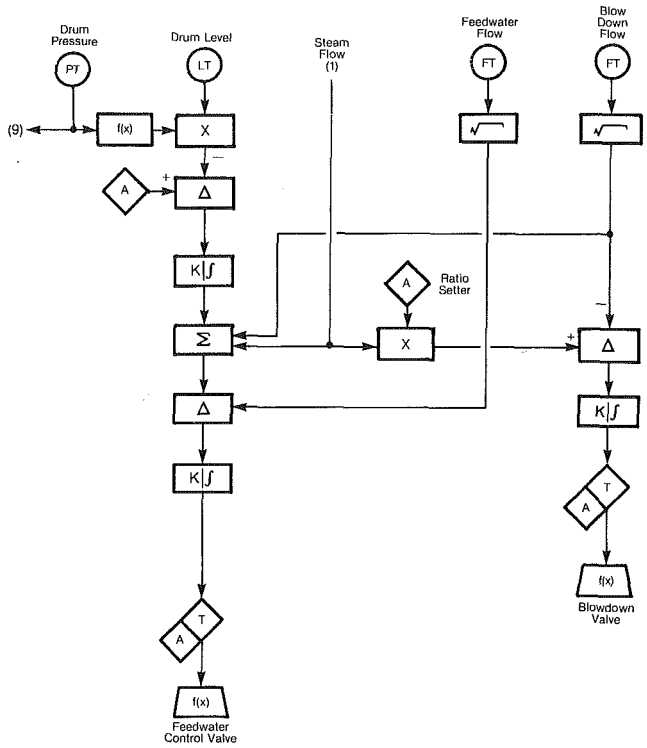

Fig. 9 Drum level control

Referring to the interaction in Fig. 3 and the matrix G in equation (2), the effects of steam temperature and the average bed temperature are included as compensation. Note that such compensatory signals come from the process values rather than the control signals. This choice was discussed along with the description of Fig. 6. Besides the pressure control loop, there are other inner loops, such as bed level and bed removal speed control.

Drum Level Control. Figure 9 describes the control logic. The drum level transmitter has drum pressure compensation. The steam flow and blowdown act as a feedforward compensation for the effect of boiler load. This compensation is in concurrence with the interaction from the bed removal speed signal (Fig. 3) as reflected by the boiler load (steam flow). The feedwater flow control is an inner loop to meter the flow of feedwater. The feedwater control valve is the final control element (Fig. 3).

Furnace Pressure Control. The control logic is described in Fig. 10. Only air flow compensation is needed as feedforward provided by the air flow demand signal in lieu of FD damper position. Several transmitters with high-low monitors are provided for safety interlocks. ID fan damper position is

[1] Scientific Apparatus Makers Association.

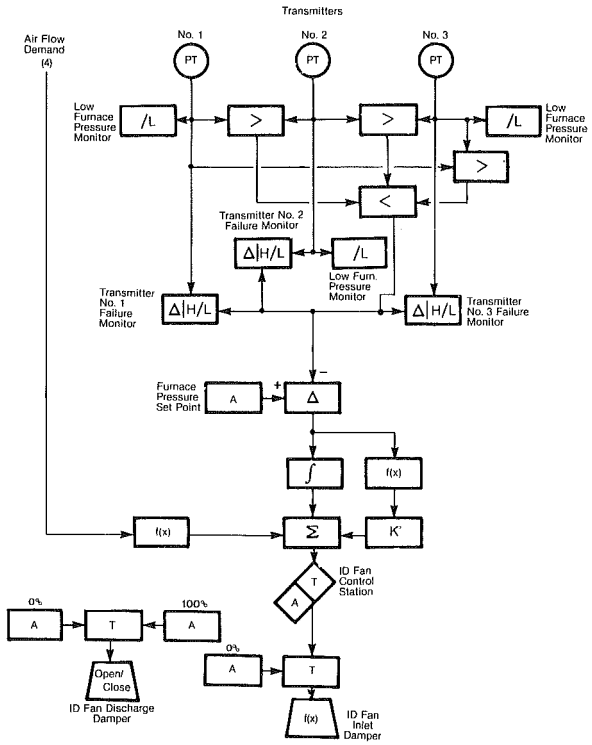

Fig. 10 Furnace pressure (draft) control

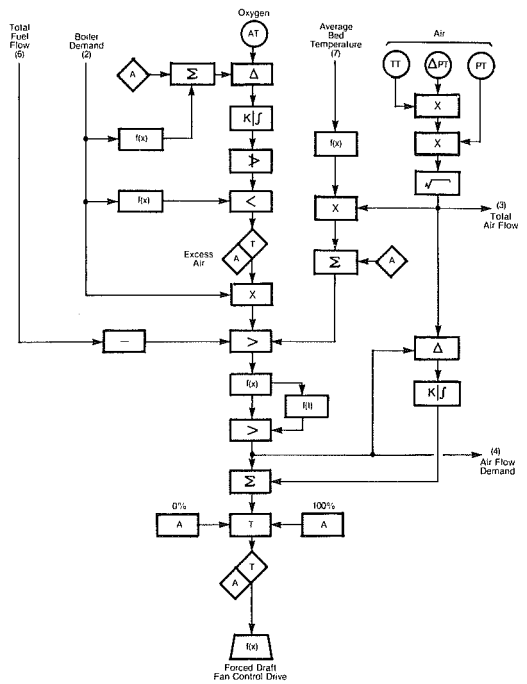

Fig. 11 Air flow control (O_2 control loop)

the final control element. The other details, such as low furnace pressure and transmitter failure monitors, are self-explanatory. These are included for safety.

Combustion Control by O_2. Figure 11 is the description of O_2 control loop. The O_2 level is affected by the load (bed level) due to the interaction from bed removal speed. It is also affected by the fuel flow, which can be represented by the bed temperature signal. The boiler demand signal, which is an indicator of the load, modifies the O_2 setting for and optimum combustion efficiency with respect to boiler load. In addition,

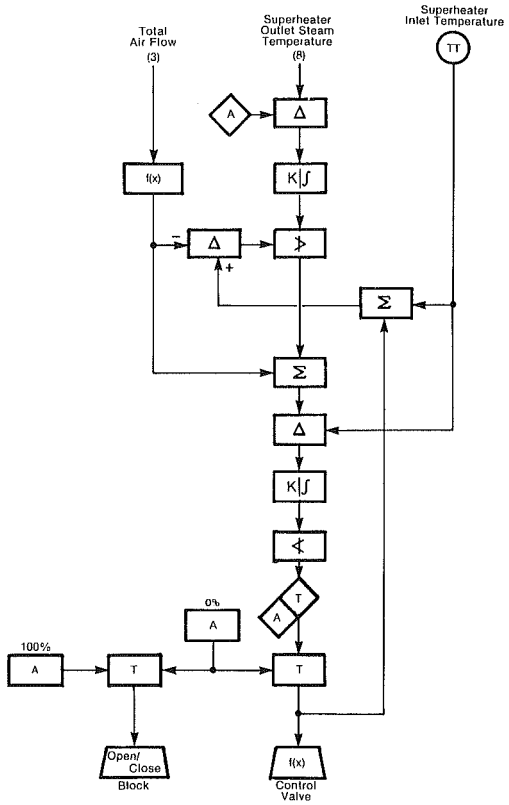

Fig. 12 Superheater steam temperature control

the cross limiting between fuel and air flow is provided to avoid the unburned combustibles under transient conditions. The low and high selectors provides cross limiting. Furthermore, the inner loop for the air flow metering is also provided. FD damper position is the final control element (Fig. 3).

SH Steam Temperature Control. The steam load (or bed removal speed) and the bed temperature (or fuel flow) variations should be compensated for. Figure 12 describes the control diagram. The total air flow can be an indication of the boiler load (bed level) as well as the fuel flow which is an indicator of the bed temperature. The total air flow compensation is satisfactory for this control loop. The inlet SH steam temperature is accounted for as an anticipatory provision to modify the control signal for spray valve.

Bed Temperature Control. The bed temperature is controlled by fuel (coal) feeders as described in Fig. 13. Bed temperature is affeced by the interactions from bed removal speed and spray valve position, which are indicators of boiler load and steam temperature, respectively (Fig. 3). The steam flow signal along with its Btu correction provides the modification for the set point. The boiler demand signal maintains an equilibrium during steady state. The steam flow signal helps the bed temperature change in the same direction as the load demand signal, during transients. Fuel feeder flows are measured and fed back for a tight control. Cross limiting (low selector) is also provided between the boiler demand (load) and air flow to avoid unburned combustibles. The control signals for coal feeders are modified based on the number of feeders on automatic operation. The other minor details are self-explanatory.

Emission Control (SO_2). The bed temperature is controlled for optimum conditions to minimize SO_2 emission. Now, the limestone feed should be manipulated to control the SO_2 at a given level as described by the control loop in Fig. 14. The control loop is compensated by the fuel flow due to the in-

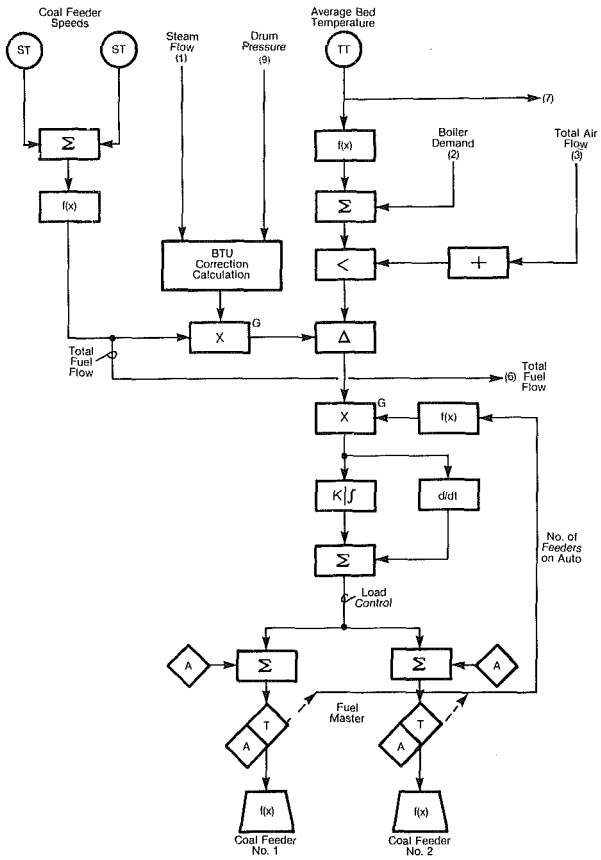

Fig. 13 Coal feeder control (bed temperature control loop)

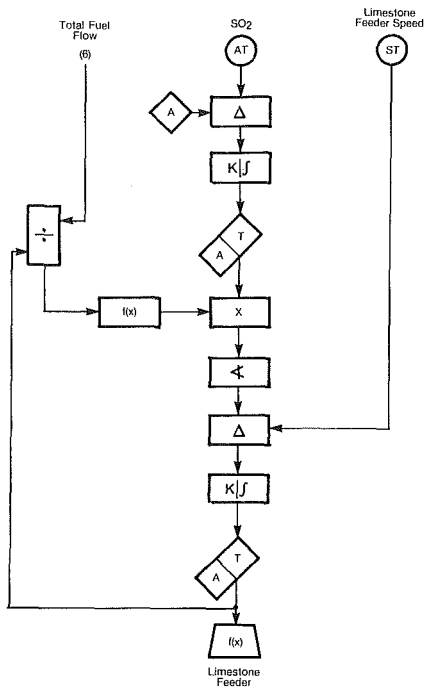

Fig. 14 Limestone feeder control (SO_2 control loop)

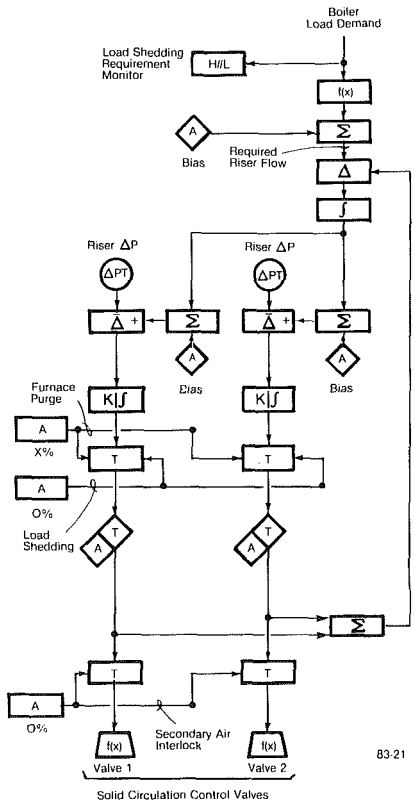

Fig. 15 Solid circulation (riser) control (one per segment)

teraction from coal flow signal. While a ratio of coal/limestone is kept as a target value, this ratio can be modified by the sulfur content of the fuel. Furthermore, the limestone feeders are metered by an inner (cascade) loop control. The diagram is simple and self-explanatory.

Control Logics for a Circulating FBB. Fine solid material is circulated throughout heat absorbing surfaces, and returned to the fluidized bed via a downflow channel sloped at the end to impart a horizontal velocity, while tossing it across the surface of the bed (Keyes et al., 1983). Thus, the bed is continuously circulated, achieving the important lateral mixing.

The entire shell, including the solids riser, is enclosed by waterwalls. There are no steam tubes in the bed; rather, superheating and steam generating take place in a convection section above the bed.

The main features, different from a conventional FBB, are as follows:

1 No tubes immersed in the fluidized bed;

2 The rapid control of the rate of solids flow provides a fast response to load changes, as well as wide range of load control.

3 All solid waste products are finely ground in the bed and separated from the flue gas by filters in the baghouse.

It is the heat transfer in the riser and return channel that distinguishes the circulating FBB from conventional FBBs. The bed temperature is maintained by the coal feed rate. The steam generation is modulated by varying the velocity of solids to the riser. There may be multiple risers (segments) that can be operated independently (in series or in parallel). There are various circulating FBB designs based on the manufacturer preference.

Only those control loops particular to circulating FBB will be discussed in the following.

Steam Pressure Control. Boiler demand development is quite similar to that shown in Fig. 7. The boiler demand is used to control the solid circulating valves to modulate the solids flow through the risers. The control logic is shown in Fig. 15. Note that for the conventional FBB (Fig. 8), the bed removal speed was controlled to modulate the bed level. Since the secondary air is used for risers for circulating FBB, the

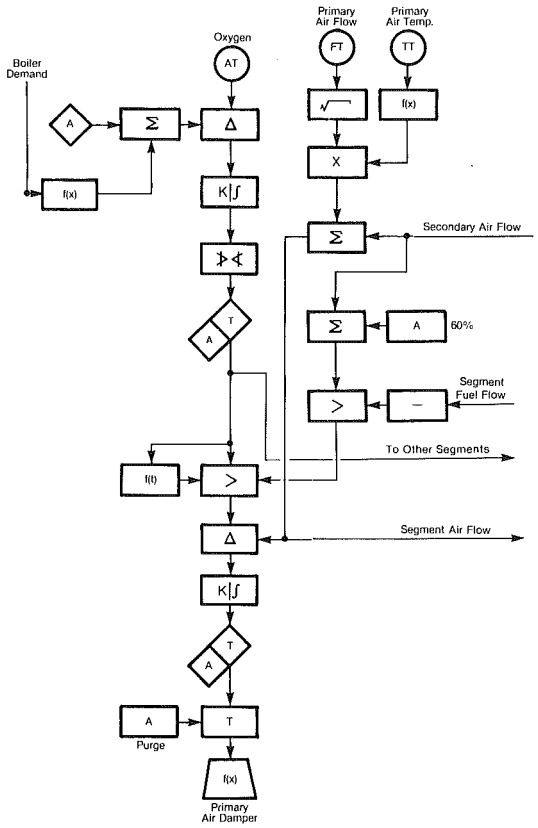

Fig. 16 Primary air flow (O_2) control (one per segment)

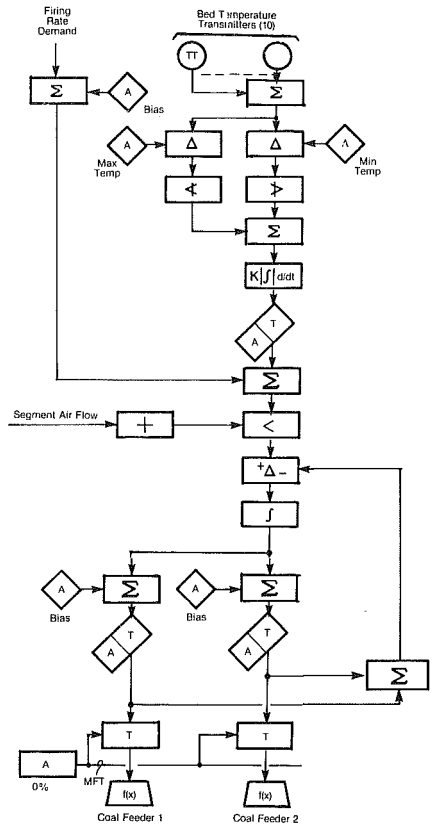

Fig. 17 Coal flow (bed temp.) control (one per segment)

riser pressure drop is taken into account along with safety interlocks. Other features such as load shedding and furnace purge are also shown.

Combusion Control by O_2. A control diagram is shown in Fig. 16. Combustion control is similar to those for the conventional AFBB (Fig. 11). However, provisions for multiple segments should be made and the secondary air flow should be coordinated. Primary air is used for bed combustion while the secondary air is for circulation. Again, boiler demand develops into O_2 setting. Secondary air flow acts as feedforward compensation. Segment fuel flow is used for cross limiting (high selector) to prevent unburned combustibles. Furthermore, another high selector downstream insures no unburned combustibles during upset conditions.

Bed Temperature Control. Bed temperature is controlled by fuel (coal) flow as shown in Fig. 17. Here, the firing rate signal acts as a feedforward compensation signal for coal feeders, since it will increase the heat transfer from the bed, which in turn affects the bed temperature. The segment air flow is used for cross limiting (low selector) to prevent unburned combustibles.

Implementation

Distributed Microprocessor System. The control logics of function blocks, which are customarily used in the control industry. These function blocks are implemented by a distributed microprocessor system having the most advanced features (Baily Controls, 1988). In this microprocessor system, each processing element is dedicated to performing some specific functions just as in the case of analog and sequential control systems. These elements are then linked to form a completely integrated process control system having a distributed architecture. The best features of both analog and digital systems are combined in this system. In addition, the

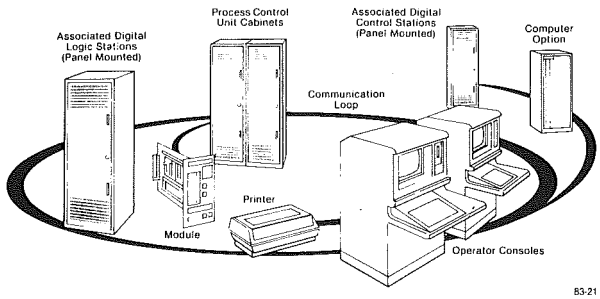

Fig. 18 NETWORK 90® system architecture

system has its own advantages. The system can interface with a computer as well.

Several features of the distributed microprocessor system are:

1 Failure of a processing element does not cause the system to shut down.

2 No programming is required; the control functions are configured easily.

3 The accuracy and flexibility features of digital algorithms are maintained.

4 Computing elements run in parallel without the drawbacks of a serial centralized computer.

5 Distributed computation is performed quickly without any communication problem as opposed to a central processor.

6 Wiring costs are greatly reduced.

7 A CRT is used instead of a panelboard, resulting in savings in control room size and cost.

The detailed information of implementing the control logics with a plant-wide coordination is given by Lukas and Smeallie (1982).

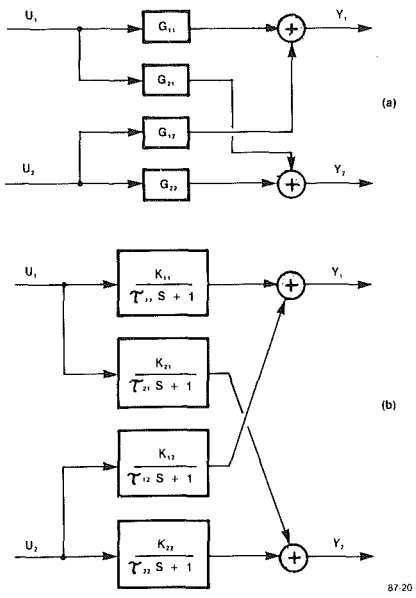

Fig. A1 Simple two-variable input/output model for state space analysis

The architecture of the distributed system is shown in the diagram in Fig. 18.

Conclusions

Systems Engineering methods have been demonstrated in controlling fluidized bed boilers. Modeling, control design, and implementation (by current devices) were the major steps. The challenges in control for efficiency and to meet pollution requirements are summarized.

The recent design and development activities are aimed mostly at overcoming current control problems and improving the process. With new designs and with the help of the current distributed microprocessor systems, FBB Technology will advance very rapidly.

References

Bailey Controls Co., 1988, *NETWORK 90 Product Specification and Application Guide*, Wickliffe, OH.

Bliss, C., 1977, "A Comparison of Conventional Oil-Fired and Fluidized Bed Coal-Fired Petroleum Refinery Atmospheric Crude Furnaces," *Proceedings of the 5th International Conference on Fluidized Bed Combustion*, Vol. II.

Brogan, W. L., 1974, *Modern Control Theory*, Quantum Publishers, New York, Chap. 16.

Datta, S., and Rovnak, J. A., 1978, "Assessment of Load Response Capability and Control Philosophy for a Power Plant Using an Atmospheric Fluidized Bed Boiler," *Proceedings of ISA 1978 Annual Conference*, pp. 137–147.

Keyes, M. A., et al., 1983, "Applications of Systems Engineering to Control Fluidized Bed Boilers," *Proceedings of the First International Fluidized Bed Combustion Symposium*, Beijing, People's Republic of China, Aug.

Lukas, M. P., and Smeallie, W. H., 1982, "Microprocessor-Based Distributed Control Systems in the Modern Power Plant," Edison Electric Institute Engineering Computer Forum, Denver, CO, Sept.

Makansi, J., and Schwieger, R., 1982, "Fluidized Bed Boilers," *Power*, Aug., special report.

Ray, A., et al., 1980, "Nonlinear Dynamic Model of a Fluidized-Bed Steam Generation System," ASME JOURNAL OF ENGINEERING FOR POWER, Vol. 102, pp. 202–208.

Schlingman, H., et al., 1979, "On-Line Process Control of a Fluidized Bed Reactor With Non-catalytic Gas/Solid Reaction," *Computers and Chemical Engineering*, Vol. 3, pp. 53–58.

Ziegler, E. N., and Meyers, R. E., 1979, "Control Technology for Coal-Fired Combustion in Northeastern U.S.," *Water, Air, and Soil Pollution*, Vol. 12, pp. 335–369.

APPENDIX

Dimensionality of State Space Approach

In order to estimate the number of state variables to be dealt with, a case of a simple example for a two input–two output process, as in Fig. A1(*a*), is worked out. The transfer function is described by

$$\begin{bmatrix} G_{11} & G_{12} \\ G_{21} & G_{22} \end{bmatrix} \begin{bmatrix} u_1 \\ u_2 \end{bmatrix} = \begin{bmatrix} y_1 \\ y_2 \end{bmatrix} \tag{A1}$$

Consider the simple first-order dynamics for each block as in Fig. A1(*b*). Define state variables x at the output of each block. The relations are written as

$$\left.\begin{aligned} x_{11} &= (K_{11}/\tau_{11})u_1 - (1/\tau_{11})x_{11} \\ x_{21} &= (K_{21}/\tau_{21})u_1 - (1/\tau_{21})x_{21} \\ x_{12} &= (K_{12}/\tau_{12})u_2 - (1/\tau_{12})x_{12} \\ x_{22} &= (K_{22}/\tau_{22})u_2 - (1/\tau_{22})x_{22} \end{aligned}\right\} \tag{A2}$$

The description in matrix form is

$$\underbrace{\begin{bmatrix} \dot{x}_{11} \\ \dot{x}_{21} \\ \dot{x}_{12} \\ \dot{x}_{22} \end{bmatrix}}_{\dot{x}} = \underbrace{\begin{bmatrix} -\frac{1}{\tau_{11}} & 0 & 0 & 0 \\ 0 & -\frac{1}{\tau_{21}} & 0 & 0 \\ 0 & 0 & -\frac{1}{\tau_{12}} & 0 \\ 0 & 0 & 0 & -\frac{1}{\tau_{22}} \end{bmatrix}}_{A} \underbrace{\begin{bmatrix} x_{11} \\ x_{21} \\ x_{12} \\ x_{22} \end{bmatrix}}_{x}$$

$$+ \underbrace{\begin{bmatrix} \frac{K_{11}}{\tau_{11}} & 0 \\ \frac{K_{21}}{\tau_{21}} & 0 \\ 0 & \frac{K_{12}}{\tau_{12}} \\ 0 & \frac{K_{22}}{\tau_{22}} \end{bmatrix}}_{B} \underbrace{\begin{bmatrix} u_1 \\ u_2 \end{bmatrix}}_{u} \tag{A3}$$

For the output, in terms of state variables,

$$\left.\begin{aligned} y_1 &= x_{11} + x_{12} \\ y_2 &= x_{22} + x_{21} \end{aligned}\right\} \tag{A4}$$

$$\underbrace{\begin{bmatrix} y_1 \\ y_2 \end{bmatrix}}_{y} = \underbrace{\begin{bmatrix} 1 & 0 & 1 & 0 \\ 0 & 1 & 0 & 1 \end{bmatrix}}_{C} \underbrace{\begin{bmatrix} x_{11} \\ x_{21} \\ x_{12} \\ x_{22} \end{bmatrix}}_{x} \tag{A5}$$

Then

$$\dot{x} = Ax + Bu$$
$$y = Cx \tag{A6}$$

where
$A = (n \times n)$ matrix, $n = 4$
$B = (n \times r)$ matrix, $r = 2$
$C = (m \times n)$ matrix, $m = 2$

The dimensions for the FBB are estimated as follows: The number of internal blocks in Fig. 3 is 18 (the number of terms in the G matrix in equation (2)). There is a minimum of 36 state variables to be defined with the simplest dynamics (first order) of each block. Considering the higher order dynamics, the number of variables could be extensive.

On-Line Performance Monitoring With Signal Validation and Uncertainty Estimation

Geun-Sun Auh
Senior Researcher,
LWR Fuel Division,
Korea Advanced Energy Research Institute,
Daedukdanji, Choong Nam, Korea

Methods are developed for performance monitoring of power plant components. On-line uncertainty estimation algorithms are developed. Since this can give new information about the validity of the measurements, proper use of performance monitoring can be achieved. A sequential fault detection method is introduced for the detection of small faults. This signal validation program gives an additional check for good inputs to the performance monitoring. Low-order models are solved using optimal estimation theory to get analytic measurements. The above algorithms are applied to heat transfer loops with real measurement data.

Introduction

The prime purpose of performance monitoring is to know the operating status of a plant and its components. The main obstacle, however, is lack of sufficient, precise, and accurate measurements. Because of this obstacle, plant engineers use existing instrumentation and assume that their instrumentation and plant are functioning without big problems.

On-line performance monitoring of a power plant is practical because of the availability of micro- and minicomputers. The on-line use of digital computers can help to solve the above measurement problems. Analytic models of plant components can give additional measurements, which are called analytic measurements. The analytic models provide a major tool for dealing with the uncertainty problems. The inputs to the analytic models are physical or other analytic measurements.

When there are more than two measurements of the same variable, they can be compared to validate the measurements. This process is generally termed signal validation.

Estimation of Uncertainties and Variables

The system model considered here is described by the following linear time-varying discrete and stochastic equations:

$$x(k)=A(k-1)+B(k-1)\ u(k-1)+w(k-1) \tag{1}$$

$$y(k)=C(k)\ x(k)+v(k) \tag{2}$$

where

x is an n-dimensional state vector
u is an m-dimensional deterministic input vector,
y is a 1-dimensional measurement vector, and
A, B, and C are deterministic matrices.

The zero-mean white noises of dynamic processes and measurements are represented by w and v, respectively.

Contributed by the Power Division for publication in the JOURNAL OF ENGINEERING FOR GAS TURBINES AND POWER. Manuscript received by the Power Division April 7, 1987.

The solutions (Auh, 1986) of the above equations are

$$x(k/k-1)=A(k-1)\ x(k-1/k-1)+B(k-1)\ u(k-1) \tag{3}$$

$$S(k/k-1)=A(k-1)\ S(k-1/k-1)\ A'(k-1)+Q(k-1) \tag{4}$$

$$r(k)=C(k)[x(k)-x(k/k-1)]+v(k) \tag{5}$$

$$\bar{r}(k)=(1/N)\sum_{i=0}^{N-1} r(k-i) \tag{6}$$

$$R(k)=(1/N-1)\sum_{i=0}^{N-1}[r(k-i)-\bar{r}(k)][r(k-i)-\bar{r}(k)]' \tag{7}$$

$$S(k/k)=S(k/k-1) - S(k/k-1)\ C'\ (k)\ [1/<C(k)\ S(k/k-1)\ C'(k) + R(k)>]C(k)\ S(k/k-1) \tag{8}$$

$$x(k/k)=x(k/k-1)+S(k/k)\ C'(k)/R(k)[y(k) - C(k)\ x(k/k-1)] \tag{9}$$

$$q(k)=x(k/k)-x(k/k-1) \tag{10}$$

$$\bar{q}(k)=(1/N)\sum_{i=0}^{N-1} q(k-i) \tag{11}$$

$$Q(k)=(1/N-1)\sum_{i=0}^{N-1}[<q(k-i)-\bar{q}(k)><q(k-i)-\bar{q}(k)>' - (N-1/N)<A(k-1-i)\ S(k-i/k-i)\ A'\ (k-1-i) - S(k-i/k-i)>] \tag{12}$$

where N is number of previous data sets used to estimate Q and R,

Q and R are covariance matrices of w and v,
S represents state estimation error covariance matrix, and
A' represents the transpose matrix of A.

$x(k/k-1)$ and $S(k/k-1)$ are estimates of x and S before using

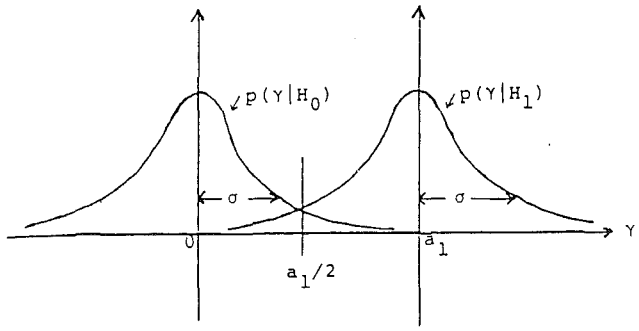

Fig. 1 Gaussian distributions of $P(\gamma|H_0)$ and $P(\gamma|H_1)$ where $P(\gamma|H_0)$ and $P(\gamma|H_1)$ denote conditional probability distribution functions of γ under hypotheses H_0 and H_1

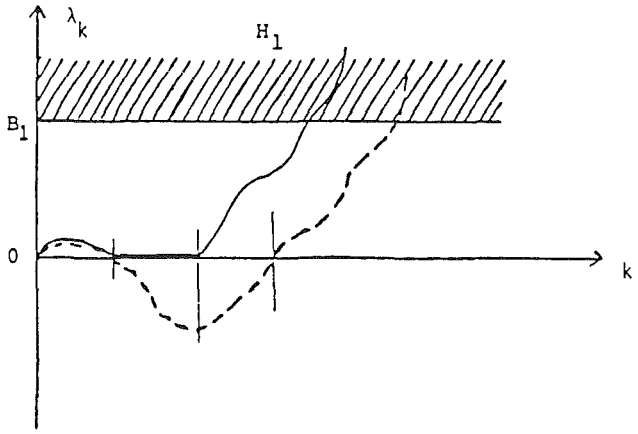

Fig. 2 Comparison of Chien's (solid line) and Wald's (dotted line) tests

the measurement information of time step k; $x(k/k)$ and $S(k/k)$ are the estimates of x and S after using the information. The above Kalman filter estimates state variables and noise variances simultaneously. This makes it possible to calculate variable uncertainties on-line.

When a system model can be described by the following equations, equations (3)–(12) can be applied:

$$P(k)=0.9P(k-1)+T(k-1)+w(k-1) \tag{13}$$

$$T(k-1)=T(k)+v(k) \tag{14}$$

where P and T are, say, pressure and temperature on the system; and T are measured. Using equations (3)–(12), $R(k)$, $x(k/k)$, and $S(k/k)$ are calculated. The square roots of $R(k)$ and $S(k/k)$ are deviations of measurement $T(k)$ and estimation of pressure $P(k)$.

Signal Validation

For many applications, measurements are sequential in nature and more information is available as time goes on. The sequential hypothesis test is a mathematical tool for handling situations of this type. The test includes automatic decisions concerning the amount of data to terminate with a decision. The following theory is based on Wald's sequential probability ratio test (Wald, 1973), which is an optimal binary hypothesis test (Wald, 1948).

Chien and Adams (1976) modified Wald's test using a feedback of the likelihood ratio function to develop a linear detection system. The modified test has shorter detection time.

Hypothesis H_0 denotes normal system and H_1 failed system (Fig. 1).

Under H_0: $E(\gamma_k)=0.0$ and $E(\gamma_k\ \gamma_k')=\sigma^2$

Under H_1: $E(\gamma_k)=a_1$ and $E(\gamma_k\ \gamma_k')=\sigma^2$

where γ_k is the difference between two measurements of the same quantity at time step k,

a_1 is the mean value of the failed γ_k, and

σ is the standard deviation of γ_k under hypotheses H_0 and H_1.

The decision function λ_k has the following recursive form:

$$\lambda_0=0.0$$

$$\lambda_k=\lambda_{k-1}+a_1/\sigma^2(\gamma_k-a_1/2) \tag{15}$$

If $\lambda_k > B_1$, decide a measurement failure

If $\lambda_k < 0.0$, set $\lambda_k=0.0$

If $0.0\le \lambda_k \le B_1$, take another sample (Fig. 2).

The detection threshold B_1 is from the following expression (Chien and Adams, 1976):

$$T=\frac{2\sigma^2}{a_1^2}(e^{B_1}-B_1-1.0) \tag{16}$$

where T is a specified mean time between false alarms.

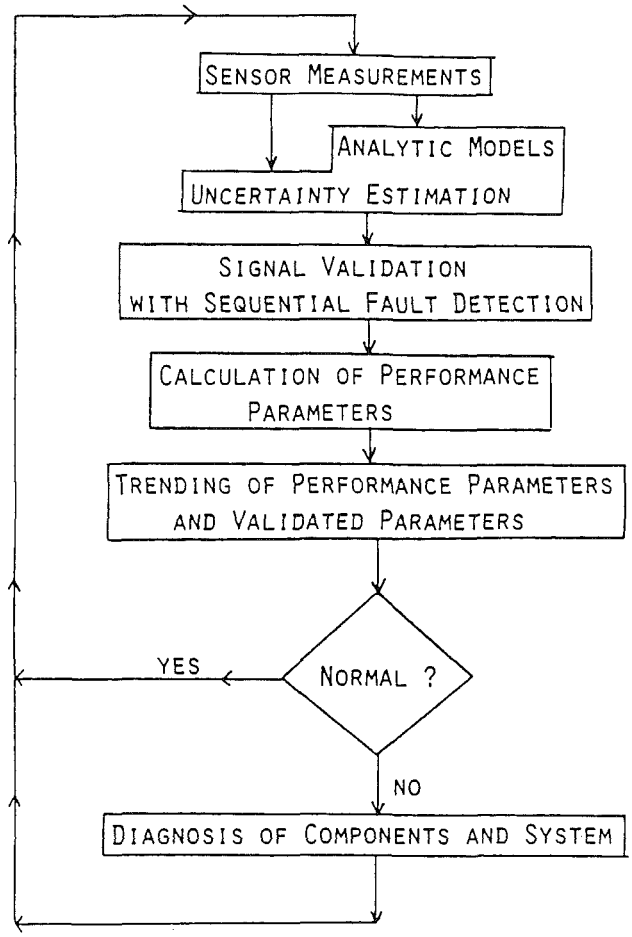

Fig. 3 Overall functional diagram

In practice, a_1 and B_1 are design parameters, and σ is from measurement characteristics. When there are two pressure measurement instruments for a steam generator, the pressure measurement can be validated using the above signal validation method. If σ, a_1 and B_1 are determined to be 65 psia, 100 psia, and 1.5 for each instrument, equations (15) are used to calculated λ_k comparing it with B_1.

Performance Monitoring

During normal operation of a plant, status is usually unknown. The actual plant can be in various states. Some component may have failed or degraded gradually to some ex-

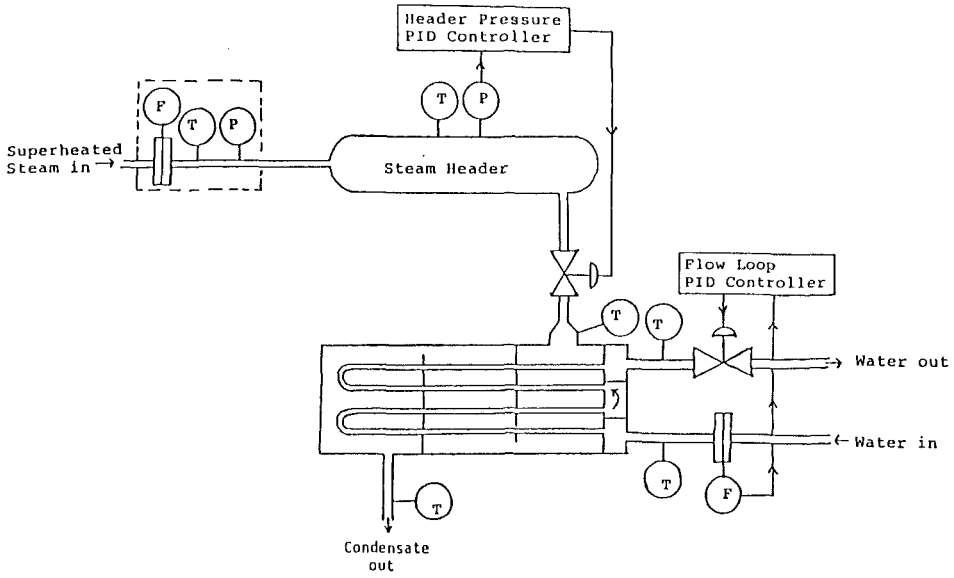

Fig. 4 Foxboro heat transfer loop

tent making the plant produce less power than designed. Other components can give failed signals even though they are functioning without problems. A good performance monitoring program should address the above situations. Such a program can give the plant personnel an accurate account of the plant. In addition, the status of plant components and various system level performances can be determined.

The ASME Performance Test Codes (PTCs) have been regarded as the most accurate measure of power plant performances, but their application cost and difficulty have precluded their use as a daily monitoring tool.

The overall process of on-line performance monitoring can be described this way (see Fig. 3). From sensor measurements and analytic models, state variables are estimated along with their uncertainties using equations (3)–(12). Faulted signals are detected through the signal validation process of equation (15). After the signal validation, we proceed to calculate the peformance parameters or indices using the validated state variables. The trends and values of these performance parameters provide indications of the system and component performances. Examples of performance parameters are thermal efficiency of a power plant and heat transfer coefficient of a heat exchanger. Note that choices of performance parameters and their definitions depend on plant specific measurements and circumstances. In relating component performance to the measured data, every effort should be made to derive performance parameters which are insensitive to the performance of other components. Deviations of the performance parameter values and key state variables can be used to diagnose the causes of degraded performances.

The overall functional diagram for signal validation, uncertainty estimation, and performance monitoring is given in Fig. 3.

Application to a Heat Transfer Loop

The Foxboro Heat Transfer Loop is shown schematically in Fig. 4. All of the indicated sensors and valves are connected to the plant computer. One possible mode of loop operation is that superheated steam goes to the steam header and then to the shell side of the heat exchanger. The inside pressure of the heat exchanger is fixed near one atmospheric pressure by admitting air from an air pusher. Cold tap water goes through the tube side of the heat exchanger to be heated. The water level on the shell side is always below the bottom of the shell for the operation of this work.

All the sensors of the heat transfer loop are used to validate signals. Three heat exchanger inlet enthalpy measurements are possible: from the orifice, steam header, and heat exchanger inlet temperature. Analytic models of the heat exchanger are used to estimate uncertainty of condensate temperature and to calculate fouling factor of the heat exchanger. Since the fouling factor is a good indication of the heat exchanges performance, it is used as a performance parameter of the heat exchanger.

By comparing two or more independent measurements of the same variable, it was possible to identify or detect small fault effects. The sequential fault detection algorithm detected the half-size fault of a single step fault detection algorithm and called the parity space fault detection algorithm (Potter and Suman, 1986).

Conclusion

Methods are developed for on-line performance monitoring of a plant. In a more general context, questions of best on-line use of given sensor complements and low-order models are answered.

The algorithms are applied to a heat transfer loop with real measurement data. The uncertainties and variables are estimated; the sequential fault detection algorithm detects small faults. It is possible to calculate the fouling factor of the heat exchanger as a performance parameter.

References

Auh, G. S., 1986, "Uncertainty Estimation and Signal Validation for Performance Monitoring of Power Plant Components," Ph.D. Thesis, Massachusetts Institute of Technology, Cambridge, MA.

Chien, T. T., and Adams, M. B., 1976, "A Sequential Failure Detection and Isolation," *IEEE Transactions on Automatic Control*, Vol. AC-21, No. 5, pp. 750–757.

Potter, J. E., and Suman, M. C., 1986, "Extension of the Midvalue Selection Technique for Redundancy Management of Inertial Sensors," *Journal of Guidance*, Vol. 9, No. 1.

Wald, A., 1973, *Sequential Analysis*, 2nd ed., Wiley, New York, NY.

Wald, A., et al., 1948, "Optimum Character of the Sequential Probability Ratio Test," *Annals of Mathematical Statistics*, Vol. 19.

J. A. Demko[1]
Assoc. Mem. ASME

G. L. Morrison
Mem. ASME

D. L. Rhode
Mem. ASME

Texas A&M University,
College Station, TX 77843

The Prediction and Measurement of Incompressible Flow in a Labyrinth Seal

Predictions and measurements were obtained for incompressible flow in a labyrinth seal for Taylor numbers of 0, 7,600, and 19,000 at an axial Reynolds number near 50,000. A hot-film anemometer with computer data acquisition was used in obtaining the measurements. The computations were made using a turbulent flow Navier–Stokes finite difference code. The QUICK differencing scheme was utilized in order to diminish false diffusion. Comparison between experiments and predictions are given for the axial and swirl velocity components and turbulent kinetic energy. Also, the substantial effect of the Taylor number on the pressure distribution is presented.

Introduction

Labyrinth seals have been used extensively to control the leakage in turbomachines. The efficiency of these seals has a significant effect on machine performance. In a gas turbine, for example, controlling the leakage between the turbine blade tips and housing has an important effect on engine efficiency (Ludwig and Bill, 1978).

Previous reviews of the available labyrinth seal leakage literature indicate that a majority of the work is related to compressible flow (Sneck, 1980; Buchter, 1980; Falseh, 1972). Most of the studies dealing with incompressible flow consider only the overall flow characteristics such as the mass flow rate for a given pressure drop across the seal. These studies rely heavily upon experimental data, which must be obtained using the specific geometry of interest. Other models utilize some idealized process with little or no emphasis on the mechanisms affecting the performance of the labyrinth seal. Better prediction of the performance of a labyrinth seal requires that these mechanisms be understood. This cannot be achieved except by investigating the flow-field details.

Measurements and predictions of the flow of water through a large scale water model were obtained by Stoff (1980). He used a straight-through seal with a rectangular-shaped cavity, which is similar to that considered in the present study. A finite difference code using pressure-velocity variables and the k–ϵ turbulence model was utilized to obtain predictions that agreed with his LDA and hot-film anemometer measurements. Swirl velocity results were presented at one axial location along with limited details about the turbulence quantities.

The flow in both a rectangular and a contoured cavity shape were predicted by Rhode et al. (1986). In that investigation, a finite difference code was developed that reduced the false diffusion error by applying a higher order differencing scheme than was used by Stoff. The verification predictions agree closely with those of Stoff and with his measurements. Also, predictions of stator wall pressure of a multicavity seal showed reasonable agreement with measurements.

The effect of Taylor number on the flow field at very low leakage rates for a rectangular cavity was given by Demko et al. (1987) and Demko (1986). When the Taylor number was increased beyond the ratio $\mathrm{Ta/Re} \sim 0.45$ a second recirculation zone formed inside the cavity. This occurrence dramatically altered the flow field, which produced a much more effective sealing, i.e. more frictional losses. However, for current practical applications this instability will not occur unless a prohibitively high shaft speed is reached.

The present study investigates the flow in a series of rectangular cavities. The geometry used in the predictions was based upon measurements of the last cavity in the test section. Measured inlet boundary conditions are used rather than assuming the flow in the cavity is streamwise periodic. Comparisons of measured velocities and turbulent kinetic energy with predictions at several locations in the cavity are presented. Comparisons of predictions with measurements are provided to assess the degree of agreement for labyrinth seal flows.

Computational Approach

The model employs the steady-state, fully elliptic Reynolds-averaged Navier–Stokes equations for turbulent flow. Closure is provided via the use of the two-equation k–ϵ turbulence model as outlined by Launder and Spalding (1974). An auxiliary relation for the effective eddy viscosity, which is based on the Boussinesq eddy viscosity concept, is utilized. It is given by

$$\mu_{\text{eff}} = \frac{C_\mu \rho k^2}{\epsilon} + \mu \tag{1}$$

The source terms for each equation and the technique used to solve the equations are presented by Rhode et al. (1986).

[1]Currently at General Dynamics, Fort Worth, TX 76101.

Contributed by the Power Division for publication in the JOURNAL OF ENGINEERING FOR GAS TURBINES AND POWER. Manuscript received by the Power Division September 30, 1987.

The k–ϵ turbulence model has been utilized for complex flows such as swirling and reacting flows by Hutchinson et al. (1976), for example. In these previous cases, disagreement between measurements and predictions was at least partially due to the fact that the model invokes an isotropic eddy viscosity, which is not entirely valid for these flows. An attempt was made to re-optimize the model constants for swirling flows by Abujelala and Lilley (1984). However, use of these new constants gave negligible change in the current predictions, so the standard set of constants was used.

Boundary Conditions. In the past, labyrinth seal simulations relied upon the assumption that the flow was streamwise periodic. Hence, the inlet values were taken as the corresponding outlet values from the previous iteration (Stoff, 1980; Rhode et al. 1986; Morrison et al., 1983). In this work, measurements were employed as inlet boundary conditions as much as possible in order to assess the predictive capability. However, there is uncertainty in these inlet measurements especially for the low swirl velocity cases. Also, various measurements at important locations near walls were not feasible with the present instrumentation. Hence a least-squares polynomial curve fit of these inlet values was employed to estimate values at the unobtainable locations. Turbulence dissipation ϵ was specified at the inlet using a turbulence length scale assumption

$$\epsilon = \frac{k^{3/2}}{0.03c} \tag{2}$$

Along solid surfaces, wall functions are introduced into the momentum equations and the turbulence energy generation terms as the appropriate boundary conditions. A detailed discussion of the use of wall functions for nonswirling flows near stationary boundaries along with an appropriate specification for turbulence dissipation near a wall were discussed by Launder and Spalding (1972, 1974).

Solution of the Difference Equations. The solution of the difference equations was obtained via the SIMPLER algorithm as presented by Patankar (1980). Convergence was considered obtained when the summation of the residual source magnitudes over the flow field was less than 0.4 percent of the inlet reference values.

The grid independence of the solutions was checked by computing one flow case each on a 20×20 grid, a 34×34 grid, and a 43×42 grid. The results of this comparison indicated that the 20×20 grid was not grid independent and that the 34×34 grid solution was essentially identical to the 43×42 grid solution.

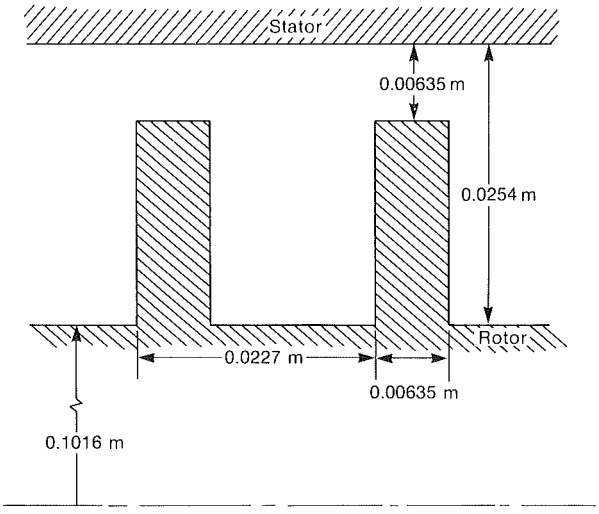

Fig. 1 Typical labyrinth seal cavity used for measurements

Experimental Apparatus and Procedure

The labyrinth seal considered in these experiments is composed of a series of five rectangular cavities as shown in Fig. 1. The shaft is concentric with respect to the stator housing and the teeth are located on the shaft. The flow enters and exits a given cavity through the small annular clearance between a tooth and the stator wall. The incompressible leakage flow is assumed to be turbulent with at least one recirculation zone within each cavity.

The water supply consisted of a 37.6 m^3 storage tank. From the tank, the water enters a centrifugal pump, which can supply a maximum of 1.5 m^3/min at 120 m of head. The pump was driven by a 56 kW motor. Following the pump, the water

Nomenclature

C_μ = turbulence model constant
c = seal clearance, m
k = turbulence kinetic energy $= 1/2(\overline{u'^2} + \overline{v'^2} + \overline{w'^2})$, m^2/s^2
k^* = dimensionless turbulent kinetic energy $= k/(1/2U_0^2)$
L = pitch of labyrinth seal teeth, m
L^* = dimensionless turbulence length scale $= k^{1.5}/(\epsilon c)$
m = mass flow rate per azimuthal unit depth, kg/m-s
P = pressure, Pa
P_i = static pressure at the cavity inlet, Pa
P_e = static presure at the cavity exit, Pa
P_{ow} = stator wall pressure at inlet to computational domain, Pa
P^* = dimensionless pressure $= (P - P_{ow})/(1/2\rho U_0^2)$
r = radial direction, m
R = radius of the rotor, m
Re = axial Reynolds number $= 2cU_0/\nu$
Ta = Taylor number $= (W_{sh}c/\nu)(c/R)^{1/2}$
U_o = spatially averaged inlet axial velocity, m/s
U^* = dimensionless mean axial velocity $= u/U_o$
$\underline{u}$ = mean axial velocity, m/s
$\overline{u'^2}$ = mean square value of the fluctuating axial velocity, m^2/s^2
V^* = dimensionless mean radial velocity $= v/U_o$
$\underline{v}$ = mean radial velocity, m/s
$\overline{v'^2}$ = mean square value of the fluctuating radial velocity, m^2/s^2
W_{sh} = peripheral velocity of the shaft, m/s
W^* = dimensionless mean azimuthal velocity $= w/W_{sh}$
$\underline{w}$ = mean azimuthal velocity, m/s
$\overline{w'^2}$ = mean square value of the fluctuating azimuthal velocity, m^2/s^2
x = axial direction, m
ϵ = turbulence dissipation rate of kinetic energy
θ = azimuthal direction
μ = absolute viscosity, kg/m-s
μ_{eff} = effective turbulent viscosity, kg/m-s
ν = kinematic viscosity, m^2/s
ρ = density, kg/m^3
ψ = stream function, kg/m-s
ψ^* = dimensionless stream function $= \psi/m$

flows through a system of strainers and filters, which remove particles larger than 10 μm from the water. Next in the flow loop were two Daniel 5.08 cm model 1503-1D 'CR' turbine flow meters in parallel. The operating range of these turbine meters was from 0.095 to 0.852 m^3/min each. The linearity and repeatability were specified by the manufacturer as ± 0.5 and ± 0.05 percent, respectively. In order to insure that the turbine meters operated well within their specified ranges during low flow testing, one of the parallel legs was turned off causing all of the flow to proceed through one turbine meter. A computerized data acquisition system was used to record all data. A Hewlett Packard 5301A counter was used to measure the flow meter output.

Upstream of the test section is a throttle valve, which regulates the supply side pressure. During any measurements, the inlet pressure to the test section was maintained at 410 kPa or above. The flow enters the test section through the top. After flowing through a small plenum, the flow immediately encounters the face of the labyrinth seal rotor. It then proceeds to flow downward past the seal stack. The seal stack consisted of five cavities similar to the one illustrated in Fig. 1. After the seal stack is another small plenum just prior to two outlets at the bottom of the test section. After the test section, there was another valve that could be adjusted to maintain the appropriate back pressure in the test section. Following the valve, the flow was piped back into the storage tank.

There were five access holes provided in each of three different cavities (the first, third, and fifth) to allow insertion of the hot-film probe. These locations were precisely drilled into the test section stator and designed to locate one position on top of each inlet and outlet tooth, one at the center of the cavity and two that were equally spaced on either side of the center of the cavity. The radial position of the probe was determined using a special traversing unit mounted to the test section. It had a resolution of 0.0254 mm. A graduated dial and vernier that was mounted on the probe shaft displayed the yaw angle of the probe. The dial and vernier had a resolution of 2 min.

The hot-film measurements of the flow field were performed using a TSI 1050 constant temperature anemometer and a TSI 1247A-10W crossed film sensor. This is a miniature probe with a nominal shaft diameter of approximately 1.52 mm. This shaft protruded into the flow only when the flow inside the cavity was measured. When the flow over the seal teeth was measured, only the small hot-film support prongs were present inside the flow field. These conditions helped to minimize disturbances generated by the probe.

The hot-wire signals were recorded by a MINC PDP 11/23 computer equipped with a 12 bit A/D with a range of ± 5.11 V and a resolution of 2.5 mV. The bridge output was read directly by the computer. Before the remainder of the measured quantities from the sensor were processed, the signal passed through a TSI 1057 signal conditioner. The signal conditioner consisted of a 1 kHz low pass filter and a 2 V suppression sampled at a rate of 2 kHz. This combination of sampling rate and low pass filter eliminated the possibility of aliasing. A spectrum analyzer was used to assure that the low pass filter did not clip the signals. The instantaneous sum (e_1+e_2), and difference (e_1-e_2) were performed by a TSI model 1063C sum and difference circuit. After each quantity was measured, the mean and mean squared deviation were calculated. When all of the necessary quantities were processed, the necessary data reduction was performed to obtain the axial and azimuthal mean velocities and turbulence intensities. The details of the data reduction may be found in Demko (1986). A directional Pitot probe was used to determine the direction of the mean velocity.

Since the anemometry is sensitive to temperature changes, the water temperature was constantly monitored during the measurement process using an Omega 199 thermocouple indicator. The water temperature is used to determine the operating temperature of the hot-film probe. The temperature difference between the water and the hot-film probe was held constant. Temperature compensation was always made before a data point was taken.

Table 1 Operating conditions

U_0, m/s	Re	Ta	Ta/Re
3.55	55,300	0	0
3.78	57,300	7,600	0.133
3.05	47,500	19,000	0.400

The hot-film measurements provided estimates on the mean axial and swirl velocity components as well as the turbulence kinetic energy at various axial and radial locations throughout the length of the labyrinth seal. Following the method outlined in Holleman (1978), the uncertainty of the mean flow velocities is estimated to be less than 18 percent of the mean inlet velocity. The uncertainty of the measurements will be less at the inlet and outlet planes since the flow velocity vector is only in the x-θ plane.

Turbulence kinetic energy was not measured directly, but estimated from measurements of the mean square velocity fluctuations in the directions along with the flow and perpendicular to the flow in the X-θ plane. Radial fluctuations could not be resolved. Taking the mean squared velocity fluctuations to be $\overline{u'^2}$ and $\overline{v'^2}$ in these two directions, respectively, and assuming that the turbulence is isotropic, the turbulence kinetic energy may be estimated as follows:

$$k=\frac{1}{2}\left[\frac{3}{2}(\overline{u'^2}+\overline{v'^2})\right] \tag{3}$$

Although anisotropic turbulence is clearly expected within the recirculation zone, it seems reasonable to assume isotropicity in the clearance region of each tooth. The basis for this assumption is that the flow in the tooth clearance region is primarily characterized by a wall layer along the stator and a separated shear layer along the dividing streamline; neither of these is expected to exhibit the highly anisotropic nature of the recirculation region.

The rotational speed of the test section was monitored by a 3000 series Bentley Nevada proximeter probe system. This system sensed the passing of the six bolts on the coupling between the variable speed motor and the test section. A Fluke digital multimeter, operated as a frequency counter, was used to monitor the rotational speed manually.

Results of Experiments and Computations

Table 1 summarizes the corresponding mean inlet axial velocity component, axial Reynolds number, Taylor number, and ratio of these two quantities for all of the flow conditions studied. These dimensionless numbers are defined by

$$\mathrm{Re}=\frac{2cU_0}{\nu} \tag{4}$$

$$\mathrm{Ta}=\frac{W_{sh}c}{\nu}\left[\frac{c}{R}\right]^{1/2} \tag{5}$$

where W_{sh} is the velocity of the peripheral edge of a labyrinth seal tooth. The ratio of Ta/Re may be used to gage swirl momentum effects to axial momentum effects. The data presented for comparison with numerical predictions were obtained in the fifth cavity.

A qualitative understanding of the flow field characteristics for all three Taylor numbers may be obtained by considering Fig. 2. Contained herein are plots of the predicted streamlines.

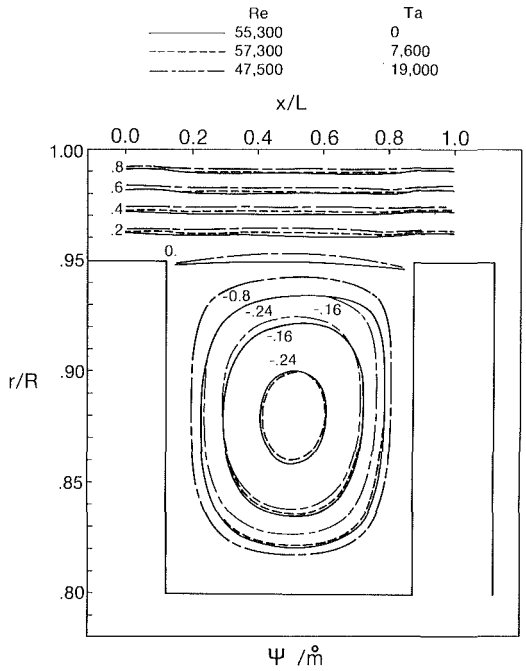

Fig. 2 Predicted streamline pattern

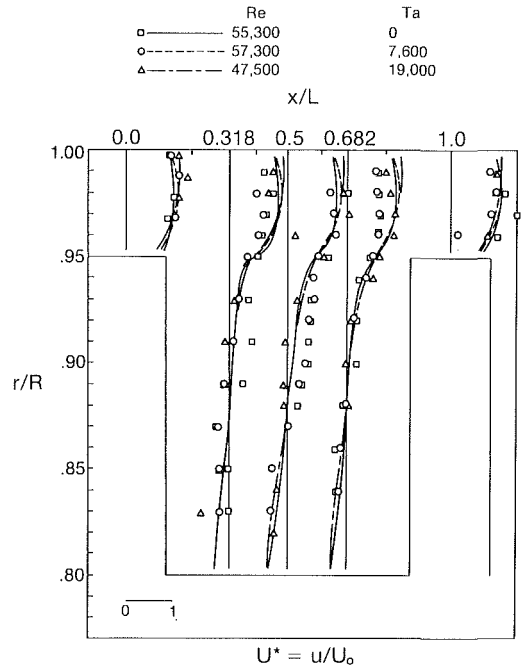

Fig. 3 Mean axial velocity

Characteristic to all three is the one large recirculation region between the teeth. It is the strongest for Ta = 19,000.

Also characteristic to all three shaft speeds is a stagnation point just below the top of the downstream tooth. Increasing the swirl velocity appears to shift the stagnation point slightly toward the top of the downstream tooth. Further, note that the dividing streamline curves outward from the cavity due to the centrifugal force. This is most noticeable at Ta = 19,000.

Figure 3 shows the axial velocity component at five axial stations. The agreement with experiment is acceptable considering the experimental and computational uncertainties discussed previously. The best agreement is in the exit plane.

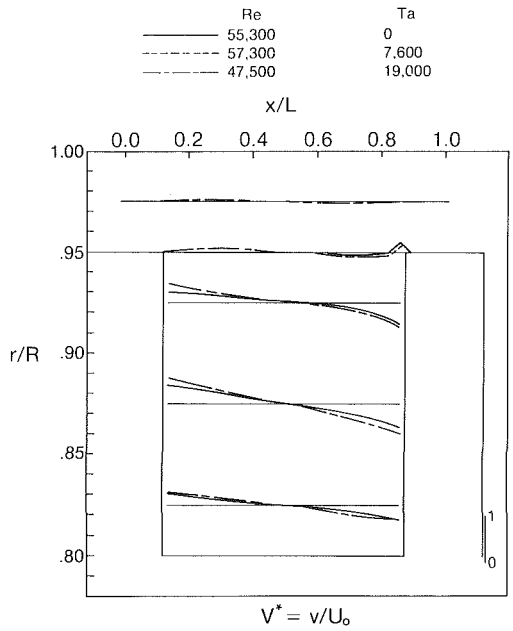

Fig. 4 Predicted mean radial velocity

One important characteristic is the large radial gradient that is present at $r/R = 0.95$. This is due to the high velocity in the leakage region adjacent to relatively low velocity in the outer portion of the recirculation zone. This is an important source of turbulence production, and in turn, viscous dissipation. For $x/L > 0.5$, these large radial gradients are diminished due to the resulting turbulent diffusion.

Figure 4 presents the predicted radial velocity component for all three Taylor numbers. There are very small radial velocities in the leakage flow region. Observe that V^*changes direction near $r/R = 0.94$ on the outlet tooth, which indicates the location of the stagnation point in this region. Swirl effects, however slight, are present. This can be seen by comparing the distributions of V^* at $r/R = 0.825$. All three Taylor numbers exhibit the same trend near the upstream tooth wall. Following the profiles toward the downstream tooth indicates that the axial gradient of V^* changes, giving lower values near the wall. This results from centrifugal forces tending to accelerate the flow slightly in opposition to its direction. These same forces are, of course, present along the upstream tooth, but the radial velocity is already positive there, so the centrifugal effect is not as evident.

Swirl velocity profiles are presented in Fig. 5 for Ta = 7,600 and 19,000, respectively. Previous computational investigations simulated the streamwise-periodic flow in a cavity downstream of the first three or four cavities. Those predictions generally yielded a mean value of W^* between 0.60–0.69, which agrees with the measurements obtained by Stoff (1980). The predictions shown here, using measured inlet profiles, yielded a significantly lower value of 0.5 for the mean value of dimensionless swirl. This is a difference of about 30 percent from previously suggested values. Using the currently measured inlet boundary conditions, measurements agree closely at $x/L = 0.5$, although with less success on either side where the radial velocity is not negligible. Good agreement with measurements is also found at the outlet.

Swirl has a pronounced effect on the predicted pressure distribution within a labyrinth seal cavity, as shown in Fig. 6. All computed pressure distributions are relative to the inlet stator wall pressure. At Ta = 0, the pressure is seen to be lowest in the central region of the cavity. As the Taylor number is increased to 7,600, the values inside the cavity decrease, while those in the jet region increase due to cen-

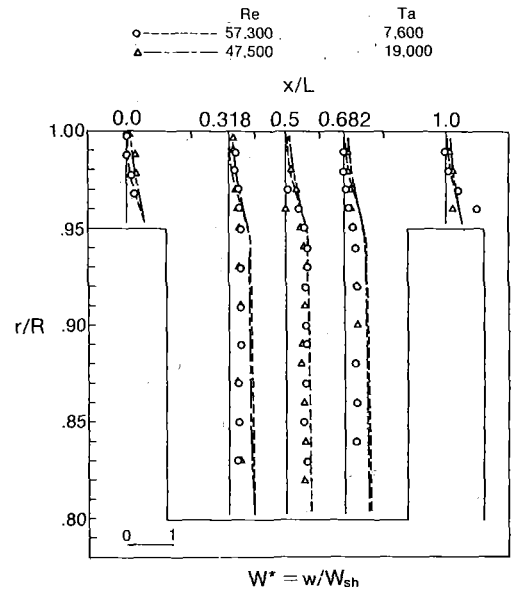

Fig. 5 Mean swirl velocity

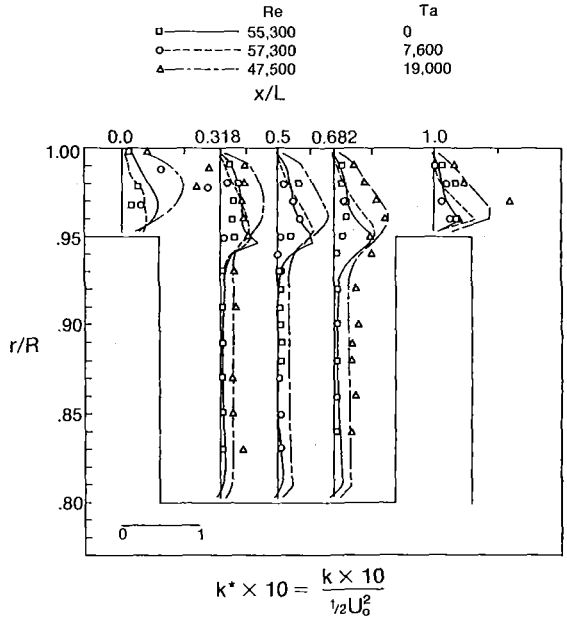

Fig. 7 Turbulence kinetic energy

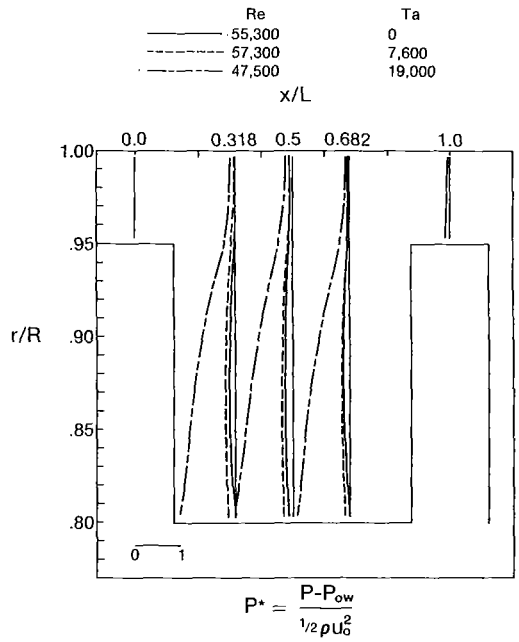

Fig. 6 Predicted relative pressure

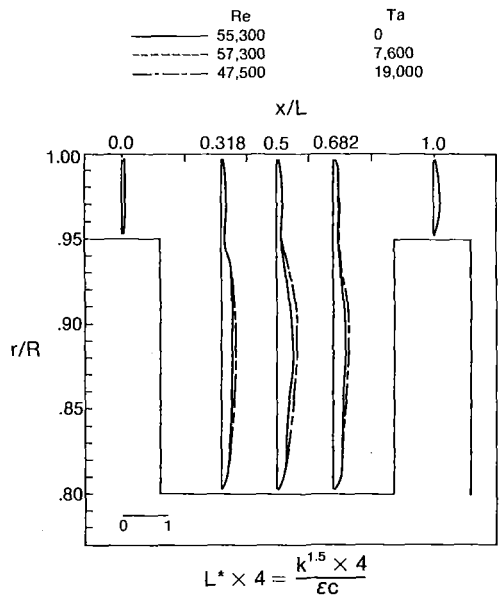

Fig. 8 Predicted length scale distributions

trifugal effects. A further increase in the Taylor number to a value of 19,000 magnifies this effect dramatically, with the lowest pressure at the base of the cavity.

The leakage flow pressure is seen to decrease in the streamwise direction until about $x/L = 0.5$. Next it increases until $x/L = 0.8$. Finally it decreases as the flow passes over the downstream tooth. This pressure variation results from a combination of viscous dissipation and the Bernoulli effect of pressure decrease at constrictions in flow area. The variation of area through which the leakage flow passes varies as indicated by the dividing streamline in Fig. 2. However, for the Ta = 19,000 case of Fig. 6, the pressure does not decrease as it passes over the downstream tooth. This is attributed to the centrifugal effect causing a rather small leakage flow area at $x/L = 0.5$. This in turn produced an unusually low pressure there via the Bernoulli effect.

Figure 7 presents radial distributions of dimensionless turbulence kinetic energy k^*. A curve fit of inlet measurements was used as the inlet boundary condition in the computations. The experimental measurements are in fair agreement with predictions made in this manner. One observation to be made regarding k^* is that production is highest in the shear layer and in the region where the flow expands over the downstream tooth. Also it is evident that the flow is neither measured nor predicted as being streamwise periodic, as the inlet and outlet profiles are different.

The predicted dimensionless length scale values are presented in Fig. 8. The characteristics are very much the same for all three conditions. These profiles show that the turbulence length scale is smaller in the leakage region than inside the cavity. The smaller length scale areas represent the regions where kinetic energy is most rapidly dissipated through viscous effects. The small length scales of the turbulence produce rapidly varying velocity gradients, which enhance the

rate at which viscous effects convert kinetic energy to heat. For $x/L < 0.5$, the smallest length scale occurs in the region along the dividing streamline. The most effective dissipation thus occurs in the shear layer that drives the recirculation zone.

Conclusion

The labyrinth seal computer code is seen to provide realistic results for straight-through labyrinths. There is no worrisome uncertainty of assuming a value for the mean flow kinetic energy carry-over coefficient, for example, which is often required in using simple algebraic models. The use of curve fits of experimental measurements for the inlet boundary conditions enhanced the level of agreement with measurements, as flow details within the facility were unknown a priori.

The results show that the Taylor number has a substantial effect on P^* and, as shown elsewhere (Demko et al., 1987; Demko, 1986), can give a different flow pattern if $Ta/Re > 0.45$. Further, as the Taylor number is increased while holding the Reynolds number constant, the Taylor number effect becomes important sooner at lower values of the Reynolds number. For the current Reynolds number near 50,000, the pressure in the cavity is dramatically altered by centrifugal effects upon increasing the Taylor number from 7600 to 19,000. Also, the centrifugal force shifts the streamlines slightly outward.

References

Abujelala, M.T., and Lilley, D.G. 1984, "Limitations and Empirical Extensions of the k-ϵ Model as Applied to Turbulent Confined Swirling Flow," presented at the AIAA 22nd Aerospace Science Meeting, Jan. 9-12, Reno, NV, Paper 84-0441.

Buchter, H.H., 1980, *Industrial Sealing Technology,* J. Wiley, New York.

Demko, J.A., Morrison, G.L., and Rhode, D.L., 1987, "Effect of Shaft Rotation on the Incompressible Flow in a Labyrinth Seal," *Journal of Propulsion and Power,* in press (also, proceedings of the 5th International Conference on Numerical Methods in Laminar and Turbulent Flow, Montreal, Canada, Aug.).

Demko, J. A., 1986, "Prediction and Measurement of Incompressible Flow in a Labyrinth Seal," PhD Dissertation, Texas A&M University, College Station, TX.

Falsen, J.I., 1972, "Review and Summary of Labyrinth Seal Theory and Design," Rocketdyne Report TMR 2115-3351.

Holleman, J.P., 1978, *Experimental Methods for Engineers,* 3rd ed., McGraw-Hill, New York.

Hutchinson, P., Khalil, E. E., Whitelaw, J. H., and Wigley, G., 1976, "The Calculation of Furnace-Flow Properties and Their Experimental Verification," ASME *Journal of Heat Transfer*, Vol. 98, pp. 276-283.

Launder, B.E., and Spalding, D.B., 1972, *Mathematical Models of Turbulence,* Academic Press, London, England.

Launder, B.E., and Spalding, D.B., 1974, "The Numerical Computation of Turbulent Flows," *Computer Methods in Applied Mechanics and Engineering,* Vol. 3, pp. 269-289.

Ludwig, L.P., and Bill, R.C., 1978, "Gas Path Sealing in Turbine Engines," NASA Technical Memorandum 73890.

Morrison, G.L., Rhode, D.L., Cogan, K.C., Chi, D., and Demko, J.A., 1983, "Labyrinth Seals for Incompressible Flow," Final Report for NASA Contract NAS8-34536; NASA Technical Brief MSF-27051.

Patankar, S.V., 1980, *Numerical Heat Transfer and Fluid Flow,* Hemisphere Publishing Corp., Washington, DC.

Rhode, D.L., Demko, J.A., Traegner, U.K., Morrison, G.L., and Sobolik, S.R., 1986, "The Prediction of Incompressible Flow in Labyrinth Seals," ASME *Journal of Fluids Engineering,* Vol. 108, pp. 19-25.

Sneck, H.J., 1980, "Labyrinth Seal Literature Survey," ASME *Journal of Lubrication Technology,* Vol. 102, pp. 579-582.

Stoff, H, 1980, "Incompressible Flow in a Labyrinth Seal," *Journal of Fluid Mechanics,* Vol. 100, pp. 817-829.

R. B. Voegtle
Manager,
Power Plant Systems—Performance.

R. H. Koppe
Manager,
Reliability and Safety Projects.

The S. M. Stoller Corporation,
Boulder, CO 80302

T. H. McCloskey
Manager,
Steam Turbine and Related Auxiliaries,
Electric Power Research Institute,
Palo Alto, CA 94303

Fossil Unit Performance—1965-1984

This paper presents an overview of the results of a study performed for EPRI covering the historical performance of fossil-fired units 200 MW and larger from 1965 through 1984. The study was based on analysis of the information collected over the years by the Equipment Availability Task Force of the Prime Movers Committee of the Edison Electric Institute (EEI), and more recently by the North American Electric Reliability Council (NERC), and covers approximately 7700 unit-years of operation at 668 individual units.

Background

In the past, EPRI and other organizations have performed or sponsored studies that have investigated the performance of fossil-fired units. Examples include Anson (1977a, 1977b), Koppe and Olson (1979), and Carlson et al. (1987). In addition, NERC regularly publishes reports such as NERC (1986) that summarize the performance of all generating units reporting data to them. The purpose of this EPRI project was to update/expand upon these studies/reports. This study was based on analysis of the unit-specific data collected by EEI/NERC and was carried out using computer programs developed by The S. M. Stoller Corporation for analysis of the EEI/NERC data base. All analyses were carried out using data in the EEI format. Data collected in the more comprehensive GADS format were converted to the EEI format by NERC. The data available for the study covered the period from 1965 through 1984.

It will not be possible in this paper to cover the results of all of the investigations performed in the project, and no attempt is made to accomplish this. Rather, we will present an overview of the project's activities, covering the types of analyses performed and providing representative results. In general, the results provided will be for coal-fired units, although the report covers all three fuel types. The main reason for this is that the coal units represent the majority of units in the data base. Since the various subgroupings of units contain more unit-years of data, trends are generally more visible and are less subject to statistical variations.

Introduction

Before getting into the discussion of the specific trends studied, an overview of the general historical performance of fossil units is useful. Figure 1 shows that over the years there has been a considerable variation in fossil unit performance. In 1965, the equivalent availability factors (EAFs) of coal-, oil-, and gas-fired units were in the 84 percent range. From the late 1960s to the mid- to late-1970s, there was a significant decline in the performance of all units, regardless of fuel type, with coal unit performance deteriorating more than that of either the oil or gas units. In recent years, the performance of all units has improved such that in 1984 there was again essentially no difference in the performance of coal, oil, and gas units. The 1984 performance level was, however, still about 6 percent lower than that in 1965. These calendar year trends should be kept in mind since they will be shown to be an important influence in all trend evaluations.

Each group of units represented in Fig. 1 contains units of differing designs (supercritical/subcritical steam pressure, balanced draft/pressurized, etc.); sizes (200 MW to 1300 MW); and vintages (units that came on line from 1953 through 1983). The purpose of the EPRI study was to explore the influence of these factors on unit performance, as well as to determine the major causes contributing to unit unavailability.

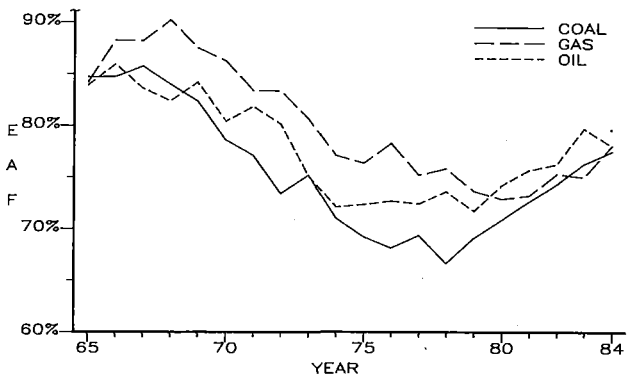

Fig. 1 Historical unit performance (EAF) of fossil-fired units

Contributed by the Power Division and presented at the Joint ASME/IEEE Power Generation Conference, Miami Beach, Florida, October 4-8, 1987. Manuscript received by the Power Division August 1, 1988. Paper No. 87-JPGC-Pwr-28.

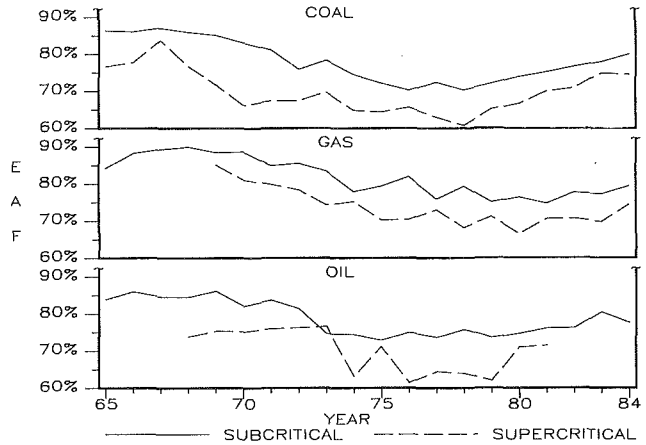

Fig. 2 Unit performance (EAF) for subcritical and supercritical coal, gas, and oil units

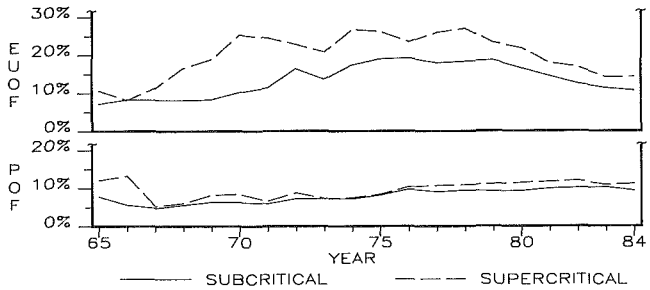

Fig. 3 Planned/unplanned contribution to coal unit unavailability

In general, the performance of the subcritical and supercritical units for each fuel type was analyzed separately. Within each unit group, the influences of factors such as size, vintage, and furnace draft were further explored. In exploring the influences of these factors and the interrelationships among them, several interesting trends were discovered. These are discussed in the following sections and summarized at the end of the paper. (Cyclone-fired units were excluded from these analyses. While these units represented a relatively small fraction of the total number of units, they were found to have a significant influence on trends. This, combined with the fact that they are no longer generally under construction – only one cyclone unit has come on line since 1976 – led to the decision to exclude them from these trend evaluations.)

Calendar Year Performance Variations for Subcritical and Supercritical Units

Since about 75 percent of the units are subcritical, one question to be answered is whether the subcritical and supercritical units have experienced the same general performance trends. Figure 2 shows the performance (EAF) for subcritical and supercritical coal-, oil-, and gas-fired units. (To make trends more visible, years represented by fewer than five units have been excluded. The absence of data in 1982 through 1984 for supercritical oil units results from most units switching their primary fuel to gas. These units are therefore included in the gas unit data for these years.) These data clearly show:

- Subcritical and supercritical units of each fuel type have indeed exhibited similar calendar year performance trends.
- The performance of the supercritical units has been below that of subcritical units regardless of primary fuel. (As will be shown later, this difference is largely due to differences in vintage and size, rather than steam pressure.)
- Since the mid- to late-1970s, the performance gap between sub- and supercritical units has generally been decreasing for coal and oil units; however, gas units have not shown the same tendency for the narrowing of the performance gap.

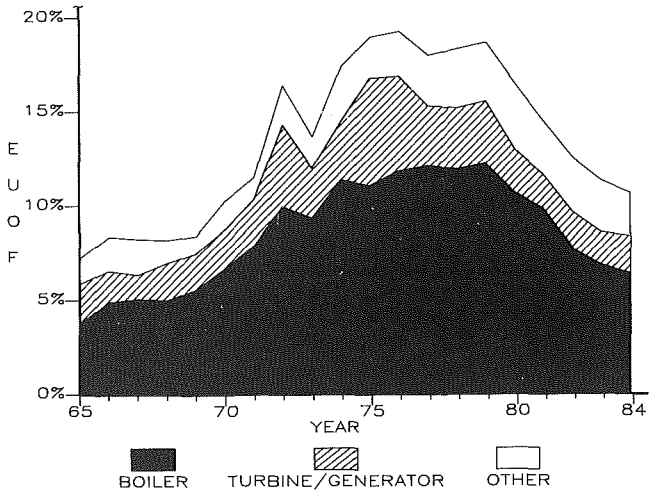

Fig. 4 EUOF contribution of major plant areas for subcritical coal units

Other observations related to the overall performance of sub- and supercritical units are:

- For all fuel types, the poorer performance of supercritical units has resulted from both planned and unplanned events; that is, the supercriticals have experienced higher planned outage factors (POF) and equivalent unplanned outage factors (EUOF).
- The calendar year EAF trends primarily result from changes in EUOF.
- Planned outage factors have generallly been increasing over the years.

These observations are illustrated in Fig. 3 for coal-fired units.

Contribution of Major Plant Areas to Unavailability

As noted above, the major influence on unit unavailability has been unplanned events (EUOF). The influence of the major areas of the plant – boiler, turbine-generator, and other equipment – on subcritical coal unit EUOF, as well as the variation of these impacts over the years, is shown in Fig. 4. Clearly, unplanned boiler-related events have been the major influence (more than half the total unit EUOF) as well as the major contributor to trends. Turbine-generator events have shown a trend generally similar (although of smaller magnitude) to that of the boiler; i.e., increasing EUOF through the mid-1970s, and generally decreasing thereafter. On the other hand, the EUOF related to other equipment generally increased through 1980 before declining.

Although boiler-related events have dominated coal unit unavailability (supercritical as well as subcritical), they have played a significantly smaller role in oil and gas units. This is shown in Fig. 5, which provides data for subcritical gas units corresponding to that in Fig. 4. In this case, the nonboiler-related EUOFs are generally larger than those of the boiler. The dominance of boiler-related events in coal units is not surprising since there is more equipment (pulverizers, feeders, precipitators, etc.) whose failure will reduce unit capability, as well as more fuel-related problems such as ash, corrosion, erosion, slagging, and fouling. It could also be expected that nonboiler-related problems would have a somewhat higher impact at the gas units since, if a unit is down less for boiler problems, there is a greater chance for other problems to occur. However, the increase in nonboiler losses at gas units

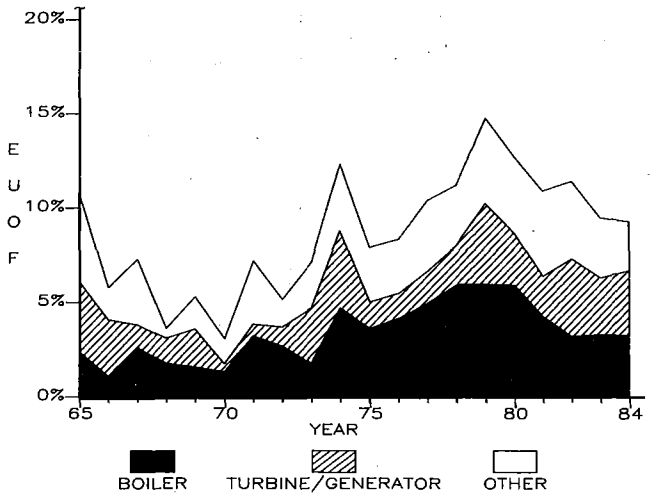

Fig. 5 EUOF contribution of major plant areas for subcritical gas units

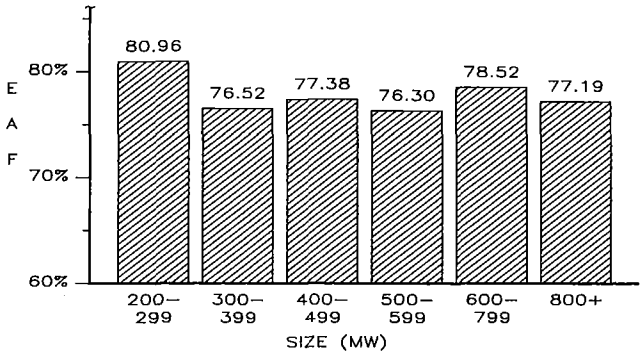

Fig. 6 EAF variation with size for subcritical coal units (1982–1984)

relative to coal units is larger than could be explained by the higher boiler availability at the gas units. No reason for this phenomenon was identified.

Performance Variation With Size

One of the areas investigated was the influence of size on unit performance. In the planning of additional generating capacity, one of the factors influencing the selection of unit size is the performance levels that might be expected for different size units. The manner in which one goes about determining the impact of size on performance can greatly influence the results. For example, all things being equal, one would generally expect some degradation in performance as size increases since larger units have more tubes that can fail, larger equipment items to repair, etc. At first glance, however, the data in Fig. 6, which cover subcritical coal units during the 1982–1984 period, do not support this conclusion. Clearly, the smaller (200–299 MW) units had higher EAFs, but above 300 MW, there appears to be no significant effect of size. If anything, there appears to be a slight tendency for EAF to increase. These trends are not influenced by differences in unit operation: amount of reserve shutdown, etc. In looking further, it was found that the distribution of units of the various vintage groups among the size ranges has influenced this result. As it turns out, for example, a significant fraction of the middle-size units (300–500 MW) were built prior to 1975 when designs tended to be less conservative, while a significant fraction of the smaller and larger units were built before 1960 or after 1975 when designs were more conservative. Also, when the larger units were first built, they represented significant extrapolations in design.

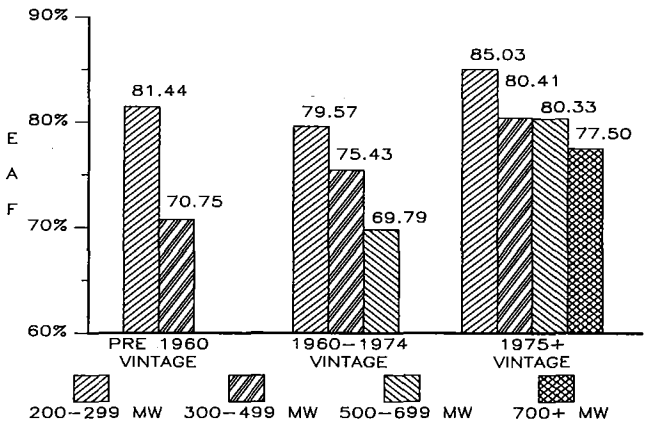

Fig. 7 Size/vintage effect for subcritical coal units (1982–1984)

Figure 7 shows the same data presented in Fig. 6, only in this case the vintage distribution is accounted for. Clearly, there is a size effect. It is particularly large in the pre-1960 vintage group – much larger than might be expected – and has diminished with subsequent vintage groups. (While the data presented are for the 1982–1984 period, a similar trend was evident for earlier time periods.) The data for earlier vintages reflect the combined effect of size and the additional problems related to design extrapolation, while the data for recent vintages appear to reflect the effect of size more directly.

Performance Variation With Vintage/Age

One of the potential relationships investigated was the influence of vintage (represented by the year the unit came on line) and age on performance. For this analysis, the units were separated into six vintage groups: pre-1960, 1960–64, 1965–69, 1970–74, 1975–79, and 1980 and after. Originally, the performance of the units in each vintage group was calculated and plotted versus the number of years of operation; however, it was observed that similar performance changes were occurring ten years into life for one vintage group, five years into life for the next, etc. When replotted versus calendar year, performance trends tended to correlate with calendar year regardless of vintage. Figure 8 shows the resulting variation in EAF with vintage for subcritical coal units. For ease in visualizing trends, each vintage group's performance is presented as the average performance over five-year periods (1965–69, 1970–74, 1975–79, and 1980–84). Also, each succeeding vintage group is represented by lines with shorter dashes, i.e., solid for oldest units to dots for the most recent vintages.

One of the observations to be made from the data is that the general calendar year trends shown in Fig. 1 – a decline in performance through the mid- to late-1970s, followed by improvement thereafter – are shown by all vintage groups. At any given point in time, units of the various vintage groups in effect represent different age groups; therefore, the data show that, regardless of age, performance was declining through the 1970s and improving in the 1980s. This is clearly indicating that calendar time and not age was the principal influence on performance. While some of the decline in performance in the 1970s could have resulted from aging, it appears the decline is more likely reflecting the general poor health of the utility industry during the period. It is clear, however, that it is not a foregone conclusion that unit performance will drop as a unit ages. This is clearly illustrated by the improving performance of all vintage groups (even the pre-1960 vintage units) in the 1980s. While it is true that aging occurs, other factors (increased emphasis on operations, maintenance and capital improvements; initiation of life extension activities; etc.), which

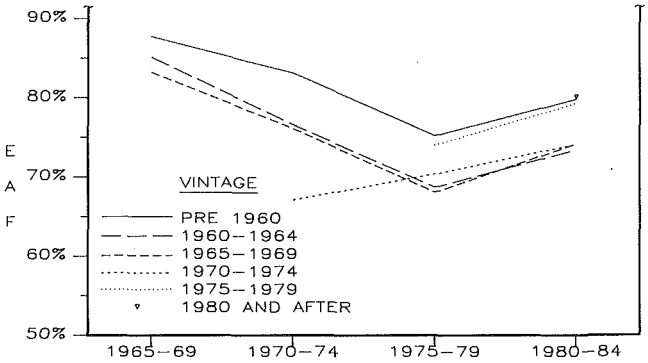

Fig. 8 Subcritical coal unit EAF trends with vintage/age

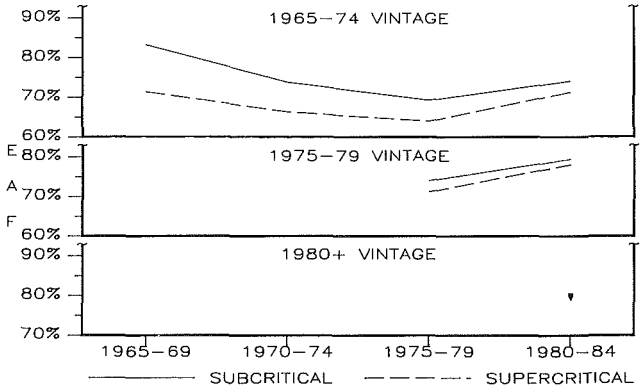

Fig. 9 Subcritical/supercritical coal unit vintage trends in EAF

have come into play in recent years, have overcome any aging effects.

The other observation to be made from Fig. 8 is the variation in performance with vintage. Figure 8 shows that the 1960–1974 vintage units have shown generally similar performance, while the earlier (pre-1960) and later (1975 and later) units have done considerably better. When unit size is accounted for, the result is somewhat different. As it turns out, essentially all of the pre-1960 units are in the 200–299 MW size range. Among these smaller units, performance tended to drop off with vintage until this trend reversed in the most recent vintage groups. Among the larger units, the predominant trend was for the early vintages to have poorer performance, with performance improving with subsequent vintages. These EAF trends appear to reflect the influences of two different factors. First, there was a general reduction in design conservatism in fossil units in the 1960s. This bottomed out in the 1966–1974 period and was followed by increased conservatism in units started up after 1975. The performance of the smaller units whose designs were relatively well established reflected these trends in design conservatism. The earliest of the larger units suffered additional problems related to extrapolation of designs from those of smaller sizes. Resolution of the design extrapolation problems at later units, combined with the trends in design conservatism, resulted in the observed improving performance with subsequent vintages. These trends can be seen in Fig. 7. When considering the 200–299 MW units, the performance drops off between the pre-1960 vintage and the 1960–1974 vintage units. Performance then improves in the 1975+ vintage group. In the case of the larger units, the earliest vintage group has the poorest performance, with subsequent vintage groups having improved performance. While this figure covers only the 1982–1984 time frame, similar trends were found over the entire 1965–1984 period. It should also be noted that similar

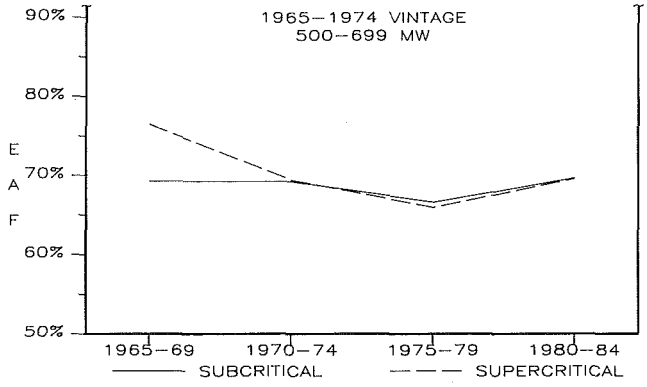

Fig. 10 Subcritical/supercritical coal unit performance

trends were found among the supercritical coal units as well as the sub- and supercritical oil and gas units.

Subcritical/Supercritical Performance Comparison

Figure 2 showed a significant performance differential between sub- and supercritical units. This straightforward comparison is however being influenced by vintage/size effects. Figure 9 illustrates the trends when vintage is accounted for, and shows the tendency for the performance differential between sub- and supercritical coal units to decrease with succeeding vintages and to decrease with time within any specific vintage group. These vintage trends have been discussed by Curley (1984, 1985) and Lofe and Richwine (1985). This is not yet the complete picture, however, because supercritical units tend to be larger in size than the subcritical units. As Fig. 10 shows, accounting for size significantly reduces the differential even among the earlier vintage units. In this case (1965–1974 vintage, 500–699 MW coal units), there is essentially no difference in performance over unit lifetimes. Overall, it appears that with size and vintage effects accounted for, the performance differential between sub- and supercritical coal units has been on the order of 1 to 2 percent. Clearly, when vintage and size effects are accounted for, the performance penalty associated with supercritical coal units is not as large as a simple comparison would indicate. The modest penalty in EAF may well be overcome by the increased efficiency of the supercritical units. Among oil and gas units, the differential has been considerably larger – between 5 and 10 percent.

Performance Variation With Furnace Draft

The influence of furnace pressure – balance draft, pressurized, converted from pressurized to balanced draft – was also investigated. Since this issue is particularly relevant to coal unit performance, this discussion will center on sub- and supercritical coal unit performance. It is interesting to note that among the subcritical coal units, roughly 30 percent were designed as pressurized (FD). About half of these were subsequently converted to balanced draft (BD). On the other hand, a little more than half of the supercritical units were designed pressurized and only 40 percent of these have subsequently been converted. There has also been a significant shift in design philosophy over the years, with the earlier and the most recent vintage units being predominantly BD and the middle vintage groups tending to FD designs. (The shift to FD designs peaked in the late 1960s when only 36 and 8 percent of the sub- and supercritical units, respectively, were designed BD.) The analysis of furnace draft effects presented below is limited to the 1960–74 and 1965–79 vintage groups for subcriticals and supercriticals, respectively, since these groups contain the

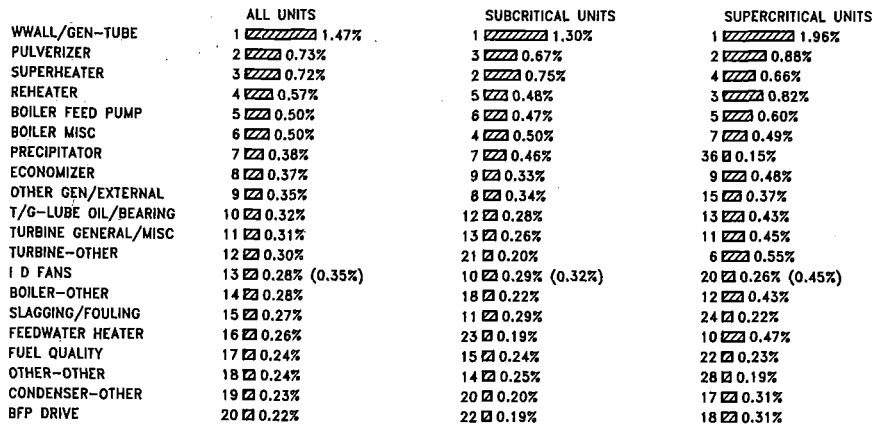

Fig. 11 Top 20 contributors to coal unit unplanned unavailability (EUOF)

largest number of units with a reasonable distribution among all designs: BD, FD, and converted.

Over the years, at least a part of the justification for the conversion of units has been an expected improvement in performance, generally on the order of 5 percent. The data below show however that in recent years (1982–1984), there was very little difference in the performance of subcritical units that were designed BD and unconverted subcritical FD units, whereas supercritical units designed BD performed 2.5 percent better than the unconverted supercritical FD units.

	EAF (percent)(1982–1984)	
	Subcritical	Supercritical
Designed BD	76.8	76.6
Unconverted FD	76.7	74.1
Difference	0.1	2.5

As it turns out, size differences have influenced this result in that the average size of the subcritical units designed BD is somewhat larger than the unconverted subcritical FD units, whereas just the opposite is true for the supercriticals. Adjusting for size differences would increase the performance differential for subcriticals and decrease it for supercriticals, resulting in a differential of about 1.5 percent in both cases. (Furnace draft was found to have no effect on the performance of oil units. There were no gas units in the data base that were designed balanced draft, therefore no comparison could be made.)

Any comparison of these results to earlier evaluations of the effects of furnace draft on unit performance is influenced by two factors that apply to both sub- and supercritical units. First, there has been a tendency for the poorer performing FD units to convert, while the better performing units do not. In addition, the performance spread between units that were designed BD and those designed FD and never converted is smaller in recent years than it has been in the past. These factors would result in earlier comparisons showing larger performance differentials than that seen in 1982–1984.

As noted above, 40 to 50 percent of the units designed FD have subsequently converted. A simple before/after analysis of the units that converted shows that the performance of both sub- and supercriticals improved after conversion (1.0 percent improvement in EAF for subcriticals and 9.1 percent for supercriticals). This comparison, however, proved to be misleading. The important consideration is how these units performed following conversion compared to how they might have been expected to perform had they not converted. For example, most supercritical units converted after 1978. Figure 2 shows this to be a period of improving performance for all supercritical coal units. Therefore, the fact that the converted units had 9 percent higher EAFs after conversion must be compared to the improvement in performance experienced by the supercriticals that had not converted. This comparison was made by establishing a baseline representing the year-by-year performance for units designed FD and which never converted. This was done for sub- and supercritical coal units. The performance of each converted unit was then compared to this baseline, again on a year-by-year basis, for those years prior to and after conversion. (The year of conversion was not included.) Given the assumption that the performance of the converted units relative to the baseline would not have changed had it not been for conversion, the average performance differentials for years before and after conversion then represents the true impact of conversion.

The results of this analysis are shown below.

	EAF relative to FD units, percent		
	Before conversion	After conversion	Improvement
Subcritical units	−6.2	−3.2	3.0
Supercritical units	−7.5	−2.7	4.8

These data show several points:

- Units that converted were among the poorer performing FD units. Prior to conversion, the units that subsequently converted were about 7 percent poorer than FD units that never converted.
- Conversion improved performance relative to the baselines; however, the converted units still had not attained the performance levels of the unconverted FD baseline units, let alone that of BD units. Following conversion, EAFs were still about 3 percent below those for the unconverted FD units.
- The true net improvement in performance following conversion was 3.0 percent for subcriticals and 4.8 percent for supercriticals compared to the 1.0 percent and 9.1 percent values derived from the simple before/after analysis. These values may overstate the effects of conversion somewhat. Since it has tended to be the poorer performing units that have converted, it is likely that additional improvements were made beyond those made at other units, and these also contributed to the observed improvement in performance. In light of the observed trends it is also likely that future conversions would produce smaller performance improvements.

Contribution of Specific Causes to Unit Unavailability

Lastly, but certainly not of least importance, was a determination of the highest impact problem areas, in terms of unplanned unavailability (EUOF), for the various unit groups. For the purpose of this study, the 230+ specific cause codes

provided in the EEI reporting format to identify problem areas were consolidated into 53 cause code groups, each of which contain either a single EEI cause code, a logical grouping of the cause codes, or alternatively all cause codes within a specific area of the plant, e.g., boiler, which were not included in one of the other groups. Figure 11 shows the relative ranking of the top 20 cause groups during the 1982–84 period. (Coal units are again chosen for illustration.) The overall rank is based on the average impact at all coal units (the first column) while the remaining columns show impact and ranking at subcritical and supercritical units. (In the case of ID fans, there are two values shown. The first value is the EUOF when averaged over all units. The value in parentheses indicates the EUOF experienced at balanced draft units or converted units following conversions. This second value represents the true impact at the units having the possibility of ID fan problems.)

These top 20 cause groups account for about 70 percent of the total unplanned unavailability for both subcritical and supercritical units. The top cause in both groups waterwall/generating tubes, accounting for 1.3 percent (11 percent of total) and 1.96 percent (13 percent of total) EUOF. (In both cases, several of the top cause groups are those labeled boiler-miscellaneous, turbine-general/miscellaneous, turbine-other, etc. The miscellaneous and general groups are cause codes used by utilities to describe any event not identified by one of the other specified cause codes. Without further information, such as the narrative that may have been provided in the event reporting, nothing can be gained related to the true cause of the lost availability. The turbine-other, boiler-other, etc., cause groups each contain several individual causes not included in other cause groups. Although collectively they may rank high, it is unlikely that any individual cause code would make a significant contribution to unavailability.)

As seen in Fig. 11, many of the same cause groups rank high for both subcritical and supercritical units, although relative rankings may differ. Significantly different rankings are not surprising, especially beyond the top 10 or 15 causes where relatively small changes in EUOF (0.1 percent) can change rank by 10 or 15 positions. In a few instances, however, there were significant differences in both impact and rank. These include the precipitator, which had a higher impact at subcriticals and turbine-other, and feedwater heater, which impacted supercriticals more. There is certainly no obvious reason related to steam pressure for the significant difference in the precipitator rankings. It is possible that depending on the specific problem (high-pressure feedwater heaters, for example) the other areas of significant difference could relate to steam pressure. Additional detailed analysis would be required to confirm this.

Conclusions

As mentioned earlier, the preceding discussion provides a general overview of the EPRI fossil plant performance study. Some of the more interesting historical performance trends observed include:

- For units of all types, calendar time and not age was the principal influence on past performance.
- Performance drops off as size increases. While this end result is not particularly surprising, the interesting point is that for coal units in particular, the size effect is not seen in a simple comparison but becomes evident only when variation in vintage is included in the analysis. The size effect is largest in early vintages and diminishes for subsequent vintages.
- Vintage is an important influence on unit performance. Among larger units (above 300 MW), the more recent vintage units generally performed better than early vintage units.
- Overall, when size and vintage effects are accounted for, the performance differential between sub- and supercritical coal units was found to be on the order of 1–2 percent. Not only has the performance differential narrowed with succeeding vintages, but after size differences are taken into account, even early units had small performance differentials. For oil and gas units, the differential was considerably larger than coal units – on the order of 5–10 percent.
- After accounting for size and vintage effects, the recent performance of coal-fired units designed balanced draft has been about 1.5 percent better than that of pressurized (never converted) units. Furnace draft had no impact on the recent performance of oil units.
- Conversion to balanced draft improved the performance of coal units. After accounting for vintage and calendar year effects, the improvement amounted to 3–5 percent. Units that had converted were among the poorer performing pressurized units, and while their performance improved, it had not reached the level of the remaining unconverted units, let alone that of balanced draft units.

Aside from the performance trends mentioned above, the study also points out the importance of correctly accounting for influencing factors in the analysis of fossil unit performance. In carrying out the various analyses, it was found that more often than not, a simple, straightforward comparison produced incorrect results. The true result surfaced only through more detailed studies that sort out the influence of various competing factors. An understanding of these influences at the unit level of performance is required in order to investigate trends effectively at the system/component level. It is also clear that any utility attempting to compare the performance of its units with that of other units must carefully account for significant characteristics in selecting comparison units. This study has shown that among those characteristics considered, fuel, size, vintage, and calendar year are significant influencing factors on unit EAF. Furnace draft (in recent years) and sub-/supercritical pressure (assuming size and vintage are properly accounted for) were found to be less of an influence than generally perceived in the past.

The information presented in the final report for the study (Voegtle and Koppe, 1988) can serve as a general reference for comparison of the performance of a specific unit or group of units; however, these performance comparisons must still be made with caution since there are many other factors, such as specific configurations, numbers of spare components, and changes in fuel quality, as well as utility- or station-specific factors, which were beyond the scope of the study, which must be considered in any meaningful detailed performance comparisons.

The results of the study also serve as a good starting point for selection of additional studies, which would investigate selected performance trends or anomalies, either at the unit or cause level, in more detail. Areas proposed for additional evaluation include the influence of changes in a unit's operating mode, the relationship between forced outage rate and output factor, and additional analyses of high impact causes (Carlson et al., 1987).

Acknowledgment

This paper summarizes work performed under EPRI Project RP 1266-31: Fossil Plant Performance Study.

References

Anson, D., 1977a, "Availability of Fossil-Fired Steam Power Plants," Electric Power Research Institute, EPRI FP-422-SR.

Anson, D., 1977b, "Availability Patterns in Fossil-Fired Steam Power Plants," Electric Power Research Institute, EPRI FP-583-SR.

Carlson, J. H., Lofe, J. S., Niebo, R. J., and Richwine, R. R., 1987,

"Availability Trend Evaluation," *Proceedings of the Fourteenth Energy Technology Conference,* Government Institutes, Inc., pp. 148–162.

Curley, G. M., 1984, "Supercritical Units – How Are They Performing?" *Proceedings of the American Power Conference*, Vol. 46, pp. 295–299.

Curley, G. M., 1985, "A View of Supercritical Fossil Steam Generators' Performance – Past, Present and Future," presented at the Joint ASME/IEEE Power Generation Conference, Milwaukee, WI, Oct. 20–24.

Koppe, R. H., and Olson, E. A. J., 1979, "Nuclear and Large Fossil Unit Operating Experience," Electric Power Research Institute, EPRI NP-1191.

Lofe, J. J., and Richwine, R. R., 1985, "Prediction of Equivalent Forced Outage Rates for Future Supercritical and Subcritical Electric Generating Units Using Learning Curve Theory: An Update and Comparison Using Data Through 1982," *Proceedings of the American Power Conference*, Vol. 47, pp. 461–467.

North American Electric Reliability Council, 1986, "Equipment Availability Report, 1976–1985."

Voegtle, R. B., and Koppe, R. H., 1988, "Fossil Unit Performance: 1965–1984," Electric Power Research Institute, EPRI CS-5627.

Spray Computations in a Centerbody Combustor

M. S. Raju

W. A. Sirignano

Department of Mechanical Engineering,
University of California, Irvine,
Irvine, CA 92717

A hybrid Eulerian–Lagrangian method is employed to model the reactive flow field of a centerbody combustor. The unsteady two-dimensional gas-phase equations are represented in Eulerian coordinates and liquid-phase equations are formulated in Lagrangian coordinates. The gas-phase equations based on the conservation of mass, momentum, and energy are supplemented by turbulence and combustion models. The vaporization model takes into account the transient effects associated with the droplet heating and liquid-phase internal circulation. The integration scheme is based on the TEACH algorithm for gas-phase equations, the Runge–Kutta method for liquid-phase equations, and linear interpolation between the two coordinate systems. The calculations show that the droplet penetration and recirculation characteristics are strongly influenced by the gas- and liquid-phase interaction in such a way that most of the vaporization process is confined to the wake region of the centerbody, thereby improving the flame stabilization properties of the flow field.

1 Introduction

The primary objective of this study is to develop an efficient solution procedure for the understanding of liquid spray combustion in a recirculating flow of bluff-body flame holders, which have been widely used in ramjet and turbojet afterburners. The design of the combustion chambers dictates the need for maintaining high combustion efficiency and low emission of NO_x and CO pollutants over a wide range of operating conditions by ensuring that most of the combustion takes place in the primary zone. The flame stabilization is influenced by the strength of the recirculating flow, spray evaporation characteristics, and energy release from the flame. The modeling of this complex flowfield is complicated by the need for accurate numerical algorithms and appropriate vaporization, turbulence, and combustion models.

Swithenbank et al. (1980) approached the problem of mathematical modeling of gas turbine combustor flows by means of three-dimensional finite difference methods incorporating spray processes and kinetic schemes. Because of the excessive computational time required to incorporate the interphase drag effects into the three-dimensional computer code, the fuel-dominant section of the combustor was treated separately as a two-dimensional case. The results of the calculations for the two-dimensional case of fuel injection in the recirculation zone behind a baffle in a cylindrical duct were summarized by Boyson and Swithenbank (1978). The droplet trajectories were determined by integrating the Lagrangian equations in a flow field obtained from separate calculations without considering the effects of liquid- and gas-phase interaction. The reported droplet trajectories were found to deviate from their initial conical path toward the flow direction in the very end of their lifetime when the droplet size becomes small due to evaporation. A similar trend in droplet behavior was observed in the calculations performed by Crowe (1974). His results also indicated a reduction in the length of the recirculation due to droplet interaction. Both the results were based on inadequate representation of the temperature field as uniform temperature was assumed to prevail over the entire flow field. Recently, El Banhawy and Whitelaw (1980) extended the PSI-CELL method of Crowe and co-workers (1974, 1977) to the case of reacting flows and predicted the flow properties of a confined swirling kerosene-spray flame. Comparison with the experimental results was found to be in general agreement and the poor predictions near the burner locations were attributed to the uncertainties associated with their calculated vaporization and spreading rates of the spray. Many of the other approaches used in spray combustion simulation can be found in the review papers by Sirignano (1983, 1986) and Faeth (1977, 1979). The solution procedure to be described herein differs from the previous studies (Faeth, 1977, 1979) in several details.

1 By retaining the time-dependent terms of the gas-phase equations, the numerical method can be used in both steady-state calculations and also unsteady calculations involving combustor instability after some modifications to account for compressible effects. The method is expected to have a better convergence rate in obtaining the steady-state solution because of the reduction in the number of iterations needed for the gas-phase equations.

2 The numerical method employs a second-order accurate interpolation procedure for evaluating gas-phase properties at the characteristic location from fixed Eulerian grid nodes and also in redistributing the source terms evaluated at characteristic locations among the fixed grid nodes surrounding the characteristic. It was indicated by Sirignano (1983) that unless a second or higher-order accurate interpola-

Contributed by the International Gas Turbine Institute for publication in the JOURNAL OF ENGINEERING FOR GAS TURBINES AND POWER. Manuscript received by the International Gas Turbine Institute February 1, 1988.

tion scheme is used that the advantage of elimination of numerical diffusion with a Lagrangian formulation for liquid phase is lost to some extent.

3 The overall vaporization is significantly affected by the large initial velocity of the liquid phase relative to the gas phase when liquid spray is injected into a recirculation zone. In this highly convective environment the transient effects remain important over the entire lifetime of a droplet for heat and mass transfer (Prakash and Sirignano, 1980). In the present study the transient effects are modeled by making use of the integral equation formulation of Tong and Sirignano (1986), which takes into account the liquid-phase internal circulation, unsteady droplet heating, and gas-phase convection.

The solution procedure and its application in predicting the flow properties of a centerbody combustor are described in the following sections.

2 Gas-Phase Equations

The governing equations based on the conservation of the gas-phase flow properties for confined subsonic recirculating flows are in general elliptic in space and parabolic in time. For axisymmetric geometries, the gas-phase equations in Eulerian coordinates can be expressed in the following form:

$$\frac{\partial \rho\phi}{\partial t} + \frac{\partial}{\partial x}\left[\rho U\phi - \Gamma_\phi \frac{\partial \phi}{\partial x}\right] + \frac{1}{y}\frac{\partial}{\partial y}\left[y\rho V\phi - y\Gamma_\phi \frac{\partial \phi}{\partial y}\right] = S_{\phi,g} + S_{\phi,l} \quad (1)$$

Table 1 contains all the relevant information pertaining to each of the dependent variables. The gas-phase equations are nondimensionalized using the inflow conditions of the combustor, which are held fixed in time for the calculations presented herein. The length scales are made dimensionless with respect to the centerbody diameter. The nondimensionalization gives rise to additional dimensionless groups, namely Re_c, M_c, and L_k.

The turbulent shear stresses are evaluated using the k–ϵ model of Launder and Spalding (1972). Use of this turbulence model implies that the influence of droplets on turbulent structure is negligible and the possible oscillatory motions have a low frequency and do not appreciably alter the turbulent properties. Note, however, that the lower frequency components of turbulent structure can be analyzed directly with the unsteady analysis. The k–ϵ model, therefore, might only be employed for the moderate frequency turbulent components. The combustion model is based on an analogous treatment of turbulent diffusion flames with the assumption that no envelope flame is present and the individual droplets act as a source of fuel vapor for the gas phase. The reaction rate is determined by taking into account the minimum of either reaction rates obtained from the eddy breakup model of Spalding (1976) or the Arrhenius reaction rate based on a single-step reaction mechanism given by Westbrook and Dryer (1984)

$$R_{fu} = \min\left\{A\left(\frac{\rho y_f}{W_f}\right)^a \left(\frac{\rho y_o}{W_o}\right)^b e^{(-E/RT)}, \frac{C_R}{W_f} g^{1/2}\left(\frac{\rho\epsilon}{k}\right)\right\} \quad (2)$$

The use of the eddy breakup model necessitates the need for the solution of an additional equation involving the square of fluctuation of concentration g. Irrespective of many deficiencies associated with these turbulent and combustion models, its application in the modeling of turbulent flames involving dilute sprays provided reasonable qualitative agreement in terms of the mean flow properties (1979).

In the present calculations, a special form of the conservation equation based on energy involving $C_p(T)$ and T is employed. The specific heat of the mixture is given by

$$C_p(T) = \sum_i y_i C_{p,i}(T) \quad (3)$$

with summation over all species. By assuming equal binary diffusion coefficients for all the species and by knowing the mass fractions of fuel and oxidizer and the stoichiometric relationship of the given hydrocarbon–air mixture, the mass frac-

Nomenclature

a = exponents of fuel mole fraction in equation (2)
b = exponent of oxidizer mole fraction in equation (2)
A' = $A(W'_c/\rho'_c)^{a+b-1}\, t'_c$ = pre-exponential coefficient in equation (2)
b_1 = $120/T'_c$ = constant in equation (22)
B_k = Spalding transfer number in equation (18)
C_D = droplet drag coefficient in equation (11)
$C(t)$ = droplet regression rate in equation (14)
C'_p = $C_p C'_{p,c}$ = specific heat, Nm/kg K
$C'_{p,c}$ = specific heat of gas at inflow, Nm/kg K
D' = binary diffusion coefficient, m^2/s
dV'_ϕ = $dV_\phi r_c'^3$ = computational cell volume for variable ϕ, m^3
E' = $E_a R' T'_c$ = activation energy, Nm/kg-mole
g' = square of concentration fluctuations
h' = $hC'_{p,c}T'_c$ = dependent variable of energy equation, Nm/kg
k' = $KU_c'^2$ = kinetic energy of turbulence, m^2/s^2
l'_k = $l_k C'_{p,c} T'_c = l_a R' T'_c/w'_f$ = heat of vaporization, Nm/kg
l_a = appears in equation (21) = $l'_k/R' T'_c/W'_f$
L_k = $r'_c/r'_{k,o}$ = ratio of characteristic length and initial drop size
m'_k = $m_k \mu'_c r'_{k,o}$ = droplet vaporization rate, kg/s
M_c = $U'_c/(\nu_c R'_c T'_c)^{1/2}$ = characteristic Mach number
n_k = number of droplets in kth Lagrangian characteristic
P' = $p\,\rho'_c U_c'^2$ = gas pressure, N/m^2
P'_n = $P_n \rho'_c U_c'^2$ = partial pressure of fuel vapor at droplet surface, N/m^2
Pe_l = liquid-phase Peclet number = $\mathrm{Re}_l \mathrm{Sc}_l$
Pr_c = gas-phase Prandtl number = $\mu'_l C'_{p,c}/k'_c$
Pr_l = liquid-phase Prandtl number = $\mu'_l C'_{p,l}/k'_l$
Q' = $QC'_{p,c}T'_c$ = heat of reaction, Nm/kg
r'_c = characteristic length, m
r'_k = $r_k r'_{k,o}$ = droplet radius, m
$r'_{k,o}$ = initial droplet radius, m
R' = universal gas constant, Nm/kg-mole K
R_{fu} = reaction rate defined in equation (2)
Re_c = gas-phase Reynolds number = $U'_c r'_c \rho'_c/\mu'_c$
Re_l = liquid-phase Reynolds number = $U'_c r'_{k,0} \rho'_l/\mu'_l$
Re_k = droplet Reynolds number defined in equation (10)
S_k = $r_k'^2/r_{k,0}'^2$ = radius squared
$S_{\phi,g}$ = source terms appearing in equation (1)

Table 1 Source terms appearing in equation (1)

Equation	ϕ	Γ_ϕ	$S_{\phi,g}$	$dV_\phi S_{\phi,\ell} = s_{\phi,\ell}$
Continuity	1	0	0	$\frac{1}{\mathrm{Re}_c}\Sigma\frac{1}{L_k}n_k m_k$
Axial momentum	U	μ_{eff}	$-\frac{\partial P}{\partial x}+\frac{\partial}{\partial x}\left(\Gamma_\phi\frac{\partial U}{\partial x}\right)+\frac{1}{y}\frac{\partial}{\partial y}\left(y\Gamma_\phi\frac{\partial V}{\partial x}\right)$	$\frac{1}{\mathrm{Re}_c}\Sigma\frac{1}{L_k}\left\{n_k m_k U_k-\frac{4\pi}{3}\rho_k r_k^3 n_k F_{\phi,k}\right\}$
Radial momentum	V	μ_{eff}	$-\frac{\partial P}{\partial y}-\frac{2\Gamma_\phi V}{y^2}+\frac{\partial}{\partial x}\left(\Gamma_\phi\frac{\partial U}{\partial y}\right)+\frac{1}{y}\frac{\partial}{\partial y}\left(y\Gamma_\phi\frac{\partial V}{\partial y}\right)$	$\frac{1}{\mathrm{Re}_c}\Sigma\frac{1}{L_k}\left\{n_k m_k V_k-\frac{4\pi}{3}\rho_k r_k^3 n_k F_{\phi,k}\right\}$
Mass fraction of fuel	y_f	Γ_{eff}	$-w_f R_{fu}$	$\frac{1}{\mathrm{Re}_c}\Sigma\frac{1}{L_k}n_k m_k$
Mass fraction of oxidizer	y_o	Γ_{eff}	$-\nu\, w_o R_{fu}$	0
Energy	h	Γ_{eff}	$(\nu_c-1)M_c^2\frac{\partial P}{\partial t}+w_f Q R_{fu}+\rho T\frac{Dc_p}{Dt}$	
			$-\frac{\partial}{\partial x}\left(\Gamma_\phi T\frac{\partial c_p}{\partial x}\right)-\frac{1}{y}\frac{\partial}{\partial y}\left(y\Gamma_\phi T\frac{\partial c_p}{\partial y}\right)$	$\frac{1}{\mathrm{Re}_c}\Sigma\frac{1}{L_k}n_k m_k\{h_s-\ell_{k,\text{eff}}\}$
Turbulent kinetic energy	k	Γ_{eff}	$\mu_t G-\rho\epsilon$	0
Turbulent energy dissipation	ϵ	Γ_{eff}	$C_1 C_\mu Gk\rho - C_2\rho\epsilon^2/k$	0
Concentration fluctuation	g	Γ_{eff}	$C_{g_1}\mu_{\text{eff}}\left[\left(\frac{\partial y_f}{\partial x}\right)^2+\left(\frac{\partial y_f}{\partial y}\right)^2\right]-C_{g_2}\rho g\frac{\epsilon}{k}$	0

Turbulence parameters

C_1	C_2	C_μ	C_{g_1}	C_{g_2}	κ	E	C_R
1.44	1.92	0.09	2.8	2.0	0.4187	9.0	1.0

$$\mu_{\text{eff}}=\frac{\mu_{la}}{\mathrm{Re}_c}+\mu_t,\quad \Gamma_{\text{eff}}=\frac{\mu_{la}}{\sigma_{\phi_{la}}\mathrm{Re}_c}+\frac{\mu_t}{\sigma_{\phi_t}},\quad \mu_t=C_\mu\rho\frac{k^2}{\epsilon},\quad G=2\left[\left(\frac{\partial U}{\partial x}\right)^2+\left(\frac{\partial V}{\partial y}\right)^2+\left(\frac{V}{y}\right)^2\right]+\left(\frac{\partial U}{\partial y}+\frac{\partial V}{\partial x}\right)^2,\quad F_{\phi,k}=\frac{d\phi_k}{dt}$$

Nomenclature (cont.)

$S_{\phi,l}$ = additional source terms of equation (1) arising from the liquid- to gas-phase interaction
Sc_c = gas-phase Schmidt number $=\mu_c'/\rho_c' D_c'$
t' = tt_c' = time, s
t_c' = r_c'/U_c' = characteristic time, s
T' = TT_c' = gas temperature, K
T_b' = $T_b\, T_c'$ = liquid boiling temperature at normal pressure, K
T_c' = characteristic temperature, K
T_k' = $T_k T_c'$ = droplet surface temperature, K
U' = UU_c' = gas velocity in axial direction, m/s
U_c' = characteristic velocity, m/s
U_k' = $U_k U_c'$ = axial component of droplet velocity, m/s
V' = $V\, U_c'$ = gas velocity in radial direction, m/s
V_k' = $V_k U_c'$ = radial component of droplet velocity, m/s
W_a' = $W_a W_c'$ = molecular weight of ith species, kg/kg-mole
x' = xr_c' = axial distance, m
y' = yr_c' = radial distance, m
y_i = mass fraction of the species
Γ_ϕ = $\Gamma_\phi \mu_c'$ = exchange coefficient in Table 1, kg/s/m
ϵ' = $\epsilon U_c'/t_c'$ = dissipation of energy, $\mathrm{m}^2/\mathrm{s}^3$
η = represents the streamline of a Hill's vortex in the circulating fluid in equations (13)–(17)
θ = half angle of the hollow-cone spray, deg
μ' = $\mu\mu_c'$ = viscosity, kg/s/m
μ_c' = viscosity of air at inflow, kg/s/m
ν = stoichiometric ratio
ν_c = ratio of specific heats
ρ' = $\rho\, \rho_c'$ = density, $\mathrm{kg/m}^3$
ρ_c' = density of air at inflow, $\mathrm{kg/m}^3$
σ_ϕ = represents Sc_c or Pr_c for variable ϕ
ϕ = represents dependent variable of equation (1)
Φ = equivalence ratio
χ_i = mole fraction of ith species

Subscripts

a = air stream
b = boiling
c = characteristic
eff = effective
f = fuel
g = gas-phase
i = species
k = droplet or Lagrangian characteristic representing a group of droplets
la = laminar
l = liquid phase
n = normal conditions
o = oxidizer
s = droplet surface
t = turbulent
w = wall
0 = liquid-phase initial conditions

tions of the remaining species N_2, CO_2, and H_2O can be easily determined in terms of simple algebraic expressions. The variation of the specific heats with temperature is considered by using polynomials of the form

$$C_{p,i} = \frac{R}{W_i}\left(C_{1i} + C_{2i}T + C_{3i}T^2 + C_{4i}T^3 + C_{5i}T^4\right) \tag{4}$$

The constants in the polynomials are compiled from CRC (1985) and Raju and Krishnamurthy (1985). The system of equations for the gas phase are completed with the following equation of state:

$$\rho = (\nu_c - 1)M_c^2 \frac{p}{RT\sum_i \frac{y_i}{W_i}} \tag{5}$$

σ_ϕ in Table 1 denotes the appropriate value of effective Prandtl or Schmidt number for each ϕ. For all the dependent variables the values chosen in the present calculations correspond to $\sigma_{\phi_{la}} = 1.0$ and $\sigma_{\phi_t} = 0.9$ with the exception of $\sigma_{\epsilon_t} = 1.217$. The discussion of the assumptions involved in the derivation of $S_{\phi,l}$ is omitted herein as it has been given by Sirignano (1983, 1985, 1986).

The implementation of the boundary conditions at the solid wall would become straightforward if the grid mesh could be made fine enough to resolve the turbulent boundary layer structure in the vicinity of the wall. Instead the source terms in the governing equations of momentum, kinetic energy, dissipation rate, and energy are modified with the introduction of wall functions. The procedure adopted for wall functions is similar to that given by Khalil et al. (1975). For the equations involving mass fractions of fuel, oxidizer, and concentration fluctuation, the flux normal to the wall is set to zero. Inflow boundary conditions for all dependent variables are prescribed. The radial velocity is set to zero at the axis of symmetry. All other boundary conditions are based on normal gradients, which are set to zero at the axis of symmetry and the outflow.

3 Liquid-Phase Equations

Among the various advantages of using the Lagrangian formulation for the liquid-phase equations are its ability to handle multivaluedness of solutions in a natural way, elimination of numerical diffusion, and restriction of the Lagrangian calculations to the region where droplets are present so that the Eulerian–Lagrangian approach can be used for very fine resolution where required (Sirignano, 1983, 1985, 1986). The liquid- and gas-phase equations are nondimensionalized with respect to the same scales. However, the droplet radius (r_k') is made dimensionless with respect to its initial radius ($r_{k,0}'$). Complete discussion of the underlying assumptions involved in the derivation of the liquid-phase equations presented herein can be found in Sirignano (1983) and Aggarwal et al. (1987).

$$\frac{dx_k}{dt} = U_k \tag{6}$$

$$\frac{dy_k}{dt} = V_k \tag{7}$$

$$\frac{dU_k}{dt} = \left\{\frac{L_k^2}{\mathrm{Re}_c\rho_k}\right\}\frac{3}{16}\frac{C_D\mu\,\mathrm{Re}_k}{r_k^2}\left[U_g - U_k\right] \tag{8}$$

$$\frac{dV_k}{dt} = \left\{\frac{L_k^2}{\mathrm{Re}_c\rho_k}\right\}\frac{3}{16}\frac{C_D\mu\,\mathrm{Re}_k}{r_k^2}\left[V_g - V_k\right] \tag{9}$$

where

$$\mathrm{Re}_k = 2\left\{\frac{\mathrm{Re}_c}{L_k}\right\}\frac{r_k\rho_g}{\mu}\left[(U_g - U_k)^2 + (V_g - V_k)^2\right]^{1/2} \tag{10}$$

$$C_D = \frac{24}{\mathrm{Re}_k}\left(1 + \frac{\mathrm{Re}_k^{2/3}}{6}\right) \tag{11}$$

Based on the Tong–Sirignano model (1986)

$$\frac{dS_k}{dt} = -2\left\{\frac{L_k^2}{\mathrm{Re}_c\rho_k}\right\}\mu\left[\frac{2}{\mu}\mathrm{Re}_k\right]^{1/2} f(B_k) \tag{12}$$

The function $f(B_k)$ is obtained from the solution of Emmon's problem. The range of validity of this function is extended in the present calculations to consider the effects of droplet condensation.

Based on the vortex model (Tong and Sirignano, 1986) for the internal droplet temperature

$$\frac{\partial T_k}{\partial t} = 17\left\{\frac{L_k}{\mathrm{Pe}_l}\right\}\frac{1}{r_k{}^2}\left[\eta\frac{\partial^2 T_k}{\partial\eta^2} + (1 + C(t)\eta)\frac{\partial T_k}{\partial\eta}\right] \tag{13}$$

where

$$C(t) = \frac{3}{17}\left\{\frac{\mathrm{Pe}_l}{L_k}\right\}r_k\frac{dr_k}{dt} \tag{14}$$

The boundary conditions for equation (13) are given by

$$t = t_{\text{injection}}, \quad T_k = T_{k,0} \tag{15}$$

$$\eta = 0, \quad \frac{\partial T_k}{\partial\eta} = \frac{1}{17}\left\{\frac{\mathrm{Pe}_l}{L_k}\right\}r_k^2\frac{\partial T_k}{\partial t} \tag{16}$$

$$\eta = 1, \quad \frac{\partial T_k}{\partial\eta} = \frac{3}{16}\left\{\frac{\mathrm{Pr}_c}{k_l}\right\}\mu\left(\frac{2}{\pi}\mathrm{Re}_k\right)^{1/2}\left[\frac{C_p(T_g - T_{k,s})}{B_k} - l_k\right]f(B_k) \tag{17}$$

$$B_k = \frac{C_p(T_g - T_{k,s})}{l_{k,\text{eff}}} = \frac{(y_{fs} - y_f)}{(1 - y_{fs})} \tag{18}$$

(Note: The Spalding number is based on y_{fs} and y_f in the present calculations.)

$$l_{k,\text{eff}} = l_k + 4\pi\left\{\frac{k_l}{\mathrm{Pr}_c}\right\}\frac{r_k^2}{m_k}\left(\frac{\partial T_k}{\partial r}\right)_s \tag{19}$$

$$y_{fs}^{-1} = 1 + \frac{W_a}{W_f}\left(\chi_{fs}^{-1} - 1\right) \tag{20}$$

Based on the assumption that the phase equilibrium exists at the droplet surface, the Clausius–Clapeyron relationship yields

$$\chi_{fs} = \frac{P_n}{p}\exp\left\{l_a\left(\frac{1}{T_b} - \frac{1}{T_{k,s}}\right)\right\} \tag{21}$$

In equation (10) the molecular viscosity is evaluated at a reference temperature using Sutherland's equation

$$\mu(T_{\text{ref}}) = \mu_C\left(\frac{T_{\text{ref}}}{T_C}\right)^{3/2}\frac{T_C + b_1}{T_{\text{ref}} + b_1} \tag{22}$$

where

$$T_{\text{ref}} = \frac{1}{3}T_g + \frac{2}{3}T_{k,s} \tag{23}$$

It is worthwhile noting that the solution to the partial differential equation (13) subjected to the boundary conditions (15)–(17) is obtained by using the integral equation formulation of Tong and Sirignano (1986). This approach reduces the problem of solving the partial differential equation to the problem of solving a system of ordinary differential equations involving a series of eigenfunctions. The regression term $C(t)$ is treated as a piecewise constant. The additional complexity of programming introduced as a result of determining the eigenvalues may be offset by the savings in computational time for the desired accuracy of solution.

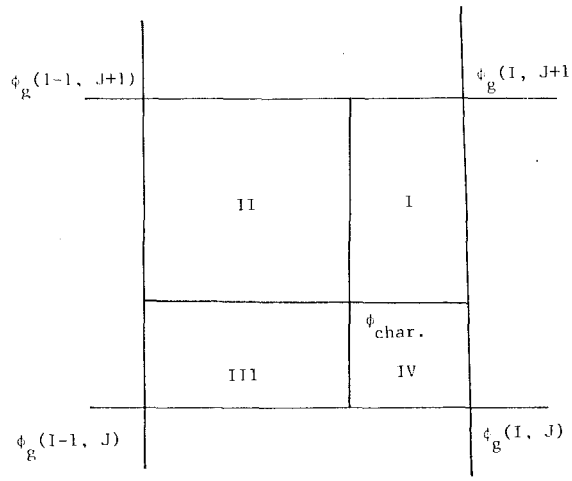

Fig. 1 Grid cell surrounding a characteristic

The Tong–Sirignano model is based on the boundary layer approximation for the gas phase and is applicable for high droplet Reynolds numbers. The model predicts low vaporization rates because of $Re_k^{1/2}$ dependence for Reynolds number of 0(1). It is, therefore, appropriate to switch from the Tong–Sirignano model to some valid low Reynolds number model as the droplet Reynolds number becomes small (Aggarwal et al., 1987). The vaporization model used for low Reynolds numbers is based on the spherically symmetric case with the correction for convective effects considered through the empirical correlations obtained from Abramzon and Sirignano (1987). The switching between the vaporization models is accomplished by replacing the term $2(2/\pi\ Re_k)^{1/2} f(b_k)$ of equations (12) and (17) by the following expressions:

$$\{1+(1+Re_k)^{1/3}\}Re_k^{0.077}\ln(1+B_k)$$

when $1 < Re_k \le 20$ or

$$\{1+(+Re_k)^{1/3}\}\ln(1+B_k)$$

when $Re_k \le 1$. The implications of switching between vaporization models need further investigation.

The droplets may evaporate, shatter, and/or reflect with reduced momentum upon droplet impingement with combustor walls. In the absence of detailed experimental verification, it is assumed that the droplets undergo instantaneous vaporization upon droplet collision with the walls (El Banhawy and Whitelaw, 1980).

4 Solution Procedure

The governing equations of the gas phase are solved using the TEACH computational procedure of Patankar (1980), where the finite-difference approximations of the derivatives with respect to the space variables are obtained by integrating the equations over a control volume surrounding the nodes of the difference mesh. Numerical integration of the equations is carried over a staggered mesh with grid nodes for the velocity components being located in the middle of the faces of the scalar variable control volume. The solution procedure of TEACH does not solve the continuity equation directly. Instead the continuity equation is satisfied indirectly by an iterative scheme known as the SIMPLE algorithm of Patankar and Spalding (1980). The velocities are first calculated from the momentum equations using a guessed pressure distribution; then the pressure distribution is adjusted so that the velocities satisfy the mass continuity equation and the whole cycle is repeated. Appropriate modifications are made to the TEACH computer code to account for the additional source terms introduced as a result of the gas- and liquid-phase interaction and the unsteady terms of the gas-phase equations.

The liquid-phase equations are advanced in time by an explicit second-order Runge–Kutta method requiring a small time step. Numerical integration of these ordinary differential equations is relatively inexpensive compared to the solution of the gas-phase equations in terms of the computational time required. The liquid- and gas-phase equations are integrated with different time steps in order to exploit fully the advantage offered by the implicit TEACH procedure used for gas-phase equations, which allows numerical integration to be carried over a large time step. Based on the known gas-phase properties the liquid-phase equations are first advanced in time from the nth time level to the $(n+1)$th time level corresponding to the gas-phase time step Δt_g. The gas-phase equations are solved next. The solution procedure for the integration of the governing equations requires: (1) interpolation of the gas-phase properties from the fixed Eulerian locations to the characteristic location; (2) integration of the liquid-phase equations over a time step $\Delta t_{l,m}$; (3) redistribution of the source terms evaluated at the characteristic location among the Eulerian nodes surrounding the characteristic; (4) Steps (1)–(3) are repeated until the liquid-phase equations are advanced over a time step Δt_g. The characteristic locations as well as the gas-phase properties are updated at the end of each time step $\Delta t_{l,m}$. Such a procedure is useful when the particles experience steep gradients. In the situations encountered otherwise it would be more appropriate to choose the characteristic location to be an average of the nth and $(n+1)$st time levels and thereby avoiding excessive computations involving interpolations. This aspect will be given future consideration along with the problem of choosing the optimum values needed for $\Delta t_{l,m}$ and Δt_g in order to enhance the rate of convergence in the steady-state calculations; (5) solve the gas-phase equations. Steps (1)–(5) are repeated until the iteration converges before advancing to the next step for unsteady calculations. In the case of steady-state calculations the solution can be directly advanced to the next time step without the need for iteration.

The interpolation scheme required in Steps (1) and (3) is a linear second-order accurate procedure. Figure 1 shows a grid cell surrounding a characteristic for the dependent variable ϕ. The gas-phase properties at the characteristic location are interpolated as follows:

$$\phi_{g,\text{char}} = (\phi_g(I, J)*\text{Vol II} + \phi_g(I, J+1)*\text{Vol III} + \phi_g(I-1, J+1)*\text{Vol IV} + \phi_g(I-1, J)*\text{Vol I})/(\text{Total cell volume}) \quad (24)$$

The source term at the grid nodes due to liquid-phase interaction is given by

$$s_{\phi l,m}(I, J) = \frac{s_{\phi l,\text{char.}}*\text{Vol II}}{\text{Total cell volume}} \quad (25)$$

and $s_{\phi l,m}(I, J+1)$, $s_{\phi l,m}(I-1, J+1)$, and $s_{\phi l,m}(I-1, J)$ are determined in a similar way. The contribution of the source terms $s_{\phi l,m}$ corresponds to a time step of $\Delta t_{l,m}$. The total contribution of these source terms over a time step Δt_g is given by

$$s_{\phi,l} = \sum_{m=1}^{M} \frac{\Delta t_{l,m}}{\Delta t_g} s_{\phi l,m} \quad (26)$$

where

$$\sum_{m=1}^{M} \Delta t_{l,m} = \Delta t_g \quad (27)$$

The relationship between $s_{\phi,l}$ and $S_{\phi,l}$ of equation (1) is given by

$$s_{\phi,l} = dV_\phi S_{\phi,l} \quad (28)$$

Depending on the relative location of the characteristic within

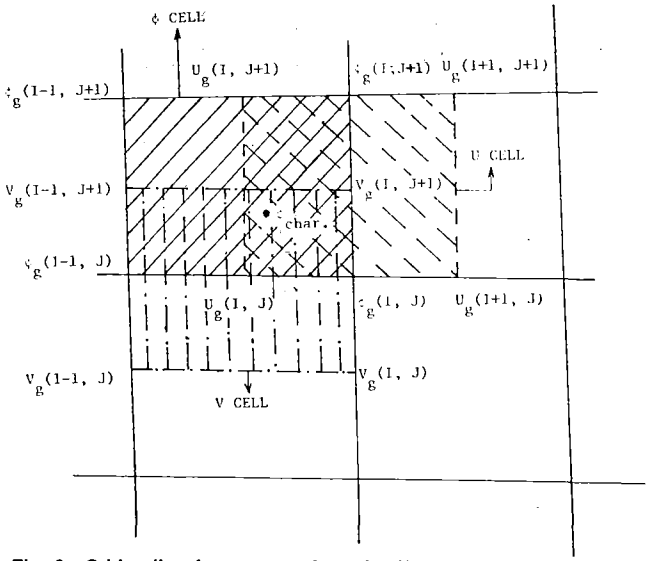

Fig. 2 Grid cells of a staggered mesh affected by the interpolation procedure

the grid cell of a scalar dependent variable different grid cells of axial and radial velocity components are affected by the interpolation procedure because of the use of a staggered grid in the TEACH computational procedure. One such configuration is shown in Fig. 2. The interpolation scheme for the dependent variables U and V is based on their respective grid cells.

5 Injection of the Particles

The injected spray is assumed to originate from the middle of the centerbody face. The droplet flow is assumed to be conical and is represented by different half-cone angles θ. Because of the axisymmetric configuration each characteristic represents a circular ring of fluid containing a definite number of droplets. The mass flow rate of the fuel is determined from the stoichiometric conditions.

$$M_f = 0.21\ \Phi\ M_a W_f/(\nu W_o) \tag{29}$$

The injection time interval for a new characteristic to appear is based on the ($\Delta x =$) Eulerian mesh size and ($U_{k,0} =$) injection velocity of the droplet. This ensures that the droplet properties are resolved on a commensurate scale with the gas-phase properties

$$dt_{\text{injection}} = \frac{\Delta x}{U_{k,0}} \tag{30}$$

The number of droplets in each characteristic is given by

$$n_k = L_k^3 \frac{M_{f,k} dt_{\text{injection}}}{\left(\frac{4}{3}\pi r_k^3 \rho_k\right)} \tag{31}$$

where

$$M_f = \Sigma M_{f,k}$$

At the time of injection the initial properties of the droplet such as $r_{k,o}$, $T_{k,0}$, velocity of the droplet $U_{k,0}$, and half cone angle θ are specified. Initially, all the characteristics are placed on the axial grid line next to the axis of symmetry. The initial velocity components of the droplet are given by

$$U_k = U_{k,0}\cos\theta \tag{32}$$

$$V_k = U_{k,0}\sin\theta \tag{33}$$

Once the droplets are injected their subsequent behavior is determined by the governing equations. When 99 percent of the mass has been evaporized the characteristic is removed from the combustor and the remaining fuel is added as vapor instantaneously.

Table 2 Values used in the computation

Parameter	Value
Combustor dimensions:	
Radius of the duct wall	0.075 m
Radius of the centerbody	0.0525 m
Length of the combustor	0.75 m
Inflow conditions of the combustor:	
Velocity, U_c'	30 m/s
Temperature, T_c'	1000 K
Pressure, P_c'	10 atm
Density, ρ_c'	3.399 kg/m^3
Turbulent kinetic energy, k_c'	0.03 $U_c'^2$ m^2/s^2
Turbulent dissipation rate, ϵ_c'	$\frac{k_c'\ c_\mu^{0.75}}{0.0009}\ \frac{\text{m}^2}{\text{s}^3}$
Duct wall temperature	700 K
Centerbody wall temperature	1000 K
Initial conditions of the liquid spray:	
Fuel	*n*-decane
Liquid density, ρ_k'	773 kg/m^3
Droplet temperature, T_K'	300 K
Droplet velocity, $U_{k,o}'$	200 m/s
Equivalence ratio, Φ	0.3

6 Results and Discussion

The numerical model is applied to predict the flow properties of a centerbody combustor. The centerbody combustor consists of a cylindrical centerbody placed coaxially in a cylindrical duct. The flow is characterized by a recirculation zone in the wake of the centerbody when incoming air passing through the annulus of the centerbody and the duct wall encounters a sudden expansion. The dimensions of the combustor along with the values used in the computation for the initial conditions of the liquid fuel and the wall and inflow boundary conditions of the gas phase are summarized in Table 2. These values correspond to $M_a = 0.9$ kg/s, $M_f = 0.018$ kg/s, and $Re_c = 2.67 \times 10^5$. The injected spray is assumed to comprise four conical streams; half-angles of the corresponding streams are given by $\theta = 5$, 15, 25, and 35 deg. The calculations are performed for two different cases involving polydisperse and monodisperse sprays, respectively. For the polydisperse spray case, each of the conical streams is discretized by four droplet groups based on different radii, $r_{k,0}' = 75$, 60, 45, and 30 μm. For the monodisperse spray case, the droplet radius is taken to be equal to 55 μm. The number of mass flow rates contained among each of the streams and droplet groups is assumed to be equal. The gas-phase calculations are performed on a grid with mesh size of 24 axial nodes $\times$20 radial nodes. For the polydisperse spray case, it takes about 1.2 h of CPU time on VAX 780 for the calculations to reach steady state using the following time steps: $\Delta t_{\text{injection}} = 1.6$ ms, $\Delta t_g = 1$ ms, and $\Delta t_{l,m} = 0.03$ ms. The corresponding time for the monodisperse spray case is about 35 min of CPU time.

The droplet trajectories and the velocity vector plot of the gas field for the polydisperse spray are shown in Figs. 3 and 4. In Fig. 3 the four droplet groups can be identified by the size of the symbol used to represent the characteristic location. The droplets enter the combustor at relatively high Reynolds numbers, $250 < Re_k < 700$. It is also observed, however, that the droplet Reynolds number falls below 50 with approximately 80 percent of the droplet lifetime still remaining. This effect can be clearly seen in the behavior of the droplet trajectories as

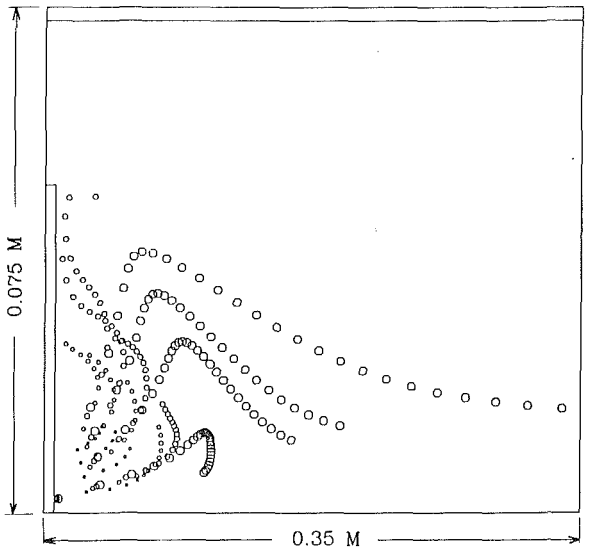

Fig. 3 Droplet trajectories for polydisperse spray

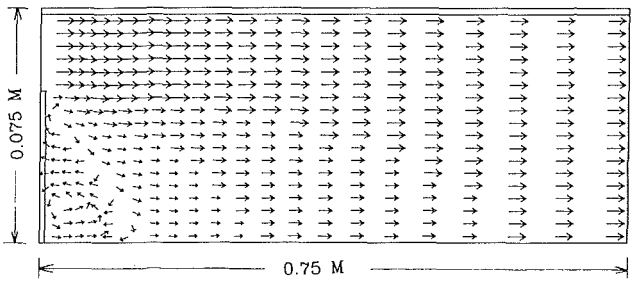

Fig. 4 Velocity vector plot for polydisperse spray

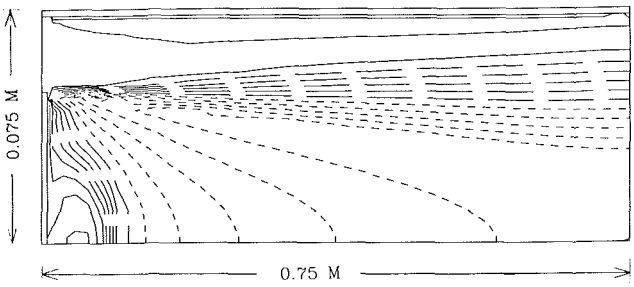

Fig. 5 Temperature contours

the entering droplets travel linearly before the drag forces cause the droplets to decelerate and the droplets assume eventually the same path dictated by the gas phase velocity. Modifications to the recirculation region are more dramatic due to droplet interaction because it would have been characterized otherwise by a single torodial vortex (Crowe, 1974; Raju and Krishnamuthy, 1985). Most of the vaporization occurs within the recirculation zone as smaller droplets are unable to penetrate downstream. This condition can lead to an excessive concentration of fuel vapor near the injection source. Droplet vaporization is completed by about $x = 0.35$ m. The calculated location of flow reversal along the centerline occurs at about 1.2 times the diameter of the centerbody. The length of the recirculation is subjected to the uncertainties of using the k–ϵ turbulence model. The discussion is limited to the results obtained for the polydisperse spray, since the behavior of the flow field for the polydisperse and monodisperse sprays is similar for the conditions considered.

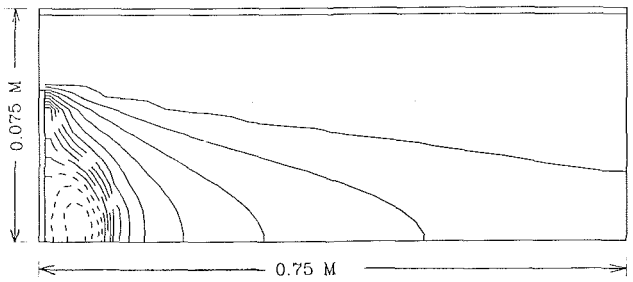

Fig. 6 Fuel mass fraction contours

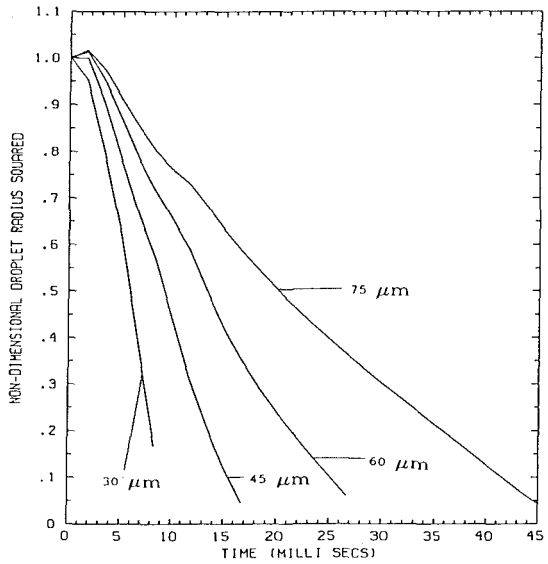

Fig. 7 Nondimensional droplet radius versus time for different droplet groups of stream, $\theta = 5$ deg

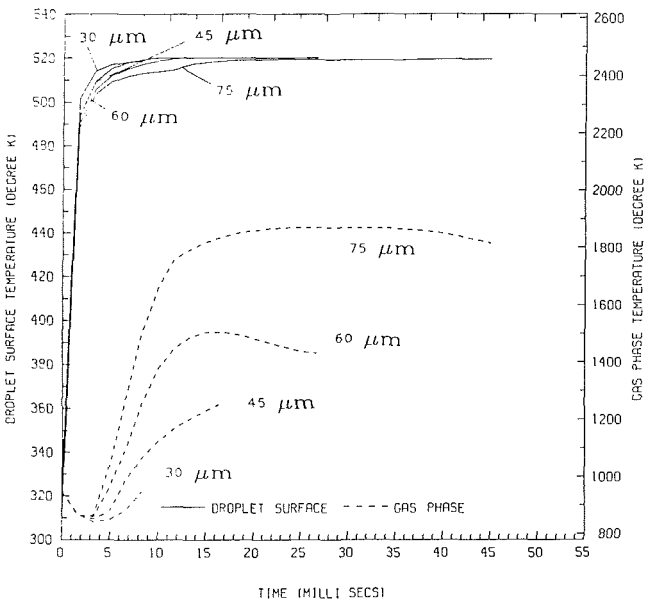

Fig. 8 Droplet surface temperature versus time for different droplet groups of the stream, $\theta = 5$ deg (also shown are the ambient gas-phase temperatures)

The temperature contours are shown in Fig. 5. The temperature difference between two adjacent contour lines is about 150 K. The maximum and minimum temperatures of the gas field are found to be 2800 K and 700 K. The solid lines represent the low-temperature region and the lines connected

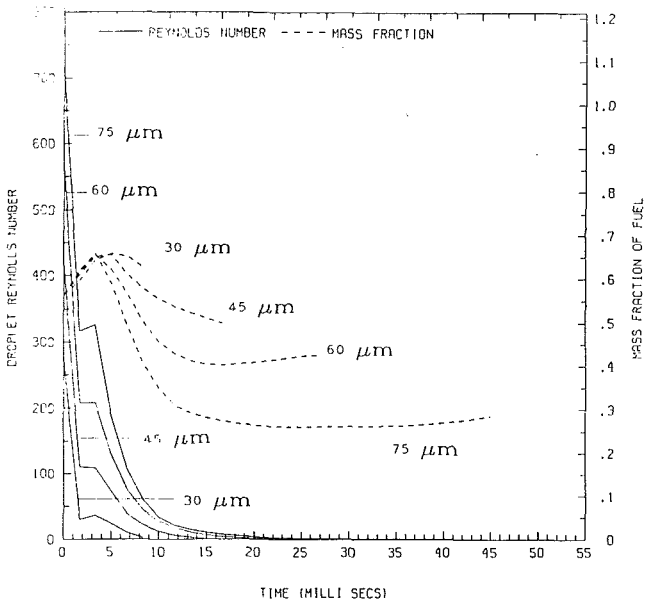

Fig. 9 Droplet Reynolds number versus time for different droplet groups of the stream, $\theta = 5$ deg (also shown are the ambient mass fractions of the fuel)

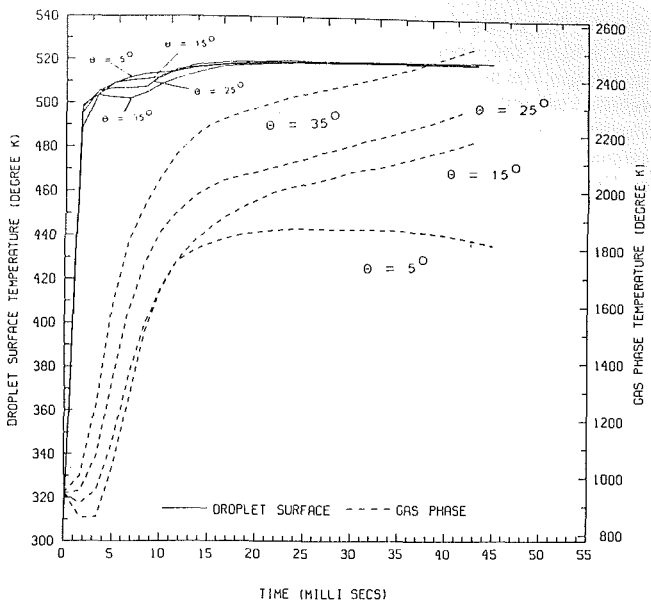

Fig. 11 Droplet surface temperature versus time for the droplet group, $r'_{k,o} = 75$ μm, among each of the different streams (also shown are the ambient gas-phase temperatures)

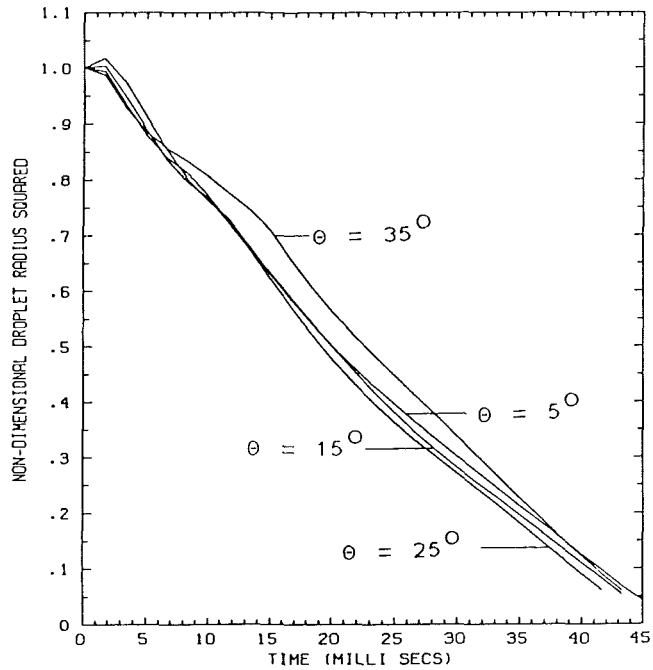

Fig. 10 Nondimensional droplet radius squared versus time for the droplet group, $r'_{k,o} = 75$ μm, among each of the different streams (also shown are the ambient gas-phase temperatures)

by the shortest dashed segments represent the high-temperature region. It can be clearly seen that the shear layer originating from the edge of the centerbody face acts as a continuous ignition source for the freshly formed mixture of fuel and air. The combustion process proceeds further downstream along the shear layer and the highest intensity combustion region is located close to the end of the combustor near the axis of symmetry. The low temperatures of the recirculation region are a result of the cooling effect of the vaporization process. This region is also characterized by large temperature gradients.

The fuel mass fraction contours of Fig. 6 are represented in a way similar to the temperature contours of Fig. 5. The values represented by the contour lines vary from 0.62 to 0.005 with the mass fraction difference between adjacent contour lines is about 0.047. The large concentration of fuel vapor in the recirculation region is due to insufficient mixing of fuel and air as the rate of air entrainment in the near-wake region is in general quite low for bluff body flame stabilizers; the air entrainment characteristics of the wake region and subsequent mixing of fuels with combustion products could be enhanced with the help of swirl and opposing jets (Lefebvre, 1983).

Figures 7–9 show the variation of droplet radius squared, droplet surface temperature, and droplet Reynolds number, respectively, with time for the different droplet groups of the stream, $\theta = 5$ deg. These figures also include the corresponding ambient conditions (gas-phase) encountered by the droplets during their lifetime. When the droplets with an initial temperature of 300 K are introduced into the combustor, the gas-phase conditions near the injection region are characterized by $y_f \sim 0.6$ and $T'_g \sim 900$ K. These conditions might likely lead to a droplet condensation because the Spalding transfer number of equation (18) can become negative if the mass fraction of fuel at the interface is less that the mass fraction of fuel at the ambient. This is indeed what happens as the droplets undergo a slight increase in radius due to condensation before they start evaporating. It takes about 10 ms for the smallest droplets to evaporate and about 45 ms for the largest droplets. It also takes longer for the largest droplets to reach the wet-bulb temperature. The droplets are observed to vaporize under changing conditions of gas-phase temperatures. The initial drop in the gas-phase temperature can be attributed to the cooling effect associated with the heatup period of the droplets. The smaller droplets are vaporizing under conditions of lower gas-phase temperatures in comparison with the larger droplets, which can penetrate farther downstream into the high temperature region. The reasons for the lower vaporization rates are mainly due to the reduction in convective effects as the droplet Reynolds number becomes small and the decrease in the Spalding transfer number as most of the vaporization is taking place under the conditions of fuel-rich surrounding medium. One would expect that the droplet Reynolds number should continue to decrease in time because of the resulting decrease in droplet relative velocity due to drag and continued decrease of the droplet radius due to evaporation. The results do indicate this trend in the behavior of the

droplet Reynolds number except for a small time period during which the increase in the density of the gas-phase outweighs the accompanied decrease in the droplet radius and relative velocity. Figures 10 and 11 show the behavior of the droplet radius squared and droplet surface temperature, respectively, for the droplet group of $r_k' = 75$ μm among each of the different streams. The relative differences among each of four streams for the droplet of the same group in terms of the droplet radius squared and droplet surface temperatures are found to be of secondary importance even though the droplets are subjected to different penetration distances and gas-phase temperatures. The results suggest that the conditions encountered by the droplet during the initial period are more significant to the vaporization process. Similar trends are observed for the monodisperse spray.

7 Conclusions

The solution procedure described has been successful in predicting the qualitative features of the centerbody flow field. Quantitative differences are expected because of the minor errors associated with the models used for turbulence, combustion and vaporization, and the idealized spray injection process. The numerical model could be improved by taking into account the influence of radiative heat transfer, particle turbulence, intermediate species of the combustion process, and the effect of variable transport coefficients on the vaporization process. The calculations indicate that the turbulent mixing rate of fuel and air in the shear layer appears to be the controlling step of the overall combustion process because of the large accumulation of fuel vapor in the recirculation for the conditions considered. Further investigation is needed with the inclusion of swirl and/or opposing jets to the present combustor configuration in order to delineate the regimes in which vaporization becomes the controlling step.

References

Abramzon, B., and Sirignano, W. A., 1987, "Numerical Simulation of Fuel Droplet Vaporization in Oscillating Flow Field," *Proceedings of 2nd ASME-JSME Thermal Engineering Joint Conference*, ASME, Vol. 1, pp. 84–95.

Aggarwal, S. K., Tong, A. Y., and Sirignano, W. A., 1987, "A Comparison of Vaporization Models in Spray Calculations," *AIAA Journal*, Vol. 22, pp. 1448–1457.

Boyson, F., and Swithenbank, J., 1978, "Spray Evaporation in Recirculating Flow," *Seventeenth Symposium (International) on Combustion*, The Combustion Institute, Pittsburgh, pp. 443–453.

CRC, 1985, *Handbook of Physics and Chemistry*, Chemical Rubber Co., Cincinnati, OH.

Crowe, C. T., 1974, "A Computational Model for the Gas-Droplet Flow Field in the Vicinity of an Atomizer," WSS/CI preprint 74-23, Western States Section/Combustion Institute.

Crowe, C. T., Sharma, M. P., and Stock, D. E., 1977, "The Particle-Source-Cell (PSI) Model for Gas-Droplet Flows," ASME *Journal of Fluids Engineering*, Vol. 99, pp. 325–332.

El Banhawy, Y., and Whitelaw, J. H., 1980, "Calculation of the Flow Properties of a Confined Kerosene-Spray Flame," *AIAA Journal*, Vol. 18, pp. 1503–1510.

Faeth, G. M., 1977, "Current Status of Droplet and Liquid Combustion," *Progress Energy Combustion Science*, Vol. 3, pp. 191–224.

Faeth, G. M., 1979, "Spray Combustion Models—A Review," AIAA preprint 79-0293, *17th Aerospace Sciences Meeting*, New Orleans, LA.

Khalil, E. E., Spalding, D. B., and Whitelaw, J. H., 1975, "The Calculation of Local Flow Properties in Two-Dimensional Furnaces," *Int. J. Heat Mass Transfer*, Vol. 18, pp. 775–791.

Launder, B. E., and Spalding, D. B., 1972, *Mathematical Models of Turbulence*, Academic Press, London, United Kingdom.

Lefebvre, A. H., 1983, *Gas Turbine Combustion*, Hemisphere Publishing Co., Washington, DC.

Patankar, S. V., 1980, *Numerical Heat Transfer and Fluid Flow*, Hemisphere Publishing Co., Washington, DC.

Prakash, S., and Sirignano, W. A., 1980, "Theory of Convective Droplet Vaporization With Unsteady Heat Transfer in the Circulating Liquid Phase," *Int. J. Heat Mass Transfer*, Vol. 23, pp. 253–268.

Raju, M. S., and Kirshnamurthy, L., 1985, "Computational Fluid Dynamic Studies of Certain Ducted Bluff-Body Flowfields Relevant to Turbojet Combustors," University of Dayton Research Institute, Dayton, OH, UDR-TR-85-83, Vol. II.

Sirignano, W. A., 1983, "Fuel Droplet Vaporization and Spray Combustion," *Progress Energy Combustion Science*, Vol. 9, pp. 291–322.

Sirignano, W. A., 1986, "The Formulation of Spray Combustion Models: Resolution Compared to Droplet Spacing," ASME *Journal of Heat Transfer*, Vol. 108, No. 3, pp. 633–639.

Sirignano, W. A., 1985, "Spray Combustion Simulation," *Numerical Simulation of Combustion Phenomena*, R. Glowinski et al., eds., Springer-Verlag, Heidelberg, Federal Republic of Germany.

Spalding, D. B., 1976, "Mathematical Models of Turbulent Flames: A Review," *Combustion Science and Technology*, Vol. 13, pp. 3–25.

Swithenbank, J., Turan, A., and Felton, P. G., 1980, "Three-Dimensional Two-Phase Mathematical Modelling of Gas Turbine Combustors," *Gas-Turbine Design Problems*, Hemisphere, Washington, DC, pp. 249–314.

Tong, A. Y., and Sirignano, W. A., 1986, "Multi-component Transient Droplet Vaporization With Internal Circulation: Integral Equation Formulation and Approximate Solution," *Numerical Heat Transfer*, Vol. 10, pp. 253–278.

Westbrook, C. K., and Dryer, F. L., 1984, "Chemical Kinetic Modeling of Hydrocarbon Combustion," *Progress Energy Combustion Science*, Vol. 10, pp. 1–57.

Irreversibility and Thermoeconomics Based Design Optimization of a Ceramic Heat Exchanger

J. Ranasinghe
Graduate Student.

S. Aceves-Saborio
Graduate Student.

G. M. Reistad
Professor and Head.

Department of Mechanical Engineering,
Oregon State University,
Corvallis, OR 97331

This paper illustrates the optimization procedure for heat exchangers residing in complex power plants. A specific case of optimizing a new technology ceramic heat exchanger, which is a part of the complex power plant, is shown. The heat exchanger design methods presented are based on two different objective functions, namely, a modified irreversibility rate based objective function proposed by the authors in earlier work and an objective function based on thermoeconomics. This paper also extends existing work by illustrating a method to obtain the cost coefficients for thermoeconomic optimization, based on the use of an overall plant simulation model. A discussion on possible methods of improving the design guideposts obtained from irreversibility minimization analysis is also presented.

Introduction

In earlier work, the authors proposed a modified irreversibility based objective function for optimization of heat exchangers (Aceves-Saborio et al., 1989). The objective function, formulated in a manner to be consistent with the logic of Boyd et al. (1981) and Le Goff and Giulietti (1982), differs from the conventional irreversibility equation by an additional term included to take into account the exergy spent in the construction of the equipment under analysis. The earlier work also showed the utility of the modified irreversibility generation equation to establish nonchanging design limits. The paper included the simplified example of a counterflow heat exchanger. Although the area of the thermoeconomic optimum heat exchanger varies as external costs change, the modified irreversibility equation was used to set a maximum value of the total area, and it was shown that under no circumstances could the optimum thermoeconomic heat exchanger have an area larger than this maximum.

The present paper builds on the previous work by showing an extended application for an emerging technology, namely, that of a ceramic heat exchanger, in this case being part of a complex power plant. The paper discusses the parameters and constraints that make designing ceramic heat exchangers different from designing metallic heat exchangers. This work further extends existing work by illustrating a method to obtain the cost coefficients necessary for thermoeconomic optimization based on the use of an overall plant simulation program.

The results include comparisons between the different objective functions for restricted (one degree of freedom) optimization. The global optimum thermoeconomic heat exchanger design is then obtained and compared to the design obtained from the modified irreversibility minimization analysis. A further discussion is included on possible methods to improve the accuracy of the design limits.

Contributed by the Advanced Energy Systems Division for publication in the JOURNAL OF ENGINEERING FOR GAS TURBINES AND POWER. Manuscript received by the Advanced Energy Systems Division March 7, 1988.

Theoretical Background

Different criteria based on the exergy concept are commonly used for performance evaluation of heat exchangers. These include irreversibility rate analysis, modified irreversibility rate analysis, and thermoeconomic analysis. The next section gives a brief description of the three criteria as used for optimization of heat exchangers. For a more complete description, including a documentation of useful theoretical contributions, the reader is referred to the recent reviews on the topic (Bejan, 1987; Gaggioli and El-Sayed, 1987; Ranasinghe et al., 1987).

Irreversibility Rate Based Objective Function. The traditional irreversibility rate based objective function for a heat exchanger, with losses due to heat transfer through finite temperature differences and pressure drops, can be expressed as

$$\dot{I}_{tot} = \dot{I}_{\Delta T} + \dot{I}_{\Delta p1} + \dot{I}_{\Delta p2} \tag{1}$$

where $\dot{I}_{\Delta T}$ is the heat transfer irreversibility, and $\dot{I}_{\Delta p1}$ and $\dot{I}_{\Delta p2}$ are the irreversibilities due to pressure drop on the two sides of the heat exchanger.

The above objective function (equation (1)) is useful to optimize fixed area heat exchangers. However, when the area is not fixed, this objective function gives the unrealistic result of an infinite area heat exchanger being the global optimum.

Thermoeconomic Objective Function. The objective function in thermoeconomic analysis is

$$C_{tot} = C_a + c_{\Delta T}\dot{I}_{\Delta T} + c_{\Delta p1}\dot{I}_{\Delta p1} + c_{\Delta p2}\dot{I}_{\Delta p2} \quad (2)$$

In this equation, C_{tot} is the total cost of operation, and $c_{\Delta T}$, $c_{\Delta p1}$, and $c_{\Delta p2}$ are the costs associated with a unit of irreversibility generation $\dot{I}_{\Delta T}$, $\dot{I}_{\Delta p1}$, and $\dot{I}_{\Delta p2}$, respectively. Again, pressure drop and heat transfer are assumed to be the major causes of irreversibility. C_a is the capital cost, to be paid along the application life of the heat exchanger t_{ap}.

The objective function given by equation (2) is preferred for commercial heat exchanger design. However, the thermoeconomic optimum designs vary with time and location. Hence, equation (2) is not useful to establish design guideposts.

Modified Irreversibility Rate Based Objective Function. The irreversibility generation objective function can be modified to include a material exergy term. The objective function becomes (Aceves-Saborio et al., 1989)

$$\dot{I}_{tot,mr} = \dot{I}_{\Delta T} + \dot{I}_{\Delta p1} + \dot{I}_{\Delta p2} + \dot{I}_m \quad (3)$$

where

$$\dot{I}_m = \mathcal{E}_m / t_{ap} \quad (4)$$

with $\mathcal{E}_m$ being the exergy value of the heat exchanger and t_{ap} the application life of the heat exchanger.

The exergy value of a heat exchanger is equal to the exergy content of the heat exchanger materials (chemical and thermomechanical exergies of the materials with respect to a dead state[1]). However, manufacturing processes have a low exergetic efficiency, and building a heat exchanger may require far more exergy than the exergy value of the heat exchanger. Including the total exergy spent in the process adds to the practicality of the results. The total exergy is calculated in terms of the overall efficiency of the process. If the exergetic efficiency ψ_m of the construction process for the heat exchanger is to be included, then the total exergy required to build the heat exchanger is

$$\mathcal{E}_{mi} = \frac{\mathcal{E}_m}{\psi_m} \quad (5)$$

The new objective function written to take into account the total exergy invested is

$$\dot{I}_{tot,mi} = \dot{I}_{\Delta T} + \dot{I}_{\Delta p1} + \dot{I}_{\Delta p2} + \dot{I}_{mi} \quad (6)$$

where

$$\dot{I}_{mi} = \frac{\mathcal{E}_{mi}}{t_{ap}} \quad (7)$$

The use of equation (3) gives results that are time and location independent. Designs obtained from equation (6) may vary as the efficiency of the construction process ψ_m changes. However, the objective function given by equation (6) is preferred over equation (3), since the low-efficiency manufacturing process has to be taken into account to obtain realistic results and the efficiency of the manufacturing process is not expected to change markedly with location and time during a significant portion of the application life of the heat exchanger. The modified irreversibility rate based objective function (equation (6)) circumvents the unrealistic result given by the traditional irreversibility rate based objective function (equation (1)) that the global optimum corresponds to an infinite area heat exchanger. The modified irreversibility rate based objective function is useful to establish design guideposts for heat exchangers (Aceves-Saborio et al., 1989).

Formulation of the Problem

The purpose of this section is to illustrate the formulation of the heat exchanger optimization problem and to give the procedure for calculating the various coefficients in the objective functions. A procedure to calculate the cost coefficients using the overall system simulation model is also presented in this section.

The new technology ceramic heat exchanger to be optimized in the present work is an air-to-gas unit with multiple passes in the gas side. A description of the base case heat exchanger,[2] as well as the power plant in which it resides, is included in the appendix.

The optimization is carried out for the heat exchanger as an isolated unit by using both the modified irreversibility minimization and the thermoeconomic analyses. In general, optimizing a plant component as a single unit does not optimize the global power plant because of the existence of interactions with the other plant components. However, the thermoeconomics-based objective function reflects the in-

[1] The dead state in this work is taken as 298 K, 1 atm, and the chemical composition as specified by Kotas (1985).

[2] The ceramic heat exchanger initially recommended for the subject power plant (Ranasinghe and Reistad, 1987) will be here referred to as the base case design.

Nomenclature

A = heat transfer surface area
c = unitary product cost
C = total cost
e = energy per unit area
$\mathcal{E}$ = exergy
I = irreversibility
ID = inside diameter of heat exchanger tube
k = constant
l = length of heat exchanger tube per single gas-side pass
M = mass of dust particle
npn = number of pipes normal to the flue gas flow direction
npp = number of pipes parallel to the flue gas flow direction
SnD = normalized pipe spacing, normal to the flue gas flow
t_{ap} = application life
V = velocity
β = cost parameter
ΔW = lost power output per unit of irreversibility
ψ = exergetic efficiency

Subscripts

a = due to heat exchanger area
$\Delta p1$ = due to pressure drop in stream 1
$\Delta p2$ = due to pressure drop in stream 2
Δpa = due to pressure drop on air side
Δpg = due to pressure drop on gas side
ΔT = due to temperature difference
e = electricity produced from power plant
$ersn$ = to cause tube erosion
m = material
mi = material, taking into account manufacturing process
mr = material, not taking into account manufacturing process
s = in the limit of small profits and labor costs
t = total, not including the heat transfer irreversibility
tot = total, including the heat transfer irreversibility

teractions with other plant components through the incremental cost coefficients used for the analysis (a method of obtaining these cost coefficients from the overall system simulation model is discussed in a later section). Therefore, if the appropriate cost coefficients are used, a thermoeconomic optimization of the heat exchanger as a single unit yields a design that optimizes the overall power plant (El-Sayed and Evans, 1970). The irreversibility minimization method does not account for the interactions with the other plant components and the results of optimizing a single unit do not correspond to the overall power plant optimum. Suggestions for overcoming this problem in a more accurate optimization model are presented in a later section.

An alternative to optimizing an isolated heat exchanger consists of optimizing the power plant as a whole with respect to the heat exchanger parameters. A global plant optimization has the advantage that it does not require a calculation of irreversibility components and cost coefficients. However, isolating the heat exchanger is sometimes advantageous, because it provides greater insight into the physical problem of the heat exchanger. Understanding the mechanism that drives the heat exchanger process toward an optimum is extremely useful if the results obtained from specific cases as the present one are to be generalized in the future. A deeper knowledge of the physical problem could also lead to innovative ideas for more efficient equipment synthesis methods for the system.

Objective Functions. The temperature of the outlet air from the ceramic heat exchanger has an upper limit. This limit is set by the maximum operating temperature of the turbine materials. A previous analysis of the power plant indicated that (as expected) the maximum plant efficiency is obtained when the air outlet temperature reaches its maximum. Reducing this temperature below its maximum does not result in any improvement, and thus the heat exchanger is optimized with this temperature fixed at its maximum allowable value. Consequently, the analysis here is limited to a constant-duty heat exchanger, with the irreversibility due to heat transfer a constant. The objective functions given by equations (2) and (6) can then be simplified as

$$C_t = C_a + c_{\Delta pa}\dot{I}_{\Delta pa} + c_{\Delta pg}\dot{I}_{\Delta pg} \tag{8}$$

$$\dot{I}_{t,mi} = \dot{I}_{\Delta pa} + \dot{I}_{\Delta pg} + \dot{I}_{mi} \tag{9}$$

where $c_{\Delta pa}$ and $c_{\Delta pg}$ are the cost coefficients associated with air-side and gas-side pressure drop irreversibilities, $\dot{I}_{\Delta pa}$ and $\dot{I}_{\Delta pg}$, respectively. The next sections show the methods for calculating the irreversibility components and the cost coefficients.

(*a*) *Irreversibility Components.* Consider the air side first. If there is no temperature rise, but only a pressure drop, the increase in entropy at the outlet is due to the pressure drop. Having calculated the increase in entropy due to the pressure drop, the corresponding irreversibility on the air side due to the pressure drop $\dot{I}_{\Delta pa}$ can be calculated. The irreversibility on the gas side can be calculated by a similar argument.

The total irreversibility in the heat exchanger, $\dot{I}_{tot}$, is the sum of the exergy loss on the air and gas sides, and the change in the temperatures and pressures on both sides has to be considered in calculating this value. The heat transfer irreversibility can hence be calculated by using the following equation:

$$\dot{I}_{\Delta T} = \dot{I}_{tot} - \dot{I}_{\Delta pa} - \dot{I}_{\Delta pg} \tag{10}$$

The heat transfer irreversibility is a constant for a fixed duty heat exchanger, and is not needed for the optimization.

(*b*) *Cost Coefficients.* The coefficients $c_{\Delta pa}$ and $c_{\Delta pg}$ are the irreversibility cost coefficients. They represent the average "lost-plant income" per unit of irreversibility generated in the heat exchanger.

The cost coefficients depend not only on heat exchanger parameters, but also on how the changes in these parameters affect other plant components. This is due to the existence of interactions between the different plant components. A general solution requires an assumption of a set of cost coefficients and an iteration in these values until convergence is reached. The heat exchanger considered in this paper is a fixed duty unit. All the temperatures and flow rates are fixed, substantially reducing the effects that changing heat exchanger parameters have in other components. Pressure drops change during the optimization process, thus changing the efficiencies of the neighboring components[3] (fan and turbine; see appendix). This situation makes it necessary to use an iterative procedure to calculate the cost coefficients. The method used is described next.

The irreversibility cost coefficients are calculated by introducing a small additional pressure drop in the side of the heat exchanger for which the cost coefficient is required. This pressure drop causes an increase in irreversibility generation and a loss of output power. The losses in output power per unit of pressure drop irreversibility in the air and gas sides are denoted here as $\Delta W_{\Delta pa}$ and $\Delta W_{\Delta pg}$, respectively. The coefficients $\Delta W_{\Delta pa}$ and $\Delta W_{\Delta pg}$ represent strictly thermodynamic parameters that depend exclusively on the power plant configuration and not on the economic environment of the power plant. The value of the output power is the cost of electricity produced from the power plant, c_e.[4] The cost coefficients (cost per unit of irreversibility) are calculated by multiplying the power loss per unit irreversibility by the cost of electricity.

Cost coefficients calculated by using this procedure are not average costs but marginal costs at the design conditions, and they are expected to vary from one design to another. However, the results obtained from the computer simulation indicate that these costs have a variation of only about 1 percent over a wide range of design conditions (Table 3). This results in the marginal costs being approximately equal to the average cost, over the domain of decision variables.

The cost of a heat exchanger as a function of its heat transfer surface area can be described, in many instances, by the relationship

$$C_a = kA^{0.6} \tag{11}$$

where k is a constant and A is the heat exchanger area (Desai, 1984). The constant k is evaluated from the base-case cost estimate for the biomass power plant ($3,000,000 for a heat exchanger with surface area of 740 m^2).

Decision Variables. The optimization process is limited to the heat exchanger. All the decision variables are chosen to be geometric heat exchanger parameters. The decision variables used here are the length and the diameter of the ceramic tubes, number of pipes normal and parallel to the flow direction, and the tube spacing. These variables also determine the size of the heat exchanger. The tube wall thickness is assumed to be equal to 6.35 mm, which is the minimum value due to strength considerations for high-pressure and temperature applications (Coombs et al., 1983).

Constraints in the Optimization Problem. The only equality constraint in the present optimization problem is the fixed duty condition for the heat exchanger. This results in one decision variable being a dependent variable, reducing the number of degrees of freedom by one.

The values of the decision variables are also constrained due

[3] Capital costs of these components may also vary as a result of the changing pressure drop. However, this change is negligible when compared to the ceramic heat exchanger capital cost.

[4] The cost of producing electricity from the power plant varies as the heat exchanger design is changed. However, these changes are small and therefore the electricity cost is taken as a constant for the present analysis.

Table 1 Constant parameters

Parameter	Air-Side	Gas-Side
Temperature in (°C)	300.0	1232.0
Temperature out (°C)	971.0	—
Mass flow rate (kg/s)	21.5	22.5
Pressure at inlet (kPa)	827.0	103.0

to reliability, manufacturing limitations, and maintenance requirements. These inequality constraints restrict the range of some decision variables.

(*a*) *Reliability Considerations.* The combustion gases from wood combustion contain some particulate matter. Excessive velocities of these dust-laden gases through the ceramic heat exchanger tubes can cause tube erosion. The maximum allowable velocity of the dust-laden flue gases, to prevent tube erosion, is given by Ranasinghe and Reistad (1987) as

$$V_{ersn} = \frac{0.0037674}{\sqrt{M}} \tag{12}$$

where V_{ersn} denotes the velocity in m/s and the mass of the impacting particles in kg is denoted by M.

For the present analysis, an unburned spherical wood particle (douglas fir) of diameter 500 μm is assumed to be the most dense particle that can escape from the combustor (Ranasinghe and Reistad, 1987). The maximum allowable velocity corresponding to such a dust particle is equal to 17.5 m/s.

(*b*) *Manufacturing Limitations.* The length of the ceramic tubes is limited by the size of the furnaces available for heat treatment, after the extrusion process (Johnson and Rowcliffe, 1986). A maximum tube length of 2.74 m is assumed for the present analysis. The maximum tube diameter that can be successfully extruded and sintered in reasonable lengths, currently, is approximately 65 mm.

(*c*) *Maintenance Requirements.* In systems involving particulate matter in the gas stream, accumulation of solid matter (slagging) has been a problem in ceramic heat exchangers. Adequate tube spacing is required for proper pipe cleaning. The tube spacing has to be determined from a knowledge of the rate of slag buildup and cleaning methods to be employed. Since this information is not available, it is assumed that the minimum gap between two tubes cannot be less than 25 mm. Optimum designs for minimum tube gaps greater than 25 mm are also presented.

Constant Parameters. The input temperature, pressure, mass flow rate, and composition of the working fluids are kept constant during the optimization. The values of these constants were obtained from running the simulation code for the power plant at design conditions. Some results are presented in Table 1. The dead state was taken as the standard atmosphere.

The ceramic heat exchanger tube material (SiC) has a chemical exergy of 27538.7 kJ/kg (Kotas, 1985), and a density of 3160 kg/m^3. The application life of the whole heat exchanger unit was assumed to be equal to 2 years.[5] The exergetic efficiency of the construction process of the heat exchanger tubes was assumed to be equal to 0.1.[6] The cost of electricity produced from the biomass power plant can vary between \$0.06/kW-h and \$0.10/kW-h, depending on the fuel prices (Huque and Reistad, 1987). The cost of electricity for the present analysis was assumed to be equal to \$0.09/kW-h.

Solution Method

The optimization procedure for the heat exchanger starts by using the simulation model for the biomass power plant to obtain the constant thermodynamic property data, flow rates, and composition of the working fluids. The ceramic heat exchanger subroutine is used as a separate module for the heat exchanger calculations. Initially, a set of decision variables is chosen. The heat exchanger subroutine calculates the thermal and flow properties of the fluids, including irreversibility generation rates. Next, the output from the heat exchanger calculations, including the value of the objective function and constraints, is fed to an optimization computer program package. New values for the design variables are subsequently generated in the optimizer and heat exchanger calculations are repeated. The iterations are continued until the objective function is optimized within the accuracy specified and all the constraints are satisfied.

For the thermoeconomic optimization, the initial cost coefficients are calculated using the base case ceramic heat exchanger configuration. Once the optimum design is calculated, new cost coefficients are calculated by using the simulation program for the biomass power plant. This procedure is continued until the designs converge to the specified accuracy.

Results

Results have been developed to indicate the specific optimal designs as well as to illustrate a comparison of the optimization with the two objective functions, $\dot{I}_{t,mi}$ and C_t. The comparison, presented first, takes a restricted—single-degree-of-freedom—case of the subject heat exchanger based on the base case design parameters previously indicated. The overall optimization presents the optimal design for the decision variables delineated above.

Comparison of Optimization for Minimum $\dot{I}_{t,mi}$ and C_t. Comparison of the optimal designs obtained with the objective functions of minimum C_t and minimum $\dot{I}_{t,mi}$ are presented for a single-degree-of-freedom optimization done around the base case design (i.e., all the design variables, other than the two decision variables chosen for the analysis, are fixed at the base case design values. The fixed duty constraint reduces the problem to a single degree of freedom). The independent decision variable chosen for this comparison is the number of pipes normal to the flue gas flow direction (npn). The dependent variable is *SnD*, the normalized center-to-center distance (center-to-center distance between two adjacent pipes normal to the flue gas flow direction divided by the outside pipe diameter).

The optimum for the objective function $\dot{I}_{t,mi}$ was evaluated and found to occur at an *npn* of 56. As discussed previously, this optimum value will not change unless the efficiency of manufacturing changes.

The optimum for the C_t objective function is expected to change with time and location and thus should be evaluated over a range of costs. The variations of costs were found to be conveniently expressed in terms of a single parameter β, which comes out of the objective function equations as follows:

$$C_t = (kA^{0.6})/t_{ap} + (c_e \Delta W_{\Delta pa})\dot{I}_{\Delta pa} + (c_e \Delta W_{\Delta pg})\dot{I}_{\Delta pg} \tag{13}$$

or, rewritten

$$C_t = c_e\{(\beta A^{0.6})/t_{ap} + \Delta W_{\Delta pa}\dot{I}_{\Delta pa} + \Delta W_{\Delta pg}\dot{I}_{\Delta pg}\} \tag{14}$$

where β is defined as k/c_e.

[5] The first few rows of the ceramic heat exchanger have to be replaced as soon as after 1 year, while some tubes can be used as long as 4–5 years. Based on these figures, an application life of 2 years is assumed, to simplify the present analysis. A penalty for a large frontal area heat exchanger, due to the reduction in application life, could be introduced in a more complete analysis.

[6] The effectiveness of the manufacturing process for carbon steel tubes is approximately 19 percent (Chapman and Roberts, 1983). The effectiveness of the manufacturing process for the ceramic tubes was not available; an effectiveness was selected at a nominal value about half that for the carbon steel tubes.

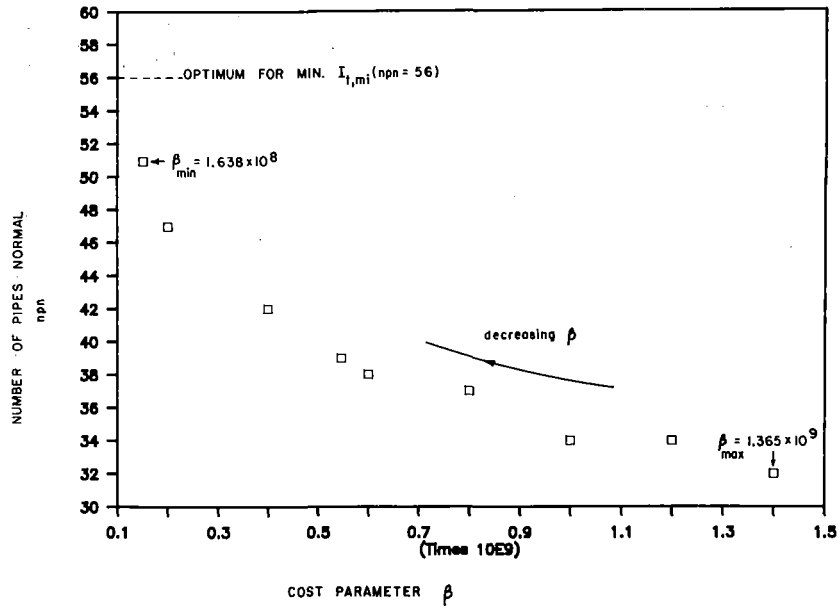

Fig. 1 Variation of the optimum number of pipes normal to the flow direction, based on the objective function C_t, as a function of the cost parameter β, for a single degree of freedom optimization around the base-case design. The optimum *npn* for minimum $I_{t,mi}$ is also indicated on the figure.

Table 2 Optimum designs for minimum $I_{t,mi}$ (base-case design included for comparison)

	npn	npp	l (m)	ID (mm)	SnD	tube gap (mm)	Δp_a (%)[1]	Δp_g (%)[1]	$\dot{I}_{t,mi}$ (kW)
Base Case	40	24	2.74	17.8	2.30	39.7	2.26	2.28	153.77
	30	42	2.74	20.3	3.64	87.4	0.71	1.45	137.52
	40	30	2.74	20.3	2.82	60.3	0.78	1.23	128.88
	50	24	2.74	20.3	2.47	48.7	0.78	0.99	124.00
	60	20	2.74	20.3	2.24	41.2	0.78	0.83	120.77
	70	16	2.74	20.3	1.93	30.9	0.89	0.91	119.00
	80	14	2.74	20.3	1.82	27.3	0.89	0.85	117.45

Note: $\dot{I}_{\Delta T}$ is constant at 1583 kW.
[1]Pressure drops expressed as a percentage of inlet pressure. The inlet pressures are 827 kPa and 103 kPa for the air and gas sides, respectively.

In the above equations c_e is the cost of electricity in \$/kJ and $\Delta W_{\Delta pa}$ and $\Delta W_{\Delta pg}$ are the lost power output from the power plant per unit of irreversibility on the air and gas sides respectively. The values of $\Delta W_{\Delta pa}$ and $\Delta W_{\Delta pg}$ for the base case design were calculated as described earlier, and are equal to 1.463 kJ/kJ and 4.762 kJ/kJ, respectively.[7] The parameter β is a function of the capital cost of the heat exchanger and the cost of electricity produced from the power plant. If the minimum possible cost of a heat exchanger of area 740 m^2 is assumed to be \$1,000,000, and the maximum possible cost is \$5,000,000, for all locations and times, the maximum and minimum values of k are 4551 and 22,757, respectively. The parameter β has its maximum value when k is a maximum and c_e is a minimum, and β is minimum when k is minimum and c_e is maximum. Hence, the maximum and minimum values of β are equal to 1.365×10^9 and 1.638×10^8, respectively. The values of β between the maximum and minimum correspond to the various combinations of the heat exchanger cost and the cost of electricity.

Figure 1 shows the optimum *npn* values for a single degree of freedom optimization of the ceramic heat exchanger with the C_t objective function. The optimum designs are presented for the total range of values of β, between its maximum and minimum. Hence, these optima represent the optimum designs for any combination of heat exchanger cost and cost of electricity. The optimum obtained from the objective function $\dot{I}_{t,mi}$ ($npn = 56$) is also indicated in this figure.

The results from the above parametric study, with a single degree of freedom, illustrate that the optimum design obtained from the thermoeconomic objective function C_t is a strong function of the cost parameters. The results also show that the objective function $\dot{I}_{t,mi}$, which is not as sensitive to time and location as C_t, yields optimum designs in the limit of exergy cost being dominant relative to labor and profits. These may readily serve as guideposts for design.

Optimum Ceramic Heat Exchanger Design. The independent decision variables for the optimization as delineated above are *npn*, *npp*, *l*, and *ID*. The dependent variable is *SnD*, the value of which is determined from the fixed duty condition. The optimum designs obtained from the modified minimum irreversibility rate criterion are initially presented, followed by the optimum designs for the minimum thermoeconomic cost criterion. Finally, the optimum designs obtained from the two criteria are compared for cost, exergy savings, and pressure drops relative to each other, and the base case design. The optimum values were reached to within a specified error of 1.25 mm for the inside tube diameter, *ID*, and 7.5 cm for the tube length per single pass on the gas side, *l*.

(*a*) *Optimum Designs for Minimum $\dot{I}_{t,mi}$.* The results from the optimization based on the criterion of minimum irreversibility, $\dot{I}_{t,mi}$, are presented in Table 2 for a range of *npn* values. The base-case design is also shown for comparison. The results are presented for a range of *npn* values because the *npn* value at each optimum determines the tube spacings,

[7]The results obtained for $\Delta W_{\Delta pa}$ and $\Delta W_{\Delta pg}$ indicate that the gas-side pressure drop irreversibility is roughly three times as valuable as the air-side pressure drop irreversibility. The reason is that gas-side pressure drops have to be overcome by feeding high-quality energy to a fan, while a pressure drop in the air-side only reduces the exergy of the air stream that has to be converted to work in the turbine (see Fig. A1).

Table 3 Optimum designs for minimum C_t (base-case design included for comparison)

	npn	npp	l (m)	ID (mm)	SnD	tube gap (mm)	Δpa_1 (%)	Δpg_1 (%)	$\Delta W_{\Delta pa}$	$\Delta W_{\Delta pg}$	C_t ($/s)
Base Case	40	24	2.74	17.8	2.30	39.7	2.26	2.28	1.463	4.762	0.0551
	30	34	2.74	15.2	3.12	59.3	4.26	2.50	1.465	4.761	0.0563
	40	25	2.74	15.2	2.55	43.3	4.43	1.98	1.479	4.772	0.0546
	50	20	2.74	15.2	2.25	35.2	4.43	1.59	1.475	4.763	0.0537
	60	18	2.59	14.0	2.17	31.4	5.55	1.44	1.484	4.778	0.0534
	70	17	2.44	14.0	2.11	29.7	4.35	1.29	1.466	4.764	0.0532
	80	15	2.44	14.0	2.00	26.7	4.28	1.13	1.472	4.769	0.0529

[1]Pressure drops expressed as a percentage of inlet pressure. The inlet pressures are 827 kPa and 103 kPa for the air and gas sides, respectively.

which can be a major design constraint. The influence of *npn* and tube spacing is discussed below.

The values of length *l* and internal diameter *ID* are constant at the optima for all *npn* values; the *l* value is optimum at its maximum while *ID* was determined to be optimum at an unconstrained value. The optimum *npp* decreases as *npn* increases. The objective function $\dot{I}_{t,mi}$ decreases with the increase in *npn*, although the rate of decrease in the objective function decreases at higher *npn*. However, the increase in *npn* corresponds to a decrease in the tube gap (as presented in Table 2), and hence becomes a constraint to the maximum possible improvement. The *npn* value of 80 corresponds to a tube gap of approximately 25 mm. Since a minimum tube gap of 25 mm was assumed for the present analysis, the overall optimum design for minimum $\dot{I}_{t,mi}$ corresponds to an *npn* value of 80.

If slag formation and cleaning requirements warrant the use of a larger tube gap, an optimum design corresponding to such a tube gap has to be chosen. For example, if a minimum tube gap of approximately 50 mm is needed, the optimum design corresponding to *npn* of 50 would satisfy this requirement (see Table 2).

The results shown in this section are designs that minimize the irreversibility of the heat exchanger taken individually, and these designs do not correspond in general with the heat exchanger that minimizes the irreversibility generation in the whole plant. However, the optimum designs presented here were observed to have the effect of increasing the overall plant net efficiency relative to the base-case design.

(*b*) *Optimum Designs for Minimum* C_t. The results from a thermoeconomic optimization of the ceramic heat exchanger are presented in Table 3. Optimum designs for different *npn* values are presented in this table. The minimum tube gap constrains the value of *npn* as in the previous case when using the objective function $\dot{I}_{t,mi}$. The optimum design corresponding to *npn* of 80 results in a minimum tube gap of approximately 25 mm, and is the overall optimum for the present thermoeconomic analysis. However, if a larger tube gap is needed, the optimum design has to be determined as described earlier.

Comparison of $\Delta W_{\Delta pa}$ and $\Delta W_{\Delta pg}$ in Table 3 shows that, as discussed previously, the pressure drop irreversibility on the gas side is approximately three times as valuable as that for the air side. It is noted that the variations of the incremental costs $\Delta W_{\Delta pa}$ and $\Delta W_{\Delta pg}$ over the range of heat exchanger design points are not very significant. (Since C_e is constant, incremental cost is proportional to ΔW.)

The thermoeconomic optimum design results in a net saving of $139,000, relative to the base-case design, over the useful life of the heat exchanger.

(*c*) *Comparison of the Optimum Designs.* The irreversibility and cost of the optimum designs presented in Tables 2 and 3 are shown in Figs. 2 and 3, respectively, as a function of the optimum *npn* with the other decision variables fixed at their optimum value. The base-case design is also indicated on these figures. As expected, designs obtained from irreversibility minimization generate less irreversibility but cost more than those obtained from thermoeconomics. The irreversibility and cost for the base case fall between both optima corresponding to the base-case *npn* ($npn = 40$), but the base-case cost is substantially higher than that at the highest *npn* ($npn = 80$), which corresponds to the optimum obtained from the present thermoeconomic analysis.

The pressure drops for the optimum designs differ substantially from those used in the base case. Gas-side pressure drops in the minimum irreversibility analysis fall below those of the base case. Air-side pressure drops in the minimum cost analysis are greater than the pressure drops of the base case. The base-case values were selected as representative of values for metallic heat exchangers. These results show that pressure drop values arbitrarily selected by a designer from past experience with metallic heat exchangers might be far from optimum for a given design condition.

As expected, the pressure drops obtained from the minimum irreversibility analysis are quite low. The thermoeconomic optimum shows that the high costs of heat exchanger area require substantially greater pressure drops than those prescribed for minimum irreversibility optimum. Because losses on the gas side are more costly than losses on the air side, the gas-side pressure drops do not increase above the minimum values of the irreversibility minimization analysis nearly as much as do those of the air side.

Discussion

This section shows how the minimum irreversibility generation optima may be used as guideposts for design. Some suggestions on how these guideposts may be improved are also included.

The cost objective function is given by equation (8). The cost of area is assumed to be proportional to the area raised to the power 0.6 (equation (11)). The total cost of the heat exchanger given by equation (11) includes the exergy cost to build the heat exchanger plus labor and profits. The exergy cost of the heat exchanger is a linear function of the area. In the limit of small labor costs and profits, the total cost is equal to the cost of the exergy, and therefore the following equation replaces equation (11) for expressing the total heat exchanger cost:

$$C_{a,s} = c_e eA = c_e \mathcal{E}_{mi}/t_{ap} = c_e \dot{I}_{mi} \tag{15}$$

where $C_{a,s}$ represents the cost of area for small profits and labor costs, *e* represents the rate of exergy, per unit area and time, spent in building the heat exchanger, and c_e is the electricity cost. Equation (15) assumes that the cost of electricity is a good average for the cost of all the exergy streams spent in producing the heat exchanger. The total cost of operation, for small profits and labor costs, reduces to

$$C_{t,s} = c_e(\dot{I}_{mi} + \Delta W_{\Delta pa}\dot{I}_{\Delta pa} + \Delta W_{\Delta pg}\dot{I}_{\Delta pg}) \tag{16}$$

The above equation reflects lower costs of area than equation (8), because equation (16) neglects profits and labor costs. Equation (16) underestimates the cost of area. Therefore, optimum designs obtained from equation (16) have a larger area, but a smaller pressure drop irreversibility compared to the optimum designs obtained from equation (8). Optimum designs from equation (16) represent guideposts for design. They set a minimum allowable value in the pressure drop and a maximum allowable value in the area, which do not change with the economic conditions.

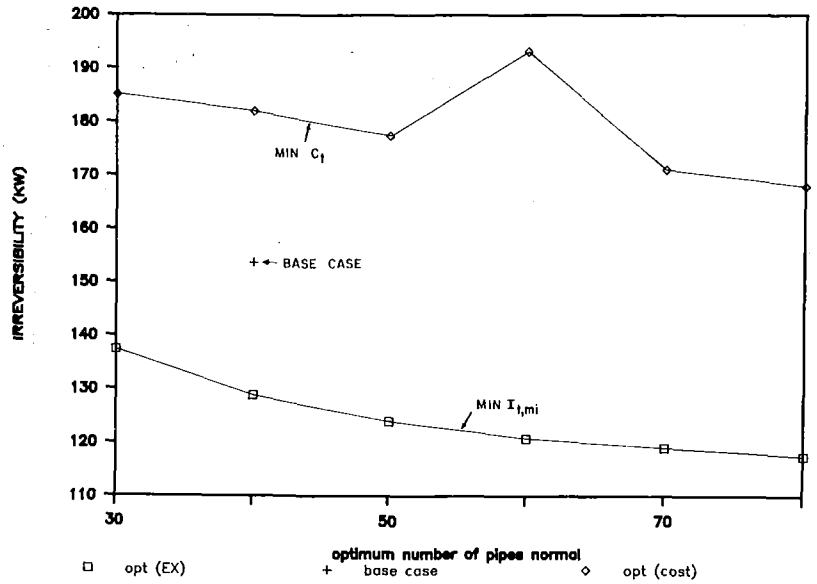

Fig. 2 Irreversibility (not including $i_{\Delta l}$) of the base case and optimum designs, as given in Tables 2 and 3

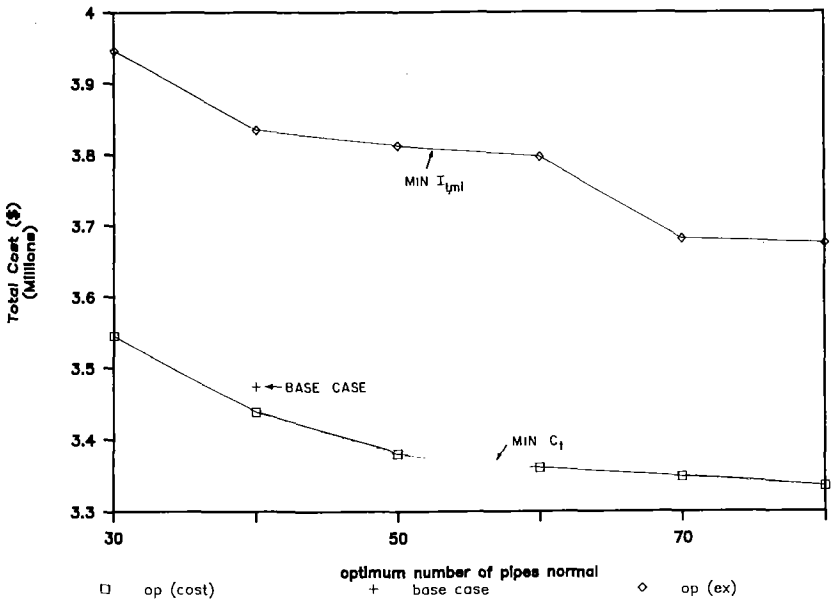

Fig. 3 Total cost (area and pressure drop irreversibility) of the base case and optimum heat exchanger designs, as given in Tables 2 and 3, during the application life of the heat exchanger

The electricity cost c_e is a constant. Dividing equation (16) by c_e does not affect the result of the optimization. Equation (16) divided by c_e results in a modified irreversibility minimization objective function where weight factors $\Delta W_{\Delta pa}$ and $\Delta W_{\Delta pg}$ have been included to take into account how the irreversibility minimization used here (equation (9)) does not take into account the values of the coefficients $\Delta W_{\Delta pa}$ and $\Delta W_{\Delta pg}$, and therefore has a more limited application to establish design guideposts. However, if the values of $\Delta W_{\Delta pa}$ and $\Delta W_{\Delta pg}$ are close to 1.0, the optima obtained from equation (9) can be used as reasonable design guideposts. The coefficients $\Delta W_{\Delta pa}$ and $\Delta W_{\Delta pg}$ differ from 1.0 because processes have exergetic efficiencies lower than 100 percent. In the limit of reversibility, the coefficients are always equal to 1.0, since all the exergy can be converted to electricity without losses. Therefore, the minimum irreversibility analysis is a nonchanging guidepost in the case that the plant operation tends to reversibility.

Another way to improve the guideposts from the present minimum irreversibility analysis is extending the system under consideration to include the turbine and the fan along with the heat exchanger. Extending the system takes into account some of the interactions with other plant components.

The need to calculate cost coefficients was cited earlier in this paper as one of the disadvantages of optimizing an isolated plant component as opposed to optimizing a global plant. In the present case, the cost coefficients were found by using the power plant simulation code. The results indicate that the gas-side pressure drop irreversibility is approximately three times as valuable as the air-side pressure drop irreversibility. Although this factor of three is specific to the system considered, it is hoped that experience with such numbers ob-

tained in the future from similar analysis of different systems can lead to the evaluation of general trends for such factors and cost coefficients.

Conclusions

This paper illustrates the optimization procedure for a heat exchanger in a complex power plant. The specific case of a ceramic heat exchanger in a biomass fueled power plant is shown. The major conclusions drawn from the work can be categorized as those of a general nature and those specific to the system evaluated. They are:

General

- The presence of an overall system simulation code allows the irreversibility costs to be readily evaluated such that thermoeconomic optimization of the heat exchanger as an isolated unit will result in optimization of the overall system with respect to the heat exchanger design variables.
- Optimization with the procedure of minimizing $I_{t,mi}$ yields reasonable guideposts for design that are useful in establishing lower and higher bounds for the design variables, but much more accurate guideposts can be obtained by modifying the analysis to take into account how each unit of irreversibility affects the power output of the system.
- Optimum pressure drops for ceramic heat exchangers need to be evaluated from an optimization rather than depend on approximate values obtained from past experience with metallic heat exchangers.

Specific

- Both optimization methods show that the optimum ceramic heat exchanger for the specific application favors a high *npn* (large width) and the maximum width is constrained by the minimum allowable tube gap.

References

Aceves-Saborio, S., Ranasinghe, J., and Reistad, G. M., 1989, "An Extension to the Irreversibility Minimization Analysis Applied to Heat Exchangers," ASME *Journal of Heat Transfer*, Vol. 111, pp. 29–36.

Bejan, A., 1987, "Thermodynamics of Heat Transfer Devices," in: *Second Law Analysis of Thermal Systems*, ASME, NY.

Boyd, J. M., Bluemel, V., Keil, T. H., Kucinkas, G. R., and Molinari, S., 1981, "The Second Law of Thermodynamics as a Criterion for Heat Exchanger Design," *Energy*, Vol. 6, pp. 603–609.

Bushnell, D. J., Reistad, G. M., Bauer, T. L., Brynjolfsson, S., and Fox, S. J., 1984, "Development of Computer Simulation of Biomass Combined-Cycle Power Plant," Final Report Part 2, USDA, Grant Nos. 59-32R6-2-141 and 83-CSRS-2-2314.

Chapman, P. F., and Roberts, F., 1983, *Metal Resources and Energy*, Butterworths, London.

Coombs, M., Kotchick, D., and Weidhaas, M., 1983, "High Temperature Ceramic Heat Exchanger Development," EPRI AP-3019, Final Report.

Dadkhah-Nikoo, A., Ranasinghe, J., Huque, Z., Bushnell, D. J., and Reistad, G. M., 1987, "Thermal Analysis, Including Off-Design, Part Load and Yearly Analysis for Final Design of Combined-Cycle Biomass Fueled Power Plants," Report 2.4, Prepared for USDA, Grant Nos. 59-32RE-2-141 and 83-CSRS-2-23-14.

Dasai, M. B., 1984, "Preliminary Cost Estimating of Process Plants," *Modern Cost Engineering: Methods and Data*, Vol. II, J. Matley, ed., McGraw-Hill, NY.

El-Sayed, Y. M., and Evans, R. B., 1970, "Thermoeconomics and the Design of Heat Systems," ASME JOURNAL OF ENGINEERING FOR POWER, Vol. 92, pp. 27–35.

Gaggioli, R. A., and El-Sayed, Y. M., 1987, "A Critical Review of Second Law Costing Methods," in: *Second Law Analysis of Thermal Systems*, M. J. Moran and E. Sciubba, eds., ASME, NY.

Huque, Z., and Reistad, G. M., 1987, "Thermal Analysis for Combined-Cycle Biomass Energy Project – Comparison With Alternative Systems," Report No. 1.7, prepared for USDA, Grant Nos. 59-32RE-2-141 and 873-CSRS-2-2314.

Johnson, S. M., and Rowcliffe, D. J., 1986, "Ceramics for Electric Power-Generating Systems," EPRI AP-4380, Final Report, SRI International, Menlo Park, CA.

Kotas, T. J., 1985, *The Exergy Method of Thermal Plant Analysis*, Butterworths, London.

LeGoff, P., and Giulietti, M., 1982, "Comparison of Economic and Energy Optimizations for a Heat Exchanger," *International Chemical Engineering*, Vol. 22, No. 2, pp. 252–268.

Ranasinghe, J., Aceves-Saborio, S., and Reistad, G. M., 1987, "Optimization of Heat Exchangers in Energy Conversion Systems," in: *Second Law Analysis of Thermal Systems*, M. J. Moran and E. Sciubba, eds., ASME, NY, pp. 29–38.

Ranasinghe, J., and Reistad, G. M., 1987, "Use of Ceramic Heat Exchangers in Wood-Fueled Power Plants," *Proc. ASME-JSME Thermal Engineering Joint Conference*, Vol. 3, pp. 163–168.

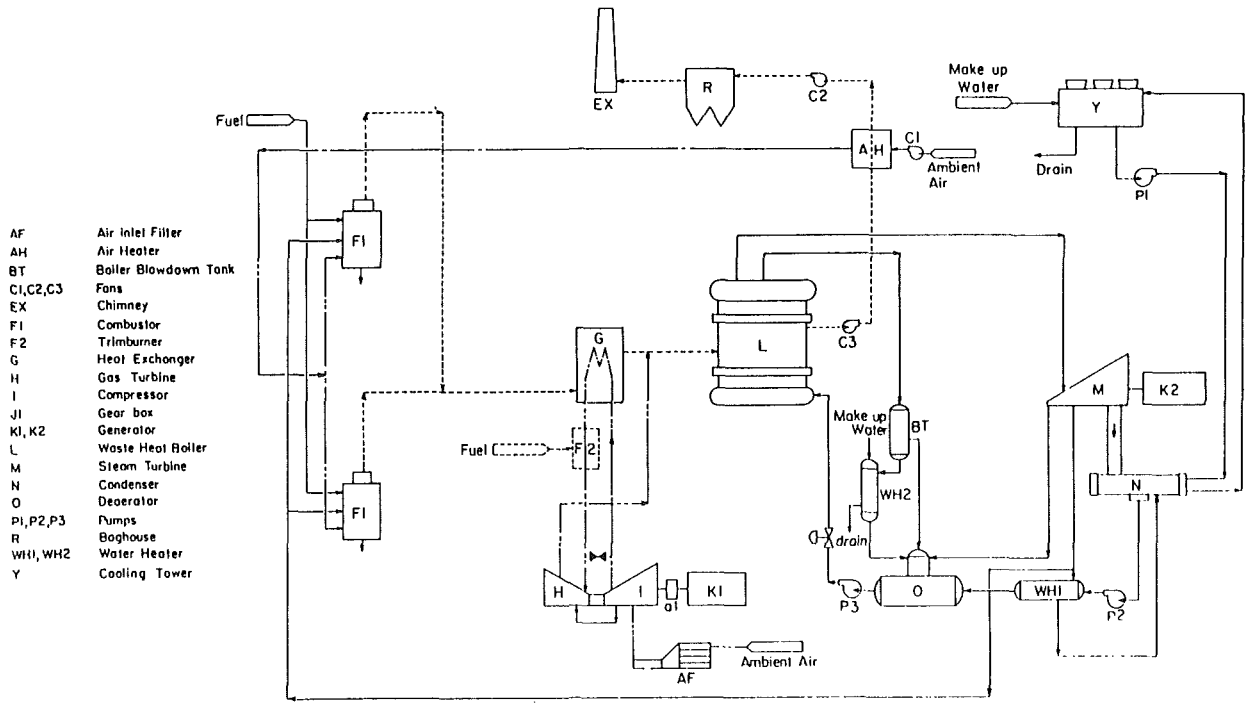

Fig. A1 Diagram of the biomass power plant

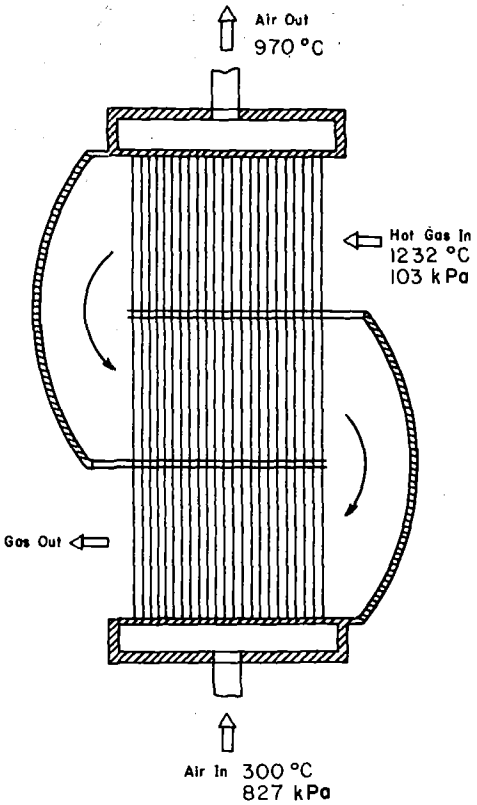

Fig. A2 Multiple gas-side pass ceramic crossflow heat exchanger recommended for use in the biomass power plant

Stephenson, J. D., and Reistad, G. M., 1988, "Analysis of a Wood-Fueled Trimburner System for Use in a Combined-Cycle, Wood-Fired Power Plant," ASME *Journal of Solar Energy Engineering*, Vol. 110, pp. 82–89.

APPENDIX

Background information is presented here on the specific biomass plant to be studied and the base-case ceramic heat exchanger design.

Biomass Power Plant

The combined-cycle biomass power plant considered for the present study is characterized by having a wood-fueled combustor, an indirect-fired gas turbine, and a Rankine steam cycle. A diagram of the plant is shown in Fig. A1. Based on the results obtained from a feasibility study of this power plant (Bushnell et al., 1984), it was concluded that heating the inlet air for the gas turbine to its rated value of 970°C was highly desirable from the viewpoint of improving the efficiency of the power plant. Two methods were considered to obtain this high gas turbine inlet temperature. One was to use a metallic heat exchanger and then a trimburner (Stephenson and Reistad, 1988), and the other was to use a high-temperature ceramic heat exchanger (Ranasinghe and Reistad, 1987).

A computer code for the steady-state simulation of the power plant and its components has been developed (Dadkhah-Nikoo et al., 1987). This code is capable of computing the overall thermal performance of the power plant and the performance of the individual plant components including their irrversibilities.

Base-Case Ceramic Heat Exchanger Design

A multiple gas-side pass, crossflow ceramic heat exchanger was selected for the biomass power plant (Ranasinghe and Reistad, 1987). A schematic diagram of the heat exchanger is shown in Fig. A2.

The tube arrangement in the fixed duty heat exchanger is in-line, and the tubes are equally spaced normal and parallel to the hot flue gas flow direction. The geometric dimensions for the base-case heat exchanger are given in Tables 2 and 3.

An Autonomous Artificial Designer of Thermal Energy Systems: Part 1—Theoretical Considerations

A. S. Kott[1]
Research Associate,
Department of Mechanical Engineering.

J. H. May
Co-director,
AIM Laboratory,
Katz Graduate School of Business.

C. C. Hwang
Associate Professor,
Department of Mechanical Engineering.

University of Pittsburgh,
Pittsburgh, PA 15261

A knowledge-based approach to automated conceptual design (flowsheet synthesis) of thermal energy systems with strong interactions between heat/power/chemical transformations is presented. The approach is based on a computer-oriented state-space search guided by specially developed heuristics, and makes use of Second Law (exergetic) analysis, rather than mimicking the strategy of a human designer. The original design problem, formulated in terms of an equipment units network, is decomposed and reduced to a level of a network of elementary processes, with a resulting reduction in the search space. A special form of fundamental equations for steady-state open thermodynamic systems, based on a "temperature interval" approach, allows one to determine the effects of work, heat and chemical interactions within the system on the magnitude of Second-Law infeasibility, and on the overall exergy loss over any particular temperature interval, prior to the completion of the design. Based on this treatment, a set of generalized transforming operators, a plausible move generator, and a state evaluation function are formulated. The search algorithm is discussed in detail.

1 Introduction

This paper focuses on the synthesis of conceptual schemes (flowsheets) of power/heating/refrigeration systems. Consider a design problem in which a number of steady-state, liquid or gas streams enter, at given thermodynamic conditions, a system to be designed, and must leave at some other required thermodynamic conditions. Within the system, these streams may interact with each other, may exchange heat with given heat sources or sinks, and may undergo various pressure changes with rejection or consumption of mechanical power. The number of possible conceptual schemes for such a system is infinite. The thermodynamic and economic effectiveness of such systems may vary widely, depending on the conceptual scheme chosen. A special case of such a problem would be the design of a power/refrigeration closed cycle to accommodate a complex combination of heat sources and sinks.

A computer-oriented technique has been developed that is capable, in either fully autonomous or human-guided mode, of generating an optimized (or at least satisfactory) scheme of a thermal system, given only a (nearly) arbitrary set of input/output flows. A human designer does not need to input any predetermined network of equipment or processes. The technique does not rely on selecting among "prepackaged" partial schemes or specialized solutions. Instead, it is guided by the fundamental considerations of eliminating sources of thermodynamic irreversibilities, while trying to avoid increases in equipment cost. The ill-structured and heuristic nature of conceptual design led the authors to consider the incorporation of Artificial Intelligence techniques into the system.

An interest in automated design of thermal systems has been gradually increasing within the last decade. Much research has appeared in the Chemical Engineering literature, where this design problem is viewed in a specific context of chemical process requirements and is called "process synthesis" or "flowsheet synthesis." A broad review of developments in the field of chemical process synthesis was presented by Nishida et al. (1981). A number of conceptual approaches to process was discussed by Siirola (1982). A large part of the flowsheet synthesis literature has been devoted to heat exchanger networks synthesis or heat integration of separation equipment. However, only a few papers deal with the simultaneous use and transformation of both heat and mechanical energy, which is the area of our research.

Shiroko and Umeda (1980) discussed a technique they called the heat availability diagram for analysis of irreversibility losses in heat exchange processes, and proposed a group of operations for pinch-point elimination. They mentioned the possibility of pressure change processes but they did not elaborate on it.

Menzies and Johnson (1972) developed a search-based method for synthesis of optimal energy recovery networks. The method featured a rigid heuristic placement of compressors and valves that precluded thermodynamic optimization of heat-power transformations.

Nishio et al. (1980) described a computerized strategy for

[1] Currently with Carnegie Group Inc., 5 PPG Place, Pittsburgh, PA 15222.

Contributed by the Advanced Energy Systems Division of The American Society of Mechanical Engineers and presented at the ASME Winter Annual Meeting, Boston, Massachusetts, December 13-18, 1987. Recipient of the E. F. Obert Outstanding Paper Award. Manuscript received by the Advanced Energy Systems Division January 19, 1988.

steam power system designs based on the use of heuristic rules intended to reduce the loss of available energy. The heuristic rules were used to choose among a number of predefined design options. Another approach (Petroulas and Reklaitis, 1984) to computer-aided synthesis of steam-power systems utilized dynamic programming and significant structural assumptions.

The danger of heuristics with structural assumptions and the advantages of a mixed-integer programming approach were discussed by Grossman (1985). An assumption of some basic "superstructure" was a requirement of the approach. This approach was used by Shelton and Grossman (1985) for the optimal synthesis of a particular type of refrigeration cascades.

Townsend and Linnhoff (1983) suggested criteria and a design method for adding a heat pump or a heat engine to a system of heating and cooling streams, and external utilities, based on a technique of "pinch technology" (Linnhoff and Flower, 1978) for synthesis of heat exchanger networks. Assumptions regarding the system structure were not required. They did not discuss a network where streams may undergo both enthalpy and pressure changes, nor did they offer a method to actually synthesize the internal structure of a heat pump or of a heat engine.

The approach presented in this paper differs from the aforementioned works in a number of ways. The approach attempts to avoid any assumptions about the structure of the system to be designed. The design process is not limited to selecting among a particular set of predefined alternatives. It addresses a problem in which power, heat, and chemical transformations are strongly interdependent, may be undergone by the same stream, and cannot be considered separately. Both economic and thermodynamic optimizations are pursued in the proposed solution. The knowledge-based solution utilizes a rigorous state-space search, which allows error recognition and backtracking.

This is the first part of a two-part paper. The first part deals with theoretical issues pertaining to the subject. Section 2 of this part discusses Artificial Intelligence aspects of the proposed approach. Section 3 formulates the design problem. In section 4 the original problem is decomposed into two simpler ones. Section 5 presents a technique of thermodynamic analysis that allows evaluation of a given design state and guides its transformation. In the second part of this paper these results are used to develop a state-space search algorithm for the solution of the design problem.

2 The Approach

Although a knowledge-based approach appeared to be attractive for the autonomous designer, strategic decisions must be made regarding the problem solving technique to use, the source of the heuristic knowledge, the search technique to use, the representation hierarchy, the completeness of the knowledge, and the handling of constraints before the system can actually be built.

One has the choice of using either heuristic search or problem reduction as an overall strategy. In engineering design, this corresponds roughly to the choice between a transformational model of design and an abstract refinement model (Mostow, 1985). Heuristic search is chosen for three reasons. First, problem reduction does not handle coupled goals well. In thermal systems, both goals and components are tightly interwoven. Second, problem reduction requires a large amount of rigidly defined structural assumptions. This conflicts with the desire to develop a conceptual designer that may be capable of some originality. Third, it is not clear that there is a good way to reduce the thermal design problem to simpler and relatively independent subproblems without imposing some major structural assumptions.

Deciding on the source of knowledge to guide the designer is even more fundamental. Should one conduct an in-depth study of an expert human designer? For the design domain it is intended to address, it is not clear that it is most desirable to have the computer mimic human reasoning process. Exploiting the computer's abilities may give a design algorithm that would be impractical or undesirable for a human design engineer, so a cognitive study of a human designer is not carried out. Of course, the ultimate design proposed must be comparable, if not identical, to that which would have been proposed by a human expert using the same design criteria. The proposed approach is based on state-space search guided by heuristics, making use of fundamental thermodynamic principles. It does not make use of a cognitive study of a human designer, using tools such as concurrent verbal protocol analysis.

In the design domain, it may be argued that the fundamental differences between humans and computers reside in that the search strategy that is optimal for a human expert is not necessarily best for a computer designer, so that a study of a human would be useful only for contrast, not for system implementation. The implication of this contention is that evaluation of the proposed system must focus on its output,

Nomenclature

A = set of available components
a = empirical coefficient associated with cost
b = empirical coefficient associated with cost
C_c = annualized cost of system components
C_e = annual cost of utilities and power
C_v = penalty for violation of constraints
DE = exergy loss within a system
DE' = Second Law infeasibility parameter
E = exergy flux
e = specific exergy for open system
F = equality constraints, or enthalpy flux
G = inequality constraints, or heat generated within a system
h = specific enthalpy
i = system's set of components
k = coupling recipe
m = mass flow rate
n_i = $+1$ if direction of process i coincides with the temperature axis and -1 if direction of process i is opposite to the temperature axis
P = penalty function
p = pressure
Q = heat input into a system, or heat transit function
S = set of elementary processes
s = specific entropy
T = temperature
W = work input into a system
X = input/output specification
x = generalized efficiency
Z = system

Subscripts

0 = refers to "dead state"
1 = temperature level 1
2 = temperature level 2
A = component A
B = component B
e = transformation into exergy
i = refers to a process (stream) i
min = minimum for a process, or for a whole system
max = maximum for a process or for a whole system
T = constant-temperature process
u = refers to a utility

Superscripts

$*$ = optimal or specified

not on how humanlike its process is, although that process must be internally consistent and logical. The objective is to automate the design process, not to automate the designer.

With regard to the hierarchy of representation, it must be determined how many levels of abstraction are needed and how the design process should maneuver between them. It is found that the problem can be decomposed into two problems, which can be viewed as two levels of abstraction: a more abstract level of elementary processes and a more detailed one of equipment units. It is also found that state evaluation can be done with only limited reference to a more detailed design level, so that search can be carried out at the more abstract level, resulting in a smaller search space. A powerful evaluation function has a massive impact on the complexity of the search.

It is realized that "look-ahead" evaluation, transformational operators, and their supporting heuristics, are available for only some of the goals and their associated cost components. How debilitating is the lack of knowledge regarding the other goals? It is found that one could construct an initial state that minimizes those costs that cannot be handled. The search proceeds from it to minimize those cost components for which one has knowledge tools available while attempting to keep increases in uncontrollable costs to a minimum.

Finally, it is decided to allow the designer to search through all states in the state space including infeasible states, because this strategy may lead to a solution faster than a strategy avoiding infeasible states. The fundamental guide to the problem is the Second Law of Thermodynamics. Here an infeasible design means a design that is infeasible with respect to the Second Law (see Section 5 below). The proposed evaluation and transformation operators can deal with such infeasible designs. The cost of such a strategy is that stopping the designer prematurely may result in an infeasible design, but the benefits of being able to take a shorter path to the solution outweigh that cost.

3 Formulation of the Design Problem

In discussing the proposed approach to the solution of the thermal system design problem, it is helpful to begin with the most general statement of the design problem and then to specialize it. In the following statement of the design problem, the treatment of Wymore (1976) with some modifications is used.

Given

- an input/output specification $X = X^*$
- feasibility constraints $F(Z) = 0$ and $G(Z) \leq 0$
- a set of available components A
- a definition of a penalty function P

Find

- a system $Z = i + k$,

where $i \in A$ is a set of components of the system, and k is a coupling recipe, defining interactions between the components, such that the input/output specification and the feasibility constraints are satisfied and P is minimized.

A set of all possible systems (including incomplete and infeasible ones) constitutes a solution space. Each element of the set is called a solution state. The design process may be viewed as a search through the solution space to find a goal state, which satisfies given input/output specifications and feasibility constraints and which minimizes a prescribed penalty function.

The way to specialize the design problem naturally follows from its general statement, that is, specialization of a design domain is accomplished by specifying the allowable types of input/output specifications, constraints, and penalty functions. In the proposed domain of thermal energy systems, interactions between components will be limited to

(1) mass exchange,
(2) heat exchange, and
(3) work exchange.

Numerous generalized components will fit the above interaction pattern; examples include turbines, compressors, heat exchangers, mixers, combustors, pumps, etc. At this time, no attempt is made to cover those components that tend to be more specific for Chemical Engineering, e.g., complex reactors and separators. When such components are present, the decomposition of the problem cannot be performed readily and requires further research.

The definition of input/output specification $X(Z)$ will be restricted to the following:

(*a*) Material streams are required to be brought from given initial chemical compositions and thermodynamic states (source states) to given final chemical/thermodynamic states (goal states); these streams are called demand streams;

(*b*) Source and goal states may be at arbitrary and different temperature and pressure levels, thus requiring both heat and work interactions to take place within the systems to be designed;

(*c*) Sources of heat or heat sinks are available over several predetermined temperature intervals; latent heat sources can be approximated using very small temperature intervals; such sources are called utility streams; their effective flow rates are not restricted;

(*d*) Sources or sinks of work are also available; and

(*e*) Additional arbitrary streams may be selected from a given set of substances and employed as working media as long as they are confined within the boundaries of the system, i.e., they do not affect input/output specifications.

The feasibility constraints $F(Z)$ and $G(Z)$ follow from

(*a*) mass balance,

(*b*) energy balance (The First Law of Thermodynamics), and

(*c*) exergy balance (The Second Law of Thermodynamics), which must be satisfied for every component or subsystem of the feasible system.

The penalty function includes three major elements:

(*a*) annualized cost of the system components C_c,
(*b*) annual cost of energy (utilities and power) C_e, and
(*c*) penalty (cost) for violation of constraints C_v, i.e.,

$$P = C_c + C_e + C_v$$

At the goal state the penalty for violation of constraints vanishes because at the goal state all constraints should be satisfied.

4 Decomposition of the Design Problem

Decomposition plays an important role in the solution of many design problems (Lien et al., 1986). When viewed in the context of the state-space search formalism, the main advantage of decomposition is a significant reduction in the solution space.

It is suggested that a major simplification of the proposed design problem can be achieved by decomposing it into two problems: inner and outer ones. The inner problem (to be solved first) deals not with a system of the components, but rather with a set of elementary processes, without specifying heat or power interactions between the processes. The desired set of elementary processes must satisfy requirements similar to those imposed on the goal state of the original, i.e., it must minimize the penalty function, and it must satisfy the input/output specification and feasibility constraints. Once such a set of elementary processes is found, it becomes an input into the outer problem: finding a network of components that approximates the optimum set of elementary processes.

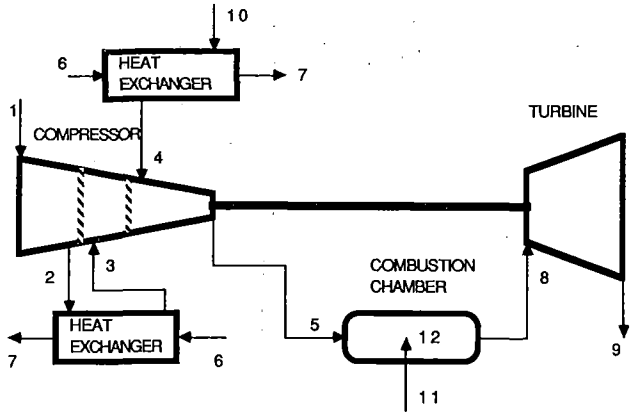

Fig. 1 System represented as a network of equipment units

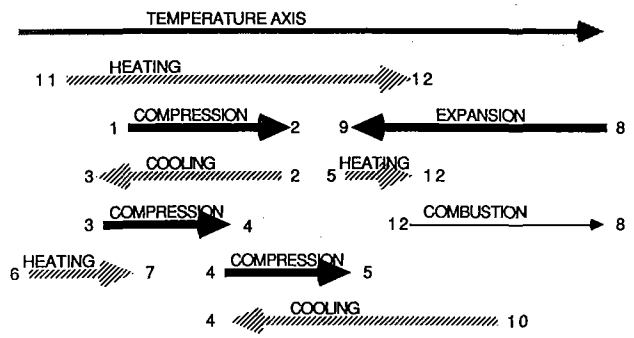

Fig. 2 System represented as a set of elementary processes

In other words, if the optimum set of elementary processes S^* is the solution of the inner problem

$$\underset{S}{\text{Min}} \{P(S) \mid X'(S) = X^*, \quad F'(S) = 0, \quad G'(S) \leq 0\}$$

and a system of components Z^* is a solution of the outer problem

$$Z^* = Z(S^*)$$

then Z^* is expected to be a solution of the original design problem

$$\underset{Z}{\text{Min}} \{P(Z) \mid X(Z) = X^*, \quad F(Z) = 0, \quad G(Z) \leq 0\}.$$

The notion of "elementary process" will be clarified next. Three types of elementary process can be distinguished: (*a*) adiabatic pressure change (compression/expansion), (*b*) isobaric enthalpy change (cooling/heating), and (*c*) adiabatic and isobaric change of chemical composition (chemical reaction). These three elementary processes allow one to approximate practically any conventional thermal energy system.

Each elementary process is associated with a single stream of material substance with a constant mass flow rate. Thus, the elementary process can be completely defined by its initial state, its final state, its mass flow rate, and two nodes, which may connect the process to other elementary processes. The demand streams can be represented by a sequence or a network of processes. Each utility stream is represented by a single enthalpy change process.

Figure 1 shows a certain system represented as a network of equipment. Figure 2 shows the same system represented as a set of elementary processes. Each elementary process is represented by an arrow directed from its initial temperature (note the axis T at the top of the picture) to its final temperature. Enthalpy change processes are shown by a gray line, pressure change processes are shown by a heavy solid line, and chemical change processes are shown by a thin solid line.

The main advantage of most decomposition techniques is reduction of the solution space. For the proposed decomposition, the solution space of the inner problem is smaller than the original one because in the inner problem most of the decisions concerning system topology are eliminated. Indeed Fig. 2, which examples a state representation for the inner problem, contains no information (and requires no decisions) about the way in which processes 2–3, 6–7, and 10–4 exchange heat; also it is unknown whether processes 1–2, 3–4, and 4–5 represent several compressors or just one; it is of no concern at this level of solution how power is being exchanged between processes 8–9, 1–2, 3–4, and 4–5, or if each of these processes is connected to a separate source or sink of power. All these decisions are removed from this level of the design activity, with resulting reduction in the solution space.

The reduction in the search space, however, by itself does not guarantee an efficient solution. Indeed, one of the requirements for an efficient search is (at least in the proposed approach) a state evaluation function. Thus the reduction in the search space achieved by a more abstract representation may be quite counterproductive if this abstraction prevents reliable evaluation of a state. It will be shown later that this is not the case in the proposed decomposition; an effective state evaluation is still possible even for a state represented by merely a set of elementary processes.

The outer problem, i.e., synthesis of equipment network from the known set of elementary processes, is not too difficult. The most formidable task, synthesis of a heat exchange network from the known set of enthalpy change processes, can be accomplished by a number of known methods. The other tasks, implementation of pressure change processes in some expansion/compression equipment and implementation of chemical changes in reactors, appear to be relatively straightforward.

The remainder of the paper is focused on the more difficult inner problem.

5 Thermodynamic Evaluation of a Design State

In order to search for a solution of the inner problem, the problem solver must be able to evaluate the thermodynamic feasibility and thermodynamic perfection of the solution state represented by a set of elementary processes. Such an analysis constitutes a core of the state evaluation function. The information about heat and power interactions between the elementary processes is not available at this level of the solution. Therefore, conventional thermodynamic analysis, in which an equipment unit or a group of units is isolated within a control volume, is not suitable here. Some other concept of control volume is needed.

A special form of fundamental equations for steady-state open thermodynamic systems based on the "temperature interval" concept introduced by Linnhoff and Flower (1978) is presented in the following. This particular treatment allows one to determine the effects of work, heat, and chemical interaction within the system on the extent of second-law infeasibility and on overall exergy loss over any particular temperature interval, prior to completion of the design. The temperature interval $(T_1; T_2)$ is defined here as an interval of temperature $T \epsilon (T_1; T_2)$ for elements in a thermodynamic system. In the example in Fig. 3, an entire design state consists of the elementary processes 1 through 7. Some segments of the processes, A–B, C–D, E–F, G–H, and J–K, are situated within the temperature interval $(T_1; T_2)$. The bounds $T = T_1$ and $T = T_2$ can be viewed as a control surface. An enthalpy flux through a boundary T is defined by

$$F(T) = \sum_i n_i h_i(T) m_i$$

where $n_i = 1$ if the direction of process i coincides with the temperature axis,
$n_i = -1$ if the direction of process i is opposite to the temperature axis,

$h_i'(T) = h_i(T)$ for $T \in (T_{i,\min}; T_{i,\max})$,

$h_i'(T) = h_i(T_{i,\min})$ for $T < T_{i,\min}$, and

$h_i'(T) = h_i(T_{i,\max})$ for $T > T_{i,\max}$.

Here $h_i(T)$ is specific enthalpy of a material substance of a process i at temperature T and at the pressure p that corresponds to temperature T in the process i. Note that this function can be double-valued if the substance is pure and a phase transition occurs at this T and p.

Consider an infinitesimal interval $(T;\ T+dT)$, which receives: dW - work input from the environment, dQ - heat input from the processes outside of $(T;\ T+dT)$, and dG - heat generated within $(T;\ T+dT)$ by chemical transformation.

The First Law of Thermodynamics for this interval is expressed as

$$F(T+dT) - F(T) = dF = dW + dQ + dG. \tag{1}$$

Integrating (1) over the interval $(T_{\min};\ T)$, where $T_{\min} = \min\{T_{i,\min}\}$, and introducing the notation

$$W(T) = \int_{T_{\min}}^{T} dW \text{ and}$$

$$G(T) = \int_{T_{\min}}^{T} dG$$

yields

$$F(T) - F(T_{\min}) = W(T) + Q(T) + G(T), \text{ or}$$

$$Q(T) = F(T) - F(T_{\min}) - W(T) - G(T) \tag{2}$$

The functions $Q = Q(T)$ is called the heat transit function. It is a net amount of heat transferred from the hotter part of the system $(T;\ T_{\max})$ (where $T_{\max} = \max\{T_{i,\max}\}$) to the colder part of the system $(T_{\min};\ T)$ across the control surface T. The Second Law of Thermodynamics requires

$Q(T) \geq 0$, or

$$F(T) - F(T_{\min}) - W(T) - G(T) \geq 0$$

$$\text{for any } T \in (T_{\min};\ T_{\max}) \tag{3}$$

Equation (3) determines the feasibility of the design state in terms of the Second Law. Any temperature interval where the heat transit function assumes a negative value is called an infeasible interval. A negative value of $Q(T)$ implies that, in violation of the Second Law, heat is transferred from the colder elements of the system to the hotter ones. Such an interval cannot correspond to any real system and must be redesigned. The same equation shows how work input and heat generation distributions along the temperature axis affect the feasibility of the design state. It also indicates possible transforming operators for the design state, as will be discussed in the second part of this paper.

Feasibility of the design state in terms of the First Law of Thermodynamics is given by the condition

$$F(T_{\max}) - F(T_{\min}) - W(T_{\max}) - G(T_{\max}) = 0 \tag{4}$$

This is obtained from equation (2) by noting that $Q(T)$ must vanish for $T = T_{\max}$. Overall change in the enthalpy flux must equal total work input plus total internal heat generation.

Next, an approximate equation for total exergy loss within the system of elementary processes will be derived. We define

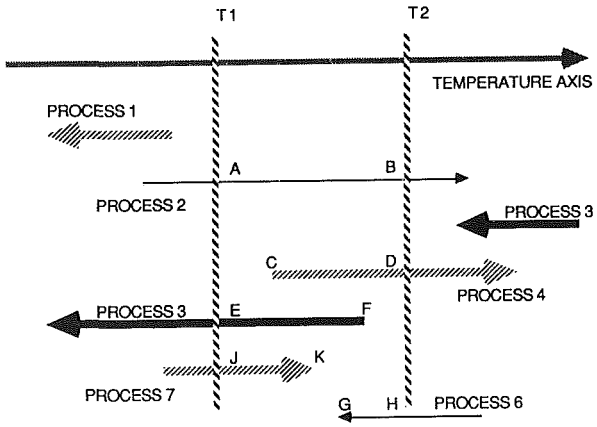

Fig. 3 Temperature interval $(T_1;\ T_2)$

an exergy flux through a boundary T in a way similar to the definition of enthalpy flux

$$E(T) = \sum_i n_i e_i'(T) m_i$$

Here the specific exergy $e_i(T)$ is defined as $(h - h_0) - T_0(s - s_0)$; chemical terms are omitted for reasons discussed by Siemons (1986). Consider again an infinitesimal interval $(T;\ T+dT)$, which receives:

dW_e – the part of dW that is transformed into exergy of the stream,
$(1 - T_0/T)dQ$ – the exergy part of the heat input, and
$(1 - T_0/T)dG$ – the exergy part of the internal heat generation.

Note that this last expression is appropriate only in such cases as combustion of fuel with a high excess air ratio, when combustion can be approximated by a heat input. Then

$$E(T+dT) - E(T) = dE(T) = dW_e + (1 - T_0/T)dQ + (1 - T_0/T)dG \tag{5}$$

Integration over the interval $(T_{\min};\ T_{\max})$ gives

$$E(T_{\max}) - E(T_{\min}) = \int_{T_{\min}}^{T_{\max}} dW_e + \int_{T_{\min}}^{T_{\max}} Q(T)\, d\left(\frac{T_0}{T}\right) + G(T_{\max})\left(1 - \frac{T_0}{T_{\max}}\right) + \int_{T_{\min}}^{T_{\max}} G(T)\, d\left(\frac{T_0}{T}\right) \tag{6}$$

Total exergy input into the interval $(T_{\min};\ T_{\max})$ consists of

- exergy of fuel, approximated as $G(T_{\max})$ (Baehr, 1973), and
- work input $W(T_{\max})$.

Total exergy loss is given by

$$DE = W(T_{\max}) + G(T_{\max}) - [E(T_{\max}) - E(T_{\min})] = \int_{T_{\min}}^{T_{\max}} (1 - x)\,dW - \int_{T_{\min}}^{T_{\max}} [Q(T) + G(T)]\, d\left(\frac{T_0}{T}\right) + G(T_{\max})\frac{T_0}{T_{\max}} \tag{7}$$

where a generalized efficiency of the pressure change process $x = dW_e/dW$ is introduced, and integration is performed over feasible intervals only.

Equation (7) provides a basis for a powerful evaluation function that can be applied to a state represented as a set of elementary processes. If all other factors are equal, a state

with higher exergy loss offers greater potential for design improvements. Furthermore, the right-hand integral of equation (7) indicates what transformation might be applied to the design state, and on what temperature interval such transformations will be particularly effective. In the second part of this paper, equation (7) is utilized to propose a state evaluation function and several state transformations.

This equation also suggests a consistent way to quantify an infeasibility of a design state. We may define a total exergy "creation" (by analogy with exergy loss) as

$$DE' = \int_{T_{\min}}^{T_{\max}} Q(T) d\left(\frac{T_0}{T}\right) \tag{8}$$

where integration is performed over infeasible intervals only. This "creation" of exergy is yet another manifestation of the Second Law violation that is implied by the infeasible intervals. Expression (8) gives one a way to compare two states in terms of feasibility violation. The state with the higher DE' violates the condition of feasibility to a greater extent. Thus, expression (8), similarly to (7), serves as a basis for both evaluation and transformation of a design state.

6 Conclusions

1 A design problem is addressed in which a structure of the design object is not determined a priori. In this situation, it is not obvious how to apply parametric optimization, integer optimization of a "superstructure," or conventional problem decomposition approaches.

2 A rigorous, nondeterministic search with specially developed analytical techniques and heuristics offers an opportunity to avoid structural assumptions about the design object. An "artificial designer" may or may not follow the same search trajectory as a human designer would.

3 An abstract representation of a thermal system by a set of elementary processes reduces the design search space without impairing design state evaluation.

The search problem in terms of physical equipment is too large and difficult to deal with directly. This can be simplified by using an alternate representation for the problem in terms of elementary processes, and then translating the optimal solution to the problem in that representation back to actual equipment. The representation in terms of elementary processes is called the "inner problem," and the search space for it is much smaller than the one for the "outer problem," in terms of actual equipment. In order to exploit the representation fully in terms of elementary processes, it must be shown that one can efficiently evaluate and search among such configurations; the former is dealt with in this paper, the latter is discussed in Part 2.

4 The technique of thermodynamic analysis presented in this paper supports formulation of a state evaluation function and of transforming operators.

The above results are utilized in the second part of this paper to develop a state-space search algorithm that enables automatic synthesis of the network of elementary processes.

References

Baehr, H. D., 1973, *Termodynamik*, Springer-Verlag, Berlin.

Grossman, I. E., 1985, "Mixed-Integer Programming Approach for the Synthesis of Integrated Process Flowsheets," *Computers and Chemical Engineering*, Vol. 9, No. 5.

Lien, K., Suzuki, G., and Westerberg, A. W., 1986, "The Role of Expert Systems Technology in Design," Report EDRC-06-13-86, Carnegie-Mellon University, Pittsburgh, PA.

Linnhoff, B., and Flower, J. R., 1978, "Synthesis of Heat Exchanger Networks," AIChE Journal, Vol. 24, pp. 633–654.

Menzies, M. A., and Johnson, A. I., 1972, "Synthesis of Optimal Energy Recovery Networks Using Discrete Methods," *Canadian Journal of Chemical Engineering*, Vol. 50, pp. 290–296.

Mostow, J., 1984, "Rutgers Workshop on Knowledge-Based Design," SIGART Newsletter, Oct., pp. 19–32.

Nishida, N., Stephanopoulos, G., and Westerberg, A. W., 1981, "A Review of Process Synthesis," AIChE Journal, Vol. 27, pp. 321–351.

Nishio, M., Johtaro, I., Shiroko, K., and Umeda, T., 1980, "A Thermodynamic Approach to Steam-Power System Design," *Industrial Engineering Chemical Process Design and Development*, No. 19, pp. 306–312.

Petroulas, T., and Reklaitis, G. V., 1984, "Computer-Aided Synthesis and Design of Plant Utility Systems," *AIChE Journal*, Vol. 30, No. 1, pp. 69–78.

Shelton, M. R., and Grossman, I. E., 1986, "Optimal Synthesis of Integrated Refrigeration Systems," Report No. EDRC-06-02-86, Carnegie-Mellon University, Pittsburgh, PA.

Shiroko, K., and Umeda, T., 1980, "A Practical Approach to Process Analysis and Improvement for Energy Conservation," *Proceedings of 1980 Conference on Industrial Energy Conservation Technology*, Houston, TX, Vol. 2, pp. 782–790.

Siemons, R. V., 1986, "Interpretation of the Exergy Equation for Steady-Flow Processes," *Energy*, Vol. II, No. 3, pp. 237–294.

Siirola, J. J., 1982, "Chemical Process Synthesis," *Chemical Engineering Education*, Vol. 16, No. 2, pp. 68–71.

Townsend, D. W., and Linnhoff, B., 1983, "Heat and Power Networks in Process Design," *AIChE Journal*, Vol. 29, No. 5, pp. 742–771.

Wymore, A. W., 1976, *Systems Engineering Methodology for Interdisciplinary Teams*, Wiley, New York.

An Autonomous Artificial Designer of Thermal Energy Systems: Part 2—Solution Algorithm

A. S. Kott[1]
Research Associate,
Department of Mechanical Engineering.

J. H. May
Co-Director,
AIM Laboratory,
Katz Graduate School of Business.

C. C. Hwang
Associate Professor,
Department of Mechanical Engineering.

University of Pittsburgh
Pittsburgh, PA 15261

A knowledge-based approach to automated conceptual design (flowsheet synthesis) of thermal energy systems with strong interactions between heat/power/chemical transformations is presented. In Part 1, formulation of a thermal design problem is stated in terms of input/output specification, component interaction, feasibility constraints, and penalty function. The problem is then decomposed in inner problems that deal with a set of elementary processes, and outer problems that find a network of components approximating the optimum set of elementary processes. A design state is evaluated using a special form of fundamental equation for steady-state open thermodynamic systems based on a "temperature interval" concept. In Part 2 of this paper, an algorithm is presented. The algorithm makes use of the state evaluation function, transformation operators, and the plausible move operator to search through a space of the design states. A simple closed-cycle gas turbine is employed to illustrate the behavior of the "artificial designer" as it advances from a certain given design to more sophisticated schemes.

1 Introduction

This is the second part of a two-part paper that focuses on the automated synthesis of conceptual schemes (flowsheets) of power/heating/refrigeration systems. The first part of the paper was devoted to the more theoretical issues pertaining to the subject. There the proposed approach was predicated on the heuristic state-space search, the design problem was reduced to a more manageable form, and a technique of thermodynamic (exergetic) analysis was developed to help guide the search. In this second part of the paper an algorithm is presented that actually solves the synthesis probem by searching through a space of the design states.

2 An Overview of the Solution Algorithm

The knowledge-based problem solver consists of three major components: a problem representation, transforming operators, and search control.

The problem representation consists of the descriptions of the design states that have been generated in the preceding steps of the solution process. The reason for keeping more than one state in the representation is the imperfection of the plausible move generator. The plausible move generator is a nondeterministic, knowledge-based instrument, and by its very nature is not expected to produce infallible decisions at each and every step. The search control mechanism must recognize a possible failure and backtrack to some earlier state; hence, the necessity to store a number of states in the representation database. Each design state is defined by a set of elementary processes. Each process is defined by two nodes, a mass flow rate, and thermodynamic and chemical conditions at the beginning and at the end of the process. Every state description also contains the value of the state evaluation function and a ranked set of transforming operators to be applied to the state. Other elements of the representation include a user-defined problem statement (demand streams, utility streams, allowable working media as discussed in Section 3, Part 1), thermodynamic properties, and cost data.

The transforming operators are discussed in Section 4. They are of two types: those that reduce infeasibility of the state and those that reduce exergy losses of the state. Each operator is a stand-alone algorithm that accepts a single state as input and returns a single transformed state. Every transformation requires a number of parameters to be available as input. These parameters describe processes to be modified and are produced by the plausible move generator.

The search control strategy is realized by means of two independent functions: a plausible move generator and a state evaluation function. The plausible move generator works along the lines sketched in Section 5. It is structured as a set of heuristics that operate on a single state and strive to find a transforming operator (along with required parameters of the operator) that produces a maximal reduction of infeasibility or exergy loss with minimum increment in other penalties. The state evaluation function (described in Section 3) is responsible for determining which of the available design states shows the most promise for the future development. This evaluation process combines equipment cost estimate for the known parts of the design, estimate of cost reduction due to potential ther-

[1] Currently with Carnegie Group Inc., Pittsburgh, PA 15222.

Contributed by the Advanced Energy Systems Division of THE AMERICAN SOCIETY OF MECHANICAL ENGINEERS and presented at the ASME Winter Annual Meeting, Boston, Massachusetts, December 13–18, 1987. Recipient of the E. F. Obert Outstanding Paper Award. Manuscript received by the Advanced Energy Systems Division January 19, 1988.

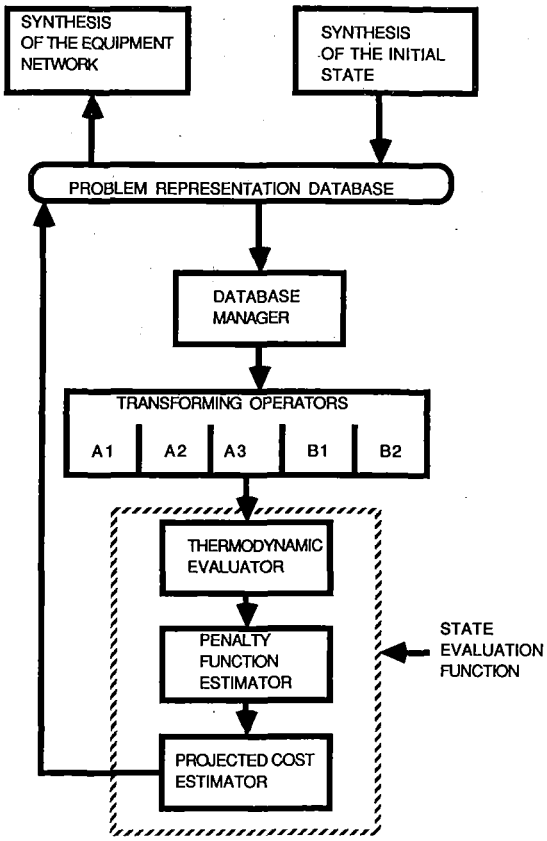

Fig. 4 Solution flowchart

modynamic improvements, and an estimate of the additional cost that would be required to eliminate infeasibilities (if any).

Figure 4 displays a flow chart of the search algorithm, and the interactions of the main components discussed above as well as some other auxiliary elements. The search starts from an initial state that can either be given by the user or generated by a computerized heuristic procedure. This step is analogous to the first guess in the iteration procedure of a numerical analysis. The synthesis of the initial state must satisfy an input/output specification (see Section 3 of Part 1), which involves material streams, and sources or sinks of heat and work. The mass balance and the energy balance are satisfied. In general, the initial state is not optimal and may be infeasible with respect to the Second Law. After several iterations, the representation database contains a number of states. The database manager sorts all the states in the database according to their projected costs. If, among the states, there are any feasible states, then the lowest cost of the feasible state is used as a benchmark to prune out (i.e., delete) the states with projected cost higher than the benchmark cost (i.e., "branch-and-bound" scheme). A copy of the best of the states in the database, the one with the minimum projected cost, is sent to the plausible move generator. The plausible move generator proposes a number of transforming operators suitable for this particular state to reduce either its infeasibility or exergy loss, ranks them, chooses the best, and sends the state to the chosen operator. The operator produces a new, presumably better, state, and transfers it to a state evaluation function.

After the evaluation, the new state returns to the database, which at this point contains all the previous states plus the new state. This iterative process terminates when the plausible move generator is unable to propose any transformations for the states remaining in the database. Then the best of the feasible states (if any) is sent to an equipment network synthesizer, which maps that state's processes into units of equipment.

Both the synthesis of the initial state and synthesis of the equipment network have been only peripheral interests of this research. Even though both of these tasks are at least partially automated in the software implementation of this algorithm, they have yet to be addressed in a more conclusive manner. The main thrust of this work is directed toward the "kernel" of the algorithm: the state evaluation function, the transforming operators, and the plausible move generator.

3 The State Evaluation Function

The state evaluation function performs several tasks. First, it conducts thermodynamic evaluation of the state, as discussed in Section 5, including computations of the functions $Q(T)$, $G(T)$, DE, and DE'. Then the expected cost of equipment is estimated using heuristic techniques (particularly that of Tjoe and Linnhoff, 1986, for total heat exchange surface) and empirical cost correlations (particularly those of Guthrie, 1969). The cost of power and utilities is calculated from the given costs per unit of power and utility consumption.

Finally, the projected cost of the state is estimated. This is the cost that is used to compare the available design states, and to decide which one is to be chosen for further development. It is different from the penalty function discussed in Section 3 of Part 1. The projected cost of the state is a lowest possible penalty function value for a hypothetical state that could be obtained from the given state using an optimum solution path. We estimate the projected cost as

$$P_{pr} = C_c + C_e - a^*DE + b^*DE'$$

where the term a^*DE accounts for potential reduction of cost due to elimination of exergy loss DE, and the term b^*DE' accounts for the cost increase required to eliminate infeasibility DE'. The empirical coefficients a and b may be viewed as the "costs" associated with exergy loss and infeasibility, respectively. These costs are initiated by the user, and are then automatically updated during the soltion process to reflect observed relations between costs, DE, and DE'. After each iteration both costs are estimated using the changes that occurred between the last two states

$$a = \frac{\partial C_c + \partial C_e + b^*\partial DE'}{\partial DE}$$

$$b = \frac{a^*\partial DE - \partial C_c - \partial C_e}{\partial DE'}$$

These values are underrelaxed by averaging them with the previously assumed values. Note that all of the above costs can be estimated while operating on the level of the abstract representation (a set of elementary processes), without involving any decisions regarding the level of component representation. The above estimation technique exploits the fact that exact projected cost has a constant value for all states on the optimal path. The accuracy of this estimate is limited because of the inevitable deviations from the optimal path and because of the inaccurate initial values of the coefficients a and b. Other techniques for estimating the terms a^*DE and b^*DE' appear to be possible: more sophisticated learning paradigms, heuristic approaches that take into account specifics of the given state, look ahead by evaluating a few moves forward from the given state, etc. In either way, the search can be made more accurate by underestimating b^*DE' and by overestimating a^*DE' (making the projected cost more optimistic, see below), but at the expense of the search efficiency.

The penalty function approach to representing infeasibility encourages the maintenance of feasibility but does not require it. If those penalty function terms are small with respect to the other costs involved, and if the space of feasible solutions is small, it is possible that our algorithm will not yield a feasible solution. We employ additional heuristics, such as retaining

the best feasible solution found so far, and biasing the search toward transformations that do not increase infeasibility, until at least one feasible solution has been found. If these are not sufficient, another recourse is to restart the problem with an increased penalty for infeasibility, as has been traditional with penalty-function-like approaches (Fiacco and McCormick, 1968).

The efficiency of the search technique is determined by the power of the heuristics that guide it. Hart, et al. (1968) and Pearl (1984) provide an overview of the use of evaluation functions to guide a search. We chose to use a variant of the A^* procedure, because it is guaranteed to terminate in an optimal path from the starting state to the goal if any such path exists (an informal discussion of the properties of A^* is given by Nilsson, 1980). The evaluation function for every node of the state-space is defined as a sum of two components: One component estimates the cost of a path from the initial node to this node (in the present case it is given by the first two terms of the projected cost), and the second component estimates the minimum cost from this node to a goal (in the present case, the last two terms of the projected cost).

The projected cost should not be too pessimistic. In other words, the projected cost for a state should not be higher than the cost of the goal state that could be obtained from the given state using an optimal solution path. It is shown by Hart (1968) that if the state evaluation function is never too pessimistic, then the optimal solution will be found eventually. On the other hand, if the projected cost is too optimistic, the "best-first" algorithm may have a tendency toward excessive backtracking, because earlier nodes of the state space will look more attractive with their over-optimistic projections than more realistic projected costs of more developed nodes.

Unfortunately, the projected cost in the present case does tend to be more optimistic for the earlier nodes (closer to the initial state), and then becomes more accurate as development proceeds toward the goal state. To alleviate this problem a back-propagation mechanism is used. The objective of the mechanism is to adjust overly optimistic costs of the earlier nodes using the evaluations of their descendant nodes. Whenever a newly created state shows a projected cost higher than the projected cost of its parent state, the projected cost of the parent state is increased; then the same procedure is applied recurrently to the "grandparent" state, etc. This dynamic adjustment reduces the amount of backtracking, although at the expense of reducing the accuracy with which the final result of the search approximates the true optimal design. Such a tradeoff between optimum and efficiency is a common feature in practical applications of heuristic search approaches.

4 Optimizing Transformations of the Design State

In Section 5, Part 1 of this paper, two important results are derived. Equations (3) and (8) define the thermodynamic feasibility of the state, while equation (7) defines the thermodynamic perfection of the state. Now these results will be used to determine generalized transforming operators, which the problem solver may apply to a given state in order to produce another state with either better feasibility or better thermodynamic performance. These operators, along with the means to rank them in order of their expected effectiveness, form the core of the plausible move generator.

Assume, in a certain design state S, that the heat transit function $Q(T)$ is negative at $T=T_1$. The problem solver wishes to find some transformation L that would produce another state $S'=L(S)$ where $Q(T_1)>0$. According to equation (2),

$$Q(T_1)=F(T_1)-F(T_{\min})-W(T_1)-G(T_1) \qquad (9)$$

For clarity we assume that all substances participating in the elementary processes are near-perfect gases or liquids, so that

$$(\partial F/\partial p)_T \simeq 0$$

although the following discussion of possible transformations would apply qualitatively to real fluids as well.

Operator A1. The simplest transforming operator starts with an introduction of a cooling utility process defined in some temperature interval below T_1 (if such a utility is available). According to the definition of $F(T)$, this change increases $Q(T_1)$ by

$$\Delta F = m_u (h_{u,\max} - h_{u,\min})$$

The same result can be obtained by increasing the mass flow rate of an existing cooling utility process or by decreasing the flow rate of an existing heating utility process (note that in such cases the designer may avoid the addition of another heat exchanger with obvious economic benefit).

In order to avoid violation of feasibility condition (4) the designer must also add a heating utility process in some temperature interval above T_1 so that

$$F(T_{\max}, S') = F(T_{\max}, S)$$

The same result can also be obtained by increasing the flow rate of an existing heating utility process or by decreasing the flow rate of an existing cooling utility, as long as that utility is located above T_1. After these additions or modifications of the utility processes are completed, the new set of processes represents a new state $S'=A1(S)$. The new state S' has an improved Second Law feasibility at least at point T_1. The First Law feasibility has not been affected, nor has compliance with the input/output specification.

Operator A2. This transformation starts by introducing an expansion process (with extraction of work) in some temperature interval below T_1. This can be accomplished in a number of ways: by introducing a new process, using a looped stream of a working medium, by replacing an existing heat exchange process, by increasing the flow rate of an existing expansion process, or by decreasing the flow rate of an existing expansion process, or by decreasing the flow rate of an existing compression process. The resulting modification is associated with work output ΔW and pressure change $\Delta P=\Delta P(\Delta W)$. From equation (9) it follows that $Q(T)$ increases by ΔW. In order to preserve compliance with the input/output specification, it is necessary to introduce a compression process in some temperature interval above T_1, acting on the same stream of substance that undergoes the expansion process added, and with the same ΔP. The compression process requires work input $\Delta W'=\Delta W'(\Delta P)$ and in general $\Delta W'>\Delta W$. This fact necessitates an addition of a cooling utility, or a decrease on a heating utility, in order to preserve compliance with the First Law.

Operator A3. This transformation affects the last member in the right-hand side of equation (9). It starts with the reduction of internal heat generation by an amount ΔG in some interval below T_1. Equation (9) asserts that this increases $Q(T_1)$ by ΔG (assuming a change in internal heat generation does not affect $F(T)$). Compliance with the input/output specification requires an offset for this modification by increasing the internal heat generation somewhere else in the system. This is done in some interval above T_1.

Now equation (7) will be considered. Attention here will be limited to an integral that describes exergy losses associated with the functions $Q(T)$ and $G(T)$

$$DE(Q, G) = -\int_{T_{\min}}^{T_{\max}} (Q+G)\, d\left(\frac{T_0}{T}\right) \qquad (10)$$

It is desirable to avoid large positive values of $Q(T)+G(T)$. According to equation (2)

$$Q(T)+G(T)=F(T)-F(T_{\min})-W(T) \qquad (11)$$

Then, in order to reduce $Q(T)+G(T)$ at some point $T=T_1$, the problem solver may apply the following transforming operators:

Operator B1. This is an analog of A1, affecting $F(T)$ in equation (11). It involves reduction of net utility heat rejection in some interval above T_1 and equal reduction of net utility heat consumption in some interval below T_1.

Operator B2. This operator is an analog of A2, targeting primarily $W(T)$ in equation (11). It involves increased work input in some interval below T_1, increased work output in the interval above T_1, and an adjustment of the utility consumption necessary for energy balance.

There is no analog to A3, however. Equation (11) shows that any redistribution of $G(T)$ will cause an equal and opposite redistribution of $Q(T)$. This conclusion is applicable only to those cases where approximations of equation (11) are valid.

5 The Plausible Move Generator.

The number of transformations applicable to a given state is infinite. Clearly, it is impossible to try all of them. The task of the plausible move generator is to propose only a few moves with the highest probability of success.

The coupling of the design goals is one of the issues involving a complicated generation of moves. For example, an attempt to reduce the exergy loss may result in increased infeasibility, and/or increased equipment cost. Another formidable difficulty arises from the single-minded, thermodynamic nature of the available transforming operators. Indeed, the solution of the design problem is characterized by the minimum value of the penalty function, which includes the annualized cost of equipment, the cost of utilities and power, and the infeasibility penalty. The transforming operators that have been devised so far are capable of reducing only some parts of these penalties. It may appear that any solution process utilizing only these operators will be able to progress toward minimization of some parts of the total cost, but not toward minimization of the total cost. These difficulties are of a rather general nature, and can be formulated in more general terms: Given a state-space search problem with a goal to minimize a total penalty function

$$P=P_A+P_B; \quad P_A, P_B>0$$

find a successful search control strategy, while knowledge-based guidance is available only for minimization of the penalty component P_B.

The following general approach to this problem is proposed:

(*a*) Find (via some heuristic technique) a state with minimum P_A; use this state as an initial point in the search. Note that this state will be, in general, infeasible and suboptimal.

(*b*) At each step of the solution, use heuristic guidance to follow the path of steepest descent, i.e., look for a move that will cause maximum reduction of cost P_B with minimum increase in cost P_A. In the present problem this means, roughly, that reduction of infeasibility or irreversibility should always be accomplished with minimum increase in the cost of equipment. This heuristic guidance is not expected to be infallible, and therefore, a "best-first" search must remain as a basic mechanism.

Obviously, such an approach is beneficial only when solution of step (*a*) (finding a state with minimum P_A) is easier than the original problem. Also, knowledge-based guidance in general is not perfect; hence this approach in general does not yield a global optimum, but rather some approximation dependent upon the accuracy of the guiding knowledge. A more detailed treatment of this subject would go beyond the scope of this paper.

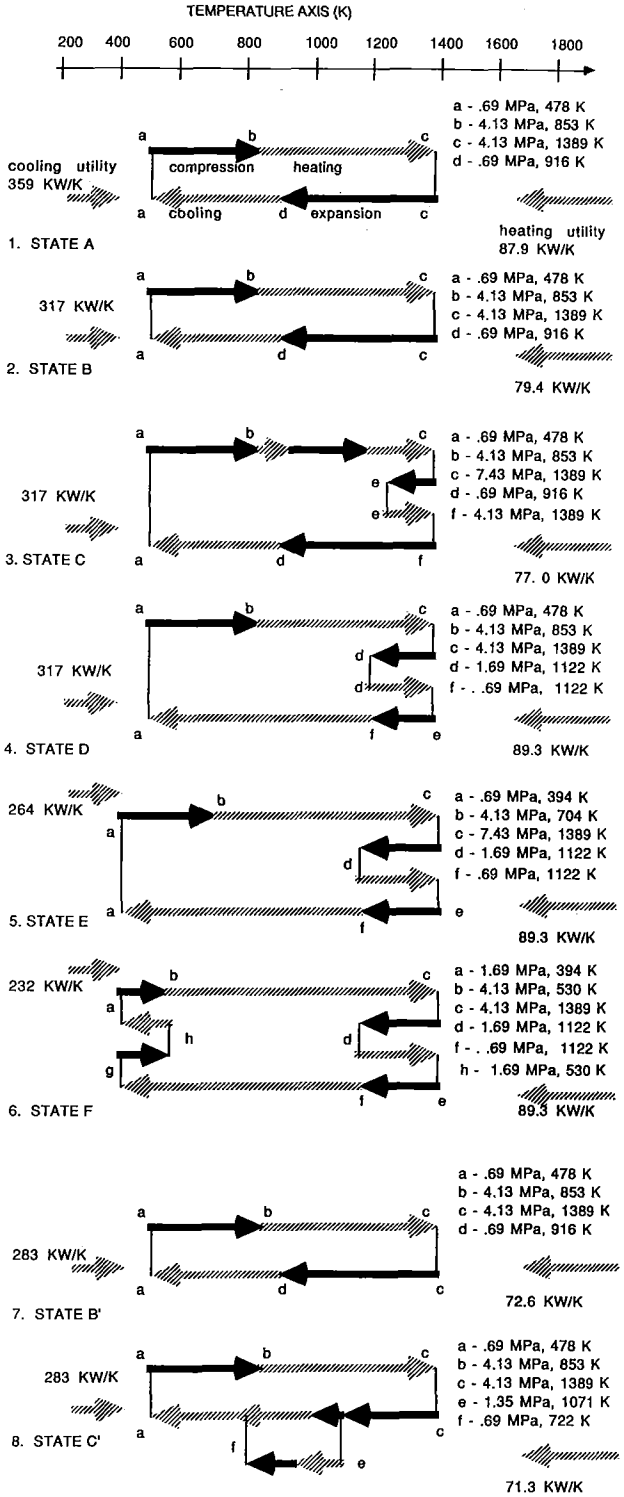

Fig. 5 Example of evolution of a closed-cycle gas turbine; design state representation

An application of each of the transforming operators involves a large number of decisions, which can be subdivided into three groups:

1 choice of an interval to be transformed,

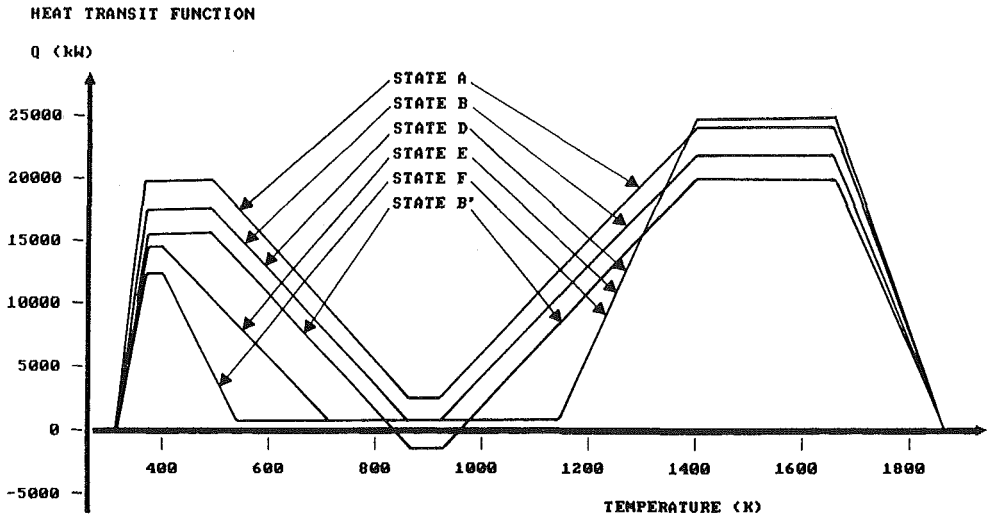

Fig. 6 Example of evolution of a closed-cycle gas turbine; heat transit function

2 choice of the processes to be included into transformation, and

3 choice of an extent of the transformation, i.e., values of ΔF, ΔW, and ΔG.

To make a choice of the target temperature interval, a heuristic rule is used that selects either an interval over which $Q(T)$ is negative and DE' is maximal over all such intervals, or an interval over which $Q(T)+G(T)$ is positive and DE is maximal over all such intervals. When there are no feasible states in the database, the infeasible interval is selected.

The choice of the processes is governed by numerous considerations. First, to qualify for inclusion into the transformation, the process must be located with respect to the target interval in such a way as to maximize the effect of the transformation within the interval and to minimize any secondary effects outside of the interval. This qualification is done by a number of heuristic rules. Secondly, the transformation must be accomplished in a most economic way; it must make use of the already existing processes whenever possible. To this end, the various alternative transformations are ranked by a number of heuristics, including:

1 An operator that executes a transformation of a state by modifying existing processes is ranked higher than one that adds new processes.

2 An operator that reduces the flow rate of an existing process is ranked higher than one that increases the flow rate.

3 An operator that eliminates an existing process is ranked higher than one that modifies it, etc.

The choice of the extent of the transformation (i.e., values of ΔF, ΔW, ΔG) does not seem to be amenable to a heuristic treatment. However, it is computationally inexpensive to introduce an inner optimization loop that searches for a value of ΔF (or ΔW, or ΔG) that minimizes the penalty function using a conventional optimization technique.

6 Example

To illustrate the proposed approach a trace is made of the behavior of the "artificial designer" as it advances from a certain given state – a simple closed-cycle gas turbine – to more sophisticated schemes.

State A, presented in Fig. 5.1, consists of four processes, forming a simple gas turbine loop, and two utility streams that satisfy heating and cooling requirements within the gas turbine cycle. No other utilities, no demand streams, and no chemical interactions are defined in this problem. Note that in the absence of chemical transformations, the function $Q(T)$ can be used to evaluate both feasibility and (partial) exergy losses in the system.

The plausible move generator detects a significant positive value for $Q(T)$ over the interval 311–1944 K as well as the availability of two utilities suitable for operator B1. Operator B1 (see Section 4) creates a new state B (see Fig. 5.2) and sends it to the state evaluation function. The latter finds that exergy loss due to heat transfer (note area under the curve $Q(T)$ on Fig. 6) has decreased with a corresponding reduction in net energy costs; the cost of utility heat exchangers has dropped as well, but a new element (a regenerator) adds cost. The projected cost of state B is estimated to be lower than that of state A. All costs in this example are referred to a unit of the power output.

In the next iteration, the plausible move generator works on state B, the highest ranking state in the representation. It targets the interval 916–1944 K due to its high DE; abandons operator B1 because a suitable utility is not available at the low end of the interval; attempts the only remaining operator B2, which forces it to limit the interval to 916–1389 K (the specified limit of preturbine temperature); and finds two alternative processes for modification *bc* and *dc*. At this point, the plausible move generator is forced to make a mistake: to pick process *bc*. By doing this, it is intended to demonstate that such an error is by no means fatal; it will be detected and recovered later. The plausible move generator does not have to be infallible. So, we force the choice of the process *bc*. Operator B2 takes process *bc* and produces (see Section 4) a state C (Fig. 5.3). The state evaluation function finds that high energy cost (due to losses in additional compression/expansion processes) plus the cost of added machinery makes the projected cost of state C very unattractive, higher than those of states A and B. Futhermore, it is even higher than the current cost of state B, and for this reason state C is deleted from the problem representation database.

In the next iteration, the best state in the database is state B again; this is an example of backtracking. Applying operator B2 to process *dc* (note that there are only two alternatives and process *bc* has been tried already), the artificial designer arrives at state D (Figs. 5.4 and 6). Then operator B2, acting on processes *ab* and *fg* over the interval 311–853 K, produces state E (Figs. 5.5 and 6). Operator B2, acting on processes *ab* and *fa* over the same interval, produces state *F* (Figs. 5.6 and 6), and so on. The process will stop when a certain predetermined goal (e.g., total cost) or limit (e.g., the number of iterations) is reached, or when the plausible move generator exhausts all options for all states in the database.

Note the versatility of operator B2: Using the same set of rules and the same operator, the artificial designer developed reheat (Fig. 5.4), reduced mean temperature difference (Fig. 5.5), and intercooling (Fig. 5.6). The motivation and the result of these transformations are reduction of the exergy loss in the system (note area under the curve $Q(T)$ on Fig. 6). Operator A2 is similarly versatile.

Now return to state A and reinitiate the process with a different cost scenario. The cost of the heating utility is increased significantly. In this case, operator B1 forces the transformation into an infeasible region (Figs. 5.7 and 6, note temperature interval with negative heat transit function). This infeasibility, however, does not necessarily mean that state B′ is hopeless and can not be an intermediate state on a path to a goal state. On the contrary, the state evaluation function finds that the projected cost of state B′ is more promising than that of state A. Indeed, even though state B′ is penalized for infeasibility, it has a much lower cost of utilities due to lower exergy loss (see Fig. 6). In the next move, operator A2 (see Section 4), acting on the partial mass flow rate of processes *cd* and *de*, produces a feasible state C′, which can be viewed as a gas turbine loop with extractive regeneration added. Eventually the "artificial designer" will have to realize that this direction of the search is not fruitful in this particular case; its evaluation of state B′ happened to be overly optimistic; it will have to backtrack to state A and try other moves.

In the actual computer run corresponding to this example the program arrived at what appeared to be an optimum scheme (for that particular set of assumptions, restrictions, and simplifications): a cycle with three intercoolings and one regeneration. This state's loss of exergy was eight times lower than in the case of a cycle with one regeneration only, and the annual profit was seven times higher. It was only marginally better than its "parent" state with two intercooling and one regeneration. It took the program 20 iterations (20 new states) to arrive at the (apparently) optimum state. Then it spent another 60 iterations trying further improvements before giving up.

7 Conclusions

1 A rigorous, nondeterministic search with specially developed analytical techniques and heuristics is capable of finding viable design solutions without being given an object's structure and without mimicking a human expert.

2 An A^*-type evaluation function supported by a back-propagation cost adjustment facilitates "best-first" search.

3 A strong heuristic operator ordering function is crucial to this design problem because the number of possible moves is unlimited, the design knowledge may be imcomplete, and design goals are coupled.

4 The ability to evaluate and to transform both feasible and infeasible (in terms of the Second Law) states appears to add to the efficiency and completeness of the design search.

5 Further research might focus on a formal evaluation of the proposed approach to design, and on improving the speed of the system. Because there does not exist a set of benchmarks against which to measure computation time, it is sufficient that the system be able to find a design configuration in a reasonable interval. Execution times are difficult to compare because of the variances in dialects of Lisp and operating system environments, but on a heavily loaded VAX running ULTRIX and Lucid Common Lisp, the generation of a new state from an existing one for a system with about 20 elementary processes took about 30-60 seconds cpu in a timesharing mode.

The proposed approach does not try to imitate a human designer, so the system's reasoning process cannot be "debugged" by comparing it to a human expert. Evaluation, in that sense, can only be carried out by examining the end product of the system and by comparing it to what would be proposed by a human, using an appropriately defined experimental plan with a variety of thermal systems. It would also be interesting to allow a human expert to criticize the system's designs, as well as to allow the system to try to improve on those of a human, to study how to quantify the elusive nature of a "good design."

Acknowledgments

The authors gratefully acknowledge the financial support given to them by Digital Equipment Corporation.

References

Barr, A., and Feigenbaum, E. A., 1981, *The Handbook of Artificial Intelligence*, Vol. 1, William Kaufmann, Los Altos, CA.

Fiacco, A. V., and McCormick, G. P., 1968, *Nonlinear Programming: Sequential Unconstrained Minimization Technique*, Wiley, New York

Guthrie, K. M., 1969, "Data and Techniques for Capital Cost Estimating," *Chemical Engineering*, Vol. 76, No. 6, pp. 114-142.

Hart, P. E., Nilsson, N. J., and Raphael, B., 1968, "A Formal Basis for the Heuristic Determination of Minimum Cost Paths," *IEEE Transactions on System Science and Cybernetics*, Vol. SSC-4(2), pp. 100-107.

Nilson, P. E., 1980, *Principles of Artificial Intelligence*, Tioga, Palo Alto, CA.

Pearl, J., 1984, *Heuristics: Intelligence Search Strategies for Computer Problem Solving*, Addison-Wesley, Reading, MA

Tjoe, T. N., and Linnhoff, B., 1966, "Using Pinch Technology for Process Retrofit," *Chemical Engineering*, Vol. 93, No. 8, pp. 47-60.

Response of Large Turbofan and Turbojet Engines to a Short-Duration Overpressure

M. G. Dunn
Physical Sciences Department,
Calspan Advanced Technology Center,
Buffalo, NY 14225

R. M. Adams

V. S. Oxford
Headquarters, Defense Nuclear Agency,
Washington, DC 20305-1000

The influences of thrust setting and overpressure level on engine operating characteristics have been obtained for two different high-thrust engines. The thrust setting was varied from engine-off to take-off rated thrust (TRT) and the overpressure was varied from 6.9 kPa (1.0 psi) to 19.4 kPa (2.8 psi). The specific engines under consideration were the Pratt/Whitney TF33 low bypass ratio turbofan and the Pratt/Whitney J57 turbojet. The experimental results suggest that overpressure has little influence on either the HP compressor speed or the exhaust gas total temperature. However, the magnitude of the overpressure has a large influence on turbine exhaust total pressure and on the inlet casing and the diffuser casing radial displacements. The J57 turbine casing was significantly influenced by the overpressure, whereas the TF33 turbine casing was relatively insensitive. The J57 inlet casing radial displacement was noticeably greater than the corresponding turbofan displacement. Even though the component radial displacements for the TF33 exceeded the steady-state red-line limit by more than 300 percent, the engine did not sustain any permanent damage. The J57 did, however, experience an internal rub at an overpressure of about 14.5 kPa (2.1 psi).

1 Introduction

The response of aircraft gas turbines to short duration sharp leading edge overpressures is an area that has been actively investigated by the Defense Nuclear Agency for the past several years. In an attempt to understand engine response to overpressure pulses better, two engines were investigated by Dunn et al. (1979), Dunn and Rafferty (1982), Padova and Dunn (1983), and Dunn et al. (1986) over the past several years. These engines were of the 600 lb and 3500 lb thrust class. More recently, two different engines of a significantly larger thrust (18,000 lb) class were subjected to overpressure pulses of substantial magnitude. An overall description of the facility and experimental technique was given in Adams and Dunn (1987) and will only briefly be summarized. This paper will deal primarily with the measurement results for both engines and a discussion of the influence of overpressure on the engine characteristics.

The measurements reported by Dunn and Rafferty (1982) were performed using a General Electric J85-5 turbojet engine. The objectives of that work were to develop an experimental technique for controlled laboratory overpressure measurements using an operating engine, and to gain an understanding of the engine response. The goal was to develop a technology that could provide the detailed data necessary to predict the general behavior of airbreathing propulsion systems. The J85 series of engines are of the 3500 lb thrust class and are used in a variety of trainer aircraft in augmented and unaugmented thrust applications. The single spool design uses eight stages of axial flow compression and two stages of turbine. One hundred percent thrust occurs at 17,800 rpm.

On the basis of the initial J85 measurements, it was concluded that: (*a*) successful development and application of the overpressure generating technique had been demonstrated, (*b*) the compressor casing radial displacement was shown to become excessive at the higher overpressures and core speeds, and (*c*) it was found that the overpressure pulse was not amplified in passing through the compressor.

The second series of engine overpressure measurements by Dunn et al. (1986) was conducted using a Williams International F107 turbofan engine. This small (600-lb thrust) engine lent itself to applying the pulses into an extended bellmouth or a S-shaped inlet duct, and at two angles other than head-on: 20 deg of yaw and from the rear (see Padova and Dunn, 1983). The particular engine used for this work was heavily instrumented and allowed much more detailed data collection and analysis of internal compression and expansion waves than was possible with the J85 instrumentation. The F107 engine has a 1:1 bypass ratio two-stage fan, and a mixed axial-centrifugal compressor. The engine has two spools, each driven by a single-stage turbine. One hundred percent thrust occurs at 61,700 rpm of the high-pressure compressor while the low-pressure compressor runs at approximately 36,000 rpm. The F107 engine exhibited no problems at the test conditions and configurations for which it has been operated. The high ro-

Contributed by the International Gas Turbine Institute and presented at the 33rd International Gas Turbine and Aeroengine Congress and Exhibition, Amsterdam, The Netherlands, June 5-9, 1988. Manuscript received by the International Gas Turbine Institute December 1, 1987. Paper No. 88-GT-273.

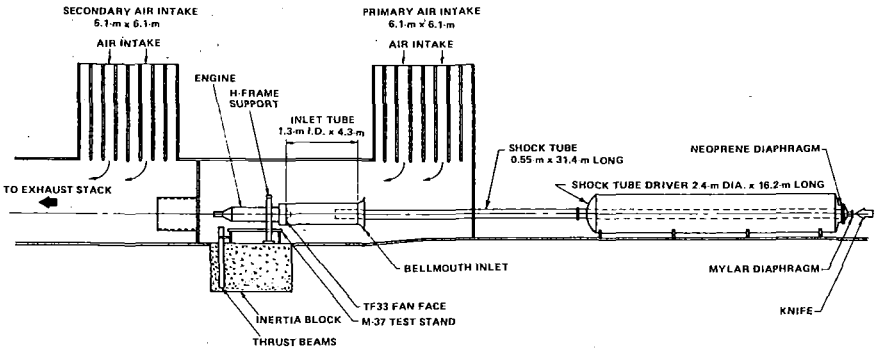

Fig. 1 Sketch of shock tube and test cell configuration

tation speeds and use of a centrifugal compressor provide less dynamic responses than the J85. Casing vibrations and radial displacements were well within manufacturer limits. While significant strides were made in understanding the blast response of engines, the variations in J85 and F107 design configuration showed that further measurements using other engines were desirable. This led to the current series using the TF33 turbofan and the J57 turbojet engines.

2 Description of Experimental Apparatus

To perform the measurements of interest, the engine was necessarily housed in an engine silencer cell to avoid excessive environmental noise pollution difficulties. The overpressure pulse is generated using a modified Ludwieg-type facility, which has been adapted to the engine silencer as shown in Fig. 1. As illustrated in Fig. 1, the engine is drawing its supply air through the open area between the shock tube and the bellmouth. The shock-generating device uses compressed air stored in a driver tube and a neoprene diaphragm initially to separate the driver gas from the shock tube. The pressure to which the driver tube is loaded determines the magnitude of the overpressure pulse. When the neoprene diaphragm is released by rapidly dropping the actuating chamber pressure, the driver-tube air expands into the shock tube, forming a shock wave within a short distance from the diaphragm, which then propagates a pulse to the operating engine. There are no fracturing diaphragm materials in the driver or driven gas supply systems, thus eliminating any foreign particles that could harm the engine. For both the TF33 and the J57 configurations, the tube was designed to deliver the shock wave directly into the inlet tube. The TF33 has a cross section of about one square meter (11 ft^2) which dictated a shock tube of 0.53-m (1.75-ft) diameter and an inlet tube of 1.32-m (4.33-ft) diameter using a ratio of 2.5:1 as verified in earlier measurements of this type by Dunn et al. (1986). For generation of pulses up to 27.6 kPa (4 psi), a driver supply tube 16.2 m (53 ft) long and 2.44 m (8.0 ft) in diameter was selected to achieve adequate volume while also assuring adequate length so that internal wave systems would lag well behind the shock wave. To deliver the upper limit of desired pressure pulses the driver supply tube must be pressurized to about 207 kPa (30 psi).

The modified Ludwieg-tube facility uses an actuating chamber and flexible diaphragm initially to isolate the supply tube from the shock tube for pressurization. Details of this design feature are given by Dunn and Rafferty (1982). This arrangement allows actuating chamber pressurization at a value slightly above (~0.5 psi) that of the supply tube, thus forcing the diaphragm against the shock-tube opening. To generate a shock wave, an air-operated cutter knife punctures the mylar diaphragm in the back of the actuating chamber, instantaneously releasing the supply air and generating the required sharp-rise pulse.

A final aspect of the shock-tube design is the interface at the engine inlet. Figure 2 is a sketch of the TF33 configuration illustrating how the shock tube is inserted into the inlet tube where the respective diameters are 0.53 m (1.75 ft) and 1.32 m (4.33 ft). The J57 configuration was similar except that the inlet tube had a smaller diameter near the compressor face. This setup allows the engine to operate at power settings up to full power, take-off rated thrust (TRT), without undue restriction of airflow. Prior to performing the overpressure measurements, the engine is calibrated with and without the shock tube installed. In addition, similar calibrations are performed with and without the 3.66-m-long inlet duct, but with the bellmouth. On the basis of these measurements, it can be shown that neither of the tubes has significant influence on the engine operation.

A calibrated bellmouth is placed at the entrance of the 3.66-m (12 ft)-long inlet duct. The overlap between shock tube exit and inlet duct entrance is critical in controlling the duration of the pulse. When the pulse exits the shock tube, an expansion wave travels back up the inlet duct toward the bellmouth. At the bellmouth, a second wave system occurs, which is then reflected back toward the engine. As this system interacts with the flow exiting the shock tube, it dissipates the sustained overpressure strength of the original shock. The geometry of the present setup provides pulse durations on the order of 20 ms as will be demonstrated.

Data are collected on the supply tube and actuating chamber pressures, pressures in the supply tube, and ambient temperatures and pressures in the test cell intake section. Figure 2 shows detailed locations of pressure measurements within the shock tubes. Data are also collected on engine operating parameters such as core and fan speed, fuel flow, inlet total pressure (P_{T2}), exhaust gas total pressure (P_{T7}), exhaust gas

Nomenclature

MRT = military rated thrust
N_2 = high-pressure compressor speed
NRT = normal rated thrust
P/P = part power
P_{S2} = static pressure at fan face (turbofan) or static pressure at low-pressure compressor (turbojet) inlet
ΔP_{S2} = change in static pressure
P_{T7} = exhaust gas total pressure
ΔP_{T7} = change in exhaust gas total pressure as a result of overpressure wave
ΔP_1 = change in stock tube sidewall static pressure at station No. 1
T_{T7} = exhaust gas total temperature

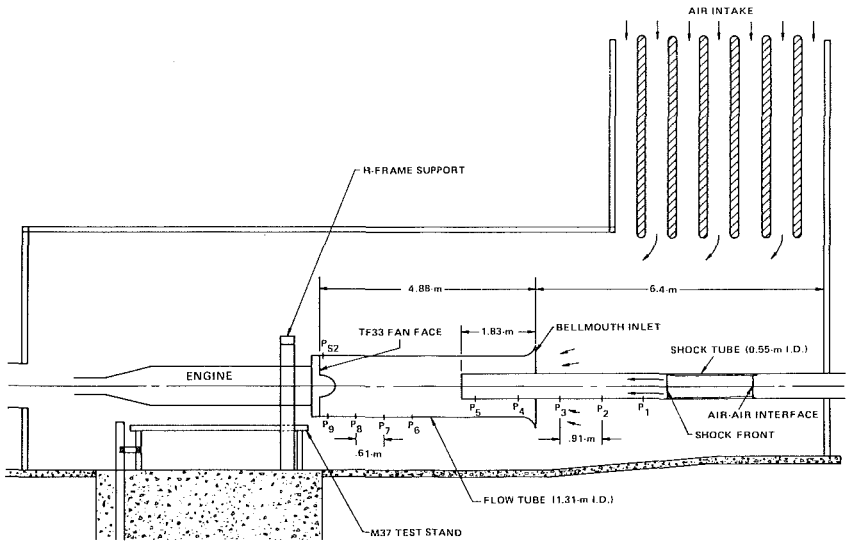

Fig. 2 Sketch of test cell configuration

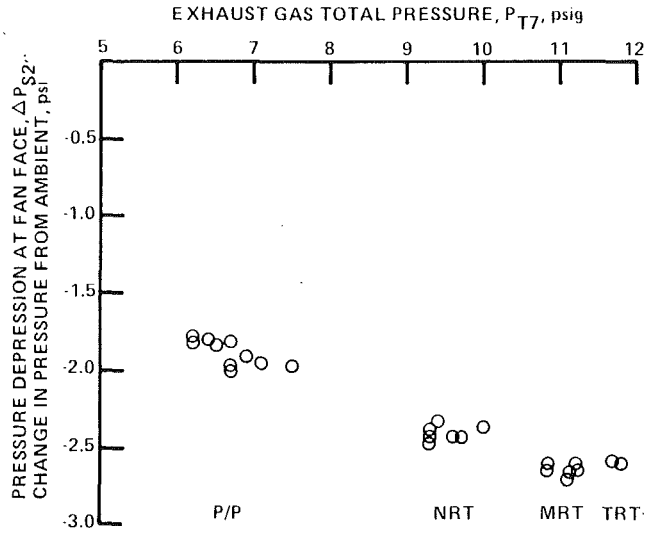

Fig. 3 Influence of thrust setting on preshock static pressure just ahead of TF33 fan face

total temperature (T_{T7}), interstage and compressor discharge pressures, and interstage bleed-door position. Accelerometers are mounted on the fan inlet casing, the diffuser casing, and the turbine casing. Data from these accelerometers are double-integrated to obtain radial displacement history during and after passage of the overpressure system through the engine.

3 Discussion of TF33 Results

With the engine and shock tube in place, the performance of the shock-tube system was validated by a series of runs including cases for which the engine was not operating and cases for which it was operating at selected thrust levels. With the engine operating, the pressure level in the shock tube prior to breaking the mylar diaphragm is reduced. Figure 3 illustrates the pressure depression measured at the fan face (ΔP_{S2}) as a function of thrust setting for part power (*P/P*), normal rated thrust (NRT), military rated thrust (MRT), and take-off rated thrust (TRT). Similar measurements were performed for all of the pressure transducers used in the system.

3.1 Influence of Engine Thrust on Static Pressure. Figures 4(*a*) and 4(*b*) present typical histories of static pressure at the sidewall of the shock tube and the static pressure at the fan face for the TF33 engine operating at MRT setting. The shock-tube pressure shown in Fig. 4(*a*) was taken from transducer P_1 in the shock tube (see Fig. 2). The shock front is shown to be quite sharp and the pulse is flat-topped for a duration on the order of 25 ms. The baseline of the shock-tube transducer is very quiet and relatively free of acoustic noise. At the end of the test time, the pressure falls rapidly to a relatively constant value that is somewhat greater than the initial pressure. The static pressure at the fan face shown in Fig. 4(*b*) also increases rapidly with the arrival of the shock wave. Shortly after arrival of the shock wave (~2.5 ms) the overpressure level is increased by reflection of the pressure pulse from one of the internal components. This reflection is felt to have come from the first or second-stage fan. About 5 ms are required for the engine to accommodate to the overpressure pulse. The duration of the test time illustrates a series of expansion and compression waves traveling into and out of the engine. Note that the time between pressure peaks during the test time is on the order of 2.7 ms corresponding to a frequency about 370 Hz. The time required for the LP compressor to make one revolution at the thrust setting consistent with the results of Fig. 4(*b*) was about 9 ms and the time for the HP compressor was about 6 ms. If these pressure fluctuations are related to rotating stall, they would be indicative of multicell stall. However, if multicell stall were present, it did not manifest itself in a destructive manner. Neither the preshock nor the postshock pressure record shown on Fig. 4(*b*) illustrate the 370 Hz pressure fluctuation that was observed during the test time. However, the character of this fan face pressure record is dependent upon the magnitude of the overpressure pulse as illustrated by comparison of Fig. 4(*b*) and Fig. 6(*d*), which were obtained for overpressures of 1.54 psi and 2.31 psi, respectively. The pressure history shown in Fig. 6(*d*) does not contain orderly pressure fluctuations in the preshock region or in the test time region, but the periodic pressure fluctuations do appear during the expansion portion of the pressure pulse. The period of the pressure fluctuation is consistent with that observed for Fig. 4(*b*). The character of this pressure record is similar to those obtained by Dunn et al. (1986) using the 40-probe distortion rake at the fan face of the F107 engine under similar experimental conditions. The pulse decays at the end of the test time and behaves similar to the shock-tube pressure record. The preshock fan face pressure record shows evidence of more acoustic noise input than was observed at the shock-tube location, but this input does not degrade the overall signal.

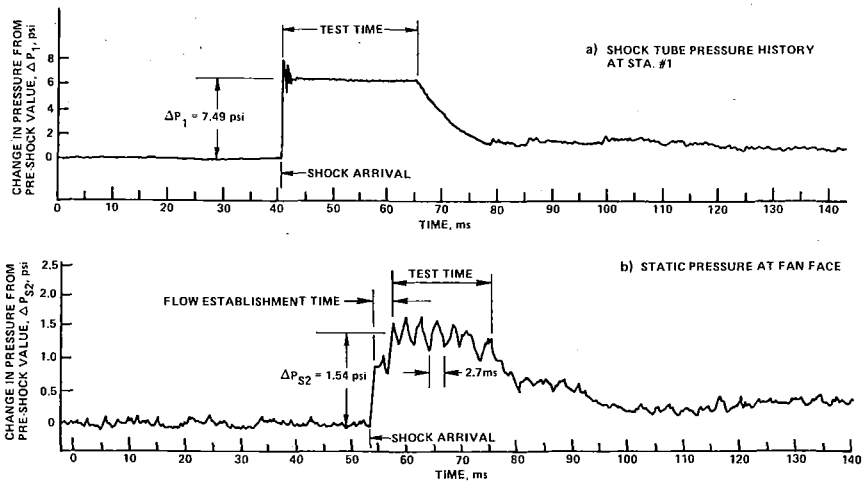

Fig. 4 Typical shock tube and fan face static pressure records for TF33 at MRT setting

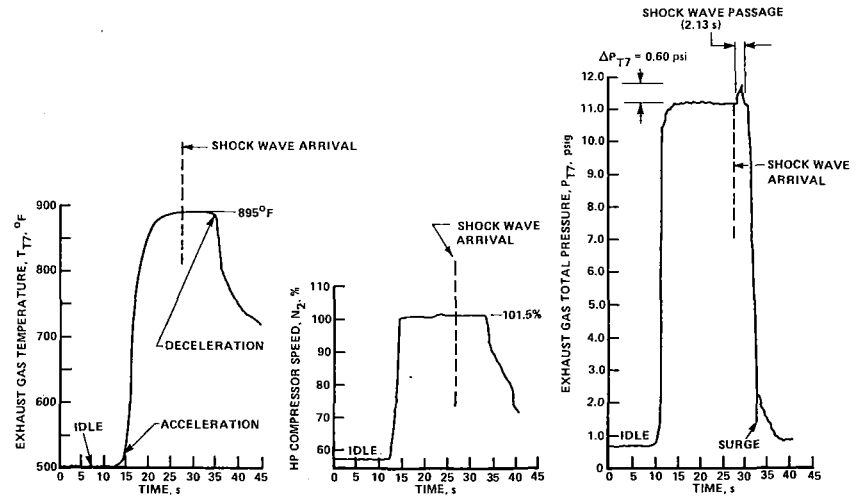

Fig. 5 History of typical engine (TF33) parameters during a 1.54 psi overpressure exposure

3.2 Influence of Overpressure on Engine Speed and Exhaust Gas Conditions. Figure 5 presents TF33 time histories of exhaust gas temperature (EGT), high-pressure compressor speed, and exhaust gas total pressure for an overpressure exposure of 1.54 psi with the engine operating at 101.5 percent of rated speed (MRT). These data were obtained using pen chart recorders and are thus recorded at a much compressed time scale compared to the linear displacement data to be shown later, but they are useful for illustrating transient conditions. For example, the exhaust gas total pressure rake does record the overpressure attributable to the shock-wave passage. The EGT, the HP compressor speed, and the bleed valve position (not shown but it was in the closed position), all held steady during shock-wave passage. At the higher thrust settings, the compressor is not choked but the turbine first-stage nozzle is very nearly choked. It would be difficult for a pressure system of the type described here to influence the EGT significantly. The rotating components of this engine have a significant inertia, making it difficult for noticeable speed changes to occur on the time scale of the pressure pulse. When the much smaller F107 engine was tested under similar overpressure conditions, the engine speed was influenced by the pressure pulse. The bleed valve was fully closed for the operating condition shown in Fig. 5 and there was no indication of an attempt to change this position during passage of the shock-wave system. At lower thrust settings, the bleed valve would be partially or fully open and could relieve the overpressure pulse as it did in the previously mentioned J85 measurements. With the engine in the "off" position, the pressure pulse caused some casing deflection (as will be described later) and also caused the compressor shafts to rotate, but otherwise passed through the engine unnoticed. In the "off" position, the bleed valve is open and tended to relieve the internal pressure.

The total pressure rake located in the TF33 exhaust gas flow did indicate an increase in pressure associated with passage of the overpressure system. The results shown in Fig. 5 for an overpressure of 1.54 psi at the fan face indicate that P_{T7} increased by at least 0.6 psi for a period of about two seconds. However, it is possible that the P_{T7} increase was greater than 0.6 psi, but because of the configuration of the exhaust gas pressure instrumentation the system was unable to respond with sufficient frequency to record the peak pressure. There are six pressure probes arranged in a ring in the exhaust passage and then manifolded together. The design of this arrangement is intended to average the circumferential pressure and thus has the effect of significantly reducing the frequency response of the measurement. If one were interested in dynamic response, this system would not be used. It should be recalled

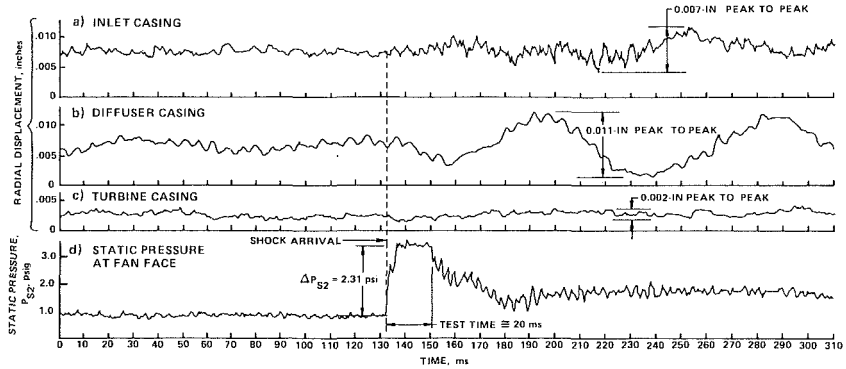

Fig. 6 Typical component radial displacement histories for TF33 at MRT setting

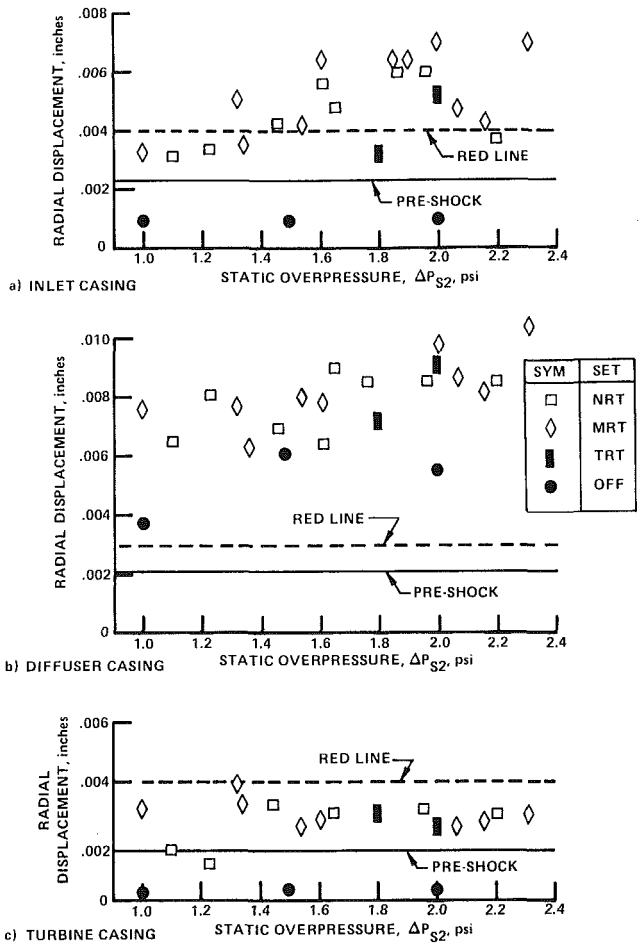

Fig. 7 Influence of overpressure on TF33 inlet, diffuser, and turbine casing displacement

that changing the instrumentation for this program was not an option because one of the objectives was to determine which of the on-board instruments would be helpful to the crew in dealing with the situation. As noted earlier, this particular run was the one for which a surge was encountered at the conclusion of a rapid deceleration. The engine was subsequently accelerated rapidly, allowed to dwell for three seconds, and then rapidly decelerated, but the surge could not be repeated.

3.3 Influence of Overpressure on Radial Displacements. Previous experience by Dunn and Rafferty (1982) with the J85 turbojet indicated that engine vibrations could be a potential difficulty. For both the TF33 and the J57, accelerometers were located on the inlet casing, the diffuser casing, and the turbine casing, and the output of these devices was doubly integrated to give an indication of radial displacement of the respective casing.

Figure 6 is typical of the measured displacement histories for the TF33 turbofan. This particular record is for a fan face overpressure of 2.31 psi for a time period of approximately 20 ms. After decay of the flat-topped portion of the pressure history, the overpressure level remains at about 1 psi above the preshock level for the duration of the record. The casings begin to respond upon arrival of the shock wave, but continue to flex for some time after the peak pressure has subsided. The turbine casing displacement is small, not being much in excess of the preshock value. The calibration procedure used here to calibrate all of the accelerometers will be described in the next paragraph. The diffuser casing displacement is much larger and the maximum peak-to-peak displacement occurs about 100 ms after shock-wave arrival. The inlet casing displacement is less than the diffuser displacement and requires more time to develop. The inlet casing displacement reaches a maximum value at about 120 ms after shock-wave arrival. These histories are all interesting but the important consideration becomes how the displacement magnitudes compare with red-line values.

It was noted above that the output signal from the engine accelerometers was doubly integrated to obtain the displacement values shown herein. The electrical cables were tightly secured to prevent erroneous signals resulting from cable vibration or "whip." The accelerometer system was designed by the engine manufacturer to have a frequency response in the range of 50 to 4000 Hz. The displacements shown on Fig. 6 have a frequency of 10 Hz (or a period of 100 ms), which is below the design frequency range of the unit. None of the vibrations experienced here were in excess of 200 Hz. A shaker unit was used to calibrate each of the accelerometers over the range of 15 to 200 Hz. It was not possible to calibrate down to the 10 Hz level but 15 Hz was felt to be sufficiently close. Over the range calibrated, the response of the inlet casing and the diffuser casing accelerometers was flat and the measured displacements are felt to be correct to within a few percent. The response of the turbine accelerometer at 15 Hz was not as good as the inlet and diffuser casing accelerometers, but it was felt to produce results correct to within 10 percent.

Figure 7 is a summary of the influence of overpressure and engine thrust on the induced casing displacements compared to the preshock and respective red-line limits for the TF33 turbofan engine. In all cases,the displacements given are peak-to-peak radial values. This particular engine was in good physical condition and all of the preshock displacement values were well below the limits. For the engine-off condition, the inlet and turbine displacements were well below the NRT, MRT,

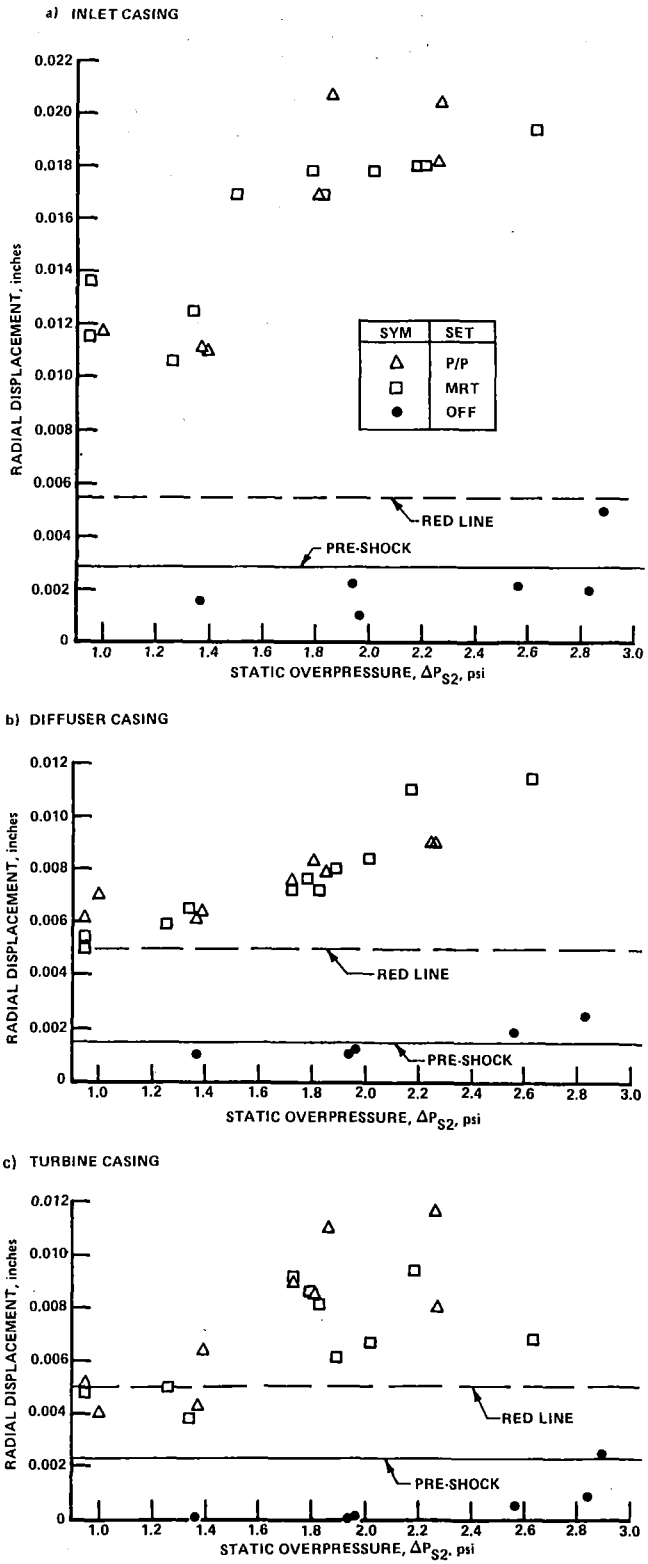

Fig. 8 Influence of overpressure on J57 inlet, diffuser, and turbine casing displacement

and TRT preshock values. However, even for the engine-off case, the diffuser casing displacement exceeded the limit. Figure 7(*a*) illustrates that below 10.4 kPa (1.5 psi) the inlet casing displacement remained at or slightly below the red-line value. For overpressures above 10.4 kPa, the red-line limit was exceeded by about 50 percent for both NRT and MRT settings. Figure 7(*b*) presents a similar comparison for the diffuser casing and shows that the limit displacement was exceeded by about 200 percent at 6.9 kPa (1.0 psi) and by more than 300 percent at 16.0 kPa (2.3 psi). This figure also illustrates that the higher thrust setting results in increased displacement for overpressures above 13.8 kPa (2.0 psi). The trend of the MRT and TRT results is to increase rapidly with increasing overpressure. It is not unreasonable to expect the diffuser casing displacement to increase with increased thrust setting. The compressor discharge pressure level also increases with thrust increase and if the overpressure is amplified in proportion to the overall compression ratio, then the discharge pressure is going to be increased accordingly. The turbine casing displacement shown in Fig. 7(*c*) does not exceed the red line regardless of the thrust setting. The pressure in the turbine section did increase as indicated by the exhaust gas total pressure increase to be described later and some influence of this increase can be seen in the results.

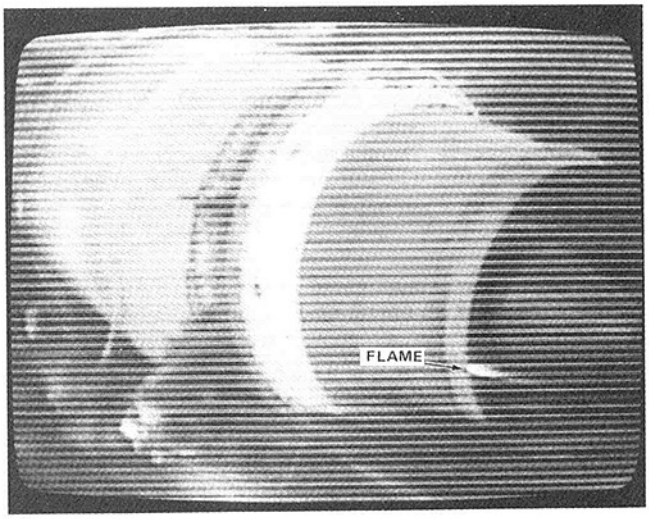

Fig. 9 Photograph of initial tailpipe flame for 2.1 psi overpressure

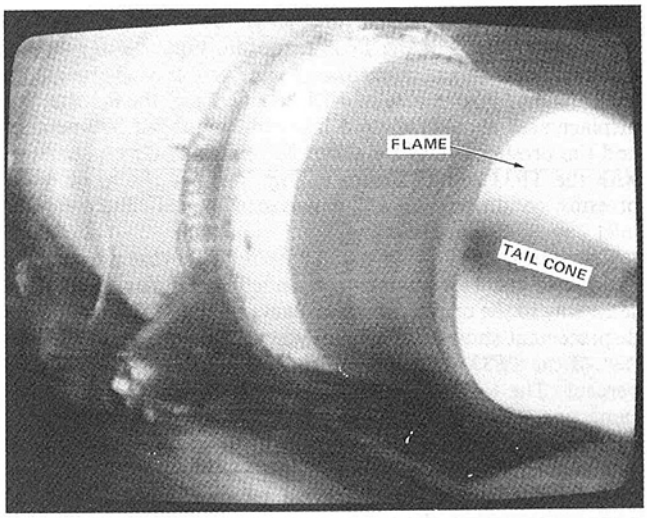

Fig. 10 Photograph of tailpipe surge during acceleration

4 Discussion of J57 Results

A video camera was used to monitor the engine exterior and the tail pipe during all of the overpressure testing. With the engine operating, the J57 had been subjected to overpressure values as high as 18.1 kPa (2.7 psi) at MRT without adverse effect, as shown on Fig. 8. Also indicated on this figure are data from engine-off measurements successfully performed at

overpressures in excess of 18.7 kPa (2.8 psi). These high-overpressure runs with the engine off were performed at the very end of the test series. On one of the repeat runs with the engine operational (prior to the engine-off runs described above) at an overpressure level of 14.1 kPa (2.1 psi) a small flame streak (see Fig. 9) and a surge (see Fig. 10) were observed to exit the tail pipe. The overpressure was then increased to about 18.1 kPa (2.7 psi) and a shower of sparks was observed to exit the tail pipe. These sparks were probably the result of an internal rub.

The engine surge experienced in the J57 overpressure experiments was not an operation-limiting event. Only a single surge would occur during each acceleration and it was possible to drive through the event and obtain satisfactory engine operation. The engine was turned off and allowed to remain inactive for a 24-hour period. When it was again started and allowed to warm up, a series of rapid accelerations produced only a single surge, suggesting that the surging problem had cleared itself.

4.1 Casing Displacement Result – TF33 versus J57. Figures 8(*b*) and 8(*c*) present the J57 diffuser casing displacement and the turbine casing displacement, respectively. The general response of the J57 turbojet to the overpressure pulse was similar to that of the TF33 turbofan. Figure 8(*a*) presents the J57 inlet casing displacement as a function of overpressure level. At an overpressure of 16.1 kPa (2.4 psi) the inlet casing displacement exceeds the red line limit by about 300 percent and the preshock level by about 600 percent. By comparison with the TF33 results shown in Fig. 7(*a*) for the same overpressure condition, the J57 experienced significantly greater inlet casing displacement.

Comparison of Figs. 7(*b*) and 8(*b*) indicates that the diffuser casings of the two engines responded in approximately the same way to the overpressure. However, the J57 turbine casing displacement shown in Fig. 8(*c*) was significantly greater than that of the TF33 and exceeded the red line limit by about 200 percent. The turbine casing accelerometer used here was the same one used for the TF33 measurements. An earlier discussion noted that the low-frequency response of this particular accelerometer was not as good as that of the inlet casing and diffuser casing accelerometers but the results are felt to be accurate to within about 10 percent. Also included on Figs. 8(*a*), 8(*b*), and 8(*c*) are the preshock displacement values, which represent measurements obtained just before shock-wave arrival with the engine operating at the desired thrust setting. The preshock displacement values were essentially independent of thrust and were all significantly below the red line limit.

As noted above, the filled circles (•) on Figs. 7 and 8 represent the casing response to the overpressure pulse with the engine off for the TF33 and the J57, respectively. The engine-off displacement measurements are all consistently below the preshock displacements with the exception of the TF33 diffuser casing result shown in Fig. 7(*b*). Also note on Fig. 7(*b*) that the preshock diffuser casing displacement is much closer to the red line limit than for the corresponding J57 component or any other component on either engine. The reason for the relatively large TF33 engine-off diffuser casing displacement is unknown at this time. The J57 engine-off displacement values were all below the preshock values, which were well below the red line limit.

4.2 Comparison of TF33 and J57 Exhaust Gas Total Pressure Results. The exhaust gas total pressure P_{T7} was monitored throughout these experiments and was found to be sensitive to the overpressure associated with the shock wave imposed on the engine face. The exhaust gas total pressure is divided by the measured inlet total pressure P_{T2} to give the engine pressure ratio (EPR), which is then displayed for the aircrew. The crew uses the EPR value to set the desired thrust condition. While the transient response of this EPR gage is

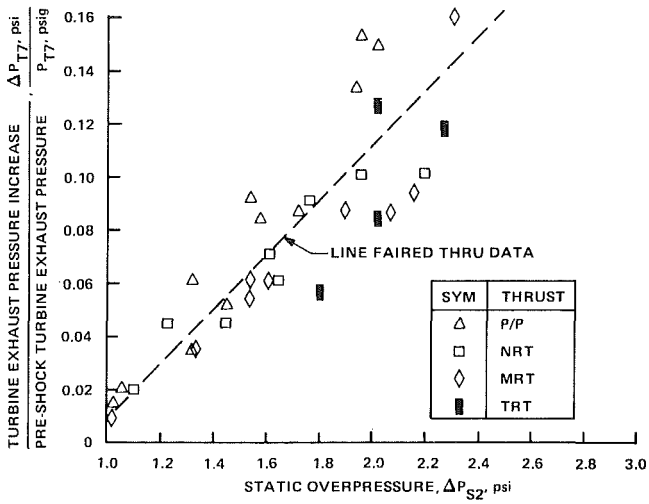

Fig. 11 Influence of fan face overpressure on tailpipe total pressure for TF33 turbofan engine

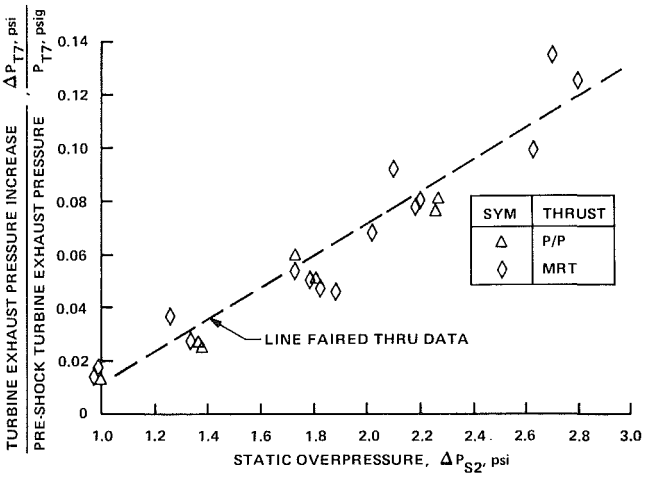

Fig. 12 Influence of compressor face overpressure on tailpipe total pressure for J57 turbojet engine

not sufficient to monitor the passage of the overpressure system, the response of the P_{T7} system is sufficient. Figure 11 illustrates the influence of overpressure imposed at the engine inlet, ΔP_{S2}, on the value of ΔP_{T7} divided by P_{T7} for the TF33 engine at four different thrust settings. The magnitude of the overpressure was in the range of 6.9 kPa (1.0 psi) to 15.9 kPa (2.3 psi). The P_{T7} history was recorded at a slow sampling frequency as illustrated on Fig. 5 and at a much higher sampling frequency using one of the channels of the recorder used to obtain the data given on Fig. 6. The magnitude of the P_{T7} increase was found to be independent of sampling frequency. Figure 11 illustrates that for the same overpressure, a higher thrust setting does not necessarily result in a larger value of $\Delta P_{T7}/P_{T7}$. As previously noted, the first-stage turbine nozzle is nearly choked at higher thrust settings but not at part power or normal rated thrust. It is not surprising that the maximum influence of overpressure on exhaust gas total pressure may not be felt at the highest thrust setting. However, the incremental change in P_{T7} does increase rapidly with increasing overpressure.

Figure 12 presents a plot corresponding to Fig. 11 for the J57 turbojet engine at two thrust settings but for a larger range of overpressure. Note that the maximum overpressure to which the J57 was subjected was 19.3 kPa (2.8 psi) as compared to 15.9 kPa (2.3 psi) for the TF33. Lines have been faired through

the data presented in Figs. 11 and 12 to illustrate the value of $\Delta P_{T7}/P_{T7}$ for the TF33 engine increases more rapidly for a given overpressure than it does for the J57. This is felt to be due to the internal geometry and operating characteristics of the respective engines. It was not possible with the particular engines used for these experiments to obtain transient pressure measurements at the low-pressure compressor exit and at the high-pressure compressor exit. These values would have been very helpful in determination of the engine response.

5 Conclusions

The response of both a TF33 turbofan engine and a J57 turbojet engine to overpressure pulses has been evaluated for overpressures from 6.9 kPa (1.0 psi) to 19.4 kPa (2.8 psi) at thrust settings from engine-off to TRT. No engine failures were encountered with either engine. The key indicators monitored for incipient engine damage were the exhaust gas total pressure, the exhaust gas total temperature, the HP compressor speed, the bleed valve position, the inlet casing radial displacement, the diffuser casing radial displacement, and the turbine casing radial displacement. For both engines, the exhaust gas total pressure probe indicated passage of the overpressure pulse even though the frequency response of the manifold system was relatively low. However, the HP compressor speed, the bleed valve position, and the EGT were all insensitive to the pressure pulse. While the transient diffuser casing radial displacement exceeded the manufacturer's steady-state maximum value by more than 300 percent, the deflection was damped before permanent engine damage could result. It is difficult to speculate how far one could push the overpressure level before permanent engine damage might occur.

Acknowledgments

The work described here was supported by the Defense Nuclear Agency under contract No. DNA 001-83-C-0182.

References

Adams, R. M., and Dunn, M. G., 1987, "Response of a Turbofan Engine to a Simulated Nuclear Blast," 10th International Symposium on Military Application of Blast Simulation, Bad Reichenhall, Federal Republic of Germany.

Dunn, M. G., Davis, A. O., and Rafferty, J. M., 1979, "Nuclear Blast Vulnerability of Airbreathing Propulsion Sytems: Laboratory Measurements and Predictive Modeling," 6th International Symposium on Military Applications of Blast Simulation, Cahors, France.

Dunn, M. G., and Rafferty, J. M., 1982, "Nuclear Blast Response of Airbreathing Propulsion Systems: Laboratory Measurements With an Operational J-85-5 Turbojet Engine," ASME JOURNAL OF ENGINEERING FOR POWER, Vol. 104, pp. 624–632.

Dunn, M. G., Padova, C., and Adams, R. M., 1986, "Response of an Operational Turbofan Engine to a Simulated Nuclear Blast," International Symposium on Turbomachinery Performance Deterioration, Atlanta, GA; also ASME *Journal of Fluids Engineering*, Vol. 109, 1987, pp. 121–129.

Padova, C., and Dunn, M. G., 1983, "Weak Shock Propagation Into a Cross-Junction Against a Jet," 14th International Symposium on Shock Tubes and Waves, Sydney, Australia.

A New Method of Modeling Underexpanded Exhaust Plumes for Wind Tunnel Aerodynamic Testing

V. Salemann

J. M. Williams

The Boeing Advanced Systems Company, Seattle, WA 98124

A new method for modeling hot underexpanded exhaust plumes with cold model scale plumes in aerodynamic wind tunnel testing has been developed. The method is applicable to aeropropulsion testing where significant interaction between the exhaust and the free stream and aftbody may be present. The technique scales the model and nozzle external geometry, including the nozzle exit area, matches the model jet to free-stream dynamic pressure ratio to full-scale jet to free-stream dynamic pressure ratio, and matches the model thrust coefficient to full-scale thrust coefficient. The technique does not require scaling of the internal nozzle geometry. A generalized method of characteristic computer code was used to predict the plume shapes of a hot (γ = 1.2) half-scale nozzle of area ratio 3.2 and of a cold (γ = 1.4) model scale nozzle of area ratio 1.3, whose pressure ratio and area ratio were selected to satisfy the above criteria and other testing requirements. The plume shapes showed good agreement. Code validity was checked by comparing code results for cold air exhausting into a quiescent atmosphere to pitot surveys and shadowgraphs of model nozzle plumes taken in a static facility.

Introduction

The work described here was performed to support a wind tunnel test of a rocket-powered crew ejection seat.* The objective of the tests was to measure the aerodynamic forces, including plume-induced forces, on a half-scale seat at transonic speeds. Testing was done at the Arnold Engineering Development Center 16 T transonic wind tunnel in Tullahoma, TN. It was to be performed at various Mach numbers, tunnel dynamic pressures, simulated rocket firing modes, and seat attitudes to measure the stability characteristics of the seat. A sketch of the ejection seat is shown in Fig. 1. The two primary rocket nozzles were located in the bottom aft corners of the seat. The rocket exhaust was highly underexpanded and was expected to present a large blockage to the oncoming flow, particularly at high angles of attack. It was felt that the induced aerodynamic effects caused by the interaction of the plume with the tunnel flow would have a significant impact on the measured aerodynamic parameters of the seat. It was decided in this case that the far field interaction of the plume with the free stream had to be modeled, not primarily the initial expansion, as is typical of models of turbojet powered aircraft. To model the far field effects correctly, the trajectory of the jet, its eventual size, and its entrainment characteristics had to be modeled.

Modeling Criteria

In planning the testing, reports from previous tests of ejec-

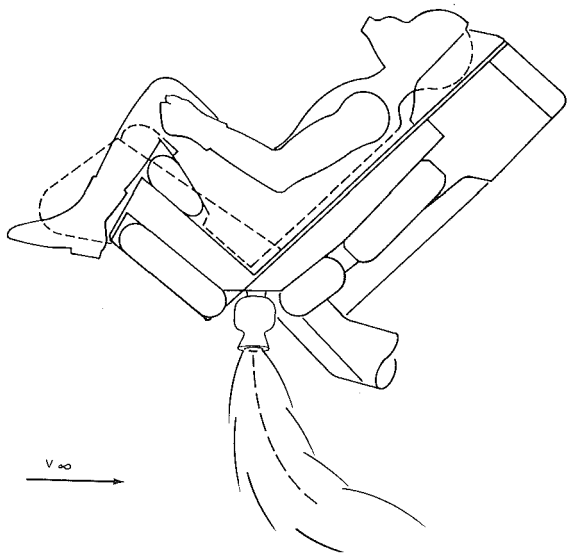

Fig. 1 CREST ejection seat at angle of attack

*Air Force CRew EScape Technologies (CREST) program, contract No. F33615-84-C-0518.

Contributed by the International Gas Turbine Institute and presented at the 33rd International Gas Turbine and Aeroengine Congress and Exhibition, Amsterdam, The Netherlands, June 5–9, 1988. Manuscript received by the International Gas Turbine Institute November 30, 1987. Paper No. 88-GT-288.

tion seats with rocket plume simulations were examined (White, 1974; Reichenau, 1977). In these wind tunnel tests the nozzle throat and exit area were scaled and the nozzle pressure ratio was reproduced. Also, since cold air with a ratio of specific heats of 1.4 was used to simulate a hot rocket exhaust with a ratio of specific heats of 1.2, the nozzle exit angle was adjusted to produce the same initial plume expansion angle with air as was predicted for the hot products of combustion under quiescent atmospheric conditions. Note that no direct consideration was given to jet deflection due to the free stream or matching of maximum plume diameter.

It will be shown that a simple geometric scaling of the nozzle exit and throat and a matching of nozzle pressure ratio in the wind tunnel does not accurately simulate the theoretical fully expanded rocket plume diameter. Consider the following example:

Full-Scale Conditions

Mach number, M	0.6	
Operating altitude	4080 ft.	(1243 m)
Static pressure, P_∞	12.69 psia	(0.8750 bar)
Free-stream dynamic pressure, q_∞	459 psf	(0.2198 bar)
Nozzle chamber total pressure, P_t	2000 psia	(137.9 bar)
Nozzle pressure ratio (NPR), P_t/P_∞	158	
Jet dynamic pressure, q_j	14707 psf	(7.042 bar)
Ratio of dynamic pressures, q_j/q_∞	32	
Fully expanded jet Mach Number, $M_{j,hot}$	3.645	
Jet specific heat ratio, γ_{hot}	1.2	
Nozzle throat area, A^*	1.94 in^2	(12.5 cm^2)
Nozzle exit area, A_{ex}	7.0 in^2	(45.2 cm^2)

The area ratio for complete expansion (A/A^*) for a pressure ratio of 158, with $\gamma = 1.2$, is 17.0 based on one-dimensional isentropic relations (calculations for this and other thermodynamic relationships are found in the appendix). Since the actual nozzle area ratio is 3.6, the jet will continue to expand externally, overshooting the fully expanded diameter and recompressing through oblique and/or normal shocks, repeating this process until shock losses, and mixing with the free stream bring the jet internal pressure to free-stream static pressure. This is illustrated by the shadowgraph picture in Fig. 2.

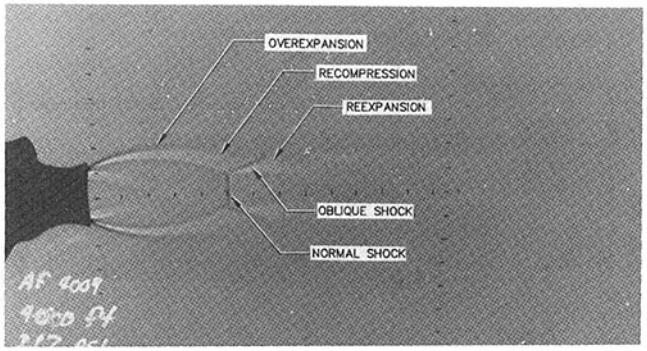

Fig. 2 Shadowgraph picture of exhaust plume

For the wind tunnel simulation of this example, the model jet medium was cold compressed air with a specific heat ratio of 1.4. Due to model and balance strength limitations, the following tunnel test conditions were selected.

Tunnel Conditions

Mach number, M_T	0.6	
Tunnel static pressure, $P_{\infty T}$	588 psf	(0.2815 bar)
Tunnel dynamic pressure, $q_{\infty T}$	150 psf	(0.0718 bar)

The area ratio for complete expansion for the same nozzle pressure ratio of 158 with $\gamma = 1.4$, based on one-dimensional assumptions, in this case is 11.0 (calculations are found in the appendix).

Let us for the moment assume that the fully expanded jet area is representative of the maximum jet diameter in the first expansion cycle. If we compare the two cases, the area ratio for the full expansion with $\gamma = 1.4$ will be 11.0, whereas with $\gamma = 1.2$ it was 17.0. Thus, if the model nozzle throat area is geometrically scaled the cold jet area will be only 65 percent of the hot jet area due to the difference in the values of specific heats. Although the nozzle exit angle can be adjusted so that the initial angle of the expanding jet relative to the jet centerline is matched (see Fig. 3), this methodology still does not match the fully expanded jet diameter, and neglects jet deflection and entrainment effects. While this type of approach may be satisfactory when the jet is aligned with the flight direction and pointed aft, it was felt to be inadequate in our case, where the jet may be pointed normal to or against the direction of flight.

Nomenclature

A_{ex} = nozzle exit area
A_{fe} = fully expanded exhaust area
A^* = nozzle throat area
d_o = nozzle exit diameter
m_{jet} = mass flow of exhaust jet
M = Mach number
M_T = tunnel Mach number
$M_{j,cold}$ = fully expanded cold jet Mach number
$M_{j,hot}$ = fully expanded hot jet Mach number
M_∞ = free-stream Mach number
NPR = nozzle pressure ratio = P_t/P_∞
NPR_{hot} = nozzle pressure of full-scale real, hot exhaust
NPR_{cold} = nozzle pressure of cold model exhaust
P = static pressure
P_∞ = free-stream static pressure
$P_{\infty T}$ = tunnel static pressure
P_t = nozzle total pressure
q = dynamic pressure
q_∞ = free-stream dynamic pressure
q_j = exhaust jet dynamic pressure
$q_{\infty T}$ = tunnel dynamic pressure
S_{ref} = reference area
V_{jet} = velocity of exhaust jet
x = axial distance from nozzle exit center
z = normal distance from nozzle exit center
x/d_o = nondimensional axial distance from nozzle exit center
z/d_o = nondimensional normal distance from nozzle exit center
γ = ratio of specific heats
γ_{hot} = ratio of specific heats of hot exhaust
γ_{cold} = ratio of specific heats of cold exhaust
δ = plume initial expansion angle
Θ_N = nozzle half-angle
ν_1 = Prandtl–Meyer angle at fully expanded jet Mach number
ν_j = Prandtl–Meyer angle at nozzle exit Mach number
ρ = air density

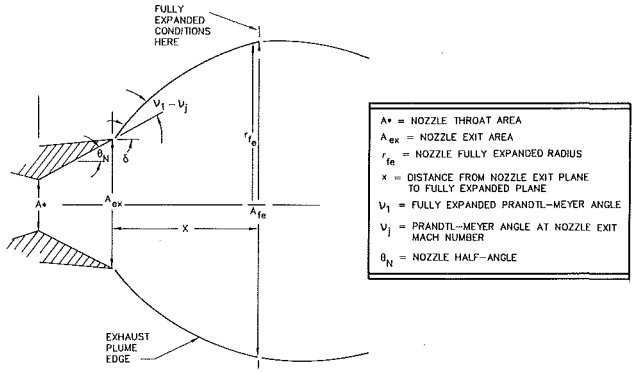

Fig. 3 Nozzle and exhaust plume

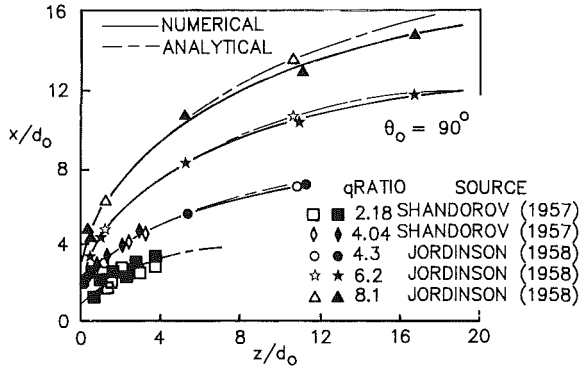

a) Plume Initial Angle 90°to Flow

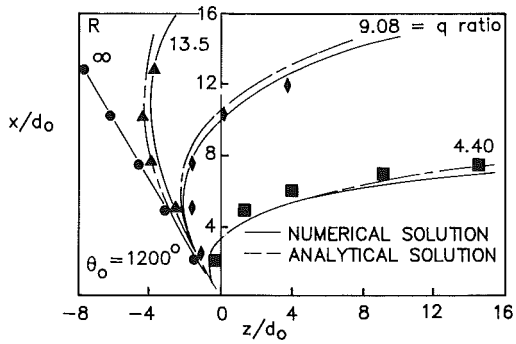

b) Plume Initial Angle 120°to Flow

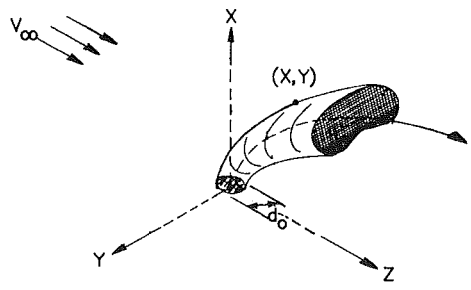

c) Diagram of Plume Bending in Flow

Fig. 4 Effect of ratio of dynamic pressures on plume bending from Braun (1969)

Therefore, new scaling parameters were examined with the goal of finding those that matched not only the initial jet expansion angle, but also the maximum diameter, its distance from the exit, the jet deflection by the free stream, and if possible, the jet entrainment.

Shandorov (1966) and Braun (1969) proposed the ratio of free-stream to jet dynamic pressure as the governing parameter for jet deflection. Amin and Chiarelli (1983) used this relationship in wind tunnel tests to correlate forces and moments and exhaust reingestion characteristics of an aircraft with thrust reversers. The effect of free-stream dynamic pressure on the plume, from Braun, is shown for various dynamic pressure ratios in Fig. 4. If the specific heat ratios of the jet and free stream are the same, matching the nozzle pressure ratio and free-stream Mach number matches the ratio of the dynamic pressures.

However, when the full-scale jet specific heat ratio is significantly different (γ = 1.2) from the model jet specific heat ratio (γ = 1.4), the nozzle pressure ratio should be adjusted such that

$$\frac{q_{j,hot}}{q_{\infty,alt.}} = \frac{q_{j,cold}}{q_{\infty,tunnel}} \tag{1}$$

Since $q = \gamma PM^2/2$, this reduces to

$$\frac{2\gamma_{hot}P_\infty M^2_{j,hot}}{2\gamma_{cold}P_\infty M^2_{\infty,alt.}} = \frac{2\gamma_{cold}P_S M^2_{j,cold}}{2\gamma_{cold}P_S M^2_T} \tag{2}$$

Since $M_T = M_\infty$

$$\left(\frac{M_{j,cold}}{M_{j,hot}}\right)^2 = \left(\frac{\gamma_{hot}}{\gamma_{cold}}\right) \tag{3}$$

Introducing

$$M^2 = \frac{2}{\gamma-1}\left[NPR^{\frac{\gamma-1}{\gamma}} - 1\right] \tag{4}$$

it can be shown that

$$NPR_{cold} = \left[\left(NPR_{hot}^{\left[\frac{\gamma-1}{\gamma}\right]_{hot}} - 1\right)\frac{\left(\frac{2\gamma}{\gamma-1}\right)_{hot}}{\left(\frac{2\gamma}{\gamma-1}\right)_{cold}} + 1\right]^{\left[\frac{\gamma}{\gamma-1}\right]_{cold}} \tag{5}$$

In the case of NPR_{hot} = 158, γ_{hot} = 1.2, γ_{cold} = 1.4, the above relationship gives a nozzle pressure ratio of 65 to be used with compressed air in the tunnel. This is considerably different from the nozzle pressure ratio of 158 for the full-scale, real nozzle with hot products of combustion. (Note that in the special case of $\gamma_{hot} = \gamma_{cold}$, as in the case of modeling propeller and rotor slipstreams and fan jets, matching NPR also matches the dynamic pressure ratio.)

Interactions between slipstreams or jets and aerodynamic surfaces generally correlate with the jet thrust coefficient as described by Pope (1947) and many others since. The thrust coefficient is described as

$$C_T = m_{jet}V_{jet}/S_{ref}\,q_\infty \tag{6}$$

As can be seen from the equation above, mass flow can be traded for velocity in models, i.e., the velocity or jet pressure ratio need not be reproduced in the model, as long as the thrust coefficient is matched by adjustments to either jet massflow or free-stream dynamic pressure. (It is assumed that this relationship will also hold in the case of aerodynamic interactions between rocket plumes and the flow around the seat.)

Using the relationship

$$m_{jet}V_{jet} = \left[(\rho VA)_{jet} \cdot V_{jet}\right]_{fully\ expanded} \tag{7}$$

$$= (\rho V^2 A)_{jet,FE} = 2q_j(A^* \cdot A_{FE}/A^*)_{jet} \tag{8}$$

Therefore

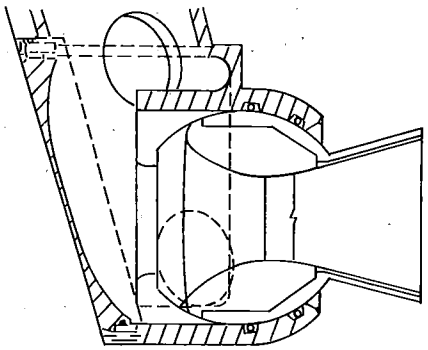

a) Geometrically Scaled Nozzle Geometry

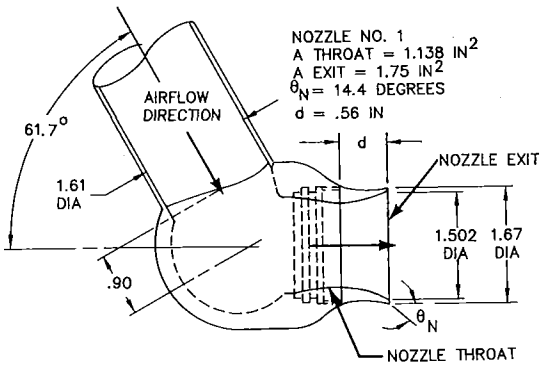

b) Model Nozzle

Fig. 5 Nozzle geometries

$$C_T = 2q_j(A^* \cdot A/A^*)_j/S_{\text{ref}}\, q_\infty \tag{9}$$

Since

$$A/A^* = \frac{1}{M}\left[\left(\frac{2}{\gamma+1}\right)\left(1+\frac{\gamma-1}{2}M^2\right)\right]^{\frac{\gamma+1}{2(\gamma-1)}} \tag{10}$$

and

$$(M_{j,\text{cold}}/M_{j,\text{hot}})^2 = \gamma_{\text{hot}}/\gamma_{\text{cold}} \tag{11}$$

It can be deduced that the ratio of $(A/A^*)_{\text{model}}$ to $(A/A^*)_{\text{F.S.}}$ is a function of the ratio of γ_{model} to $\gamma_{\text{full-scale}}$ only and that to match C_T at a scaled value of S_{ref}, the nozzle throat area A^* cannot be scaled but must be adjusted such that the fully expanded jet area is scaled. Scaling of the fully expanded jet area is satisfied by matching the dynamic pressure ratio and thrust coefficient.

This analysis also shows that geometric scaling of the nozzle throat and exit and matching of the nozzle pressure ratio produces a scaled fully expanded plume only when the specific heat ratios of the full-scale and model scale plume are close.

With the other requirements met, the remaining requirement important to simulating the near-field effect of the plume is the initial jet expansion angle. This expansion angle can be matched by proper selection of the model nozzle exit half-angle. The following equation from Latvala (1961) and Pindzola (1965) was used to set the nozzle half-angle and thus the initial expansion angle of the plume (δ) (see Fig. 3):

$$\delta = \nu_1 - \nu_j + \Theta_N$$

where δ = plume initial expansion angle; ν_1 = fully expanded Prandtl-Meyer angle; ν_j = Prandtl-Meyer angle at nozzle exit Mach number; Θ_N = nozzle half-angle.

The initial plume expansion angle was calculated for the full-scale nozzle using NPR_{hot}, γ = 1.2, and Θ_N = 15 deg.

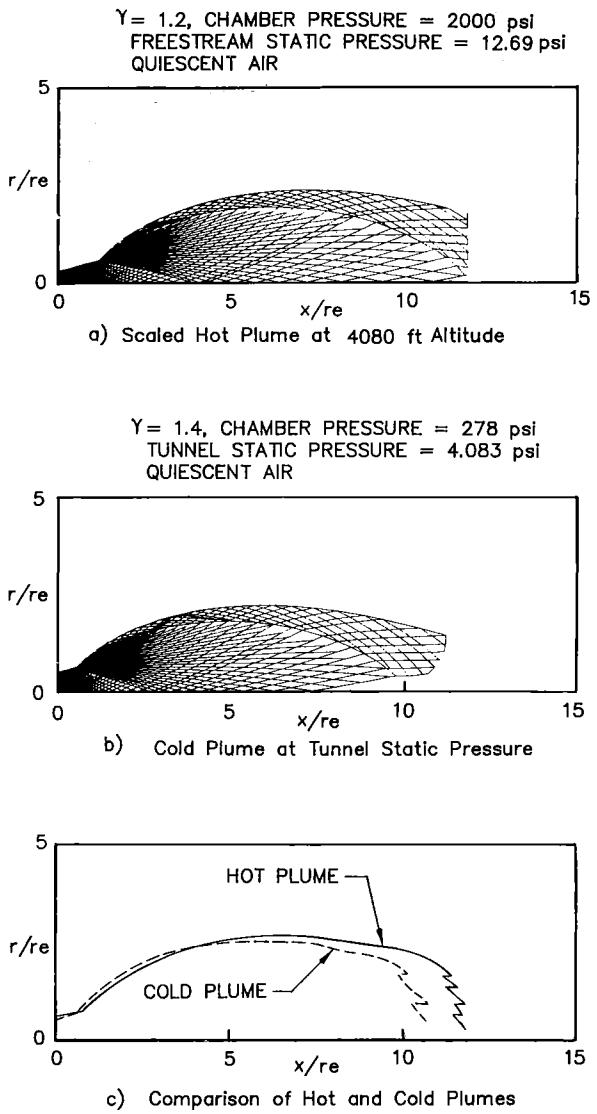

Fig. 6 MOCHA plume simulations

The sidewall angle of the model nozzle was set to give the same expansion angle with γ = 1.4 and NPR_{cold}. Summarizing, the modeling criteria chosen were:

1 Scale exterior contours of the model seat and nozzle exit area according to geometric scale factor
2 Match dynamic pressure ratio (q_j/q_∞)
3 Match thrust coefficient (C_T)
4 Match nozzle initial expansion angle (δ)

Using the above modeling criteria a set of nozzles were designed and constructed to simulate the full scale nozzle at M = 0.6, 4080 ft (1243 m) in the wind tunnel at q = 150 psf (0.0718 bar). The geometrically scaled full-scale and model scale nozzles are shown in Fig. 5.

Experimental Results and Discussion

Theoretical Validation of Selected Modeling Parameters. After the design of the nozzles was completed, a generalized method-of-characteristics computer code (MOCHA) was used to predict the plume shapes of representative hot and cold plumes exhausting into quiescent air and a comparison of plume shapes was made.

The hot plume prediction was done for quiescent conditions with an ambient static pressure corresponding to M = 0.6,

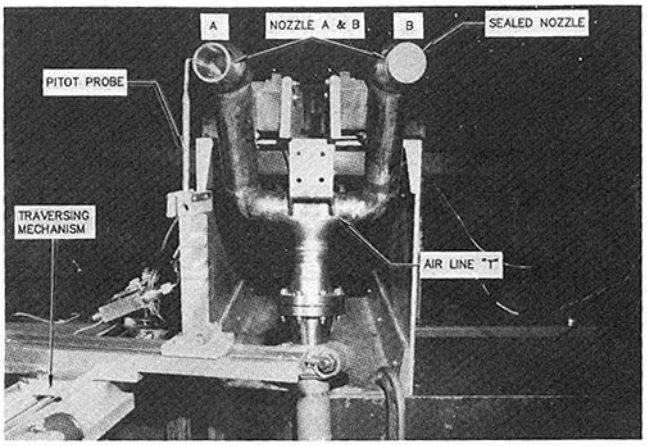

Fig. 7 Nozzles in static test facility

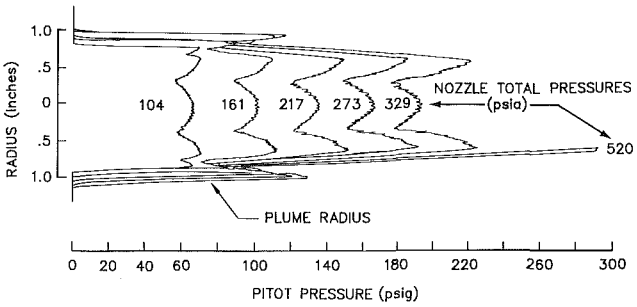

Fig. 8(a) Survey 0.25 in. from exit

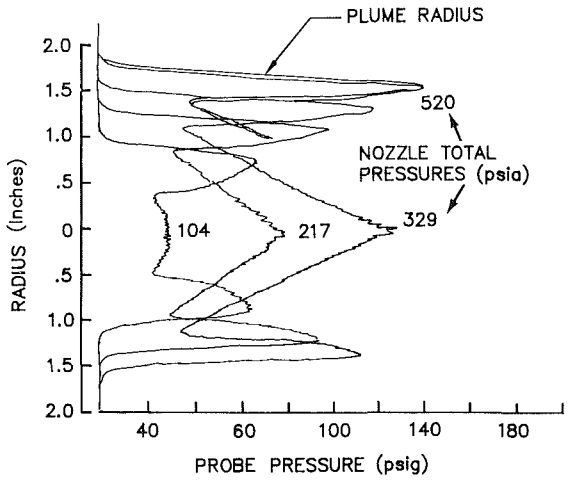

Fig. 8(b) Survey 1.5 in. from exit

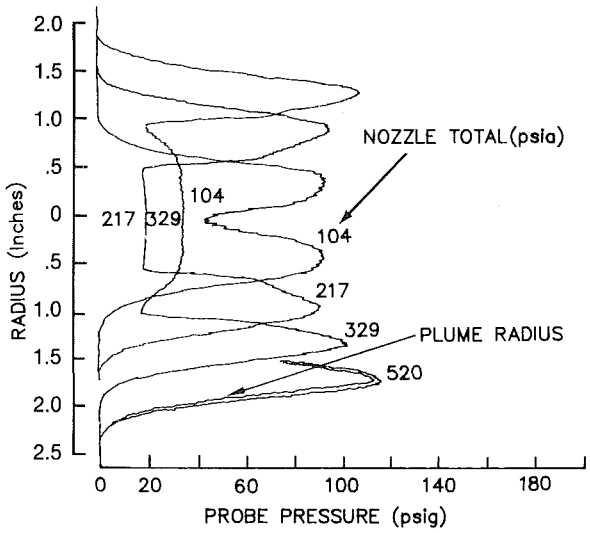

Fig. 8(c) Survey 3 in. from exit

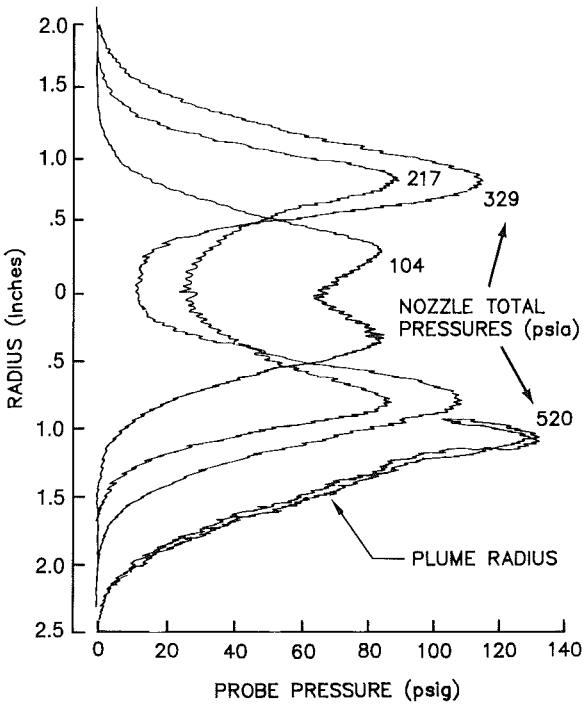

Fig. 8(d) Survey 6 in. from exit

4080 ft (1243 m) altitude and rocket chamber pressure of 2000 psi (137.9 bar). This resulted in a nozzle pressure ratio of 158. A value of 1.2 was used for the ratio of specific heats of the products of combustion. Full-scale nozzle geometry was used, but plots were normalized by the nozzle exit diameter. Results for the simulated hot plume are shown on Fig. 6(*a*).

The cold plume prediction was also done at quiescent conditions (Fig. 6*b*). The ambient static pressure corresponded to that seen in a tunnel operating at M = 0.6 and at a dynamic pressure of 150 psf (0.0718 bar). This is considerably lower than the full-scale dynamic pressure of 459 psf (0.2198 bar), which corresponds to M = 0.6 at 4080 ft (1243 m). The use of cold air with $\gamma = 1.4$ and the abovedescribed modeling criteria resulted in a model nozzle pressure ratio of 65, a much lower area ratio and different exit angle than those of the full-scale nozzle (see Fig. 5).

Figure 6(*c*) shows a comparison of the plume shapes of the two cases described above. The figure demonstrates that the cold and hot plume maximum diameters agree closely, as do the initial expansion angles of the plumes. The location of the strong shock (Mach disk) relative to the nozzle exit cannot be determined from this analysis since the (MOCHA) code cannot calculate through a strong shock.

Experimental Code Validation. Nozzle static tests were performed in an atmospheric test stand (Fig. 7). Pitot pressure surveys with a traversing probe in the nozzle throat and exhaust plume were made at various nozzle total pressures. Plume radius estimates were made from these at the highest nozzle total pressure achievable in the test facility, 520 psi (35.85 bar), which corresponds to a nozzle pressure ratio of 35. While this pressure ratio was well below the desired scaled nozzle pressure

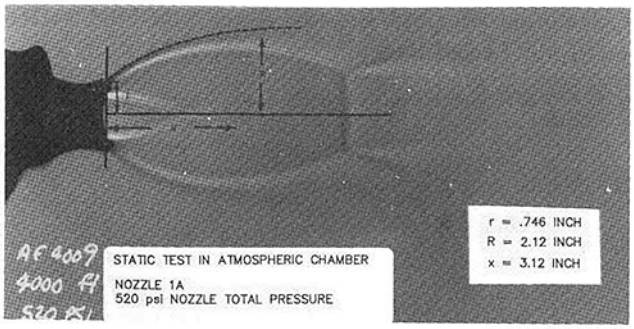

Fig. 9 Shadowgraph photo of plume

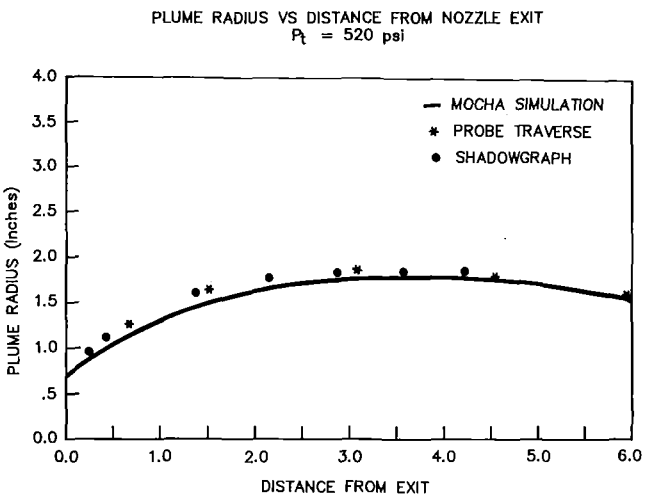

Fig. 10 Comparison of plume radii

ratio, it was high enough to result in considerable external expansion. Shadowgraph pictures of the nozzle flow were also taken. MOCHA predictions were then made at the highest achievable nozzle pressure ratio of 35 to verify that the code predicts plume shapes accurately.

Pitot pressure surveys of the plume for various nozzle total pressures and distances from the nozzle exit are shown in Fig. 8. Figure 8 shows that the plume is symmetric about the center of the nozzle exit. The variation of pitot pressure with radius and distance from the exit in the plume is primarily caused by variations in Mach number with radius and distance, due to external expansion of the plume. High local Mach numbers result in high normal shock losses at the pitot probe and therefore, low pitot readings. Low pitot readings, therefore, do not necessarily imply low total pressure. The plume radius for a nozzle total pressure of 520 psi (35.85 bar) was measured at each survey station in the middle of the viscous transition (Figs. 8*a–d*).

A shadowgraph picture of the plume for a nozzle total pressure of 520 psi (35.85 bar) is shown in Fig. 9. From this picture the shape of the plume was also estimated. The estimated edge of the plume is indicated in the figure as a dashed line.

Predictions of the plume shape at the nozzle total pressure mentioned above were made using MOCHA. A plot of the plume shape from MOCHA predictions, pitot surveys, and shadowgraph data is shown in Fig. 10. It can be seen here that the MOCHA prediction agrees closely with the shadowgraph and pressure survey. This verifies that the MOCHA code is able to predict the shape of an exhaust plume properly in quiescent air and validates MOCHA predictions at higher pressure ratios that could not be duplicated in the static test facility.

Results and Conclusions

A method for modeling hot highly underexpanded exhaust plumes with cold air for aerodynamic testing has been described. The method is (1) scaling external geometry (including only the nozzle exit area), (2) matching dynamic pressure ratio, (3) matching thrust coefficient, and (4) matching plume initial expansion angle.

A computational code was run to compare hot and cold plume shapes resulting from the application of the above modeling laws for nozzles exhausting into still air. The plume shapes agreed well.

Finally, a static test of the model nozzle was run. The experimental results agreed with the predictions, thus validating the computational code. Since the code was validated and the two plumes simulated by the code agreed, it follows that the modeling method is valid for static conditions.

It is recommended that comparisons of predictions to data be made for hot and cold plumes (with specific heat ratios of 1.2 and 1.4, respectively) exhausting at various angles into a moving stream. Hot tests could be accomplished by firing small rockets in propulsion tunnels. Such a test would represent the final validation of the scaling method proposed.

The modeling method described can be applied widely to aerodynamic modeling, particularly in cases where the limitations of the test facility (i.e., tunnel dynamic pressure, facility pressure, mass flow, balance loads) require wind tunnel operation at other than full-scale dynamic pressure ratios. It should not be limited to rockets, but also applied to the modeling of other high-temperature and low-γ jets such as high-temperature turbojets and hypersonic jets.

Acknowledgments

The authors wish to express their gratitude to Dale C. Barr for his work in generating the MOCHA code solutions.

References

Amin, N. F., and Richards, C. J., 1983, "Thrust Reverser Exhaust Plume Reingestion Tests for a STOL Fighter Model," Paper No. AIAA-83-1229.

Braun, G. W., and McAllister, J. D., 1969, "Cross Wind Effects on Trajectory and Cross Sections of Turbulent Jets," NASA SP-218 or NASA N70-11836.

Chiarelli, C., 1983, "Wind Tunnel Evaluation of Tactical Aircraft Stability and Control as Affected by Nozzle Thrust Reverser Parameter Variations," Paper No. AIAA-83-1228.

Latvala, E. K., and Anderson, T. P., 1961, "Studies of the Spreading of Rocket Exhaust Jets at High Altitudes," *Ballistic Missles and Space Technology*, Vol. 11, Pergamon Press, pp. 77–91.

Pindzola, M., 1965, "Boundary Simulation Parameters for Underexpanded Jets in Quiescent Atmosphere," Technical Report AEDC-TR-65-6, Arnold Engineering Developmental Center, Air Force Systems Command, Arnold Air Force Station, TN.

Pope, A., 1947, *Wind Tunnel Testing*, Wiley, New York.

Reichenau, D. E. A., 1977, "Aerodynamic Characteristics of a B-1 Ejection Seat Escape System With Rocket Plume Simulation at Mach Numbers from 0.6 Through 1.5," Technical Report AEDC-TR-77-36, Arnold Engineering Developmental Center, Air Force Systems Command, Arnold Air Force Station, TN.

Shandorov, G. S., 1966, "Calculation of a Jet Axis in a Drifting Flow," NASA TT F-10,638.

White, B. J., 1974, "Aeromechanical Properties of Ejection Seat Escape Systems," Technical Report AFFDL-TR-74-57, Air Force Flight Dynamics Laboratory, Wright-Patterson AFB, OH.

APPENDIX

Calculation of Full-Scale Hot Exhaust Values

Altitude = 4080 ft

$P_\infty = 12.69$ psia, $\gamma = 1.2$

$P_t = 2000$ psia

$P_t/P_\infty = 2000/12.69 = 157.6 =$

$$\left[1+\frac{\gamma-1}{2}\left(M_{j,hot}\right)^2\right]^{\frac{\gamma}{\gamma-1}}$$

$$M_{j,hot}=\left[\left((P_t/P_\infty)^{\frac{\gamma-1}{\gamma}}-1\right)\frac{2}{\gamma-1}\right]^{\frac{1}{2}}$$

$$=\left[\left((157.6)^{\frac{1.2-1}{1.2}}-1\right)\frac{2}{1.2-1}\right]^{\frac{1}{2}}=3.645$$

$$A/A^*=\frac{1}{M}\left[\left(\frac{2}{\gamma+1}\right)\left(1+\frac{\gamma-1}{2}M^2\right)\right]^{\frac{\gamma+1}{2(\gamma-1)}}$$

$$=\frac{1}{3.645}\left[\left(\frac{2}{1.2+1}\right)\left(1+\frac{1.2-1}{2}3.645^2\right)\right]^{5.5}=17.0$$

Calculation of Cold Exhaust Conditions for a Geometrically Scaled Nozzle

$$P_t/P_{\infty_{tun}}=157.6=\left[1+\frac{\gamma-1}{2}\left(M_{j,cold}\right)^2\right]^{\frac{\gamma}{\gamma-1}}\text{with }\gamma=1.4$$

$$M_{j,cold}=\left[\left(157.6\right)^{0.2857}-1\right)\frac{2}{1.4-1}\Bigg]^{\frac{1}{2}}=4.028$$

$$A/A^*=\frac{1}{M}\left[\left(\frac{2}{\gamma+1}\right)\left(1+\frac{\gamma-1}{2}M^2\right)\right]^{\frac{\gamma+1}{2(\gamma-1)}}$$

$$=\frac{1}{4.028}\left[\left(\frac{2}{1.4+1}\right)\left(1+\frac{1.4-1}{2}4.028^2\right)\right]^{3.0}=11.0$$

ERRATA

Errata for "Improvement of Emissions From Diesel Engines" by T. Morimatsu, T. Okazaki, T. Furuya, and H. Furukawa, published in the July 1988 issue of the ASME JOURNAL OF ENGINEERING FOR GAS TURBINES AND POWER, Vol. 110, pp. 343–348:

In Figs. 13 and 14, the ordinate axis is labeled incorrectly. The numbers 0.1, 0.2, 0.3, and 0.4 should be changed to 0.180, 0.359, 0.539, and 0.719, respectively.